

**SYNTHESIS AND CHARACTERIZATION OF COPPER-EXCHANGED  
ZEOLITE CATALYSTS AND KINETIC STUDIES ON NO<sub>x</sub> SELECTIVE  
CATALYTIC REDUCTION WITH AMMONIA**

by

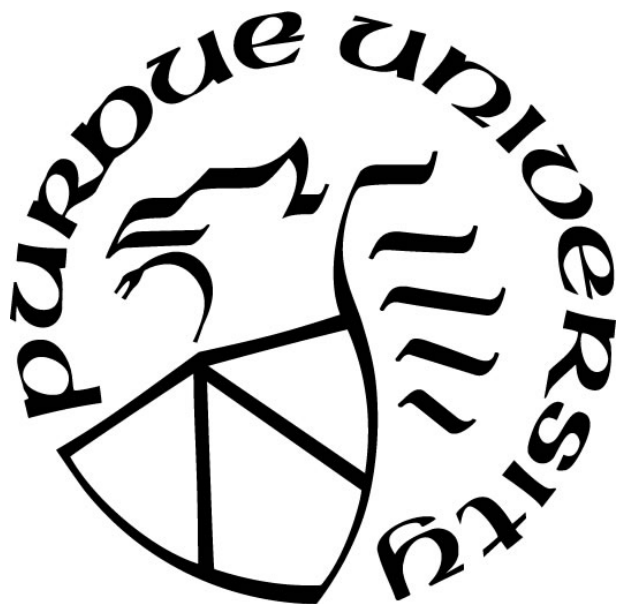
**Arthur Jayang Shih**

**A Dissertation**

*Submitted to the Faculty of Purdue University*

*In Partial Fulfillment of the Requirements for the degree of*

**Doctor of Philosophy**



Davidson School of Chemical Engineering

West Lafayette, Indiana

December 2018

**THE PURDUE UNIVERSITY GRADUATE SCHOOL**  
**STATEMENT OF COMMITTEE APPROVAL**

Dr. Fabio H. Ribeiro, Chair

Davidson School of Chemical Engineering

Dr. Rajamani Gounder

Davidson School of Chemical Engineering

Dr. Jeffrey Greeley

Davidson School of Chemical Engineering

Dr. Aleksey Yezerets

Cummins Incorporated

**Approved by:**

Dr. John Morgan

Head of the Graduate Program

*For my parents who brought me into this utterly bizzare, fuzzy, but fascinating world.*

*This is also for all those who hold a version of me in their entanglements of neurons located within the confines of their nervous system – family, friends, colleagues from Michigan and Purdue, and strangers who I have bumped into from adventures around the universe.*

The image displays a musical score for a Flute and Piano. The score is written in 2/4 time and consists of two systems of music, measures 1 through 8. The Flute part is in the upper staff, and the Piano part is in the lower staff. The key signature has one flat (B-flat). The score includes dynamic markings: *mf* (mezzo-forte) and *p* (piano). The first system (measures 1-4) shows a melodic line in the flute with a series of eighth and quarter notes, and a piano accompaniment of eighth notes. The second system (measures 5-8) continues the melodic line, with a crescendo leading to a final measure marked *rit.* (ritardando). The piano accompaniment in the second system features a more complex rhythmic pattern with some chords.

## ACKNOWLEDGMENTS

What I have personally accomplished, I owe to my teachers, mentors, students, colleagues, friends, and family. Scientists and engineers do not work alone, and although a Ph.D. may seem like an individual endeavor, many have contributed. First and foremost, I thank my family (the ABCD family): my father Albert Jaumin Shih, my mother Alice Huishan Chang, and my siblings Brenda, Christopher, and Deanna. I also thank my granduncle and his family (Yen-Jer (Frank), Jane, and Karen Shih) for their support over the last decade.

Many teachers and have mentors encouraged, molded, and shaped me over the years: my 5<sup>th</sup> grade teacher Mrs. Rock from AB Combs Elementary School in Raleigh, NC, teachers from Pioneer High School in Ann Arbor, MI: Ms. Vincent, Mrs. Washabaugh, Mr. Armstrong, Mrs. Hochrein, Mrs. Dickson, Mr. Snapir, Mr. David Leach, and Mrs. Nancy Waring, professors at the University of Michigan: Thomas Wang, Raul Kopelman, Ralph Yang, H. Scott Fogler, Susan Montgomery, Lola Eniola Adefeso, Nina Lin, Charles Monroe, Suljo Linic, Andrew Tadd, Scott Boerma, and John Pasquale. Technical communication lecturers Dr. Elaine Wisniewski and Dr. Christian Casper for their guidance and instruction on organizing, designing, and presenting technical presentations and reports. Former graduate student instructors and teaching assistants: Professor Elizabeth Stewart (Worcester Polytechnic), Ryan Huang, Professor Mohammad Fallahi-Sichani (U. Michigan). Professors at Purdue University, in particular my advisor Fabio Ribeiro, and others from the Purdue Catalysis Center: W. Nicholas Delgass, Rajamani Gounder, Jeffrey Miller, Jeffrey Greeley, Mahdi Abu-Omar, Christina Li, and Pelin Liao.

Friends and colleagues from many facets of my life have supported me, drove me insane, and kept me sane – simultaneously like Schrödinger’s cat. The Bubblez Gang for their friendship and encouragement during my high school years: Alvin Siu, Han Zhang, Prateek Garg, Stephanie Yan, Ruixin Shi, Ian Paschal, Gaurav Kulkarni. Former UMich classmates who also pursued graduate school, of whom I had the pleasure of interacting with during my time at Purdue: Danielle Mai (UIUC, MIT), Michael Boyd (Stanford), Lawrence Lai (MIT), Carlos Pons Siepermann (MIT), Vincent Tocco (Florida), Lian Zhu (Princeton), Natalie Eyke (MIT), Nicholas Burtch (Georgia Tech). Tej Choksi for his mentorship during the advisor selection process. The SCR Dynasty: Anuj Verma, Shane Bates, Atish Parekh, Jonatan Albarracin-Caballero, Ishant Khurana, Lucia Perez Ramirez, Andres Pena Lozano, Juan González, John Di Iorio, Casey Jones, Trevor Lardinois, and Brandon Bolton. Former and current Ribeiro Group members: James W. Harris, Yanran Cui, Cory Milligan, Han-Ting Tseng, Jeremy Arvay, Richard Caulkins, Garrett Mitchell, Abhijit Talpade, John Degenstein, Viktor Cybulskis, McKay Easton, Zhe Li, Ian Smith, Michael Detwiler, Shankali Pradhan, Harsavardhan Choudhari, Amir Gharachorlou, Dhariya Mehta, Kaiwalya Sabnis, Fred Sollberger, and Vinod Venkatakrishnan. Everyone in the Purdue Catalysis Center, of which there are too many to name. Yury Zvinevich for his knowledge, assistance, and patience on building and fixing scientific equipment. Computational, experimental, and industrial collaborators: Aída Luz Villa Hogun, William F. Schneider, Aleksey Yezerets, Ashok Kumar, Krishna Kamasamudram, Jinyong Luo, Saurabh Joshi, Juan González, Trunjoyojo Anggara, Christopher Paolucci, Hui Li, Sichi Li, and Yujia Wang. Other amazing friends who constantly deal with and partake with my shenanigans: Ayşe



Eren, Ian Smith, Akila Paneer, Jimmy Tang, Helen Sun, Arthur Dysart, Joseph Kubal, and Michael Cordon. The Dungeons & Dragons group: Joseph Kubal, Leo Miroshnik, Ian Smith, Richard Caulkins, Brandon Bukowski, Nathan Davis, Jeremy Arvay, Pushkar Ghanekar, and Jason Wickham. The WERQ group: Laura Wilcox, Juan Carlos Vega Vila, Clarie Nimlos, and Nicole Libretto. Professors from the Purdue Band and Orchestras program for the opportunity to participate and perform music: Ishbah Cox, Matthew Conaway, Jay Gephart, John Williams, and Jonathan Sweet. Members of the Bollywood fusion rock band Tatvam who I had the pleasure to practice and perform with: Ananya Sheth, Prieston Lobo, Anamika Shreevastava, Sai Prashanth, Hridya Nelson, Parul Verma, Spencer T aylor, and Kia Rahmani.

I also want to thank a number of colleagues for opportunities, guidance, and sage wisdom on teaching and education: H. Scott Fogler for the opportunity to maintain his website and develop educational material during my time at Michigan, Philip Wankat and Matthew Ohland for an inspirational course on Engineering Education, Richard Felder and Rebecca Brent for delivering educational workshops at Purdue, Kendall Thomson and Osman Başaran for the opportunity to TA fluid mechanics with them, the 150 students I had the pleasure to TA - many of which I still keep in touch with to this day, and Joanne Lax and Linda Mason for offering and organizing professional development workshops to the university.

There are a number of unsung heros who ensure that business and research progress smoothly and safely. Gabriela Nagy for her efforts in maintaining a safety culture for the school. The ChE Graduate Office, Business Office, and Building Services: Courtney Eddy, Jill Vigar, Lynly Horine, Yvette Rosas, Aimee Mansfield, Janni Mamph, Jeff Valley, Nick Humphrey, Jason Davenport, Catherine (Katie) Field, Bev Johnson, Corwin Green, and the building custodians: Linda Wesley, Jim, Skyler, Virginia, Viktor, Gabby, and Chris.

I also want to to thank my office in FRNY 2123 (40°25'46.0"N, 86°54'51.2"W, 670 ft above sea level), and my laboratory in FRNY 3182 (40°25'47.0"N, 86°54'50.9"W, 700 ft above sea level), and my bedroom (40°27'18.2"N, 86°55'50.1"W, 660 ft above sea level). Since time and space are intertwined, a part of myself with always have a connection with those coordinates due to a degree of entanglement that occurs between particles.

Lastly, I would like to acknowledge financial support provided by the National Science Foundation GOALI program under award number 1258715-CBET, the Department of Energy vehicle technology program under contract number DE-EE0003977, and that provided by Cummins, Inc. I also thank Chuck Peden (PNNL), Feng Gao (PNNL), Janos Szanyi (PNNL), Jean-Sabin McEwen (Washington State University) and their research groups for fruitful technical discussions as part of the collaborative NSF GOALI project.

To reiterate, although a Ph.D. may seem like an individual endeavor, many have contributed; this adventure has been laden with support from teachers, mentors, students, colleagues, friends, and family. This dissertation is a tribute to them, and their desire to change the world for the better.

## TABLE OF CONTENTS

ACKNOWLEDGMENTS .....	4
TABLE OF CONTENTS.....	6
LIST OF TABLES .....	12
LIST OF FIGURES .....	15
ABSTRACT.....	39
1. INTRODUCTION .....	43
1.1 Energy Outlook.....	43
1.2 The Increased Consumption of Fossil Fuels and Subsequent Increase in Pollution.....	44
1.3 Aftertreatment Technologies for Gasoline and Diesel Engines.....	45
1.4 Chemical Environment in the Aftertreatment System.....	48
1.5 The Selective Catalytic Reduction of NO <sub>x</sub> from Diesel Exhaust .....	49
1.6 Parallel and Competing Reactions .....	50
1.7 Catalysts for SCR.....	50
1.8 Chemistry of Zeolites.....	51
1.9 Cu ion-exchange into chabazite zeolite supports.....	53
1.10 Copper Site Location and Speciation in Cu-SSZ-13.....	53
1.11 Standard SCR Kinetics collected over a number of laboratory and commercial catalysts .....	54
2. EXPERIMENTAL.....	56
2.1 Catalyst Synthesis .....	56
2.1.1 Hydrothermal Synthesis of SSZ-13 Si:Al = 4.5 .....	56
2.1.2 Hydrothermal Synthesis of SSZ-13 Si:Al = 15 and 25.....	56
2.1.3 Hydrothermal Synthesis of Si:Al = 100.....	57
2.1.4 Hydrothermal Synthesis of Beta.....	57
2.1.5 Commercial ZSM-5 .....	57
2.1.6 Work-up to H-zeolites .....	57
2.1.7 Copper Ion Exchange .....	57
2.2 Characterization Methods .....	58

2.2.1	XRD.....	58
2.2.2	AAS .....	58
2.2.3	NH <sub>3</sub> -TPD .....	59
2.2.4	Al-NMR.....	60
2.2.5	SEM and EDS.....	60
2.2.6	Ar-micropore .....	61
2.2.7	Co-exchange .....	61
2.2.8	UV-Visible-NIR .....	61
2.2.9	FTIR.....	61
2.2.10	Cu-edge XAS .....	62
2.3	Kinetics Procedures and confirmation of absence of mass/heat transfer effects.....	65
2.3.1	Loading the catalyst bed .....	65
2.3.2	Pre-treatment and stabilization under standard SCR conditions .....	65
2.3.3	Kinetics, turnover frequencies, and reactant orders.....	65
3.	METHODS TO TITRATE, COUNT, AND CLOSE SITE BALANCES ON H-SSZ-13 AND CU-SSZ-13 MATERIALS USING NH <sub>3</sub> AS A TITRANT .....	67
3.1	Abstract.....	67
3.2	Introduction.....	67
3.3	Experimental Methods .....	68
3.4	Results and Discussion .....	69
3.4.1	Site Balance Equations .....	69
3.4.2	Quantitative methods for selectively titrating Brønsted Acid sites in H-ZSM-5 and H-SSZ-13 materials using gas-phase ammonia or liquid-phase ammonium as a probe molecule.....	70
3.4.3	Quantitative methods for selectively titrating Brønsted Acid sites in Cu-SSZ-13 materials using gas-phase ammonia or liquid-phase ammonium as a probe molecule .....	74
3.4.4	Identification of two active Cu sites: ZCuOH and Z <sub>2</sub> Cu .....	75
3.4.4.1	Evidence 1: Quantification of Brønsted acid sites on Cu-SSZ-13 exchanged with Cu <sup>2+</sup> cations .....	75
3.4.4.2	Evidence 2: Quantification of Brønsted acid sites on Cu-SSZ-13 with reduced Cu <sup>1+</sup> cations .....	76

3.4.4.3	Evidence 3: DFT calculations and Monte Carlo Simulations .....	77
3.4.4.4	Evidence 4: Cobalt Exchange.....	77
3.4.4.5	Evidence 5: FTIR spectroscopy.....	78
3.4.5	Behavior of two Cu species under standard SCR.....	79
3.4.6	Method to quantify NH <sub>3</sub> -Cu coordination numbers on NH <sub>3</sub> saturated Cu-SSZ-13 materials.....	80
3.5	Conclusions.....	87
3.6	Acknowledgements.....	87
3.7	Supplementary Information .....	88
4.	DYNAMIC AND REVERSIBLE INTERCONVERSION OF Z <sub>2</sub> Cu AND ZH/ZCuOH SITES IN Cu-SSZ-13.....	91
4.1	Abstract.....	91
4.2	Introduction.....	92
4.3	Experimental Methods.....	92
4.3.1	Cu-SSZ-13 sample preparation and selective NH <sub>3</sub> titration of residual Brønsted Acid sites .....	92
4.3.2	Aqueous Cu(NO <sub>3</sub> ) <sub>2</sub> treatment of a calcined Cu-SSZ-13 material .....	93
4.3.3	H <sub>2</sub> O vapor treatment of a calcined Cu-SSZ-13 material .....	93
4.4	Results and Discussion .....	93
4.5	Conclusions.....	108
4.6	Acknowledgements.....	108
4.7	Supplementary Information .....	108
5.	NATURE OF Cu SPECIES DURING STANDARD SCR.....	110
5.1	Abstract.....	110
5.2	Introduction.....	110
5.2.1	Rationally piecing together the standard SCR mechanism like a mosaic .....	110
5.2.2	Development of the proposed standard SCR mechanism.....	112
5.3	Results and Discussion .....	114
5.3.1	Cu ions in Cu-SSZ-13 under go a reduction-oxidation reaction during NH <sub>3</sub> -SCR. ....	114
5.3.2	NO + NH <sub>3</sub> is necessary to reduce Cu(II) to Cu(I) .....	115
5.3.3	O <sub>2</sub> or NO <sub>2</sub> can oxidize Cu(I) to Cu(II).....	119

5.3.4	The incomplete mosaic .....	122
5.4	Conclusions .....	123
5.5	Supplementary Information .....	123
5.5.1	Transition from $\text{NH}_3$ promotion to $\text{NH}_3$ inhibition with increasing $\text{NH}_3$ concentrations during standard SCR catalysis over Cu-SSZ-13 .....	123
6.	METHOD OF USING NO AS A PROBE MOLEULE TO QUANTIFY FRACTION OF PAIRABLE $\text{Cu(I)(NH}_3)_2$ IN CU-SSZ-13 MATERIALS .....	127
6.1	Abstract .....	127
6.2	Introduction .....	128
6.3	Experimental Methods .....	128
6.3.1	Measuring the fraction of oxidizable $\text{Cu(I)(NH}_3)_2$ using XANES .....	128
6.3.2	Measuring the fraction of oxidizable $\text{Cu(I)(NH}_3)_2$ using NO titration .....	128
6.4	Results and Discussion .....	129
6.4.1	Scheme 1: Titrating $(\text{NH}_3)_2\text{Cu(I)-O}_2\text{-Cu(I)(NH}_3)_2$ species using concurrent flow of NO + $\text{NH}_3$ .....	129
6.4.2	Scheme 2: Titrating $(\text{NH}_3)_2\text{Cu(I)-O}_2\text{-Cu(I)(NH}_3)_2$ species using a flow of NO then a flow of NO + $\text{NH}_3$ .....	131
6.4.3	Parity Plot: Titrating $(\text{NH}_3)_2\text{Cu(I)-O}_2\text{-Cu(I)(NH}_3)_2$ species using a flow of NO then a flow of NO + $\text{NH}_3$ .....	135
6.4.4	Detailed Procedure: Titrating $(\text{NH}_3)_2\text{Cu(I)-O}_2\text{-Cu(I)(NH}_3)_2$ species using a flow of NO then a flow of NO + $\text{NH}_3$ .....	136
6.5	Conclusions .....	137
6.6	Acknowledgements .....	138
6.7	Supplementary Information .....	138
6.7.1	Staility of $(\text{NH}_3)_2\text{Cu(I)-O}_2\text{-Cu(I)(NH}_3)_2$ dimers in the presence of $\text{H}_2\text{O}$ .....	138
6.7.2	Using the NO titration method to test a sample unable to be tested using XAS .....	139
6.7.3	Cu density is not the only descriptor required to explain the fraction of $(\text{NH}_3)_2\text{Cu(I)-O}_2\text{-Cu(I)(NH}_3)_2$ dimer complexes that can be formed from $\text{O}_2$ -titrating $\text{Cu(I)(NH}_3)_2$ .....	142
7.	SPECTROSCOPIC AND KINETIC RESPONSE OF CU-SSZ-13 TO $\text{SO}_2$ EXPOSURE AND IMPLICATIONS FOR $\text{NO}_x$ SELECTIVE CATALYTIC REDUCTION .....	146
7.1	Abstract .....	146

7.2	Introduction.....	146
7.3	Experimental Methods .....	150
7.3.1	Synthesis, sulfation, and de-sulfation of Cu-zeolites.....	150
7.3.2	Catalyst Characterization.....	151
7.3.3	Measurement of SCR kinetic details .....	153
7.3.4	DFT Simulation details.....	154
7.4	Results and Discussion .....	157
7.4.1	Nature of interactions between sulfur species with $Z_2Cu$ and $ZCuOH$ sites .....	157
7.4.2	Kinetic behavior of sulfated Cu-SSZ-13 catalysts after desulfation .....	162
7.4.3	Structures and energies of sulfur species bound to Cu sites .....	165
7.5	Conclusions.....	168
7.6	Acknowledgements.....	169
7.7	Supplementary Information .....	170
7.7.1	Elemental Analysis and Titration .....	170
7.7.2	Reaction Kinetics.....	172
7.7.3	Additional Characterization (TGA, $NO_2$ selectivity) on $ZCuOH$ S:Cu = 1.44 model catalyst .....	189
7.7.4	UV-Visible, XANES, EXAFS, $N_2$ Micropore, and Ar micropore on model $ZCuOH$ and $Z_2Cu$ materials .....	191
7.7.5	Parity plot between fractional increase in the SCR rate versus fractional decrease in sulfur content after regeneration .....	206
7.7.6	SEM and crystallite size plots on sulfated and regenerated $ZCuOH$ and $Z_2Cu$ model materials.....	207
7.7.7	Transmission FTIR spectra on $ZCuOH$ and $Z_2Cu$ model materials .....	209
7.7.8	Kinetic comparison of Cu-SAPO-34 materials in the literature to the Cu-SSZ-13 materials reported here .....	210
7.7.9	Error Propagation equations used for determining reaction rate confidence intervals.. .....	211
8.	SYNTHESIS OF CU-SSZ-13 MATERIALS WITH $CU_xO_y$ SPECIES .....	212
8.1	Abstract.....	212
8.2	Experimental Methods .....	212

8.2.1 Procedure to determine Cu-precipitation pH.....	212
8.3 Results and Discussion .....	212
8.3.1 Effect of pH on $\text{Cu}(\text{NO}_3)_2$ precipitation with $\text{NH}_4\text{OH}$ addition .....	212
8.3.2 Effect of Cu Precipitates on Cu-speciation on Cu-zeolites .....	214
8.3.3 Implications of Cu-Precipitation.....	218
8.4 Conclusions.....	218
8.5 Acknowledgements.....	219
APPENDIX A. BACK-OF-THE-ENVELOPE CALCULATIONS AND DERIVATIONS .....	220
APPENDIX B. HYDROTHERMAL SYNTHESIS AND CHARACTERIZATION OF CHABAZITE.....	226
APPENDIX C. AQUEOUS CU-EXCHANGE OF CU INTO SSZ-13 CHABAZITE SUPPORTS .....	235
APPENDIX D. LOW TEMPERATURE (30 TO 150°C) NO OXIDATION OVER H-SSZ-13 AND CU-SSZ-13 MATERIALS DURING STANDARD SCR CONDITIONS .....	237
APPENDIX E. CU-NA-ZSM-5 CO-CATION EXCHANGE KINETICS .....	245
APPENDIX F. ADSORPTION ENERGIES AND SCALING RELATIONSHIPS OF $\text{NH}_x$ , $\text{NO}_x$ , $\text{SO}_x$ , AND $\text{CH}_x$ OVER METAL-SSZ-13 ZEOLITES .....	249
APPENDIX G. CU- AND FE-ZEOLITES AT THE TOP OF THE VOLCANO.....	256
APPENDIX H. $\text{NH}_3$ OXIDATION KINETICS OVER CU-SSZ-13 .....	261
APPENDIX I. CU-ION MOBILITY AND KINETIC STUDIES.....	265
APPENDIX J. DEACTIVATION OF CU-ZSM-5.....	268
APPENDIX K. $\text{N}_2\text{O}$ FORMATION ON $\text{Cu}_x\text{O}_y$ , $\text{Z}_2\text{Cu}$ , AND $\text{ZCuOH}$ SITES DURING STANDARD SCR AND IMPACT OF SULFUR POISONS .....	270
APPENDIX L. OBSERVED PHENOMENON WHEN STANDARD SCR GASES ARE BUBBLED THROUGH AQUEOUS $\text{Cu}(\text{NO}_3)_2$ .....	280
REFERENCES .....	283
VITA .....	304
PUBLICATIONS.....	305

## LIST OF TABLES

<b>Table 1.</b> Typical composition in real diesel exhaust collected by Linnell et al. [24] compared to simulated diesel exhaust conditions recommended by Cummins Inc. n.r. = not reported. ....	49
<b>Table 2.</b> Compilation of differential standard SCR kinetics collected under negligible heat/mass transfer conditions on a variety of catalysts active for standard SCR. (n.m. = not measured) *errors for activation energies and reaction orders are 95% confidence intervals from experiments performed in our work.....	55
<b>Table 3.</b> NH <sub>3</sub> :Al molar ratios on H-SSZ-13, H-ZSM-5, and H-Beta materials. Errors on the Si:Al ratio are $\pm 25\%$ . Errors on the NH <sub>3</sub> :Al ratio are $\pm 0.1$ . *Samples from Zeolyst, Incorporated **Sample from Professor Enrique Iglesia's research group ***Sample synthesized in-house using methods outlined in Section 1.13 .....	71
<b>Table 4.</b> NH <sub>3</sub> :Al ratios measured using five different methods on a H-ZSM-5 material and H-SSZ-13 material. ....	73
<b>Table 5.</b> Governing equations from combining the Cu-exchange balance and NH <sub>3</sub> adsorption balance equations. ....	82
<b>Table 6.</b> Experimental NH <sub>3</sub> coordination numbers on the four different types of Cu species. ....	84
<b>Table 7.</b> Summary of BA deactivation experiments of H-SSZ-13 Si:Al = 4.5 samples .....	89
<b>Table 8.</b> List of all possible combinations of sites and proximal sites, and their most stable form assuming that Cu and H are allowed to exchange/hop and if CuOH and proximal H <sup>+</sup> sites are allowed to condense. ....	101
<b>Table 9.</b> List of possible mechanisms with scenarios with two Z <sub>2</sub> CuOH/CuOH (two ZCuOH's at a paired anionic site) negated.....	106
<b>Table 10.</b> Three samples run to validate NO titration procedure. Repeats were made for two of the samples. Parity plot is shown in Figure 60. ....	135
<b>Table 11.</b> List of all Cu-SSZ-13 samples whose fraction of oxidizable Cu(I)(NH <sub>3</sub> ) <sub>2</sub> via O <sub>2</sub> -titration has been measured experimentally using XAS and/or NO titration. n.m. = not measured. ....	140
<b>Table 12.</b> List of samples with similar Cu densities (0.22 to 0.27 Cu per 1000 Å <sup>3</sup> ), their CuOH fraction, Si:Al molar ratio, and oxidizable Cu(I) using XAS. ....	144



<b>Table 13.</b> Apparent activation energies and reactant orders on unsulfated ZCuOH and Z <sub>2</sub> Cu model catalysts collected under “10% O <sub>2</sub> SCR” conditions (300 ppm NO, 300 ppm NH <sub>3</sub> , 10% O <sub>2</sub> , 2% H <sub>2</sub> O, 8% CO <sub>2</sub> , balance N <sub>2</sub> at 473 K) and “60% O <sub>2</sub> SCR” conditions (300 ppm NO, 300 ppm NH <sub>3</sub> , 60% O <sub>2</sub> , 2% H <sub>2</sub> O, 8% CO <sub>2</sub> , balance N <sub>2</sub> at 473 K).....	158
<b>Table 14.</b> NH <sub>3</sub> :S values calculated from excess NH <sub>3</sub> storage on Cu-SSZ-13 catalysts after dry SO <sub>2</sub> poisoning. Corresponding S:Cu loadings on the four samples are also included for comparison. ....	167
<b>Table 15.</b> SCR apparent activation energies (E <sub>app</sub> ) on model catalysts after sulfation and desulfation treatments. (n.m. = not measured).....	184
<b>Table 16.</b> SCR apparent NO orders on model catalysts after sulfation and desulfation treatments. (n.m. = not measured). ....	184
<b>Table 17.</b> SCR apparent O <sub>2</sub> orders on model catalysts after sulfation and desulfation treatments. (n.m. = not measured). ....	185
<b>Table 18.</b> SCR apparent NH <sub>3</sub> orders on model catalysts after sulfation and desulfation treatments. (n.m. = not measured). ....	185
<b>Table 19.</b> SCR apparent CO <sub>2</sub> orders on model catalysts after sulfation and desulfation treatments. (n.m. = not measured). ....	186
<b>Table 20.</b> SCR apparent H <sub>2</sub> O orders on model catalysts after sulfation and desulfation treatments. (n.m. = not measured). ....	186
<b>Table 21.</b> Apparent activation energies and reaction orders an unsulfated Cu-SSZ-13 catalyst with a low Cu and Al density (0.1 Cu wt%, Si:Al = 100) under “10% O <sub>2</sub> SCR” conditions (300 ppm NO, 300 ppm NH <sub>3</sub> , 10% O <sub>2</sub> , 2.5% H <sub>2</sub> O, 8% CO <sub>2</sub> , balance N <sub>2</sub> at 473 K).....	189
<b>Table 22.</b> Ambient and dehydrated (573 K in dry air) XANES Cu(II) fractions observed on fresh, sulfated, and desulfated Cu-SSZ-13 catalysts using Cu(I)(NH <sub>3</sub> ) <sub>2</sub> and Cu(II) references. (n.m. not measured).....	192
<b>Table 23.</b> Operando XANES Cu(II) fractions observed on fresh, sulfated, and desulfated Cu-SSZ-13 catalysts using Cu(I)(NH <sub>3</sub> ) <sub>2</sub> and Cu(II) references. (n.m. not measured).....	193
<b>Table 24.</b> In situ XANES Cu(II) fractions after reduction with NH <sub>3</sub> + NO and subsequent reoxidation with O <sub>2</sub> observed on fresh, sulfated, and desulfated Cu-SSZ-13 catalysts using Cu(I)(NH <sub>3</sub> ) <sub>2</sub> and Cu(II) references. (n.m. not measured). ....	193

<b>Table 25.</b> Ambient and dehydrated (573 K in dry air) EXAFS Cu coordination numbers observed on fresh, sulfated, and desulfated Cu-SSZ-13 catalysts. (n.m. = not measured).....	194
<b>Table 26.</b> Operando EXAFS Cu coordination numbers observed on fresh, sulfated, and desulfated Cu-SSZ-13 catalysts. (n.m. = not measured).....	194
<b>Table 27.</b> In situ EXAFS coordination numbers after reduction with $\text{NH}_3 + \text{NO}$ and subsequent reoxidation with $\text{O}_2$ observed on Cu coordination numbers observed on fresh, sulfated, and desulfated Cu-SSZ-13 catalysts. (n.m. = not measured).....	195
<b>Table 28.</b> Governing equations used to calculate reaction rate normalized per mass catalyst, mol Cu, and (mol Cu –mol S). Concentrations of NO ( $C_{\text{NO,in}}$ and $C_{\text{NO,out}}$ ) are in ppm. ....	211
<b>Table 29.</b> Error propagation equations used to calculate reaction rate errors normalized per mass catalyst, mol Cu, and (mol Cu –mol S). Concentrations of NO ( $C_{\text{NO,in}}$ and $C_{\text{NO,out}}$ ) are in ppm. ....	211
<b>Table 30.</b> Energy density (watt-hours) for gasoline, diesel, and a smartphone battery. ....	220
<b>Table 31.</b> Rate of energy transfer for transferring energy into a gasoline automobile, electric car, and cell phone. *3000 mAh * (1 Ah /1000 mAh) *3.7 V = 14.8 Wh .....	221
<b>Table 32.</b> The fraction of tetrahedral and octahedral Al measured by quantifying the area under the curve for the tetrahedral feature (60 ppm chemical shift) and octahedral feature (-5 ppm chemical shift).s .....	227
<b>Table 33.</b> Summary SEM results for SSZ-13.....	233
<b>Table 34.</b> Qualitative comparisons between FD and LCAO modes. ....	250
<b>Table 35.</b> Fraction of Cu species on $\text{Cu}_x\text{O}_y$ , $\text{Z}_2\text{Cu}$ , and $\text{ZCuOH}$ model materials. *The fraction of $\text{Cu}_x\text{O}_y$ sites were estimated from differential SCR rates. The ratio of the actual measured SCR rate on the material with $\text{Cu}_x\text{O}_y$ to the expected SCR rate assuming all its Cu were $\text{Z}_2\text{Cu}$ was used to estimate the fraction of $\text{Cu}_x\text{O}_y$ .....	273
<b>Table 36.</b> SCR reaction rates and apparent activation energies compared to the $\text{N}_2\text{O}$ formation rates and activation energies on $\text{Cu}_x\text{O}_y$ , $\text{Z}_2\text{Cu}$ , and $\text{ZCuOH}$ model materials (300 ppm $\text{NH}_3$ , 300 ppm NO, 10% $\text{O}_2$ , 8% $\text{CO}_2$ , 2.5% $\text{H}_2\text{O}$ , balance $\text{N}_2$ , 200°C). The ratio of the $\text{N}_2\text{O}$ formation rate and SCR NO reduction rate is tabulated in the right-most column. ....	273
<b>Table 37.</b> Impact of sulfation and desulfation on $\text{N}_2\text{O}$ formation rates on model $\text{Z}_2\text{Cu}$ and $\text{ZCuOH}$ Cu-SSZ-13. ....	274

## LIST OF FIGURES

<b>Figure 1.</b> United States NO <sub>x</sub> Production by Sector. Data adapted from EPA NO <sub>2</sub> Risk and Exposure Assessment Report [13].	44
<b>Figure 2.</b> NO <sub>x</sub> emission regulations since the United States Clean Air Act of 1970. Data adapted from Cummins Sustainability Report [7].	45
<b>Figure 3.</b> Oxygen concentration in % in the air-fuel mixture before injection into the engine as the function of the air-to-fuel ratio (right y-axis). The rate of fuel consumption during engine operation as a function of the air-to-fuel ratio (left y-axis).	46
<b>Figure 4.</b> Catalytic conversion of carbon monoxide (CO), hydrocarbons (HC), and nitrogen oxide (NO) through a commercial three-way catalyst as a function of Air-to-fuel ratio. (Figure adapted from Takeuchi et al. [16]).	47
<b>Figure 5.</b> Schematic of a typical diesel exhaust aftertreatment system. [17]	47
<b>Figure 6.</b> Chabazite unit cell adapted from the International Zeolite Association [34].	51
<b>Figure 7.</b> Transmission <i>operando</i> XAS (red vector from I <sub>0</sub> to I <sub>t</sub> ) was collected while simultaneously collecting differential intrinsic reaction rates (blue vector from “reactant gases in” to “gases out”). The term <i>operando</i> refers to a technique that combines kinetic performance and evaluation of the catalyst structure in a single experiment under reaction conditions.	64
<b>Figure 8.</b> Left: The differential intrinsic rates (blue diamonds) must match the intrinsic rates collected in the laboratory reactor (green squares) for the XAS spectra to be called <i>operando</i> . If it does not, the spectra is simply <i>in-situ</i> . Right: <i>Operando</i> Cu k-edge XAS spectra (two blue curves) plotted with the standard Cu(I)(NH <sub>3</sub> ) <sub>2</sub> standard spectra (black curve with highest peak at 8.982 keV) and the Cu(II) standard spectra (black curve with no feature at 8.982 keV).	64
<b>Figure 9.</b> NH <sub>3</sub> concentrations during saturation and temperature programmed desorption (TPD).	68
<b>Figure 10.</b> H-ZSM-5 (Si:Al = 12.5) materials were saturated to steady state with 500 ppm NH <sub>3</sub> in balance He at 433 K. NH <sub>3</sub> desorption rates plotted versus temperature on a sample without purge (light trace) and purging with 800 sccm 2.5% H <sub>2</sub> O in balance He at 433 K for 8 hours (dark trace).	70
<b>Figure 11.</b> mols NH <sub>3</sub> per gram zeolite on H-SSZ-13, H-ZSM-5, and H-Beta materials.	72

- Figure 12.** Parity plot that compares the mols of  $\text{NH}_3$  per gram catalyst compared to the mols of Al per gram catalyst on H-SSZ-13, H-Beta, and H-ZSM-5 materials. .... 72
- Figure 13.** Cu-SSZ-13 (Si:Al = 4.5, Cu:Al = 0.12, Cu wt% = 2.3) material was saturated to steady state with 500 ppm  $\text{NH}_3$  in balance He at 433 K.  $\text{NH}_3$  desorption rates (a.u.) plotted versus temperature on a sample without purge (light trace), purging with 800 sccm dry He at 433 K for 5 hours (medium trace), and purging with 800 sccm 2.5%  $\text{H}_2\text{O}$  in balance He at 433 K for 8 hours (dark trace). .... 74
- Figure 14.** Number of residual BA sites normalized to the number of paired BA sites ( $\text{H}:\text{Al}_f$ ) on samples with varying levels of Metal-loadings ( $\text{M}:\text{Al}_f$ ). *Dashed lines* represent predicted number of residual BA sites assuming Cu exchanges at paired  $\text{Al}_f$  sites (at a 1:2 Cu: $\text{H}^+$  ratio) to saturation as predicted by Method 1 (Monte Carlo simulations) then continues to exchange at isolated  $\text{Al}_f$  sites (at a 1:1 Cu: $\text{H}^+$  ratio). *Circles* represent data collected for Co-SSZ-13 samples exchanged to saturation of paired  $\text{Al}_f$ . *Diamonds* represent data collected for Cu-SSZ-13 samples for a series of metal loadings. .... 75
- Figure 15.** The number of additional BA sites generated after reduction using  $\text{NH}_3$  and NO for Cu-SSZ-13. *Dashed lines* represent predicted number of additional BA sites generated for SSZ-13 with Si:Al of 4.5, 15, and 25, assuming isolated  $\text{Cu}^{2+}$  reduction to  $\text{Cu}^+$  generates a residual BA site and that  $[\text{CuOH}]^+$  reduction does not. *Data points* represent the measured increase in BA sites after reduction with  $\text{NH}_3$  and NO for Cu-SSZ-13 with varying Cu:Al and Si:Al ratios. .... 76
- Figure 16.** Schematic displaying the generation of a BA site after reduction of isolated  $\text{Cu}^{2+}$  sites in a reductive  $\text{NH}_3$  and NO environment (300 ppm NO + 300 ppm  $\text{NH}_3$ , in balance He, 200°C). .... 77
- Figure 17.** Comparison of the three methods that can be used to quantify number of paired  $\text{Al}_f$  sites. .... 78
- Figure 18.** FTIR spectra collected for a Cu-SSZ-13 Si:Al = 15 at various Cu loadings. An increase in Cu loading lead to an increase in  $[\text{CuOH}]^+$  peaks at  $3650\text{ cm}^{-1}$  and a decrease in BA peaks at  $3590\text{ cm}^{-1}$ . .... 79
- Figure 19.** Left: Integrated areas of  $[\text{CuOH}]^+$  feature at  $3650\text{ cm}^{-1}$  plotted as a function of Cu loading. Right: Integrated areas of BA sites feature at  $3590\text{ cm}^{-1}$  plotted as a function of Cu loading..... 79

- Figure 20.** SCR rate plotted against Cu wt% for samples with primarily isolated  $\text{Cu}^{2+}$  active sites (blue), exclusively  $[\text{CuOH}]^+$  active sites (red), and a mixture of isolated  $\text{Cu}^{2+}$  and  $[\text{CuOH}]^+$  active sites. .... 80
- Figure 21.**  $\text{NH}_3$ :Al molar storage ratios after  $\text{NH}_3$  titration and dry He flush plotted versus Cu:Al molar ratio on a number model ZCuOH (yellow),  $\text{Z}_2\text{Cu}$  (red), and materials with a mix of both sites (blue). The dashed linear lines exhibit slopes of 0, 1, and 2..... 83
- Figure 22.**  $\text{NH}_3$ :Al molar storage ratios after reduction with NO and  $\text{NH}_3$ , then  $\text{NH}_3$  titration and dry He flush plotted versus Cu:Al molar ratio on a number model ZCuOH (yellow) and  $\text{Z}_2\text{Cu}$  (red) Cu-SSZ-13 materials. The dashed linear lines exhibit slopes of 0, 1, and 2..... 83
- Figure 23.**  $\text{Cu}^{1+}$  fraction measured using XANES on two model  $\text{Z}_2\text{Cu}$  materials and on one model ZCuOH material, all with different Cu loadings. .... 86
- Figure 24.** Residual BA site quantification on Cu-SSZ-13 Si:Al = 4.5 on H-SSZ-13 Cu-exchanged with pH control to 5 with addition of 0.1M  $\text{NH}_4\text{OH}$  (*black diamonds*), and H-SSZ-13 Cu-exchanged without pH control (*red diamonds*) ..... 88
- Figure 25.** The molar NO:Cu fraction consumed after flowing NO (300 ppm NO in balance He, 200°C) through a sample saturated with  $\text{NH}_3$  (300 ppm  $\text{NH}_3$  in balance He, 200°C) and flushed with dry He. 95% confidence intervals are  $\pm 0.1$ ..... 90
- Figure 26.**  $\text{NH}_3$  TPD profiles before (orange) and after (blue) calcination on four model samples. .... 94
- Figure 27.**  $\text{NH}_3$  TPD shows a 1:1 loss in H for every exchanged Cu on Cu-SSZ-13 materials before calcination..... 95
- Figure 28.** Left:  $\text{NH}_3$  TPD profiles on an uncalcined (orange) and calcined (blue) Cu-SSZ-13 Si:Al = 4.5, Cu:Al = 0.23. Right:  $\text{NH}_3$  TPD profiles after flowing  $\text{H}_2\text{O}$  vapors at 30°C (2.5  $\text{H}_2\text{O}$  wt% in balance He, 800 sccm, 2 mg catalyst) for 24 hours (orange), after calcination (blue), and after exposure to standard SCR gases for 72 hours (black). .... 96
- Figure 29.** H:Al values measured from  $\text{NH}_3$  on TPD after a variety of post-calcination treatments. From left-to-right: (1) calcined Cu-SSZ-13 (Si:Al = 4.5, Cu wt% = 3.8), (2) uncalcined Cu-SSZ-13 after exposure to aqueous  $\text{Cu}(\text{NO}_3)_2$  for 24 hours\* (Si:Al = 4.5, Cu wt% = 4.3), (3) calcined Cu-SSZ-13 (Si:Al = 4.5, Cu wt% = 4.3), (4) calcined Cu-SSZ-13 vapor  $\text{H}_2\text{O}$  exposed at 30°C for 24 hours\*\*, (5) calcined Cu-SSZ-13 \*100 mL 0.1 M  $\text{Cu}(\text{NO}_3)_2$  + 0.1 g Cu-

SSZ-13 (Si:Al = 4.5, Cu wt% = 3.8), 24°C for 24 h **2.5% H <sub>2</sub> O in 500 mL N <sub>2</sub> through 1.76 mg Cu-SSZ-13 (Si:Al = 4.5, Cu wt% = 4.3) for 24h .....	97
<b>Figure 30.</b> Arrhenius plot collected on Cu-SSZ-13 (Si:Al = 4.5, Cu wt% = 4.3) before and after the vapor H <sub>2</sub> O treatment. ....	98
<b>Figure 31.</b> Schematic illustrating the reversibility of ZH/ZCuOH and Z <sub>2</sub> Cu sites at paired anionic sites on the zeolite framework.....	98
<b>Figure 32.</b> Six different types of possible sites on Cu-SSZ-13.....	99
<b>Figure 33.</b> One-site, two-site, and three-site models account for ion-exchange between Cu <sup>2+</sup> ions and H <sup>+</sup> ions between paired and unpaired sites proximal to none, one other, or two other paired or unpaired sites, respectively.....	100
<b>Figure 34.</b> Attempt to quantify the mols of H <sub>2</sub> O released during dehydration of Z <sub>2</sub> H/CuOH species on a model Z <sub>2</sub> Cu Cu-SSZ-13 material (Si:Al = 4.5, Cu:Al = 0.21). ....	109
<b>Figure 35.</b> Nature of the nature of two Cu <sup>2+</sup> active sites on Cu-SSZ-13 materials after calcination (treatment by flowing dry air at 600°C for 6 hours) and return to ambient hydrated conditions (ambient air, 20°C). ....	111
<b>Figure 36.</b> The reversible interconversion of Z <sub>2</sub> H/CuOH and Z <sub>2</sub> Cu sites from the removal of water via heat oxidative heat treatment or the low-temperature (20 to 30°C) introduction of water via exposure to aqueous media or vapor treatment.....	112
<b>Figure 37.</b> Proposed mechanistic pathways for the standard SCR reaction on isolated Cu <sup>2+</sup> ( <i>left</i> ) and [CuOH] <sup>+</sup> ( <i>right</i> ) active sites. Figure adapted from Paolucci et al. [109]. ....	113
<b>Figure 38.</b> Steady-state <i>operando</i> Cu(I) fractions plotted versus the Cu wt%. ....	114
<b>Figure 39.</b> Updated molecular mosaic for the nature of Cu ions in Cu-SSZ-13 during standard SCR reaction conditions (300 ppm NH <sub>3</sub> , 300 ppm NO, 10% O <sub>2</sub> , 7% CO <sub>2</sub> , 2.5% H <sub>2</sub> O, balance N <sub>2</sub> , 200°C).....	115
<b>Figure 40.</b> Adsorption energies of individual SCR gas molecules to Cu <sup>2+</sup> sites on Cu-SSZ-13 (top). Bader charge oxidation states of Cu <sup>2+</sup> sites on Cu-SSZ-13 after adsorption of individual SCR gases (bottom). ....	116
<b>Figure 41.</b> Fraction of Cu(I) ions during standard SCR and after NH <sub>3</sub> , NO, and O <sub>2</sub> cutoff at 200°C. We observe that gas mixture that leads to the greatest reduction of Cu(II) to Cu(I) is NO+NH <sub>3</sub> . Two Cu-SSZ-13 Si:Al = 4.5 with Cu:Al molar ratios of 0.11 (dark bars) and 0.16 (light bars) were used.....	117

- Figure 42.** XANES and EXAFS spectra collected on a ZCuOH model material (Cu-SSZ-13 Si:Al = 15, Cu:Al = 0.44) and Z<sub>2</sub>Cu model material (Cu-SSZ-13 Si:Al = 4.5, Cu:Al = 0.08). . 118
- Figure 43.** Updated molecular mosaic for the nature of Cu ions in Cu-SSZ-13 during standard SCR reaction conditions (300 ppm NH<sub>3</sub>, 300 ppm NO, 10% O<sub>2</sub>, 7% CO<sub>2</sub>, 2.5% H<sub>2</sub>O, balance N<sub>2</sub>, 200°C). 118
- Figure 44.** Adsorption energies of individual SCR gas molecules to Cu(I) sites on Cu-SSZ-13 (top). Bader charge oxidation states of Cu(I) sites on Cu-SSZ-13 after adsorption of individual SCR gases (bottom). 119
- Figure 45.** Transient NO<sub>2</sub> (left graph) and O<sub>2</sub> (right graph) titrations of Cu(I)(NH<sub>3</sub>)<sub>2</sub> sites on three Cu-SSZ-13 with different Cu wt% 's. The three horizontal bars on the right graph represent the fraction of oxidizable Cu(I) predicted from Monte Carlo simulations, assuming that Cu with diffusion spheres of 9 Å are only able to pair and oxidize if their diffusion spheres overlap. ... 120
- Figure 46.** The fraction of unoxidized Cu(I)(NH<sub>3</sub>)<sub>2</sub> remaining after titration of Cu-SSZ-13 with O<sub>2</sub>. The lines represent the predicted fraction of oxidizable Cu from computation assuming that each Cu electrostatically tethered to the framework can only move up to 9 Å (solid red line).. 121
- Figure 47.** Updated molecular mosaic for the nature of Cu ions in Cu-SSZ-13 during standard SCR reaction conditions (300 ppm NH<sub>3</sub>, 300 ppm NO, 10% O<sub>2</sub>, 7% CO<sub>2</sub>, 2.5% H<sub>2</sub>O, balance N<sub>2</sub>, 200°C). 122
- Figure 48.** Holes in the current molecular mosaic for the nature of Cu ions in Cu-SSZ-13 during standard SCR reaction conditions (300 ppm NH<sub>3</sub>, 300 ppm NO, 10% O<sub>2</sub>, 7% CO<sub>2</sub>, 2.5% H<sub>2</sub>O, balance N<sub>2</sub>, 200°C) 122
- Figure 49.** Intrinsic rates dependent on NH<sub>3</sub> pressure (left) and Arrhenius plots (right) on a Cu-SSZ-13 sample (Si:Al = 15, Cu wt% = 2.9, Cu:Al = 0.44) collected under standard SCR conditions (300 ppm NO, 50 to 2000 ppm NH<sub>3</sub>, 2 to 60% O<sub>2</sub>, 8% CO<sub>2</sub>, 2.5% H<sub>2</sub>O, balance N<sub>2</sub> at 200°C). All reaction rates are differential **except** for the 60% O<sub>2</sub> rate at the lowest NH<sub>3</sub> pressure (NH<sub>3</sub> conversion was 26%). 125
- Figure 50.** The standard SCR NH<sub>3</sub> order on a Cu-SSZ-13 sample (Si:Al = 15, Cu wt% = 2.9, Cu:Al = 0.44) collected at O<sub>2</sub> pressures ranging from 2% to 60%. 125
- Figure 51.** Intrinsic rates dependent on NH<sub>3</sub> pressure (left) and Arrhenius plots (right) on a Cu-SSZ-13 sample (Si:Al = 15, Cu wt% = 2.9, Cu:Al = 0.44) collected under standard SCR conditions (300 ppm NO, 50 to 2000 ppm NH<sub>3</sub>, 10% O<sub>2</sub>, 8% CO<sub>2</sub>, 2.5% H<sub>2</sub>O, balance N<sub>2</sub> at 160

to 240°C). All reaction rates are differential **except** for the 240°C rate at the lowest NH<sub>3</sub> pressure (NH<sub>3</sub> conversion was 30%)..... 126

**Figure 52.** The standard SCR NH<sub>3</sub> order on a Cu-SSZ-13 sample (Si:Al = 15, Cu wt% = 2.9, Cu:Al = 0.44) collected at temperatures ranging from 160 to 240°C..... 126

**Figure 53.** Reaction schematic that illustrates the formation of (NH<sub>3</sub>)<sub>2</sub>Cu(I)-O<sub>2</sub>-Cu(I)(NH<sub>3</sub>)<sub>2</sub> dimers from O<sub>2</sub> and two Cu(I)(NH<sub>3</sub>)<sub>2</sub> species whose diffusion spheres in Cu-SSZ-13 overlap. 127

**Figure 54.** Schematic that summarizes the treatments exposed to Cu-SSZ-13 at 200°C to count the fraction of oxidizable Cu(I)(NH<sub>3</sub>)<sub>2</sub>. In summary, (1) starting out with a calcined Cu-SSZ-13 with all Cu oxidized to Cu<sup>2+</sup>, reduce all the Cu<sup>2+</sup> to Cu(I)(NH<sub>3</sub>)<sub>2</sub>, (2) oxidize the Cu(I)(NH<sub>3</sub>)<sub>2</sub> with O<sub>2</sub> to form (NH<sub>3</sub>)<sub>2</sub>Cu(I)-O<sub>2</sub>-Cu(I)(NH<sub>3</sub>)<sub>2</sub> dimers, (4) activate NO and reform Cu(I)(NH<sub>3</sub>)<sub>2</sub> under a flow of NO + NH<sub>3</sub>..... 130

**Figure 55.** The mols of NO consumed per mol Cu after flowing a reductive mixture of NO + NH<sub>3</sub> to form Cu(I)(NH<sub>3</sub>)<sub>2</sub> (300 ppm NO, 300 ppm NH<sub>3</sub>, balance He) (blue diamonds). After O<sub>2</sub> oxidation (10% O<sub>2</sub> in balance He) of Cu(I)(NH<sub>3</sub>)<sub>2</sub>, an inert N<sub>2</sub> flush (600 sccm) was performed for six different flushing times between 0 to 120 minutes before flowing the NO + NH<sub>3</sub> reductive mixture (300 ppm NO, 300 ppm NH<sub>3</sub>, balance He). Again, the NO:Cu molar ratio was calculated during this second reduction and quantified (red squares). Tests were run on a Cu-SSZ-13 with Si:Al = 4.5, Cu:Al = 0.21, Cu wt% = 3.8..... 130

**Figure 56.** Schematic that summarizes the treatments exposed to Cu-SSZ-13 at 200°C to count the fraction of oxidizable Cu(I)(NH<sub>3</sub>)<sub>2</sub>. In summary, (1) starting out with a calcined Cu-SSZ-13 with all Cu oxidized to Cu<sup>2+</sup>, reduce all the Cu<sup>2+</sup> to Cu(I)(NH<sub>3</sub>)<sub>2</sub>, (2) oxidize the Cu(I)(NH<sub>3</sub>)<sub>2</sub> with O<sub>2</sub> to form (NH<sub>3</sub>)<sub>2</sub>Cu(I)-O<sub>2</sub>-Cu(I)(NH<sub>3</sub>)<sub>2</sub> dimers, (3) activate NO with the dimers, (4) reform Cu(I)(NH<sub>3</sub>)<sub>2</sub> using a flow of NO + NH<sub>3</sub>..... 132

**Figure 57.** NO concentrations measured in the reactor effluent during five step-wise treatments of Cu-SSZ-13 in order to quantify NO consumption (per Cu) in treatment steps 2, 4, and 5 above, which correspond to different steps in the proposed standard SCR cycle. Red and blue traces indicate experiments with the blank reactor and catalyst-loaded reactor, respectively. .... 133

**Figure 58.** The consumption of NO plotted as a molar NO:Cu ratio after reduction of a calcined Cu-SSZ-13 with NO + NH<sub>3</sub> (blue diamonds), exposing the catalyst to NO in balance He (red square) after flushing the catalyst with inert for 30 minutes after O<sub>2</sub> saturation, and finally flowing NO and NH<sub>3</sub> (green triangle). Varying inert flushing times after O<sub>2</sub> saturation of



$\text{Cu(1)(NH}_3)_2$  between 0 to 120 minutes were run before feeding NO. Two Cu-SSZ-13 samples, one with all  $\text{Cu}^{2+}$  as  $\text{Z}_2\text{Cu}$  (Si:Al = 15, Cu wt% = 0.5) (left graph) and one with all  $\text{Cu}^{2+}$  ZCuOH (Si:Al = 15, Cu wt% = 2.0,  $\text{Na}^+$ -free hydrothermal synthesis) (right graph)..... 134

**Figure 59.** The sum of the second and third NO:Cu molar ratios from Figure 58. Two Cu-SSZ-13 samples, one with all  $\text{Cu}^{2+}$  as  $\text{Z}_2\text{Cu}$  (Si:Al = 15, Cu wt% = 0.5) (left graph) and one with all  $\text{Cu}^{2+}$  ZCuOH (Si:Al = 15, Cu wt% = 2.0,  $\text{Na}^+$ -free hydrothermal synthesis) (right graph)..... 134

**Figure 60.** Parity plot between the fraction of oxidized  $\text{Cu(1)(NH}_3)_2$  measured using the NO titration method versus the fraction of oxidized  $\text{Cu(1)(NH}_3)_2$  measured using XAS. The dashed line represents the 1:1 parity line between the two axes..... 136

**Figure 61.** The consumption of NO plotted as a molar NO:Cu ratio after reduction of a calcined Cu-SSZ-13 with NO +  $\text{NH}_3$  (blue diamonds), exposing the catalyst to NO in balance  $\text{N}_2$  (red square) after flushing the catalyst with 2.5%  $\text{H}_2\text{O}$  in balance inert for 15 minutes after  $\text{O}_2$  saturation, and finally flowing NO and  $\text{NH}_3$  (green triangle). Two Cu-SSZ-13 samples, one with all  $\text{Cu}^{2+}$  as  $\text{Z}_2\text{Cu}$  (Si:Al = 15, Cu wt% = 0.5) (left graph) and one with all  $\text{Cu}^{2+}$  ZCuOH (Si:Al = 15, Cu wt% = 2.0,  $\text{Na}^+$ -free hydrothermal synthesis) (right graph)..... 139

**Figure 62.** Fraction of  $\text{Cu(1)(NH}_3)_2$  in Cu-SSZ-13 oxidized using  $\text{O}_2$  using XANES (purple circles) and the NO titration method (green triangles) plotted versus the Cu density of the samples tested. .... 141

**Figure 63.** Parity plot between the fraction of oxidized  $\text{Cu(1)(NH}_3)_2$  measured using the NO titration method versus the fraction of oxidized  $\text{Cu(1)(NH}_3)_2$  predicted from computation. .... 141

**Figure 64.** The fraction of unoxidized  $\text{Cu(1)(NH}_3)_2$  remaining after titration of Cu-SSZ-13 with  $\text{O}_2$ . The lines represent the predicted fraction of oxidizable Cu from computation assuming that each Cu electrostatically tethered to the framework can only move up to 9 Å (solid red line) and 7 Å (dashed blue line) from the anionic Al. Three Cu-SSZ-13 samples have all their  $\text{Cu}^{2+}$  species as  $\text{Z}_2\text{Cu}$  (red circles) and the remaining three have all or most of their  $\text{Cu}^{2+}$  species as CuOH (green/blue circles)..... 142

**Figure 65.** Parity plot between the unoxidized Cu(1) from the computational model compared to the unoxidized Cu(1) measured from XAS. .... 143

**Figure 66.** Illustration demonstrating that  $\text{Cu(1)(NH}_3)_2$  formed from  $\text{Z}_2\text{Cu}$  species have a slightly larger diffusion sphere (red cloud), likely owing to the possibility that  $\text{H}^+$  and  $\text{Cu(1)(NH}_3)_2$  can exchange and hop between a paired Al, thereby increasing the volume able to be reached by the

$\text{Cu(1)(NH}_3)_2$ . Conversely,  $\text{ZCuOH}$  species have a slightly smaller diffusion sphere likely owing to the fact that it is only electrostatically tethered to one anionic site. .... 143

**Figure 67.** There is a correlation between the fraction of oxidizable  $\text{Cu(I)(NH}_3)_2$  and the  $\text{CuOH}$  fraction (left) and also a correlation between the fraction of oxidizable  $\text{Cu(I)(NH}_3)_2$  and the  $\text{Si:Al}$  molar ratio (right). Four  $\text{Cu-SSZ-13}$  samples with similar  $\text{Cu}$  densities (0.22 to 0.27  $\text{Cu}$  per 1000  $\text{\AA}^3$ ) were used. .... 145

**Figure 68.** Proposed differences the diffusion radius of  $\text{Cu(I)(NH}_3)_2$  species anchored at a paired anionic site (left) and an isolated anionic site (right). Illustration demonstrates that  $\text{Cu(1)(NH}_3)_2$  formed from  $\text{Z}_2\text{Cu}$  species have a slightly larger diffusion sphere (red cloud), likely owing to the possibility that  $\text{H}^+$  and  $\text{Cu(1)(NH}_3)_2$  can exchange and hop between a paired  $\text{Al}$ , thereby increasing the volume able to be reached by the  $\text{Cu(1)(NH}_3)_2$ . Conversely,  $\text{ZCuOH}$  species have a slightly smaller diffusion sphere likely owing to the fact that it is only electrostatically tethered to one anionic site. .... 145

**Figure 69.** Normalized micropore volume (BET-surface areas derived from  $\text{N}_2$  adsorption) with increasing  $\text{S}$  content reported by Ham et al. [128], Brookshear et al. [132], Wijayanti et al. [131], and Shen et al. [133] when  $\text{Cu-zeolites}$  are poisoned with  $\text{SO}_2$ , or with  $\text{SO}_2$  and  $\text{NH}_3$  concurrently. .... 148

**Figure 70.** Molecular structure of a  $\text{SSZ-13 (CHA)}$  cage, with the  $1\text{Al (ZCuOH)}$  and  $2\text{Al (Z}_2\text{Cu)}$   $\text{Cu}$  sites on the right. Red, yellow, green, gray, and pink spheres correspond to  $\text{O}$ ,  $\text{Si}$ ,  $\text{Al}$ ,  $\text{Cu}$ , and  $\text{H}$  atoms, respectively. .... 154

**Figure 71.** Experimental  $\text{S:Cu}$  ratios (left) and computed  $\text{SO}_2$  binding energies to  $\text{Cu}$  from DFT (right). .... 157

**Figure 72.** Reaction rates and apparent activation energies for  $\text{ZCuOH}$  (red) and  $\text{Z}_2\text{Cu}$  (blue) model materials after sulfation. SCR conditions are 300 ppm  $\text{NO}$ , 300 ppm  $\text{NH}_3$ , 60%  $\text{O}_2$ , 2%  $\text{H}_2\text{O}$ , 8%  $\text{CO}_2$ , balance  $\text{N}_2$  at 473 K. .... 159

**Figure 73.** Diffuse reflectance UV-Visible spectra on  $\text{ZCuOH}$  (left) and  $\text{Z}_2\text{Cu}$  (right) after partial dehydration at 523 K under dry air. .... 161

**Figure 74.** Sulfur K-edge XANES measured ex situ at ambient conditions of  $\text{ZCuOH}$  (left) and  $\text{Z}_2\text{Cu}$  (right) samples treated with  $\text{SO}_2$  and  $\text{O}_2$  at either 200°C or 400 °C. .... 162

**Figure 75.**  $\text{S:Cu}$  ratios before (solid bars) and after desulfation (hatched bars) on  $\text{ZCuOH}$  and  $\text{Z}_2\text{Cu}$  model materials. .... 163

- Figure 76.** Reaction rates and apparent activation energies for ZCuOH and Z<sub>2</sub>Cu model materials after sulfation (filled) and desulfation (hollow). SCR conditions are 300 ppm NO, 300 ppm NH<sub>3</sub>, 60% O<sub>2</sub>, 2% H<sub>2</sub>O, 8% CO<sub>2</sub>, balance N<sub>2</sub> at 473 K. Arrows indicate the starting and ending samples after desulfation, and thus how the apparent activation energy changes after desulfation. .... 163
- Figure 77.** Fresh, sulfated, and desulfated samples that exhibit the same apparent activation energy collapse to the same turnover rate when normalized to (mol<sub>Cu</sub> – mol<sub>S</sub>). .... 165
- Figure 78.** First-principles phase diagram for S<sub>w</sub>O<sub>x</sub>H<sub>y</sub>N<sub>z</sub> species on a ZCuOH site vs temperature and NH<sub>3</sub> partial pressure at 1 atm total pressure and 20 ppm SO<sub>2</sub>, 10% O<sub>2</sub>, and 5% H<sub>2</sub>O. Molecular structures corresponding to each region indicated by numbers. Gray, red, yellow, green, blue, orange, and white spheres correspond to Cu, O, Si, Al, N, S, and H atoms, respectively. Zeolite framework included only when directly hosting Cu or H. .... 166
- Figure 79.** First-principles phase diagram for S<sub>w</sub>O<sub>x</sub>H<sub>y</sub>N<sub>z</sub> species on a Z<sub>2</sub>Cu site vs temperature and NH<sub>3</sub> partial pressure at 1 atm total pressure and 20 ppm SO<sub>2</sub>, 10% O<sub>2</sub>, and 5% H<sub>2</sub>O. Molecular structures corresponding to each region indicated by numbers. Gray, red, yellow, green, blue, orange, and white spheres correspond to Cu, O, Si, Al, N, S, and H atoms, respectively. Zeolite framework included only when directly hosting Cu or H. .... 166
- Figure 80.** Molar S:Cu ratios measured using EDS and ICP on sulfated ZCuOH model catalysts after heating to 523 K under dry air (100 mg sample, 200 mL min<sup>-1</sup> for 6 hours) and dehydrated at 150°C under vacuum (< 5 μmHg, 30 mg sample) for 4 hours. .... 170
- Figure 81.** Excess molar NH<sub>3</sub>:S ratios relative to the unsulfated materials were measured from NH<sub>3</sub> titration of both Brønsted and Lewis acid sites. The mols of NH<sub>3</sub> that displaced the volume of gas in the reactor was quantified using a blank reactor and subtracted to determine the NH<sub>3</sub>:S ratio for the catalyst. .... 170
- Figure 82.** Parity plot confirming that NH<sub>3</sub> storage (NH<sub>3</sub>:Al) can be quantified during NH<sub>3</sub> saturation at 160°C or during TPD. Quantifying NH<sub>3</sub> storage during NH<sub>3</sub> saturation is particularly useful for materials that are temperature sensitive or for instruments that cannot handle desorption species (e.g. sulfur oxides). .... 171
- Figure 83.** Arrhenius plots (left) and rate dependent on temperature (right) on sulfated ZCuOH model catalyst (filled black square) and post-sulfation heat treated catalyst (100 mg sample, 523

K 200 mL min<sup>-1</sup> dry air for 6 hours) (hollow squares) during standard SCR conditions (300 ppm NO, 300 ppm NH<sub>3</sub>, 10% O<sub>2</sub>, 8% CO<sub>2</sub>, 2.5% H<sub>2</sub>O, balance N<sub>2</sub> at 473 K)..... 172

**Figure 84.** Arrhenius plots (left) and rate dependent on temperature (right) on sulfated ZCuOH model catalyst after continuous exposure to a range of SCR conditions (150 to 700 ppm NO, 150 to 2000 ppm NH<sub>3</sub>, 0.4 to 70% O<sub>2</sub>, 0 to 15% CO<sub>2</sub>, 0 to 2.5% H<sub>2</sub>O, balance N<sub>2</sub> at 423 to 523 K). Repeat returns to standard SCR conditions (300 ppm NO, 300 ppm NH<sub>3</sub>, 10% O<sub>2</sub>, 8% CO<sub>2</sub>, 2.5% H<sub>2</sub>O, balance N<sub>2</sub> at 473 K) were collected on Day 0 (filled black squares), Day 14 (grey squares), and Day 24 (hollow squares). ..... 172

**Figure 85.** Arrhenius plots (left) and rate dependent on temperature (right) on fresh (black diamond), sulfated (black square and triangle), and desulfated (hollow square and triangle) ZCuOH model catalysts during standard SCR conditions (300 ppm NO, 300 ppm NH<sub>3</sub>, 10% O<sub>2</sub>, 8% CO<sub>2</sub>, 2.5% H<sub>2</sub>O, balance N<sub>2</sub> between 423 and 523 K) ..... 173

**Figure 86.** Arrhenius plots (left) and rate dependent on temperature (right) on fresh (black diamond), sulfated (black square and triangle), and desulfated (hollow square and triangle) ZCuOH model catalysts during high O<sub>2</sub> SCR conditions (300 ppm NO, 300 ppm NH<sub>3</sub>, 60% O<sub>2</sub>, 8% CO<sub>2</sub>, 2.5% H<sub>2</sub>O, balance N<sub>2</sub> between 423 and 523 K) ..... 173

**Figure 87.** Arrhenius plots (left) and rate dependent on temperature (right) on fresh (black diamond), sulfated (black square and triangle), and desulfated (hollow square and triangle) Z<sub>2</sub>Cu model catalysts during standard SCR conditions (300 ppm NO, 300 ppm NH<sub>3</sub>, 10% O<sub>2</sub>, 8% CO<sub>2</sub>, 2.5% H<sub>2</sub>O, balance N<sub>2</sub> between 423 and 523 K at 1 atm) ..... 174

**Figure 88.** Arrhenius plots (left) and rate dependent on temperature (right) on fresh (black diamond), sulfated (black square and triangle), and desulfated (hollow square and triangle) Z<sub>2</sub>Cu model catalysts during high O<sub>2</sub> SCR conditions (300 ppm NO, 300 ppm NH<sub>3</sub>, 60% O<sub>2</sub>, 8% CO<sub>2</sub>, 2.5% H<sub>2</sub>O, balance N<sub>2</sub> between 423 and 523 K at 1 atm) ..... 174

**Figure 89.** Linearized O<sub>2</sub> order plots (left) and rate dependent on O<sub>2</sub> concentration plots (right) on fresh (black diamond), sulfated (black square and triangle), and desulfated (hollow square and triangle) ZCuOH model catalysts during SCR conditions (300 ppm NO, 300 ppm NH<sub>3</sub>, 2 to 70% O<sub>2</sub>, 8% CO<sub>2</sub>, 2.5% H<sub>2</sub>O, balance N<sub>2</sub> at 473 K and 1 atm) ..... 175

**Figure 90.** Linearized O<sub>2</sub> order plots (left) and rate dependent on O<sub>2</sub> concentration plots (right) on fresh (black diamond), sulfated (black square and triangle), and desulfated (hollow square and

triangle)  $Z_2Cu$  model catalysts during SCR conditions (300 ppm NO, 300 ppm  $NH_3$ , 2 to 70%  $O_2$ , 8%  $CO_2$ , 2.5%  $H_2O$ , balance  $N_2$  at 473 K and 1 atm)..... 175

**Figure 91.** Linearized  $NH_3$  order plots (left) and rate dependent on  $NH_3$  concentration plots (right) on fresh (black diamond), sulfated (black square and triangle), and desulfated (hollow square and triangle)  $ZCuOH$  model catalysts during standard SCR conditions (300 ppm NO, 150 to 2000 ppm  $NH_3$ , 10%  $O_2$ , 8%  $CO_2$ , 2.5%  $H_2O$ , balance  $N_2$  at 473 K and 1 atm)..... 176

**Figure 92.** Linearized  $NH_3$  order plots (left) and rate dependent on  $NH_3$  concentration plots (right) on fresh (black diamond), sulfated (black square and triangle), and desulfated (hollow square and triangle)  $ZCuOH$  model catalysts during high  $O_2$  SCR conditions (300 ppm NO, 150 to 2000 ppm  $NH_3$ , 60%  $O_2$ , 8%  $CO_2$ , 2.5%  $H_2O$ , balance  $N_2$  at 473 K and 1 atm)..... 176

**Figure 93.** Linearized  $NH_3$  order plots (left) and rate dependent on  $NH_3$  concentration plots (right) on fresh (black diamond), sulfated (black square and triangle), and desulfated (hollow square and triangle)  $Z_2Cu$  model catalysts during standard SCR conditions (300 ppm NO, 150 to 2000 ppm  $NH_3$ , 10%  $O_2$ , 8%  $CO_2$ , 2.5%  $H_2O$ , balance  $N_2$  at 473 K and 1 atm)..... 177

**Figure 94.** Linearized  $NH_3$  order plots (left) and rate dependent on  $NH_3$  concentration plots (right) on fresh (black diamond), sulfated (black square and triangle), and desulfated (hollow square and triangle)  $Z_2Cu$  model catalysts during high  $O_2$  SCR conditions (300 ppm NO, 150 to 2000 ppm  $NH_3$ , 60%  $O_2$ , 8%  $CO_2$ , 2.5%  $H_2O$ , balance  $N_2$  at 473 K and 1 atm)..... 177

**Figure 95.** Linearized NO order plots (left) and rate dependent on NO concentration plots (right) on fresh (black diamond), sulfated (black square and triangle), and desulfated (hollow square and triangle)  $ZCuOH$  model catalysts during standard SCR conditions (150 to 700 ppm NO, 300 ppm  $NH_3$ , 10%  $O_2$ , 8%  $CO_2$ , 2.5%  $H_2O$ , balance  $N_2$  at 473 K and 1 atm)..... 178

**Figure 96.** Linearized NO order plots (left) and rate dependent on NO concentration plots (right) on fresh (black diamond), sulfated (black square and triangle), and desulfated (hollow square and triangle)  $ZCuOH$  model catalysts during high  $O_2$  SCR conditions (150 to 500 ppm NO, 300 ppm  $NH_3$ , 60%  $O_2$ , 8%  $CO_2$ , 2.5%  $H_2O$ , balance  $N_2$  at 473 K and 1 atm)..... 178

**Figure 97.** Linearized NO order plots (left) and rate dependent on NO concentration plots (right) on fresh (black diamond), sulfated (black square and triangle), and desulfated (hollow square and triangle)  $Z_2Cu$  model catalysts during standard SCR conditions (150 to 700 ppm NO, 300 ppm  $NH_3$ , 10%  $O_2$ , 8%  $CO_2$ , 2.5%  $H_2O$ , balance  $N_2$  at 473 K and 1 atm)..... 179

**Figure 98.** Linearized NO order plots (left) and rate dependent on NO concentration plots (right) on fresh (black diamond), sulfated (black square and triangle), and desulfated (hollow square and triangle)  $Z_2Cu$  model catalysts during high  $O_2$  SCR conditions (150 to 500 ppm NO, 300 ppm  $NH_3$ , 60%  $O_2$ , 8%  $CO_2$ , 2.5%  $H_2O$ , balance  $N_2$  at 473 K and 1 atm)..... 179

**Figure 99.** Linearized  $H_2O$  order plots (left) and rate dependent on  $H_2O$  concentration plots (right) on fresh (black diamond) and desulfated (hollow square and triangle)  $ZCuOH$  model catalysts during standard SCR conditions (300 ppm NO, 300 ppm  $NH_3$ , 10%  $O_2$ , 8%  $CO_2$ , 0 to 2.5%  $H_2O$ , balance  $N_2$  at 473 K and 1 atm).  $H_2O$  orders were not collected for the sulfated  $ZCuOH$  model catalyst. .... 180

**Figure 100.** Linearized  $H_2O$  order plots (left) and rate dependent on  $H_2O$  concentration plots (right) on fresh (black diamond) and desulfated (hollow square and triangle)  $ZCuOH$  model catalysts during high  $O_2$  SCR conditions (300 ppm NO, 300 ppm  $NH_3$ , 60%  $O_2$ , 8%  $CO_2$ , 0 to 2.5%  $H_2O$ , balance  $N_2$  at 473 K and 1 atm).  $H_2O$  orders were not collected for the sulfated  $ZCuOH$  model catalyst. .... 180

**Figure 101.** Linearized  $H_2O$  order plots (left) and rate dependent on  $H_2O$  concentration plots (right) desulfated (hollow square and triangle)  $Z_2Cu$  model catalysts during standard SCR conditions (300 ppm NO, 300 ppm  $NH_3$ , 10%  $O_2$ , 8%  $CO_2$ , 0 to 2.5%  $H_2O$ , balance  $N_2$  at 473 K and 1 atm).  $H_2O$  orders were not collected for the fresh and sulfated  $Z_2Cu$  model catalyst. .... 181

**Figure 102.** Linearized  $H_2O$  order plots (left) and rate dependent on  $H_2O$  concentration plots (right) on desulfated (hollow square and triangle)  $Z_2Cu$  model catalysts during high  $O_2$  SCR conditions (300 ppm NO, 300 ppm  $NH_3$ , 60%  $O_2$ , 8%  $CO_2$ , 0 to 2.5%  $H_2O$ , balance  $N_2$  at 473 K and 1 atm).  $H_2O$  orders were not collected for the fresh and sulfated  $Z_2Cu$  model catalyst. .... 181

**Figure 103.** Linearized  $CO_2$  order plots (left) and rate dependent on  $CO_2$  concentration plots (right) on desulfated (hollow square and triangle)  $ZCuOH$  model catalysts during standard SCR conditions (300 ppm NO, 300 ppm  $NH_3$ , 10%  $O_2$ , 0 to 15%  $CO_2$ , 2.5%  $H_2O$ , balance  $N_2$  at 473 K and 1 atm).  $CO_2$  orders were not collected experimentally for the fresh and sulfated  $ZCuOH$  model catalyst. .... 182

**Figure 104.** Linearized  $CO_2$  order plots (left) and rate dependent on  $CO_2$  concentration plots (right) on desulfated (hollow square and triangle)  $ZCuOH$  model catalysts during high  $O_2$  SCR conditions (300 ppm NO, 300 ppm  $NH_3$ , 60%  $O_2$ , 0 to 15%  $CO_2$ , 2.5%  $H_2O$ , balance  $N_2$  at 473 K

and 1 atm). CO<sub>2</sub> orders were not collected experimentally for the fresh and sulfated ZCuOH model catalyst. .... 182

**Figure 105.** Linearized CO<sub>2</sub> order plots (left) and rate dependent on CO<sub>2</sub> concentration plots (right) on desulfated (hollow square and triangle) Z<sub>2</sub>Cu model catalysts during standard SCR conditions (300 ppm NO, 300 ppm NH<sub>3</sub>, 10% O<sub>2</sub>, 0 to 15% CO<sub>2</sub>, 2.5% H<sub>2</sub>O, balance N<sub>2</sub> at 473 K and 1 atm). CO<sub>2</sub> orders were not collected experimentally for the fresh and sulfated Z<sub>2</sub>Cu model catalyst. .... 183

**Figure 106.** Linearized CO<sub>2</sub> order plots (left) and rate dependent on CO<sub>2</sub> concentration plots (right) on desulfated (hollow square and triangle) Z<sub>2</sub>Cu model catalysts during high O<sub>2</sub> SCR conditions (300 ppm NO, 300 ppm NH<sub>3</sub>, 60% O<sub>2</sub>, 0 to 15% CO<sub>2</sub>, 2.5% H<sub>2</sub>O, balance N<sub>2</sub> at 473 K and 1 atm). CO<sub>2</sub> orders were not collected experimentally for the fresh and sulfated Z<sub>2</sub>Cu model catalyst. .... 183

**Figure 107.** Standard SCR (300 ppm NO, 300 ppm NH<sub>3</sub>, 10% O<sub>2</sub>, 2.5% H<sub>2</sub>O, 8% CO<sub>2</sub>, in balance N<sub>2</sub>, at 200°C) rate, and apparent activation energy on unsulfated Cu-SSZ-13 samples with low Cu loadings (< 1 wt%). The catalyst with the lowest Cu and Al density (0.1 Cu wt%, Si:Al = 100) exhibited a drop in the apparent activation energy compared to other catalysts (Cu wt% from 0.2 to 0.8, Si:Al from 4.5 to 25)..... 187

**Figure 108.** Standard SCR (300 ppm NO, 300 ppm NH<sub>3</sub>, 10% O<sub>2</sub>, 2.5% H<sub>2</sub>O, 8% CO<sub>2</sub>, in balance N<sub>2</sub>, at 200°C) Arrhenius plot of an unsulfated Cu-SSZ-13 catalysts with a low Cu and Al density (0.1 Cu wt%, Si:Al = 100)..... 187

**Figure 109.** Standard SCR (300 ppm NO, 300 ppm NH<sub>3</sub>, 10% O<sub>2</sub>, 2.5% H<sub>2</sub>O, 8% CO<sub>2</sub>, in balance N<sub>2</sub>, at 200°C) order plots on an unsulfated Cu-SSZ-13 catalyst with a low Cu and Al density (0.1 Cu wt%, Si:Al = 100). The NO, NH<sub>3</sub>, O<sub>2</sub>, H<sub>2</sub>O, and CO<sub>2</sub> orders are 0.6, 0.0, 0.9, 0.0, and 0.0, respectively. .... 188

**Figure 110.** Thermogravimetric analysis (TGA) of sulfated Cu-SSZ-13 catalysts in a dry He environment (10 mg sample, ramp from ambient temperature to 1273 K with a ramp rate of 10 K min<sup>-1</sup>). Collected on a Thermal Analysis (TA) Instruments Simultaneous DSC/TGA (SDT) Q600. .... 189

**Figure 111.** Selectivities toward NO oxidation under standard (10% O<sub>2</sub>) SCR conditions (left), and selectivities toward NO oxidation under high O<sub>2</sub> (60% O<sub>2</sub>) SCR conditions, on Cu-SSZ-13 poisoned with increasing S content..... 190

<b>Figure 112.</b> Diffuse reflectance UV-Visible spectra on ZCuOH (left) and Z <sub>2</sub> Cu (right) collected under ambient conditions (298 K, ambient air). .....	191
<b>Figure 113.</b> The micropore volume measured with Ar for Z <sub>2</sub> Cu invariant with increasing S wt% with increasing sulfation on sulfated materials before saturation with NH <sub>3</sub> (left), and after saturation with NH <sub>3</sub> (right). .....	196
<b>Figure 114.</b> Micropore volumes measured using N <sub>2</sub> on samples that were either co-poisoned with NH <sub>3</sub> and SO <sub>2</sub> , or poisoned with SO <sub>2</sub> then saturated with NH <sub>3</sub> . .....	197
<b>Figure 115.</b> Argon adsorption isotherms (87 K) of sulfated ZCuOH model samples before NH <sub>3</sub> saturation (left) and after NH <sub>3</sub> saturation (right).....	198
<b>Figure 116.</b> Argon adsorption isotherms (87 K) of sulfated Z <sub>2</sub> Cu model samples before NH <sub>3</sub> saturation (left) and after NH <sub>3</sub> saturation (right).....	198
<b>Figure 117.</b> Relevant CHA XRD peaks indexed to diffraction planes for estimation of the CHA cage volume increase from XRD. ....	200
<b>Figure 118.</b> XRD peak shifts at 9.5° for Cu-SSZ-13 catalysts poisoned with only dry SO <sub>2</sub> (left) and NH <sub>3</sub> saturated after dry SO <sub>2</sub> poisoning (right) for ZCuOH (diamonds) and Z <sub>2</sub> Cu (squares). .....	201
<b>Figure 119.</b> XRD peak shifts at 13° for Cu-SSZ-13 catalysts poisoned with only dry SO <sub>2</sub> (left) and NH <sub>3</sub> saturated after dry SO <sub>2</sub> poisoning (right) for ZCuOH (diamonds) and Z <sub>2</sub> Cu (squares). .....	201
<b>Figure 120.</b> XRD patterns on Z <sub>2</sub> Cu model catalysts after dry sulfation (left) and after NH <sub>3</sub> saturation (right). Samples on the right were saturated with 500 ppm NH <sub>3</sub> at 453 K until saturation, then flushed with dry N <sub>2</sub> at 453 K and cooled to room temperature.....	202
<b>Figure 121.</b> XRD patterns on ZCuOH model catalysts after dry sulfation (left) and after NH <sub>3</sub> saturation (right). Samples on the right were saturated with 500 ppm NH <sub>3</sub> at 453 K until saturation, then flushed with dry N <sub>2</sub> at 453 K and cooled to room temperature.....	202
<b>Figure 122.</b> XRD patterns narrowed in on diffraction peaks at 9.5° 2θ for Z <sub>2</sub> Cu model catalysts after dry sulfation (left) and after NH <sub>3</sub> saturation (right). Samples on the right were saturated with 500 ppm NH <sub>3</sub> at 453 K until saturation, then flushed with dry N <sub>2</sub> at 453 K and cooled to room temperature. ....	203
<b>Figure 123.</b> XRD patterns narrowed in on diffraction peaks at 13° 2θ for Z <sub>2</sub> Cu model catalysts after dry sulfation (left) and after NH <sub>3</sub> saturation (right). Samples on the right were saturated	



with 500 ppm  $\text{NH}_3$  at 453 K until saturation, then flushed with dry  $\text{N}_2$  at 453 K and cooled to room temperature. .... 203

**Figure 124.** XRD patterns narrowed in on diffraction peaks at  $9.5^\circ 2\theta$  for ZCuOH model catalysts after dry sulfation (left) and after  $\text{NH}_3$  saturation (right). Samples on the right were saturated with 500 ppm  $\text{NH}_3$  at 453 K until saturation, then flushed with dry  $\text{N}_2$  at 453 K and cooled to room temperature. .... 204

**Figure 125.** XRD patterns narrowed in on diffraction peaks at  $13^\circ 2\theta$  for ZCuOH model catalysts after dry sulfation (left) and after  $\text{NH}_3$  saturation (right). Samples on the right were saturated with 500 ppm  $\text{NH}_3$  at 453 K until saturation, then flushed with dry  $\text{N}_2$  at 453 K and cooled to room temperature. .... 204

**Figure 126.** % increase in micropore volume measured using Ar micropore and XRD peak shifts on the  $\text{Z}_2\text{Cu}$  model material. .... 205

**Figure 127.** Fractional increase in the SCR rate after desulfation plotted versus the fractional increase in S content after desulfation. The dashed line represents parity. Error bars are 95% confidence intervals calculated from error propagation. .... 206

**Figure 128.** SEM images of unsulfated, sulfated ( $400^\circ\text{C}$   $\text{SO}_2$ ), and desulfated ZCuOH and  $\text{Z}_2\text{Cu}$  samples. .... 207

**Figure 129.** Crystallite size distribution histograms derived from SEM images. The legend reports mean average crystallite diameters with 5% confidence intervals as errors. .... 208

**Figure 130.** FTIR spectra normalized to mass of catalyst of ZCuOH (left) and  $\text{Z}_2\text{Cu}$  (right) catalysts after sulfur poisoning. .... 209

**Figure 131.** Standard SCR (300 ppm NO, 300 ppm  $\text{NH}_3$ , 10%  $\text{O}_2$ , 2.5%  $\text{H}_2\text{O}$ , 8%  $\text{CO}_2$ , in balance  $\text{N}_2$ , at  $200^\circ\text{C}$ ) rate, apparent activation energy, and reaction orders for sulfated Cu-SSZ-13 (red and blue) and Cu-SAPO-34 (green). .... 210

**Figure 132.** Precipitation pH curves for  $\text{Cu}(\text{NO}_3)_2$  (*black squares*) and  $\text{Cu}(\text{Acetate})$  (*black circles*) using  $\text{NH}_4\text{OH}$  as a base to increase the pH. If final equilibrium pH and Cu molarities fall above the curve,  $\text{Cu}_2(\text{OH})_2$  precipitates were observed. If final equilibrium pH and Cu molarities fall below the curve, then all Cu species are aqueous. Literature values for  $\text{Cu}(\text{NO}_3)_2$  precipitation from Baes and Mesmer ([168], *hollow square*) and Regalbuto and Miller ([166], *cross-hatched square*) are also plotted. .... 213

**Figure 133.** Concentration of  $\text{Cu}(\text{NO}_3)_2$  and pH important at equilibrium during Cu-exchange for all Cu-zeolite (SSZ-13, ZSM-5, and Beta) samples Cu-exchanged. Cu-exchanged zeolites that did not exhibit black  $\text{Cu}_x\text{O}_y$  clusters after calcination are represented as *blue diamonds*. Cu-exchanged zeolites that did exhibit black  $\text{Cu}_x\text{O}_y$  clusters after calcination are represented as *orange diamonds*. The precipitation pH for  $\text{Cu}(\text{NO}_3)_2$  is represented by black squares the precipitation curve model (*light red trace*). 215

**Figure 134.** The SCR NO consumption reaction rate normalized per gram of catalyst plotted versus the Cu wt% (top) and the SCR NO consumption apparent activation energy plotted versus the Cu wt% (bottom). Standard SCR conditions (300 ppm NO, 300 ppm  $\text{NH}_3$ , 10%  $\text{O}_2$ , 7%  $\text{CO}_2$ , 2.5%  $\text{H}_2\text{O}$ , balance  $\text{N}_2$ , 200°C). Cu-SSZ-13 catalysts with Si:Al molar ratios of 4.5 and 15 and Cu wt%s between 0 and 19 were synthesized and used for this study. The blue shaded area between 0 to 4 wt% represents samples with all Cu as ionic  $\text{Cu}^{2+}/\text{Cu}^{1+}$  species. The grey shaded area between 4 to 19 wt% represents samples that contain bulk  $\text{Cu}_x\text{O}_y$  species. 216

**Figure 135.** Catalytic activities of four different sites present on Cu-SSZ-13 (Brønsted acid sites,  $\text{Z}_2\text{Cu}$  sites,  $\text{ZCuOH}$  sites, and  $\text{Cu}_x\text{O}_y$  cluster sites) for four different reactions (fast SCR [171], standard SCR [43,109], dry NO oxidation [122],  $\text{NH}_3$  oxidation (Appendix H). Check marks indicate that the particular site is active for and catalyzes the particular reaction, X marks indicate that particular site is not active for the particular reaction, and question marks indicate that it is uncertain whether the particular site is active. 217

**Figure 136.** XRD spectra on the H-form of all SSZ-13 (top), ZSM-5 (middle) , and Beta (bottom) zeolite supports used. Peak locations were consistent for those of SSZ-13, ZSM-5, and Beta, respectively. 226

**Figure 137.**  $^{27}\text{Al}$ -NMR spectra collected on H-SSZ-13 with Si:Al ratios of 4.5, 15, and 25. . 227

**Figure 138.** Calibration curve to convert a measured normalized intensity of  $\text{NH}_3$  in the AutoChemII-MSD to the actual mol  $\text{NH}_3 \text{ g}^{-1}$  desorbed from the sample during TPD. The mol  $\text{NH}_3 \text{ g}^{-1}$  desorbed from the sample can be used to determine the  $\text{NH}_3$ :Al ratio of zeolites, which is equal to the H:Al ratio assuming each  $\text{NH}_3$  truly titrates one BA site during liquid  $\text{NH}_4$ -exchange. 228

**Figure 139.** Scanning electron microscopy (SEM) and electron dispersive x-ray spectroscopy (EDS) used to determine distributions of Si and Al in the commercial H-ZSM-5 with Si:Al = 12.5 at resolutions of 10  $\mu\text{m}$  (a) and 100  $\mu\text{m}$  (b), Si:Al = 18 at resolutions of 10  $\mu\text{m}$  (c) and 100

$\mu\text{m}$ (d), and Si:Al = 30 at resolutions of 10 $\mu\text{m}$ (e) and 100 $\mu\text{m}$ (f) In all images, a green pixel represents the detection of Si atoms and a red pixel represents the detection of Al atoms. ....	229
<b>Figure 140.</b> SEM images on H-SSZ-13 Si:Al = 4.5 .....	230
<b>Figure 141.</b> SEM images on H-SSZ-13 Si:Al = 15 .....	231
<b>Figure 142.</b> SEM images on H-SSZ-13 Si:Al = 25 synthesized via direct tumbling 10 days at 160°C. ....	232
<b>Figure 143.</b> SEM images on H-SSZ-13 Si:Al = 80 synthesized in a static Parr reactor for 10 days at 160°C with stirring every 2 days via 3-minute agitation without opening the Parr reactor. HF was not added.....	232
<b>Figure 144.</b> BA counts measured using liquid $\text{NH}_4\text{NO}_3$ exchange and TPD using the AutoChemII-MSD and calibration curve for three representative commercial H-ZSM-5 samples with Si:Al = 12.5, 18, and 30.....	234
<b>Figure 145.</b> Centrifuge test performed on three representative commercial H-ZSM-5 samples with Si:Al = 12.5 (a), Si:Al = 18 (b), and Si:Al = 30 (c). ....	234
<b>Figure 146.</b> Cu-exchange isotherms for various zeolite supports for samples consisting of primarily $\text{Cu}^{2+}$ species coordinated to two framework Al (top graph), and CuOH species coordinated to one framework Al (bottom graph). ....	236
<b>Figure 147.</b> Arrhenius plot of the forward NO oxidation reaction rate between temperatures of 30 and 160°C and a feed composition of 1000 ppm NO, 5% $\text{O}_2$ , in balance $\text{N}_2$ . Forward NO oxidation rates are collected by Loiland et al. [177] on Si-CHA (red squares), H-SSZ-13 (blue circles), and Na-SSZ-13 (orange circles). Forward NO oxidation rates were also collected on Cu-SSZ-13 (Si:Al = 4.5, Cu wt% = 3.8) in the presence of 2% $\text{H}_2\text{O}$ (purples x's) and absence of $\text{H}_2\text{O}$ (green triangles). ....	239
<b>Figure 148.</b> Arrhenius plots for the NO consumption rates (blue diamonds) during standard SCR gas conditions (300 ppm NO, 300 ppm $\text{NH}_3$ , 10% $\text{O}_2$ , 7% $\text{CO}_2$ , 2.5% $\text{H}_2\text{O}$ in balance $\text{N}_2$ between temperatures of 40°C and 180°C on a Cu-SSZ-13 sample (Si:Al = 4.5, Cu wt% = 3.8, Cu:Al = 0.21). ....	241
<b>Figure 149.</b> NO selectivity to $\text{NO}_2$ during standard SCR gas feed conditions between 180 to 40°C on a Cu-SSZ-13 sample (Si:Al = 4.5, Cu wt% = 3.8, Cu:Al = 0.21). NO selectivity $\text{N}_2$ and $\text{H}_2\text{O}$ via standard SCR is 100% at 180°C, but decreases to 30% at 150°C at which the selectivity	

stabilizes out between 150 and 40°C. Between this temperature range the NO selectivity is 70% to NO<sub>2</sub>. ..... 241

**Figure 150.** Arrhenius plots for the forward NO consumption rates during standard SCR gas conditions (300 ppm NO, 300 ppm NH<sub>3</sub>, 10% O<sub>2</sub>, 7% CO<sub>2</sub>, 2.5% H<sub>2</sub>O in balance N<sub>2</sub> between temperatures of 40°C and 180°C on a series of Cu-SSZ-13 samples with different Al and Cu densities (top graph). NO selectivity to NO<sub>2</sub> during standard SCR gas feed conditions between 180 to 40°C on a series of Cu-SSZ-13 samples with different Al and Cu densities (bottom graph). ..... 242

**Figure 151.** Apparent activation energies at 70°C on the series of Cu-SSZ-13 samples with varying Al and Cu densities (top graph). Forward NO reaction rates at 70°C under standard SCR gas conditions (300 ppm NO, 300 ppm NH<sub>3</sub>, 10% O<sub>2</sub>, 7% CO<sub>2</sub>, 2.5% H<sub>2</sub>O in balance N<sub>2</sub>) (bottom graph). ..... 243

**Figure 152.** The NO oxidation rate with a standard SCR gas feed (300 ppm NO, 300 ppm NH<sub>3</sub>, 10% O<sub>2</sub>, 7% CO<sub>2</sub>, 2.5% H<sub>2</sub>O, balance N<sub>2</sub>) decreases with increasing sulfation, suggesting that sulfur species decrease the reaction rate by either removing confining environments, restricting access to Cu sites, or a combination of both. .... 244

**Figure 153.** Effect of Na:Al ratio on the (a) SCR NO consumption rate normalized per mol Cu, (b) Eapp, and (c) NH<sub>3</sub>, NO, and O<sub>2</sub> orders. All four samples have the same Cu wt% of 1.00 ± 0.05, but varying Na<sup>+</sup> loadings between 0.00 to 0.25. .... 246

**Figure 154.** Arrhenius plots of the four Cu-Na-ZSM-5 samples tested for standard SCR rate. The temperature used was 190°C with feed conditions of 320 ppm NH<sub>3</sub>, 320 ppm NO, 10% O<sub>2</sub>, 7% CO<sub>2</sub>, and 3.5% H<sub>2</sub>O. NH<sub>3</sub> orders were taken with NH<sub>3</sub> concentrations ranging from 150 ppm and 500 ppm NH<sub>3</sub>. NO orders were taken with NO concentrations ranging from 100ppm and 500 ppm NO. O<sub>2</sub> orders were taken with O<sub>2</sub> concentrations ranging from 2% to 15%..... 247

**Figure 155.** UV-Visible spectra on BaSO<sub>4</sub> baseline powder, H-ZSM-5 (Si:Al = 12.5), and four different Cu-Na-ZSM-5 materials with the same Cu:Al molar ratio of 0.11, but different Na:Al ratios ranging from 0.00 to 0.23..... 248

**Figure 156.** Screenshot of the CHA unit cell from the International Zeolite Association (IZA) website. Image was generated using an atomic simulation environment (ASE) python code [183]. ..... 249

<b>Figure 157.</b> Schematic illustrating the computations necessary to determine the adsorption energy ( $\text{NH}_3$ , blue, used as illustration) of adsorbates on a Cu atom (brown) in the SSZ-13 framework (tan = silicon, dark tan = aluminum, red = oxygen).....	250
<b>Figure 158.</b> Chabazite energies computed using LCAO for a $\text{Cu}^{2+}$ charge balanced by two framework Al in a six membered ring at 1 nearest-neighbor (NN), 2 NN, and 3 NN positions.	251
<b>Figure 159.</b> Parity plot between computed Cu-O distances between $\text{Cu}^{2+}$ and framework O atoms in the chabazite 6 membered ring computed in this work compared to those reported by McEwen et al. [184].....	251
<b>Figure 160.</b> Tabulated list of adsorbates and metals used in this study. The yellow arrow points to the location of the metal center in the chabazite unit cell.....	253
<b>Figure 161.</b> Scaling relations for $\text{NH}_x$ on metal-SSZ-13. ....	253
<b>Figure 162.</b> Scaling relations for $\text{NO}_x$ and $\text{N}_2\text{O}$ on metal-SSZ-13. ....	253
<b>Figure 163.</b> Scaling relations for $\text{CH}_x$ on metal-SSZ-13.....	254
<b>Figure 164.</b> Scaling relations for $\text{SO}_x$ on metal-SSZ-13.....	254
<b>Figure 165.</b> NO consumption SCR reaction rates normalized per gram of material plotted versus the metal wt% (left). NO consumption SCR reaction rates normalized per mol metal loaded versus the metal wt%. ....	257
<b>Figure 166.</b> DFT-computed $\text{NH}_3$ binding energies onto a variety of $\text{M}^{2+}$ sites charged balanced by two anionic sites on a SSZ-13 framework. ....	258
<b>Figure 167.</b> Experimentally measured standard SCR reaction rates normalized per mol active metal plotted versus the DFT-computed binding energies. Cu-zeolites turns over the fastest, Fe- and Ag- with mediocre rates, and Ru-, W-, and Co- with poor rates. ....	259
<b>Figure 168.</b> Experimentally measured standard SCR apparent activation energies plotted versus the DFT-computed binding energies. The increase in apparent activation energy with increasing binding energy may be due to electronic effects of isolated metal active sites. ....	259
<b>Figure 169.</b> $\text{NH}_3$ oxidation rates (300 ppm $\text{NH}_3$ , 10% $\text{O}_2$ , 2.5% $\text{H}_2\text{O}$ , in balance $\text{N}_2$ , 300°C) as a function of the Cu wt% collected on Cu-SSZ-13 materials with different Al and Cu densities (left graph). The square root of the $\text{NH}_3$ oxidation rate plotted versus the Cu wt% results in a linear relationship (right graph). ....	262
<b>Figure 170.</b> $\text{NH}_3$ oxidation rates normalized per gram of catalyst as a function of $\text{O}_2$ concentration on a series of Cu-SSZ-13 catalysts with varying Cu densities. Samples with Si:Al	

ratios of 4.5 (red), 15 (blue), and 25 (green) were tested. Two Cu-SSZ-13 Si:Al =15 catalysts with the same Al density and Cu density, but different Al distributions were also tested -- NH<sub>3</sub> reaction rates between these two samples matched within error. .... 262

**Figure 171.** Apparent activation energies, NH<sub>3</sub> order, and O<sub>2</sub> orders for NH<sub>3</sub> oxidation (300 ppm NH<sub>3</sub>, 10% O<sub>2</sub>, balance N<sub>2</sub>, 300°C) on a series of Cu-SSZ-13 materials without co-feeding H<sub>2</sub>O (solid shapes) and with co-feeding 2.5% H<sub>2</sub>O (hollow shapes). .... 263

**Figure 172.** Cu(II) fraction transients measured as a function of time on a Cu-SSZ-13 catalyst (Si:Al = 15, Cu wt% = 3) during NH<sub>3</sub> saturation at 200°C of a calcined catalyst with only Cu(II) (left graph). Steady state Cu(I) fractions after NH<sub>3</sub> saturation with O<sub>2</sub> (red squares) and with only NH<sub>3</sub> (blue diamonds) (right graph). .... 263

**Figure 173.** Three possible pathways for NH<sub>3</sub> oxidation: (1) direct oxidation to N<sub>2</sub> and H<sub>2</sub>O, (2) Oxidation to NO, then to N<sub>2</sub> and H<sub>2</sub>O via standard SCR, (3) oxidation to NO<sub>2</sub>/NO, then to N<sub>2</sub> and H<sub>2</sub>O via fast SCR. .... 264

**Figure 174.** SCR reaction rate on a physical mixture of Cu-SiO<sub>2</sub> and H-SSZ-13 as a function of time. The physical mixture was activated at 237°C (blue triangles) and 330°C (red circles). ... 265

**Figure 175.** Arrhenius plots of activated Cu-SiO<sub>2</sub> and H-SSZ-13 physical mixtures after activation at 237°C (red squares) and 330°C (green triangles). The reaction rate on Cu-SiO<sub>2</sub> is represented by the blue diamond. .... 266

**Figure 176.** Arrhenius plot for the proton transport rate measured from Impedance Spectroscopy (IS) over a H-ZSM-5 material (Si:Al = 60) in the presence of 1% H<sub>2</sub>O (grey circles), 100 ppm NH<sub>3</sub> (black circles), and dehydrated (black x's). Figure adapted from Franke et al. [200,201]. 266

**Figure 177.** Arrhenius plots for the consumption of NO during standard SCR feed conditions for a Cu-SSZ-13 catalyst with most Cu ions as Z<sub>2</sub>Cu (left) and as ZCuOH (right). .... 267

**Figure 178.** Arrhenius plots for the initial rate of decrease after cutting off NH<sub>3</sub> from a catalyst operating at differential steady state under standard SCR conditions (300 ppm NH<sub>3</sub>, 300 ppm NO, 10% O<sub>2</sub>, 7% CO<sub>2</sub>, 2.5% H<sub>2</sub>O, balance N<sub>2</sub> at temperatures between 160 to 240°C) on a Cu-SSZ-13 material (Si:Al = 4.5 ,Cu:Al = 0.21). Fitting the initial rate to a first order rate law gives a better fit than fitting it to a second order rate law. .... 267

**Figure 179.** NH<sub>3</sub> concentration over an initially fresh Cu-ZSM-5 catalyst over the course of exposure to standard SCR conditions (300 ppm NH<sub>3</sub>, 300 ppm NO, 10% O<sub>2</sub>, 8% CO<sub>2</sub>, 2.5% H<sub>2</sub>O, balance N<sub>2</sub>) at 400°C for 40 hours. .... 268

- Figure 180.** Standard SCR reaction rates on fresh Cu-ZSM-5 catalyst after exposure to standard SCR conditions (300 ppm NH<sub>3</sub>, 300 ppm NO, 10% O<sub>2</sub>, 7% CO<sub>2</sub>, 2.5% H<sub>2</sub>O, balance N<sub>2</sub>) at 400°C for 40 hours. The apparent activation energy at 200°C decreases from 60 kJ mol<sup>-1</sup> to 30 kJ mol<sup>-1</sup> ..... 269
- Figure 181.** Arrhenius plots for the SCR NO reduction rate (black diamonds) and the N<sub>2</sub>O formation rate during SCR (black crosses) on model Cu<sub>x</sub>O<sub>y</sub>, Z<sub>2</sub>Cu, and ZCuOH Cu-SSZ-13 materials. Standard SCR conditions were used (300 ppm NH<sub>3</sub>, 300 ppm NO, 10% O<sub>2</sub>, 8% CO<sub>2</sub>, 2.5% H<sub>2</sub>O, balance N<sub>2</sub>, 150 to 250°C). ..... 272
- Figure 182.** The N<sub>2</sub>O formation rate over Z<sub>2</sub>Cu (hollow triangles) and ZCuOH (hollow diamonds) Cu-SSZ-13 catalysts before and after sulfur poisoning and after desulfation. The presence of sulfation suppresses the N<sub>2</sub>O formation rate with ZCuOH exhibiting the largest decrease in N<sub>2</sub>O formation after sulfur poisoning. .... 275
- Figure 183.** Although the presence of sulfur suppresses both the standard SCR and N<sub>2</sub>O formation rate, the N<sub>2</sub>O formation rate is suppressed to greater extents than the standard SCR rate after sulfation and desulfation on the model ZCuOH Cu-SSZ-13 (diamonds). Sulfation suppresses the N<sub>2</sub>O formation rate and standard SCR rate by approximately equal extents on model Z<sub>2</sub>Cu Cu-SSZ-13 (triangles). ..... 276
- Figure 184.** The N<sub>2</sub>O formation apparent activation energy does not change within error with increasing sulfur poisoning on both model Z<sub>2</sub>Cu (hollow triangles) and ZCuOH (hollow diamonds) Cu-SSZ-13 materials. The standard SCR apparent activation energy decreases with increasing sulfur poisoning on ZCuOH model Cu-SSZ-13 (solid diamonds), but does not change with increasing sulfur poisoning on Z<sub>2</sub>Cu model Cu-SSZ-13 (solid triangles). ..... 277
- Figure 185.** Arrhenius plots of standard SCR rates (black diamonds) and N<sub>2</sub>O formation rates during standard SCR (crosses) on (a) unsulfated, (b) 200°C SO<sub>2</sub>, (c) 400°C SO<sub>2</sub>, (d) 200°C SO<sub>2</sub> desulfated, (e) 400°C SO<sub>2</sub> desulfated model ZCuOH catalysts. .... 278
- Figure 186.** Arrhenius plots of standard SCR rates (black diamonds) and N<sub>2</sub>O formation rates during standard SCR (crosses) on (a) unsulfated, (b) 200°C SO<sub>2</sub>, (c) 400°C SO<sub>2</sub>, (d) 200°C SO<sub>2</sub> desulfated, (e) 400°C SO<sub>2</sub> desulfated model Z<sub>2</sub>Cu catalysts. .... 279
- Figure 187.** Photo of the vacuum filter Erlenmeyer flask setup for bubbling SCR gases through a Cu(NO<sub>3</sub>)<sub>2</sub> solution. .... 280

**Figure 188.**  $\text{NH}_3$  concentration as a function of time through a blank Erlenmeyer flask (grey trace), water (black trace), and 1.0 M  $\text{Cu}(\text{NO}_3)_2$  (dashed black trace). At time zero the SCR mixture started flowing at time zero. The breakthrough time delay before appearance of  $\text{NH}_3$  into the MKS FTIR 2030 is due to  $\text{NH}_3$  displacing the inert  $\text{N}_2$  in the piping and Erlenmeyer flask.

..... 282

**Figure 189.**  $\text{NO}$  concentration as a function of time through a blank Erlenmeyer flask (grey trace), water (black trace), and 1.0 M  $\text{Cu}(\text{NO}_3)_2$  (dashed black trace). The standard SCR mixture started flowing at time zero. The breakthrough time delay before appearance of  $\text{NO}$  into the MKS FTIR 2030 is due to  $\text{NO}$  displacing the inert  $\text{N}_2$  in the piping and Erlenmeyer flask..... 282



## LIST OF ABBREVIATIONS

Abbreviation	Meaning
NO <sub>x</sub>	Nitrogen oxides (x = 1,2)
NH <sub>3</sub>	Ammonia
PM	Particulate matter
SO <sub>x</sub>	Sulfur oxides
HC	Hydrocarbons
H <sub>2</sub> O	Water
O <sub>2</sub>	Oxygen
CO <sub>2</sub>	Carbon dioxide
He	Helium
Ar	Argon
Co	Cobalt
Cu	Copper
Fe	Iron
-OH	Hydroxide ligand
BA	Brønsted Acid
Al <sub>f</sub>	Framework-Aluminum
Si:Al	Silicon to Aluminum ratio
Cu:Al <sub>f</sub>	Copper to framework-Aluminum ratio
DOC	Diesel Oxidation Catalyst
LNT	Lean NO <sub>x</sub> Traps
NSR	NO <sub>x</sub> Storage and Reduction
SCR	Selective Catalytic Reduction
CHA	<b>Ch</b> abazite framework (includes SSZ-13 and SAPO-34)
MFI	<b>M</b> ordenite <b>F</b> ramework <b>I</b> nverted framework (includes ZSM-5)
FAU	<b>Fau</b> jasite framework (includes zeolite Y)
SSZ-13	aluminosilicate zeolite with the CHA framework
SAPO-34	<b>Silico</b> aluminum <b>phosph</b> ate molecular sieve with the CHA framework
ZSM-5	aluminosilicate zeolite with the MFI framework ( <b>Z</b> eolite <b>S</b> ocony <b>M</b> obil-5)

Y	aluminosilicate zeolite with the FAU framework
6MR	Six-membered ring
8MR	Eight-memberd ring
TOR	Turnover Rate (rate per active site)
RLS	Rate limiting step
M	Molar (moles per liter)
TPD	Temperature Programmed Desorption
UV-Vis-NIR	Ultraviolet-Visible-Near Infrared spectroscopy
XAS	X-ray Absorption Spectroscopy
XANES	X-ray Absorption Near-Edge Spectroscopy
EXAFS	Extended X-ray Absorption Fine Structure
IR	Infrared spectroscopy
XRD	X-ray Diffraction
AAS	Atomic Absorption Spectroscopy
SEM	Scanning Electron Microscopy
EDS	Electron Dispersive Spectroscopy
DFT	Density Functional Theory

## ABSTRACT

Author: Shih, Arthur, J. Doctor of Philosophy in Chemical Engineering

Institution: Purdue University

Degree Received: December 2018

Title: Synthesis and Characterization of Copper-Exchanged Zeolite Catalysts and Kinetic Studies on NO<sub>x</sub> Selective Catalytic Reduction with Ammonia

Committee Chair: Ribeiro, Fabio, H.

Although Cu-SSZ-13 zeolites are used commercially in diesel engine exhaust after-treatment for abatement of toxic NO<sub>x</sub> pollutants via selective catalytic reduction (SCR) with NH<sub>3</sub>, molecular details of its active centers and mechanistic details of the redox reactions they catalyze, specifically of the Cu(I) → Cu(II) oxidation half-reaction, are not well understood. A detailed understanding of the SCR reaction mechanism and nature of the Cu active site would provide insight into their catalytic performance and guidance on synthesizing materials with improved low temperature (< 473 K) reactivity and stability against deactivation (e.g. hydrothermal, sulfur oxides). We use computational, titration, spectroscopic, and kinetic techniques to elucidate (1) the presence of two types of Cu<sup>2+</sup> ions in Cu-SSZ-13 materials, (2) molecular details on how these Cu cations, facilitated by NH<sub>3</sub> solvation, undergo a reduction-oxidation catalytic cycle, and (3) that sulfur oxides poison the two different types of Cu<sup>2+</sup> ions to different extents at via different mechanisms.

Copper was exchanged onto H-SSZ-13 samples with different Si:Al ratios (4.5, 15, and 25) via liquid-phase ion exchange using Cu(NO<sub>3</sub>)<sub>2</sub> as the precursor. The speciation of copper started from the most stable Cu<sup>2+</sup> coordinated to two anionic sites on the zeolite framework to [CuOH]<sup>+</sup> coordinated to only one anionic site on the zeolite framework with increasing Cu:Al ratios. The number of Cu<sup>2+</sup> and [CuOH]<sup>+</sup> sites was quantified by selective NH<sub>3</sub> titration of the number of residual Brønsted acid sites after Cu exchange, and by quantification of Brønsted acidic Si(OH)Al and CuOH stretching vibrations from IR spectra. Cu-SSZ-13 with similar Cu densities and anionic framework site densities exhibit similar standard SCR rates, apparent activation energies, and orders regardless of the fraction of Z<sub>2</sub>Cu and ZCuOH sites, indicating that both sites are equally active within measurable error for SCR.

The standard SCR reaction uses  $O_2$  as the oxidant ( $4NH_3 + 4NO + O_2 \rightarrow 6H_2O + 4N_2$ ) and involves a Cu(I)/Cu(II) redox cycle, with Cu(II) reduction mediated by NO and  $NH_3$ , and Cu(I) oxidation mediated by NO and  $O_2$ . In contrast, the fast SCR reaction ( $4NH_3 + 2NO + 2NO_2 \rightarrow 6H_2O + 4N_2$ ) uses  $NO_2$  as the oxidant. Low temperature (437 K) standard SCR reaction kinetics over Cu-SSZ-13 zeolites depend on the spatial density and distribution of Cu ions, varied by changing the Cu:Al and Si:Al ratio. Facilitated by  $NH_3$  solvation, mobile Cu(I) complexes can dimerize with other Cu(I) complexes within diffusion distances to activate  $O_2$ , as demonstrated through X-ray absorption spectroscopy and density functional theory calculations. Monte Carlo simulations are used to define average Cu-Cu distances. In contrast with  $O_2$ -assisted oxidation reactions,  $NO_2$  oxidizes single Cu(I) complexes with similar kinetics among samples of varying Cu spatial density. These findings demonstrate that low temperature standard SCR is dependent on Cu spatial density and requires  $NH_3$  solvation to mobilize Cu(I) sites to activate  $O_2$ , while in contrast fast SCR uses  $NO_2$  to oxidize single Cu(I) sites.

We also studied the effect of sulfur oxides, a common poison in diesel exhaust, on Cu-SSZ-13 zeolites. Model Cu-SSZ-13 samples exposed to dry  $SO_2$  and  $O_2$  streams at 473 and 673 K. These Cu-SSZ-13 zeolites were synthesized and characterized to contain distinct Cu active site types, predominantly either divalent  $Cu^{2+}$  ions exchanged at proximal framework Al sites ( $Z_2Cu$ ), or monovalent  $CuOH^+$  complexes exchanged at isolated framework Al sites ( $ZCuOH$ ). On the model  $Z_2Cu$  sample, SCR turnover rates (473 K, per Cu) catalyst decreased linearly with increasing S content to undetectable values at equimolar S:Cu molar ratios, while apparent activation energies remained constant at  $\sim 65 \text{ kJ mol}^{-1}$ , consistent with poisoning of each  $Z_2Cu$  site with one  $SO_2$ -derived intermediate. On the model  $ZCuOH$  sample, SCR turnover rates also decreased linearly with increasing S content, yet apparent activation energies decreased monotonically from  $\sim 50$  to  $\sim 10 \text{ kJ mol}^{-1}$ , suggesting that multiple phenomena are responsible for the observed poisoning behavior and consistent with findings that  $SO_2$  exposure led to additional storage of  $SO_2$ -derived intermediates on non-Cu surface sites. Changes to  $Cu^{2+}$  charge transfer features in UV-Visible spectra were more pronounced for  $SO_2$ -poisoned  $ZCuOH$  than  $Z_2Cu$  sites, while X-ray diffraction and micropore volume measurements show evidence of partial occlusion of microporous voids by  $SO_2$ -derived deposits, suggesting that deactivation may not only reflect

Cu site poisoning. Density functional theory calculations are used to identify the structures and binding energies of different  $\text{SO}_2$ -derived intermediates at  $\text{Z}_2\text{Cu}$  and  $\text{ZCuOH}$  sites. It is found that bisulfates are particularly low in energy, and residual Brønsted protons are liberated as these bisulfates are formed. These findings indicate that  $\text{Z}_2\text{Cu}$  sites are more resistant to  $\text{SO}_2$  poisoning than  $\text{ZCuOH}$  sites, and are easier to regenerate once poisoned.

# 1. INTRODUCTION

## 1.1 Energy Outlook

Energy is one of the grand challenges of our time. The world is dependent on fossil fuels (coal, oil, natural gas), and its demand for energy has and is growing rapidly. On the basis of joules, the world energy consumption of fossil fuels has increased from near 0% in 1800, to 40% in 1900, to 60% in 2000, and to 70% in 2018, relative to the total amount of energy consumed during that particular year [1,2]. The world energy consumption of energy from renewable sources have increased from ~3% in 2000 to ~7% in 2018 as renewable energy continues to gain importance. With the recent boom in shale gas resources in the United States [2,3], and subsequent decrease in fuel prices, it is expected that our dependence on fuel will continue in the near future. To prepare for the end of our dependence on fossil fuels as we know it, a push to develop technologies that derive energy from alternative sources (preferably renewable) in addition to technologies that store or transport energy has become more and more prevalent over the last few decades.

The convenience and price of fossil fuels, stemming primarily from the infrastructure of drilling, refining, distributing, and consuming fossil fuels built over the century will be a challenge to beat. For instance, from back-of-the-envelope calculations (Appendix A.1) the amount of energy in a full tank of gasoline (~15 gallons) is enough energy to charge 50,000 smartphones. Better yet, all this energy can be transferred from the pump to the tank in just 1 to 3 minutes, equivalent to an energy transfer rate of 1,000,000 watts (Joules per second). In comparison, the energy transfer rate while charging an electric vehicle is approximately 1,000 watts (three orders of magnitude slower) and the energy transfer rate while charging a cell phone is approximately 5 watts (five orders of magnitude slower). The point is, for another energy source to truly beat gasoline, additional factors beyond price (such as the high energy transfer rate convenience of gasoline stations) play an integral role. Fossil fuels are here to stay for the near future as alternate technologies become cheaper and more convenient through continued research, development, and commercialization.

## 1.2 The Increased Consumption of Fossil Fuels and Subsequent Increase in Pollution

When drilling for oil took off in the late 1800s, fuels in the gasoline and diesel range were in such low demand that it was dirt cheap. Interestingly, kerosene was the most sought after fraction of fuel [4]. With the invention of the combustion engine, its application in automobiles, and the government's investment in building and maintaining a transportation systems conducive to personal vehicles (pushed partially by car companies), gasoline and diesel demand skyrocketed throughout the 1900s, leading to an increase in production and additional air pollution from personal vehicles [5].

It was not until environmental (acid rain), human health (respiratory irritation and diseases), and global (visibility, warming) issues became prevalent when communities started cracking down on the issue [5]. In the 1970, the United States Environmental Protection Agency was established to maintain and enforce pollution prevention programs and energy conservation efforts [6]. EPA identified six criteria air pollutants: carbon monoxide (CO), ozone (O<sub>3</sub>), lead, nitrogen oxides (NO<sub>x</sub>), particulate matter (PM), and sulfur oxides (SO<sub>x</sub>) and set upper emission limits that became more and more stringent over time, allowing industries enough to plan and invest in researching and developing technologies to adapt to the new regulations [7] (Figure 1). NO<sub>x</sub> gases are released by two major sources: stationary sources such as power plants, and mobile sources such as vehicles. Mobile sources of NO<sub>x</sub> emissions contribute to the majority of all NO<sub>x</sub> emissions in the US (Figure 1), of which approximately half are due to lean-burn diesel engines. [8–12]

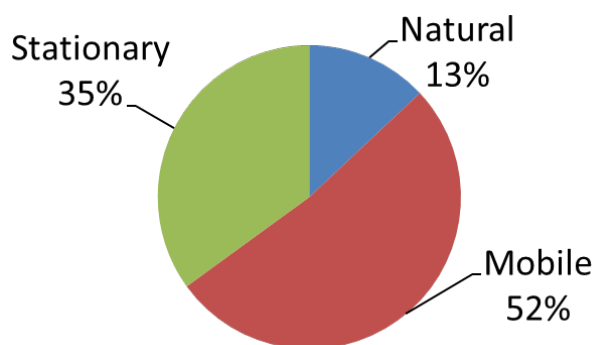


**Figure 1.** United States NO<sub>x</sub> Production by Sector. Data adapted from EPA NO<sub>2</sub> Risk and Exposure Assessment Report [13].

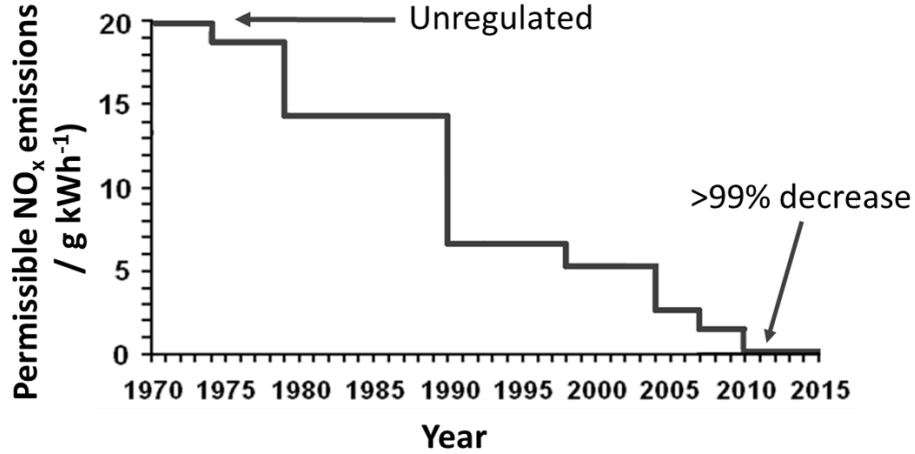
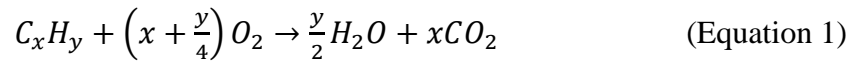


**Figure 2.** NO<sub>x</sub> emission regulations since the United States Clean Air Act of 1970. Data adapted from Cummins Sustainability Report [7].

### 1.3 Aftertreatment Technologies for Gasoline and Diesel Engines

Gasoline engines feed in hydrocarbon fuel (gasoline) and oxygen (from the air) in stoichiometric ratios such that complete combustion to only H<sub>2</sub>O and CO<sub>2</sub> occurs (ideally) by the time the exhaust leaves the tailpipe, as represented by Equation 1, where C<sub>x</sub>H<sub>y</sub> is the hydrocarbon fuel molecule with x carbons and y hydrogens.



Gasoline engines are inefficient in utilizing the total chemical energy stored between hydrogen-carbon bonds in the gasoline hydrocarbon fuel. In a 1993 study by Cheng et al. [14], 10% of gasoline leaves the engine block unburned. In more recent studies, it is reported that 100 ppm of hydrocarbons exit gasoline engines unburned, equivalent to approximately 0.7% of the gasoline injected into the engine [15]. This unburned hydrocarbon is accompanied with a stoichiometric amount of carbon monoxide in addition to nitrogen oxides, which are formed N<sub>2</sub> and O<sub>2</sub> in the air itself is combusted at the high temperatures (>700°C), Equation 2.

$$\%O_2 = 20 \cdot \frac{(A:F)}{(A:F)+1} \quad (\text{Equation 3})$$



The oxygen concentration in an air-fuel mixture increases with increasing air-to-fuel ratio (Equation 3, Figure 3). Keeping the air-fuel mixture injection rate into the engine constant and increase in the air-to-fuel ratio leads to a decrease in the amount of fuel per injection, and thus a decrease in fuel consumption (Figure 3).

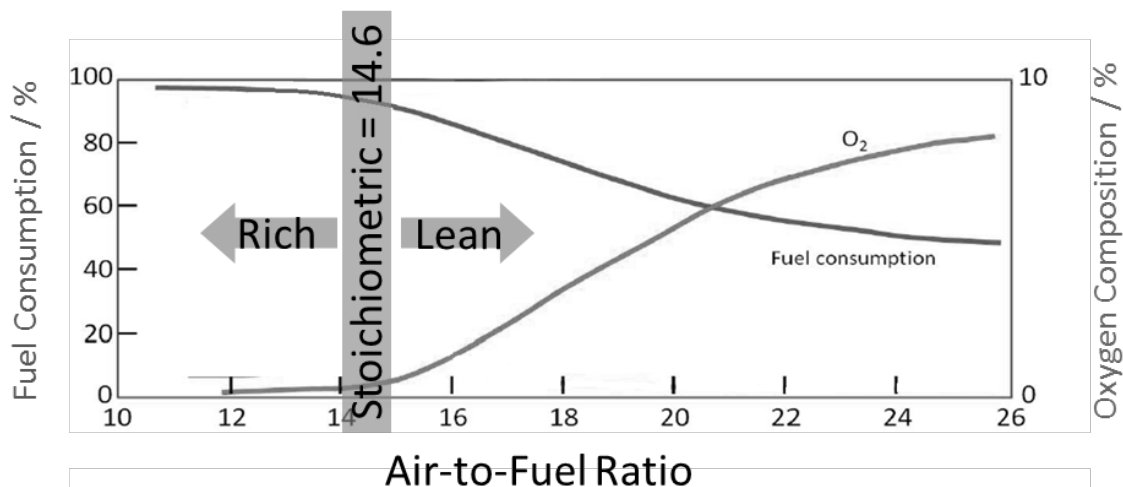


**Figure 3.** Oxygen concentration in % in the air-fuel mixture before injection into the engine as the function of the air-to-fuel ratio (right y-axis). The rate of fuel consumption during engine operation as a function of the air-to-fuel ratio (left y-axis).

One caveat of diesel engines is that the nature of the exhaust pollutants is different than those that are released from a gasoline engine. Diesel engines produce more particulate matter (e.g. soot) and because of the increase in oxygen during combustion, much more nitrogen oxides and less carbon monoxide and unburned hydrocarbons leave the engine.

The pollutants from gasoline engine exhaust (unburned hydrocarbons, carbon monoxide, and nitrogen oxides) are released in stoichiometric proportions and are converted to harmless  $O_2$ ,  $N_2$ ,  $H_2O$ , and  $CO_2$  via several reduction and oxidation routes (Equations 4 to 6) through a three way catalyst. As demonstrated by Takeuchi et al. [16], the three-way-catalyst displays high activity only when the air-to-fuel ratio, and thus exhaust pollutants are stoichiometric ( $A:F = 14.7$ ).

Three-way-catalysts do not perform for air-to-fuel ratios less than 14 or greater than 15 (**Figure 4**).

Reduction of nitrogen oxides:  $2NO_x \rightarrow xO_2 + N_2$  (Equation 4)

Oxidation of carbon monoxide:  $2CO + O_2 \rightarrow 2CO_2$  (Equation 5)

Oxidation of unburned hydrocarbons:  $C_xH_y + \left(x + \frac{y}{4}\right) O_2 \rightarrow \frac{y}{2} H_2O + xCO_2$  (Equation 6)

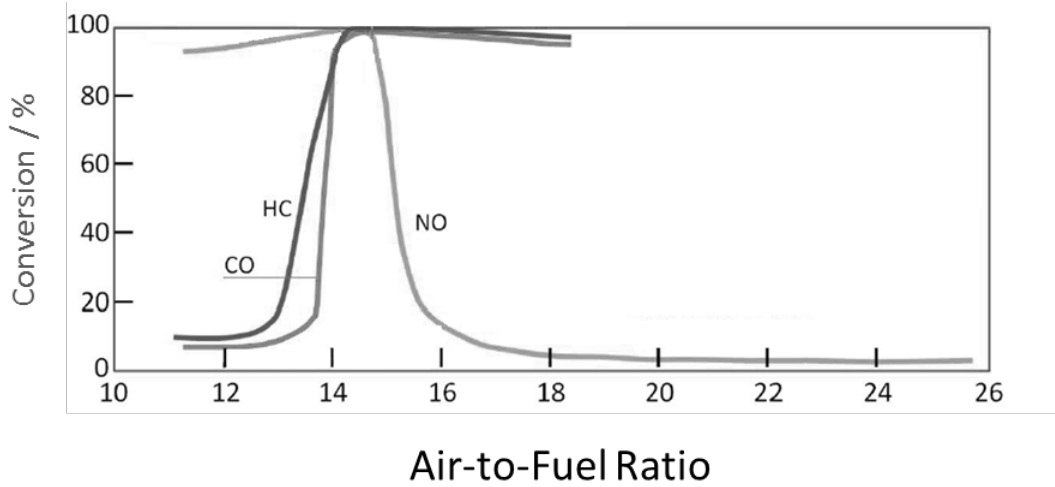


**Figure 4.** Catalytic conversion of carbon monoxide (CO), hydrocarbons (HC), and nitrogen oxide (NO) through a commercial three-way catalyst as a function of Air-to-fuel ratio. (Figure adapted from Takeuchi et al. [16])

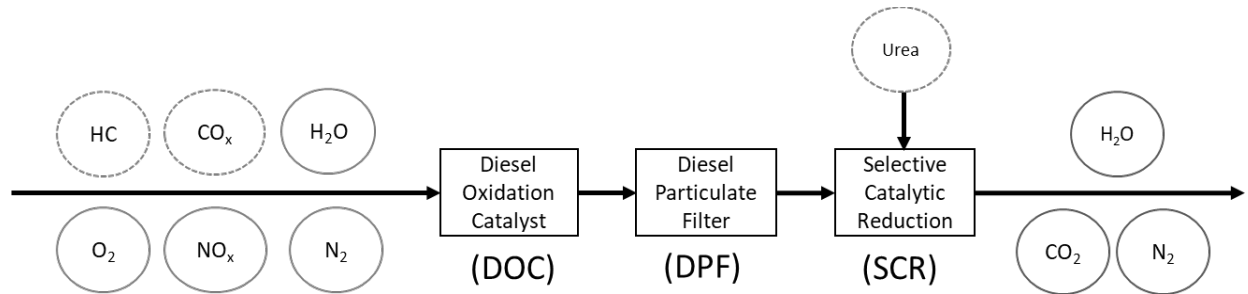


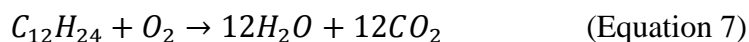
**Figure 5.** Schematic of a typical diesel exhaust aftertreatment system. [17]

Due to the extreme loss in activity (from near 100% conversion to less than 10% conversion) through a three-way-catalyst at air-to-fuel mixtures relevant to diesel engines (A:F between 17 to 80), automobile and engine manufacturers had to come up with a new solution. Decades of research and development since the 1970s has lead a diesel aftertreatment system where filter and catalytic reactors are placed in series to clean up diesel exhaust before release into the atmosphere (Figure 5). Exhaust from lean-burn diesel engines pass through three treatment stages after combustion: a diesel oxidation catalyst (DOC) to oxidize unburned hydrocarbons, a

particulate filter (PF) to remove particulates, and a selective catalytic reduction (SCR) reactor to reduce  $\text{NO}_x$  to  $\text{H}_2\text{O}$  and  $\text{N}_2$  in the presence of reductant (often  $\text{NH}_3$  or hydrocarbons) [9,18–20]. Due to the excess oxygen (Air-to-fuel ratio  $> 15$ ) in lean-burn diesel exhaust, reducing  $\text{NO}_x$  in the SCR reactor is difficult without the presence of a reductant and catalyst. Stoichiometric injection of reductant (as  $\text{H}_2$ ,  $\text{NH}_3$ , or hydrocarbons) into lean-burn engine exhaust has been studied over a variety of catalysts including base-oxides, noble metals, activated carbon, and metal-exchanged zeolites [21–23].

#### 1.4 Chemical Environment in the Aftertreatment System

Linnell et al. [24] used a diesel engine typical of motor coaches in cities and subjected it to rpm's ranging from 800 to 2000 with a range of loads. They analyzed the composition of the diesel exhaust directly leaving the engine using an FTIR, calorimetry, and gas chromatography. Table 1 shows the results of their measurements compared to the measurements we use in our simulated diesel exhaust. We do not co-feed hydrocarbons or carbon monoxide in our simulated diesel exhaust because the diesel oxidation catalyst upstream of the selective catalytic reduction catalyst would oxidize the hydrocarbons and carbon monoxide to  $\text{H}_2\text{O}$  and  $\text{CO}_2$ . To properly compare these values with the values recommended by our collaborators at Cummins Incorporated, we assume all the carbon monoxide and hydrocarbons oxidize to  $\text{CO}_2$  and  $\text{H}_2\text{O}$ . The average chemical formula for diesel fuel is  $\text{C}_{12}\text{H}_{24}$  [25], so Equation 7 was used to estimate the amount of  $\text{H}_2\text{O}$  and  $\text{CO}_2$  formed from the combustion of unburned diesel hydrocarbons through the diesel oxidation catalyst (DOC) upstream of the SCR catalyst.



The recommended simulated diesel exhaust concentrations fall within the range reported by Linnell et al. [24].

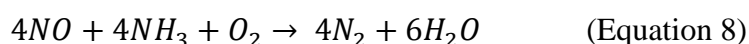
**Table 1.** Typical composition in real diesel exhaust collected by Linnell et al. [24] compared to simulated diesel exhaust conditions recommended by Cummins Inc. n.r. = not reported.

Molecule	Linnell et al.	Linnell et al. (assuming complete oxidation of CO and HC through DOC)	Simulated Diesel Exhaust
H <sub>2</sub> O	15400 to 87000	15800 to 88400	20000
CO <sub>2</sub>	17000 to 140000	17500 to 146000	80000
HC	33 to 120	0	0
CO	170 to 4800	0	0
NO	42 to 1000	42 to 1000	300
NO <sub>2</sub>	40 to 400	40 to 400	0
O <sub>2</sub>	n.r.	n.r.	10
SO <sub>2</sub>	6 to 90	6 to 90	0

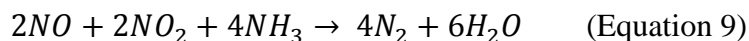
The temperature of diesel engine exhaust was reported by Gonzalez et al. [26] and Hussain et al. [27]. Both studies measured the temperature of the diesel exhaust with the engine running under various levels of load to be between the ambient outside temperature and 315°C. In reality, the upper limit of the exhaust temperature is 700°C due to the temperatures required to combust captured particulate matter in the particulate filter to CO<sub>2</sub> [9]. The temperature recommended by Cummins Incorporated was 200°C because the catalyst will spend most of its life around 200°C as the truck drives on the highway, well within the temperature range measured by Gonzalez et al. [26] and Hussain et al. [27].

### 1.5 The Selective Catalytic Reduction of NO<sub>x</sub> from Diesel Exhaust

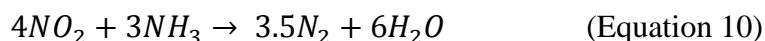
Several reactions are involved with the standard catalytic reduction (SCR) of NO<sub>x</sub> with NH<sub>3</sub> as a reductant. Today's diesel exhaust contains NO<sub>x</sub> mostly in the form of NO [28]. This particular reaction scheme is called standard SCR, Equation 8.



When a mixture of NO and NO<sub>2</sub> are present in a ratio of 1:1, the reaction proceeds faster, and is called the fast SCR reaction, shown below:



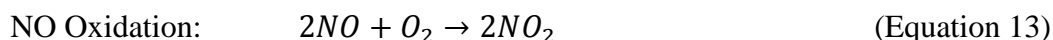
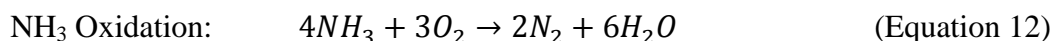
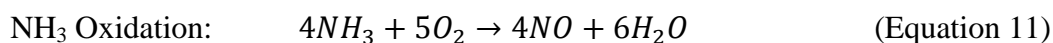
When an NO:NO<sub>2</sub> ratio exists higher than 1:1, NO<sub>2</sub> can react with NH<sub>3</sub> by itself, which has been called slow SCR, however, it is been seen to exhibit similar rates as standard SCR despite its name [28].



Together, these three reactions form the most common SCR reactions encountered under various gas conditions.

## 1.6 Parallel and Competing Reactions

Due to the presence of excess O<sub>2</sub> (~100000 ppm, 3 orders of magnitude higher than NH<sub>3</sub> and NO) in the presence of NH<sub>3</sub> (~300 ppm) and NO (~300 ppm), the oxidation of NH<sub>3</sub> (Equation 11 and Equation 12), oxidation of NO (Equation 13), and formation of N<sub>2</sub>O can also be energetically favorable pathways on the multi-dimensional reaction landscape [29]. The selectivity to these undesirable reactions depends on the catalyst, and its environment (gas concentrations, temperature).



## 1.7 Catalysts for SCR

Studies on metal-exchanged zeolites indicate that the presence of transition metals incorporated in the zeolite increase its activity for standard SCR. [28,30,31] Copper-exchanged chabazite (e.g. Cu-SSZ-13, Cu-SAPO-34) and iron-exchanged chabazite (Fe-CHA) are used commercially due to its increased resistance to hydrothermal aging and high activity at low-temperatures (~200°C) for Cu and high-temperatures (>300°C) for Fe [32,33] compared to catalysts synthesized with other zeolite supports. Although these materials are used commercially, their behavior still changes in unpredictable ways under SCR conditions and in even more unpredictable ways after hydrothermal deactivation or sulfur poisoning. Thus, the development of a predictive molecular

model of catalyst synthesis, preparation, and performance under all operating conditions is necessary to improve engine efficiency within emission constraints.

## 1.8 Chemistry of Zeolites

Zeolites are microporous crystalline aluminosilicate materials constructed from tetrahedral silicon (4+ charge) and tetrahedral aluminum (3+ charge) atoms connected by oxygen (2- charge) atoms. The International Zeolite Association (IZA) maintains a database with structural information on all zeolite types and to this day there are 232 synthesized zeolite frameworks, with 40 of them occurring naturally in nature [34].

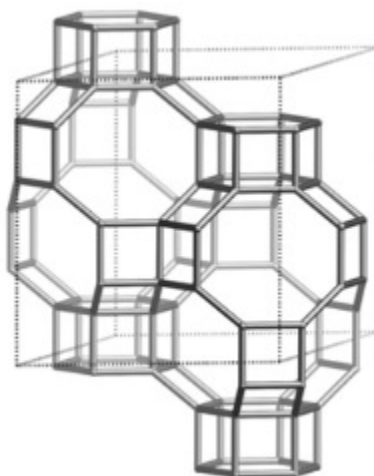


**Figure 6.** Chabazite unit cell adapted from the International Zeolite Association [34].

For illustration, a chabazite (CHA) zeolite will be used (Figure 6). Each straight line represents a bond between a Si or Al atom bridge by an oxygen atom, and each tetrahedral intersection represents a Si or Al atom. Since Al has a charge one lower than Si, an anionic site is introduced into the zeolite framework when an Al is introduced into the framework. This anionic site is charge balanced by extraframework cations (e.g.  $\text{Na}^+$ ,  $\text{H}^+$ ,  $\text{Cu}^+$ ,  $\text{Cu}^{2+}$ ).

Defects can also occur in the zeolite. At the edge of a zeolite crystallite, there are a number of terminal silanol groups (Si-OH) at Si that do not exhibit any neighboring Si or Al atoms. In addition, unstable Al in the zeolite framework can also exist as octahedral extraframework Al

atoms if that configuration is energetically more stable than in the tetrahedral framework-state. It has been demonstrated that the presence or absence of water is enough to interconvert Al between these two states [35,36].

## 1.9 Cu ion-exchange into chabazite zeolite supports

Several methods to get Cu on to chabazite zeolites are reported in the literature. In summary, they are: (1) one-shot Cu ion-exchange [37–43], (2) multiple Cu ion-exchanges in series [40,41,44], (3) incipient wetness impregnation (IWI) [45], (4) solid-State Exchange [46–50], and one-pot hydrothermal synthesis [51–53]. It is unclear whether one particular method produces materials with a higher rate per active site due to the lack of differential reaction rates in the literature, which would allow for proper comparison of rates. Commercially, the ideal catalyst would demonstrate sufficient activity without being overly expensive (time and cost) from its synthesis and manufacture.

## 1.10 Copper Site Location and Speciation in Cu-SSZ-13

The standard SCR research community has persevered to determine the location of the metal active sites on Cu-SSZ-13 under a wide variety of conditions including ambient, dehydrated, and standard SCR conditions [41,42,54–58]. Combining insight from DFT calculations and experiments, the community has converged on the claim that Cu is most stable when coordinated to the framework in the 6-membered ring (6MR) [54–56,59,60], and that once all the sites in the 6MR are filled, move on to coordinate to the 8-membered ring (8MR) [41,57].

With respect to speciation, several research groups have claimed isolated  $\text{Cu}^{2+}$  species [43,55,56,61,62],  $[\text{CuOH}]^+$  species [46,63], and Cu-O<sub>x</sub>-Cu dimeric species [62–64] as active sites on Cu-zeolites. These results may seem contradictory, but we will demonstrate how these contradictory results can be elucidated by tracking the synthesis, pre-treatment, and conditions at which the catalysts are studied. A number of studies have observed a change in the standard SCR kinetics at high temperature ( $>300^\circ\text{C}$ ) and have attributed it to a decrease in the  $\text{NH}_3$  storage capacity at those high temperatures, where  $\text{NH}_3$  is observed to desorb [63,65,66]. This change in kinetics at low ( $\sim 200^\circ\text{C}$ ) and high ( $>300^\circ\text{C}$ ) temperatures suggest that the SCR mechanism or rate limiting step(s) change due to changes in the intermediate coverages.

Studies on the mechanism on standard SCR since the 1970s have mostly been on vanadium oxide supported on titanium oxide, along with Cu- and Fe- exchanged zeolites. Literature agrees



that the mechanism involves a redox cycle with evidence stemming from cutoff experiments and XANES [40,43,56]. How reactant molecules interact and react with the metal active sites is still under heavy debate [30,43,57,65,67–73], in particular the oxidation half-cycle [43,68,74].

### **1.11 Standard SCR Kinetics collected over a number of laboratory and commercial catalysts**

Differential standard SCR kinetics have been collected on a wide variety of catalysts including vanadium oxide supported on titanium oxide, and Cu- and Fe- exchanged zeolites. A representative sample of kinetics collected using a variety of materials under differential conversion and negligible heat/mass-transfer limited conditions at temperatures between 150 and 300°C are reported in Table 2.

The apparent activation energy and reaction orders across all types of catalysts seem to be comparable, suggesting that the standard SCR mechanism may be similar between all these materials, with differences in the overall reaction rate stemming primarily from the transition metal active site's ability to adsorb reactants, react, and desorb products.

**Table 2.** Compilation of differential standard SCR kinetics collected under negligible heat/mass transfer conditions on a variety of catalysts active for standard SCR. (n.m. = not measured)

\*errors for activation energies and reaction orders are 95% confidence intervals from experiments performed in our work.

Catalyst	Apparent Activation Energy / kJ mol <sup>-1</sup> ( $\pm 7$ )*	NO Order ( $\pm 0.1$ )*	NH <sub>3</sub> Order ( $\pm 0.1$ )*	O <sub>2</sub> Order ( $\pm 0.1$ )*	Reference
V <sub>2</sub> O <sub>5</sub> /TiO <sub>2</sub>	48.5	1	0	n.m.	[75,76]
V <sub>2</sub> O <sub>5</sub> /Al <sub>2</sub> O <sub>3</sub>	n.m.	1	0	n.m.	[75,76]
V <sub>2</sub> O <sub>5</sub> /TiO <sub>2</sub>	n.m.	1	0	0.3 – 0.5	[77]
V <sub>2</sub> O <sub>5</sub> /TiO <sub>2</sub>	n.m.	1	0	0.2 – 0.5	[78]
V <sub>2</sub> O <sub>5</sub> /Al <sub>2</sub> O <sub>3</sub>	n.m.	1	0	0.4	[78]
V <sub>2</sub> O <sub>5</sub> /SiO <sub>2</sub> -TiO <sub>2</sub>	n.m.	0.5 – 0.6	-0.2 – 0.3	n.m.	[79]
V <sub>2</sub> O <sub>5</sub> /WO <sub>3</sub> -TiO <sub>2</sub>	n.m.	n.m.	-0.1 – 0.0	0.0 – 0.5	[80]
Mn <sub>2</sub> O <sub>3</sub> -WO <sub>3</sub> /Al <sub>2</sub> O <sub>3</sub>	n.m.	n.m.	0	0.1 – 0.5	[81]
Fe/Y	31 – 69	0.8 – 1.0	-0.4 – 0.1	n.m.	[82]
Fe/ZSM-5	n.m.	n.m.	n.m.	0.5	[83]
Cu/ZSM-5	35 – 60	1	n.m.	0.6	[84]
Cu/ZSM-5	38 – 77	0.5 – 0.7	-0.5 – -0.3	0.4 – 0.7	Purdue
Cu/SSZ-13	62	1	0	n.m.	[57]
Cu/SSZ-13	42 – 71	0.7-0.9	-0.3 – 0.1	0.1 – 0.5	[43]
Cu/SSZ-13	42 – 74	0.4 – 0.9	-0.7 – 0.1	0.3 – 0.9	Purdue
<b>Overall range</b>	<b>31- 77</b>	<b>0.4 - 1</b>	<b>-0.7 – 0.3</b>	<b>0.0 – 0.9</b>	

## 2. EXPERIMENTAL

This section will describe experimental procedures that span several chapters. Specialized procedures specific to a particular chapter will be introduced in that chapter.

### 2.1 Catalyst Synthesis

#### 2.1.1 Hydrothermal Synthesis of SSZ-13 Si:Al = 4.5

As-synthesized SSZ-13 (AS-SSZ-13) with a Si:Al ratio of 4.5 was synthesized based off a procedure developed by Zones, and later modified by Fickel et al. [54,85–87] 37.5 g of sodium silicate (Sigma Aldrich) was mixed with 30.0 g of 0.1 M NaOH (Alfa Aesar), 48.0 g of water and stirred for 15 minutes at ambient conditions. 3.75 g of NH<sub>4</sub>-Y (Zeolyst CBV100) was added to the mixture and stirred for 30 minutes at ambient conditions. 15.75 g of trimethyladamantylammonium hydroxide (Sachem, 25%) was added to the mixture and stirred for an additional 30 minutes. The resulting gel was transferred to Teflon-lined Parr autoclaves and loaded into a 140°C tumbling oven. The autoclaves were removed and quenched in H<sub>2</sub>O at room temperature after 6 to 10 days (typically 10 days).

#### 2.1.2 Hydrothermal Synthesis of SSZ-13 Si:Al = 15 and 25

As-synthesized SSZ-13 (AS-SSZ-13) with Si:Al ratios of 15 and 25 were synthesized using a recipe reported by Zones [34,88]. For the AS-SSZ-13 Si:Al = 15 zeolite, 28.4 g of trimethyladamantylammonium hydroxide (Sachem, 25%) was mixed with 71.4 g of H<sub>2</sub>O, 0.87 g of aluminum hydroxide (SPI Pharma, 99.9%), and 34.6 g of 1.0 M NaOH (Alfa Aesar), then stirred for 15 minutes at ambient conditions. 10 g of fumed silica (Cab-o-sil M-5) was added to the mixture and stirred for 2 hours at ambient conditions. The resulting gel was transferred to Teflon-lined Parr autoclaves and loaded into a 160°C tumbling oven. The autoclaves were removed and quenched in static H<sub>2</sub>O at room temperature after 10 days. The AS-SSZ-13 Si:Al = 25 sample followed the same procedure, but with 0.43 g of Al(OH)<sub>3</sub> instead.

### 2.1.3 Hydrothermal Synthesis of Si:Al = 100

The AS-SSZ-13 Si:Al = 100 sample was synthesized using the same procedure as the AS-SSZ-13 Si:Al = 15 and 25, but with addition of equimolar  $\text{Al}(\text{OH})_3$  (SPI Pharma, 99.9%) and HF (40 wt%, Sigma Aldrich) (0.13 g of  $\text{Al}(\text{OH})_3$  and 0.8 g of HF)

### 2.1.4 Hydrothermal Synthesis of Beta

As-synthesized Beta (AS-BEA) was synthesized using a procedure reported by Chang and Fan et al [89]. 0.7 g of NaOH pellets (Macon Fine Chem., 98%) was dissolved in 82.8 g tetraethylammonium hydroxide (Sigma Aldrich, 35% in  $\text{H}_2\text{O}$ ) for 15 minutes. 125.0 g Colloidal silica (HS-30, Sigma Aldrich, 30%) and 10.4 g of aluminum isopropoxide (Sigma Aldrich, 98%) was then added to the vessel. The resulting solution was capped and stirred for 24 hours. The solution was transferred to Teflon-lined Parr autoclaves and loaded into a 140°C static oven. The autoclaves were removed and quenched in  $\text{H}_2\text{O}$  at room temperature after 10 days.

### 2.1.5 Commercial ZSM-5

Commercial  $\text{NH}_4$ -ZSM-5 samples with Si:Al = 13 (CBV2314) and 30 (CBV5524G) were purchased from Zeolyst.

### 2.1.6 Work-up to H-zeolites

The as-synthesized zeolites were washed with Millipore UHP water and acetone until a pH of 8, then and dried between 50 to 100°C. The sample was crushed into a fine powder and calcined in a packed-bed flow-through furnace at 600°C in dry air (Indiana Oxygen, AirZero) for six hours with a ramp rate of 0.5°C min<sup>-1</sup> from ambient temperature to remove the template. The resulting Na-zeolite was then ion-exchanged in a 0.1 M solution of  $\text{NH}_4\text{NH}_3$  (Sigma Aldrich, 99.999%) at 80°C for 10+ hours. The solution was washed with  $\text{H}_2\text{O}$  and dried at 50°C. The resulting  $\text{NH}_4$ -zeolite (in addition to commercial  $\text{NH}_4$ -zeolites) was then calcined at 550°C in dry air (Indiana Oxygen, AirZero) for 6 hours with a ramp rate of 0.5°C min<sup>-1</sup> from ambient temperature.

### 2.1.7 Copper Ion Exchange

The parent H-zeolite was weighed and stirred vigorously in  $\text{H}_2\text{O}$  at 40°C for 30 minutes. A prepared 100 mL  $\text{Cu}(\text{NO}_3)_2$  solution with molarities ranging from 0.001 M to 0.100 M was added to the H-zeolite mixture. 0.1 M  $\text{NH}_4\text{OH}$  (Sigma Aldrich, 28%, diluted with Millipore

water) was added dropwise to adjust and maintain the pH of the solution at  $4.9 \pm 0.1$ . The solution was stirred until the pH stabilizes at  $\sim 4.9$  at  $40^\circ\text{C}$ , which typically takes 6+ hours. The resulting Cu-zeolite was centrifuged out and washed with 100 mL  $\text{H}_2\text{O}$  3 times then dried at  $50^\circ\text{C}$  to  $100^\circ\text{C}$ . The Cu-zeolite was then calcined in air at  $550^\circ\text{C}$  for 6 hours with a ramp rate of  $0.5^\circ\text{C min}^{-1}$  from ambient temperature. Once cool, the samples are pelleted and sieved to retain 125 to 250  $\mu\text{m}$  particles (W.S. TYLER No. 60 and No. 120 all-stainless-steel).

## **2.2 Characterization Methods**

### **2.2.1 XRD**

Powder X-ray diffraction (XRD) data were collected on a SmartLab Rigaku diffractometer using a Cu  $\text{K}(\alpha)$  radiation source operated at 1.76 kW. Two sample holders were used. For one, approximately 0.6 g of sample were loaded in a sample holder with a depth of 2 mm. The second, about 0.05 g of sample were loaded in a sample holder with a depth of 0.2 mm. Patterns were obtained from  $4$  to  $40^\circ 2\theta$  using a step size of  $0.01^\circ 2\theta$  and scan rate  $0.05^\circ 2\theta \text{ min}^{-1}$  at ambient conditions. XRD patterns were used to confirm the presence of peaks characteristic to a desired framework.

### **2.2.2 AAS**

Elemental analysis to measure the Si:Al and Cu:Al of the dissolved sample was performed using atomic absorption spectroscopy (AAS) on a Perkin-Elmer AAnalyst 300. Approximately 20 mg of sample were dissolved in 2 mL of HF (Mallenkrodt, 40 wt%) for 8+ hours in a high-density-polyethylene (HDPE) bottle, then diluted with between 50 to 120 mL deionized water (Millipore, Synergy UV Water Purification System,  $18.2 \text{ M}\Omega \text{ cm}^{-1}$  resistivity). Proper PPE, engineering controls, and emergency exposure precautions must be taken as HF is an extremely corrosive chemical and will directly attack calcium in human flesh. 1000 ppm standards for copper (Sigma Aldrich TraceCERT, 1000 mg/L Cu in nitric acid), silicon (Sigma Aldrich TraceCERT, 1000 mg/L Si in NaOH), aluminum (Sigma Aldrich TraceCERT, 1000 mg/L Al in nitric acid), and sodium (Sigma Aldrich TraceCERT, 1000 mg/L Na in nitric acid) were diluted to two to three concentrations within the linear calibration range in clean HDPE bottles for use as standards. Care must be taken to minimize contamination since ppm levels of contaminants and skew runs. A test we used to ensure bottles were clean was to fill the bottle with Millipore water, and to test

if the AAS detected trace amounts of Si, Al, Na, or Cu. During each run, a calibration (absorbance vs concentration) was generated at the beginning and end of each run to ensure that absorbances do not drift by more than 5% throughout the run. Each calibration and sample bottle was shaken vigorously before collecting concentrations to eliminate possible concentration gradients due to gravimetric separation.

### 2.2.3 NH<sub>3</sub>-TPD

H<sup>+</sup> sites on H-SSZ-13 and oxidized and reduced forms of Cu-SSZ-13 samples were measured using the NH<sub>3</sub> titration procedure described by Di Iorio et al. [90] Oxidizing pre-treatment involved heating in synthetic air (commercial grade, Indiana Oxygen) at 773 K while the reducing pre-treatment involved flowing 500 ppm NO (from 3.6% NO/Ar, Praxair) +500 ppm NH<sub>3</sub>(from 3% NH<sub>3</sub> in Ar, Praxair) at 473 K for 2 hours. 30 to 50 mg of each sample, in either its oxidized or reduced forms, was saturated with 500 ppm NH<sub>3</sub> diluted with UHP He (99.999% , Indiana Oxygen) at 433 K for 2 hr with a total flow rate of 350 mL min<sup>-1</sup>. Following this NH<sub>3</sub> saturation step, the sample was flushed with 2.5-3.0% water in UHP He (wet purge) for 8 hours at the same flow rate to desorb NH<sub>3</sub> bound to non-protonic sites. This wet purge was followed by a temperature programmed desorption (TPD) in UHP He from 433 K to 820 K at a ramp rate of 0.167 K s<sup>-1</sup>. The total moles of NH<sub>3</sub> desorbed during the TPD were measured using on-board calibrations in a MKS Multigas 2030 gas-phase FT-IR spectrometer [91]

Additional TPD experiments on H-zeolites were performed on a Micrometrics AutoChemII 2920 Chemisorption Analyzer equipped with an Agilent 5975C mass selective detector (MSD) was used to quantify the number of Brønsted acid sites per gram. TPD was performed on NH<sub>3</sub>-zeolite (sieved to particle diameters between 125 μm and 250 μm) secured between two quartz wool plugs in a quartz U-tube with a ramp of 10°C min<sup>-1</sup> from ambient temperature to 500°C under 50 mL min<sup>-1</sup> helium (UHP, 99.999%, Indiana Oxygen). The m/z of desorbed species, temperature, and thermal conductivity of the outlet gas stream were collected with respect to time during the TPD. Immediately following TPD, an argon (UHP, 99.999%, Indiana Oxygen) injection from a 0.5 cm<sup>3</sup> sample loop was used as an internal standard to correct for instrumental drift in the MSD signal over time. The argon pulse was produced by flowing 35 mL min<sup>-1</sup> Ar into a 0.5 cm<sup>3</sup> sample loop then injecting it into a 50 mL min<sup>-1</sup> He stream; the argon pulse is

broadened using a 200 mL expander after which its  $m/z = 40$  signal intensity is collected with respect to time by the MSD.

Contributions from fragments of  $H_2O$  ( $m/z = 18$ ) were scaled to the fragments of  $H_2O$  and  $NH_3$  ( $m/z = 17$ ) and removed to produce a signal only resulting from  $NH_3$ . The area of the  $NH_3$  feature ( $m/z = 17$ ) was normalized to the area of the Argon pulse ( $m/z = 40$ ) to determine the number of available Brønsted acid (BA) sites using an in-house intensity-to BA calibration curve.

Selective  $NH_3$  titration of Brønsted acid sites was used to quantify the number of Brønsted acid sites, as described in our previous publications [90,91]. Briefly, 500 ppm of  $NH_3$  in balance  $N_2$  is flown through the catalyst at 433 K until saturation, then a stream of 2%  $H_2O$  in balance  $N_2$  is used to flush out  $NH_3$  bound to Lewis acidic Cu sites until steady state. At this point, temperature-programmed desorption (TPD) is performed and the  $NH_3:Al$  is determined from integrating and quantifying the TPD profile.

#### 2.2.4 Al-NMR

$^{27}Al$  MAS NMR spectra were recorded on H-SSZ-13 to estimate the fraction of framework ( $Al_f$ ) and extraframework Al ( $Al_{ex}$ ) species present in each material. Spectra of H-SSZ-13 were collected using a Chemagnetics CMX400 400 MHz spectrometer in a wide-bore 9.4 Tesla magnet at the Purdue Interdepartmental NMR Facility. Spectra were acquired at ambient conditions from 456 scans with 12.5  $\mu s$  pulses and a 2 s delay and were measured at 104.24 MHz and a MAS rate of 5 kHz. Zeolite samples were hydrated by holding for > 48 hours in a desiccator containing a saturated potassium chloride (KCl) solution prior to packing in a 4mm  $ZrO_2$  rotor.

#### 2.2.5 SEM and EDS

Scanning electron microscopy (SEM) and energy dispersive spectroscopy (EDS) images on Zeolyst H-ZSM-5 samples were recorded using a Hitachi S-4800 microscope operating at an acceleration voltage of 25 kV at the Burke Nanotechnology Center at Purdue University. SEM and EDS images on H-SSZ-13 were recorded using a FEI Quanta 3D FEG<sup>®</sup> Dual-Beam SEM at the Life Science Microscopy Facility at Purdue University.

### 2.2.6 Ar-micropore

Argon (87 K) and nitrogen (77 K) micropore measurements were collected on a Micromeritics Accelerated Surface Area and Porosimetry (ASAP) 2020 system. Samples were first pelleted and sieved to retain particles between 180-250  $\mu\text{m}$  in diameter, degassed by heating 0.03–0.05 g of sample to 393 K ( $0.167\text{ K s}^{-1}$ ) under high vacuum ( $<5\text{ }\mu\text{mHg}$ ) for 2 h, and then further heated to 623 K ( $0.167\text{ K s}^{-1}$ ) under high vacuum ( $<5\text{ }\mu\text{mHg}$ ) for 8 hours. Extrapolation of the linear volumetric uptake during mesopore filling ( $\sim 0.08\text{--}0.30\text{ P/P}_0$ ) to zero relative pressure gave an estimate for the volume of adsorbed gas in micropores ( $\text{cm}^3\text{ g cat}^{-1}$  at STP).

### 2.2.7 Co-exchange

0.1 g of a H-SSZ-13 zeolite was stirred in 100 mL of 0.25 M  $\text{Co}(\text{NO}_3)_2$  for 24 hours, washed 5 times with 50 mL of water each. The Co:Al exchange ratio at saturation of paired  $\text{Al}_\text{f}$  sites was quantified using AAS.

### 2.2.8 UV-Visible-NIR

The UV-Visible-NIR spectra of H- and Cu-zeolites were taken at ambient conditions (calcined beforehand in air at  $550^\circ\text{C}$  for 6 hours and exposed to  $\sim 25^\circ\text{C}$  in air) with a Varian Cary 5000<sup>®</sup> UV-VIS-NIR spectrophotometer and Harrick-Scientific Praying-Mantis<sup>®</sup> diffuse reflectance optics and cell. Barium sulfate ( $\text{BaSO}_4$ , Sigma-Aldrich, 99%) was used for zero-absorbance background scans for background correction. UV-Visible-NIR spectra were collected with a scan speed of  $2000\text{ cm}^{-1}\text{ min}^{-1}$  from 4000 to  $50000\text{ cm}^{-1}$ . A mass of approximately 0.1 to 0.2 g of sample packed and flattened in a sample cup using a clean microscope slide where UV-Visible-NIR measurements were then performed. For Cu-zeolites, UV-Vis-NIR spectra show two bands, which are assigned to a  $\text{Cu}^{2+}$  d-d transition at  $\sim 12000\text{ cm}^{-1}$  and a charge transfer ( $\text{O}\rightarrow\text{Cu}$ ) at  $\sim 47000\text{ cm}^{-1}$ , as reported in the literature.[43,55,92]

### 2.2.9 FTIR

IR data were collected using a Nicolet 6700 FTIR spectrometer equipped with a liquid nitrogen cooled mercury cadmium telluride (MCT) detector. Experiments were performed in a custom designed transmission FTIR cell. [93] About 35-40 mg of each catalyst sample was loaded in the form of a self-supported wafer, 2 cm in diameter. All samples were treated with 10%  $\text{O}_2$  (UHP



grade O<sub>2</sub>, Indiana Oxygen diluted with UHP grade He, Indiana Oxygen) at 400 °C for 30 min and then cooled down in the same gas flow to 200 °C. All reported spectra were collected at 200 °C with a resolution of 4 cm<sup>-1</sup>, averaged over 1000 scans and baseline corrected for direct comparison. The IR spectrum of the H-form was subtracted from the corresponding spectrum for each Cu-SSZ-13 sample to obtain a difference spectrum. All spectra were first normalized by their T-O-T vibrations between 2082 and 1589 cm<sup>-1</sup>. Difference spectra were obtained by subtracting the spectrum of H/SSZ-13 from each of the individual Cu/SSZ-13 sample spectra.

### 2.2.10 Cu-edge XAS

X-ray absorption spectroscopy (XAS) experiments were carried out at Sector 10 of the Advanced Photon Source at Argonne National Laboratory [94,95]. Spectra were collected at both beamlines, 10-ID and 10-BM.

For *in situ* experiments using a six-shooter cell that allows the simultaneous treatment of six samples, 10 – 15 mg of each sample was loaded. All spectra were collected in the step scan mode. Gas treatments were performed in the lab and the samples were transferred to the beamline and cooled down to room temperature before collecting spectra. The samples were oxidized in a 20% O<sub>2</sub>/He (UHP grade, Airgas) flow, whereas the reducing treatments used either UHP He (Airgas) at 400 °C, 3.5% H<sub>2</sub>/He (UHP, Airgas) at 250 °C or 1500 ppm NH<sub>3</sub> (3% NH<sub>3</sub>/Ar, Praxair) + 1500 ppm NO (0.3% NO/N<sub>2</sub>, Airgas) at 400 °C. The total flow rate in each case was 100 ml min<sup>-1</sup> and samples were exposed to the corresponding gas conditions for 45 min.

For *operando* and *in-situ* experiments performed in a glassy carbon reactor, 5 to 20 mg of sample was diluted with spherical carbon beads to minimize beam absorption [96]. For *operando* XAS experiments, a standard SCR gas mixture was introduced to the reactor. H<sub>2</sub>O was introduced into a N<sub>2</sub> (UHP, Airgas) and CO<sub>2</sub> (HP, Airgas) through a PermaPure MH<sup>®</sup> humidifier. Then, NO (3000 ppm in N<sub>2</sub>, Matheson Tri-Gas), O<sub>2</sub> (20% in He, Airgas) were added to the stream. NH<sub>3</sub> (3000 ppm in He, Matheson Tri-gas) was added last to minimize the formation of NH<sub>4</sub>NO<sub>3</sub>. The reaction mixture was preheated to 473 K using preheater coil upstream of the reactor. NO<sub>x</sub>, NH<sub>3</sub>, H<sub>2</sub>O, CO<sub>2</sub> concentrations were measured using a Multi-Gas 2030<sup>®</sup> FTIR gas analyzer during *operando* and *in situ* experiments.

For both experiments utilizing both the six-shooter cell and the glassy carbon reactor, the Cu metal foil spectrum was calibrated to 8979 eV for the Cu K-edge. In addition, Cu metal foil spectrum was simultaneously collected while measuring sample spectra in the energy range from 8700 eV to 9890 eV. All spectra were normalized using a 1<sup>st</sup> order polynomial in the pre-edge region and a 3<sup>rd</sup> order polynomial in the post-edge region. EXAFS data was fit from  $k = 2.7$  to  $\sim 11 \text{ \AA}^{-1}$ . Linear combination XANES fits to determine the Cu(I) – Cu(II) fractions under *operando* conditions were carried out using the appropriate references as explained in our previous publications. [43,68,97] For both *operando* and *in situ* experiments, concentrations were stabilized through a bypass before exposure to the catalyst bed. XAS spectra were collected in an energy range between 8700 and 9890 eV for samples held under different gas conditions, and between 8700 and 9780 eV for *operando* experiments. Once exposed to the catalyst, XAS spectra were taken approximately every 2 min until stabilization.

Sulfated catalysts were not calcined prior to exposure to gases and were not exposed to temperatures greater than 523 K to prevent desorption of sulfur species. For both *operando* and *in-situ* experiments, concentrations were stabilized through a bypass before exposure to the catalyst bed. XAS spectra were collected in an energy range between 8700 and 9890 eV for samples held under different gas conditions, and between 8700 and 9780 eV for *operando* experiments. Once exposed to the catalyst, XAS spectra were taken approximately every 2 min until stabilization.

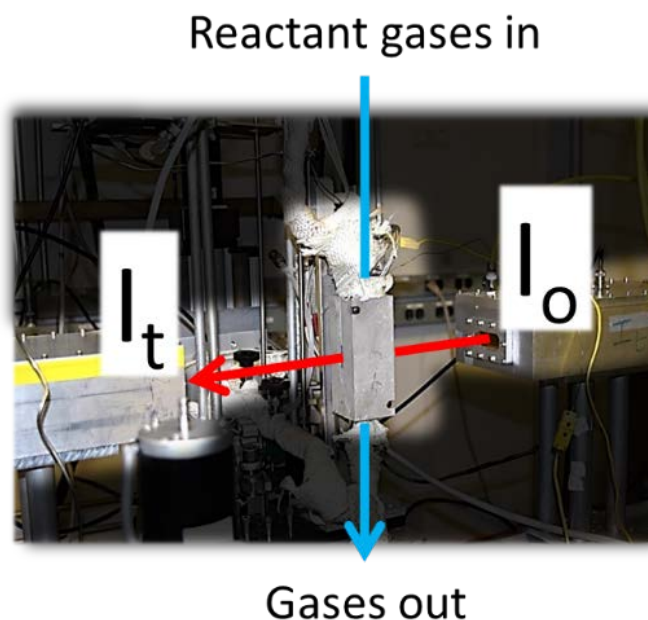


**Figure 7.** Transmission *operando* XAS (red vector from  $I_o$  to  $I_t$ ) was collected while simultaneously collecting differential intrinsic reaction rates (blue vector from “reactant gases in” to “gases out”). The term *operando* refers to a technique that combines kinetic performance and evaluation of the catalyst structure in a single experiment under reaction conditions.

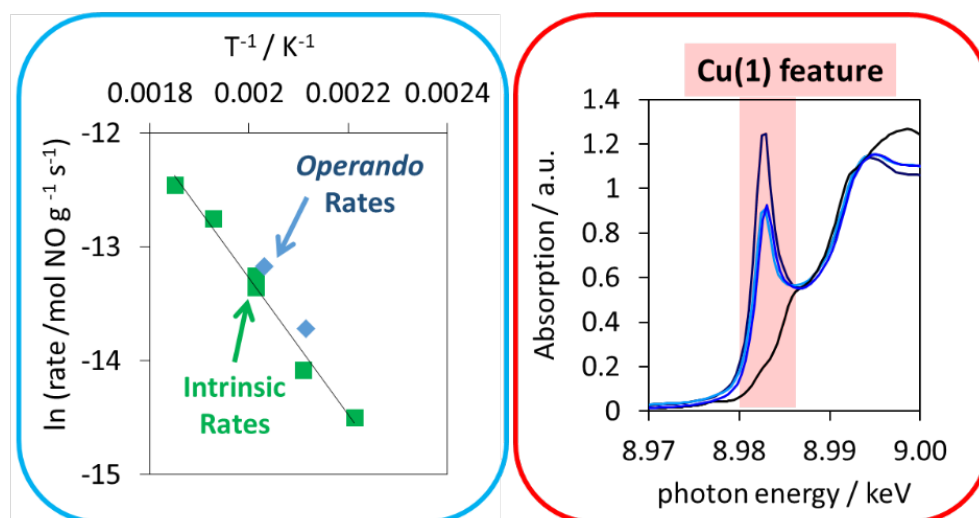


**Figure 8.** Left: The differential intrinsic rates (blue diamonds) must match the intrinsic rates collected in the laboratory reactor (green squares) for the XAS spectra to be called *operando*. If it does not, the spectra is simply *in-situ*. Right: *Operando* Cu k-edge XAS spectra (two blue curves) plotted with the standard Cu(I)(NH<sub>3</sub>)<sub>2</sub> standard spectra (black curve with highest peak at 8.982 keV) and the Cu(II) standard spectra (black curve with no feature at 8.982 keV).

## **2.3 Kinetics Procedures and confirmation of absence of mass/heat transfer effects.**

### **2.3.1 Loading the catalyst bed**

10 to 50 mg of sieved (125 to 250 microns diameter) zeolite sample was diluted in 30 to 40 mg of silica gel (Fisher Chemical, Catalog No. S817-1) and loaded in a quartz tube-reactor between two quartz wool plugs. The quartz tube-reactor was attached to the deNO<sub>x</sub> rig where two thermocouples were placed immediately above and below the catalyst in the reactor for proper measurement of the temperature of the catalyst. Quartz beads were placed upstream of the catalyst on a wire mesh to ensure plug-flow of reactants through the catalyst. The loaded reactor was leak checked in He for 30 minutes at 5 psig.

### **2.3.2 Pre-treatment and stabilization under standard SCR conditions**

After loading and leak checking the reactor, the catalyst was calcined at 450°C for 30 minutes under 750 mL min<sup>-1</sup> dry air (20% O<sub>2</sub> in N<sub>2</sub>). After the reactor cooled down to temperatures between 150°C and 250°C, the catalyst was stabilized for 8 hours under standard SCR conditions. Standard SCR conditions were 750 mL min<sup>-1</sup> to 2000 mL min<sup>-1</sup> of ~300 ppm NO (3.6% NO/Ar Praxair), ~300 ppm NH<sub>3</sub> (3.0% NH<sub>3</sub>/Ar, Praxair), 8% CO<sub>2</sub> (liquid, Indiana Oxygen), 10% O<sub>2</sub> (99.5%, Indiana Oxygen), 2.5% H<sub>2</sub>O (UHP Millipore water), in balance N<sub>2</sub> (boil-off liquid nitrogen) at 200°C.

### **2.3.3 Kinetics, turnover frequencies, and reactant orders**

Steady-state differential reactor and bypass concentrations of NO, NO<sub>2</sub>, N<sub>2</sub>O, H<sub>2</sub>O, and NH<sub>3</sub>, and were detected and measured using a MultiGas 2030 Fourier transform infrared (FTIR) spectrometry gas analyzer from MKS. The rates at 200°C and apparent activation energy ( $E_{app}$ ) were calculated by varying temperature measured by the thermocouples above and below the catalyst at five or more temperatures between 150°C and 250°C. The conversions of NO and NH<sub>3</sub> at steady state were checked to ensure the assumption of differential conditions still hold (< 20% conversion).

The reaction orders of NO, NH<sub>3</sub>, and O<sub>2</sub> were collected by varying the concentrations of each reactant species. The reaction orders were determined by computing the slope when the natural

logarithm of the rate was plotted against the natural logarithm of the concentration of the reactant of interest.

### 3. METHODS TO TITRATE, COUNT, AND CLOSE SITE BALANCES ON H-SSZ-13 AND CU-SSZ-13 MATERIALS USING NH<sub>3</sub> AS A TITRANT

#### 3.1 Abstract

Zeolites, due to their well-defined crystal structure and presence of framework Al that lead to anionic framework sites lend themselves favorably to quantitative titrations, notably by using (1) extraframework cations that charge balance the anionic framework sites, and (2) probe molecules that adsorb on these extraframework cations. Brønsted acid sites on Cu-exchanged SSZ-13 can be titrated selectively using gaseous ammonia when NH<sub>3</sub> bound to Lewis acid sites and physisorbed. NH<sub>3</sub> are purged off in 2% H<sub>2</sub>O in balance inert at 433 K. Using this method, we probe the coordination nature of Cu cations in Cu-SSZ-13 by counting residual Brønsted acid (BA) sites. IR spectroscopy to detect and quantify BA sites and CuOH species provided spectroscopic evidence of the nature of the Cu species beyond simply its coordination number with the framework. Results suggest the presence of two major Cu species: isolated Cu<sup>2+</sup> ions coordinated to two framework oxygens, and [CuOH]<sup>+</sup> coordinated one framework oxygen. These two sites exhibit comparable standard SCR rates, apparent activation energies, and orders regardless of the fraction of Cu<sup>2+</sup> to [CuOH]<sup>+</sup> sites. Another titration method that selectively titrates Brønsted acid sites in addition to Lewis acidic Cu<sup>2+</sup> cations involves flushing in dry inert after NH<sub>3</sub> saturation. It was experimentally observed that the NH<sub>3</sub> coordination numbers to Cu<sup>2+</sup> are one ligand lower than that predicted from DFT calculations.

#### 3.2 Introduction

Amines are promising as titrant molecules for acid sites due to their extra pair of electrons. Specifically, n-propylamine (and other alkylamines) are protonated only by accessible H<sup>+</sup> (Brønsted acid sites), which decomposes to NH<sub>3</sub> and C<sub>3</sub>H<sub>6</sub> (or other hydrocarbons in the case of other alkylamines) upon heating [98–100]. N-propylamine adsorbed onto Lewis-acid sites or physisorbed will stay as n-propylamine when desorbed upon heating. This allows us to quantify the number of Brønsted and Lewis acid sites on materials such as silicas [36] and zeolites [90,91]. Bates et al. [91] demonstrated that though n-propylamine can titrate acid sites on H-ZSM-5 (a

medium-pore zeolite, openings  $< 5.5 \text{ \AA}$ ), it cannot titrate acid sites on H-SSZ-13 (a small pore zeolite, openings  $< 3.8 \text{ \AA}$ ). They performed this by comparing the number of  $\text{NH}_3$  released during TPD after saturation with  $\text{NH}_3$  and n-propylamine probe molecules and observed parity between the  $\text{NH}_3:\text{Al}$  counts for H-ZSM-5, but not for H-SSZ-13.

It is unclear whether the low amount of n-propylamine able to adsorb into SSZ-13 compared to  $\text{NH}_3$  is due to steric hinderance from the small  $< 3.8 \text{ \AA}$  pores in SSZ-13, or due to increased diffusion limitations in H-SSZ-13 compared to H-ZSM-5 that resulted in H-SSZ-13 not reaching a true steady-state before the TPD. If the former is true, then saturating a H-SSZ-13 to infinite time with n-propylamine will result in less  $\text{NH}_3$  release per gram compared to when  $\text{NH}_3$  is used as the titrant. If the latter is true, then saturating a H-SSZ-13 to infinite time with n-propylamine would result in the same amount of  $\text{NH}_3$  released per gram compared to when  $\text{NH}_3$  is used as the titrant. Steric effects may also increase with increasing Al density (decreasing Si:Al), as the number Brønsted acid sites in each zeolite cage are unable to accommodate multiple n-propylamine or  $\text{NH}_3$  molecules during the titration. a

### 3.3 Experimental Methods

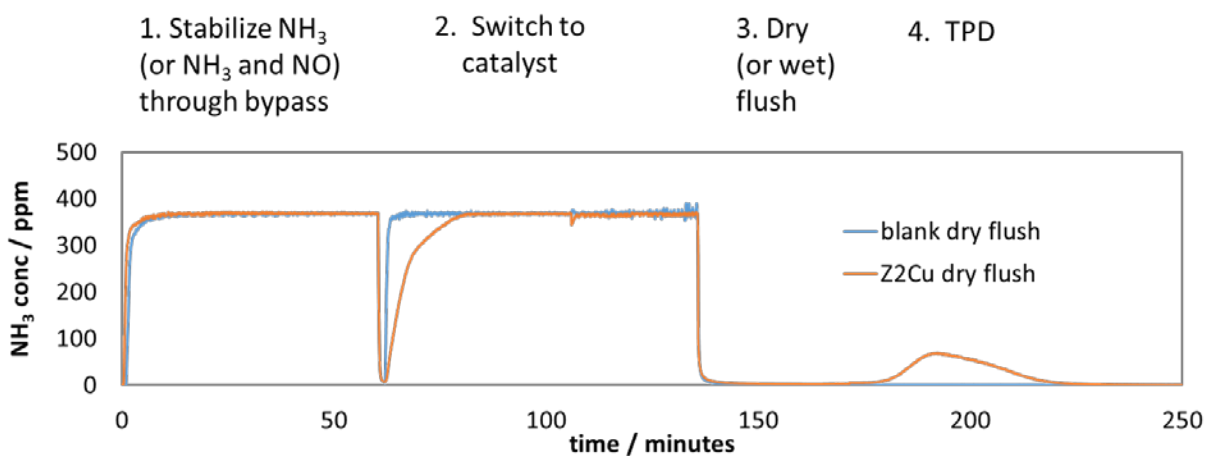


**Figure 9.**  $\text{NH}_3$  concentrations during saturation and temperature programmed desorption (TPD).

### 3.4 Results and Discussion

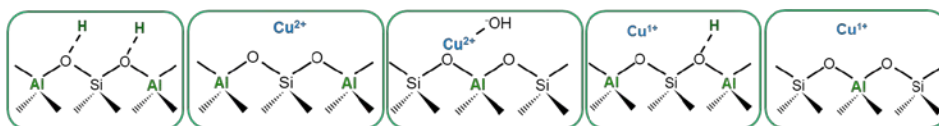
#### 3.4.1 Site Balance Equations

The well-defined zeolite crystal structure and presence of Al in the framework that can electrostatically tether cations (e.g.  $H^+$ ,  $Cu^{2+}$  and other Cu ion species) makes quantifying and titrating sites a promising endeavor. Since the anionic sites on the zeolite stemming from framework Al can charge balance cations, and an adsorbent probe molecule can also be used as a titrant, two general site balance equations can be written: One for the electrostatically tethered cations, and another for the probe molecule. Titration techniques can be complementary to spectroscopical techniques and in some cases can provide experimental evidence to truly compliment spectroscopy.

Equation 14 and 15 assumes that all anionic sites are initially charge balance by hydrogen ions (leading to Brønsted acid sites), and that Cu (and perhaps other cations) are ion-exchanged into the zeolite as a variety of different species. The “...” is a placeholder for other extralattice cationic species that may charge balance anionic sites in the zeolite framework.

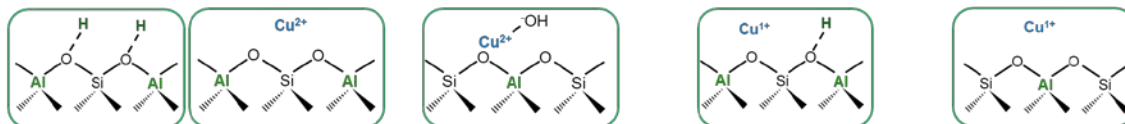
$$n_{BA} = n_{BA_{residual}} + N_{Z_2Cu} \cdot n_{Z_2Cu} + N_{ZCuOH} \cdot n_{ZCuOH} + N_{ZCuZH} \cdot n_{ZCuZH} + N_{ZCu} \cdot n_{ZCu} + \dots$$

(Equation 14)



$$n_{PM} = n_{BA_{residual}} + N_{NH_3, Z_2Cu} \cdot n_{Z_2Cu} + N_{NH_3, ZCuOH} \cdot n_{ZCuOH} + (N_{NH_3, ZCuZH} + 1) \cdot n_{ZCuZH} + N_{NH_3, ZCu} \cdot n_{ZCu} + \dots$$

(Equation 15)



To use these equations, a method was that selectively titrates Brønsted acid sites over Cu sites was developed.



### 3.4.2 Quantitative methods for selectively titrating Brønsted Acid sites in H-ZSM-5 and H-SSZ-13 materials using gas-phase ammonia or liquid-phase ammonium as a probe molecule

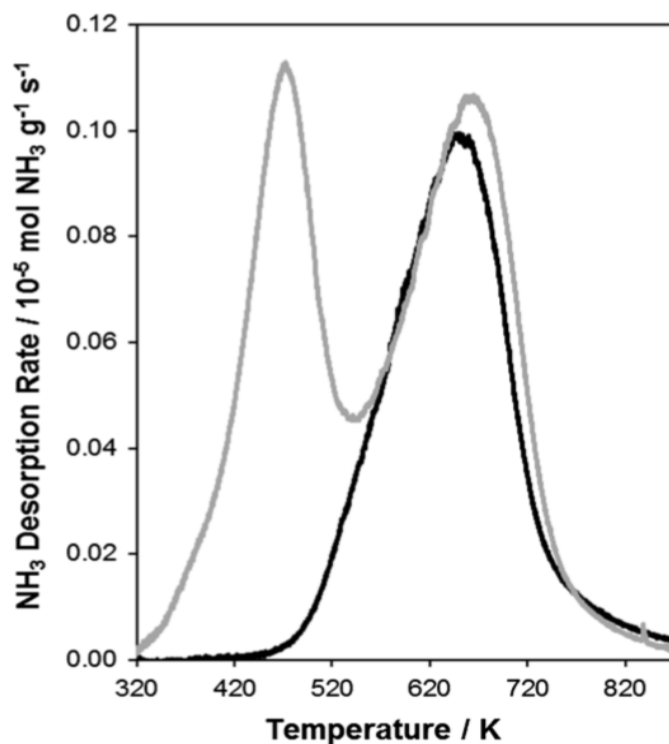


**Figure 10.** H-ZSM-5 (Si:Al = 12.5) materials were saturated to steady state with 500 ppm  $\text{NH}_3$  in balance He at 433 K.  $\text{NH}_3$  desorption rates plotted versus temperature on a sample without purge (light trace) and purging with 800 sccm 2.5%  $\text{H}_2\text{O}$  in balance He at 433 K for 8 hours (dark trace).

As shown in Figure 10, the TPD profile for H-ZSM-5 exhibits two features when saturated with  $\text{NH}_3$  to steady-state with no post-saturation flush, indicating that there are at least two sites that adsorb  $\text{NH}_3$ . The lowest temperature feature (470 K) disappears when the H-ZSM-5 is flushed with dry or wet He post saturation, resulting in the presence of only one desorption peak. We assign the lower temperature feature (470 K) to  $\text{NH}_3$  physisorbed and weakly bound to the surface of the zeolite and the higher temperature feature (650 K) to  $\text{NH}_3$  desorbing from Brønsted acid sites.

It should be noted that the temperature at which the  $\text{NH}_3$  desorption peak occurs is not fixed as it depends on a number of factors such as space velocity (amount of catalyst loaded and inert flow rate), the density of  $\text{NH}_3$  in the material, the particle size of the catalyst, among others. During the TPD, the  $\text{NH}_3$  experiences re-adsorption and re-desorption until it leaves the bed. This phenomenon combined with the residence time distribution of the  $\text{NH}_3$  leaving the bed will lead to shifts in the peak temperature if the space velocity and density of  $\text{NH}_3$  in the material are not held constant between runs. Thus, making claims based off peak shifts may be erroneous.

To further determine whether assigning the higher temperature feature to  $\text{NH}_3$  desorbing from Brønsted acid sites, we measured the mols of  $\text{NH}_3$  desorbed per gram a number of H-ZSM-5 and H-SSZ-13 catalysts with varying Al densities (varying Si:Al ratios), Figure 11. We observe that there is a linear relation between the anionic site density and mols of  $\text{NH}_3$  desorbed per gram, further providing evidence for assigning the desorption feature at 650 K to be from Brønsted acid sites (Figure 12).

**Table 3.**  $\text{NH}_3$ :Al molar ratios on H-SSZ-13, H-ZSM-5, and H-Beta materials. Errors on the Si:Al ratio are  $\pm 25\%$ . Errors on the  $\text{NH}_3$ :Al ratio are  $\pm 0.1$ .

\*Samples from Zeolyst, Incorporated

\*\*Sample from Professor Enrique Iglesia's research group

\*\*\*Sample synthesized in-house using methods outlined in Section 1.13

Sample	Si:Al	$\text{NH}_3$ :Al	Origin
H-ZSM-5	12.5	0.95	Zeolyst CBV 2314*
H-ZSM-5	18	0.70	Zeolyst CBV 3024E*
H-ZSM-5	30	0.95	Zeolyst CBV 5524G*
H-ZSM-5	43	0.80	Berkeley**
H-ZSM-5	89	0.55	Zeolyst CBV 1502*
H-SSZ-13	4.5	0.65	In-house***
H-SSZ-13	15	0.95	In-house***
H-SSZ-13	25	0.95	In-house***
H-SSZ-13	100	0.95	In-house***
H-Beta	11.5	0.95	In-house***

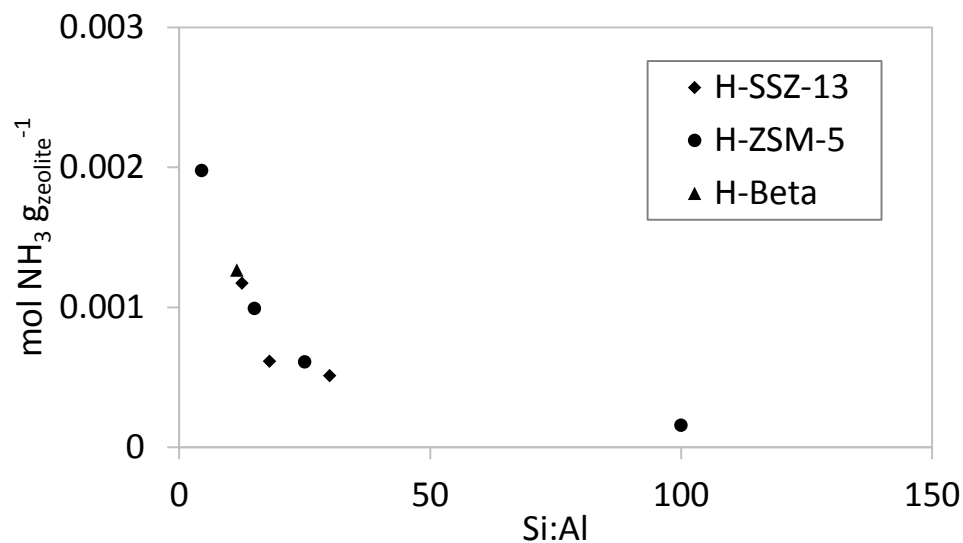


**Figure 11.** mols  $\text{NH}_3$  per gram zeolite on H-SSZ-13, H-ZSM-5, and H-Beta materials.

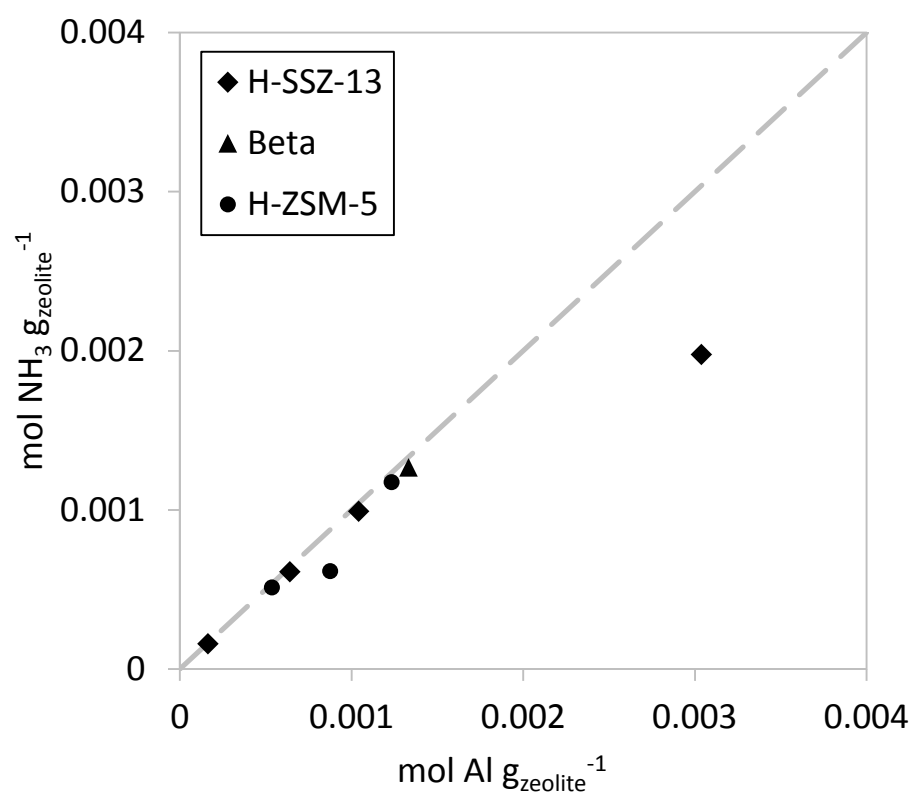


**Figure 12.** Parity plot that compares the mols of  $\text{NH}_3$  per gram catalyst compared to the mols of Al per gram catalyst on H-SSZ-13, H-Beta, and H-ZSM-5 materials.

Titration of Brønsted acid sites can also be achieved using aqueous  $\text{NH}_4\text{NO}_3$  at  $80^\circ\text{C}$ , drying in an oven at  $200^\circ\text{C}$ , then quantifying the number of  $\text{NH}_4$  sites via desorption of  $\text{NH}_3$  by TPD.

$\text{NH}_3:\text{Al}$  ratios on a H-ZSM-5 and H-SSZ-13 material using this method match those measured from gas-phase  $\text{NH}_3$  titration and flush, Table 4.

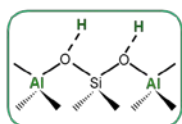
**Table 4.**  $\text{NH}_3:\text{Al}$  ratios measured using five different methods on a H-ZSM-5 material and H-SSZ-13 material.

Zeolite	Si:Al	H:Al	H:Al	H:Al	H:Al	H:Al
		Gas-phase $\text{NH}_3$ at $160^\circ\text{C}$ wet flush	Gas-phase $\text{NH}_3$ at $200^\circ\text{C}$ wet flush	Gas-phase $\text{NH}_3$ at $160^\circ\text{C}$ dry flush	Gas-phase $\text{NH}_3$ at $200^\circ\text{C}$ dry flush	$\text{NH}_4\text{NO}_3$ at $80^\circ\text{C}$ aqueous exchange
H-ZSM-5	12.5	0.92	0.95	0.93	0.93	0.93
H-SSZ-13	4.5	0.65	0.62	0.65	0.65	0.65

With the evidence provided, titration of  $\text{NH}_3$  using either gas-phase  $\text{NH}_3$  saturation at  $160^\circ\text{C}$  and purge or liquid-phase  $\text{NH}_4\text{NO}_3$  titration are methods that can selectively titrate only Brønsted acid sites in H-ZSM-5 and H-SSZ-13. As such, the general cation site balance (Equation 14) can be simplified to the following expression:

Copper Exchange Balance:

$$n_{\text{BA}} = n_{\text{BA}_{\text{residual}}} + N_{\text{ZrCu}} \times \text{Cu} + N_{\text{ZCuOH}} \times \text{OH} + N_{\text{ZCuZr}} \times \text{Zr} + N_{\text{ZCu}} \times \text{Cu}$$



### 3.4.3 Quantitative methods for selectively titrating Brønsted Acid sites in Cu-SSZ-13 materials using gas-phase ammonia or liquid-phase ammonium as a probe molecule

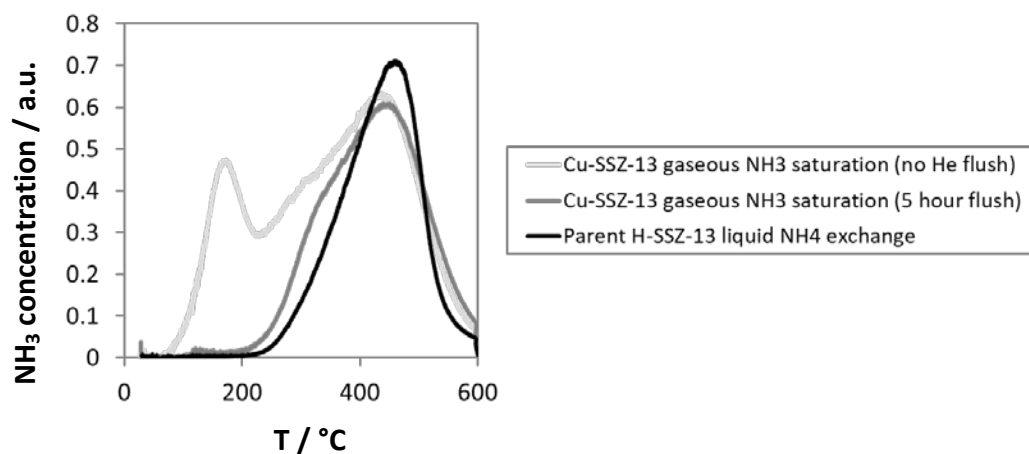


**Figure 13.** Cu-SSZ-13 (Si:Al = 4.5, Cu:Al = 0.12, Cu wt% = 2.3) material was saturated to steady state with 500 ppm  $\text{NH}_3$  in balance He at 433 K.  $\text{NH}_3$  desorption rates (a.u.) plotted versus temperature on a sample without purge (light trace), purging with 800 sccm dry He at 433 K for 5 hours (medium trace), and purging with 800 sccm 2.5%  $\text{H}_2\text{O}$  in balance He at 433 K for 8 hours (dark trace).

As shown in Figure 13, the TPD profile for Cu-SSZ-13 exhibits at least three features when saturated with  $\text{NH}_3$  to steady-state with no post-saturation flush, indicating that there are at least three sites that adsorb  $\text{NH}_3$ . The lowest temperature feature (470 K) disappears when the Cu-SSZ-13 is flushed with dry He post-saturation, resulting in the presence of only two desorption peaks. When the Cu-SSZ-13 is flushed with wet He post-saturation, the intermediate desorption peak (650 K) disappears, leaving one desorption peak behind. We assign the lower temperature feature (470 K) to  $\text{NH}_3$  physisorbed and weakly bound to the surface of the zeolite, the intermediate temperature feature (640 K) to  $\text{NH}_3$  coordination to Lewis acidic sites (e.g. Cu ions), and the higher temperature feature (650 K) to  $\text{NH}_3$  desorbing from Brønsted acid sites. If these assignments are true, then the number of Brønsted Acid sites should decrease as the number of Cu sited at anionic sites increase. Recent DFT studies by Chen et al. [101] revisit these assignments and assign the low temperature feature (< 473 K) to  $\text{NH}_3$  desorbing from Lewis-acidic Cu(II) ion sites, the intermediate temperature feature (523 to 623 K) Lewis acidic Cu(I) and Cu(II) sites, and the high temperature feature to Brønsted sites in addition to Cu(I) and Cu(II) complexes.

### 3.4.4 Identification of two active Cu sites: ZCuOH and Z<sub>2</sub>Cu

#### 3.4.4.1 Evidence 1: Quantification of Brønsted acid sites on Cu-SSZ-13 exchanged with Cu<sup>2+</sup> cations

The number of residual BA sites were quantified by selectively titrating BA sites by adsorbing NH<sub>3</sub> and measuring its amount by TPD using methods reported by Bates et al.[91] and Di Iorio et al. [90] for a number of Cu-SSZ-13 (exchanged to a variety of metal loadings, diamonds in Figure 14). For each of the three H-SSZ-13 samples of different Si:Al ratio, Cu first exchanges onto the zeolite with a 1:2 (Cu:H<sup>+</sup>) stoichiometry to saturation of paired Al<sub>f</sub> sites, and then with a 1:1 ratio at higher Cu loadings. For example, H-SSZ-13 with Si:Al = 15 (grey diamonds) exchanges with a 1:2 (Cu:H<sup>+</sup>) ratio up to a Cu:Al<sub>f</sub> of 0.12 then with a 1:1 ratio at Cu loadings above a Cu:Al<sub>f</sub> of 0.12.

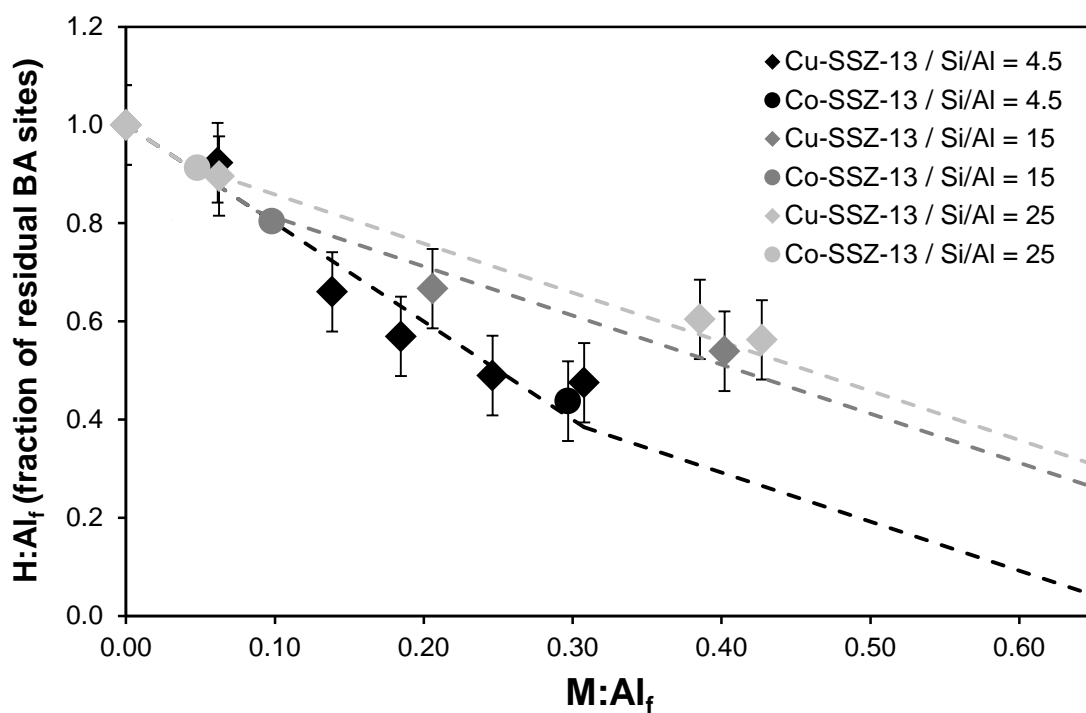


**Figure 14.** Number of residual BA sites normalized to the number of paired BA sites (H:Al<sub>f</sub>) on samples with varying levels of Metal-loadings (M:Al<sub>f</sub>). *Dashed lines* represent predicted number of residual BA sites assuming Cu exchanges at paired Al<sub>f</sub> sites (at a 1:2 Cu:H<sup>+</sup> ratio) to saturation as predicted by Method 1 (Monte Carlo simulations) then continues to exchange at isolated Al<sub>f</sub> sites (at a 1:1 Cu:H<sup>+</sup> ratio). *Circles* represent data collected for Co-SSZ-13 samples exchanged to saturation of paired Al<sub>f</sub>. *Diamonds* represent data collected for Cu-SSZ-13 samples for a series of metal loadings.

In addition to measuring the number of BA sites on oxidized Cu-SSZ-13 as shown in Figure 14, the number of BA sites on Cu-SSZ-13 after reduction of  $\text{Cu}^{2+}$  to  $\text{Cu}^+$  with  $\text{NH}_3$  and NO were also measured. Results in Figure 15 suggest  $\text{Cu}^{2+}$  ions coordinated two to framework  $\text{Al}_f$  generate an additional BA site after reduction with  $\text{NH}_3$  and NO, however reduced  $[\text{CuOH}]^+$  do not (shown schematically in Figure 16).

### 3.4.4.2 Evidence 2: Quantification of Brønsted acid sites on Cu-SSZ-13 with reduced $\text{Cu}^{1+}$ cations

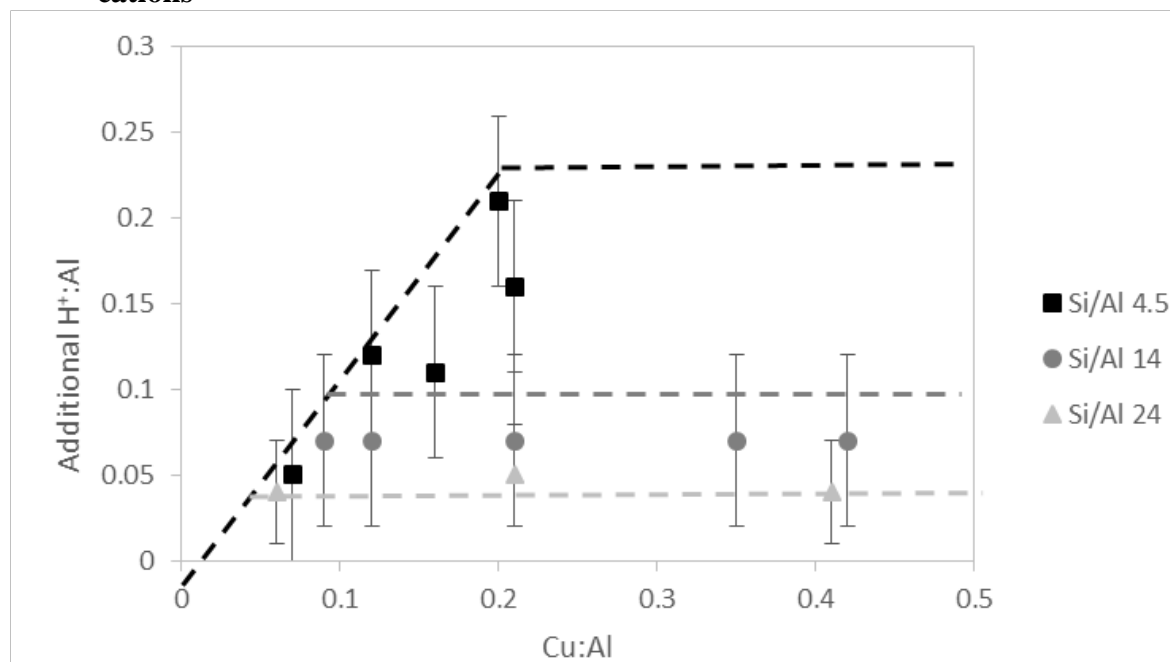


**Figure 15.** The number of additional BA sites generated after reduction using  $\text{NH}_3$  and NO for Cu-SSZ-13. **Dashed lines** represent predicted number of additional BA sites generated for SSZ-13 with Si:Al of 4.5, 15, and 25, assuming isolated  $\text{Cu}^{2+}$  reduction to  $\text{Cu}^+$  generates a residual BA site and that  $[\text{CuOH}]^+$  reduction does not. **Data points** represent the measured increase in BA sites after reduction with  $\text{NH}_3$  and NO for Cu-SSZ-13 with varying Cu:Al and Si:Al ratios.

The dashed lines in Figure 15 represent the number of expected additional BA sites after reduction with  $\text{NH}_3$  and NO for three different Si:Al ratios if only isolated  $\text{Cu}^{2+}$  ions generate BA sites.

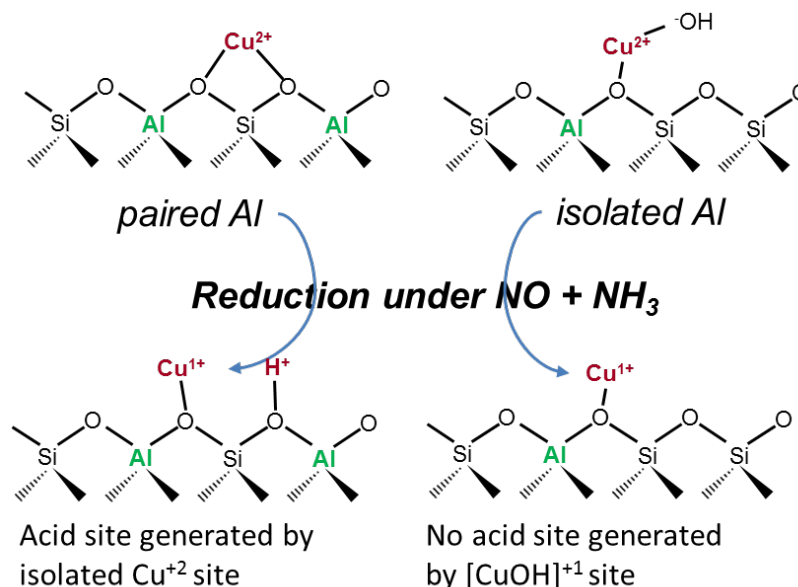


**Figure 16.** Schematic displaying the generation of a BA site after reduction of isolated Cu<sup>2+</sup> sites in a reductive NH<sub>3</sub> and NO environment (300 ppm NO + 300 ppm NH<sub>3</sub>, in balance He, 200°C).

### 3.4.4.3 Evidence 3: DFT calculations and Monte Carlo Simulations

From DFT calculations, the most stable Al<sub>f</sub> pairs reside in chabazite six-membered rings (6-MR).[43] The maximum number of Al<sub>f</sub> pairs in 6-MRs has been computed assuming a random Al<sub>f</sub> distribution and Lowenstein's Rule [102] for a range of Si:Al ratios and they are 0.20, 0.11, and 0.05 for SSZ-13 with Si:Al ratios of 4.5, 15, and 25, respectively.[43]

### 3.4.4.4 Evidence 4: Cobalt Exchange

Co<sup>2+</sup> is an ideal titrant to probe the number of paired anionic sites that can to charge balance Cu<sup>2+</sup> due to its similar atomic diameter to Cu and also due to its preference to stay in the 2+ oxidation state [103]. The number of paired anionic sites were determined by selectively exchanging paired Al<sub>f</sub> with Co<sup>2+</sup> to saturation following methods reported and developed by Dedeczek [104] and Di Iorio [105], then using elemental analysis to measure the Co:Al molar ratio. The maximum number of paired sites measured from Co-exchange matches the predicted number of maximum paired sites for SSZ-13 assuming a random distribution of Al<sub>f</sub> (Figure 17). It should be noted that SSZ-13 syntheses that include a Na:Al ratio of 1 in its hydrothermal synthesis gel seem to be randomly distributed. Synthesis recipes with Na:Al ratios that deviates from 1 can lead to non-random distributions of Al<sub>f</sub> as demonstrated by Di Iorio and Gounder [105] where decreasing the



Na:Al ratio decreases the number of paired anionic sites and increasing the Na:Al ratio increases the number of paired anionic sites. Being able to measure the fraction of paired  $\text{Al}_f$  and isolated (unpaired)  $\text{Al}_f$  allows us to further support and explain why Cu speciates as  $\text{Z}_2\text{Cu}$  to a particular extent before speciating as  $\text{ZCuOH}$ .

Results from Figure 15 suggest that the total number of paired sites (height of plateau) can also be measured experimentally by taking a Cu-SSZ-13 sample where all paired  $\text{Al}_f$  sites have been saturated with isolated  $\text{Cu}^{2+}$  ions (with or without the presence of  $[\text{CuOH}]^+$  species) and measuring the number of additional BA sites generated after  $\text{NH}_3 + \text{NO}$  reduction. Measured paired  $\text{Al}_f$  on our SSZ-13 samples using this methods is compared to the Co-titrations method and from Monte Carlo statistical counting in Figure 17.

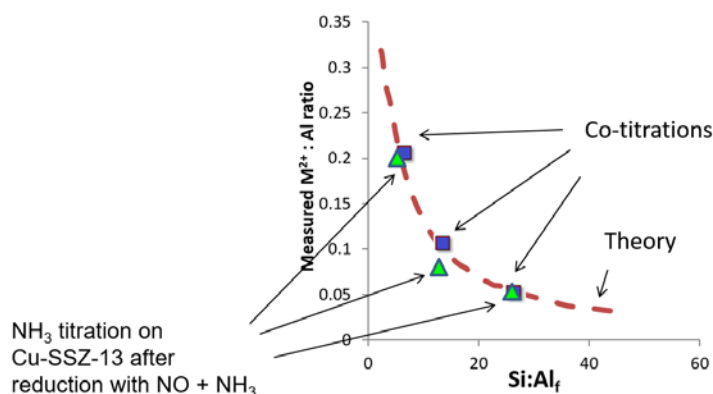


**Figure 17.** Comparison of the three methods that can be used to quantify number of paired  $\text{Al}_f$  sites.

#### 3.4.4.5 Evidence 5: FTIR spectroscopy

IR spectroscopy was used to measure the increase in  $[\text{CuOH}]^+$  and decrease of BA stretching frequencies with increasing Cu-loading for SSZ-13 samples with  $\text{Si}:\text{Al} = 15$  (Figure 18). Features at  $3650\text{ cm}^{-1}$  characteristic of  $[\text{CuOH}]^+$  and at  $3590\text{ cm}^{-1}$  characteristic of BA sites were integrated and quantified [106,107]. Quantification of the  $[\text{CuOH}]^+$  and BA site features (Figure 19) suggests that Cu species without an  $-\text{OH}$  ligand are present at Cu loadings below  $\text{Cu}:\text{Al} = 0.12$  (e.g.  $\text{Cu}^{2+}$ ), and that  $[\text{CuOH}]^+$  species above  $\text{Cu}:\text{Al} = 0.12$  are present, as represented by a linear increase in the  $[\text{CuOH}]^+$  feature in the IR. Additionally, quantification of the BA peak at  $3590\text{ cm}^{-1}$  suggests that  $\text{Cu}^{2+}$  species titrate twice as many  $\text{H}^+$  sites as  $[\text{CuOH}]^+$  species, which is the same result obtained with  $\text{NH}_3$ -TPD in Figure 14.

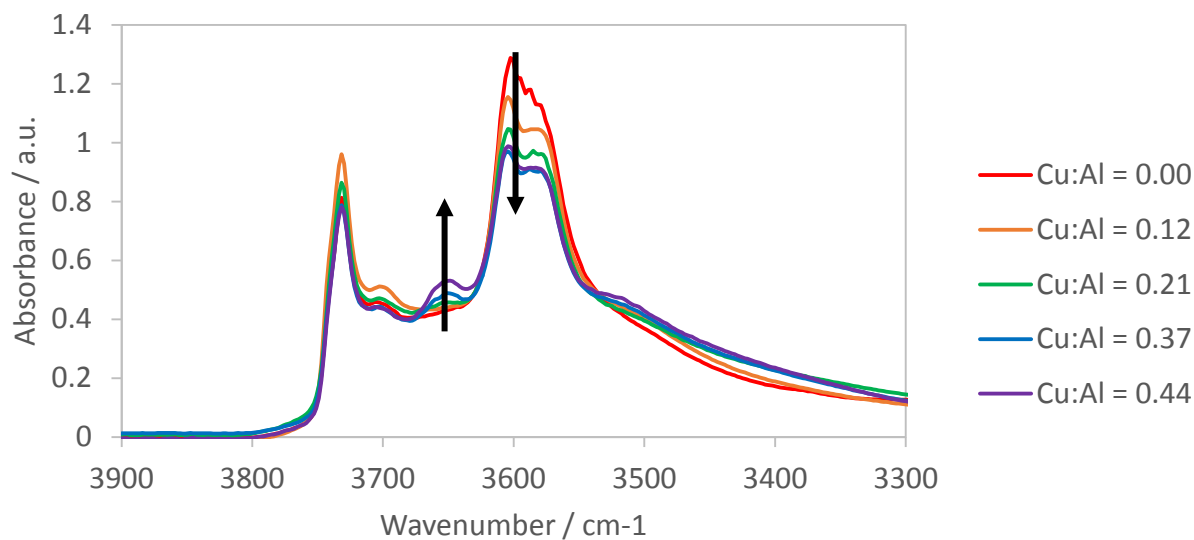


**Figure 18.** FTIR spectra collected for a Cu-SSZ-13 Si:Al = 15 at various Cu loadings. An increase in Cu loading lead to an increase in  $[\text{CuOH}]^+$  peaks at  $3650\text{ cm}^{-1}$  and a decrease in BA peaks at  $3590\text{ cm}^{-1}$ .

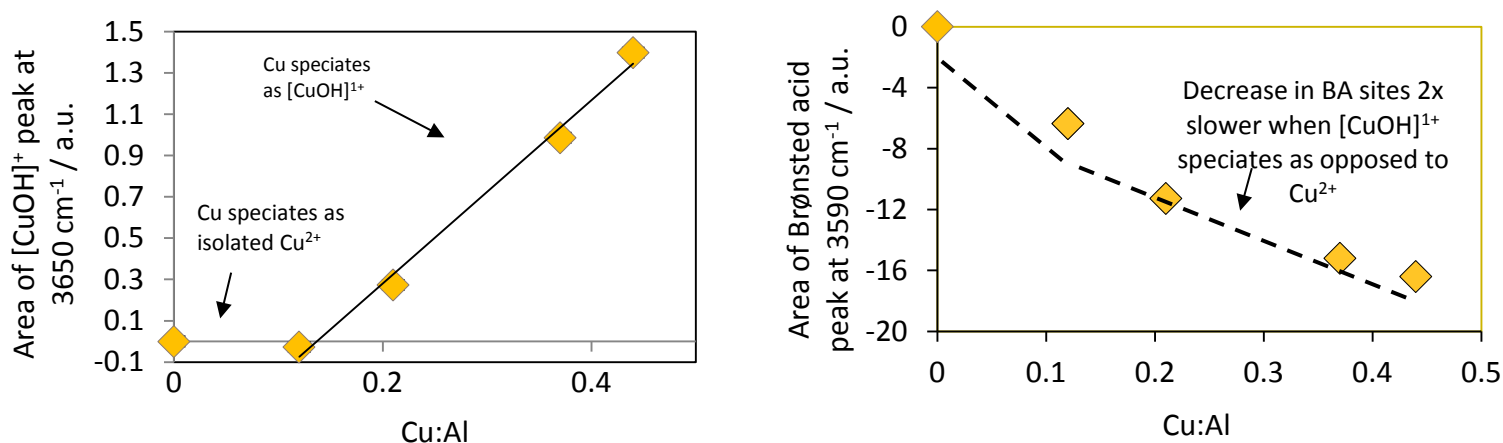


**Figure 19.** Left: Integrated areas of  $[\text{CuOH}]^+$  feature at  $3650\text{ cm}^{-1}$  plotted as a function of Cu loading. Right: Integrated areas of BA sites feature at  $3590\text{ cm}^{-1}$  plotted as a function of Cu loading.

### 3.4.5 Behavior of two Cu species under standard SCR

Cu-SSZ-13 samples shown in Figure 20 exhibit similar activation energies ( $68 \pm 7\text{ kJ mol}^{-1}$ ), NO orders ( $0.7 \pm 0.1$ ),  $\text{NH}_3$  orders ( $0.0 \pm 0.1$ ), and  $\text{O}_2$  orders ( $0.4 \pm 0.1$ ) regardless of the amount and fraction of  $\text{Cu}^{2+}$  and  $[\text{CuOH}]^+$  species. In addition, the rate per mole of Cu (proportional to the

value of the slope in Figure 20) stays constant regardless of whether the Cu active sites speciate as  $[\text{CuOH}]^+$  or  $\text{Cu}^{2+}$ . Note that for the Si:Al = 4.5 samples Cu is exchanged as  $\text{Cu}^{2+}$  whereas for Si:Al = 15 a mixture of  $[\text{CuOH}]^+$  and  $\text{Cu}^{2+}$  sites. The yellow circle designates a Cu-SSZ-13 Si:Al = 15 with only isolated  $\text{Al}_f$  sites (no paired  $\text{Al}_f$ ), so only  $[\text{CuOH}]^+$  speciates (also confirmed with  $\text{NH}_3$ -TPD, data not shown). Thus, the kinetics (rate per Cu active site, activation energy, and orders) between the two Cu active site species are statistically indistinguishable.

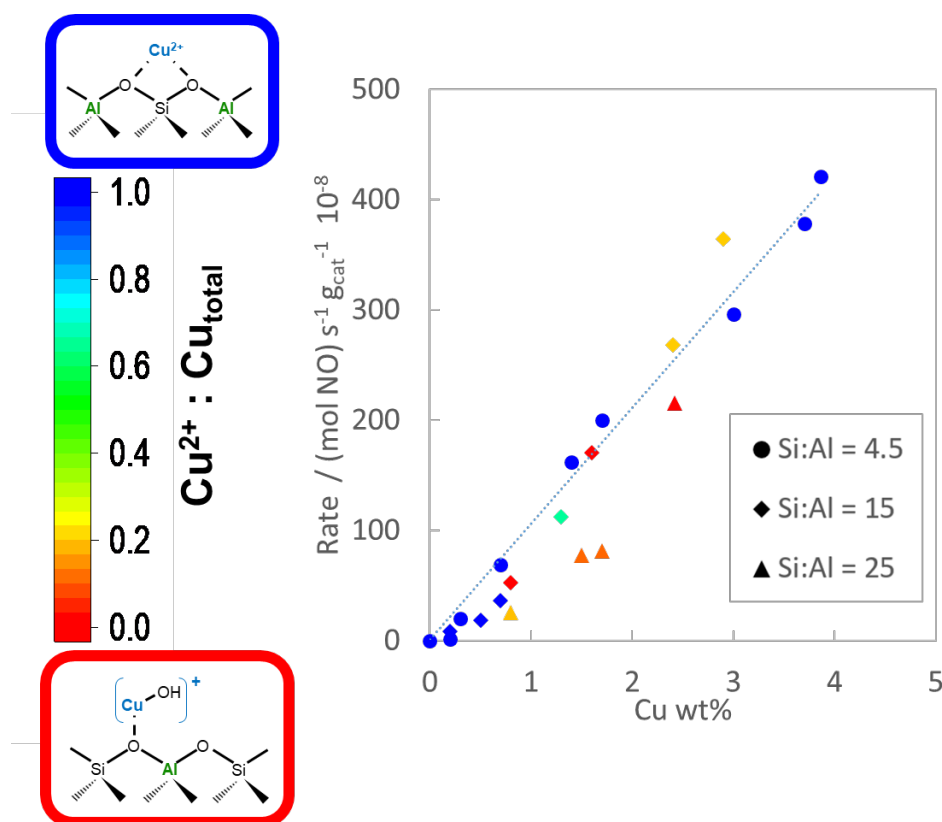


**Figure 20.** SCR rate plotted against Cu wt% for samples with primarily isolated  $\text{Cu}^{2+}$  active sites (blue), exclusively  $[\text{CuOH}]^+$  active sites (red), and a mixture of isolated  $\text{Cu}^{2+}$  and  $[\text{CuOH}]^+$  active sites.

### 3.4.6 Method to quantify $\text{NH}_3$ -Cu coordination numbers on $\text{NH}_3$ saturated Cu-SSZ-13 materials

Having established that  $\text{Cu}^{2+}$  ions come in two flavors ( $\text{Z}_2\text{Cu}$ ,  $\text{ZCuOH}$ ), understanding the  $\text{NH}_3$  coordination nature on these two different sites is important in predicting and quantifying the  $\text{NH}_3$  saturation capability of Cu-SSZ-13 materials.

Returning to the general copper exchange balance, we have established the following constants:

$$N_{Z_2Cu} = 2$$

$$N_{ZCuOH} = 1$$

$$N_{ZCuZH} = 2$$

$$N_{ZCu} = 1$$

These constants tell us that Cu in the form of  $Z_2Cu$  charge balances two anionic framework sites, that  $ZCuOH$  charge balances only one anionic framework site,  $ZCuZH$  charge balances two anionic framework sites, and that  $ZCu$  charge balances one anionic framework site. Knowing the values of these coordination constants allow us to reduce the number of degrees of freedom, allowing us to understand the coordination between  $NH_3$  and ionic Cu species.

To determine the number of  $NH_3$  coordinated to the oxidized and reduced forms of  $Z_2Cu$  and  $ZCuOH$  species, we select model materials that have 100% of its ionic Cu as  $Z_2Cu$  (Cu-SSZ-13 Si:Al = 4.5, Cu:Al = 0.21) and 100% of its ionic Cu as  $ZCuOH$  (Cu-SSZ-13 Si:Al = 15, Cu:Al = 0.17, Na-free hydrothermal synthesis). Combining the copper-exchange balance with the  $NH_3$ -adsorption site balances equations, substituting the coordination numbers between Cu sites and the anionic sites on the zeolite framework, and neglecting the terms that relate to sites not present on the model material, we arrive at four governing equations each with only one unknown (Table 5).

**Table 5.** Governing equations from combining the Cu-exchange balance and NH<sub>3</sub> adsorption balance equations.

State of Cu	Cu species	Governing Equation
100% Oxidized	Z <sub>2</sub> Cu	$n_{NH_3} = (N_{NH_3, Z_2Cu} - 2)n_{Z_2Cu} + n_{BA}$
100% Reduced	Z <sub>2</sub> Cu	$n_{NH_3} = (N_{NH_3, ZCuOH} - 1) \cdot n_{ZCuOH} + n_{BA}$
100% Oxidized	ZCuOH	$n_{NH_3} = (N_{NH_3, ZCuZH} - 1) \cdot n_{ZCuZH} + n_{BA}$
100% Reduced	ZCuOH	$n_{NH_3} = (N_{NH_3, ZCu} - 1) \cdot n_{ZCu} + n_{BA}$

Note that all these equations are linear relationships. Plotting the molar NH<sub>3</sub>:Al ratio versus the molar Cu:Al ratio for a number of oxidized and reduced model Z<sub>2</sub>Cu and model ZCuOH samples. Equating the slopes to the value in the governing equation's parentheses listed in Table 5 allows us to solve for  $N_{NH_3}$ .

Figure 21 plots the molar NH<sub>3</sub>:Al ratios versus molar Cu:Al ratios for a number of H-SSZ-13 and oxidized (calcination in 20% O<sub>2</sub> in balance N<sub>2</sub> at 500°C) Cu-SSZ-13 materials that exhibit a range of ZCuOH and Z<sub>2</sub>Cu species. Figure 22 plots the molar NH<sub>3</sub>:Al ratios versus molar Cu:Al ratios for a number of reduced (300 ppm NH<sub>3</sub> + 300 ppm NO in balance He until steady state) Cu-SSZ-13 materials that exhibit a range of ZCuOH and Z<sub>2</sub>Cu species. Table 6 lists our experimentally measured NH<sub>3</sub>-Cu coordination numbers compared with those reported by Luo et al. [108] and Paolucci et al. [109]. These results are consistent with the coordination numbers experimentally measured by Luo et al. [108], but are not consistent with those predicted by DFT computation in Paolucci et al. [109].

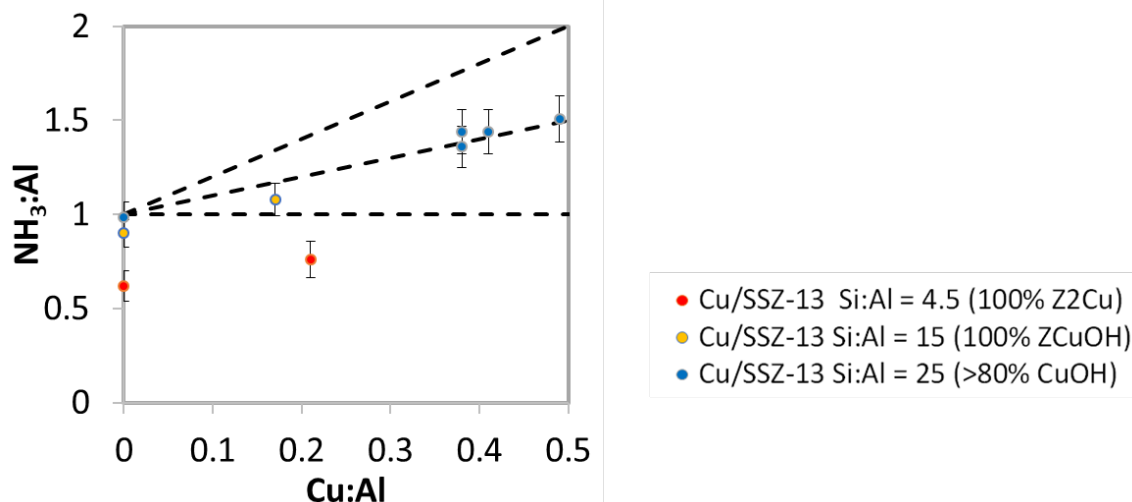


**Figure 21.**  $\text{NH}_3:\text{Al}$  molar storage ratios after  $\text{NH}_3$  titration and dry He flush plotted versus  $\text{Cu}:\text{Al}$  molar ratio on a number model  $\text{ZCuOH}$  (yellow),  $\text{Z}_2\text{Cu}$  (red), and materials with a mix of both sites (blue). The dashed linear lines exhibit slopes of 0, 1, and 2.

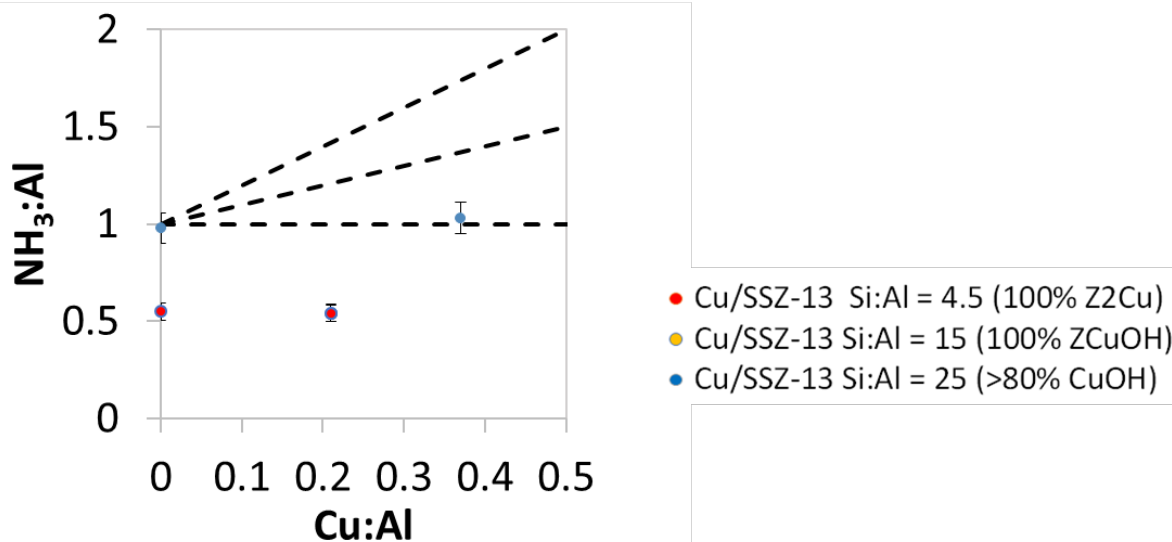


**Figure 22.**  $\text{NH}_3:\text{Al}$  molar storage ratios after reduction with  $\text{NO}$  and  $\text{NH}_3$ , then  $\text{NH}_3$  titration and dry He flush plotted versus  $\text{Cu}:\text{Al}$  molar ratio on a number model  $\text{ZCuOH}$  (yellow) and  $\text{Z}_2\text{Cu}$  (red)  $\text{Cu}$ -SSZ-13 materials. The dashed linear lines exhibit slopes of 0, 1, and 2.

**Table 6.** Experimental  $\text{NH}_3$  coordination numbers on the four different types of Cu species.

State of Cu	Cu species	$N_{\text{NH}_3}$	Luo et al.	Paolucci et al.
100% Oxidized	$\text{Z}_2\text{Cu}$	$2.7 \pm 0.3$	3	4
100% Reduced	ZH/ZCu	$1.0 \pm 0.3$	1	2
100% Oxidized	ZCuOH	$2.1 \pm 0.4$	2	3
100% Reduced	ZCu	$1.2 \pm 0.3$	1	2

The inconsistency between the experimental  $\text{NH}_3$ -Cu coordination numbers and the expected  $\text{NH}_3$ -Cu coordination numbers are not understood. We will discuss a few possible explanations below.

The first possible explanation lies in the assumptions that go into the model to generate the  $\text{NH}_3$  phase diagrams in Paolucci et al. [109]. The biggest assumption is the entropy assumption; if our conditions are near a phase transition, what we observe experimentally could be either phase. The conditions at which the Cu-SSZ-13 materials are ammonia saturated (300 ppm  $\text{NH}_3$  in the absence of  $\text{O}_2$  at  $180^\circ\text{C}$ ), are near a phase transition for  $\text{Z}_2\text{Cu}$  but not near a phase transition for ZCuOH the phase diagram computed by Paolucci et al. [109]. This could possibly explain the lower  $\text{NH}_3$ -Cu coordination number observed for our  $\text{Z}_2\text{Cu}$  materials.

Since the phase diagrams in Paolucci et al. [109] also suggest that  $\text{NH}_3$  may reduce  $\text{Cu}^{2+}$  ions in the absence of  $\text{O}_2$ , the fraction of  $\text{Cu}^{1+}$  on three Cu-SSZ-13 samples (two with only  $\text{Z}_2\text{Cu}$  sites and one with ZCuOH) after  $\text{NH}_3$  saturation at  $200^\circ\text{C}$  was collected in Sector 10-ID at the Advanced Photon Source at Argonne National Laboratory, Figure 23. This data suggests that  $\text{NH}_3$  itself is able to reduce  $\text{Cu}^{2+}$  to  $\text{Cu}^{1+}$  species regardless of speciation. If 50 to 90% of the  $\text{Cu}^{2+}$  reduces to  $\text{Cu}^{1+}$ , and four  $\text{NH}_3$  coordinates to  $\text{Z}_2\text{Cu}$  and three  $\text{NH}_3$  coordinates to ZH/ZCu, and one less  $\text{NH}_3$  it will be able to explain why we observe an average coordination number of  $2.7 \pm 0.3$  across all  $\text{Z}_2\text{Cu}$  model materials. This ~50% reduction in ZCuOH sites can also possibly explain the lower measured coordination number of  $2.1 \pm 0.4$ . The observation that  $\text{NH}_3$  itself can reduce  $\text{Cu}^{2+}$  to  $\text{Cu}^{1+}$ , however cannot explain why we observe a coordination number of 1 for the  $\text{Z}_2\text{Cu}$  and ZCuOH materials after  $\text{NO} + \text{NH}_3$  reduction, inconsistent with

those predicted using DFT and the EXAFS coordination number of 2 observed after in-situ NO + NH<sub>3</sub> reduction of Cu<sup>2+</sup> to Cu<sup>1+</sup>.

The fact that NH<sub>3</sub> itself is able to reduce Cu<sup>2+</sup> also brings up two pressing questions: (1) are we using the correct references to quantify Cu<sup>1+</sup> and Cu<sup>2+</sup> fractions, and (2) how is this observation consistent with the NH<sub>3</sub> saturation and TPD methods we developed to count residual Brønsted Acid sites?

With regards to the first question regarding Cu<sup>1+</sup> and Cu<sup>2+</sup> references, it has been demonstrated that the white-line intensity in the XANES is affected by the nature of the environment surrounding Cu<sup>1+</sup>. The introduction of new ligands or atomic coordinations to a Cu ion will affect the intensity of the Cu(I) feature at 8.982 keV. For example, the reference used for 100% Cu(I) on NH<sub>3</sub>-saturated Cu-SSZ-13 and Cu(I) oxide vary by a factor of two in intensity due to changes in the Cu's coordination environment [109–111]. This phenomenon affects our ability to reliably use linear-combination fitting to quantitatively determine the fraction of Cu<sup>2+</sup> that truly reduces to Cu<sup>1+</sup>. It still allows us to qualitatively observe whether particular in-situ treatments are able to reduce Cu<sup>2+</sup> to Cu<sup>1+</sup>. As shown in Table 6, since a NH<sub>3</sub> coordination number of one is experimentally observed for both ZCu and Z<sub>2</sub>H/Cu species, it is thereby possible that when Cu is reduced by only NH<sub>3</sub> (in the absence NO) the reduced Cu<sup>1+</sup> species may still be coordinated framework. This is highly likely since Cu<sup>1+</sup> species prefer to coordinate to two ligands from ligand-field theory [112]. The nature (oxidation state, coordination nature, and thus mobility) of Cu ions in Cu-SSZ-13 is dependent on its environment (e.g. gas conditions, temperature) [109], so it is not surprising that perturbing the Cu-SSZ-13 away from standard SCR conditions (300 ppm NO, 300 ppm NH<sub>3</sub>, 10% O<sub>2</sub>, 7% CO<sub>2</sub>, 2.5% H<sub>2</sub>O, in balance N<sub>2</sub>, 200°C) to a reductive NO + NH<sub>3</sub> environment (300 ppm NO + 300 ppm NH<sub>3</sub>, in balance He, 200°C), to a simply NH<sub>3</sub>-rich environment (300 ppm NH<sub>3</sub> in balance He, 180°C) will result in Cu with different oxidation states and coordination.



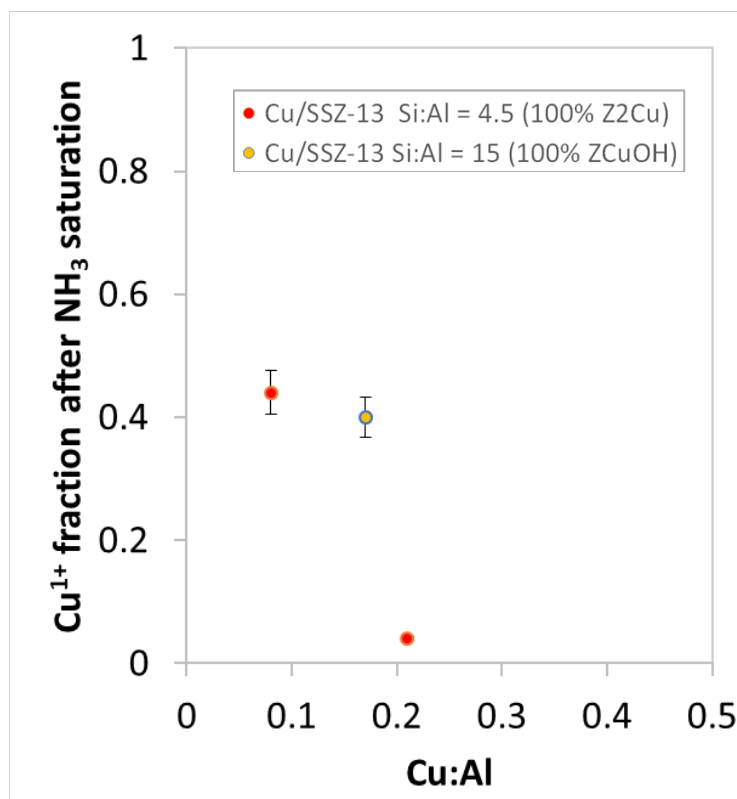


**Figure 23.** Cu<sup>1+</sup> fraction measured using XANES on two model Z<sub>2</sub>Cu materials and on one model ZCuOH material, all with different Cu loadings.

With regards to the second question regarding our NH<sub>3</sub> TPD procedure, we have demonstrated that subjecting Cu-SSZ-13 to an NH<sub>3</sub> rich environment (300 ppm NH<sub>3</sub> in balance He, 160°C) allows us to count the number of residual Brønsted Acid sites that are charge-balanced by only H<sup>+</sup> and not oxidized Cu<sup>2+</sup> species either as ZCuOH or Z<sub>2</sub>Cu [109]. XAS demonstrated that NH<sub>3</sub> itself does reduce Cu<sup>2+</sup> to Cu<sup>1+</sup> during the NH<sub>3</sub> saturation step (Figure 21), and that the number of residual Brønsted Acid sites on Cu-SSZ-13 materials with Cu species all initially in the Cu<sup>2+</sup> state quantified using this technique point to Z<sub>2</sub>Cu sites displacing two H<sup>+</sup> cations, and ZCuOH sites displacing one H<sup>+</sup> cation. This technique also indicated that the reduction of Z<sub>2</sub>Cu with a reductive NO + NH<sub>3</sub> environment (300 ppm NO + 300 ppm NH<sub>3</sub>, in balance He, 200°C) generates an additional Brønsted Acid site proportional to the number of Z<sub>2</sub>Cu species. Taken together, these experimental observations point to the assertion that Z<sub>2</sub>Cu species generate a residual Brønsted Acid site when subjected to a reductive NO + NH<sub>3</sub> environment, but may or may not generate a residual Brønsted Acid site (The NH<sub>3</sub>:Cu coordination ratio on Z<sub>2</sub>H/Cu is 1,

so  $\text{NH}_3$  can choose to site at the anionic site or with the Cu) when subjected to an  $\text{NH}_3$  rich environment. If  $\text{NH}_3$  chooses to site at the  $\text{H}^+$  site, then this would indicate that during  $\text{NH}_3$  saturation,  $\text{Z}_2\text{Cu}$  sites that are reduced by only  $\text{NH}_3$  to  $\text{Cu}^{1+}$  are coordinated only to the zeolite framework and no  $\text{NH}_3$  ligands. If  $\text{NH}_3$  chooses to coordinate with  $\text{Cu}^{1+}$ , then the anionic site would be charged balanced by a  $\text{H}^+$  rather than an  $\text{NH}_4^+$ . If the preference for  $\text{NH}_3$  between both states are close with a low-enough energy barrier between the two states, then we expect  $\text{NH}_3$  to dynamically switch between the two states.

### 3.5 Conclusions

A technique to selectively titrate Brønsted acid sites on Cu-SSZ-13 was developed. This technique involves saturating the Cu-SSZ-13 material with 500 ppm  $\text{NH}_3$  at 433 K, flushing out  $\text{NH}_3$  bound to Lewis acidic Cu(II) sites in 2%  $\text{H}_2\text{O}$  in balance inert at 433 K, then performing a temperature programmed desorption to quantify the remaining adsorbed  $\text{NH}_3$ . Using this method, along with supporting computational (Monte Carlo), and spectroscopic (FTIR) evidence, we propose the presence of two Cu species: isolated  $\text{Cu}^{2+}$  ions that saturates paired framework anionic sites to saturation first, and  $[\text{CuOH}]^+$  that continues to site at isolated framework anionic sites. These two sites exhibit comparable standard SCR rates, apparent activation energies, and orders regardless of the fraction of  $\text{Cu}^{2+}$  to  $[\text{CuOH}]^+$  sites. Another titration method that selectively titrates Brønsted acid sites in addition to Lewis acidic  $\text{Cu}^{2+}$  cations involves flushing in dry inert after  $\text{NH}_3$  saturation. It was experimentally observed that the  $\text{NH}_3$  coordination numbers to  $\text{Cu}^{2+}$  are one ligand lower than that predicted from DFT calculations.

### 3.6 Acknowledgements

The author acknowledges Dr. Anuj Verma and Dr. Shane Bates for their assistance and time in discussion the  $\text{NH}_3$  titration method. Professor Rajamani Gounder has been a steady presence who offers advice and insight throughout the years on titration methods. The author also acknowledges Ishant Khurana ( $\text{NH}_3$  TPD), Dr. Atish Parekh (FTIR), and John Di Iorio (Cobalt exchange) for collecting the majority of the data using the techniques that appear in parentheses after their name.

### 3.7 Supplementary Information

#### Aqueous low cation ( $\text{Cu}^{2+}$ and $\text{NH}_4^+$ ) exchange

$\text{NH}_3$ -TPD quantification of residual BA sites in Figure 14 exhibit an outlier for the lowest Cu-exchanged Si:Al = 4.5 sample (circled in black in Figure 24). Residual BA sites were quantified on Cu-SSZ-13 exchanged without pH control was performed on a series of 3 samples, shown as red diamonds in Figure 24. This data suggests that H-SSZ-13 Si:Al = 4.5 will lose 80% of its BA sites from just exposure to water at room temperature ( $\text{pH} < 2$ ). The addition of  $\text{Cu}^{2+}$  cations into the exchange solution suppresses the deactivation of BA sites. The addition of  $\text{Cu}^{2+}$  cations in addition to  $\text{NH}_4^+$  cations in the form of  $\text{NH}_4\text{OH}$  to increase the pH to 5 suppresses the deactivation of BA sites even further. H-SSZ-13 samples with Si:Al = 15 and 25 do not exhibit this unusual decrease in BA sites, possibly due to the higher stability of  $\text{Al}_f$  in these materials.

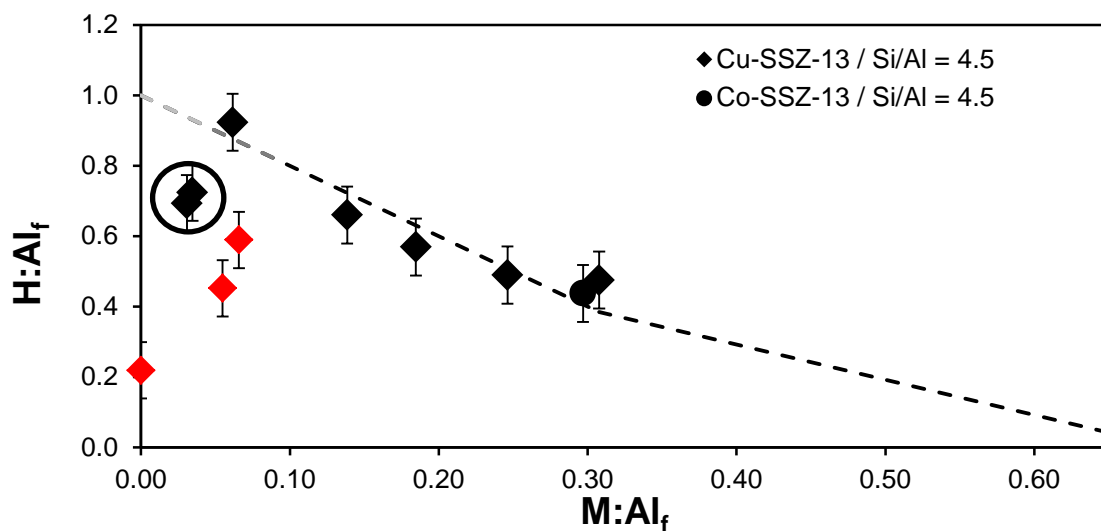


**Figure 24.** Residual BA site quantification on Cu-SSZ-13 Si:Al = 4.5 on H-SSZ-13 Cu-exchanged with pH control to 5 with addition of 0.1M  $\text{NH}_4\text{OH}$  (**black diamonds**), and H-SSZ-13 Cu-exchanged without pH control (**red diamonds**)

When low concentrations of  $\text{Cu(II)}$  and  $\text{NH}_4^+$  are present during aqueous-phase Cu exchange of H-SSZ-13 (Si:Al=5) at ambient conditions, we observed a 40-80% decrease in the number of Brønsted acid sites relative to the parent SSZ-13. These observations suggest that significant structural changes occur to framework Al atoms (e.g., dealumination) in high Al content H-SSZ-13 zeolites synthesized by the FAU-to-CHA conversion methods at low pH values and low concentrations of cations (80% loss in  $\text{H}^+$  sites when no Cu is present), consistent with reports

that cations exchange  $H^+$  sites to stabilize framework Al against dealumination. The addition of  $NH_4OH$  to maintain a pH of 5 during the exchange of low concentrations of Cu cations mitigated Al structural changes and only resulted in a decrease of 25% of the number of Brønsted acid sites (black diamonds). We have previously reported  $NH_3$  TPD data that quantified the loss of  $\approx 0.25$   $H^+$ :Al for this SSZ-13 sample (Si:Al=5, Cu:Al=0.02),<sup>5</sup> which is much larger than expected from the Cu:H 2:1 exchange stoichiometry (0.04 H:Al for a Cu:Al=0.02).

### Calcination and storage at ambient conditions

For samples with a high BA density (H-SSZ-13 Si:Al = 4.5), significant deactivation of BA sites occur when the H-zeolite is exposed to certain conditions, as summarized in Table 7. H-SSZ-13 readily loses BA sites after storage at ambient conditions, after calcination in breathing air, and exposure to water under ambient conditions. Slight modifications in the hydrothermal synthesis procedure (increasing the length of hydrothermal synthesis from 6 to 10 days, and slow cooling the as-synthesized sample after hydrothermal synthesis in air vs fast-cooling by quenching in water) do not affect the final  $H^+$ :Al<sub>f</sub> of the sample. The first two treatments do not deactivate BA sites for samples with lower BA densities (H-SSZ-13 with Si:Al = 15 and Si:Al = 25). The third treatment (stirring the H-zeolite in water under ambient conditions for 24 hours) has not been tested on the samples with lower BA densities.

**Table 7.** Summary of BA deactivation experiments of H-SSZ-13 Si:Al = 4.5 samples

Treatment Condition	$H^+$ :Al <sub>tot</sub> before ( $\pm 0.1$ )	$H^+$ :Al <sub>tot</sub> after ( $\pm 0.1$ )
Store H-SSZ-13 at ambient conditions for 1 year	0.63	0.44
Calcine H-SSZ-13 with breathing air for 10 hours at 600°C	0.87	0.73
Stir in water at ambient conditions for 24 hours	0.87	0.22
Synthesize H-SSZ-13 Si:Al = 4.5 for 6 days vs 10 days	0.75 (6-day synthesis)	0.76 (10-day synthesis)
Synthesize H-SSZ-13 Si:Al = 4.5 with slow air-cool vs. water-quench.	0.74 (air-cool)	0.75 (water-quench)

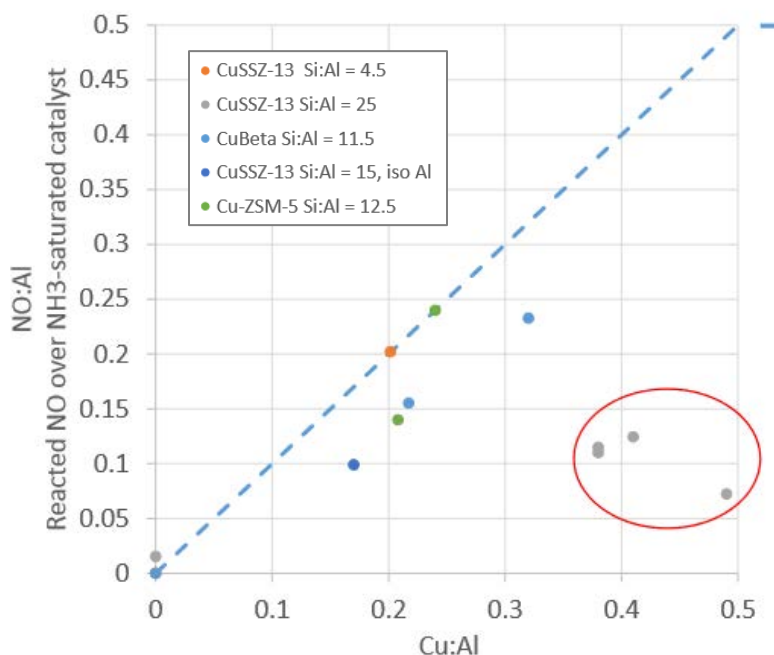


**Figure 25.** The molar NO:Cu fraction consumed after flowing NO (300 ppm NO in balance He, 200°C) through a sample saturated with NH<sub>3</sub> (300 ppm NH<sub>3</sub> in balance He, 200°C) and flushed with dry He. 95% confidence intervals are  $\pm 0.1$ .

In Figure 25, a variety of Cu-zeolites with varying Si:Al ratios and speciation were saturated with 500 ppm NH<sub>3</sub> at 160°C, then flushed with dry inert at 160°C. This saturation method is expected to result in NH<sub>3</sub> titrating both Brønsted acid and Lewis acidic (Cu ions) sites. A stream of 500 ppm NO was then introduced to the material and the molar NO:Al consumed was quantified. We expect the NO to react with NH<sub>3</sub> coordinated to Lewis acidic Cu ions to reduce the Cu(II) to Cu(I). The parity between the molar NO:Al ratio and molar Cu:Al ratio supports this hypothesis, but samples with a Si:Al = 25 are outliers, exhibiting molar NO:Al ratios 60 to 90% lower than parity. This could be due to the fact that most of the Cu in these Si:Al = 25 materials are CuOH (note that a model CuOH material with Si:Al = 15 (labeled as isoAl) synthesized using methods reported in Di Iorio et al. [105] have error bars too high to statistically distinguish whether it's an outlier or not). It could also be due to the fact that these samples have the lowest Brønsted acid density of all other samples tested.

## 4. DYNAMIC AND REVERSIBLE INTERCONVERSION OF $Z_2Cu$ AND $ZH/ZCuOH$ SITES IN $Cu-SSZ-13$

### 4.1 Abstract

Cu-zeolites are versatile due to their ability to catalyze a variety of reactions such as the selective catalytic reduction of  $NO_x$ , methane oxidation to methanol, dry NO oxidation, among others [1-3]. For each of these reactions, the identify of the active site is different for each reaction, as demonstrated by the experimental observation that some materials (e.g.  $Cu-SSZ-13$ ,  $Si:Al = 4.5$ ,  $Cu:Al = 0.21$ , all  $Z_2Cu$ ) are active for standard SCR, but not active for dry NO oxidation, indicating that understanding, synthesizing, and controlling the nature of Cu species will be able to allow us to increase the density of sites that are more active for a desired chemistries.

Immediately after ion-exchange, ionic Cu speciates as either  $Z_2H/CuOH$  or  $ZCuOH$  (Z indicates an anionic zeolite framework oxygen,  $H_2O$  molecules solvated to Cu are not shown for clarity). Upon dehydration or calcination,  $Z_2H/CuOH$  condenses into  $Z_2Cu$  as evidenced by the stoichiometric loss of BA sites from selective  $NH_3$  titration. It is demonstrated that  $Z_2Cu$  sites can be reversibly converted to  $Z_2H/CuOH$  sites via exposure to  $H_2O$  either at  $20^\circ C$  in liquid aqueous media or at  $30^\circ C$  with 2.5%  $H_2O$  in the vapor phase. Subsequent calcination of these  $Z_2H/CuOH$  species revert them back to  $Z_2Cu$  species, as probed by selective  $NH_3$  titration of residual Brønsted acid sites.

To garner an idea of how the possible implication of  $Cu^{2+}$  and  $H^+$  exchange between proximal anionic sites on the zeolite framework may also explain the phenomeon observed, we list all the reaction combinations that could explain the reversible  $Z_2H/CuOH$  and  $Z_2Cu$  phemomenon and sorted them into groups that involve  $Z_2CuOH/CuOH$  species, those that require  $Cu^{2+}$  and  $H^+$  ion exchange, those that do not, and those that do not change. We hope that this preliminary listing of possible reaction pathways will pave the way for computational studies to look into whether  $Cu^{2+}-H^+$  exchange between anionic sites is facile and whether other species such as  $Z_2H/CuOH$  are energetically favorable in the presence of  $H_2O$  ligands compared to  $Z_2Cu$ .

This study opens avenues to better understand the nature of the active site for various reactions, and to strategically synthesize Cu-zeolites with different fractions of these active sites.

## 4.2 Introduction

A number of studies report the intriguing observation that ZCuOH sites are able to convert to Z<sub>2</sub>Cu sites during thermal treatments (in the presence or absence of water). Luo et al. [108] quantified the increase of NH<sub>3</sub> coordinated to Lewis acidic Cu sites and decrease in Brønsted acidic H-sites from TPD after hydrothermal treatments of a Cu-SSZ-13 material at 600°C for various times. Luo et al. attributed this observation to the interconversion of ZCuOH sites to Z<sub>2</sub>Cu sites during hydrothermal steaming. In the study published by Song et al. [113], the fraction of Z<sub>2</sub>Cu, ZCuOH, and Cu<sub>x</sub>O<sub>y</sub> species after hydrothermal aging for 16 hours at temperatures between 550 and 900°C were quantified using elemental analysis (ICP) and EPR. They also measured the interconversion of ZCuOH sites to Z<sub>2</sub>Cu sites after hydrothermal steaming using NH<sub>3</sub> TPD, with the interconversion halting at 700°C. Song et al. [113] also took their Cu-SSZ-13 samples post-hydrothermal steaming and experimentally quantified the number of paired anionic sites using cobalt exchange [105]. A study by Sushkevich et al. [114] quantified the fraction of hydrated Cu(II), dehydrated Cu(II), and Cu(I) species on calcined and uncalcined Cu-MOR samples. They observed that uncalcined Cu-MOR samples contained a higher fraction of hydrated Cu(II) below temperature of 650 K than the calcined counterpart. It is also observed that the temperature of autoreduction of Cu(II) into Cu(I) in He flow is lower for the uncalcined material versus the calcined material, indicating that the different states of Cu in the two materials somehow lead to different reactivities during He autoreduction.

## 4.3 Experimental Methods

### 4.3.1 Cu-SSZ-13 sample preparation and selective NH<sub>3</sub> titration of residual Brønsted Acid sites

The experimental methods to prepare Cu-SSZ-13 materials and quantify the number of residual is the same as report in Section 1.13.3, with one minor difference: no calcination step in dry air after drying in the oven at 100°C overnight. The samples were sieved then loaded into the reactor

as illustrated in Section 1.14.1. The  $\text{NH}_3\text{:Al}$  ratio prior to calcination were then determined from  $\text{NH}_3$ -TPD (Section 1.13.3) and atomic absorption elemental analysis (Section 1.13.2).

Once the  $\text{NH}_3$  TPD reached and held its peak temperature ( $\sim 600^\circ\text{C}$ ) for 30 minutes in dry He, the gas environment was switched over to 20%  $\text{O}_2$  in balance He, thereby calcining the catalyst as the catalyst cooled down to  $160^\circ\text{C}$  over the course of 4 to 5 hours.

Once the catalyst has stabilized at  $160^\circ\text{C}$ , the 20%  $\text{O}_2/\text{He}$  gas environment was switched to dry He. The reactor and bypass lines were flushed with dry He (1200 sccm dry He, 30 minutes) to remove excess  $\text{O}_2$  prior to repeating the  $\text{NH}_3$ -TPD to determine the  $\text{NH}_3\text{:Al}$  ratio post-calcination.

#### **4.3.2 Aqueous $\text{Cu}(\text{NO}_3)_2$ treatment of a calcined Cu-SSZ-13 material**

To determine whether immersing a calcined Cu-SSZ-13  $\text{Z}_2\text{Cu}$  model material (Cu-SSZ-13 Si:Al = 4.5, Cu wt% = 3.8) to aqueous water can convert  $\text{Z}_2\text{Cu}$  to  $\text{ZCuOH}$  sites, we immersed 0.1 g of the calcined Cu-SSZ-13 sample in 100 mL of 0.1 M  $\text{Cu}(\text{NO}_3)_2$  at  $24^\circ\text{C}$  for 24 h in an 250 mL Erlenmeyer flask. A magnetic Teflon stirbar stirred the solution vigorously at 500 rpm for 24 hours. The sample was then washed with 50 mL of  $\text{H}_2\text{O}$  three times and left to dry overnight in a  $100^\circ\text{C}$  oven. Once dry, the catalyst was sieved and loaded into a flow-through reactor before subjected to  $\text{NH}_3$  saturation and  $\text{NH}_3$  TPD protocol for selectively measuring residual Brønsted acid sites.

#### **4.3.3 $\text{H}_2\text{O}$ vapor treatment of a calcined Cu-SSZ-13 material**

To determine whether immersing a calcined Cu-SSZ-13  $\text{Z}_2\text{Cu}$  model material (Cu-SSZ-13 Si:Al = 4.5, Cu wt% = 4.3) to water vapor can convert  $\text{Z}_2\text{Cu}$  to  $\text{ZCuOH}$  sites, we sieved, calcined, and loaded 1.76 mg of the model material into a flow-through reactor. 500 sccm of a 2.5%  $\text{H}_2\text{O}$  in balance  $\text{N}_2$  stream was flown through the catalyst at  $30^\circ\text{C}$  for 24 hours. Once complete, the catalyst was subjected to our standard  $\text{NH}_3$  saturation and  $\text{NH}_3$  TPD protocol for selectively measuring residual Brønsted acid sites.

### **4.4 Results and Discussion**

Four model H-SSZ-13 materials were Cu-exchanged via aqueous  $\text{Cu}(\text{NO}_3)_2$ , and dried in a  $100^\circ\text{C}$  oven. The number of residual Brønsted Acid sites on these uncalcined materials were



quantified via selective  $\text{NH}_3$  titration, and quantified again after calcination. The  $\text{NH}_3$  TPD profiles shown in Figure 26 indicate that a decrease in the number of residual Brønsted Acid sites are observed only for model  $\text{Z}_2\text{Cu}$  materials and not for model  $\text{ZCuOH}$  materials. Quantifying the  $\text{NH}_3:\text{Al}$  on the model  $\text{Z}_2\text{Cu}$  materials before and after calcination (Figure 27) indicates that the  $\text{NH}_3:\text{Al}$  measured on uncalcined samples are consistent with Cu siting as  $\text{ZCuOH}$  species regardless of the presence of paired anionic sites. These results suggest that after calcination, the  $\text{ZCuOH}$  transforms into  $\text{Z}_2\text{Cu}$  species until saturation of paired anionic sites, then the rest of the  $\text{ZCuOH}$  remains as  $\text{ZCuOH}$ . We propose that the precursor to  $\text{Z}_2\text{Cu}$  species are  $\text{Z}_2\text{H}/\text{CuOH}$  species that form either directly from the aqueous ion-exchange process, or form from  $\text{CuOH}^+/\text{H}^+$  exchange or migration during the calcination process.

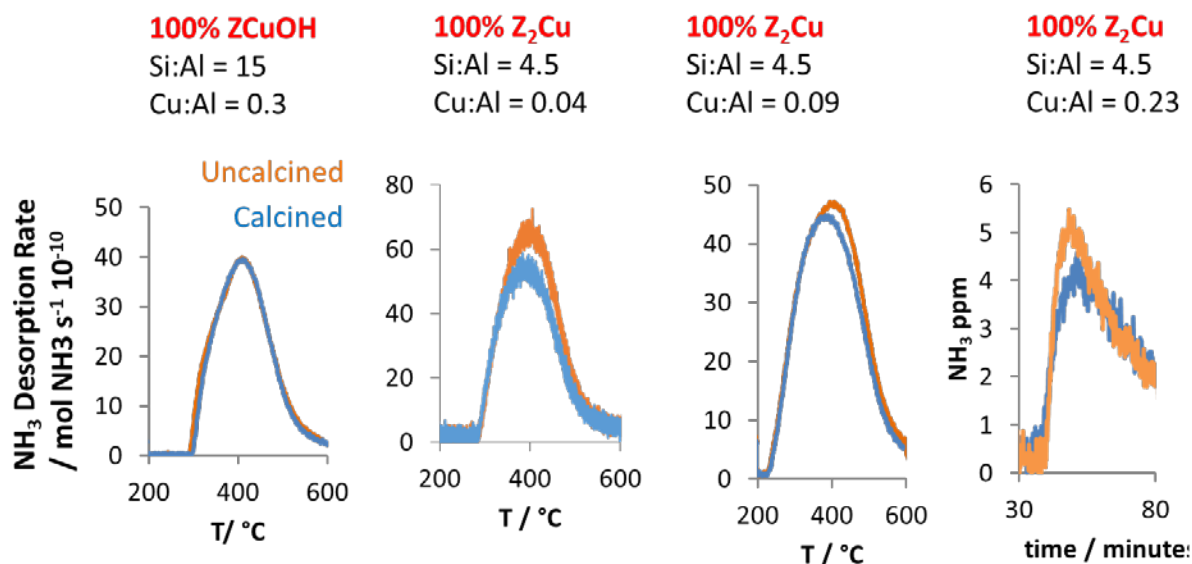


**Figure 26.**  $\text{NH}_3$  TPD profiles before (orange) and after (blue) calcination on four model samples.

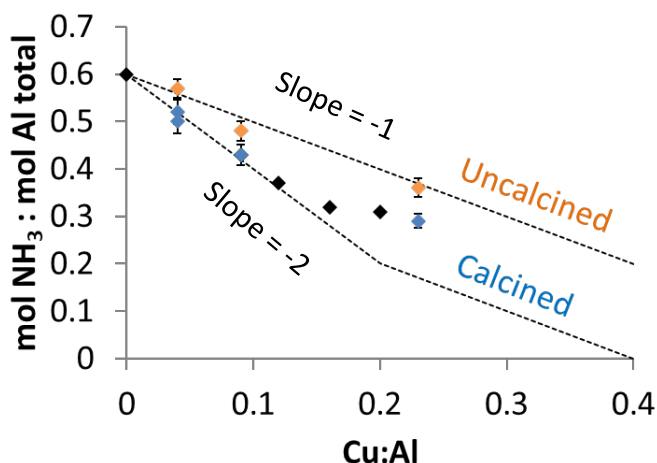


**Figure 27.**  $\text{NH}_3$  TPD shows a 1:1 loss in H for every exchanged Cu on Cu-SSZ-13 materials before calcination

Since calcination can convert  $\text{Z}_2\text{H}/\text{CuOH}$  sites to  $\text{Z}_2\text{Cu}$  and  $\text{H}_2\text{O}$ , one may question whether this process is reversible – whether subjecting  $\text{Z}_2\text{Cu}$  to an excess of  $\text{H}_2\text{O}$  can revert its chemical nature to  $\text{Z}_2\text{H}/\text{CuOH}$ . To test this, we designed a set of two experiments, the procedures of which can be found in Section 3.3.2 and Section 3.3.3.

The first experiment consisted of immersing a calcined Cu-SSZ-13 with only  $\text{Z}_2\text{Cu}$  sites (Cu-SSZ-13 Si:Al = 4.5, Cu:Al = 0.21) to a dilute 0.1 M  $\text{Cu}(\text{NO}_3)_2$  solution at  $24^\circ\text{C}$  for 24 hours. Since we immerse the Cu-SSZ-13 into an aqueous solution, ion exchange between the Cu ions in the zeolite and in the solution will occur until steady state equilibrium is achieved. Because of this, elemental analysis using AAS was performed on the sample after exposure to aqueous conditions, indicating that the Cu:Al increased from 0.21 to 0.23.  $\text{NH}_3$  TPD on the aqueous-treated Cu-SSZ-13 sample indicates that the  $\text{NH}_3$ :Al is indicative of all Cu existing as only  $\text{ZCuOH}$  species (Figure 28, left, orange) since a slope of -1 indicates that each  $\text{Cu}^{2+}$  displaces only one Brønsted  $\text{H}^+$  site even with the presence of paired anionic sites on the SSZ-13 framework. The residual proton count after a subsequent calcination suggests that Cu exists as  $\text{Z}_2\text{Cu}$  (Figure 28, left, blue) since a slope of -2 indicates that each  $\text{Cu}^{2+}$  displaces two Brønsted  $\text{H}^+$  sites. This sample was then exposed to 2.5% at  $30^\circ\text{C}$  for 24 hours before another  $\text{NH}_3$  TPD was performed (Figure 28, right, orange), indicative that exposure to  $\text{H}_2\text{O}$  vapor at  $30^\circ\text{C}$  can also revert  $\text{Z}_2\text{Cu}$  to  $\text{Z}_2\text{H}/\text{CuOH}$  species without changing the overall Cu density of the Cu-SSZ-13

material. A subsequent calcination and  $\text{NH}_3$  TPD was performed to confirm that the  $\text{Z}_2\text{H}/\text{CuOH}$  sites formed can revert back to  $\text{Z}_2\text{Cu}$  (Figure 28, right, blue). Figure 29 plots the quantified  $\text{NH}_3:\text{Al}$  ratios after each  $\text{H}_2\text{O}$  treatment and calcination, indicating that  $\text{Z}_2\text{H}/\text{CuOH}$  and  $\text{Z}_2\text{Cu}$  sites are indeed reversible.

After exposing the Cu-SSZ-13 to standard SCR conditions and collecting differential rates, selective  $\text{NH}_3$  titration of the residual acid sites was performed (Figure 28, right, black). The number of residual acid sites indicate that the Cu-SSZ-13 material after exposure to standard SCR conditions contain a mixture of Cu species bound to two anionic sites and Cu species bound to one anionic site in the framework. This may suggest that during standard SCR,  $-\text{OH}$  ligands dynamically and reversibly appear and disappear on  $\text{Cu}^{2+}$  active sites as the reaction turns over. From the current understanding of the low temperature ( $200^\circ\text{C}$ ) standard SCR mechanism over Cu-SSZ-13, this proposal is plausible since the  $\text{Cu}(\text{I})(\text{NH}_3)_2$  intermediate is the same regardless of whether it's precursor is  $\text{Z}_2\text{Cu}$  or  $\text{ZCuOH}$  [115]. This indicates that  $\text{CuOH}$  site and ammonium ion likely occurs at paired anionic sites during the standard SCR reaction.

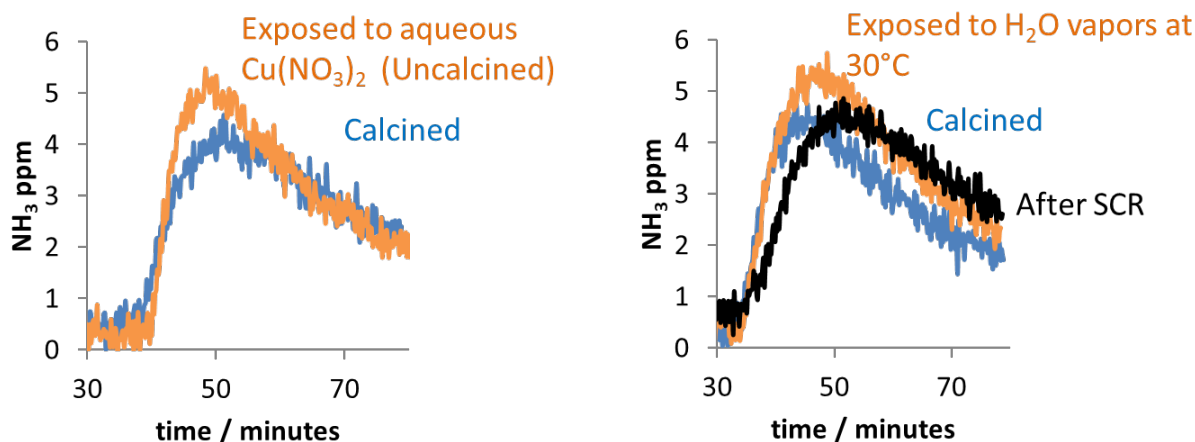


**Figure 28.** Left:  $\text{NH}_3$  TPD profiles on an uncalcined (orange) and calcined (blue) Cu-SSZ-13 Si:Al = 4.5, Cu:Al = 0.23. Right:  $\text{NH}_3$  TPD profiles after flowing  $\text{H}_2\text{O}$  vapors at  $30^\circ\text{C}$  (2.5  $\text{H}_2\text{O}$  wt% in balance He, 800 sccm, 2 mg catalyst) for 24 hours (orange), after calcination (blue), and after exposure to standard SCR gases for 72 hours (black).

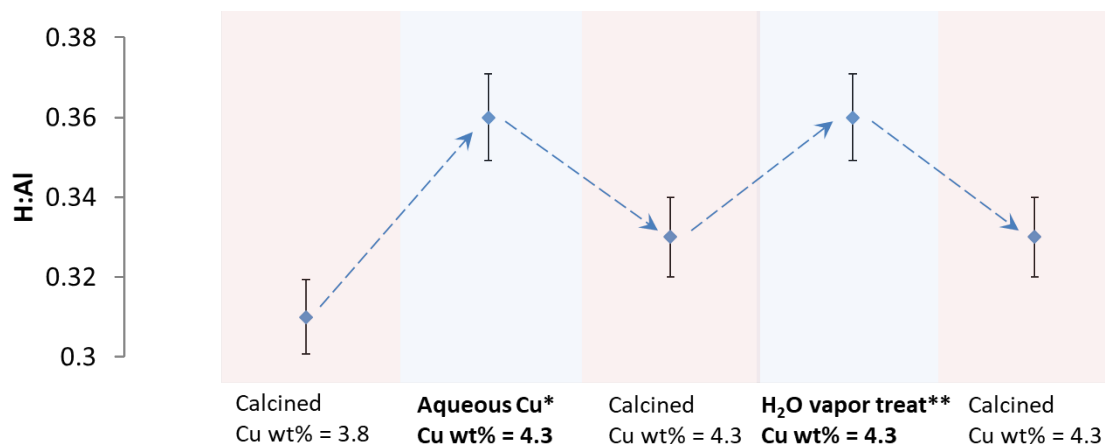


**Figure 29.** H:Al values measured from  $\text{NH}_3$  on TPD after a variety of post-calcination treatments. From left-to-right: (1) calcined Cu-SSZ-13 (Si:Al = 4.5, Cu wt% = 3.8), (2) uncalcined Cu-SSZ-13 after exposure to aqueous  $\text{Cu}(\text{NO}_3)_2$  for 24 hours\* (Si:Al = 4.5, Cu wt% = 4.3), (3) calcined Cu-SSZ-13 (Si:Al = 4.5, Cu wt% = 4.3), (4) calcined Cu-SSZ-13 vapor  $\text{H}_2\text{O}$  exposed at  $30^\circ\text{C}$  for 24 hours\*\*, (5) calcined Cu-SSZ-13

\*100 mL 0.1 M  $\text{Cu}(\text{NO}_3)_2$  + 0.1 g Cu-SSZ-13 (Si:Al = 4.5, Cu wt% = 3.8),  $24^\circ\text{C}$  for 24 h

\*\*2.5%  $\text{H}_2\text{O}$  in 500 mL  $\text{N}_2$  through 1.76 mg Cu-SSZ-13 (Si:Al = 4.5, Cu wt% = 4.3) for 24h

Standard SCR reaction Arrhenous plots collected before and after vapor treatment confirm that after the vapor treatment did not affect the overall rate on the catalyst (Figure 30). The standard SCR rate collected before and after the aqueous  $\text{Cu}(\text{NO}_3)_2$  treatment also exhibited the same reaction rate normalized mol Cu of  $7 \cdot 10^{-11} \text{ mol}_{\text{NO}} \text{ mol}_{\text{Cu}}^{-1} \text{ s}^{-1}$  under standard SCR conditions at  $200^\circ\text{C}$ , indicating that the Cu sites did not deactivate.

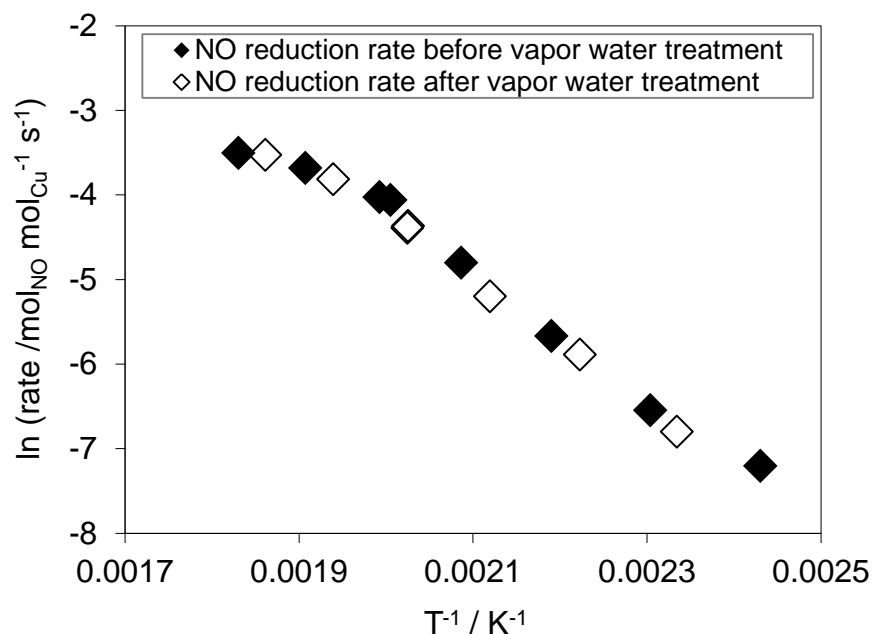


**Figure 30.** Arrhenius plot collected on Cu-SSZ-13 (Si:Al = 4.5, Cu wt% = 4.3) before and after the vapor  $\text{H}_2\text{O}$  treatment.

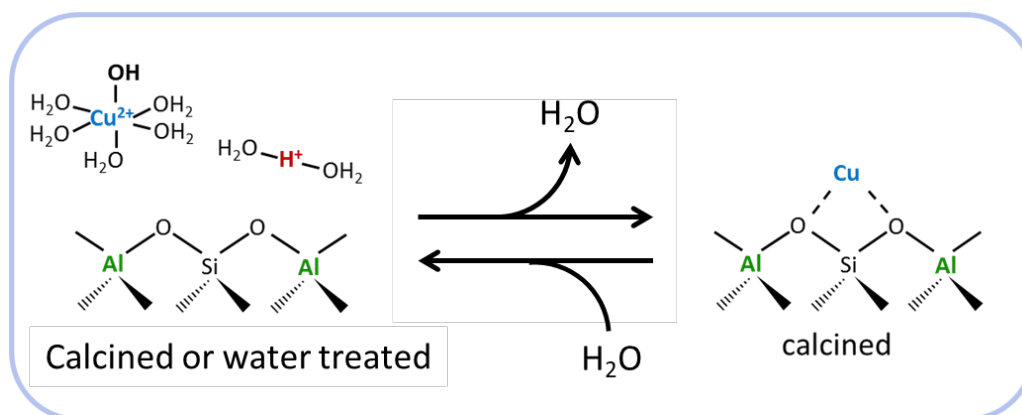


**Figure 31.** Schematic illustrating the reversibility of ZH/ZCuOH and  $\text{Z}_2\text{Cu}$  sites at paired anionic sites on the zeolite framework.

It is difficult to collect spectroscopic data to further support these claims since the presence of water before thermal condensation makes it difficult to discern Cu-OH stretches from other -OH stretches from  $\text{H}_2\text{O}$  [116]. To this, we turn our focus toward computation in hopes that listing out all possible mechanistic pathways to form these  $\text{Z}_2\text{H}/\text{CuOH}$  sites prior to condensation into  $\text{Z}_2\text{Cu}$  and  $\text{H}_2\text{O}$  may open our eyes to the list of plausible reaction schemes. Though no DFT study has

been performed, we hope that having a table of DFT-computed energies with and without H<sub>2</sub>O ligands may shed insight into this phenomenon.

We first define six possible different types of sites that can be found on a Cu-SSZ-13 material. These sites are shown in Figure 32 and include isolated Al sites, paired Al sites, and all the combinations of H<sup>+</sup>, CuOH, and Cu<sup>2+</sup> that can charge balance these sites. To garner an understanding of how neighboring sites may cause ion-exchange hopping, we consider all combinations of the six sites displayed in Figure 32 and asked ourselves how having one, two, or three of these three sites in proximity to each other (Figure 33) (close enough to facilitate ion-exchange between Cu<sup>2+</sup> species and H<sup>+</sup> species) can lead to mechanisms that are consistent with our observations from NH<sub>3</sub>-TPD.

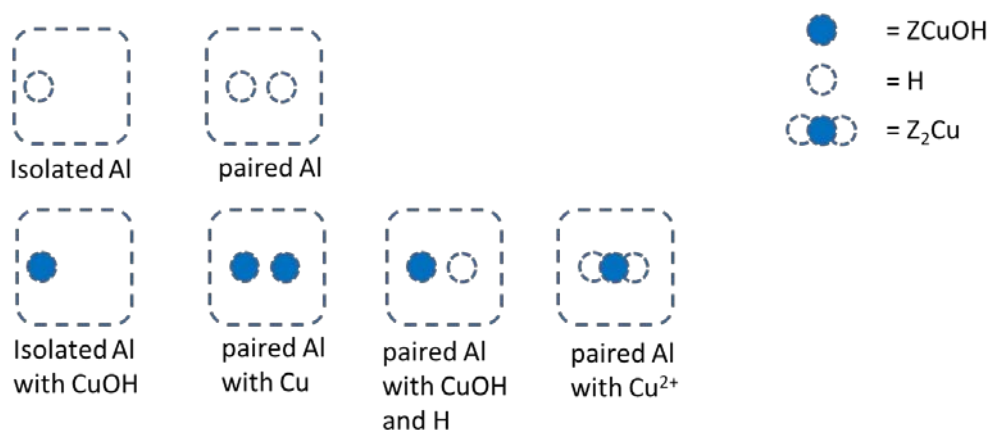


**Figure 32.** Six different types of possible sites on Cu-SSZ-13.

One-site model



Two-site model



Three-site model

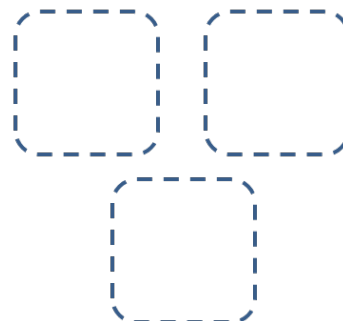


**Figure 33.** One-site, two-site, and three-site models account for ion-exchange between  $\text{Cu}^{2+}$  ions and  $\text{H}^+$  ions between paired and unpaired sites proximal to none, one other, or two other paired or unpaired sites, respectively.

To avoid repeated combinations and combinations that are consistent with the observations made from  $\text{NH}_3$  TPD, the following rules are also applied:

- Cu sites only as ZCuOH after aqueous ion-exchange
- Sites that have no Cu are represented by an H, even though they could easily be a  $\text{NH}_4^+$
- Species can spatially exchange with other species, thereby hop between anionic Al sites
- The following permutations are considered equivalent, and will not be double counted.
  - $\text{ZH/ZCuOH} = \text{ZCuOH/ZH}$
  - $\text{ZH} + \text{ZCuOH} = \text{ZCuOH} + \text{H}$
  - $\text{ZH/ZCuOH} + \text{ZCuOH} = \text{ZCuOH} + \text{ZH/ZCuOH}$
  - $\text{ZH} + \text{ZH} + \text{ZCuOH} = \text{ZH} + \text{ZCuOH} + \text{ZH} = \text{ZCuOH} + \text{ZH} + \text{ZH}$
  - $\text{ZH} + \text{ZCuOH} + \text{ZCuOH} = \text{ZCuOH} + \text{ZCuOH} + \text{ZH} = \text{ZCuOH} + \text{ZH} + \text{ZCuOH}$
  - $\text{ZH} + \text{ZH} + \text{ZH/ZCuOH} = \text{ZH} + \text{ZH/ZCuOH} + \text{ZH} = \text{ZH/ZCuOH} + \text{ZH} + \text{ZH}$
  - $\text{ZH} + \text{ZH/ZCuOH} + \text{ZH/ZCuOH} = \text{ZH/ZCuOH} + \text{ZH/ZCuOH} + \text{ZH} =$   
 $\text{ZH/ZCuOH} + \text{ZH} + \text{ZH/ZCuOH}$

Table 8 lists all combinations of the sites shown in Figure 32 and Figure 33 while following the restrictions listed above.

**Table 8.** List of all possible combinations of sites and proximal sites, and their most stable form assuming that Cu and H are allowed to exchange/hop and if CuOH and proximal H<sup>+</sup> sites are allowed to condense.

Numb er of Sites	Permutation	Possible products after calcination	Comments	ZCuOH/ZCuO H present in reactant?	ZCuOH/ZCuO H present in products?	Does CuOH hop?
1	ZH	ZH	Did not change			
1	ZCuOH	ZCuOH	Did not change			
1	ZH/ZH	ZH/ZH	Did not change			
1	ZH/ZCuOH	Z <sub>2</sub> Cu + H <sub>2</sub> O	Condensed			
1	ZCuOH/ZCuOH	ZCuOH/ZCuOH	Did not change	✓	✓	
2	ZH + ZH	ZH + ZH	Did not change			
2	ZH + ZCuOH	ZH + ZCuOH	Cu could have hopped			
2	ZCuOH + ZCuOH	ZCuOH + ZCuOH	Did not change			
2	ZH + ZH/ZH	ZH + ZH/ZH	Did not change			
2	ZH + ZH/ZCuOH	ZH + Z <sub>2</sub> Cu + H <sub>2</sub> O	Condensed			
2	ZH + ZCuOH/ZCuOH	ZCuOH + Z <sub>2</sub> Cu + H <sub>2</sub> O	Cu could have hopped then condensed	✓		✓
2	ZCuOH + ZH/ZH	ZH + Z <sub>2</sub> Cu + H <sub>2</sub> O	Cu could have hopped then condensed			✓
2	ZCuOH + ZH/ZCuOH	ZCuOH + Z <sub>2</sub> Cu + H <sub>2</sub> O	Condensed			
2	ZCuOH + ZCuOH/ZCuOH	ZCuOH + ZCuOH/ZCuOH	Did not change	✓	✓	



2	ZH/ZH + ZH/ZH	ZH/ZH + ZH/ZH	Did not change			
2	ZH/ZH + ZH/ZCuOH	ZH/ZH + Z <sub>2</sub> Cu + H <sub>2</sub> O	Condensed			
2	ZH/ZH + ZCuOH/ZCuOH	Z <sub>2</sub> Cu + Z <sub>2</sub> Cu + 2H <sub>2</sub> O	Cu could have hopped then condensed	✓		✓
2	ZH/ZCuOH + ZH/ZCuOH	Z <sub>2</sub> Cu + Z <sub>2</sub> Cu + 2H <sub>2</sub> O	Condensed			
2	ZCuOH/ZCuOH + ZH/ZCuOH	ZCuOH/ZCuOH + Z <sub>2</sub> Cu + H <sub>2</sub> O	Condensed, ZCuOH/ZCuOH present after calcination	✓	✓	
2	ZCuOH/ZCuOH + ZCuOH/ZCuOH	ZCuOH/ZCuOH + Z <sub>2</sub> Cu + H <sub>2</sub> O	Did not change, ZCuOH/ZCuOH present after calcination	✓	✓	
3	ZH + ZH + ZH	ZH + ZH + ZH	Did not change			
3	ZH + ZH+ ZCuOH	ZH + ZH+ ZCuOH	Did not change			
3	ZH + ZCuOH + ZCuOH	ZH + ZCuOH + ZCuOH	Did not change			
3	ZCuOH + ZCuOH + ZCuOH	ZCuOH + ZCuOH + ZCuOH	Did not change			
3	ZH + ZH + ZH/ZH	ZH + ZH + ZH/ZH	Did not change			
3	ZH + ZH+ ZH/ZCuOH	ZH + ZH+ Z <sub>2</sub> Cu + H <sub>2</sub> O	Condensed			
3	ZH + ZCuOH + ZH/ZH	ZH + ZH+ Z <sub>2</sub> Cu + H <sub>2</sub> O	Cu could have hopped then condensed			✓
3	ZH + ZCuOH + ZH/ZCuOH	ZH + ZCuOH + Z <sub>2</sub> Cu + H <sub>2</sub> O	Condensed			

3	ZCuOH + ZCuOH + ZH/ZH	ZH + ZCuOH + Z <sub>2</sub> Cu + H <sub>2</sub> O	Cu could have hopped then condensed			✓
3	ZH + ZH + ZCuOH/ZCuOH	ZH + ZCuOH + Z <sub>2</sub> Cu + H <sub>2</sub> O	Cu could have hopped then condensed	✓		✓
3	ZCuOH + ZCuOH + ZH/ZCuOH	ZCuOH + ZCuOH + Z <sub>2</sub> Cu + H <sub>2</sub> O	Condensed			
3	ZH + ZCuOH + ZCuOH/ZCuOH	ZCuOH + ZCuOH + Z <sub>2</sub> Cu + H <sub>2</sub> O	Cu could have hopped then condensed	✓		✓
3	ZCuOH + ZCuOH + ZCuOH/ZCuOH	ZCuOH + ZCuOH + ZCuOH/ZCuOH	Did not change, ZCuOH/ZCuOH present after calcination	✓	✓	
3	ZH + ZH/ZH + ZH/ZH	ZH + ZH/ZH + ZH/ZH	Did not change			
3	ZH + ZH/ZH + ZH/ZCuOH	ZH + ZH/ZH + Z <sub>2</sub> Cu + H <sub>2</sub> O	Condensed			
3	ZCuOH + ZH/ZH + ZH/ZH	ZH + ZH/ZH + Z <sub>2</sub> Cu + H <sub>2</sub> O	Cu could have hopped then condensed			✓
3	ZCuOH + ZH/ZH + ZH/ZCuOH	ZH + Z <sub>2</sub> Cu + Z <sub>2</sub> Cu + 2H <sub>2</sub> O	Cu could have hopped then condensed			✓
3	ZH + ZH/ZCuOH + ZH/ZCuOH	ZH + Z <sub>2</sub> Cu + Z <sub>2</sub> Cu + 2H <sub>2</sub> O	Condensed			
3	ZH + ZH/ZH + ZCuOH/ZCuOH	ZH + Z <sub>2</sub> Cu + Z <sub>2</sub> Cu + 2H <sub>2</sub> O	Cu could have hopped then condensed	✓		✓
3	ZCuOH + ZH/ZH + ZCuOH/ZCuOH	ZCuOH + Z <sub>2</sub> Cu + Z <sub>2</sub> Cu + 2H <sub>2</sub> O	Cu could have hopped then	✓		✓

			condensed			
3	ZCuOH + ZH/ZCuOH + ZH/ZCuOH	ZCuOH + Z <sub>2</sub> Cu + Z <sub>2</sub> Cu + 2H <sub>2</sub> O	Condensed			
3	ZH + ZCuOH/ZCuOH + ZH/ZCuOH	ZCuOH + Z <sub>2</sub> Cu + Z <sub>2</sub> Cu + 2H <sub>2</sub> O	Cu could have hopped then condensed	✓		✓
3	ZH + ZCuOH/ZCuOH + ZCuOH/ZCuOH	ZCuOH + ZCuOH/ZCuOH + Z <sub>2</sub> Cu + H <sub>2</sub> O	Cu could have hopped then condensed, ZCuOH/ZCuOH present after calcination	✓	✓	✓
3	ZCuOH + ZH/ZCuOH + ZCuOH/ZCuOH	ZCuOH + ZCuOH/ZCuOH + Z <sub>2</sub> Cu + H <sub>2</sub> O	Condensed, ZCuOH/ZCuOH present after calcination	✓	✓	
3	ZCuOH + ZCuOH/ZCuOH + ZCuOH/ZCuOH	ZCuOH + ZCuOH/ZCuOH + ZCuOH/ZCuOH	Did not change, ZCuOH/ZCuOH present after calcination	✓	✓	
3	ZH/ZH + ZH/ZH + ZH/ZH	ZH/ZH + ZH/ZH + ZH/ZH	Did not change			
3	ZH/ZH + ZH/ZH + ZH/ZCuOH	ZH/ZH + ZH/ZH + Z <sub>2</sub> Cu + H <sub>2</sub> O	Condensed			
3	ZH/ZH + ZH/ZH + ZCuOH/ZCuOH	ZH/ZH + Z <sub>2</sub> Cu + Z <sub>2</sub> Cu + 2H <sub>2</sub> O	Cu could have hopped then condensed	✓		✓
3	ZH/ZH + ZH/ZCuOH + ZH/ZCuOH	ZH/ZH + ZH/ZCuOH + ZH/ZCuOH	Condensed			
3	ZH/ZH + ZH/ZCuOH + ZCuOH/ZCuOH	Z <sub>2</sub> Cu + Z <sub>2</sub> Cu + Z <sub>2</sub> Cu + 3H <sub>2</sub> O	Cu could have hopped then	✓		✓

			condensed			
3	ZH/ZCuOH + ZH/ZCuOH + ZH/ZCuOH	ZH/ZCuOH + ZH/ZCuOH + ZH/ZCuOH	Condensed			
3	ZH/ZCuOH + ZH/ZCuOH + ZCuOH/ZCuOH	ZCuOH/ZCuOH +Z <sub>2</sub> Cu + Z <sub>2</sub> Cu + 2H <sub>2</sub> O	Condensed, ZCuOH/ZCuOH present after calcination	✓	✓	
3	ZH/ZH + ZCuOH/ZCuOH + ZCuOH/ZCuOH	ZCuOH/ZCuOH +Z <sub>2</sub> Cu + Z <sub>2</sub> Cu + 2H <sub>2</sub> O	Cu could have hopped then condensed, ZCuOH/ZCuOH present after calcination	✓	✓	✓
3	ZH/ZCuOH + ZCuOH/ZCuOH + ZCuOH/ZCuOH	Z <sub>2</sub> Cu + ZCuOH/ZCuOH + ZCuOH/ZCuOH + H <sub>2</sub> O	Condensed, ZCuOH/ZCuOH present after calcination	✓	✓	
3	ZCuOH/ZCuOH + ZCuOH/ZCuOH + ZCuOH/ZCuOH	ZCuOH/ZCuOH + ZCuOH/ZCuOH + ZCuOH/ZCuOH	Did not change, ZCuOH/ZCuOH present after calcination	✓	✓	

Since ZCuOH/ZCuOH is likely more unstable than Z<sub>2</sub>Cu and likely will not occur unless at high Cu loadings, we will neglect reactions that involve those species in the reactant or products. DFT computation of the stability of these species compared to other comparable species that could form is required to further justify or debunk this assumption. Table 9 lists the remaining 34 possible mechanisms sorted by three criteria: (1) whether CuOH needs to ion-exchange hop with a H<sup>+</sup> prior to condensation to form Z<sub>2</sub>Cu (5 scenarios), (2) whether Z<sub>2</sub>H/CuOH can condense to form Z<sub>2</sub>Cu without the need of any ion-exchange hopping (14 scenarios), (3) whether nothing changed between the reactants and products (15 scenarios).

**Table 9.** List of possible mechanisms with scenarios with two  $Z_2CuOH/CuOH$  (two  $ZCuOH$ 's at a paired anionic site) negated.

Number of Sites	Permutation	Possible products after calcination	Comments
2	$ZCuOH + ZH/ZH$	$ZH + Z_2Cu + H_2O$	Cu hopped then condensed
3	$ZH + ZCuOH + ZH/ZH$	$ZH + ZH + Z_2Cu + H_2O$	Cu hopped then condensed
3	$ZCuOH + ZCuOH + ZH/ZH$	$ZH + ZCuOH + Z_2Cu + H_2O$	Cu hopped then condensed
3	$ZCuOH + ZH/ZH + ZH/ZH$	$ZH + ZH/ZH + Z_2Cu + H_2O$	Cu hopped then condensed
3	$ZCuOH + ZH/ZH + ZH/ZCuOH$	$ZH + Z_2Cu + Z_2Cu + 2H_2O$	Cu hopped then condensed
1	$ZH$	$ZH$	Did not change
1	$ZCuOH$	$ZCuOH$	Did not change
1	$ZH/ZH$	$ZH/ZH$	Did not change
2	$ZH + ZH$	$ZH + ZH$	Did not change
2	$ZCuOH + ZCuOH$	$ZCuOH + ZCuOH$	Did not change
2	$ZH + ZH/ZH$	$ZH + ZH/ZH$	Did not change
2	$ZH/ZH + ZH/ZH$	$ZH/ZH + ZH/ZH$	Did not change
3	$ZH + ZH + ZH$	$ZH + ZH + ZH$	Did not change
3	$ZH + ZH + ZCuOH$	$ZH + ZH + ZCuOH$	Did not change
3	$ZH + ZCuOH + ZCuOH$	$ZH + ZCuOH + ZCuOH$	Did not change
3	$ZCuOH + ZCuOH + ZCuOH$	$ZCuOH + ZCuOH + ZCuOH$	Did not change
3	$ZH + ZH + ZH/ZH$	$ZH + ZH + ZH/ZH$	Did not change

3	ZH + ZH/ZH + ZH/ZH	ZH + ZH/ZH + ZH/ZH	Did not change
3	ZH/ZH + ZH/ZH + ZH/ZH	ZH/ZH + ZH/ZH + ZH/ZH	Did not change
1	ZH/ZCuOH	Z <sub>2</sub> Cu + H <sub>2</sub> O	Condensed
2	ZH + ZCuOH	ZH + ZCuOH	Cu could have hopped
2	ZH + ZH/ZCuOH	ZH + Z <sub>2</sub> Cu + H <sub>2</sub> O	Condensed
2	ZCuOH + ZH/ZCuOH	ZCuOH + Z <sub>2</sub> Cu + H <sub>2</sub> O	Condensed
2	ZH/ZH + ZH/ZCuOH	ZH/ZH + Z <sub>2</sub> Cu + H <sub>2</sub> O	Condensed
2	ZH/ZCuOH + ZH/ZCuOH	Z <sub>2</sub> Cu + Z <sub>2</sub> Cu + 2H <sub>2</sub> O	Condensed
3	ZH + ZH+ ZH/ZCuOH	ZH + ZH+ Z <sub>2</sub> Cu + H <sub>2</sub> O	Condensed
3	ZH + ZCuOH + ZH/ZCuOH	ZH + ZCuOH + Z <sub>2</sub> Cu + H <sub>2</sub> O	Condensed
3	ZCuOH + ZCuOH + ZH/ZCuOH	ZCuOH + ZCuOH + Z <sub>2</sub> Cu + H <sub>2</sub> O	Condensed
3	ZH + ZH/ZH + ZH/ZCuOH	ZH + ZH/ZH + Z <sub>2</sub> Cu + H <sub>2</sub> O	Condensed
3	ZH + ZH/ZCuOH + ZH/ZCuOH	ZH + Z <sub>2</sub> Cu + Z <sub>2</sub> Cu + 2H <sub>2</sub> O	Condensed
3	ZCuOH + ZH/ZCuOH + ZH/ZCuOH	ZCuOH + Z <sub>2</sub> Cu + Z <sub>2</sub> Cu + 2H <sub>2</sub> O	Condensed
3	ZH/ZH + ZH/ZH + ZH/ZCuOH	ZH/ZH + ZH/ZH + Z <sub>2</sub> Cu + H <sub>2</sub> O	Condensed
3	ZH/ZH + ZH/ZCuOH + ZH/ZCuOH	ZH/ZH + Z <sub>2</sub> Cu + Z <sub>2</sub> Cu + 2H <sub>2</sub> O	Condensed
3	ZH/ZCuOH + ZH/ZCuOH + ZH/ZCuOH	Z <sub>2</sub> Cu + Z <sub>2</sub> Cu + Z <sub>2</sub> Cu + 3H <sub>2</sub> O	Condensed

## 4.5 Conclusions

In summary, high temperature ( $>350^{\circ}\text{C}$ ) dehydration condenses  $\text{ZCuOH/ZH}$  into  $\text{Z}_2\text{Cu}$ .

Tracking the synthesis and treatment history can allow us to understand seemingly conflicting results from the literature.  $\text{Z}_2\text{Cu}$  and  $\text{Z}_2\text{H/CuOH}$  can dynamically and reversibly interconvert with calcination and low temperature ( $<50^{\circ}\text{C}$ )  $\text{H}_2\text{O}$  treatments. Finally, to further understand all possible mechanisms, from combinatorial analysis, we generated a list of 35 possible condensation mechanisms that are consistent with the  $\text{NH}_3:\text{Al}$  observations from our previous studies [43,68,109] and the new data collected in this study. It is our hopes that these 35 possible mechanisms can be labeled as likely possible or not possible from DFT energy calculations of the sites with and without  $\text{H}_2\text{O}$  ligands.

## 4.6 Acknowledgements

The author acknowledges Ishant Khurana, Trevor Lardinois, Juan Gonzalez, Lucia Perez, and Andres Pena Lozano for discussions.

## 4.7 Supplementary Information

To further confirm that  $\text{Cu}^{2+}$  at paired anionic sites do speciate as  $\text{Z}_2\text{H/CuOH}$  after aqueous ion-exchange or low-temperature ( $20$  to  $30^{\circ}\text{C}$ )  $\text{H}_2\text{O}$  treatments, an attempt to quantify the amount of  $\text{H}_2\text{O}$  evolved during condensation of  $\text{Z}_2\text{H/CuOH}$  to  $\text{Z}_2\text{Cu}$  was carried out, Figure 34.

Unfortunately, we were unable to deconvolute  $\text{H}_2\text{O}$  desorbing from the condensation of  $\text{Z}_2\text{H/CuOH}$  to  $\text{Z}_2\text{Cu}$  from  $\text{H}_2\text{O}$  ligands simply desorbing from  $\text{Cu}^{2+}$  cations or other locations on the Cu-SSZ-13 material.

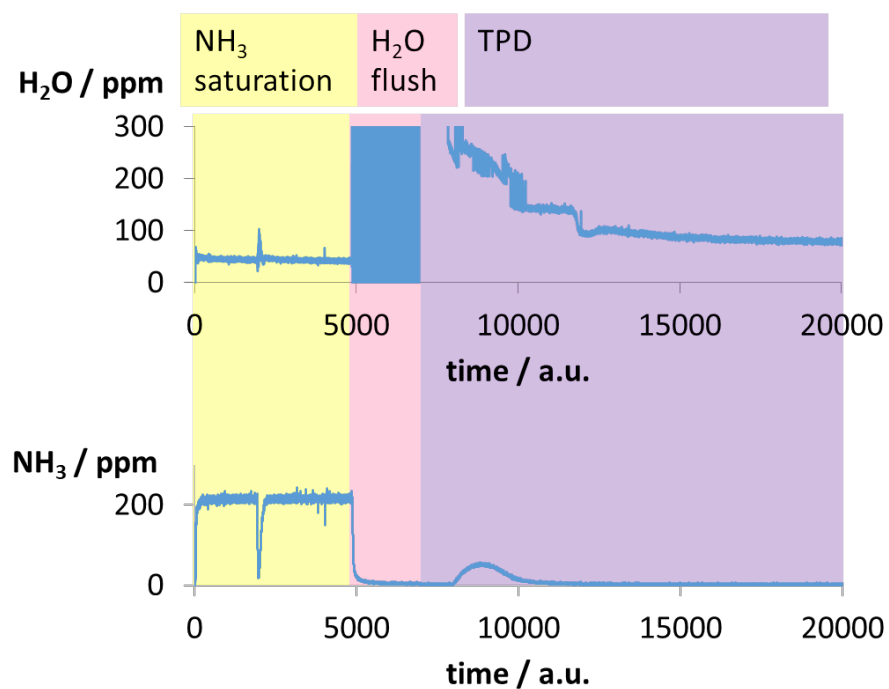


**Figure 34.** Attempt to quantify the mols of H<sub>2</sub>O released during dehydration of Z<sub>2</sub>H/CuOH species on a model Z<sub>2</sub>Cu Cu-SSZ-13 material (Si:Al = 4.5, Cu:Al = 0.21).



## 5. NATURE OF CU SPECIES DURING STANDARD SCR

### 5.1 Abstract

Having established that  $\text{Cu}^{2+}$  sites are active for the standard  $\text{NH}_3$ -SCR reaction via the Koros-Nowak criterion, we explore and piece together the molecular picture of the active sites in this chapter. From *operando* XAS experiments, we discover that under reaction conditions, Cu exists in two oxidation state:  $\text{Cu}^{2+}$  and  $\text{Cu}^{1+}$ , which provides evidence that Cu undergoes a reduction-oxidation reaction during catalysis. Furthermore, DFT calculations and in-situ XAS provide evidence that the reduction half-cycle requires  $\text{NO} + \text{NH}_3$ , and results in the formation of  $\text{Cu(I)(NH}_3)_2$  species. We then provide evidence from Monte-Carlo simulations and *in-situ* XAS that the oxidation of  $\text{Cu(I)(NH}_3)_2$  is not mean-field and is a function of the Cu density in Cu-SSZ-13.

### 5.2 Introduction

#### 5.2.1 Rationally piecing together the standard SCR mechanism like a mosaic

As advised by Professor. W. Nicholas Delgass, “The objective of life’s career is to build a mosaic of the connections of the physical world... when you see evidence, try to fit it into your mosaic. [Ask yourself] what do I know about the chemical world and why would that happen?” [117]. This chapter will step the reader through the iterative process of designing and collecting evidence and updating our current mosaic of the standard SCR catalytic cycle. The understanding of the nature of the Cu ions under different environmental conditions (gas pressures and temperature) are represented in black rectangles with curved corners in figures. In the spirit of “building the mosaic”, the molecular picture in these figures will be gradually refined as evidence is presented.

As introduced in the previous two chapters, two  $\text{Cu}^{2+}$  species ( $\text{Z}_2\text{Cu}$  and  $\text{ZCuOH}$ ) exist on Cu-SSZ-13 materials after aqueous Cu exchange, calcination, and return to ambient hydrated conditions at  $25^\circ\text{C}$ , as summarized in Figure 35. To reiterate, we use titration (selective  $\text{NH}_3$  titration of residual Brønsted Acid sites, selective  $\text{Co}^{2+}$  titration of paired anionic sites in CHA), spectroscopy (FTIR to identify and quantify Brønsted Acid sites and Cu-OH stretching

frequencies), and computation (Monte Carlo simulations to quantify paired anionic sites) to piece together this molecular picture. Each  $\text{Cu}^{2+}$  exhibits six  $\text{H}_2\text{O}$  molecules, as evidenced from EXAFS coordination numbers. The presence of a UV-Visible d-d transition suggests that the axial  $\text{H}_2\text{O}$  ligands exhibit longer Cu-O bonds than the other four equatorial  $\text{H}_2\text{O}$  ligands because of the Jahn-Teller distortion, which states the slight asymmetry in the ligands the d bands to split ever so slightly, leading to electronic excitation features in spectroscopy such as UV-Visible [112].

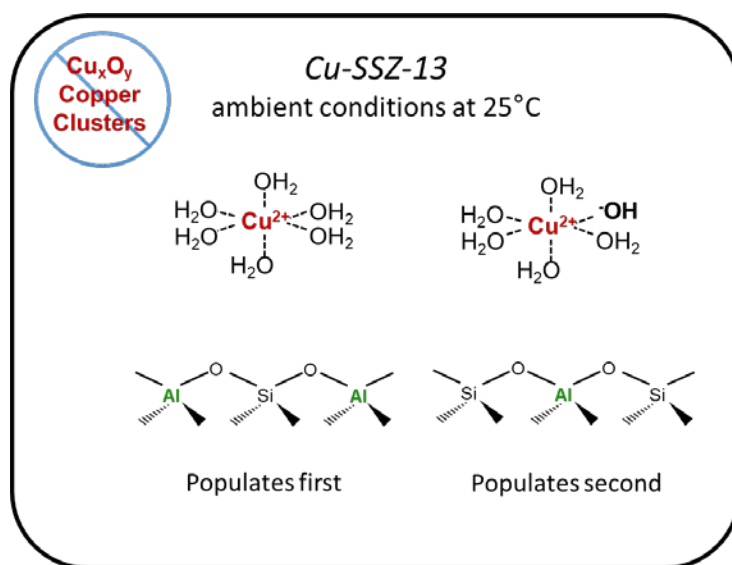


**Figure 35.** Nature of the nature of two  $\text{Cu}^{2+}$  active sites on Cu-SSZ-13 materials after calcination (treatment by flowing dry air at 600°C for 6 hours) and return to ambient hydrated conditions (ambient air, 20°C).

It was demonstrated using selective  $\text{NH}_3$  titration of residual acid sites that after aqueous Cu-exchange and prior to calcination,  $\text{ZCuOH}$  sites at paired anionic sites as  $\text{Z}_2\text{H}/\text{CuOH}$ . Upon calcination these molecular species condense to  $\text{Z}_2\text{Cu}$  sites, and can be reverted back to  $\text{Z}_2\text{H}/\text{CuOH}$  species after low temperature (20 to 30°C) exposures to water either in the aqueous phase or vapor phase, Figure 36. Subsequent calcinations revert these species back to  $\text{Z}_2\text{Cu}$ .

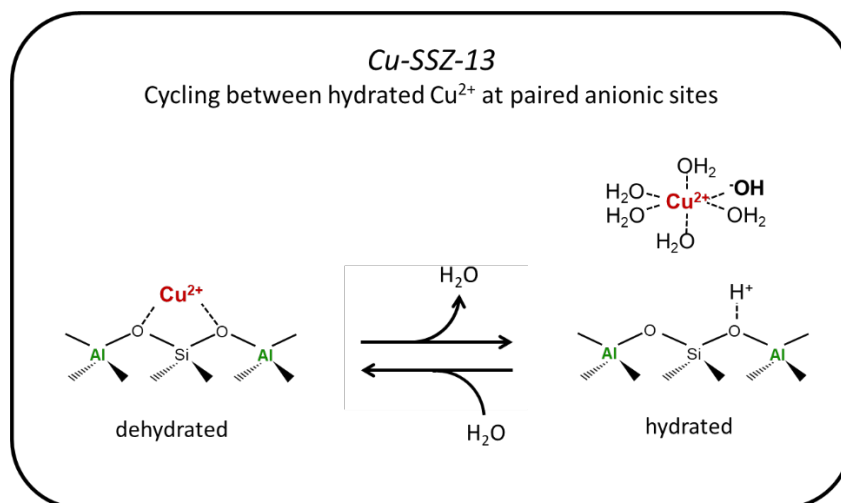


**Figure 36.** The reversible interconversion of  $\text{Z}_2\text{H}/\text{CuOH}$  and  $\text{Z}_2\text{Cu}$  sites from the removal of water via heat oxidative heat treatment or the low-temperature (20 to  $30^\circ\text{C}$ ) introduction of water via exposure to aqueous media or vapor treatment.

### 5.2.2 Development of the proposed standard SCR mechanism

The proposed standard SCR redox mechanism has been extended from the isolated  $\text{Cu}^{2+}$  active site model from Bates et al. [43] to include  $[\text{CuOH}]^+$  as an active site. [68] As shown in Figure 20, both active sites exhibit the same TOR within error. Both mechanisms are similar in that their reduction half-cycle requires consumption of an  $\text{NH}_3$  and  $\text{NO}$  and that their oxidation half-cycles require the consumption of  $\text{NH}_3$ ,  $\text{NO}$ , and  $\text{O}_2$ . Major differences are that reducing the isolated  $\text{Cu}^{2+}$  active site produces an isolated  $\text{Cu}^{1+}$  with a generated BA sites whereas reducing  $[\text{CuOH}]^+$  produces an isolated  $\text{Cu}^{1+}$  with no generation of a BA site (since there are no  $\text{Al}_f$  nearby), consistent with the  $\text{NH}_3$ -TPD results on both oxidized and reduced Cu-SSZ-13 samples in Figure 15 and Figure 16. Another major difference is that the mechanism for  $[\text{CuOH}]^+$  as the active site produces an additional  $\text{H}_2\text{O}$  in the reduction half-cycle (produced from removing the  $-\text{OH}$  ligand) and one less  $\text{H}_2\text{O}$  in the oxidation half-cycle ( $-\text{OH}$  ligand added to  $\text{Cu}^{2+}$ ).

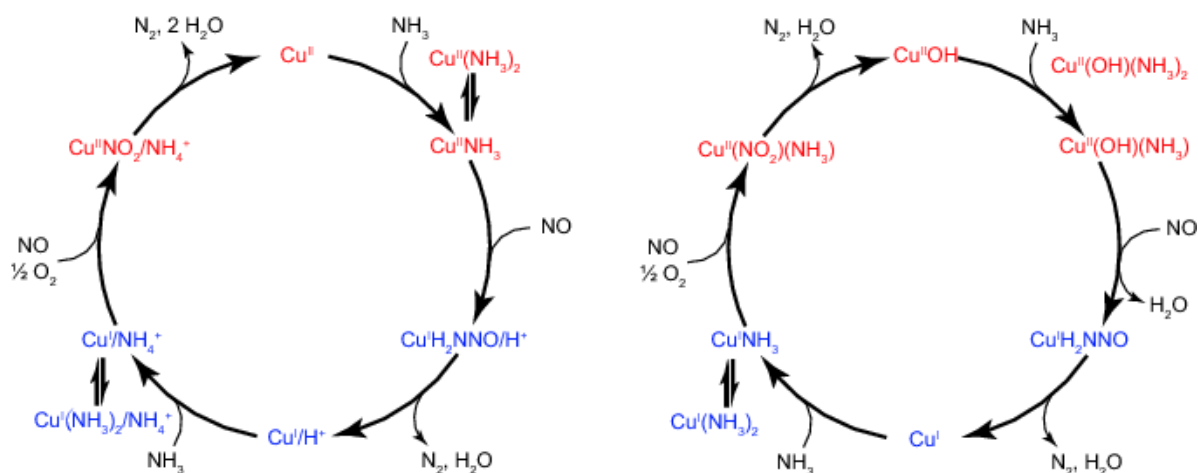


**Figure 37.** Proposed mechanistic pathways for the standard SCR reaction on isolated  $\text{Cu}^{2+}$  (left) and  $[\text{CuOH}]^+$  (right) active sites. Figure adapted from Paolucci et al. [109].

One major drawback of our proposed mechanism is that the oxidation half-cycle requires the use of a  $\frac{1}{2} \text{O}_2$ . Three standard SCR oxidation half-cycles have been proposed for variety of catalysts (namely Cu-zeolites, Fe-zeolites, and Vanadia):

- $\text{O}_2$  and  $\text{NO}$  coordinate as a  $\text{NO}_3$  intermediate to isolated  $\text{Cu}^+$ . [65,67,118,119]
- Oxidant denoted as  $\frac{1}{2} \text{O}_2$  [43,68,84,120]
- NO oxidation of  $\text{NO} + \text{O}_2$  to  $\text{NO}_2$ , which in turn acts as an oxidant in lieu of  $\text{O}_2$ . [121]

The way  $\text{O}_2$  participates in any of the three proposals above is not satisfactory.  $\text{O}_2$  and  $\text{NO}$  coordinating to an isolated  $\text{Cu}^{1+}$  site would require a triple-collision (since  $\text{NO}$  and  $\text{O}_2$  do not readily adsorb on  $\text{Cu}^{1+}$  under standard SCR conditions [68]). Leaving it as  $\frac{1}{2} \text{O}_2$  is physically not reasonable, and may imply that more than one  $\text{Cu}^{1+}$  site is required (i.e. Cu-dimers) or that the cycle has to turn around twice to consume an  $\text{O}_2$ . The NO oxidation of  $\text{NO} + \text{O}_2$  to  $\text{NO}_2$  is reasonable, however, the sites at which NO oxidation occurs (if it occurs at all), or how one could collect convincing evidence for the formation of these  $\text{NO}_2$  species is also unknown.

Verma et al. studied the dry NO oxidation reaction on our Cu-SSZ-13 samples [122] to probe the oxidation half-cycle but no correlation between dry NO oxidation kinetics and the oxidation half-cycle kinetics during standard SCR has been discovered.

### 5.3 Results and Discussion

#### 5.3.1 Cu ions in Cu-SSZ-13 under go a reduction-oxidation reaction during NH<sub>3</sub>-SCR

From this understanding of Cu<sup>2+</sup> species under oxidative and/or hydrated conditions, we will subject the Cu-SSZ-13 catalyst to the standard SCR environment (300 ppm NO, 300 ppm NH<sub>3</sub>, 10% O<sub>2</sub>, 7% CO<sub>2</sub>, 2.5% H<sub>2</sub>O, balance N<sub>2</sub>, 200°C). *Operando* XANES quantifies the fraction of Cu(I) simultaneously while measuring the intrinsic reaction rate, Figure 38. We observe that Cu exists in Cu(I) and Cu(II) oxidation states during steady state standard SCR and that the fraction of Cu(I) is highest (near 100% Cu(I)) at low Cu wt% 's and lowest (near 100% Cu(II)) at high Cu wt% 's. This suggests that Cu undergoes a Cu(II)/Cu(I) reduction-oxidation catalytic cycle during standard SCR, and illustrated in Figure 39.

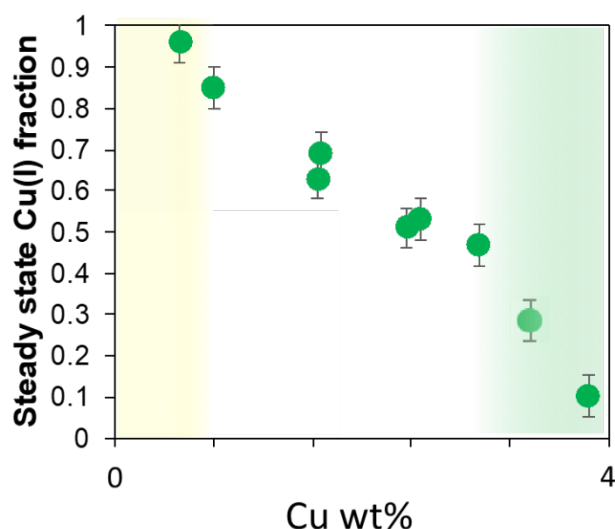


**Figure 38.** Steady-state *operando* Cu(I) fractions plotted versus the Cu wt%.

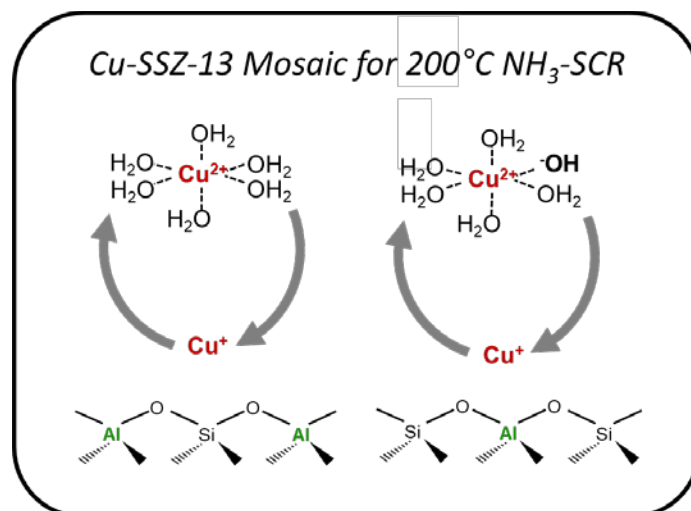


**Figure 39.** Updated molecular mosaic for the nature of Cu ions in Cu-SSZ-13 during standard SCR reaction conditions (300 ppm NH<sub>3</sub>, 300 ppm NO, 10% O<sub>2</sub>, 7% CO<sub>2</sub>, 2.5% H<sub>2</sub>O, balance N<sub>2</sub>, 200°C).

### 5.3.2 NO + NH<sub>3</sub> is necessary to reduce Cu(II) to Cu(I)

To shed light onto what drives Cu(II) to reduce to Cu(I), we looked at the adsorption energies of individual SCR molecules onto Cu-SSZ-13 (Figure 40). NH<sub>3</sub> and H<sub>2</sub>O exhibit the strongest affinity to Cu(II) species, with NH<sub>3</sub> ligands slightly more stable than H<sub>2</sub>O. The badger charge of the Cu(II) after adsorption of each individual standard SCR gas molecule indicates that an individual molecule is insufficient to reduce Cu(II) to Cu(I) by itself. NO + NH<sub>3</sub> together, however, is able to reduce Cu(II) to Cu(I), and testing other combinations experimentally (NO + O<sub>2</sub>, NH<sub>3</sub> + O<sub>2</sub>, NO + NH<sub>3</sub>, Figure 41) confirms that NO + NH<sub>3</sub> is the only combination that's able to reduce Cu(II) to Cu(I).

Additionally, coordination numbers measured from EXAFS indicate a coordination number four after exposure to NH<sub>3</sub> + O<sub>2</sub> (300 ppm NH<sub>3</sub>, 10% O<sub>2</sub>, balance N<sub>2</sub>, 200°C), consistent with NH<sub>3</sub> ligands arranged in a square planar fashion around Cu<sup>2+</sup>. Z<sub>2</sub>Cu sites would coordinate to four NH<sub>3</sub> ligands while ZCuOH coordinate to three NH<sub>3</sub> ligands and one –OH ligand. After reduction of Cu(II) to Cu(I) with NO + NH<sub>3</sub>, the coordination number of Cu(I) decreases to two. Paired with the fact that the –OH ligand on Cu(II) must leave as H<sub>2</sub>O due to atomic balance, the reduced species for both Z<sub>2</sub>Cu and ZCuOH are thus identical Cu(I)(NH<sub>3</sub>)<sub>2</sub>.

With this pool of evidence, the standard SCR mosaic presented in Figure 39 is updated to the mosaic presented in Figure 43, with two notable differences: (1) replacement of  $\text{H}_2\text{O}$  ligands with  $\text{NH}_3$  ligands, leading to four-coordinated  $\text{Cu(II)}$  and two-coordinated  $\text{Cu(I)}$  species, and (2) addition of  $\text{NO} + \text{NH}_3$  molecules to reduce  $\text{Cu(II)}$  to  $\text{Cu(I)(NH}_3)_2$ .

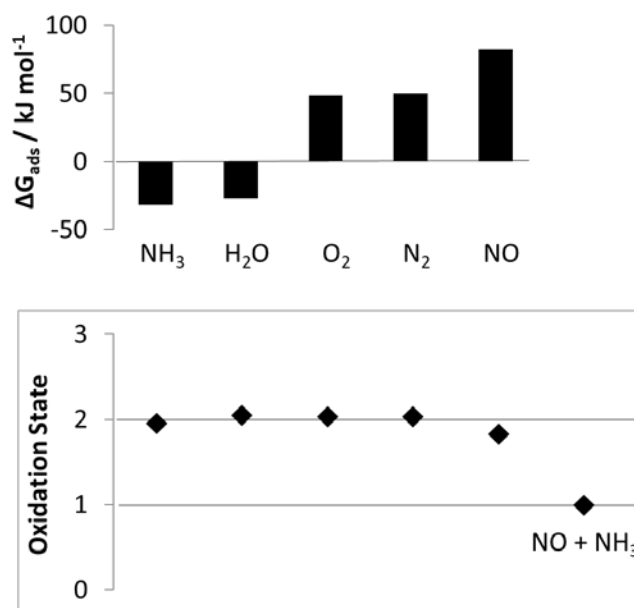


**Figure 40.** Adsorption energies of individual SCR gas molecules to  $\text{Cu}^{2+}$  sites on Cu-SSZ-13 (top). Bader charge oxidation states of  $\text{Cu}^{2+}$  sites on Cu-SSZ-13 after adsorption of individual SCR gases (bottom).

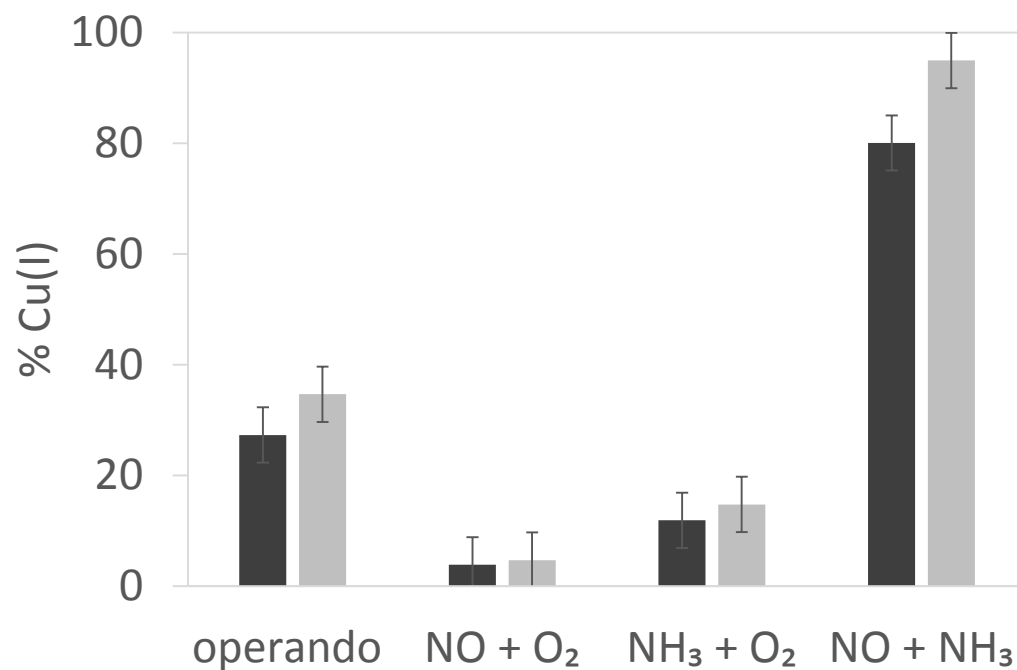


**Figure 41.** Fraction of Cu(I) ions during standard SCR and after NH<sub>3</sub>, NO, and O<sub>2</sub> cutoff at 200°C. We observe that gas mixture that leads to the greatest reduction of Cu(II) to Cu(I) is NO+NH<sub>3</sub>. Two Cu-SSZ-13 Si:Al = 4.5 with Cu:Al molar ratios of 0.11 (dark bars) and 0.16 (light bars) were used.



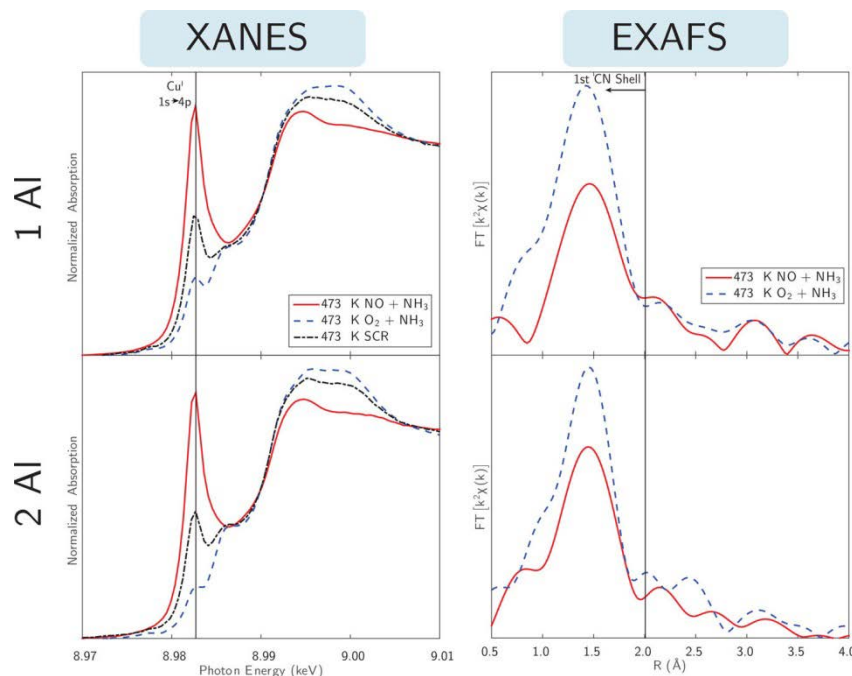


**Figure 42.** XANES and EXAFS spectra collected on a ZCuOH model material (Cu-SSZ-13 Si:Al = 15, Cu:Al = 0.44) and Z<sub>2</sub>Cu model material (Cu-SSZ-13 Si:Al = 4.5, Cu:Al = 0.08).

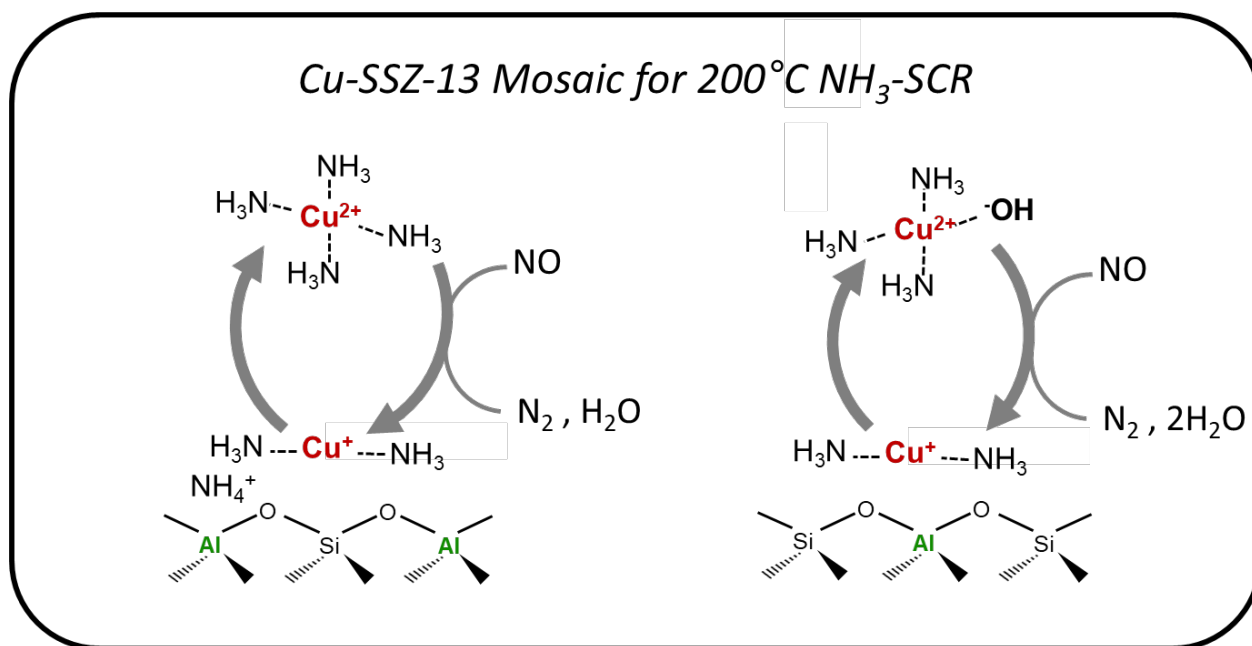


**Figure 43.** Updated molecular mosaic for the nature of Cu ions in Cu-SSZ-13 during standard SCR reaction conditions (300 ppm NH<sub>3</sub>, 300 ppm NO, 10% O<sub>2</sub>, 7% CO<sub>2</sub>, 2.5% H<sub>2</sub>O, balance N<sub>2</sub>, 200°C).

### 5.3.3 O<sub>2</sub> or NO<sub>2</sub> can oxidize Cu(I) to Cu(II)

With the current mechanistic picture, all that's left is to continue along and start piecing together the oxidation half-cycle. The adsorption energies of individual SCR molecules onto Cu(I) are shown in Figure 44 (top) indicate that NO<sub>2</sub> binds strongest to Cu(I), followed by NH<sub>3</sub> and H<sub>2</sub>O. Bader charges of the Cu(I), however, indicate that NO<sub>2</sub> followed by O<sub>2</sub> are the best SCR molecules to oxidize Cu(I) to Cu(II). We performed in-situ O<sub>2</sub> and NO<sub>2</sub> titration experiments on Cu-SSZ-13 pre-treated in a reducing NO + NH<sub>3</sub> gas feed (300 ppm NO, 300 ppm NH<sub>3</sub>, balance N<sub>2</sub>, 200°C) to reduce all the Cu to Cu(I)(NH<sub>3</sub>)<sub>2</sub>, Figure 45. Results show that NO<sub>2</sub> is able to oxidize Cu(I)(NH<sub>3</sub>)<sub>2</sub> to Cu(II) by itself at similar rates and to the same extent (100% oxidized) independent of the Cu density, indicating that NO<sub>2</sub> is a single-site oxidant. O<sub>2</sub>, however, oxidizes only a fraction of Cu(I)(NH<sub>3</sub>)<sub>2</sub>, with oxidizable fraction increasing with Cu density. This observation suggests that O<sub>2</sub> likely requires two Cu(I)(NH<sub>3</sub>)<sub>2</sub> to form a relevant SCR intermediate.

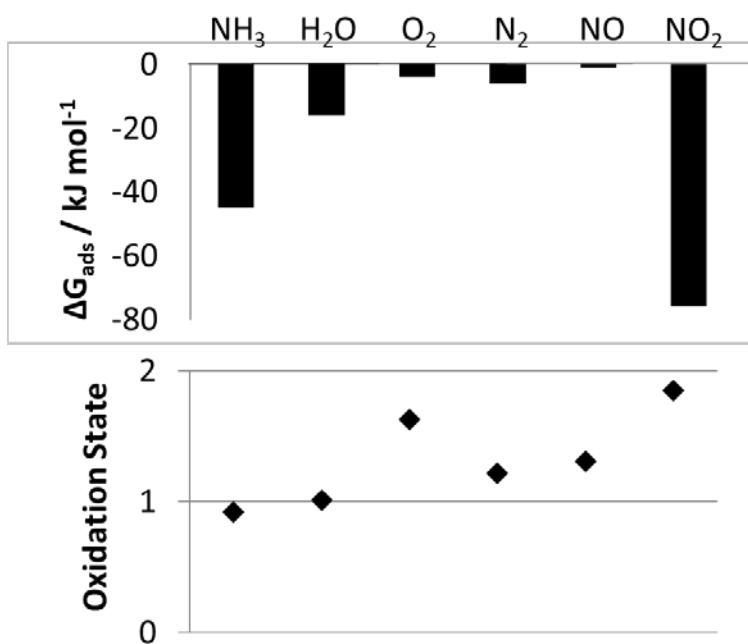


**Figure 44.** Adsorption energies of individual SCR gas molecules to Cu(I) sites on Cu-SSZ-13 (top). Bader charge oxidation states of Cu(I) sites on Cu-SSZ-13 after adsorption of individual SCR gases (bottom).

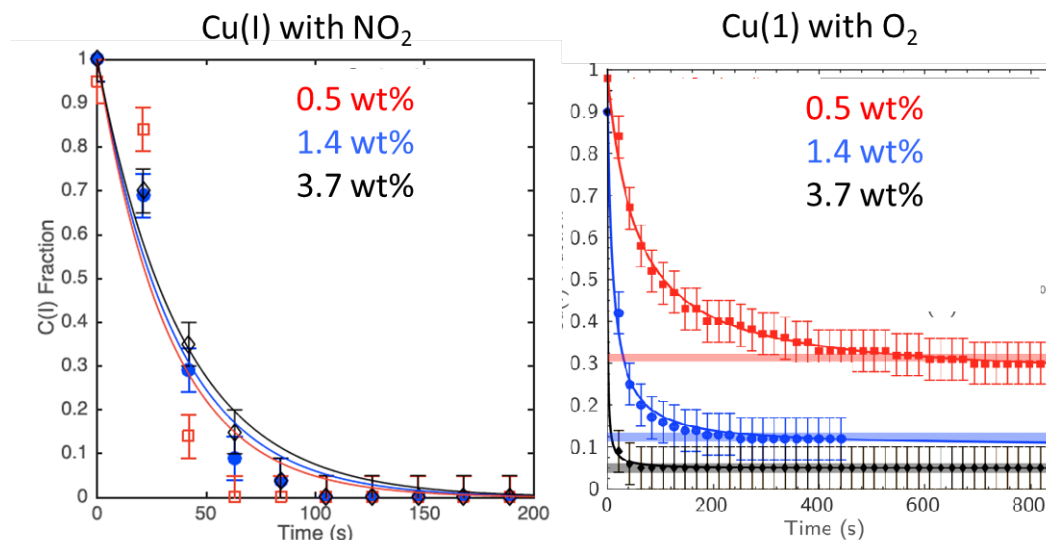


**Figure 45.** Transient  $\text{NO}_2$  (left graph) and  $\text{O}_2$  (right graph) titrations of  $\text{Cu(I)(NH}_3)_2$  sites on three Cu-SSZ-13 with different Cu wt% 's. The three horizontal bars on the right graph represent the fraction of oxidizable Cu(I) predicted from Monte Carlo simulations, assuming that Cu with diffusion spheres of 9 Å are only able to pair and oxidize if their diffusion spheres overlap.

Monte Carlo simulations are used to define average Cu-Cu distances and climbing-image nudged elastic band calculations were used to calculate Cu diffusion energies between CHA cages for Cu ions electrostatically tethered to an isolated anionic site [123]. It was determined that this particular Cu site can travel up to 9 Å from its anionic framework site. Randomly scattering Cu ions at a pre-defined density in a volume and drawing 9 Å diffusion spheres allows us to quantify the fraction of pair-able Cu, as shown by the solid red curve in Figure 46. Three model Cu-SSZ-13 catalysts with different Cu densities were tested and the experimental fraction of  $\text{O}_2$  oxidizable  $\text{Cu(I)(NH}_3)_2$  quantified by XANES are in parity with the predicted fraction of  $\text{Cu(I)(NH}_3)_2$  species with overlapping diffusion spheres. This observation of Cu being able to diffuse a limited distance while still electrostatically tethered to its anionic framework sites opens doors and opportunities with regards to mechanistic understanding of reactions over metal-zeolites with electrostatically tethered metal centers.

Revising the mosaic of our SCR mechanism, Figure 47 replaces Figure 43 with an updated understanding of the oxidation half cycle. Two additions are made: (1)  $\text{NO}_2$  can oxidize single  $\text{Cu(I)(NH}_3)_2$  sites back to  $\text{Cu(II)}$ , and (2)  $\text{O}_2$  can form  $(\text{NH}_3)_2\text{Cu(I)-O}_2\text{-Cu(I)(NH}_3)_2$  dimeric

intermediates when two  $\text{Cu(I)(NH}_3)_2$  diffusion spheres intersect. The electron balance and thus formal oxidation states of Cu on this  $(\text{NH}_3)_2\text{Cu(I)-O}_2\text{-Cu(I)(NH}_3)_2$  dimeric intermediate is uncertain; the Cu should have a formal oxidation state of Cu(III) since  $\text{O}_2$  is a four-electron oxidant. At this point in the mechanism, to close the molecular balance, our proposed  $(\text{NH}_3)_2\text{Cu(I)-O}_2\text{-Cu(I)(NH}_3)_2$  dimeric intermediate must react with two NO and four  $\text{NH}_3$  molecules to drive the oxidation back to  $\text{Cu(II)(NH}_3)_4$  and  $\text{Cu(II)(NH}_3)_3(\text{OH})$  sites.

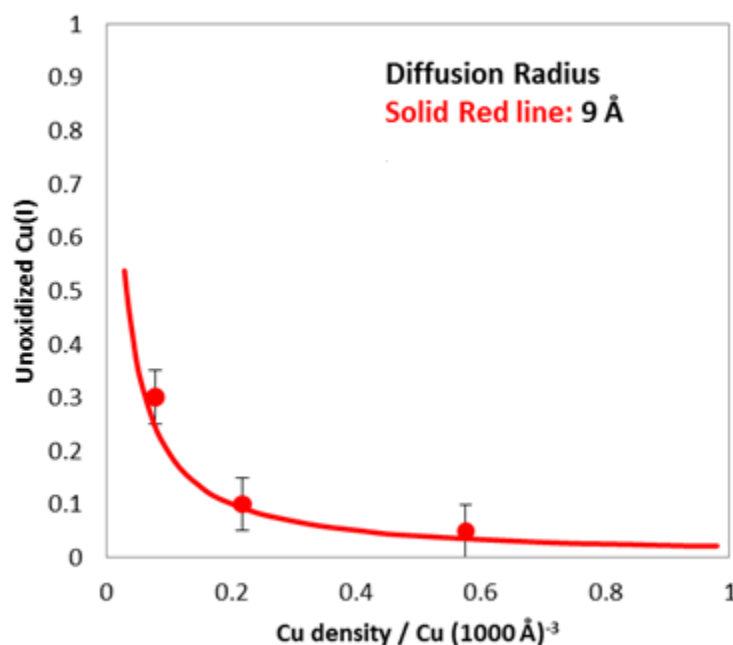


**Figure 46.** The fraction of unoxidized  $\text{Cu(I)(NH}_3)_2$  remaining after titration of Cu-SSZ-13 with  $\text{O}_2$ . The lines represent the predicted fraction of oxidizable Cu from computation assuming that each Cu electrostatically tethered to the framework can only move up to 9 Å (solid red line).

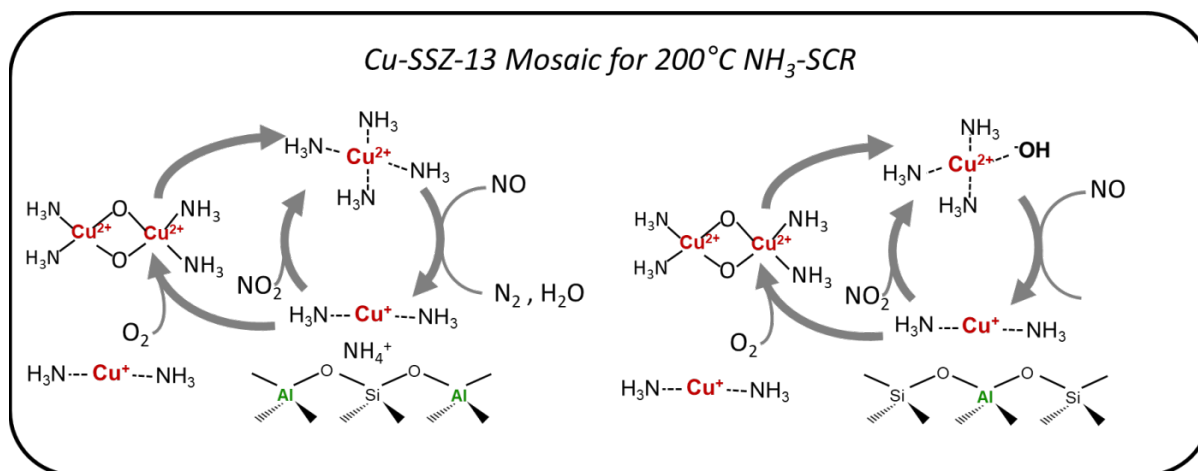


**Figure 47.** Updated molecular mosaic for the nature of Cu ions in Cu-SSZ-13 during standard SCR reaction conditions (300 ppm NH<sub>3</sub>, 300 ppm NO, 10% O<sub>2</sub>, 7% CO<sub>2</sub>, 2.5% H<sub>2</sub>O, balance N<sub>2</sub>, 200°C).

### 5.3.4 The incomplete mosaic

How does NO activate the dissociation of our proposed (NH<sub>3</sub>)<sub>2</sub>Cu(I)-O<sub>2</sub>-Cu(I)(NH<sub>3</sub>)<sub>2</sub> dimeric intermediate into Cu(II)(NH<sub>3</sub>)<sub>4</sub> and Cu(II)(NH<sub>3</sub>)<sub>3</sub>(OH) sites (Figure 48)? Evidence for how this phenomenon occurs is currently lacking, but from a chemistry and molecular balance standpoint, two NO molecules must attack and dissociate the bonds between oxygen and Cu, and four NH<sub>3</sub> molecules must adsorb back onto Cu to form the NH<sub>3</sub> saturated Cu(II) intermediate.

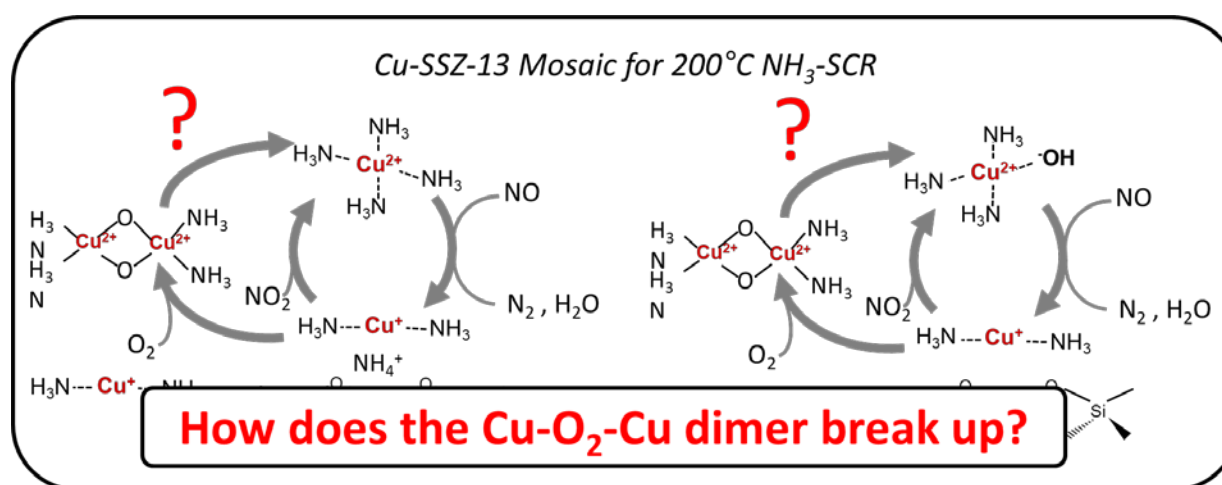


**Figure 48.** Holes in the current molecular mosaic for the nature of Cu ions in Cu-SSZ-13 during standard SCR reaction conditions (300 ppm NH<sub>3</sub>, 300 ppm NO, 10% O<sub>2</sub>, 7% CO<sub>2</sub>, 2.5% H<sub>2</sub>O, balance N<sub>2</sub>, 200°C)

## 5.4 Conclusions

Using the variety of tools in our arsenal, we were able to clear up (a bit) and begin to piece together mechanistic details of how Cu active sites in Cu-SSZ-13 turnover. The standard SCR reaction uses  $O_2$  as the oxidant ( $4NH_3 + 4NO + O_2 \rightarrow 6H_2O + 4N_2$ ) and involves a Cu(I)/Cu(II) redox cycle, with Cu(II) reduction mediated by NO and  $NH_3$ , and Cu(I) oxidation mediated by NO and  $O_2$ . In contrast, the fast SCR reaction ( $4NH_3 + 2NO + 2NO_2 \rightarrow 6H_2O + 4N_2$ ) uses  $NO_2$  as the oxidant. Low temperature (437 K) standard SCR reaction kinetics over Cu-SSZ-13 zeolites depend on the spatial density and distribution of Cu ions, varied by changing the Cu:Al and Si:Al ratio. Facilitated by  $NH_3$  solvation, mobile Cu(I) complexes can dimerize with other Cu(I) complexes within diffusion distances to activate  $O_2$ , as demonstrated through X-ray absorption spectroscopy and density functional theory calculations. Monte Carlo simulations are used to define average Cu-Cu distances. In contrast with  $O_2$ -assisted oxidation reactions,  $NO_2$  oxidizes single Cu(I) complexes with similar kinetics among samples of varying Cu spatial density. These findings demonstrate that low temperature standard SCR is dependent on Cu spatial density and requires  $NH_3$  solvation to mobilize Cu(I) sites to activate  $O_2$ , while in contrast fast SCR uses  $NO_2$  to oxidize single Cu(I) sites.

## 5.5 Supplementary Information

### 5.5.1 Transition from $NH_3$ promotion to $NH_3$ inhibition with increasing $NH_3$ concentrations during standard SCR catalysis over Cu-SSZ-13

A recent study by Marberger et al. [124] explored the origins of  $NH_3$  inhibition of the standard SCR rate over Cu-SSZ-13 catalysts. They proposed *in situ* XAS transient  $NH_3$  cutoff experiments that  $NH_3$  inhibition was due to  $NH_3$  preventing  $Cu(I)(NH_3)_2$  from oxidizing, thus decreasing the rate of re-oxidation back to  $Cu(II)(NH_3)_4$ , and that at higher temperatures where  $NH_3$  is more readily desorbed,  $NH_3$  does not inhibit the reoxidation of Cu(I) to Cu(II) as readily.

To explore whether Cu-SSZ-13 operating under the oxidation rate limited regime (2%  $O_2$  during standard SCR) or reduction rate limited regime (60%  $O_2$  during standard SCR) affects the  $NH_3$  inhibition, we collected  $NH_3$  reactant orders on a Cu-SSZ-13 sample (Si:Al = 15, Cu wt% = 2.9,

Cu:Al = 0.44) when subjected to SCR conditions with 2%, 10%, and 60% O<sub>2</sub> (Figure 49). The NH<sub>3</sub> orders at 300 ppm NH<sub>3</sub> were quantified by the slope on the ln-ln plot (Figure 49, right) and plotted in Figure 50. We do not see a change in the NH<sub>3</sub> order within statistical error. To explore whether Cu-SSZ-13 at operating under temperatures ranging from 160 to 240°C also do not exhibit changes in the NH<sub>3</sub> order within error (Figure 51 and Figure 52).

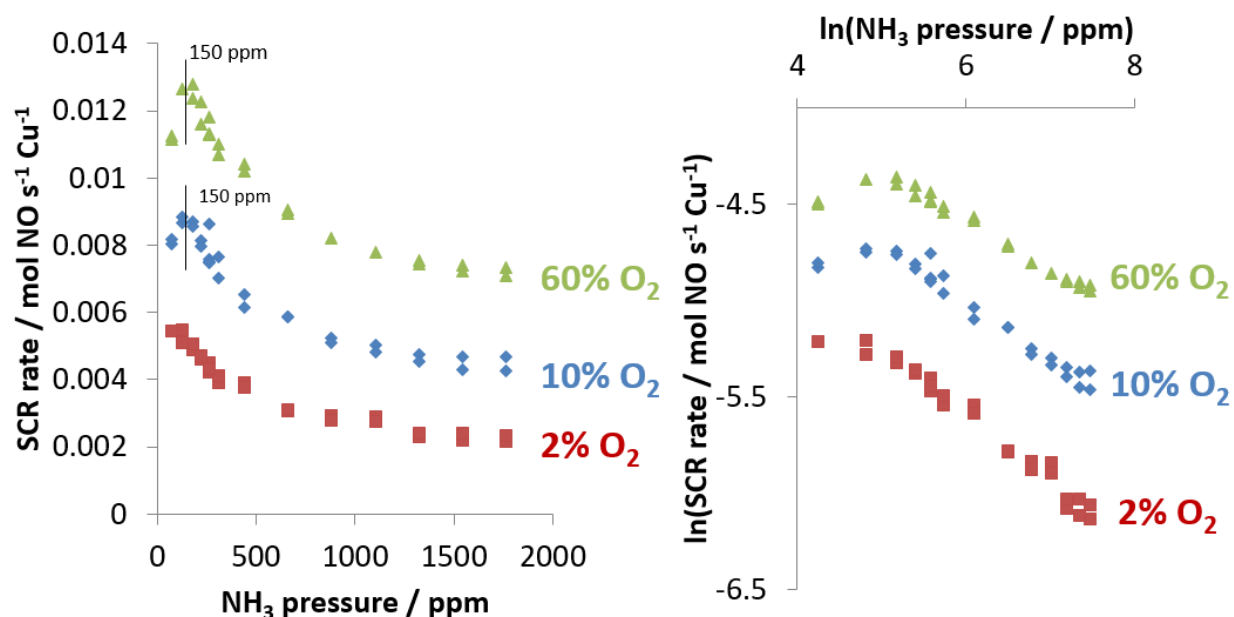


**Figure 49.** Intrinsic rates dependent on NH<sub>3</sub> pressure (left) and Arrhenius plots (right) on a Cu-SSZ-13 sample (Si:Al = 15, Cu wt% = 2.9, Cu:Al = 0.44) collected under standard SCR conditions (300 ppm NO, 50 to 2000 ppm NH<sub>3</sub>, 2 to 60% O<sub>2</sub>, 8% CO<sub>2</sub>, 2.5% H<sub>2</sub>O, balance N<sub>2</sub> at 200°C). All reaction rates are differential **except** for the 60% O<sub>2</sub> rate at the lowest NH<sub>3</sub> pressure (NH<sub>3</sub> conversion was 26%).

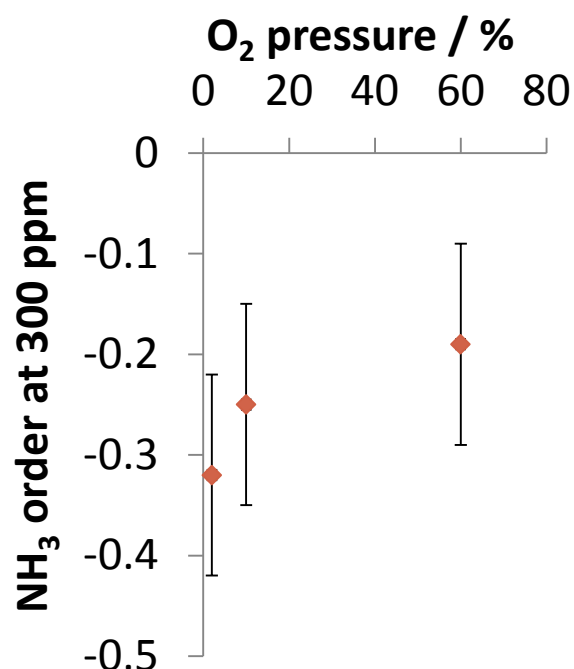


**Figure 50.** The standard SCR NH<sub>3</sub> order on a Cu-SSZ-13 sample (Si:Al = 15, Cu wt% = 2.9, Cu:Al = 0.44) collected at O<sub>2</sub> pressures ranging from 2% to 60%.



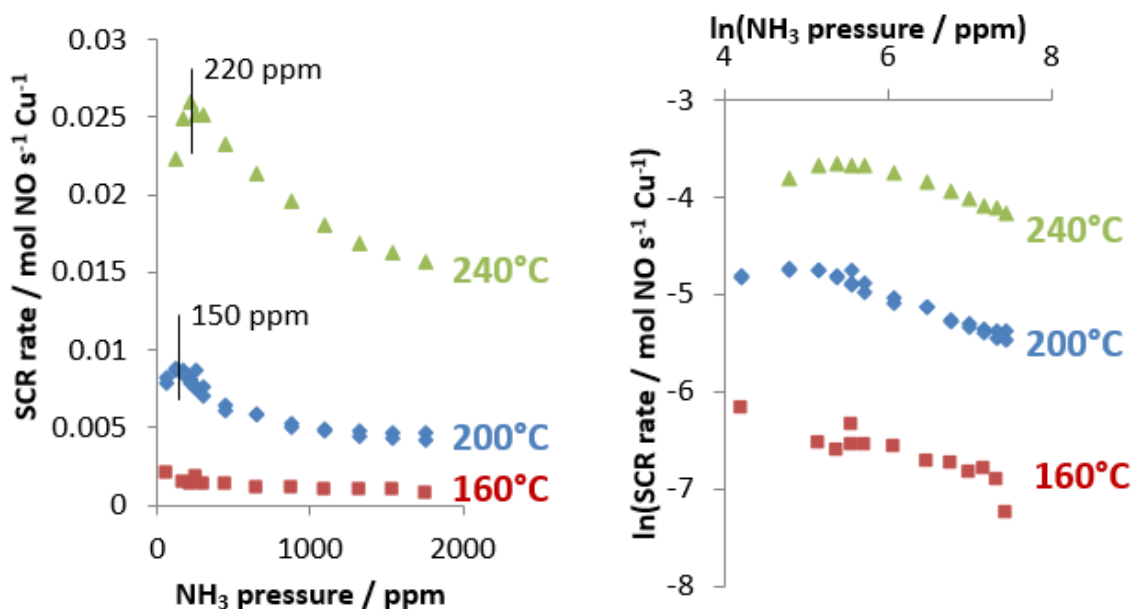


**Figure 51.** Intrinsic rates dependent on NH<sub>3</sub> pressure (left) and Arrhenius plots (right) on a Cu-SSZ-13 sample (Si:Al = 15, Cu wt% = 2.9, Cu:Al = 0.44) collected under standard SCR conditions (300 ppm NO, 50 to 2000 ppm NH<sub>3</sub>, 10% O<sub>2</sub>, 8% CO<sub>2</sub>, 2.5% H<sub>2</sub>O, balance N<sub>2</sub> at 160 to 240°C). All reaction rates are differential **except** for the 240°C rate at the lowest NH<sub>3</sub> pressure (NH<sub>3</sub> conversion was 30%).

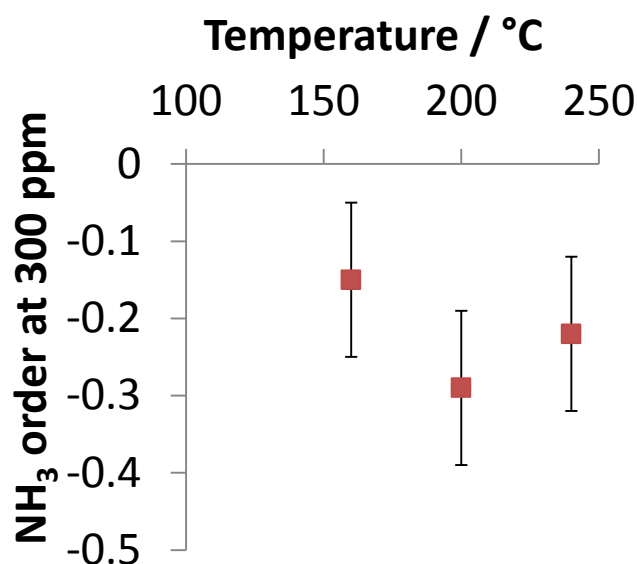


**Figure 52.** The standard SCR NH<sub>3</sub> order on a Cu-SSZ-13 sample (Si:Al = 15, Cu wt% = 2.9, Cu:Al = 0.44) collected at temperatures ranging from 160 to 240°C.

## 6. METHOD OF USING NO AS A PROBE MOLECULE TO QUANTIFY FRACTION OF PAIRABLE $\text{Cu(I)(NH}_3)_2$ IN $\text{Cu-SSZ-13}$ MATERIALS

### 6.1 Abstract

Oxygen-bridged Cu(1) dimers are a relevant intermediate for the low temperature ( $200^\circ\text{C}$ ) standard SCR reaction using  $\text{NH}_3$  as a reductant over  $\text{Cu-SSZ-13}$ . It has been demonstrated that Cu ions are electrostatically tethered to anionic sites in the chabazite framework and have an accessible diffusion sphere (radius of  $9 \text{ \AA}$ ) from that anionic site, limited by electrostatic forces and barriers arising from sterics of traveling through 8-membered rings in the zeolite framework. XAS was used to first ensure all the  $\text{Cu}^{2+}$  reduced to  $\text{Cu(I)(NH}_3)_2$  under a stream of  $\text{NO} + \text{NH}_3$  in balance inert, then oxidation with  $\text{O}_2$  to form the  $\text{O}_2\text{-Cu(I)(NH}_3)_2$  complex. We use XANES to quantify the extent of oxidation through linear combination of the  $\text{Cu}^{1+}$  pre-edge feature and observe that the fraction of oxidizable Cu to form these  $\text{O}_2\text{-Cu(I)(NH}_3)_2$  complexes matches the predicted number of oxidizable Cu from Monte Carlo simulations. These Monte Carlo simulations assume (1) a random distribution of Cu, (2) that Cu and H cannot ion-exchange or “hop”, (3) that Cu is mobile to an extent of  $9 \text{ \AA}$ , and (4) that only Cu whose diffusion spheres overlap can form dimers. Although XAS is a powerful technique, it is not widely accessible and is expensive and time consuming. In this chapter, we discuss the development and implication of an in-lab titration technique that quantifies the fraction of pairable  $\text{Cu(I)(NH}_3)_2$  using in-situ pre-treatments and NO as a probe molecule.

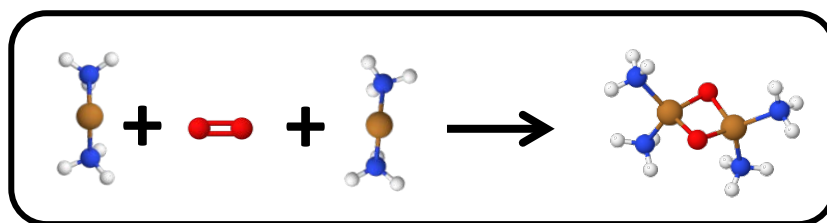


**Figure 53.** Reaction schematic that illustrates the formation of  $(\text{NH}_3)_2\text{Cu(I)-O}_2\text{-Cu(I)(NH}_3)_2$  dimers from  $\text{O}_2$  and two  $\text{Cu(I)(NH}_3)_2$  species whose diffusion spheres in  $\text{Cu-SSZ-13}$  overlap.

## 6.2 Introduction

With the discovery of mobile  $\text{Cu(I)(NH}_3)_2$  species that are only able to turn over if during standard SCR catalysis in Cu-SSZ-13 [123,125], methods to be able to count the fraction of active  $\text{Cu(I)(NH}_3)_2$  coupled with a push to develop a non mean-field model to explain observed reaction rates have taken off.

Gao et al. [125], demonstrated from DFT calculations and kinetics that a relevant intermediate in the standard SCR catalytic cycle involves an  $\text{O}_2$ -bridged  $\text{Cu(I)(NH}_3)_2$  dimer. Paolucci et al. [123], further provided evidence from in-situ XAS transient experiments from flowing  $\text{O}_2$  over Cu-SSZ-13 whose Cu ions all exist as  $\text{Cu(I)(NH}_3)_2$  that not all  $\text{Cu(I)(NH}_3)_2$  is able to pair, as evidenced by the observation that the fraction of oxidizable  $\text{Cu(I)(NH}_3)_2$  decreases with decreasing Cu density. It was also shown that this decrease matches quantitatively with computation under the restriction that where number of  $\text{Cu(I)(NH}_3)_2$  species can only oxidize when paired via an  $\text{O}_2$  bridge if its diffusion sphere is limited to 9 to 10 Å from its anionic charge balancing site on the framework .

## 6.3 Experimental Methods

### 6.3.1 Measuring the fraction of oxidizable $\text{Cu(I)(NH}_3)_2$ using XANES

Experimental procedures for collecting and measuring XANES spectra can be found in Section 2.5.10. To measure the fraction of oxidizable  $\text{Cu(I)(NH}_3)_2$ , we first reduce a Cu-SSZ-13 catalyst at  $\text{NO} + \text{NH}_3$  stream (300 ppm NO, 300 ppm  $\text{NH}_3$ , balance  $\text{N}_2$ ,  $200^\circ\text{C}$ ). After confirming that all the Cu has reduced, the  $\text{NH}_3$  stream is cut off for 30 seconds prior to switching the NO flow ( $\sim 300$  ppm NO in balance  $\text{N}_2$ ,  $200^\circ\text{C}$ ) with  $\text{O}_2$  (10%  $\text{O}_2$  in balance  $\text{N}_2$ ). The switch between NO and  $\text{O}_2$  is considered time  $t = 0$  and the final fraction of oxidized Cu measured using XANES and the final Cu-ligand coordination numbers measured using EXAFS were collected. Analysis details are found in Section 2.5.10.

### 6.3.2 Measuring the fraction of oxidizable $\text{Cu(I)(NH}_3)_2$ using NO titration

Though XAS provides useful information about the fraction of  $\text{Cu(I)(NH}_3)_2$  that's able to spatially pair and oxidize via forming an  $\text{O}_2$  bridge, it is time consuming and requires the use of

XAS, which is not an easily accessible spectroscopic technique in our day. To this end, we developed a technique that mimics the state of the catalyst during the in-situ XAS switching experiments in a laboratory flow-through reactor that uses NO as a probe tritrant.

From the current understanding of the standard SCR mechanism and standard SCR atomic balance, each Cu in the dimer will require one NO to dissociate the dimer, and another NO to reduce it back to  $\text{Cu(I)(NH}_3)_2$  [123]. This indicates that the fraction of oxidizable  $\text{Cu(I)(NH}_3)_2$  via pairing with a bridging  $\text{O}_2$  can potentially be titrated with NO and calculated using Equation 16, where  $(\text{NO}:\text{Cu})_{\text{second}}$  represents the molar NO:Cu consumed after titration of the  $(\text{NH}_3)_2\text{Cu(I)-O}_2\text{-Cu(I)(NH}_3)_2$  dimers with NO. The rationale behind will be explained more detail in the following section.

$$\text{fraction of oxidizable Cu(1)} = \frac{(\text{NO}:\text{Cu})_{\text{second}}}{2} \quad (\text{Equation 16})$$

The remainder of this chapter will step through the experiments we performed and the results we obtained to develop this NO titration method to count  $(\text{NH}_3)_2\text{Cu(I)-O}_2\text{-Cu(I)(NH}_3)_2$  dimers.

## 6.4 Results and Discussion

### 6.4.1 Scheme 1: Titrating $(\text{NH}_3)_2\text{Cu(I)-O}_2\text{-Cu(I)(NH}_3)_2$ species using concurrent flow of NO + $\text{NH}_3$

The first titration trial run involved flowing 10%  $\text{O}_2$  over a Cu-SSZ-13 material ( $\text{Si:Al} = 4.5$ ,  $\text{Cu:Al} = 0.21$ ,  $\text{Cu wt\%} = 3.8$ ) with all Cu as  $\text{Cu(I)(NH}_3)_2$  until steady state, then flowing NO +  $\text{NH}_3$  through the catalyst to quantify the number of NO consumed, Figure 54. As shown in Figure 55, immediately switching  $\text{O}_2$  (10%  $\text{O}_2$ , balance  $\text{N}_2$ ,  $200^\circ\text{C}$ ) with NO +  $\text{NH}_3$  (300 ppm NO, 300 ppm  $\text{NH}_3$ , balance  $\text{N}_2$ ,  $200^\circ\text{C}$ ) leads to a NO:Cu molar consumption of 5. From Equation 16, this indicates that the fraction of pairable Cu is 2.5, much greater than the value of 0.9 measured using XAS. We hypothesize that the molar NO:Cu ratio of 2.5 occurred because residual  $\text{O}_2$  in the presence of NO +  $\text{NH}_3$  caused a number of sites to turnover more than once, leading to an excess consumption of NO, thereby skewing this titration method rendering it not useful for our needs.

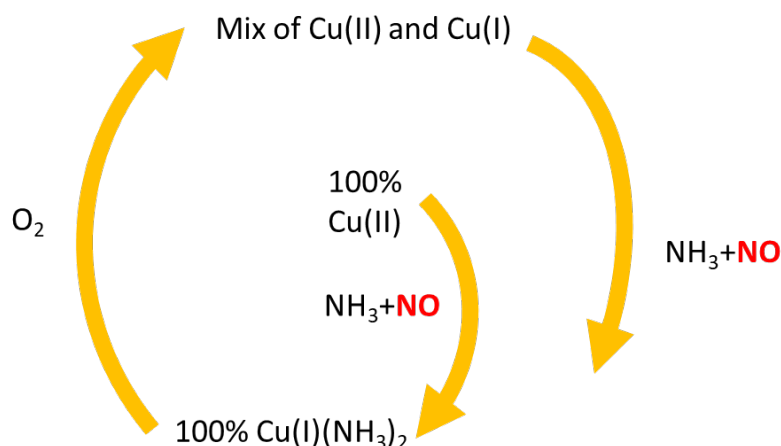


**Figure 54.** Schematic that summarizes the treatments exposed to Cu-SSZ-13 at 200°C to count the fraction of oxidizable Cu(I)(NH<sub>3</sub>)<sub>2</sub>. In summary, (1) starting out with a calcined Cu-SSZ-13 with all Cu oxidized to Cu<sup>2+</sup>, reduce all the Cu<sup>2+</sup> to Cu(I)(NH<sub>3</sub>)<sub>2</sub>, (2) oxidize the Cu(I)(NH<sub>3</sub>)<sub>2</sub> with O<sub>2</sub> to form (NH<sub>3</sub>)<sub>2</sub>Cu(I)-O<sub>2</sub>-Cu(I)(NH<sub>3</sub>)<sub>2</sub> dimers, (4) activate NO and reform Cu(I)(NH<sub>3</sub>)<sub>2</sub> under a flow of NO + NH<sub>3</sub>.

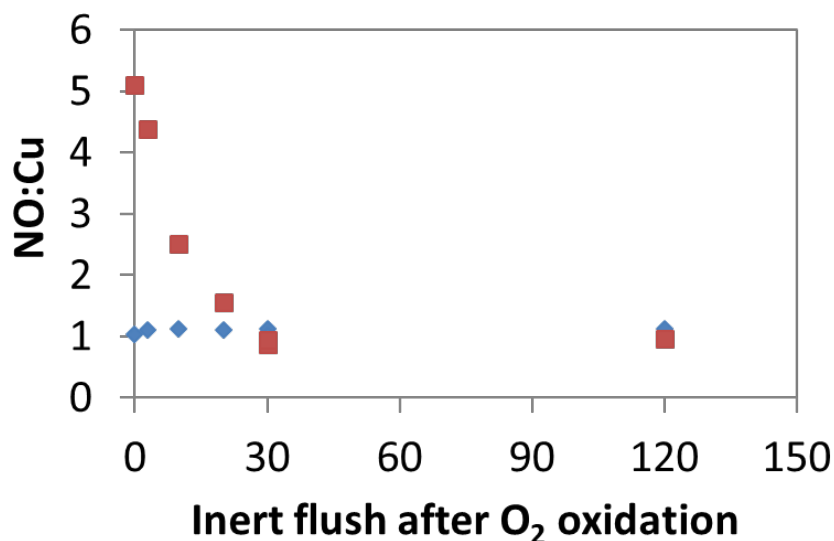


**Figure 55.** The mols of NO consumed per mol Cu after flowing a reductive mixture of NO + NH<sub>3</sub> to form Cu(I)(NH<sub>3</sub>)<sub>2</sub> (300 ppm NO, 300 ppm NH<sub>3</sub>, balance He) (blue diamonds). After O<sub>2</sub> oxidation (10% O<sub>2</sub> in balance He) of Cu(I)(NH<sub>3</sub>)<sub>2</sub>, an inert N<sub>2</sub> flush (600 sccm) was performed for six different flushing times between 0 to 120 minutes before flowing the NO + NH<sub>3</sub> reductive mixture (300 ppm NO, 300 ppm NH<sub>3</sub>, balance He). Again, the NO:Cu molar ratio was calculated during this second reduction and quantified (red squares). Tests were run on a Cu-SSZ-13 with Si:Al = 4.5, Cu:Al = 0.21, Cu wt% = 3.8.

To avoid the issue of overconsumption of NO due to the brief simultaneous presence of NO, NH<sub>3</sub>, and O<sub>2</sub>, an inert flushing step with dry N<sub>2</sub> was added post O<sub>2</sub>-titration of the pair-able Cu(I)(NH<sub>3</sub>)<sub>2</sub> sites. Figure 55 plots the resulting NO:Cu molar ratios after inert flushing with times between 0 to 120 minutes of the (NH<sub>3</sub>)<sub>2</sub>Cu(I)-O<sub>2</sub>-Cu(I)(NH<sub>3</sub>)<sub>2</sub> dimers. We observe a decrease in the molar NO:Cu ratios between 0 to 30 minutes of flushing with N<sub>2</sub>, which may indicate that it takes 30 minutes to flush out a sufficient amount of the 10% O<sub>2</sub> initially present in the reactor to prevent Cu sites from turning over more than once during titration. We obtain the same molar NO:Cu ratio for 30 minutes and 120 minutes of inert flushing after O<sub>2</sub>-titration, indicating that for the mass of sample loaded (~10 mg) and N<sub>2</sub> flow rate used (600 sccm), 30 minutes flushing is sufficient enough to ensure enough O<sub>2</sub> has been flushed out of the system to avoid Cu sites from turning over more than once after feeding NO and NH<sub>3</sub>. It should also be noted that the blue triangles in Figure 55 indicates the molar NO:Cu consumed during the reduction of the calcined Cu-SSZ-13 catalyst with NO + NH<sub>3</sub>. The molar NO:Cu is within error of 1, confirming that it only requires one NO during a flow of NO + NH<sub>3</sub> to reduce one Cu(II) to Cu(I).

We obtain a molar NO:Cu ratio of 1 after feeding NO + NH<sub>3</sub> after flushing O<sub>2</sub> out of the system with inert post O<sub>2</sub>-titration. Since half of 1 is 0.5, this value indicates that the fraction of pairable Cu(I)(NH<sub>3</sub>)<sub>2</sub> measured using this method is 0.5, which does not match the measured value of 0.9 using XAS. Molecularly, it is possible that (NH<sub>3</sub>)<sub>2</sub>Cu(I)-O<sub>2</sub>-Cu(I)(NH<sub>3</sub>)<sub>2</sub> dimers are unstable and break apart in inert. If this is the case, then the destruction of about half of the (NH<sub>3</sub>)<sub>2</sub>Cu(I)-O<sub>2</sub>-Cu(I)(NH<sub>3</sub>)<sub>2</sub> dimers occurred within the first 30 minutes of inert flushing since the molar NO:Cu ratio did not change between 30 and 120 minutes of inert flushing.

#### **6.4.2 Scheme 2: Titrating (NH<sub>3</sub>)<sub>2</sub>Cu(I)-O<sub>2</sub>-Cu(I)(NH<sub>3</sub>)<sub>2</sub> species using a flow of NO then a flow of NO + NH<sub>3</sub>**

Since it is hypothesized that (NH<sub>3</sub>)<sub>2</sub>Cu(I)-O<sub>2</sub>-Cu(I)(NH<sub>3</sub>)<sub>2</sub> dimers may be unstable under inert flow, a method to quantify the number of NO required to convert each Cu in the dimer into Cu(I)(NH<sub>3</sub>)<sub>2</sub> was devised, as shown in Figure 57. In short, the method follows the same procedure as that outlined Figure 54 except rather than flushing the (NH<sub>3</sub>)<sub>2</sub>Cu(I)-O<sub>2</sub>-Cu(I)(NH<sub>3</sub>)<sub>2</sub> dimers with inert to flush out O<sub>2</sub>, we skip the flushing step and immediately flow 300 ppm NO in balance N<sub>2</sub> after cutting off O<sub>2</sub>. Once stable, 300 ppm NH<sub>3</sub> is added to the gas stream, resulting in additional consumption of NO. The fraction of NO consumed during initial reduction of Cu(II)

to Cu(I) using NO + NH<sub>3</sub> is referred to as (NO:Cu)<sub>first</sub>. The fraction of NO consumed during exposure of (NH<sub>3</sub>)<sub>2</sub>Cu(I)-O<sub>2</sub>-Cu(I)(NH<sub>3</sub>)<sub>2</sub> dimers to NO in balance N<sub>2</sub> is referred to as (NO:Cu)<sub>second</sub>. The fraction of NO consumed after NH<sub>3</sub> is added to the NO flow is referred to as (NO:Cu)<sub>third</sub>. The final state of the Cu-SSZ-13 material after these sequential treatments is thus, Cu(I)(NH<sub>3</sub>)<sub>2</sub>. Since each Cu in the dimer will require one NO to dissociate the dimer, and another NO to reduce it back to Cu(I)(NH<sub>3</sub>)<sub>2</sub> [123], the fraction of oxidizable Cu(I) can be measured using Equation 17.

$$\text{fraction of oxidizable Cu(1)} = \frac{(\text{NO:Cu})_{\text{second}} + (\text{NO:Cu})_{\text{third}}}{2} \quad (\text{Equation 17})$$

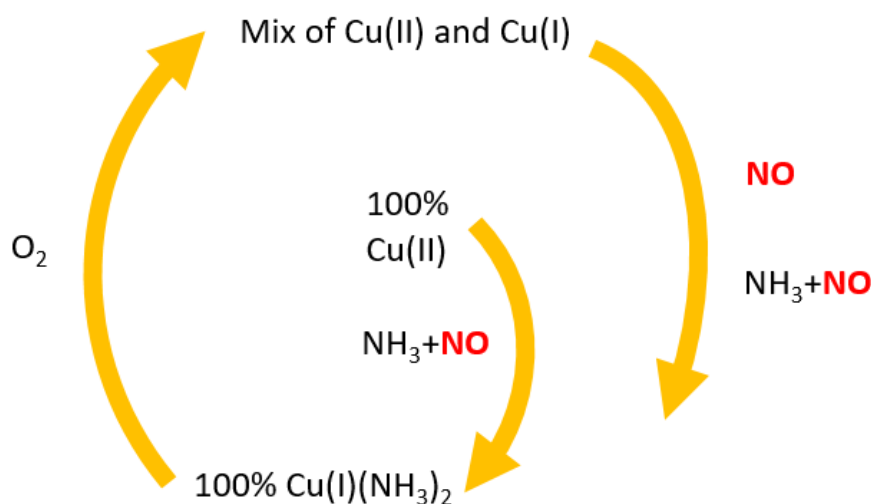


**Figure 56.** Schematic that summarizes the treatments exposed to Cu-SSZ-13 at 200°C to count the fraction of oxidizable Cu(I)(NH<sub>3</sub>)<sub>2</sub>. In summary, (1) starting out with a calcined Cu-SSZ-13 with all Cu oxidized to Cu<sup>2+</sup>, reduce all the Cu<sup>2+</sup> to Cu(I)(NH<sub>3</sub>)<sub>2</sub>, (2) oxidize the Cu(I)(NH<sub>3</sub>)<sub>2</sub> with O<sub>2</sub> to form (NH<sub>3</sub>)<sub>2</sub>Cu(I)-O<sub>2</sub>-Cu(I)(NH<sub>3</sub>)<sub>2</sub> dimers, (3) activate NO with the dimers, (4) reform Cu(I)(NH<sub>3</sub>)<sub>2</sub> using a flow of NO + NH<sub>3</sub>.

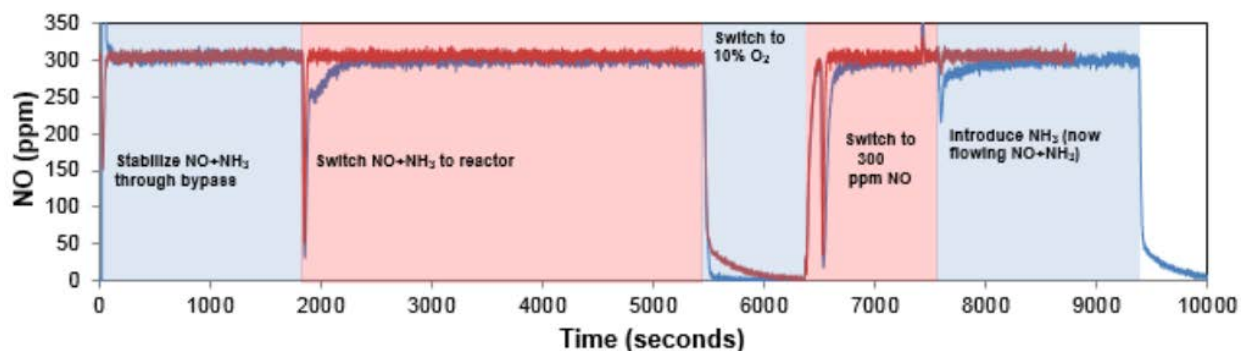


**Figure 57.** NO concentrations measured in the reactor effluent during five step-wise treatments of Cu-SSZ-13 in order to quantify NO consumption (per Cu) in treatment steps 2, 4, and 5 above, which correspond to different steps in the proposed standard SCR cycle. Red and blue traces indicate experiments with the blank reactor and catalyst-loaded reactor, respectively.

We note that it is likely that dry NO oxidation occurs over the material, however with such a low reaction rate at 200°C (two orders of magnitude slower than SCR) [43,122] and the exponential decrease of O<sub>2</sub> from 10% to near 0% over the course of 30 minutes, the number of NO molecules consumed during NO oxidation is negligible compared to the total amount of NO consumed during this step.

Since it is still uncertain whether (NH<sub>3</sub>)<sub>2</sub>Cu(I)-O<sub>2</sub>-Cu(I)(NH<sub>3</sub>)<sub>2</sub> dimers dissociate during inert flush with N<sub>2</sub>, flushing time experiments that varied the O<sub>2</sub> flushing time between 0 to 120 minutes on two model Cu-SSZ-13 materials (the first Si:Al = 4.5, Cu wt% = 3.7 with all ionic copper speciating as Z<sub>2</sub>Cu, the second Si:Al = 15 [105], Cu wt% = 2.0 with all ionic copper speciating as ZCuOH) were performed, Figure 58. For both samples, we observe a decrease in the (NO:Cu)<sub>second</sub> molar ratio with increasing inert flushing time post O<sub>2</sub>-titration. On the Z<sub>2</sub>Cu model sample, we observe a decrease in the (NO:Cu)<sub>third</sub> molar ratio with increasing inert flushing time post O<sub>2</sub>-titration. On the ZCuOH model sample, we observe an increase in the (NO:Cu)<sub>third</sub> molar ratio with increasing inert flushing time post O<sub>2</sub>-titration. We do not understand why this occurs, but summing up the (NO:Cu)<sub>second</sub> and (NO:Cu)<sub>third</sub> molar ratios (Figure 59) gives us two tell-tale pieces of information. First, that the model Z<sub>2</sub>Cu catalyst exhibits an overall decrease in the NO:Cu molar ratio with increasing inert flushing time post O<sub>2</sub>-saturation while the model ZCuOH catalyst exhibits no significant decrease in the NO:Cu molar



ratio with increasing inert flushing time post  $O_2$  saturation. The rationale behind why we observe this is unknown. The second tell-tale piece of information is that with no flush post  $O_2$  saturation, the fraction of oxidizable  $Cu(1)(NH_3)_2$  with  $O_2$  is parity with the fraction experimentally measured using XAS.

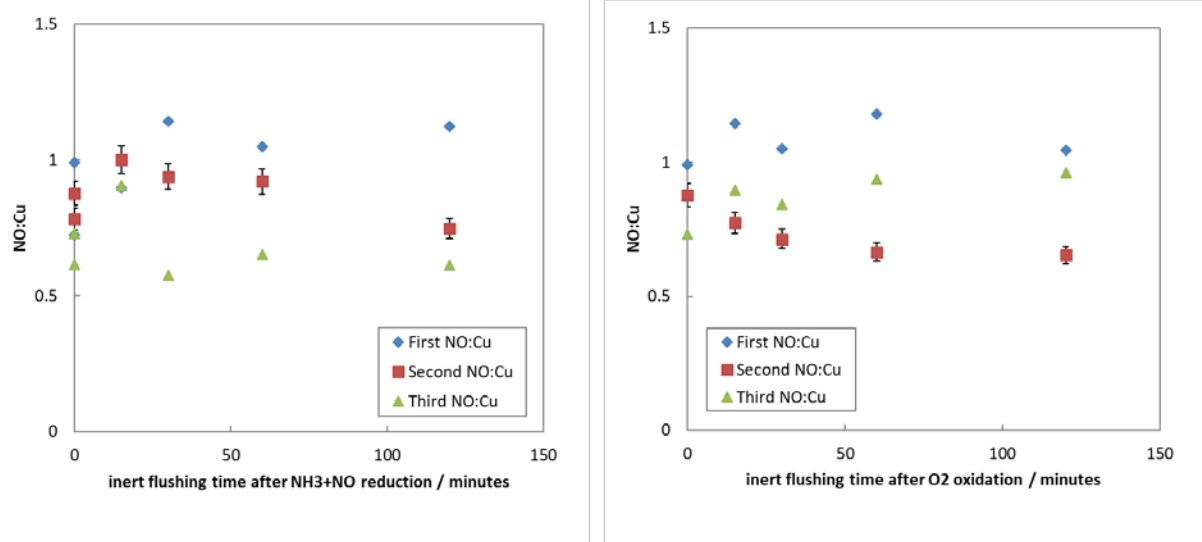


**Figure 58.** The consumption of NO plotted as a molar NO:Cu ratio after reduction of a calcined Cu-SSZ-13 with NO +  $NH_3$  (blue diamonds), exposing the catalyst to NO in balance He (red square) after flushing the catalyst with inert for 30 minutes after  $O_2$  saturation, and finally flowing NO and  $NH_3$  (green triangle). Varying inert flushing times after  $O_2$  saturation of  $Cu(1)(NH_3)_2$  between 0 to 120 minutes were run before feeding NO. Two Cu-SSZ-13 samples, one with all  $Cu^{2+}$  as  $Z_2Cu$  (Si:Al = 15, Cu wt% = 0.5) (left graph) and one with all  $Cu^{2+}$  ZCuOH (Si:Al = 15, Cu wt% = 2.0,  $Na^+$ -free hydrothermal synthesis) (right graph)

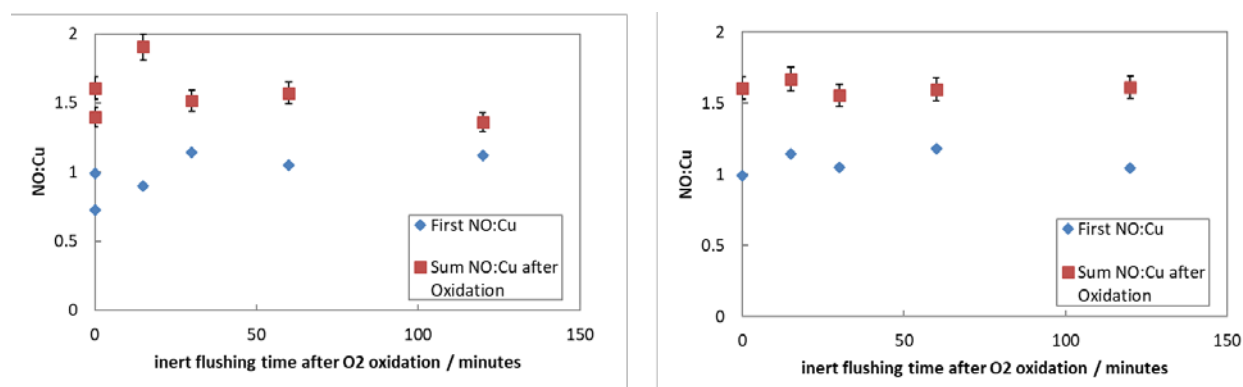


**Figure 59.** The sum of the second and third NO:Cu molar ratios from Figure 58. Two Cu-SSZ-13 samples, one with all  $Cu^{2+}$  as  $Z_2Cu$  (Si:Al = 15, Cu wt% = 0.5) (left graph) and one with all  $Cu^{2+}$  ZCuOH (Si:Al = 15, Cu wt% = 2.0,  $Na^+$ -free hydrothermal synthesis) (right graph)

### 6.4.3 Parity Plot: Titrating $(\text{NH}_3)_2\text{Cu(I)}\text{-O}_2\text{-Cu(I)(NH}_3)_2$ species using a flow of NO then a flow of NO + $\text{NH}_3$

Three samples whose fraction of oxidizable  $\text{Cu(I)(NH}_3)_2$  has been collected from in situ XAS were subjected to the NO titration technique developed in the previous section. Table 10 lists the samples and the experimentally determined oxidizable Cu(I) fractions from XAS and from NO titration. The oxidizable Cu(I) fractions measured using XAS and NO titration are shown in Figure 60. The five data points all scatter around the dashed 1:1 parity line, indicating that the NO titration method (more detailed procedure outlined in Section 6.4.4) is an alternative to in-situ XAS experiments that can be performed in any standard laboratory flow reactor equipped with an instrument that can detect NO concentrations with at least 0.5 second time resolution. This NO titration technique can also be used to quantify the fraction of pair-able  $\text{Cu(1)(NH}_3)_2$  for samples whose Cu loadings are less than 0.5 wt% due to the inability of XAS to collect Cu-edge spectra with acceptable signal-to-noise ratios.

**Table 10.** Three samples run to validate NO titration procedure. Repeats were made for two of the samples. Parity plot is shown in Figure 60.

Si:Al	Cu wt%	Cu / 1000 Angstroms <sup>3</sup>	Oxidized Cu(1) XAS	Oxidized Cu(1) NO titration
4.5	3.7	0.58	0.95	1.0
15	0.5	0.08	0.70	0.67
15	0.5	0.08	0.70	0.77
4.5	1.4	0.22	0.90	0.66
4.5	1.4	0.22	0.90	1.1

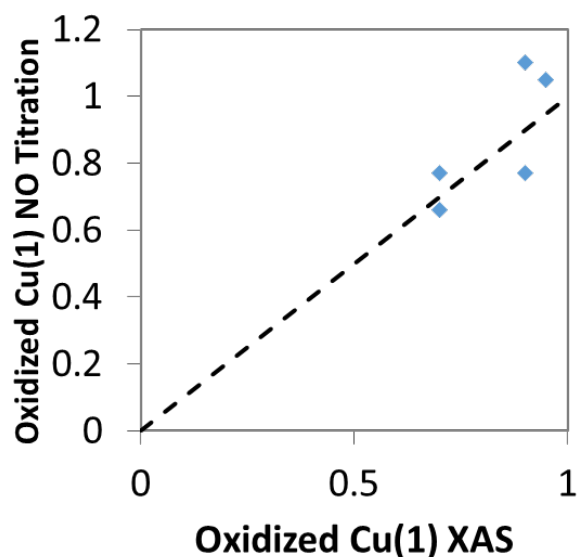


**Figure 60.** Parity plot between the fraction of oxidized  $\text{Cu(1)(NH}_3)_2$  measured using the NO titration method versus the fraction of oxidized  $\text{Cu(1)(NH}_3)_2$  measured using XAS. The dashed line represents the 1:1 parity line between the two axes.

#### 6.4.4 Detailed Procedure: Titrating $(\text{NH}_3)_2\text{Cu(I)-O}_2\text{-Cu(I)(NH}_3)_2$ species using a flow of NO then a flow of NO + $\text{NH}_3$

The reversibility of  $\text{O}_2$  oxidation of copper diamine species after reduction with NO and  $\text{NH}_3$  back to Cu(1) diamine was performed using NO as a probe molecule. Samples were prepared and loaded (~10 to 20 mg) into the same reactor system used for SCR kinetics (Section 1.14.1). All flow rates used in the following procedure are 600 sccm.

The catalyst was calcined under 20%  $\text{O}_2$  (99.5%, Indiana Oxygen) in balance He (99.999%, Indiana Oxygen) with a ramp rate of  $1^\circ\text{C min}^{-1}$  to  $550^\circ\text{C}$  and cooled to  $200^\circ\text{C}$  to ensure that 100% of the Cu oxidized and to ensure that there is no adsorbed water or  $\text{NH}_3$  on the catalyst. The catalyst and bypass was then flushed with He for 30 minutes each to ensure there is no residual  $\text{O}_2$  gas in the reactor or bypass.

A 300 ppm NO (3.5% NO/Ar, Praxair) and 300 ppm  $\text{NH}_3$  (3.0%  $\text{NH}_3$ /Ar, Praxair) mixture in balance He (99.999%, Indiana Oxygen) was stabilized through the bypass for 15 minutes then switched to the catalyst for a 1 hour reduction. The fraction of NO:Cu consumed was quantified using the difference between the unloaded blank reactor and loaded reactor.  $\text{NH}_3$  and NO flows

were then immediately switched with a 10% O<sub>2</sub> in balance He stream for 15 minutes. During this step the catalyst turns over a few times due to the brief but simultaneous presence of NH<sub>3</sub>, NO, and O<sub>2</sub> in the reactor. However, the steady state values represents the catalyst oxidized to its furthest extent, as evidenced by transient XANES. The flow was then redirected through the bypass and a 300 ppm NO in He stream stabilized for 2 minutes. This flow was directed to the reactor for 15 minutes and the NO:Cu consumed during this step was quantified using the same method as earlier. During this step there was no NH<sub>3</sub> simultaneously present with NO and O<sub>2</sub> in the reactor as the NH<sub>3</sub> spike was from the static NH<sub>3</sub> that remained in the bypass from the initial NO+NH<sub>3</sub> reduction. A 300 ppm NO and 300 ppm NH<sub>3</sub> in He stream was then flown directly to the catalyst for 30 minutes. Again, the NO:Cu consumed during this step was quantified. Our results show that takes  $1.08 \pm 0.11$  NO:Cu to reduce a fully oxidized Cu-SSZ-13 catalyst to a fully reduced catalyst. After O<sub>2</sub> oxidation, it takes a NO:Cu of  $0.98 \pm 0.10$  to fully oxidize the Cu dimer to Cu(II), and after addition of NH<sub>3</sub> to the NO it takes another NO:Cu of  $1.07 \pm 0.11$  to fully reduce the catalyst back to Cu(I). These NO titration ratios are consistent with our proposed mechanism where 1 NO:Cu is consumed to fully reduce an oxidized Cu to a reduced Cu, and another 2 NO:Cu is required to fully reduce only the copper oxidized by O<sub>2</sub> to Cu(I).

## 6.5 Conclusions

Oxygen-bridged Cu(1) dimers are a relevant intermediate for the low temperature (200°C) standard SCR reaction using NH<sub>3</sub> as a reductant over Cu-SSZ-13. It has been demonstrated that Cu ions are electrostatically tethered to anionic sites in the chabazite framework and has an accessible diffusion sphere (radius of 9 Å) from that anionic site, limited by electrostatic forces and barriers arising from sterics of traveling through 8-membered rings in the zeolite framework. XAS was used to first ensure all the Cu<sup>2+</sup> reduced to Cu(1)(NH<sub>3</sub>)<sub>2</sub> under a stream of NO + NH<sub>3</sub> in balance inert, then oxidation with O<sub>2</sub> to form the O<sub>2</sub>-Cu(1)(NH<sub>3</sub>)<sub>2</sub> complex. We use XANES to quantify the extent of oxidation through linear combination of the Cu<sup>1+</sup> pre-edge feature and observe that the fraction of oxidizable Cu to form these O<sub>2</sub>-Cu(1)(NH<sub>3</sub>)<sub>2</sub> complexes matches the predicted number of oxidizable Cu from Monte Carlo simulations. These Monte Carlo simulations assume (1) a random distribution of Cu, (2) that Cu and H cannot ion-exchange or “hop”, (3) that Cu is mobile to an extent of 9 Å, and (4) that only Cu whose diffusion spheres overlap can form dimers. Although XAS is a powerful technique, it is not widely accessible and

is expensive and time consuming. In this chapter, we discuss the development and implication of an in-lab titration technique that quantifies the fraction of pairable  $\text{Cu(I)(NH}_3)_2$  using in-situ pre-treatments and NO as a probe molecule.

## 6.6 Acknowledgements

The author would like to acknowledge Ishant Khurana for insight, advice, and discussions throughout the entire process of developing this titration method.

## 6.7 Supplementary Information

### 6.7.1 Stability of $(\text{NH}_3)_2\text{Cu(I)-O}_2\text{-Cu(I)(NH}_3)_2$ dimers in the presence of $\text{H}_2\text{O}$

The stability of  $(\text{NH}_3)_2\text{Cu(I)-O}_2\text{-Cu(I)(NH}_3)_2$  dimers in the presence of 2.5%  $\text{H}_2\text{O}$  in balance  $\text{N}_2$  was probed using NO as a titrant molecule, using the procedure outlined in Section 5.4.4, but with a  $\text{H}_2\text{O}$  flushing step inserted between  $\text{O}_2$  oxidation and NO introduction. Figure 61 demonstrates that with increasing  $\text{H}_2\text{O}$  flushing time, the number of NO that reacts decreases with increasing  $\text{H}_2\text{O}$  flushing time. It is uncertain from Figure 61 whether the number of NO that reacts will eventually reach zero when flushed with water sufficient time, or whether it'll level off at a non-zero value. If the value levels off at zero, then it indicates that all  $(\text{NH}_3)_2\text{Cu(I)-O}_2\text{-Cu(I)(NH}_3)_2$  dimers formed are able to be rendered unable to activate NO from a water flush. If the value levels off at a non-zero value, then it indicates that there are at least two pools of  $(\text{NH}_3)_2\text{Cu(I)-O}_2\text{-Cu(I)(NH}_3)_2$  dimers: (1) those that are able to be rendered unable to activate NO from a water flush and (2) those who are resistant enough to  $\text{H}_2\text{O}$  and are able to activate NO even after exposure to  $\text{H}_2\text{O}$ .

It is also uncertain how the ligands in the  $(\text{NH}_3)_2\text{Cu(I)-O}_2\text{-Cu(I)(NH}_3)_2$  dimer complex respond to  $\text{H}_2\text{O}$ . It is possible that  $\text{H}_2\text{O}$  displaces the  $\text{NH}_3$  ligands while maintaining the  $\text{O}_2$ -bridged dimer complex, and it is also possible that  $\text{H}_2\text{O}$  not only displaces the  $\text{NH}_3$  ligands, but also destroys the  $\text{O}_2$ -bridge. Regardless of what the final state of the  $(\text{NH}_3)_2\text{Cu(I)-O}_2\text{-Cu(I)(NH}_3)_2$  dimer complex looks like after exposure to  $\text{H}_2\text{O}$ , it is evident from Figure 61 that those species are not able to activate NO.

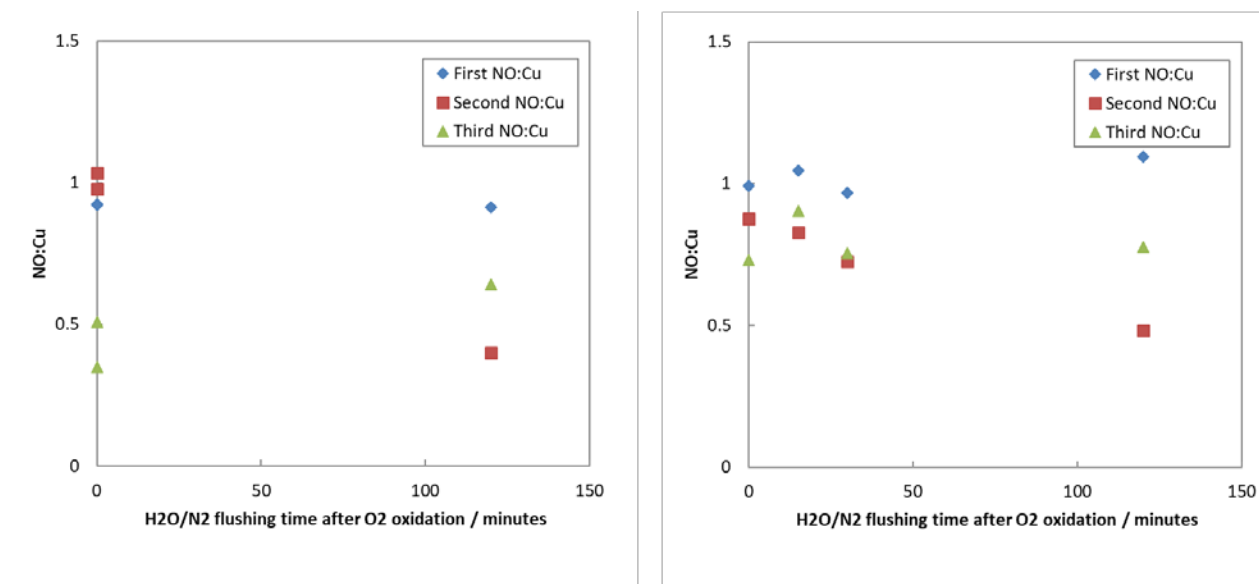


**Figure 61.** The consumption of NO plotted as a molar NO:Cu ratio after reduction of a calcined Cu-SSZ-13 with NO + NH<sub>3</sub> (blue diamonds), exposing the catalyst to NO in balance N<sub>2</sub> (red square) after flushing the catalyst with 2.5% H<sub>2</sub>O in balance inert for 15 minutes after O<sub>2</sub> saturation, and finally flowing NO and NH<sub>3</sub> (green triangle). Two Cu-SSZ-13 samples, one with all Cu<sup>2+</sup> as Z<sub>2</sub>Cu (Si:Al = 15, Cu wt% = 0.5) (left graph) and one with all Cu<sup>2+</sup> ZCuOH (Si:Al = 15, Cu wt% = 2.0, Na<sup>+</sup>-free hydrothermal synthesis) (right graph)

### 6.7.2 Using the NO titration method to test a sample unable to be tested using XAS

Table 11 lists all the samples whose fraction of oxidizable Cu(I)(NH<sub>3</sub>)<sub>2</sub> has been experimentally measured using either in-situ XAS and/or NO titration. Figure 62 plots the oxidizable Cu(I) fraction collected from XAS (purple circles), NO titration (green triangles) and computation (red lines). We first point out the Cu-SSZ-13 (Si:Al = 100, Cu wt% = 0.11) sample (green triangle with the lowest Cu density in Figure 62) whose fraction of oxidizable Cu is unable to be determined using in-situ XAS because its low Cu wt% (< 0.5 wt%) increase the signal-to-noise ratio to significantly higher than its typical  $\pm 5\%$ . Fortunately, NO titration is a technique that can count the fraction of oxidizable Cu(I)(NH<sub>3</sub>)<sub>2</sub> for samples with Cu wt%'s lower than 0.5. Though computation predicts that only 20% of the Cu(I)(NH<sub>3</sub>)<sub>2</sub> are able to oxidize to (NH<sub>3</sub>)<sub>2</sub>Cu(I)-O<sub>2</sub>-Cu(I)(NH<sub>3</sub>)<sub>2</sub> dimer, we experimentally measure from NO titration that 60% is able to activate NO, which does not match with computational expectations, as shown by the outlier in Figure 63.

**Table 11.** List of all Cu-SSZ-13 samples whose fraction of oxidizable  $\text{Cu(I)(NH}_3)_2$  via  $\text{O}_2$ -titration has been measured experimentally using XAS and/or NO titration. n.m. = not measured.

Si:Al	Cu wt%	Cu / 1000 $\text{\AA}^3$	Cu:Al	Oxidized Cu(I) XAS	Oxidized Cu(I) NO titration	Oxidized Cu(I) Computation
4.5	1.4	0.22	0.08	0.90	1.10	0.88
4.5	1.4**	0.22	0.08	0.90	0.66	0.88
4.5	3.7	0.58	0.21	0.95	1.05	0.95
15	0.5	0.08	0.08	0.70	0.66	0.70
15	0.5**	0.08	0.08	0.70	0.77	0.70
15*	1.6	0.24	0.20	0.78	n.m.	0.89
15	1.7	0.27	0.22	0.80	n.m.	0.90
15	2.0	0.31	0.24	n.m.	0.80	0.91
15	2.0**	0.31	0.24	n.m.	0.70	0.91
25	1.6	0.25	0.25	0.75	n.m.	0.89
100	0.11	0.017	0.1	n.m.	0.70	0.20

\*sample hydrothermally synthesized in the absence of  $\text{Na}^+$ , which leads all Cu speciating as  $\text{ZCuOH}$  after aqueous Cu-exchange.

\*\*sample is a repeat of the sample listed on the line immediately above the double asterisk.

It is currently unknown why this particular sample deviates from the computational model. It is possible that one or more of the assumptions that go into the model breaks down as Cu and Al densities decrease, or it is possible that the chemical phenomenon occurring during the NO titration method is different for samples with dilute Cu versus samples with higher Cu densities. If the  $(\text{NH}_3)_2\text{Cu(I)-O}_2\text{-Cu(I)(NH}_3)_2$  dimer is the only species that activates NO, then 60% of the  $\text{Cu(I)(NH}_3)_2$  are able to form the  $(\text{NH}_3)_2\text{Cu(I)-O}_2\text{-Cu(I)(NH}_3)_2$  dimer complex. Why is a higher fraction of  $\text{Cu(I)(NH}_3)_2$  able to pair than expected? Perhaps the  $(\text{NH}_3)_2\text{Cu(I)-O}_2\text{-Cu(I)(NH}_3)_2$  dimer is not formed, and some single-site Cu are able to activate NO after  $\text{O}_2$ -titration, similar to the oxidation half cycle in the reaction proposed by Janssens et al.[118]. Perhaps it is due to Cu being able to hop and exchange with neighboring Brønsted acid sites; this scenario is not as likely because of the dilute anionic site density (Si:Al = 100) compared to other samples collected with higher anionic site density (Si:Al = 4.5 to 25).

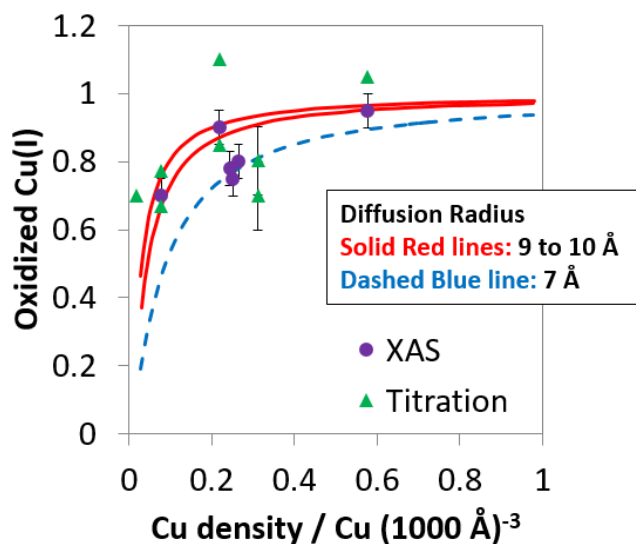


**Figure 62.** Fraction of Cu(1)(NH<sub>3</sub>)<sub>2</sub> in Cu-SSZ-13 oxidized using O<sub>2</sub> using XANES (purple circles) and the NO titration method (green triangles) plotted versus the Cu density of the samples tested.

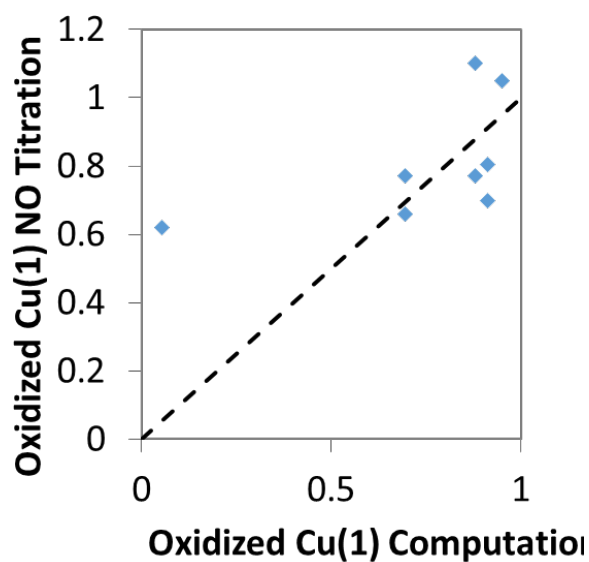


**Figure 63.** Parity plot between the fraction of oxidized Cu(1)(NH<sub>3</sub>)<sub>2</sub> measured using the NO titration method versus the fraction of oxidized Cu(1)(NH<sub>3</sub>)<sub>2</sub> predicted from computation.



### 6.7.3 Cu density is not the only descriptor required to explain the fraction of $(\text{NH}_3)_2\text{Cu(I)}\text{-O}_2\text{-Cu(I)(NH}_3)_2$ dimer complexes that can be formed from $\text{O}_2$ -titrating $\text{Cu(I)(NH}_3)_2$

On the topic of Cu hopping and exchanging with neighboring extraframework moieties, We observe that the experiential XAS results do not match well with the computational results, specifically for a series of four Cu-SSZ-13 samples with similar Cu densities (0.22 to 0.27 Cu per  $1000 \text{ \AA}^3$ ), tabulated in Table 12. Since changes in the fraction of  $\text{O}_2$ -oxidizable  $\text{Cu(I)(NH}_3)_2$  is independent of the Cu density, a search for descriptors that could assist in explaining why certain samples with the same Cu density are able to exhibit higher fraction of pair-able  $\text{Cu(I)(NH}_3)_2$ .

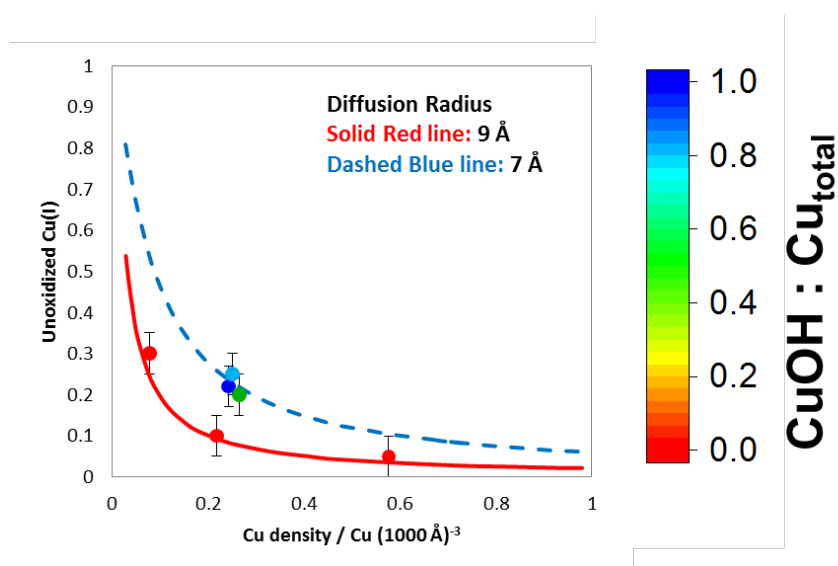


**Figure 64.** The fraction of unoxidized  $\text{Cu(I)(NH}_3)_2$  remaining after titration of Cu-SSZ-13 with  $\text{O}_2$ . The lines represent the predicted fraction of oxidizable Cu from computation assuming that each Cu electrostatically tethered to the framework can only move up to 9 Å (solid red line) and 7 Å (dashed blue line) from the anionic Al. Three Cu-SSZ-13 samples have all their  $\text{Cu}^{2+}$  species as  $\text{Z}_2\text{Cu}$  (red circles) and the remaining three have all or most of their  $\text{Cu}^{2+}$  species as CuOH (green/blue circles).

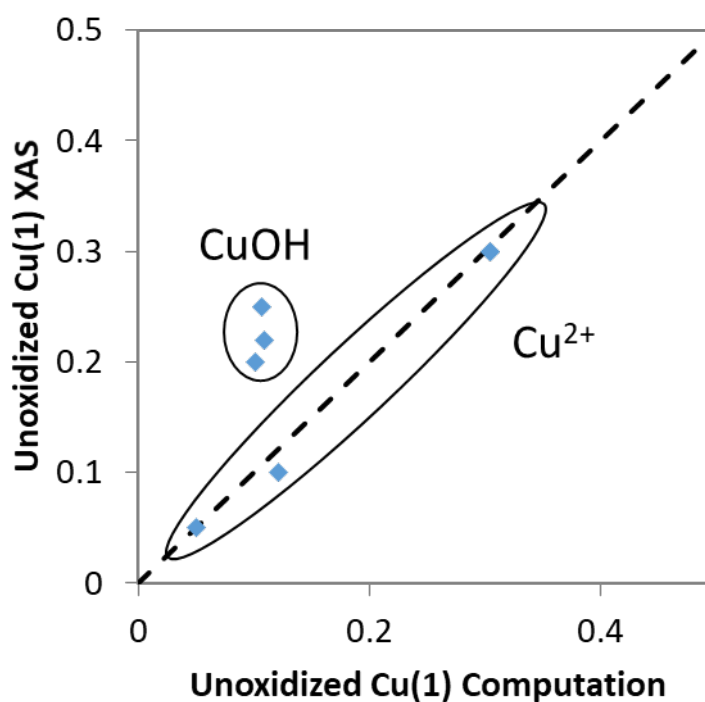


**Figure 65.** Parity plot between the unoxidized Cu(1) from the computational model compared to the unoxidized Cu(1) measured from XAS.



**Figure 66.** Illustration demonstrating that Cu(1)(NH<sub>3</sub>)<sub>2</sub> formed from Z<sub>2</sub>Cu species have a slightly larger diffusion sphere (red cloud), likely owing to the possibility that H<sup>+</sup> and Cu(1)(NH<sub>3</sub>)<sub>2</sub> can exchange and hop between a paired Al, thereby increasing the volume able to be reached by the Cu(1)(NH<sub>3</sub>)<sub>2</sub>. Conversely, ZCuOH species have a slightly smaller diffusion sphere likely owing to the fact that it is only electrostatically tethered to one anionic site.

Figure 67 plots the fraction of pair-able  $\text{Cu(I)(NH}_3)_2$  as a function of the ZCuOH fraction and as a function of the Si:Al ratio. We observe that increasing the ZCuOH ratio correlates with a decrease in the fraction of pair-able  $\text{Cu(I)(NH}_3)_2$  while increasing the Si:Al ratio correlates with a decrease in the fraction of pair-able  $\text{Cu(I)(NH}_3)_2$ . Perhaps an increase in the anionic density (decrease in Si:Al ratio) is able to confer the ability of Cu to ion-exchange hop, thereby increasing its diffusion sphere and increasing its fraction of pair-able  $\text{Cu(I)(NH}_3)_2$ . From a mobility standpoint,  $\text{Cu(I)(NH}_3)_2$  species stemming from  $\text{Z}_2\text{Cu}$  sites would be expected to exhibit a higher diffusion radius if  $\text{Cu(I)(NH}_3)_2$  can swap between either anionic site in the paired Al at a rate that's faster or equal to the rate of standard SCR. This would render  $\text{Cu(I)(NH}_3)_2$  sites that are formed from ZCuOH sites at isolated Al sites with a lower diffusion radius. Figure 68 illustrates the proposed differences in the diffusion radius of  $\text{Cu(I)(NH}_3)_2$  species at paired and isolated anionic sites.

**Table 12.** List of samples with similar Cu densities (0.22 to 0.27 Cu per 1000  $\text{\AA}^3$ ), their CuOH fraction, Si:Al molar ratio, and oxidizable Cu(I) using XAS.

Si:Al	Cu wt%	Cu / 1000 $\text{\AA}^3$	Cu:Al	CuOH fraction	Oxidized Cu(I) XAS
4.5	1.4	0.22	0.08	0.00	0.90
15	1.6	0.24	0.20	0.40	0.78
15	1.7	0.27	0.22	0.45	0.80
25	1.6	0.25	0.25	0.68	0.75

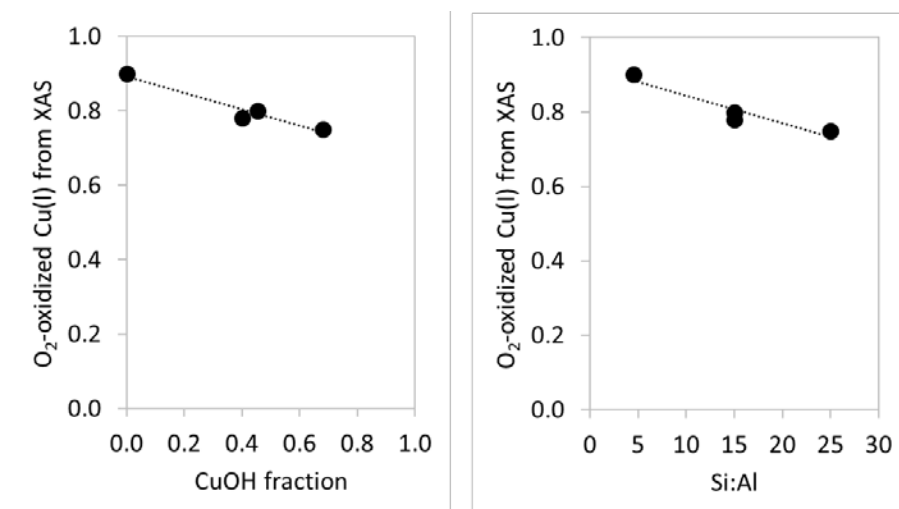


**Figure 67.** There is a correlation between the fraction of oxidizable Cu(I)(NH<sub>3</sub>)<sub>2</sub> and the CuOH fraction (left) and also a correlation between the fraction of oxidizable Cu(I)(NH<sub>3</sub>)<sub>2</sub> and the Si:Al molar ratio (right). Four Cu-SSZ-13 samples with similar Cu densities (0.22 to 0.27 Cu per 1000 Å<sup>3</sup>) were used.

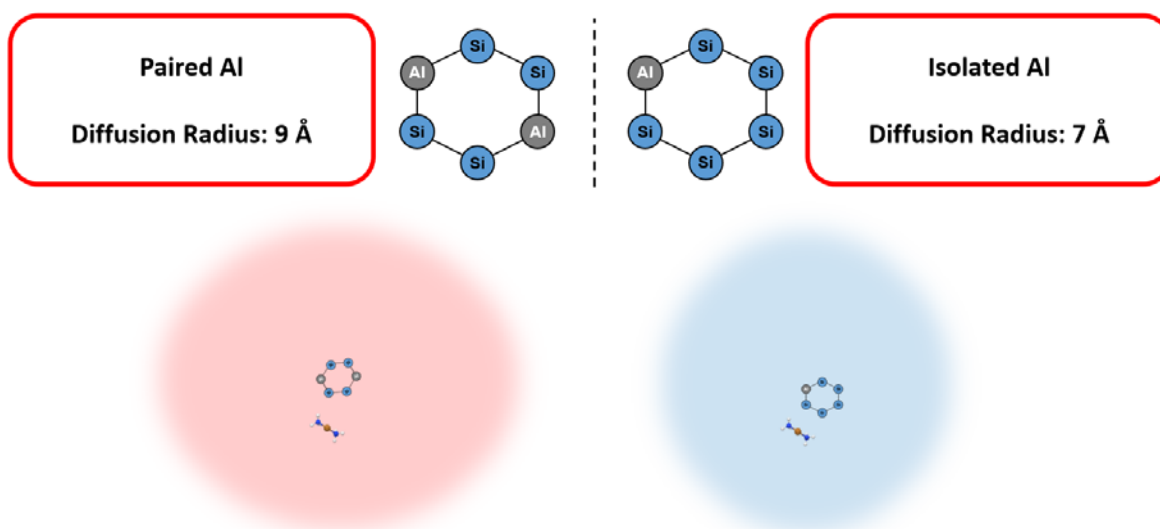


**Figure 68.** Proposed differences the diffusion radius of Cu(I)(NH<sub>3</sub>)<sub>2</sub> species anchored at a paired anionic site (left) and an isolated anionic site (right). Illustration demonstrates that Cu(I)(NH<sub>3</sub>)<sub>2</sub> formed from Z<sub>2</sub>Cu species have a slightly larger diffusion sphere (red cloud), likely owing to the possibility that H<sup>+</sup> and Cu(I)(NH<sub>3</sub>)<sub>2</sub> can exchange and hop between a paired Al, thereby increasing the volume able to be reached by the Cu(I)(NH<sub>3</sub>)<sub>2</sub>. Conversely, ZCuOH species have a slightly smaller diffusion sphere likely owing to the fact that it is only electrostatically tethered to one anionic site.

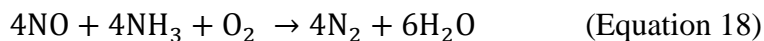
## 7. SPECTROSCOPIC AND KINETIC RESPONSE OF CU-SSZ-13 TO SO<sub>2</sub> EXPOSURE AND IMPLICATIONS FOR NO<sub>x</sub> SELECTIVE CATALYTIC REDUCTION

### 7.1 Abstract

The effects of sulfur poisoning on Cu-SSZ-13 zeolites, used commercially for the selective catalytic reduction (SCR) of nitrogen oxides (NO<sub>x</sub>) with ammonia, were studied by exposing model Cu-zeolite powder samples to dry SO<sub>2</sub> and O<sub>2</sub> streams at 473 and 673 K, and then analyzing the surface intermediates formed using spectroscopic and kinetic assessments. Model Cu-SSZ-13 zeolites were synthesized to contain distinct Cu active site types, predominantly either divalent Cu<sup>2+</sup> ions exchanged at proximal framework Al (Z<sub>2</sub>Cu), or monovalent CuOH<sup>+</sup> complexes exchanged at isolated framework Al (ZCuOH). SCR turnover rates (473 K, per Cu) decreased linearly with increasing S content to undetectable values at equimolar S:Cu ratios, consistent with poisoning of each Cu site with one SO<sub>2</sub>-derived intermediate. Cu and S K-edge X-ray absorption spectroscopy and density functional theory calculations are used to identify the structures and binding energies of different SO<sub>2</sub>-derived intermediates at Z<sub>2</sub>Cu and ZCuOH sites, revealing that bisulfates are particularly low in energy, and residual Brønsted protons are liberated at Z<sub>2</sub>Cu sites as bisulfates are formed. Molecular dynamics simulations also show that Cu sites bound to one HSO<sub>4</sub> are immobile, but become liberated from the framework and more mobile when bound to two HSO<sub>4</sub>. These findings indicate that Z<sub>2</sub>Cu sites are more resistant to SO<sub>2</sub> poisoning than ZCuOH sites, and are easier to regenerate once poisoned.

### 7.2 Introduction

Sulfur levels in diesel fuel were regulated by the Environmental Protection Agency (EPA) in 1993 to “low-sulfur” contents (500 ppm) [126], and further in 2006 to “ultra-low sulfur” diesel fuel (15 ppm) [127]. Sulfur oxides (SO<sub>x</sub>, x = 2,3) formed during the combustion of diesel fuel cause deactivation of the Cu-SSZ-13 zeolite catalysts used for the selective catalytic reduction of nitrogen oxides (NO<sub>x</sub>, x = 1,2) with ammonia (NH<sub>3</sub>-SCR), which for the “standard” reaction stoichiometry is shown in Equation 18:



Strategies to reverse the deactivation of  $\text{SO}_x$ -poisoned Cu-SSZ-13 zeolites typically involve high temperature (673-1073 K) regeneration treatments. A molecular understanding of how  $\text{SO}_x$ -derived species poison different Cu site types in Cu-SSZ-13 zeolites would aid in developing additional strategies for regenerating sulfur poisoned materials and designing catalysts that would be more resistant to sulfur poisoning.

A significant body of prior work has studied the effects of sulfur poisoning on Cu-zeolites within the context of  $\text{NH}_3$ -SCR, by monitoring the decrease the micropore volume as a function of sulfur content, as summarized in Figure 69. On Cu-MOR zeolites with increasing sulfur content, Ham et al. observed a decrease in  $\text{NO}_x$  conversion (during standard  $\text{NH}_3$ -SCR) and a concurrent decrease in the BET-derived surface area measured by  $\text{N}_2$  adsorption [128–130]. Several groups have reported similar observations on Cu-CHA poisoned concurrently with  $\text{SO}_2$  and  $\text{NH}_3$ , including Wijayanti et al. for Cu-SAPO-34 and Brookshear et al. for Cu-SSZ-13 [131,132], and this evidence was used to propose pore-blocking with sulfur-derived species to be the dominant mechanism of sulfur poisoning. Cu-SAPO-34 poisoned only with  $\text{SO}_2$  in the absence of  $\text{NH}_3$ , however, did not cause decreases in BET-derived surface areas with increasing sulfur content, leading Shen et al. to propose that sulfur-derived species were bound chemically at Cu sites to cause inhibition or deactivation [133]. Sulfur temperature programmed desorption (TPD) experiments have also demonstrated that  $\text{SO}_2$  storage is negligible on H-form zeolites, and significant amounts of sulfur are stored only on Cu-containing zeolites [133–135].

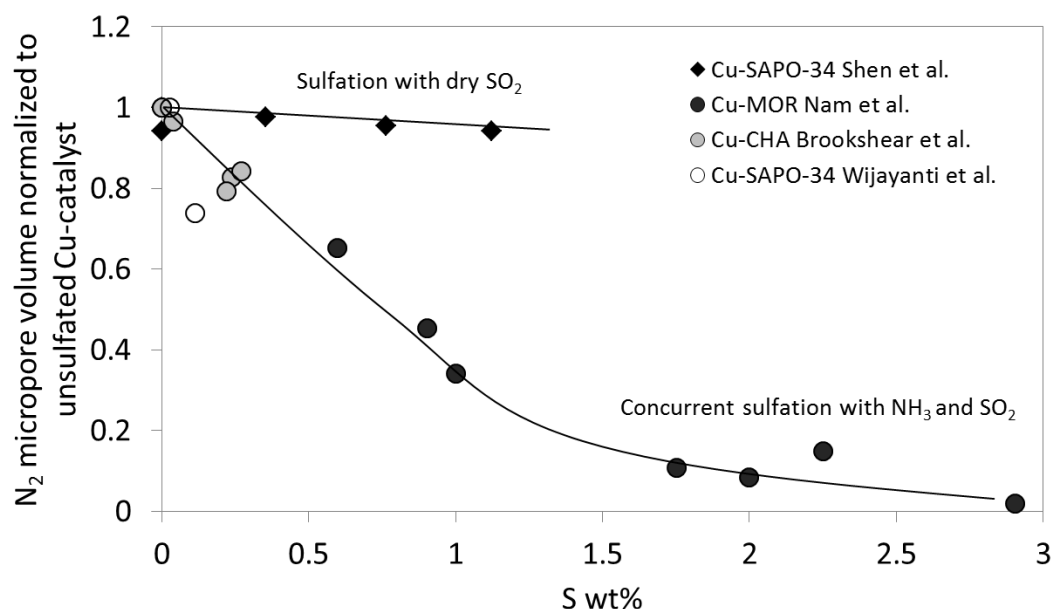


**Figure 69.** Normalized micropore volume (BET-surface areas derived from N<sub>2</sub> adsorption) with increasing S content reported by Ham et al. [128], Brookshear et al. [132], Wijayanti et al. [131], and Shen et al. [133] when Cu-zeolites are poisoned with SO<sub>2</sub>, or with SO<sub>2</sub> and NH<sub>3</sub> concurrently.

Several studies have also reported the effects of SO<sub>2</sub> poisoning of Cu-zeolites, in the presence of other molecules relevant to NH<sub>3</sub>-SCR catalysis. Oxidation catalysts upstream of the SCR catalyst in diesel exhaust aftertreatment systems oxidize SO<sub>2</sub> to SO<sub>3</sub>, and the fraction of SO<sub>3</sub> increases with temperature until thermodynamic equilibrium among SO<sub>2</sub>, O<sub>2</sub>, and SO<sub>3</sub> is reached [136–138]. Cheng et al. reported that the presence of SO<sub>3</sub> poisons a Cu-zeolite catalyst (framework not specified) to a greater extent than just SO<sub>2</sub> alone [139]. X-ray photoelectron spectroscopy (XPS) was used to show that the surface sulfur species (S<sup>6+</sup>) are in the same compound (SO<sub>4</sub><sup>2-</sup>) regardless of whether SO<sub>3</sub> was present or not during poisoning treatments. Hammershøi et al. [140] and Wijayanti et al. [141] demonstrated that the presence of H<sub>2</sub>O, NH<sub>3</sub>, and NO<sub>x</sub> species during SO<sub>2</sub> poisoning affects the total sulfur storage on Cu-CHA materials. Specifically, Hammershøi et al. [142] measured higher S:Cu ratios on Cu-SAPO-34 poisoned in the presence of NH<sub>3</sub>-SCR gases at low temperature (<573 K), than when poisoned in the presence of only O<sub>2</sub> and H<sub>2</sub>O at higher temperatures (>573 K).

Understanding the details of desulfation processes is also important in developing catalyst regeneration strategies, given Cu-CHA catalysts only partially recover NH<sub>3</sub>-SCR reactivity after

desulfation [134,135,137,143,144]. Hammershøi et al. reported that successive desulfation treatments of Cu-SSZ-13 under  $\text{NH}_3$ -SCR conditions (823 K) can only regenerate ~80% of the rate (per mass, 2-30%  $\text{NO}_x$  conversion) of unpoisoned samples [140]. Furthermore, Hammershøi et al. reported that desulfation under  $\text{NH}_3$ -SCR conditions does not occur until temperatures higher than 573 K, consistent with sulfur desorption temperatures from TPD experiments [134,139,140,144–146]. Kumar et al. [147] and Ando et al. [148] demonstrated that desulfation treatments are more effective in a reducing environment ( $\text{NO} + \text{NH}_3$ ,  $\text{NH}_3$ ,  $\text{C}_3\text{H}_6$ ,  $n\text{-C}_{12}\text{H}_{16}$ ) than in a more oxidizing environment at moderate temperatures ca. 623 K, allowing for catalyst regeneration on-stream without a significant temperature increase. These authors proposed that sulfur-poisoned Cu sites were regenerated by initiating the redox cycling of Cu from the  $2+$  to  $1+$  oxidation state under reducing environments. In contrast, temperatures up to 823 K are required to regenerate Cu under more oxidative conditions, such as the standard  $\text{NH}_3$ -SCR gas environment.

Since the discovery and implementation of Cu-SSZ-13 zeolites for  $\text{NH}_3$ -SCR nearly a decade ago, a significant amount of research has been performed to identify the nature of Cu active sites and the  $\text{NH}_3$ -SCR reaction mechanism. Three major conclusions from studying unpoisoned Cu-SSZ-13 catalysts are: (1)  $\text{NH}_3$ -SCR involves a  $\text{Cu}^{2+}/\text{Cu}^+$  redox process, (2) at low temperatures (<573 K), the SCR active sites are derived from isolated Cu cations that are exchanged to anionic Al sites in the zeolite framework, and (3) there are pool of active Cu sites include two distinct types of exchanged Cu ions present as  $\text{CuOH}^+$  ( $\text{ZCuOH}$ ) and  $\text{Cu}^{2+}$  ( $\text{Z}_2\text{Cu}$ ) sites that are respectively charge compensated by one and two framework Al [65,68,96,106,109,149]. Evidence for  $\text{Cu}^{2+}/\text{Cu}^+$  redox cycling during standard  $\text{NH}_3$ -SCR was obtained from observing mixtures of Cu(I) and Cu(II) states during in situ and in operando XAS [68,115]. The two distinct Cu site types in Cu-SSZ-13 have been observed using infrared spectroscopy (DRIFTS, FTIR) to identify and quantify the (O-H) stretching vibration at  $3660\text{ cm}^{-1}$  for Cu-OH sites,  $\text{H}_2$ -temperature programmed reduction ( $\text{H}_2$ -TPR), Rietveld refinement of XRD patterns [41,54,150], Cu: $\text{H}^+$  site exchange stoichiometries, FTIR, and DFT calculations. These characterization studies conclude that Cu ions exchange in SSZ-13 preferentially exchange as  $\text{Z}_2\text{Cu}$  to saturation, then as  $\text{ZCuOH}$  [109]. Recently, it was reported that another relevant intermediate during low



temperature ( $<573$  K)  $\text{NH}_3$ -SCR includes transiently-formed dimeric Cu-oxo complexes formed via reaction of two  $\text{NH}_3$ -solvated Cu(I) complexes ( $\text{Cu}(\text{NH}_3)_2^+$ ) with  $\text{O}_2$  [125,151].

The effects of sulfur poisoning on  $\text{Z}_2\text{Cu}$  and  $\text{ZCuOH}$  site types have been reported by Luo et al. [150] and Jangjou et al. [144,150]. Luo et al. measured DRIFTS spectra on a Cu-SSZ-13 sample containing a mixture of  $\text{ZCuOH}$  ( $950\text{ cm}^{-1}$ ) and  $\text{Z}_2\text{Cu}$  ( $900\text{ cm}^{-1}$ ) sites, and found that sulfur poisoning caused full suppression of the  $\text{ZCuOH}$  peak but only minor suppression of the  $\text{Z}_2\text{Cu}$  peak, leading to the proposal that  $\text{Z}_2\text{Cu}$  sites are less susceptible to sulfur poisoning because they are stabilized with one more anionic charge in the zeolite framework than  $\text{ZCuOH}$  sites. Jangjou et al. studied a Cu-SAPO-34 sample containing with a mixture of  $\text{ZCuOH}$  and  $\text{Z}_2\text{Cu}$  sites and concluded that sulfur deactivates  $\text{ZCuOH}$  sites through chemical poisoning and  $\text{Z}_2\text{Cu}$  sites via pore blocking, using in situ DRIFTS and NO as a probe molecule [143].

Here, we build on this prior work to investigate how  $\text{SO}_2$  poisons  $\text{ZCuOH}$  sites and  $\text{Z}_2\text{Cu}$  sites in Cu-SSZ-13 zeolites, by combining an approach that interprets changes in  $\text{NH}_3$ -SCR kinetic parameters with varying sulfur content, structural characterization of surface species using spectroscopy (XAS, UV-Visible, FTIR) and titration ( $\text{NH}_3$ ) methods, and density functional theory (DFT) calculations. Kinetic measurements (reaction rate, reaction orders, and apparent activation energy) provide insights on the effects of sulfur poisoning and regeneration on  $\text{ZCuOH}$  and  $\text{Z}_2\text{Cu}$  sites. We find that the sulfur poisons both  $\text{ZCuOH}$  and  $\text{Z}_2\text{Cu}$  sites to inactive states, resulting in a constant SCR turnover rate when normalized by the number of residual unpoisoned Cu sites ( $\text{mol Cu} - \text{mol S}$ ).

## 7.3 Experimental Methods

### 7.3.1 Synthesis, sulfation, and de-sulfation of Cu-zeolites

In this paper, two model catalysts were synthesized, one with a Si:Al of 4.5 with a Cu wt% of 3.8 (100%  $\text{Z}_2\text{Cu}$ , 0%  $\text{ZCuOH}$ ) and one with a Si:Al of 25 with a Cu wt% of 1.5 (80%  $\text{ZCuOH}$ , 20%  $\text{Z}_2\text{Cu}$ ) using methods reported in Section 1.12. The relative fraction of  $\text{Z}_2\text{Cu}$  and  $\text{ZCuOH}$  active sites were confirmed using Cu elemental analysis and selective titration of Brønsted acid sites

using  $\text{NH}_3$ , as outlined in our previous publication [109]. Sulfation treatments were performed by saturating 0.5 g of sieved catalyst in a flowing stream of  $\text{N}_2$  ( $600 \text{ mL min}^{-1}$ ) containing 100 ppm  $\text{SO}_2$  at 473 K or 673 K for a pre-determined time, such that the cumulative molar exposure was  $\text{S}:\text{Cu} = 5$ . Sulfated sample names are preceded by 473 K  $\text{SO}_2$  or 673 K  $\text{SO}_2$  to denote sulfation treatments at 473 K and 673 K, respectively.

Desulfation treatments of sulfated samples were performed in a reductive environment in flowing  $\text{N}_2$  ( $800 \text{ mL min}^{-1}$ ) containing of 500 ppm  $\text{NH}_3$  and 500 ppm  $\text{NO}$  at 673 K. Typically, 0.02 to 0.05 g of each sulfated catalyst was heated to 673 K in dry nitrogen (liquid nitrogen boil-off, Linde) with a ramp rate of 283 K per minute, then exposed to flowing  $\text{NH}_3$  and  $\text{NO}$  stream for a pre-determined time, such that the cumulative molar exposure of  $\text{NO}:\text{S}$  was 100. The desulfated catalysts were then cooled to ambient temperature in  $\text{N}_2$  flow.

### 7.3.2 Catalyst Characterization

Bulk Si, Al and Cu contents in all Cu-SSZ-13 samples was determined by atomic absorption spectroscopy (AAS) (Details in Section 1.13.2). Si, Al, Cu, and S were also measured using inductively coupled plasma – optical emission spectroscopy (ICP-OES) on an iCAP 7400 ICP-OES analyzer. Samples were prepared by acid microwave digestion. For ICP-OES sample preparation, about 30 mg of sample is transferred to a Teflon liner with 9 mL of  $\text{HNO}_3$ , 3 mL  $\text{HF}$ , and a stirbar, then heated while stirring to 503 K (temperature reached in 5 minutes) and holding at 503 K for 20 minutes. Next, the sample was allowed to cool to ambient temperature for 1 hour, after which point 10 mL of 4% boric acid was added. The sample was heated while stirring to 453 K in 4 minutes and held for 15 minutes. Once cooled, the resulting liquid was diluted to 100 mL.

SEM, XRD, and UV-Vis was also performed to characterize the catalysts. Experimental details can be found in Section 1.13. UV-Vis-NIR spectroscopy was used to identify changes in the coordination of copper active sites in sulfated Cu-SSZ-13, as evidence of  $\text{SO}_2$  binding to Cu species. Also, the formation of intermediate  $\text{NH}_4\text{-SO}_x$ -like species was studied by collecting spectra after saturating the samples with 500 ppm  $\text{NH}_3$  at 298 K and 473 K. UV-Vis-NIR spectra from  $4000$  to  $50000 \text{ cm}^{-1}$  and scan speed of  $2000 \text{ cm}^{-1} \text{ min}^{-1}$  were collected on a Cary 5000®

UV-VIS-NIR spectrophotometer equipped with a Harrick-Scientific Praying-Mantis<sup>®</sup> diffuse reflectance optics and cell. BaSO<sub>4</sub> (99%, Sigma-Aldrich) was used as a background correction. All samples were dehydrated (O<sub>2</sub> activated) with 100 mL min<sup>-1</sup> air (99.99%, Indiana Oxygen) at 523 K for 6 h before analysis. The low dehydration temperature of 523 K was selected to avoid desorption of sulfur species [134,139,140,144–146].

Argon (87 K) and nitrogen (77 K) micropore measurements were collected on a Micromeritics Accelerated Surface Area and Porosimetry (ASAP) 2020 system and were used to probe changes in accessible catalyst volumes after sulfation treatments. Prior to analysis, 15 to 30 mg of unsulfated Cu-SSZ-13 samples were degassed at 673 K under vacuum (<5  $\mu$ torr) for 12 h and were compared to the same samples degassed at 423 K under vacuum (<5  $\mu$ torr) for 4 h. Both degas treatments resulted in measurement of the same micropore volume within error, thus the lower temperature degas treatment was performed on the sulfated samples before collecting micropore volumes. Subjecting a sulfated sample to the 423 K degas treatment did not result in a significant decrease in sulfur content, as measured by ICP (Figure 80).

Fluorescence sulfur K-edge X-ray absorption spectroscopy (XAS) was performed at Sector 9-BM of the Advanced Photon Source at Argonne National Laboratory. Samples were pressed into circular wafers (8 mm x 0.5 mm) and adhered to carbon tape, then transferred to a He-purged chamber to minimize losses in fluorescence signal. Energies were calibrated using a sodium thiosulfate pre-edge feature at 2469.20 eV. XAS spectra were collected in an energy range between 2420 and 2550 eV. Since sulfur content on all samples were low (<1 wt%), dilution was not performed to minimize self-absorption. The sulfur content was not constant enough for quantitative analysis. XANES spectra are plotted as the ratio of the intensity of the total fluorescence signal to the intensity of the excitation radiation as a function of the photon energy. Pre-edge and post-edge spectra were normalized to 0 and 1, respectively.

A method that quantifies only NH<sub>3</sub> adsorbed on Brønsted acid sites and Lewis acidic Cu sites, and not physisorbed on the zeolite structure, was developed. The procedure involves saturation of the catalyst in a packed bed reactor with 500 ppm NH<sub>3</sub> in balance N<sub>2</sub> at 433 K (Figure 81). On unsulfated samples, the NH<sub>3</sub>:Al quantified from NH<sub>3</sub> consumption during the saturation step, and

from  $\text{NH}_3$  formation during the TPD step, were identical within error (Figure 82). The parity in  $\text{NH}_3/\text{Al}$  measured during saturation and during TPD allow quantifying the ammonia stored on sulfated Cu-SSZ-13 materials without desorbing sulfur, which can damage downstream equipment.

### 7.3.3 Measurement of SCR kinetic details

Ammonia selective catalytic reduction ( $\text{NH}_3$ -SCR) of  $\text{NO}_x$  kinetic data were measured in a down-flow 3/8" ID tubular quartz reactor, as described earlier in section 2.6. The only deviation from the reported procedure in section 2.6 is that the fresh and sulfated catalysts were not calcined in dry air at elevated temperatures ( $\sim 773$  K) prior to collecting reaction kinetics due to sulfur desorption at temperature higher than 573 K [137]. Dehydrating the catalyst with dry air at 523 K does not affect the SCR reaction rate (Figure 83). In addition, continuous exposure to SCR gases between 423 and 523 K for 24 consecutive days did not affect the SCR reaction rate (Figure 84).  $\text{NO}$ ,  $\text{NO}_2$ ,  $\text{NH}_3$ ,  $\text{CO}_2$ ,  $\text{N}_2\text{O}$ , and  $\text{H}_2\text{O}$  concentration data were recorded every 0.95 seconds using a MKS MultiGas 2030 gas-phase Fourier transform infrared (FTIR) spectrometer with on-board calibrations. Reaction temperatures were collected using two Omega® K-type 1/16" OD thermocouples with one placed in contact with the quartz wool above the top of the bed and the second placed in contact with the quartz frit below the bottom of the bed. The temperature difference was always within 3 K during steady state SCR catalysis. Total flow rates were measured using a soap bubble gas flow meter.

In the limit of differential NO conversion, the gas concentrations and catalyst bed temperature can be assumed constant, allowing the differential NO conversion rate to be calculated using Equation 19:

$$-r_{\text{NO}} = \frac{(C_{\text{NO},in} - C_{\text{NO},out})}{1000000} \frac{P\dot{V}_{total}}{RT} \quad (\text{Equation 19})$$

where  $C$  is the concentrations of NO in ppm before and after the catalyst bed,  $\dot{V}_{total}$  is the total flow rate,  $P$  is 1 atm,  $T$  is ambient temperature, and  $R$  is the gas constant. The experimental data

are fitted to a power law rate expression (Equation 20) where  $k_{app}$  (Equation 21) is the apparent rate constant and  $\alpha$ ,  $\beta$ ,  $\gamma$ ,  $\delta$ , and  $\epsilon$  are the apparent reaction orders with respect to concentrations of NO, NH<sub>3</sub>, O<sub>2</sub>, H<sub>2</sub>O, and CO<sub>2</sub>, respectively.

$$-r_{NO} = k_{app} C_{NO}^{\alpha} C_{NH_3}^{\beta} C_{O_2}^{\gamma} C_{H_2O}^{\delta} C_{CO_2}^{\epsilon} \quad (\text{Equation 20})$$

$$k_{app} = A_0 \exp\left(-\frac{E_{a,app}}{RT}\right) \quad (\text{Equation 21})$$

All reported rates are free of external diffusion limitations (independent of space velocity) and internal diffusion limitations, evident in turnover rates that are similar for crystallite sizes ranging from 0.5 to 2.5 microns [43,109,152].

### 7.3.4 DFT Simulation details

Calculations were performed within periodic triclinic SSZ-13 supercell that contains 12 T-sites [30], consistent with our previous studies [43,109,151]. Figure 70(a) shows the structure of one chabazite (CHA) cage with some atoms presented as spheres to highlight the ring structures. Figure 70(b) shows the Z<sub>2</sub>Cu site where 2 Al (“Z”) atoms were substituted in the 6-membered ring (6MR). Figure 70(c) shows the ZCuOH site where 1 Al atom was substituted.

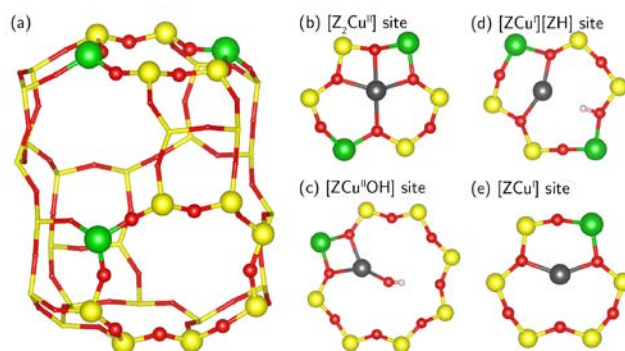


**Figure 70.** Molecular structure of a SSZ-13 (CHA) cage, with the 1Al (ZCuOH) and 2Al (Z<sub>2</sub>Cu) Cu sites on the right. Red, yellow, green, gray, and pink spheres correspond to O, Si, Al, Cu, and H atoms, respectively.

To locate the minimum energy structures reported here, we first performed ab initio molecular dynamics (AIMD) simulations at 473 K for 30 ps on candidate structures using the Car-Parrinello molecular dynamics software (CPMD) [153]. Calculations were performed within the Perdew-Becke-Erzenhof (PBE) generalized gradient approximation (GGA) [154–156], ions described with Vanderbilt ultrasoft pseudopotentials [157] and plane waves cut off at 30 Ry. Simulations were run in the canonical (NVT) ensemble with 0.6 fs timesteps. A Nose-Hoover thermostat was used to control temperature to 473 K. Low energy geometry snapshots were extracted from the trajectories and optimized to obtain the local minima energy and structure at 0 K. At least two low energy configurations were extracted from the trajectories and relaxed to ensure consistency. Subsequent geometry optimizations were performed within the Vienna Ab initio Simulation Package (VASP) software [158]. Plane wave cutoff was 400 eV and the Brillouin zone sampled at the  $\Gamma$ -point, as appropriate for a solid insulator. Electronic energies were converged to  $10^{-6}$  eV and geometries relaxed until atomic forces were less than  $0.01 \text{ eV } \text{\AA}^{-1}$  using the hybrid screened-exchange method of Heyd-Scuseria-Erzenhof (HSE06) and D2 for dispersion corrections. Charge analysis was performed by the method of Bader, and reported normalized to  $\text{Cu}^{2+}$  and  $\text{Cu}^+$  references ( $\text{Z}_2\text{Cu}$  and  $\text{ZCu}$ ). We report Bader charges as a superscript to Cu (i.e.  $\text{Cu}^{\text{I}}$  and  $\text{Cu}^{\text{II}}$ ).

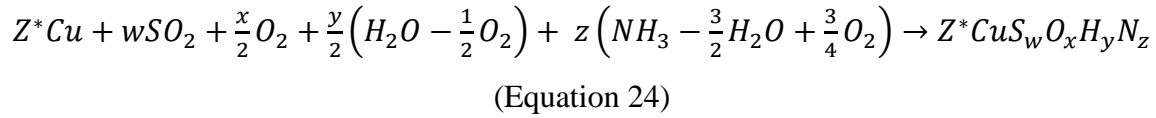
The relative mobility of the Cu centers was quantified by running 150 ps of AIMD within CPMD and following the method described in a previous publication [109]. In order to sample possible configurations efficiently, we performed five independent 30 ps AIMD simulations starting from geometries slightly perturbed (maximum perturbation =  $0.1 \text{ \AA}$ ) from the equilibrium geometry. From each of the five simulations, 12 ps was used for equilibration and 18 ps was used for data collection.

We report the free energies of formation of various combinations of  $\text{S}_w\text{O}_x\text{H}_y\text{N}_z$  on Cu sites with respect to  $\text{SO}_2$ ,  $\text{O}_2$ ,  $\text{H}_2\text{O}$ , and  $\text{NH}_3$ :

$$\Delta G_{w,x,y,z}^{\text{form}}(T, \Delta\mu_{\text{SO}_2}, \Delta\mu_{\text{O}_2}, \Delta\mu_{\text{H}_2\text{O}}, \Delta\mu_{\text{NH}_3}) = \Delta E_{w,x,y,z}^{\text{form}} - w\Delta\mu_{\text{SO}_2} - \frac{x}{2}\Delta\mu_{\text{O}_2} - \frac{y}{2}(\Delta\mu_{\text{H}_2\text{O}} - \frac{1}{2}\Delta\mu_{\text{O}_2}) - z(\Delta\mu_{\text{NH}_3} - \frac{3}{2}\Delta\mu_{\text{H}_2\text{O}} + \frac{3}{4}\Delta\mu_{\text{O}_2}) - T\Delta S(T) \text{ (Equation 22)}$$

$$\Delta E_{w,x,y,z}^{\text{form}} = E_{Z^*CuS_wO_xH_yN_z} - E_{Z^*Cu} - wE_{SO_2} - \frac{x}{2}E_{O_2} - \frac{y}{2}\left(E_{H_2O} - \frac{1}{2}E_{O_2}\right) - z\left(E_{NH_3} - \frac{3}{2}E_{H_2O} + \frac{3}{4}E_{O_2}\right) \quad (\text{Equation 23})$$

where  $Z^*Cu$  (\* = 1,2) represents either a Cu bound near one Al or two Al placed as third nearest neighbors (3NN) position in the 6MR.  $\Delta E_{w,x,y,z}^{\text{form}}$  is the formation energy of reaction:



computed using the HSE06-D2 optimized energies of all species. To compute free energies, we neglect  $PV$  and heat capacity differences between the adsorbate-free and adsorbate-covered Cu sites and compute their entropy difference using a previously reported correlation derived from ab initio potential of mean force (PMF) free energy simulations [32],  $\Delta_{\text{ads}}S^0 = -0.35S^{\text{o, i.g.}}_{\text{total}}$  for the  $ZCuOH$  site and  $\Delta_{\text{ads}}S^0 = -0.51S^{\text{o, i.g.}}_{\text{total}}$  for the  $Z_2Cu$  site [109,159].  $\Delta\mu_{SO_2}$ ,  $\Delta\mu_{O_2}$ ,  $\Delta\mu_{H_2O}$ ,  $\Delta\mu_{NH_3}$  are difference in ideal gas chemical potential ( $\mu$ ) between 0 K and the desired temperature ( $T$ ) and pressure ( $P$ ). We used the  $\Delta H^0$  and  $\Delta S^0$  values from the JANAF table [160] to calculate the  $\Delta\mu$  at each discrete temperature (0 K, 100 K, etc, up to 1000 K), and linearly interpolated any other temperatures in between those discrete points.

## 7.4 Results and Discussion

### 7.4.1 Nature of interactions between sulfur species with $Z_2Cu$ and $ZCuOH$ sites

Elemental analysis results (AAS, ICP, EDS) of the model Cu-SSZ-13 catalysts before and after various  $SO_2$  sulfation treatments ( $600 \text{ mL min}^{-1}$  of 100 ppm  $SO_2$  in balance  $N_2$  at 473 K or 673 K to reach a cumulative sulfur exposure of  $S:Cu = 5$ ) are reported in Figure 71. For a given sulfation treatment,  $ZCuOH$  sites stored more sulfur (per Cu) than  $Z_2Cu$  sites, consistent with the more exothermic DFT-computed binding energy of  $SO_2$  and  $SO_3$  species on  $ZCuOH$  than on  $Z_2Cu$  (Figure 71, right). Yang et al. [161] studied the  $SO_2$  poisoning behavior on Cu-SAPO-34 computationally, and also reported that  $SO_2$  prefers to adsorb on  $ZCuOH$  sites rather than  $Z_2Cu$  sites. Computational studies by Yang et al. [161] and Hammershøi et al. [142] report that  $SO_2$  prefers to adsorb on  $Cu^+$  sites over  $Cu^{2+}$  sites, regardless of whether the framework is Cu-SSZ-13 or Cu-SAPO-34. The sulfur uptake increases at higher temperatures (Figure 71), as also reported by Hammershøi et al. for sulfation of Cu-SAPO-34 and Cu-SSZ-13 with  $SO_2$  in the presence of  $O_2$  and  $H_2O$  [142,162].

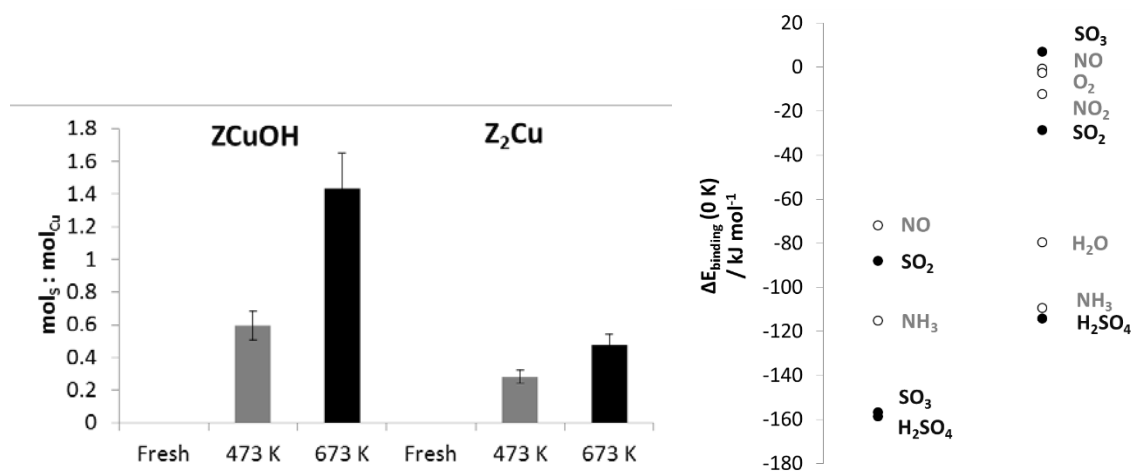


**Figure 71.** Experimental S:Cu ratios (left) and computed  $SO_2$  binding energies to Cu from DFT (right).

$NH_3$ -SCR kinetic parameters (apparent activation energies, apparent reaction orders) were measured on the two model Cu-SSZ-13 samples at standard  $O_2$  feed compositions (10%) and excess  $O_2$  feed compositions (60%) and are reported in Table 13 (activation energy and reaction order plots for all samples can be found in Figure 85 to Figure 106 and Table 15). All kinetic



parameters on the ZCuOH and Z<sub>2</sub>Cu samples, when measured with 10% O<sub>2</sub> in the feed stream (Table 14), suggest both samples likely have different rate limiting steps under these conditions, which may preclude straightforward comparisons of their kinetic behavior. In contrast, when kinetic parameters were measured with 60% O<sub>2</sub> in the feed stream (Table 13), the apparent activation energy (ca. 50 kJ/mol) and apparent NO orders (~1) became similar, suggesting that rates are limited by single-site NO + NH<sub>3</sub> reduction [43,68,115] and measurements made under these conditions could facilitate more direct comparisons between the two samples. The dependence of SCR turnover rates and apparent activation energy on S content for both model Cu-SSZ-13 samples is shown in Figure 72. With increasing S content, the SCR rate (per Cu site) decreases linearly to undetectable values at a S:Cu ratio of 1, while apparent activation energies appear constant (40-55 kJ/mol), suggesting equimolar poisoning of each Cu active site by an SO<sub>2</sub>-derived intermediate.

**Table 13.** Apparent activation energies and reactant orders on unsulfated ZCuOH and Z<sub>2</sub>Cu model catalysts collected under “10% O<sub>2</sub> SCR” conditions (300 ppm NO, 300 ppm NH<sub>3</sub>, 10% O<sub>2</sub>, 2% H<sub>2</sub>O, 8% CO<sub>2</sub>, balance N<sub>2</sub> at 473 K) and “60% O<sub>2</sub> SCR” conditions (300 ppm NO, 300 ppm NH<sub>3</sub>, 60% O<sub>2</sub>, 2% H<sub>2</sub>O, 8% CO<sub>2</sub>, balance N<sub>2</sub> at 473 K).

	E <sub>app</sub>		NO		O <sub>2</sub>		NH <sub>3</sub>	
	10% O <sub>2</sub>	60% O <sub>2</sub>	order	order	order	order	order	order
	SCR	SCR	SCR	SCR	SCR	SCR	SCR	SCR
ZCuOH	52	46	0.60	0.90	0.65	0.37	-0.40	-0.63
Z <sub>2</sub> Cu	69	54	0.90	0.94	0.30	0.02	0.00	-0.04

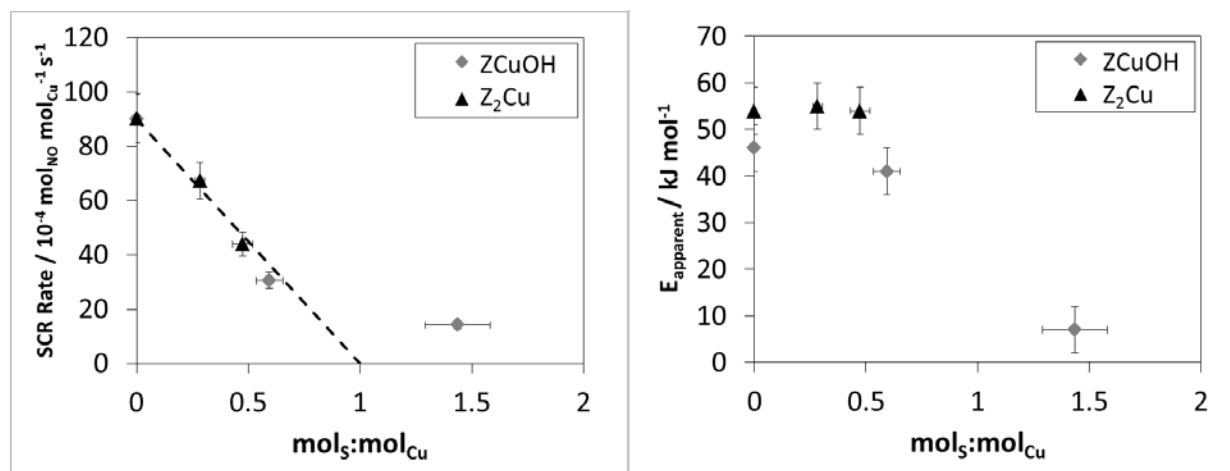
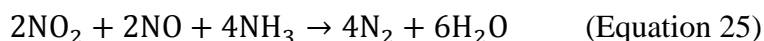


**Figure 72.** Reaction rates and apparent activation energies for ZCuOH (red) and Z<sub>2</sub>Cu (blue) model materials after sulfation. SCR conditions are 300 ppm NO, 300 ppm NH<sub>3</sub>, 60% O<sub>2</sub>, 2% H<sub>2</sub>O, 8% CO<sub>2</sub>, balance N<sub>2</sub> at 473 K.

We note that one ZCuOH sample was poisoned to an excess value of S:Cu of 1.4, and does not follow the equimolar poisoning behavior indicated by the dashed line in Figure 72. This suggests that there are likely two forms of S on this sample, those poisoning Cu sites and those that are bound elsewhere on the sample. The  $E_{\text{app}}$  value of 14  $\text{kJ mol}^{-1}$  on this sample is also much lower than on the other samples; in fact, the apparent activation energy and reaction orders on this sulfated sample is similar to those measured on a Cu-SSZ-13 sample with a Cu wt% = 0.1 and Si:Al = 100 (Table 21 and Figure 107 to Figure 109), suggesting that it may be plausible that sulfur poisoning decreases the effective spatial density of active Cu sites to low values.

Thermogravimetric analysis (TGA) indicates that the ZCuOH sample poisoned to a S:Cu of 1.4 contain a higher fraction of species that desorb at 1000 K, compared to other sulfated samples (Figure 110). Interestingly, under SCR conditions at 473 K, this sample is not 100% selective toward SCR, but shows 20% selectivity toward NO oxidation to NO<sub>2</sub> (Figure 111). This suggests that other pathways involving the formation of NO<sub>2</sub> and subsequent reaction of NO<sub>2</sub> with NH<sub>3</sub> via fast SCR pathways (Equation 25) on acid sites or Cu sites, may convolute analysis of SCR kinetic parameters and precludes direct comparison with the kinetic data measured on the other SO<sub>2</sub>-poisoned samples.



SCR rate measurements (normalized per mol Cu) decrease with S content on the two model Cu-SSZ-13 catalysts studied here, consistent with each S poisoning one ZCuOH or Z<sub>2</sub>Cu site. Several studies, however, have suggested that sulfur causes different poisoning mechanisms on ZCuOH and Z<sub>2</sub>Cu sites [143,144,150], including preventing access of SCR reactants to the active site, and binding directly to and electronically modifying the active site [131,132]. Diffuse reflectance UV-Visible spectra were measured on the model ZCuOH and Z<sub>2</sub>Cu samples before and after sulfation treatments (Figure 73). Spectra collected under ambient conditions (Figure 112) indicate that water solvates Cu ions, making it difficult to discern structural and electronic differences between ZCuOH and Z<sub>2</sub>Cu sites. Upon partial dehydration (523 K in dry air, to avoid desorption of sulfur), however, qualitative differences become discernable in the d-d transition and charge transfer regions [106,109]. For the ZCuOH sample, three of the four features in the d-d transition region disappear with increasing S content; however, this ZCuOH model sample contains some residual Z<sub>2</sub>Cu sites (20%), so it is uncertain whether the features remaining after S-poisoning reflects Z<sub>2</sub>Cu sites or ZCuOH sites. In contrast, for the Z<sub>2</sub>Cu sample, the d-d transition feature does not change significantly with S content, suggesting that sulfur more weakly affects the electronic nature of Z<sub>2</sub>Cu compared to ZCuOH. In the charge transfer region, sulfation causes the appearance of a feature at lower wavenumbers (38,000 cm<sup>-1</sup>) than is typical Cu-O framework charge transfer features (45,000-50,000 cm<sup>-1</sup>) in unsulfated catalysts [106], and this feature was more pronounced for SO<sub>2</sub>-poisoned ZCuOH sites, consistent with the observation from the d-d region that sulfur species interact more strongly with ZCuOH sites.

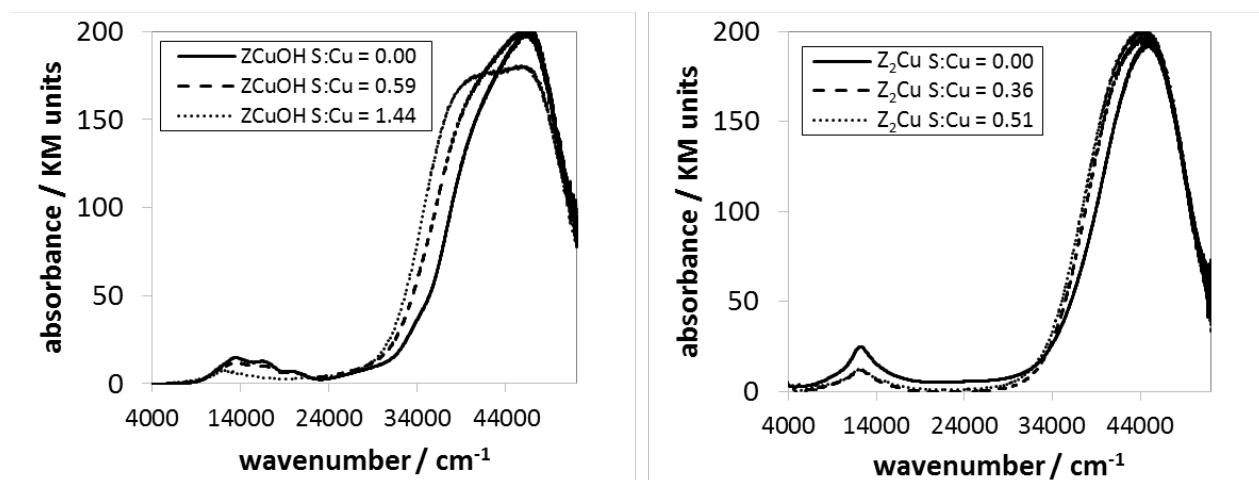


**Figure 73.** Diffuse reflectance UV-Visible spectra on ZCuOH (left) and  $Z_2Cu$  (right) after partial dehydration at 523 K under dry air.

In situ and in operando XAS was used to probe changes in the Cu oxidation state after sulfation. The introduction of sulfur species to the sample introduces sufficient complexity in deconvoluting XANES features, so accurate quantification becomes more complicated (details in Supp. Info.). The fraction of reducible  $Cu^{2+}$  before and after sulfation was estimated after reducing the catalyst with  $NO + NH_3$ . We observe that sulfation decreases the fraction of reducible Cu from 100% on the unsulfated catalysts to about 70% on all four sulfated catalysts (Table 24). Operando XAS was used to probe how sulfur affects the oxidation for both ZCuOH and  $Z_2Cu$  model catalysts. The introduction of sulfur increased the operando Cu(II)/Cu(I) fraction for the ZCuOH model catalyst. Unfortunately, the unsulfated  $Z_2Cu$  catalyst already had an operando Cu(II)/Cu(I) fraction of 0.9, making it difficult to discern possible increases in Cu(II)/Cu(I) fraction after sulfation (Table 23). In addition, average Cu coordination numbers on ZCuOH materials increased after sulfation, but average Cu coordination number on our  $Z_2Cu$  model material did not exhibit an increase in coordination number after sulfation, an observation that is consistent with observations from UV-visible (Table 25).

S K-edge XAS was used to probe the state of the sulfur species bound to the Cu sites. Ex situ XANES spectra were collected on the  $Z_2Cu$  and ZCuOH samples sulfated at either 473 K or 673 K, each of these samples exposed to 300 ppm  $NH_3$  at 473 K for 1 hour, and each of these

samples exposed to standard SCR gas mix for 30 min. Figure 74 plots all the normalized XANES spectra for the  $Z_2Cu$  samples (Figure 74 (a)) and the  $ZCuOH$  samples (Figure 74 (b)). All 12 spectra show a single prominent peak at 2480 eV, indicating the presence of  $S^{6+}$  species, regardless of sulfation and any subsequent gas treatment conditions. There is no other feature in between 2470 eV and 2477 eV, which rules out the presence of sulfur in other oxidation states (e.g.  $S^{2-}$  and  $S^{4+}$ ).

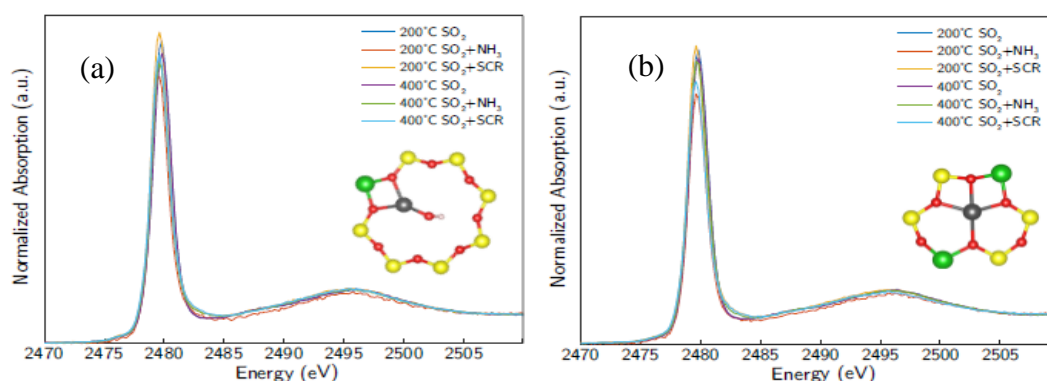


**Figure 74.** Sulfur K-edge XANES measured ex situ at ambient conditions of  $ZCuOH$  (left) and  $Z_2Cu$  (right) samples treated with  $SO_2$  and  $O_2$  at either 200°C or 400 °C.

#### 7.4.2 Kinetic behavior of sulfated Cu-SSZ-13 catalysts after desulfation

The four sulfated catalysts were desulfated in a reductive  $NO + NH_3$  feed (300 ppm  $NO$ , 300 ppm  $NH_3$ , balance  $N_2$ , 673 K) until a cumulative molar exposure of  $NO:S$  of 100 was obtained [147]. Elemental analysis results are shown in Figure 75. Successive desulfations were not performed due to experimental limitations on the amount of sample studied. Hammershøi et al. reports that 20% of sites appear to be irreversibly poisoned with sulfur [140].

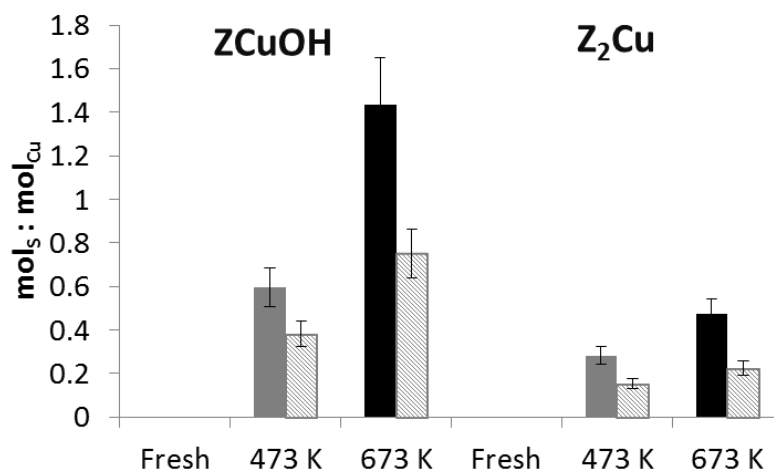


**Figure 75.** S:Cu ratios before (solid bars) and after desulfation (hatched bars) on ZCuOH and Z<sub>2</sub>Cu model materials.

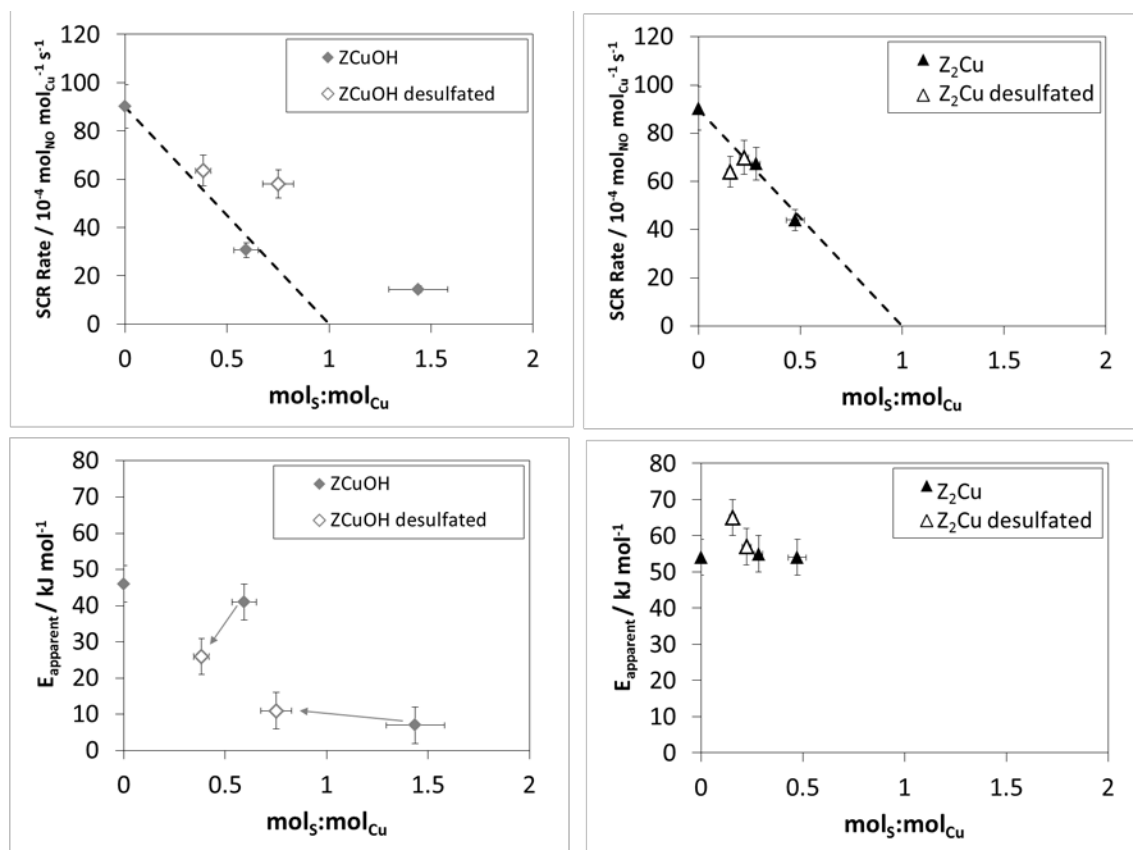


**Figure 76.** Reaction rates and apparent activation energies for ZCuOH and Z<sub>2</sub>Cu model materials after sulfation (filled) and desulfation (hollow). SCR conditions are 300 ppm NO, 300 ppm NH<sub>3</sub>, 60% O<sub>2</sub>, 2% H<sub>2</sub>O, 8% CO<sub>2</sub>, balance N<sub>2</sub> at 473 K. Arrows indicate the starting and ending samples after desulfation, and thus how the apparent activation energy changes after desulfation.

The SCR reaction rates and activation energies measured on desulfated samples containing ZCuOH and  $Z_2Cu$  sites are shown in Figure 76. After desulfation of  $Z_2Cu$  sites, the recovered rates increased proportionally to the number of sulfur species removed during desulfation, and the apparent activation energy and reaction orders on the desulfated catalysts do not change within error (Figure 76, Figure 127). This indicates that the sulfation is reversible and results in the apparent loss of  $Z_2Cu$  active sites. In contrast, rates measured on desulfated ZCuOH samples do not recover to the original rates when S content is accounted for, suggesting that some ZCuOH sites are deactivated irreversibly by sulfur species. The reaction rate on the desulfated ZCuOH catalyst initially poisoned to a S:Cu value  $> 1$  shows a reaction rate that is higher than other catalysts at the same S:Cu ratio, suggesting that desulfation preferentially removed sulfur bound to the Cu over other types of sulfur species stored on the sample (Figure 127). Another possible explanation is that sulfur bound to ZCuOH sites allow catalytic turnover at a lower (but non-zero) rate than unsulfated ZCuOH. There is not enough evidence to distinguish between the two proposals, but quantifying number of sulfur bound to Cu or elsewhere (possibly via S-TPD) may provide more insight. It is also important to note that the model ZCuOH sample does have 20%  $Z_2Cu$  sites, and based on the  $Z_2Cu$  desulfation data, we expect the sulfur bound to those sites to be able to be removed.

Jangjou et al. [144] observed a significant decrease (by 30 to 40 kJ mol<sup>-1</sup>) in the standard SCR apparent activation energy after sulfation of  $Z_2Cu$  and ZCuOH materials. The apparent activation energies for  $Z_2Cu$  returned to its original value of 88 kJ mol<sup>-1</sup> after each stepwise desulfation in 10% O<sub>2</sub>/N<sub>2</sub> at 723, 773, then 823 K. The same stepwise desulfation on their ZCuOH material resulted in a gradual increase, and thus recovery, of the apparent activation energy. These results, together with our kinetic results, suggest that a decrease in the apparent activation energy will likely be observed on both  $Z_2Cu$  and ZCuOH materials at high enough sulfur loadings, and that it would be easier to recover apparent activation energies on  $Z_2Cu$  materials than ZCuOH materials.

Taken together, we present quantitative evidence that sulfur poisons and deactivates both ZCuOH and  $Z_2Cu$  sites in an equimolar ratio at S:Cu  $< 1$ , but via two different mechanisms involving both site blocking and pore volume occlusion. The fact that the apparent activation energy and reaction orders do not change during the sulfation and desulfation process results in a

constant turnover rate, when the reaction rate is normalized to the number of unpoisoned Cu sites ( $\text{mol Cu} - \text{mol S}$ ) (Figure 77).

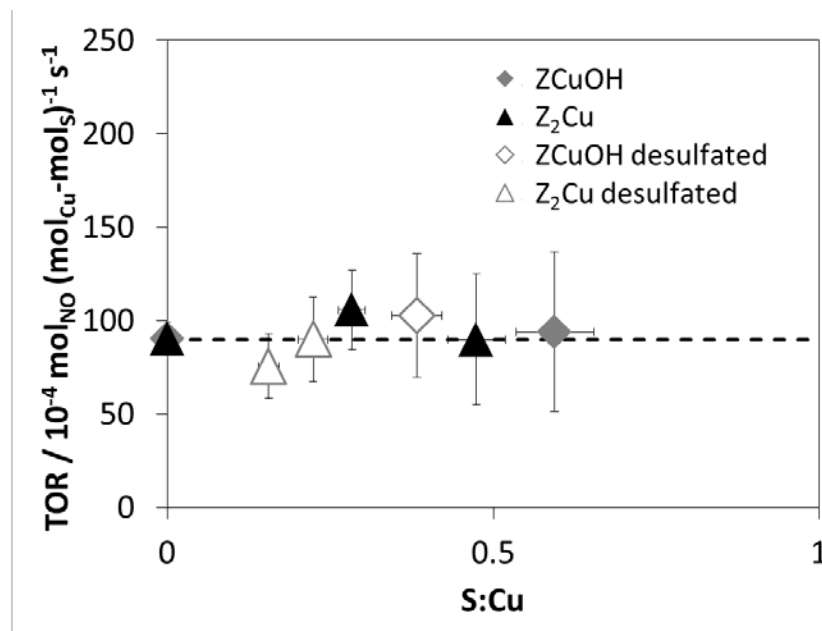


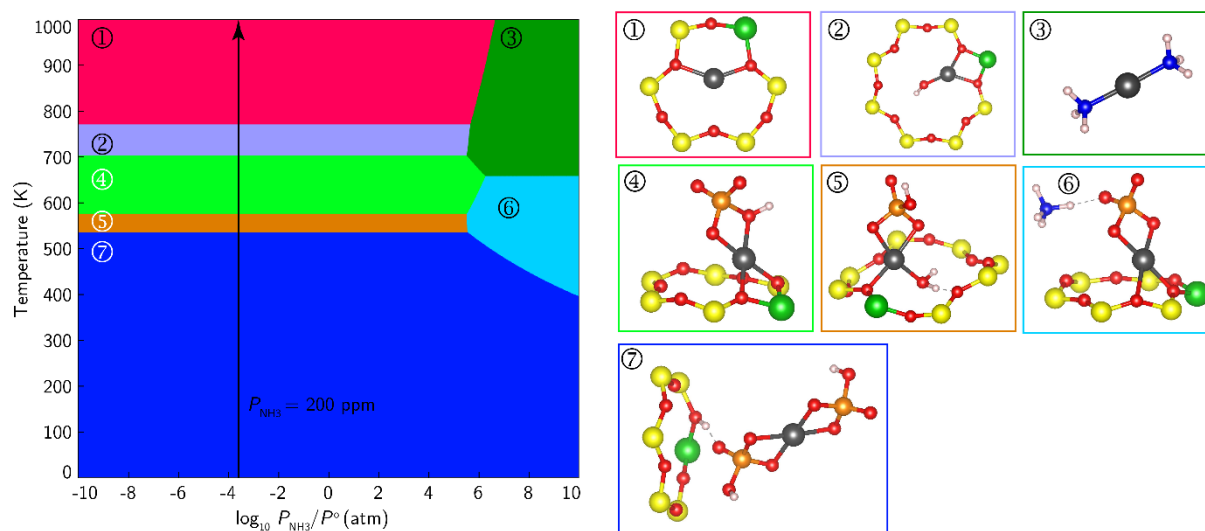
**Figure 77.** Fresh, sulfated, and desulfated samples that exhibit the same apparent activation energy collapse to the same turnover rate when normalized to  $(\text{mol}_{\text{Cu}} - \text{mol}_{\text{S}})$ .

### 7.4.3 Structures and energies of sulfur species bound to Cu sites

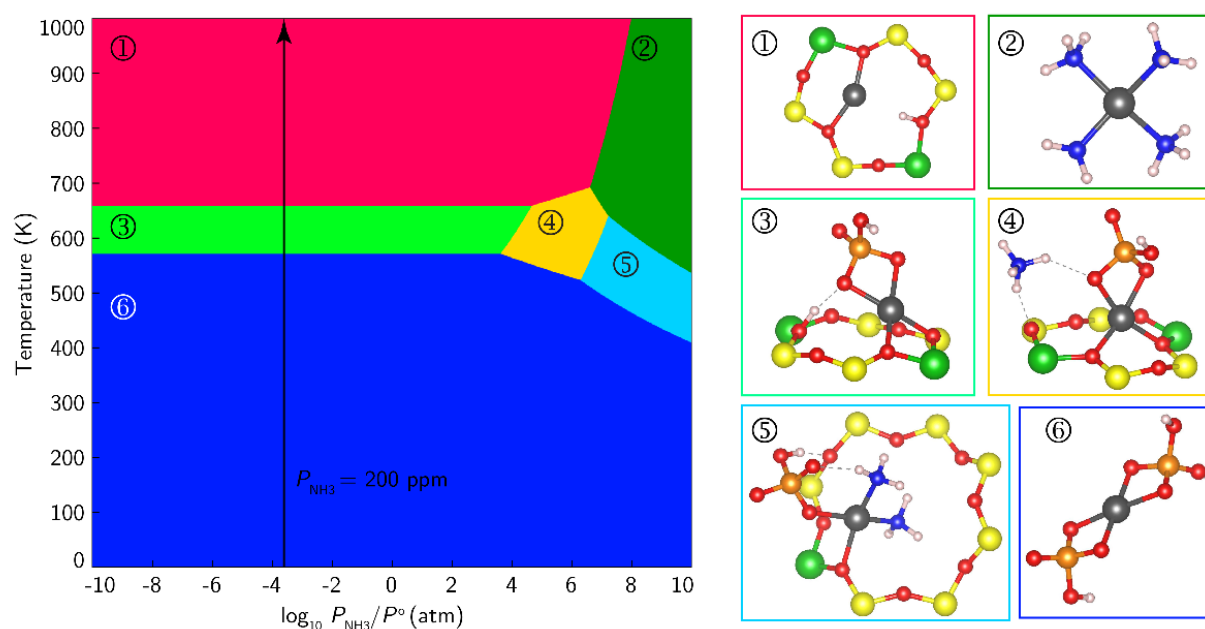
We used DFT calculations and first-principles thermodynamics [109] to explore the differences in response of  $\text{Z}_2\text{Cu}$  and  $\text{ZCuOH}$  sites to exposure to  $\text{SO}_2$ ,  $\text{H}_2\text{O}$ ,  $\text{O}_2$ , and  $\text{NH}_3$  as a function of temperature and exposure conditions. We drew on literature results [144,161,163] and chemical intuition to construct a variety of candidate structures containing up to two  $\text{SO}_x$  combined with  $\text{NH}_3$  and  $\text{H}_2\text{O}$ . We considered chemically relevant S/O/H compounds ( $\text{SO}_2$ ,  $\text{SO}_3$ , sulfide, (bi)sulfite, (bi)sulfate) as ligands with and without OH,  $\text{H}_2\text{O}$ ,  $\text{NH}_4^+$  and  $\text{NH}_3$  ligands. We annealed using AIMD at 473 K and relaxed to obtain final DFT formation energies.

Figure 78 and Figure 79 show the equilibrium phase diagrams for  $\text{ZCuOH}$  and  $\text{Z}_2\text{Cu}$  sites, respectively, as a function of  $\text{NH}_3$  pressure and temperature at 20 ppm  $\text{SO}_2$ , 10%  $\text{O}_2$ , and 5%  $\text{H}_2\text{O}$ , 1 atm total pressure, all chosen to be consistent with experimental exposure conditions. These diagrams report the thermodynamic equilibrium species without consideration of formation kinetics, and thus must be interpreted appropriately.





**Figure 78.** First-principles phase diagram for  $S_wO_xH_yN_z$  species on a ZCuOH site vs temperature and  $NH_3$  partial pressure at 1 atm total pressure and 20 ppm  $SO_2$ , 10%  $O_2$ , and 5%  $H_2O$ . Molecular structures corresponding to each region indicated by numbers. Gray, red, yellow, green, blue, orange, and white spheres correspond to Cu, O, Si, Al, N, S, and H atoms, respectively. Zeolite framework included only when directly hosting Cu or H.



**Figure 79.** First-principles phase diagram for  $S_wO_xH_yN_z$  species on a  $Z_2Cu$  site vs temperature and  $NH_3$  partial pressure at 1 atm total pressure and 20 ppm  $SO_2$ , 10%  $O_2$ , and 5%  $H_2O$ . Molecular structures corresponding to each region indicated by numbers. Gray, red, yellow, green, blue, orange, and white spheres correspond to Cu, O, Si, Al, N, S, and H atoms, respectively. Zeolite framework included only when directly hosting Cu or H.

Across the entire composition space, save for the highest temperature region of the ZCuOH diagram, Cu is present in the 2+ oxidation state, and all S species are present as bisulfate ( $\text{HSO}_3^-$ ), consistent with the Cu and S oxidation states observed in the XAS above. Further,  $\text{Cu}^{2+}$  is always present in four-fold coordination consistent with EXAFS analysis (Table 25). The left sides of the diagrams correspond to  $\text{SO}_2$  exposure in the absence of  $\text{NH}_3$ . In this limit, the most stable species on both Cu sites contain two bisulfate ligands at low temperature, transitioning to a single bisulfate at temperatures closer to those relevant to experimental dosing and consistent with the uptake stoichiometry of 1 S: 1 Cu. The temperature to fully desorb sulfur is predicted to be upwards of  $100^\circ\text{C}$  higher on ZCuOH than  $\text{Z}_2\text{Cu}$ . A key difference between the two sites is the predicted creation of a new Brønsted acid site upon sulfation for  $\text{Z}_2\text{Cu}$  but not ZCuOH.

To test this prediction, we employed methods we have developed previously to selectively quantify  $\text{NH}_3$  adsorbed on Brønsted acid and Cu sites, while excluding physisorbed  $\text{NH}_3$  [90,91]. Table 14 reports the number of excess  $\text{NH}_3$  (per S), relative to the unsulfated Cu-SSZ-13 samples:

$$\text{NH}_3:\text{S} = \frac{(\text{mol NH}_3 \text{ on sulfated sample}) - (\text{mol NH}_3 \text{ on unsulfated sample})}{(\text{mol S on sulfated sample})} \quad (\text{Equation 26})$$

**Table 14.**  $\text{NH}_3:\text{S}$  values calculated from excess  $\text{NH}_3$  storage on Cu-SSZ-13 catalysts after dry  $\text{SO}_2$  poisoning. Corresponding S:Cu loadings on the four samples are also included for comparison.

	S:Cu	$\text{NH}_3:\text{S}$
ZCuOH	0.59	$-0.2 \pm 0.2$
ZCuOH	1.44	$0.0 \pm 0.2$
$\text{Z}_2\text{Cu}$	0.36	$1.2 \pm 0.2$
$\text{Z}_2\text{Cu}$	0.51	$0.9 \pm 0.2$

Zhang et al. [135] observed a 2:1 molar increase in the excess released  $\text{NH}_3$  to excess released  $\text{SO}_2$  ratio after concurrent sulfation with  $\text{NH}_3$  and  $\text{SO}_2$  over a commercial Cu-SAPO-34 catalyst, and claimed that a 2:1 stoichiometry could be due to the formation of ammonium bisulfate. In addition, Jangjou et al. [144] demonstrated that sulfur bound to ZCuOH and  $\text{Z}_2\text{Cu}$  sites likely desorb at different temperatures, with sulfur bound to ZCuOH desorbing at a higher temperature ( $580^\circ\text{C}$ ) than  $\text{Z}_2\text{Cu}$  ( $380^\circ\text{C}$ ). The relative S:Cu ratio from these two desorption features correlated with the fraction of ZCuOH and  $\text{Z}_2\text{Cu}$  on their parent Cu-SSZ-13 samples.

We observe that sulfation does not change the total  $\text{NH}_3$ -storage capacity on the model ZCuOH catalyst, but increases the  $\text{NH}_3$  storage capacity by a ratio of 1  $\text{NH}_3$ :S for the model  $\text{Z}_2\text{Cu}$  catalyst (Table 14). The excess 1:1  $\text{NH}_3$ :S molar ratio on sulfated- $\text{Z}_2\text{Cu}$  sites may reflect storage at excess Brønsted acid sites after sulfation, consistent with DFT predictions that the sulfation of  $\text{Z}_2\text{Cu}$  sites results in the generation of new Brønsted acid sites.

## 7.5 Conclusions

The effects of dry  $\text{SO}_2$  poisoning at 473 and 673 K were studied on two model Cu-SSZ-13 catalysts, synthesized to contain predominantly  $\text{Z}_2\text{Cu}$  sites or ZCuOH sites. ZCuOH sites are more prone to  $\text{SO}_2$ -poisoning than  $\text{Z}_2\text{Cu}$  sites, reflected in the larger amounts of  $\text{SO}_2$ -derived intermediates that were stored on the model ZCuOH sample than on the  $\text{Z}_2\text{Cu}$  sample upon exposure to the same sulfation treatment. SCR rates (473 K, per Cu) decrease proportionally with the S:Cu ratio on the  $\text{Z}_2\text{Cu}$  and ZCuOH samples, while apparent activation energies are unaffected, consistent with equimolar Cu site poisoning by each  $\text{SO}_2$ -derived intermediate. Additional  $\text{SO}_2$  storage is also observed on non-Cu sites in the ZCuOH sample, and evidence is provided for partial micropore occlusion by  $\text{SO}_2$ -derived species. Computation shows that bisulfates are particularly low in energy, that  $\text{Z}_2\text{Cu}$  and ZCuOH can take up one or two bisulfates, and that residual Brønsted acid sites are liberated as these bisulfates are formed. Dynamic simulations also show that  $\text{Cu}^{2+}$  bound to one  $\text{HSO}_4$  is immobile, but those bound to two are liberated from the framework and are mobile. Taken together, experimental and theoretical characterizations support the hypothesis that  $\text{Z}_2\text{Cu}$  sites are more resistant to  $\text{SO}_2$  poisoning than ZCuOH sites, and can be regenerated more easily once poisoned.

## **7.6 Acknowledgements**

We thank the researchers in the Cummins Emissions Team for helpful technical discussions. We also thank Haiying Chen (Johnson Matthey), William Epling (Virginia), Ton V.W. Janssens (Umicore Denmark ApS), Feng Gao (PNNL), and Chuck Peden (PNNL) for discussions at the 2018 Crosscut Lean Exhaust Emissions Reduction Simulations (CLEERS) meeting.

## 7.7 Supplementary Information

### 7.7.1 Elemental Analysis and Titration

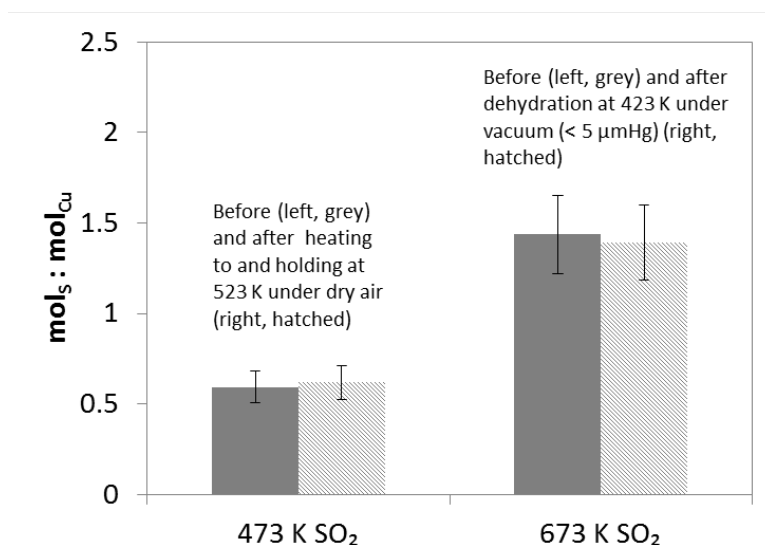


**Figure 80.** Molar S:Cu ratios measured using EDS and ICP on sulfated ZCuOH model catalysts after heating to 523 K under dry air (100 mg sample, 200 mL min<sup>-1</sup> for 6 hours) and dehydrated at 150°C under vacuum (< 5 μmHg, 30 mg sample) for 4 hours.

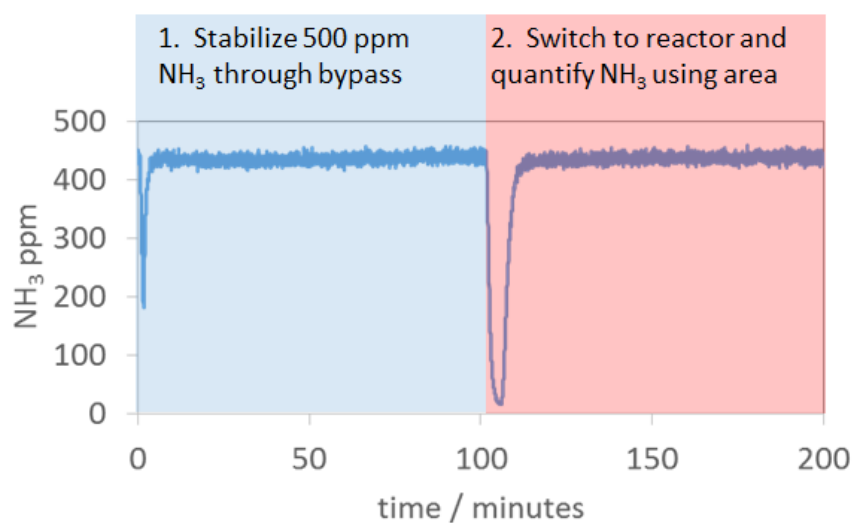


**Figure 81.** Excess molar NH<sub>3</sub>:S ratios relative to the unsulfated materials were measured from NH<sub>3</sub> titration of both Brønsted and Lewis acid sites. The mols of NH<sub>3</sub> that displaced the volume of gas in the reactor was quantified using a blank reactor and subtracted to determine the NH<sub>3</sub>:S ratio for the catalyst.

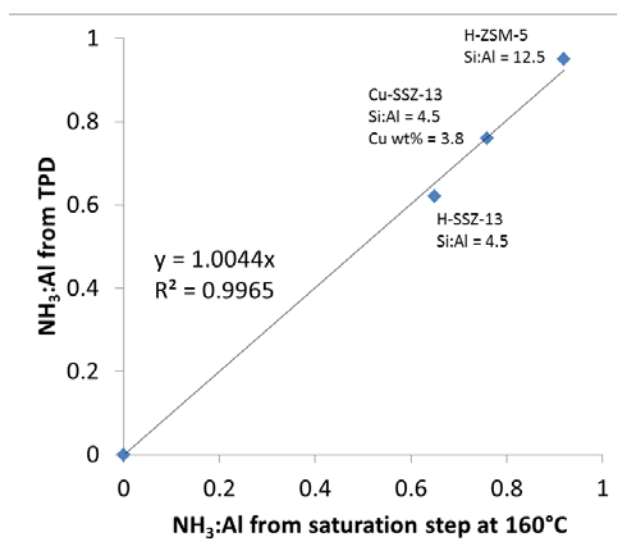


**Figure 82.** Parity plot confirming that NH<sub>3</sub> storage (NH<sub>3</sub>:Al) can be quantified during NH<sub>3</sub> saturation at 160°C or during TPD. Quantifying NH<sub>3</sub> storage during NH<sub>3</sub> saturation is particularly useful for materials that are temperature sensitive or for instruments that cannot handle desorption species (e.g. sulfur oxides).

## 7.7.2 Reaction Kinetics

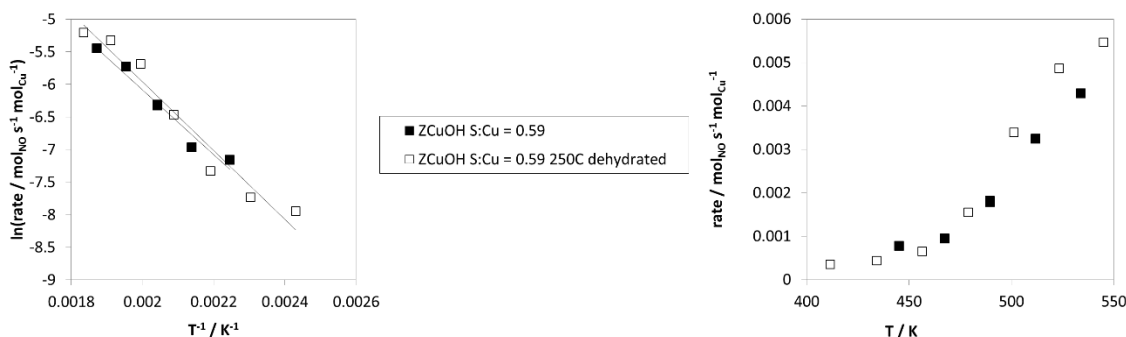


**Figure 83.** Arrhenius plots (left) and rate dependent on temperature (right) on sulfated ZCuOH model catalyst (filled black square) and post-sulfation heat treated catalyst (100 mg sample, 523 K 200 mL min<sup>-1</sup> dry air for 6 hours) (hollow squares) during standard SCR conditions (300 ppm NO, 300 ppm NH<sub>3</sub>, 10% O<sub>2</sub>, 8% CO<sub>2</sub>, 2.5% H<sub>2</sub>O, balance N<sub>2</sub> at 473 K)

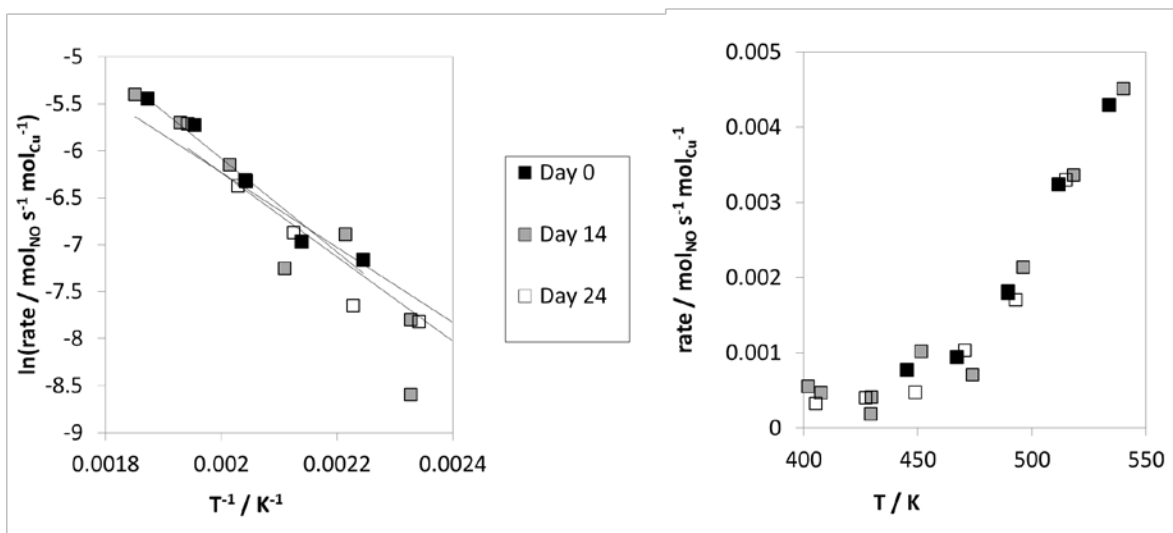


**Figure 84.** Arrhenius plots (left) and rate dependent on temperature (right) on sulfated ZCuOH model catalyst after continuous exposure to a range of SCR conditions (150 to 700 ppm NO, 150 to 2000 ppm NH<sub>3</sub>, 0.4 to 70% O<sub>2</sub>, 0 to 15% CO<sub>2</sub>, 0 to 2.5% H<sub>2</sub>O, balance N<sub>2</sub> at 423 to 523 K). Repeat returns to standard SCR conditions (300 ppm NO, 300 ppm NH<sub>3</sub>, 10% O<sub>2</sub>, 8% CO<sub>2</sub>, 2.5% H<sub>2</sub>O, balance N<sub>2</sub> at 473 K) were collected on Day 0 (filled black squares), Day 14 (grey squares), and Day 24 (hollow squares).

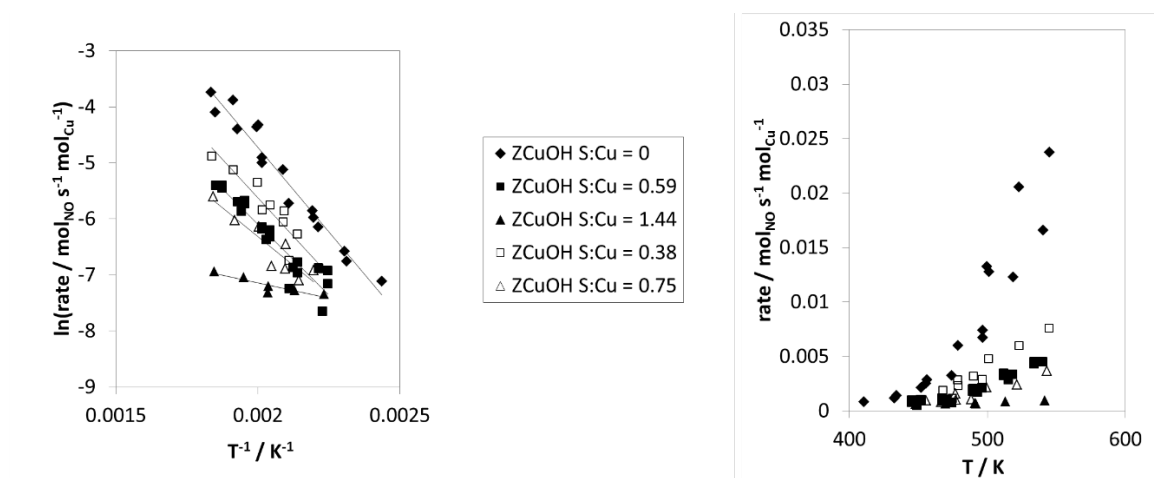


**Figure 85.** Arrhenius plots (left) and rate dependent on temperature (right) on fresh (black diamond), sulfated (black square and triangle), and desulfated (hollow square and triangle) ZCuOH model catalysts during standard SCR conditions (300 ppm NO, 300 ppm NH<sub>3</sub>, 10% O<sub>2</sub>, 8% CO<sub>2</sub>, 2.5% H<sub>2</sub>O, balance N<sub>2</sub> between 423 and 523 K)

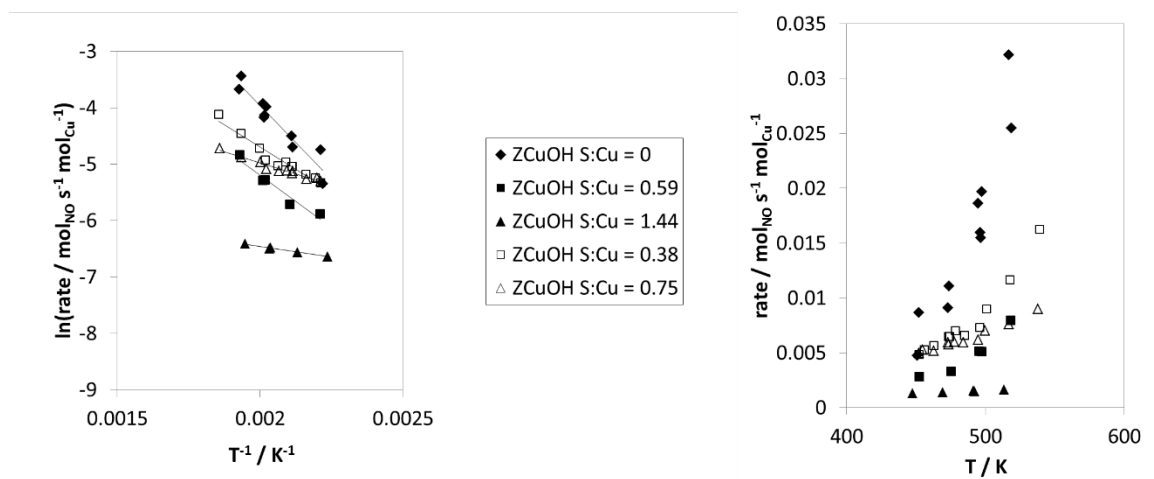


**Figure 86.** Arrhenius plots (left) and rate dependent on temperature (right) on fresh (black diamond), sulfated (black square and triangle), and desulfated (hollow square and triangle) ZCuOH model catalysts during high O<sub>2</sub> SCR conditions (300 ppm NO, 300 ppm NH<sub>3</sub>, 60% O<sub>2</sub>, 8% CO<sub>2</sub>, 2.5% H<sub>2</sub>O, balance N<sub>2</sub> between 423 and 523 K)



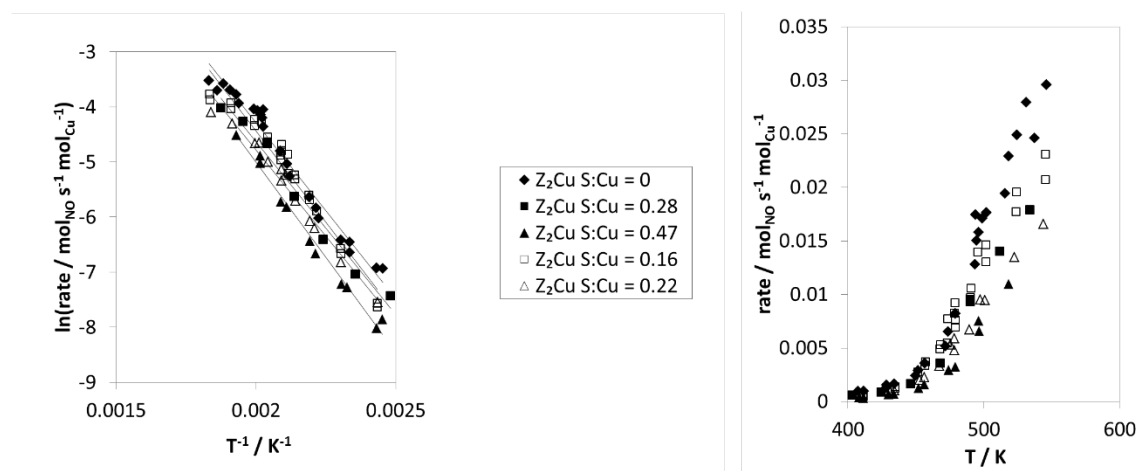


**Figure 87.** Arrhenius plots (left) and rate dependent on temperature (right) on fresh (black diamond), sulfated (black square and triangle), and desulfated (hollow square and triangle)  $\text{Z}_2\text{Cu}$  model catalysts during standard SCR conditions (300 ppm NO, 300 ppm  $\text{NH}_3$ , 10%  $\text{O}_2$ , 8%  $\text{CO}_2$ , 2.5%  $\text{H}_2\text{O}$ , balance  $\text{N}_2$  between 423 and 523 K at 1 atm)

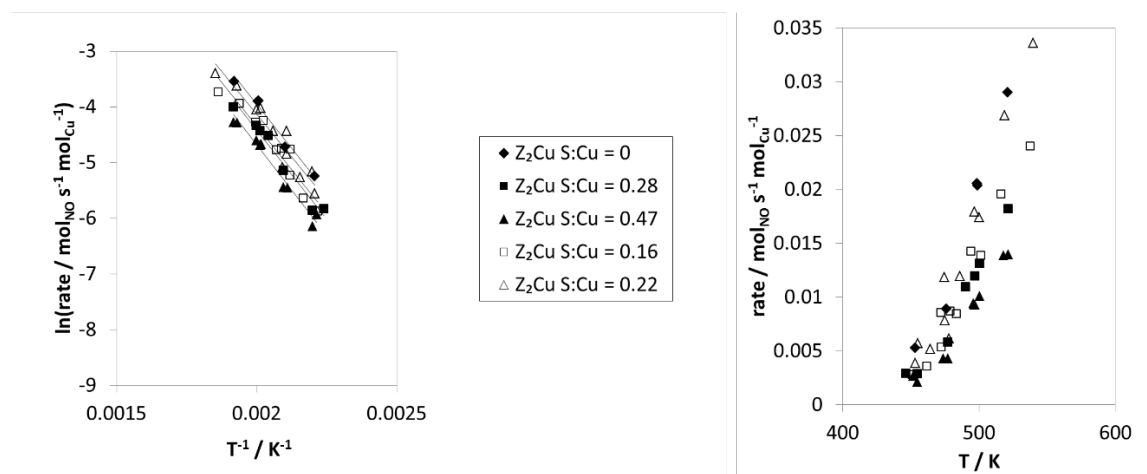


**Figure 88.** Arrhenius plots (left) and rate dependent on temperature (right) on fresh (black diamond), sulfated (black square and triangle), and desulfated (hollow square and triangle)  $\text{Z}_2\text{Cu}$  model catalysts during high  $\text{O}_2$  SCR conditions (300 ppm NO, 300 ppm  $\text{NH}_3$ , 60%  $\text{O}_2$ , 8%  $\text{CO}_2$ , 2.5%  $\text{H}_2\text{O}$ , balance  $\text{N}_2$  between 423 and 523 K at 1 atm)

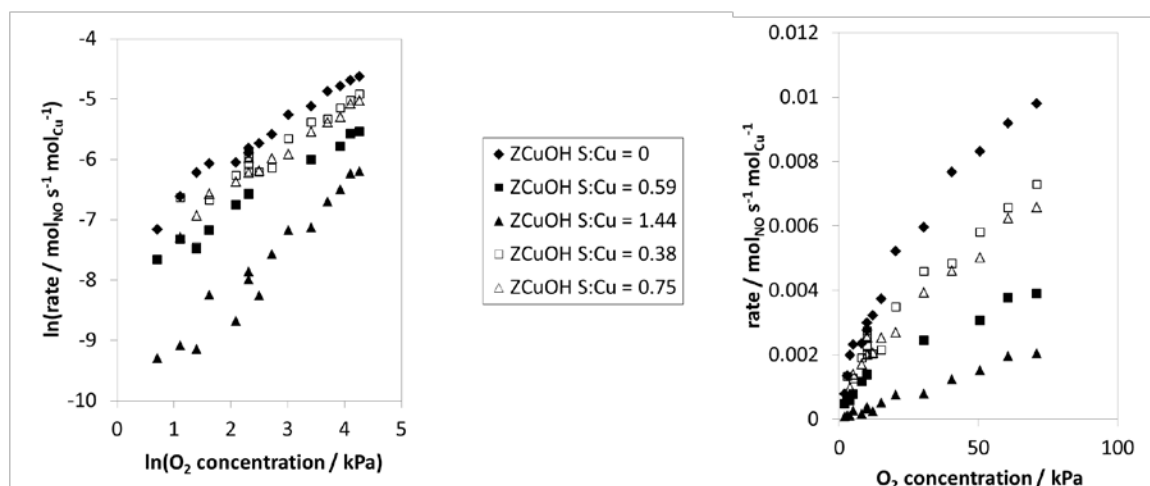


**Figure 89.** Linearized  $O_2$  order plots (left) and rate dependent on  $O_2$  concentration plots (right) on fresh (black diamond), sulfated (black square and triangle), and desulfated (hollow square and triangle) ZCuOH model catalysts during SCR conditions (300 ppm NO, 300 ppm  $NH_3$ , 2 to 70%  $O_2$ , 8%  $CO_2$ , 2.5%  $H_2O$ , balance  $N_2$  at 473 K and 1 atm)

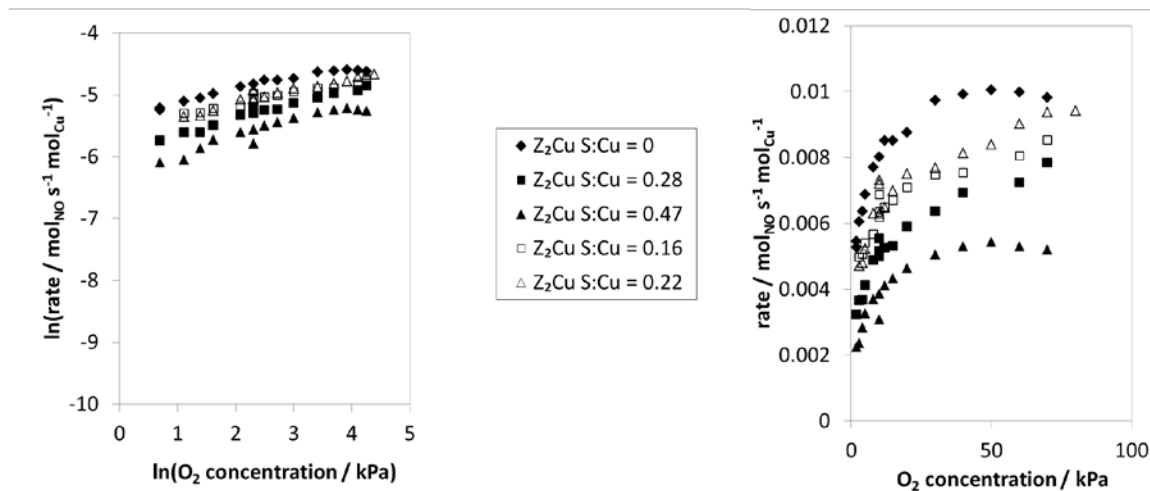


**Figure 90.** Linearized  $O_2$  order plots (left) and rate dependent on  $O_2$  concentration plots (right) on fresh (black diamond), sulfated (black square and triangle), and desulfated (hollow square and triangle)  $Z_2Cu$  model catalysts during SCR conditions (300 ppm NO, 300 ppm  $NH_3$ , 2 to 70%  $O_2$ , 8%  $CO_2$ , 2.5%  $H_2O$ , balance  $N_2$  at 473 K and 1 atm)

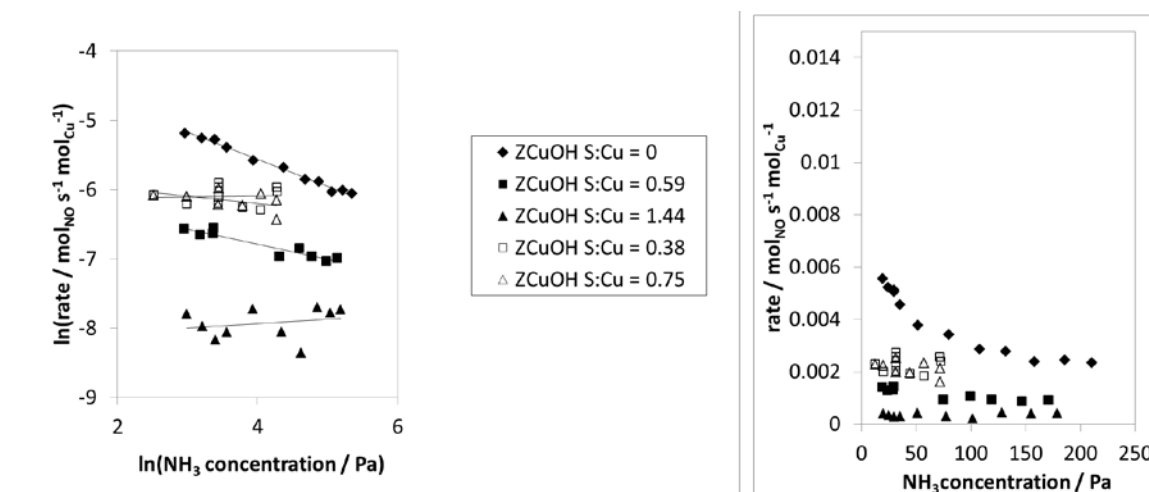


**Figure 91.** Linearized  $\text{NH}_3$  order plots (left) and rate dependent on  $\text{NH}_3$  concentration plots (right) on fresh (black diamond), sulfated (black square and triangle), and desulfated (hollow square and triangle) ZCuOH model catalysts during standard SCR conditions (300 ppm NO, 150 to 2000 ppm  $\text{NH}_3$ , 10%  $\text{O}_2$ , 8%  $\text{CO}_2$ , 2.5%  $\text{H}_2\text{O}$ , balance  $\text{N}_2$  at 473 K and 1 atm)

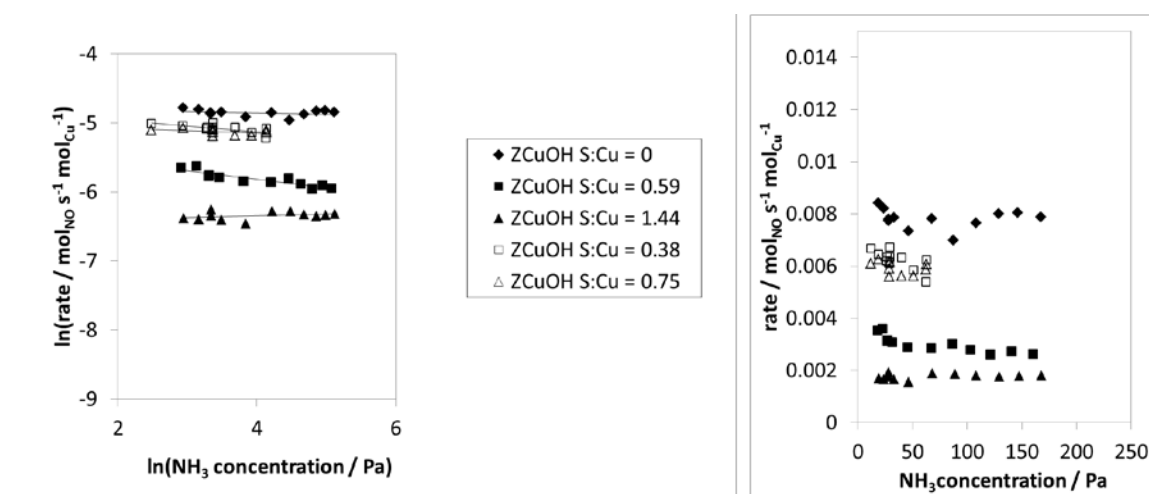


**Figure 92.** Linearized  $\text{NH}_3$  order plots (left) and rate dependent on  $\text{NH}_3$  concentration plots (right) on fresh (black diamond), sulfated (black square and triangle), and desulfated (hollow square and triangle) ZCuOH model catalysts during high  $\text{O}_2$  SCR conditions (300 ppm NO, 150 to 2000 ppm  $\text{NH}_3$ , 60%  $\text{O}_2$ , 8%  $\text{CO}_2$ , 2.5%  $\text{H}_2\text{O}$ , balance  $\text{N}_2$  at 473 K and 1 atm)

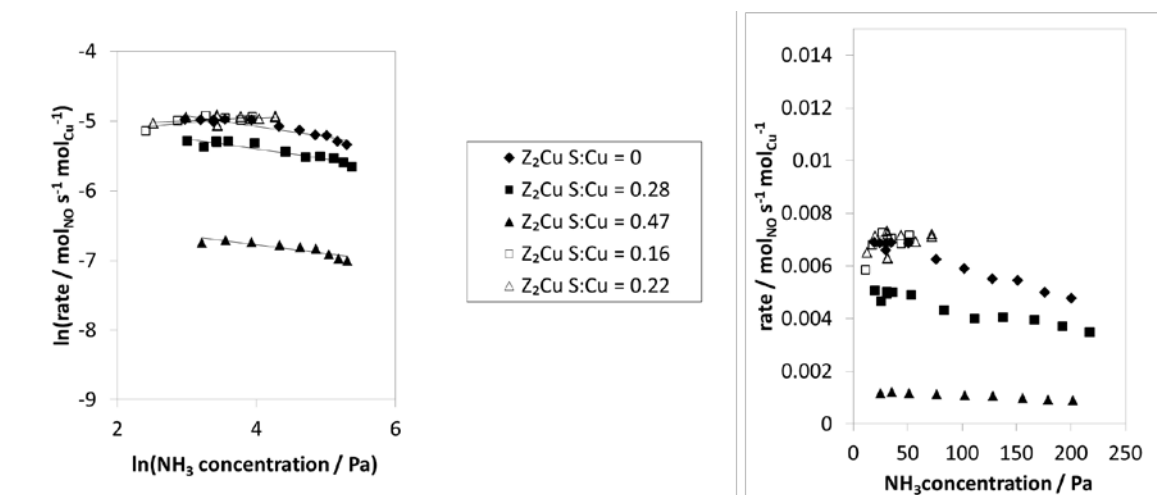


**Figure 93.** Linearized  $\text{NH}_3$  order plots (left) and rate dependent on  $\text{NH}_3$  concentration plots (right) on fresh (black diamond), sulfated (black square and triangle), and desulfated (hollow square and triangle)  $\text{Z}_2\text{Cu}$  model catalysts during standard SCR conditions (300 ppm NO, 150 to 2000 ppm  $\text{NH}_3$ , 10%  $\text{O}_2$ , 8%  $\text{CO}_2$ , 2.5%  $\text{H}_2\text{O}$ , balance  $\text{N}_2$  at 473 K and 1 atm)

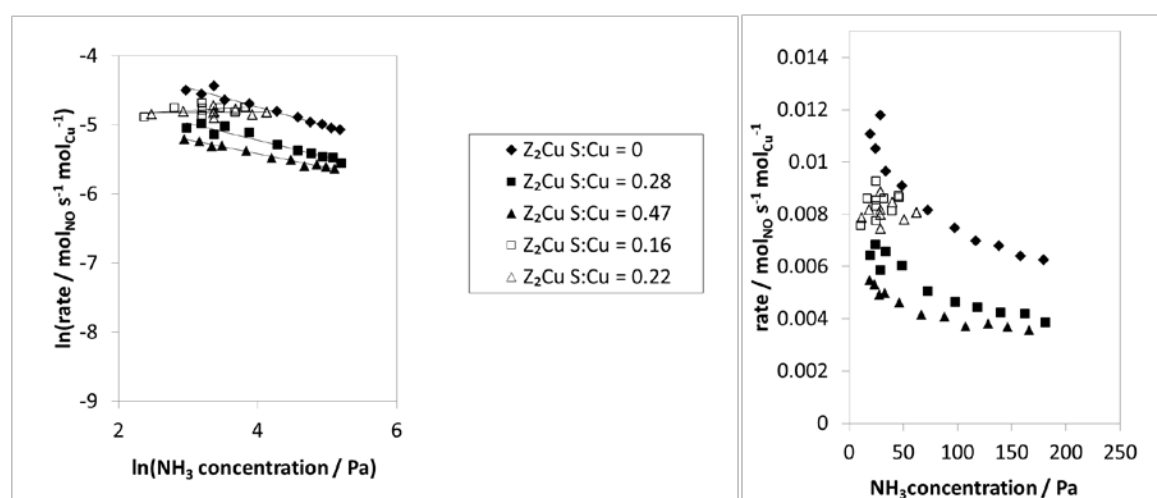


**Figure 94.** Linearized  $\text{NH}_3$  order plots (left) and rate dependent on  $\text{NH}_3$  concentration plots (right) on fresh (black diamond), sulfated (black square and triangle), and desulfated (hollow square and triangle)  $\text{Z}_2\text{Cu}$  model catalysts during high  $\text{O}_2$  SCR conditions (300 ppm NO, 150 to 2000 ppm  $\text{NH}_3$ , 60%  $\text{O}_2$ , 8%  $\text{CO}_2$ , 2.5%  $\text{H}_2\text{O}$ , balance  $\text{N}_2$  at 473 K and 1 atm)

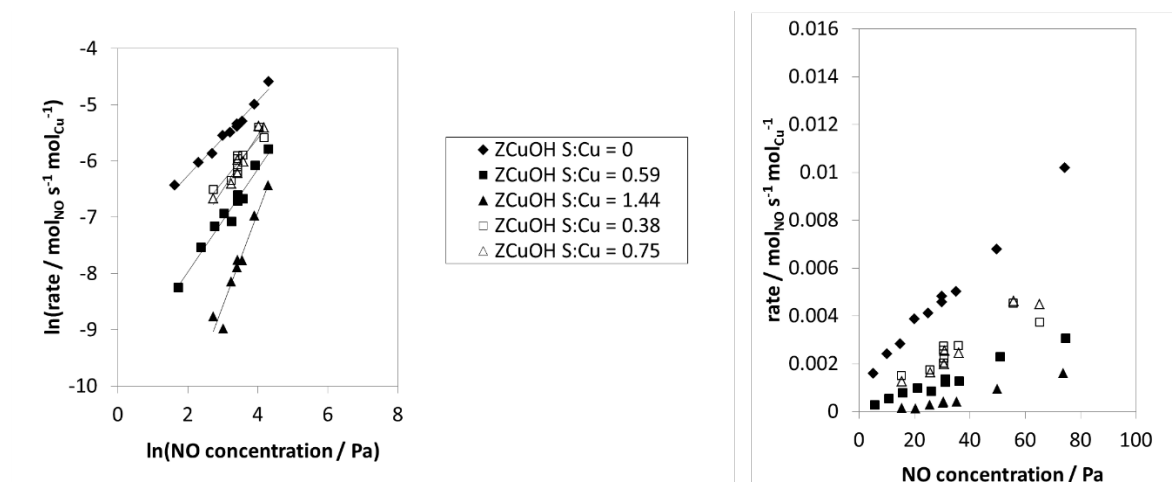


**Figure 95.** Linearized NO order plots (left) and rate dependent on NO concentration plots (right) on fresh (black diamond), sulfated (black square and triangle), and desulfated (hollow square and triangle) ZCuOH model catalysts during standard SCR conditions (150 to 700 ppm NO, 300 ppm  $\text{NH}_3$ , 10%  $\text{O}_2$ , 8%  $\text{CO}_2$ , 2.5%  $\text{H}_2\text{O}$ , balance  $\text{N}_2$  at 473 K and 1 atm)

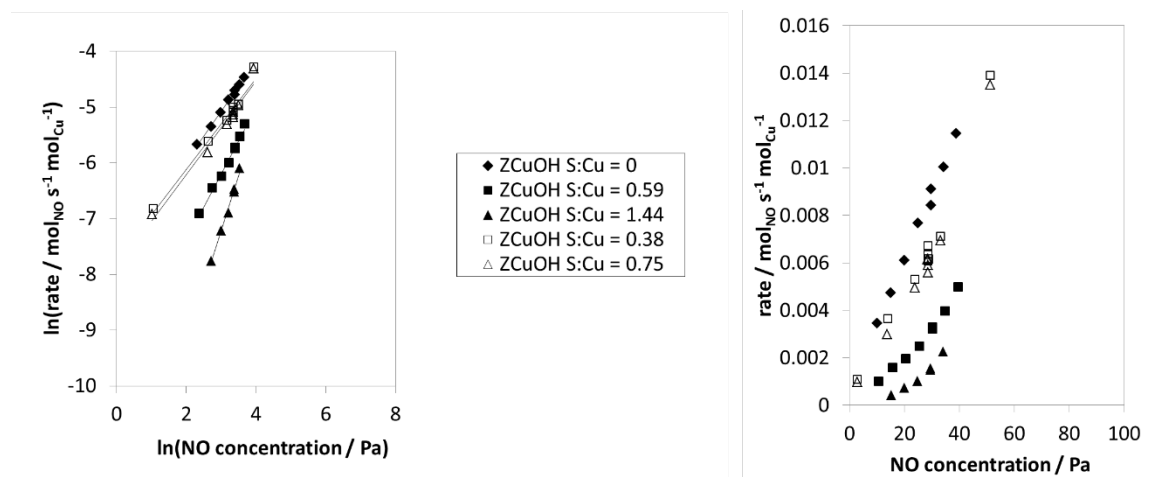


**Figure 96.** Linearized NO order plots (left) and rate dependent on NO concentration plots (right) on fresh (black diamond), sulfated (black square and triangle), and desulfated (hollow square and triangle) ZCuOH model catalysts during high  $\text{O}_2$  SCR conditions (150 to 500 ppm NO, 300 ppm  $\text{NH}_3$ , 60%  $\text{O}_2$ , 8%  $\text{CO}_2$ , 2.5%  $\text{H}_2\text{O}$ , balance  $\text{N}_2$  at 473 K and 1 atm)

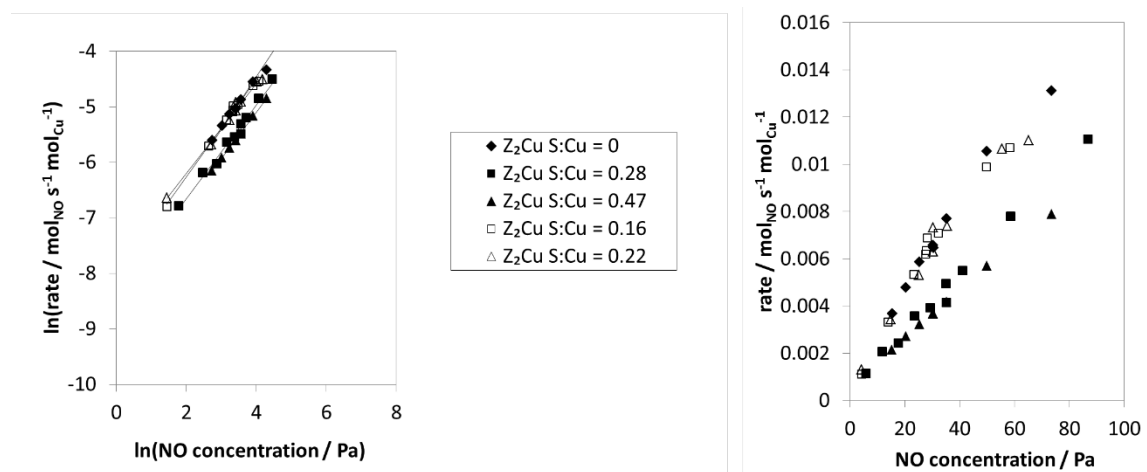


**Figure 97.** Linearized NO order plots (left) and rate dependent on NO concentration plots (right) on fresh (black diamond), sulfated (black square and triangle), and desulfated (hollow square and triangle)  $\text{Z}_2\text{Cu}$  model catalysts during standard SCR conditions (150 to 700 ppm NO, 300 ppm  $\text{NH}_3$ , 10%  $\text{O}_2$ , 8%  $\text{CO}_2$ , 2.5%  $\text{H}_2\text{O}$ , balance  $\text{N}_2$  at 473 K and 1 atm)

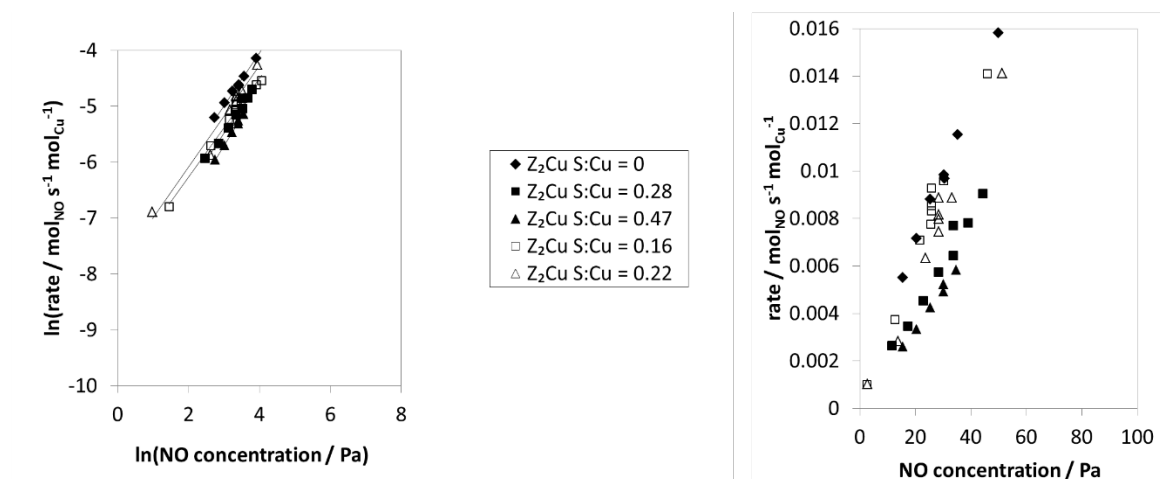


**Figure 98.** Linearized NO order plots (left) and rate dependent on NO concentration plots (right) on fresh (black diamond), sulfated (black square and triangle), and desulfated (hollow square and triangle)  $\text{Z}_2\text{Cu}$  model catalysts during high  $\text{O}_2$  SCR conditions (150 to 500 ppm NO, 300 ppm  $\text{NH}_3$ , 60%  $\text{O}_2$ , 8%  $\text{CO}_2$ , 2.5%  $\text{H}_2\text{O}$ , balance  $\text{N}_2$  at 473 K and 1 atm)

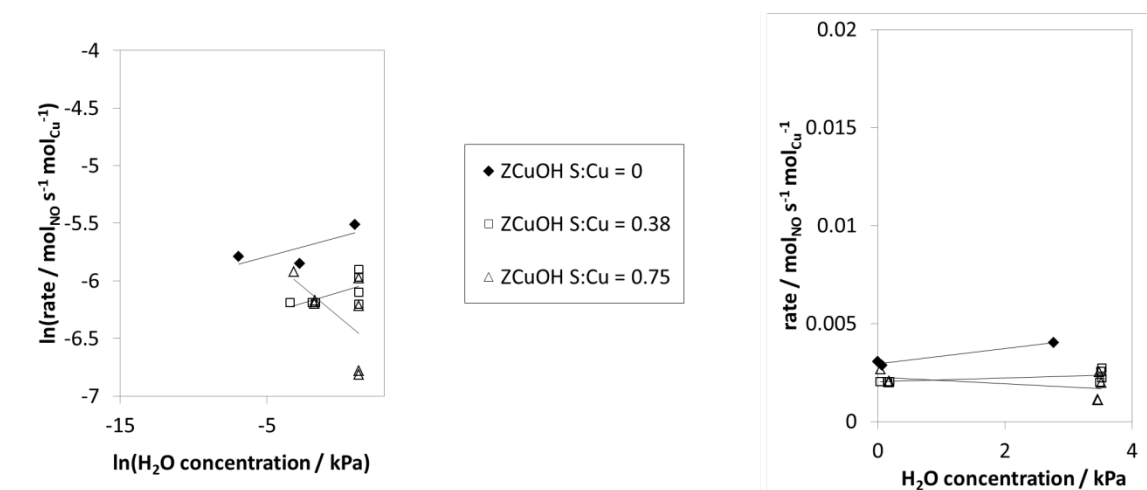


**Figure 99.** Linearized H<sub>2</sub>O order plots (left) and rate dependent on H<sub>2</sub>O concentration plots (right) on fresh (black diamond) and desulfated (hollow square and triangle) ZCuOH model catalysts during standard SCR conditions (300 ppm NO, 300 ppm NH<sub>3</sub>, 10% O<sub>2</sub>, 8% CO<sub>2</sub>, 0 to 2.5% H<sub>2</sub>O, balance N<sub>2</sub> at 473 K and 1 atm). H<sub>2</sub>O orders were not collected for the sulfated ZCuOH model catalyst.

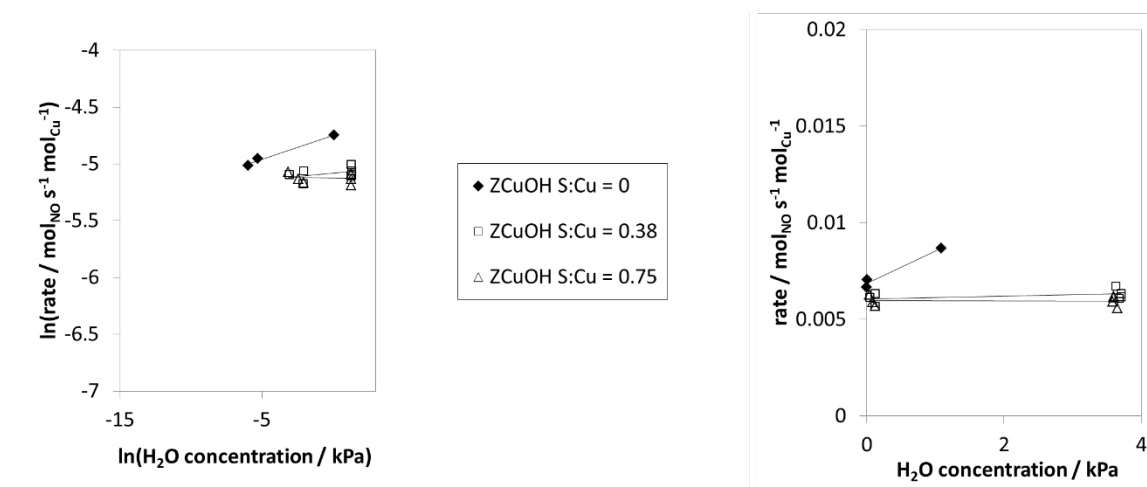


**Figure 100.** Linearized H<sub>2</sub>O order plots (left) and rate dependent on H<sub>2</sub>O concentration plots (right) on fresh (black diamond) and desulfated (hollow square and triangle) ZCuOH model catalysts during high O<sub>2</sub> SCR conditions (300 ppm NO, 300 ppm NH<sub>3</sub>, 60% O<sub>2</sub>, 8% CO<sub>2</sub>, 0 to 2.5% H<sub>2</sub>O, balance N<sub>2</sub> at 473 K and 1 atm). H<sub>2</sub>O orders were not collected for the sulfated ZCuOH model catalyst.

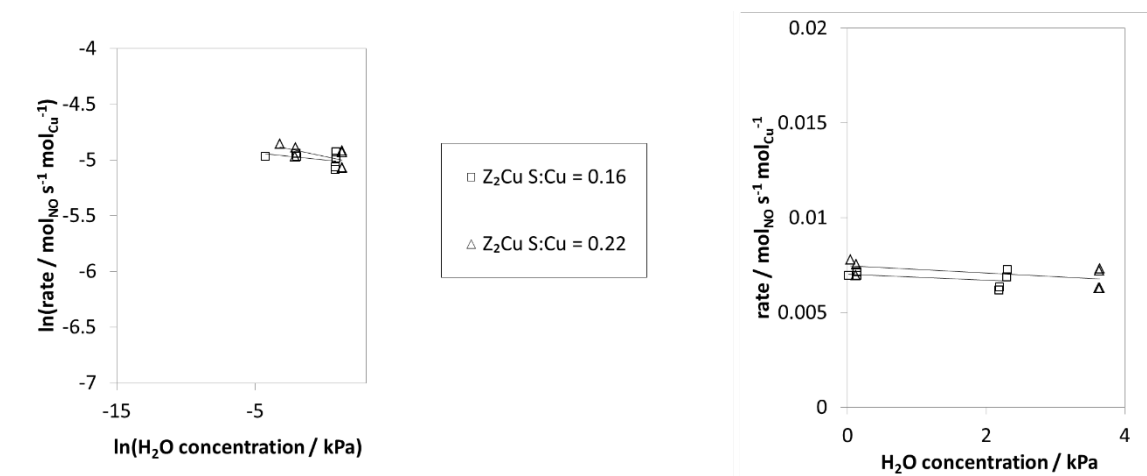


**Figure 101.** Linearized H<sub>2</sub>O order plots (left) and rate dependent on H<sub>2</sub>O concentration plots (right) desulfated (hollow square and triangle) Z<sub>2</sub>Cu model catalysts during standard SCR conditions (300 ppm NO, 300 ppm NH<sub>3</sub>, 10% O<sub>2</sub>, 8% CO<sub>2</sub>, 0 to 2.5% H<sub>2</sub>O, balance N<sub>2</sub> at 473 K and 1 atm). H<sub>2</sub>O orders were not collected for the fresh and sulfated Z<sub>2</sub>Cu model catalyst.

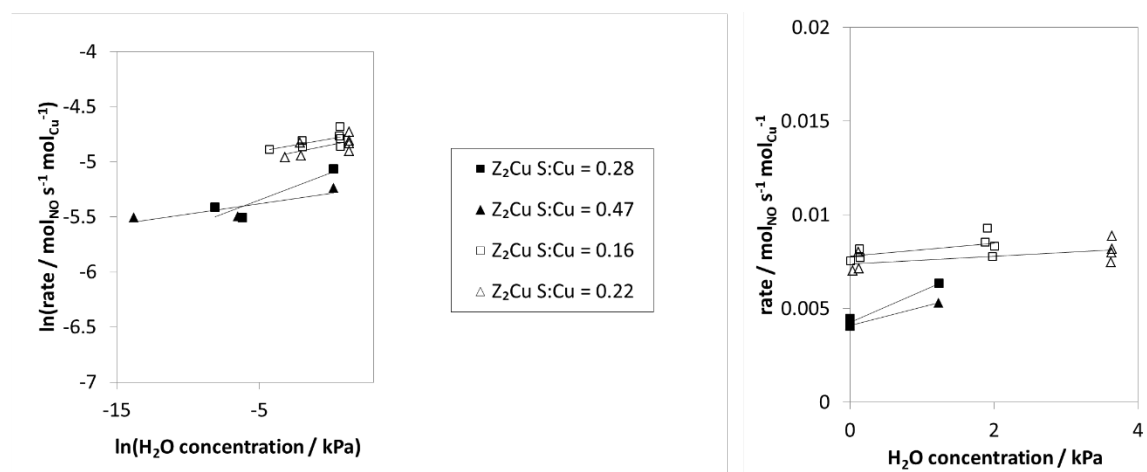


**Figure 102.** Linearized H<sub>2</sub>O order plots (left) and rate dependent on H<sub>2</sub>O concentration plots (right) on desulfated (hollow square and triangle) Z<sub>2</sub>Cu model catalysts during high O<sub>2</sub> SCR conditions (300 ppm NO, 300 ppm NH<sub>3</sub>, 60% O<sub>2</sub>, 8% CO<sub>2</sub>, 0 to 2.5% H<sub>2</sub>O, balance N<sub>2</sub> at 473 K and 1 atm). H<sub>2</sub>O orders were not collected for the fresh and sulfated Z<sub>2</sub>Cu model catalyst.



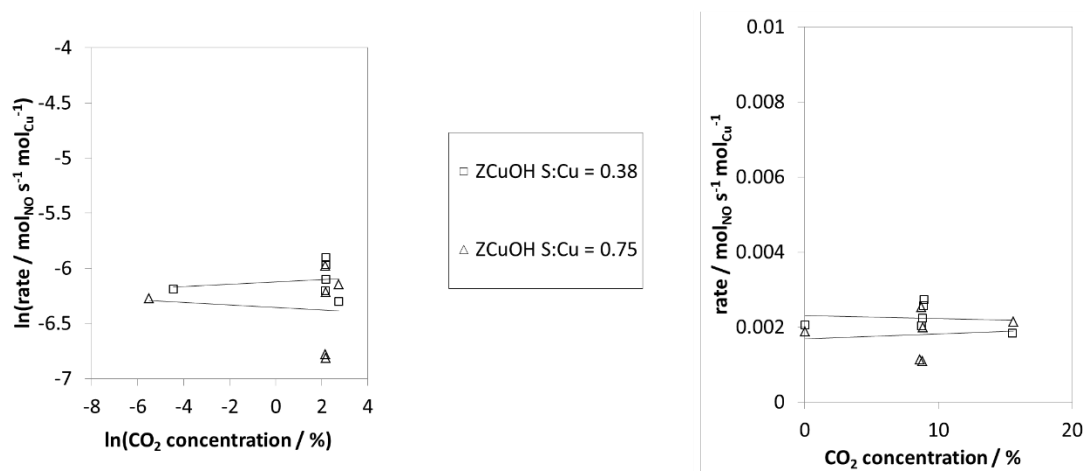


**Figure 103.** Linearized CO<sub>2</sub> order plots (left) and rate dependent on CO<sub>2</sub> concentration plots (right) on desulfated (hollow square and triangle) ZCuOH model catalysts during standard SCR conditions (300 ppm NO, 300 ppm NH<sub>3</sub>, 10% O<sub>2</sub>, 0 to 15% CO<sub>2</sub>, 2.5% H<sub>2</sub>O, balance N<sub>2</sub> at 473 K and 1 atm). CO<sub>2</sub> orders were not collected experimentally for the fresh and sulfated ZCuOH model catalyst.

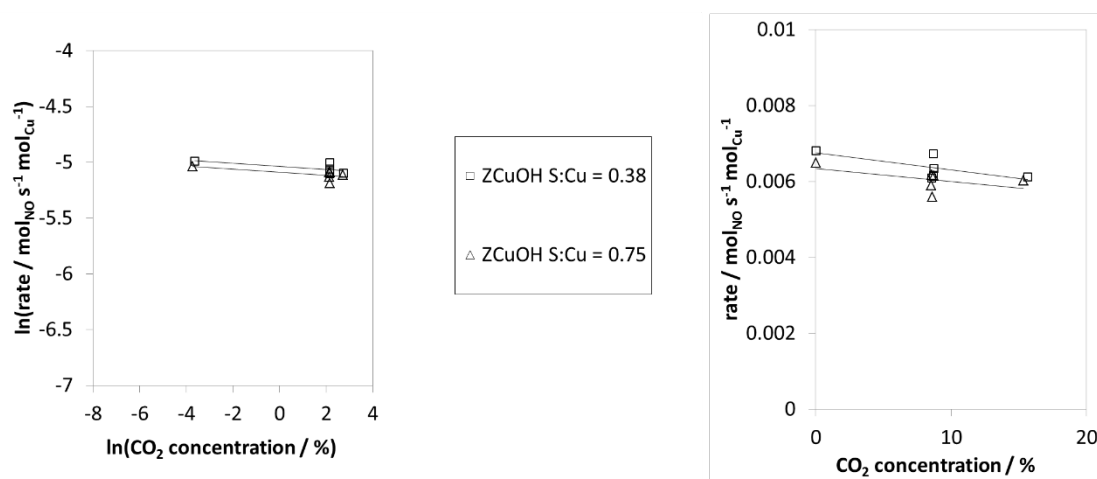


**Figure 104.** Linearized CO<sub>2</sub> order plots (left) and rate dependent on CO<sub>2</sub> concentration plots (right) on desulfated (hollow square and triangle) ZCuOH model catalysts during high O<sub>2</sub> SCR conditions (300 ppm NO, 300 ppm NH<sub>3</sub>, 60% O<sub>2</sub>, 0 to 15% CO<sub>2</sub>, 2.5% H<sub>2</sub>O, balance N<sub>2</sub> at 473 K and 1 atm). CO<sub>2</sub> orders were not collected experimentally for the fresh and sulfated ZCuOH model catalyst.

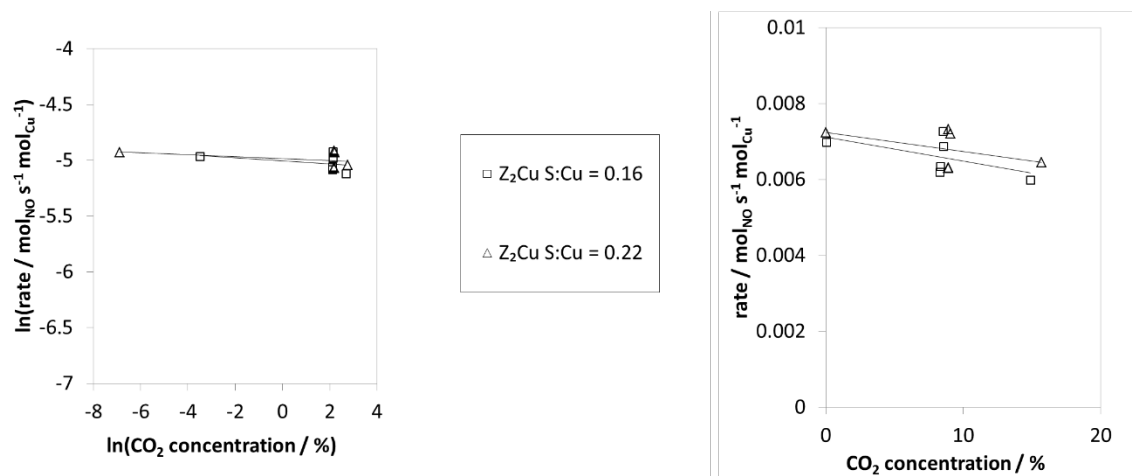


**Figure 105.** Linearized CO<sub>2</sub> order plots (left) and rate dependent on CO<sub>2</sub> concentration plots (right) on desulfated (hollow square and triangle) Z<sub>2</sub>Cu model catalysts during standard SCR conditions (300 ppm NO, 300 ppm NH<sub>3</sub>, 10% O<sub>2</sub>, 0 to 15% CO<sub>2</sub>, 2.5% H<sub>2</sub>O, balance N<sub>2</sub> at 473 K and 1 atm). CO<sub>2</sub> orders were not collected experimentally for the fresh and sulfated Z<sub>2</sub>Cu model catalyst.

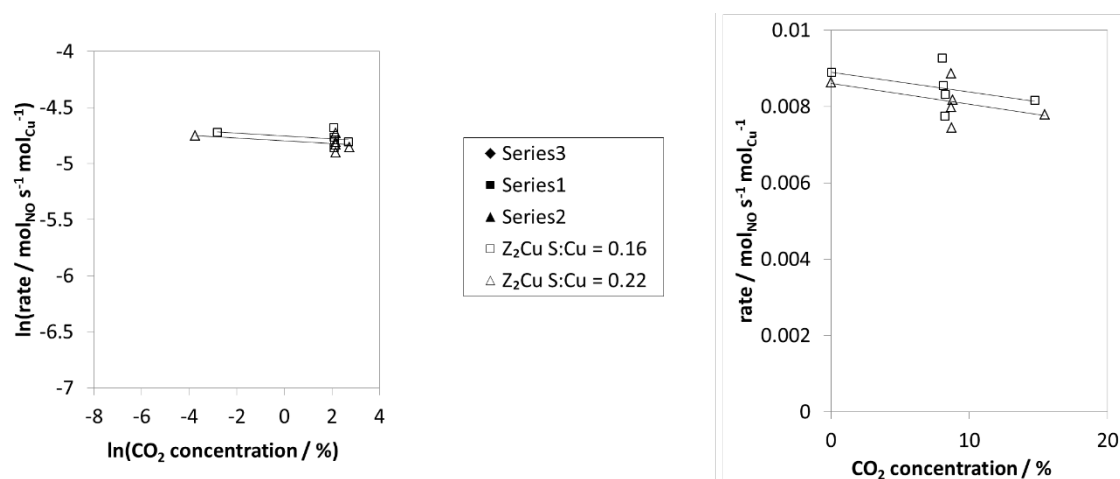


**Figure 106.** Linearized CO<sub>2</sub> order plots (left) and rate dependent on CO<sub>2</sub> concentration plots (right) on desulfated (hollow square and triangle) Z<sub>2</sub>Cu model catalysts during high O<sub>2</sub> SCR conditions (300 ppm NO, 300 ppm NH<sub>3</sub>, 60% O<sub>2</sub>, 0 to 15% CO<sub>2</sub>, 2.5% H<sub>2</sub>O, balance N<sub>2</sub> at 473 K and 1 atm). CO<sub>2</sub> orders were not collected experimentally for the fresh and sulfated Z<sub>2</sub>Cu model catalyst.

**Table 15.** SCR apparent activation energies ( $E_{app}$ ) on model catalysts after sulfation and desulfation treatments. (n.m. = not measured).

Sample	S:Cu	$E_{app}$	
		SCR with 10% O <sub>2</sub>	SCR with 60% O <sub>2</sub>
ZCuOH fresh	0.00	52	46
ZCuOH 473 K SO <sub>2</sub>	0.59	42	41
ZCuOH 673 K SO <sub>2</sub>	1.44	15	7
ZCuOH 473 K SO <sub>2</sub> – desulfated	0.38	38	26
ZCuOH 673 K SO <sub>2</sub> – desulfated	0.75	34	11
Z <sub>2</sub> Cu fresh	0.00	69	54
Z <sub>2</sub> Cu 473 K SO <sub>2</sub>	0.28	73	55
Z <sub>2</sub> Cu 673 K SO <sub>2</sub>	0.47	72	54
Z <sub>2</sub> Cu 473 K SO <sub>2</sub> – desulfated	0.16	62	65
Z <sub>2</sub> Cu 673 K SO <sub>2</sub> – desulfated	0.22	61	57

**Table 16.** SCR apparent NO orders on model catalysts after sulfation and desulfation treatments. (n.m. = not measured).

Sample	S:Cu	NO order	
		SCR with 10% O <sub>2</sub>	SCR with 60% O <sub>2</sub>
ZCuOH fresh	0.00	0.60	0.90
ZCuOH 473 K SO <sub>2</sub>	0.59	0.90	1.20
ZCuOH 673 K SO <sub>2</sub>	1.44	1.70	2.00
ZCuOH 473 K SO <sub>2</sub> – desulfated	0.38	0.77	0.82
ZCuOH 673 K SO <sub>2</sub> – desulfated	0.75	0.97	0.84
Z <sub>2</sub> Cu fresh	0.00	0.90	0.94
Z <sub>2</sub> Cu 473 K SO <sub>2</sub>	0.28	0.80	0.98
Z <sub>2</sub> Cu 673 K SO <sub>2</sub>	0.47	0.80	0.97
Z <sub>2</sub> Cu 473 K SO <sub>2</sub> – desulfated	0.16	0.82	0.94
Z <sub>2</sub> Cu 673 K SO <sub>2</sub> – desulfated	0.22	0.81	0.91

**Table 17.** SCR apparent O<sub>2</sub> orders on model catalysts after sulfation and desulfation treatments.  
(n.m. = not measured).

Sample	S:Cu	O <sub>2</sub> order	
		SCR with 10% O <sub>2</sub>	SCR with 60% O <sub>2</sub>
ZCuOH fresh	0.00	0.65	0.37
ZCuOH 473 K SO <sub>2</sub>	0.59	0.60	0.60
ZCuOH 673 K SO <sub>2</sub>	1.44	0.90	0.90
ZCuOH 473 K SO <sub>2</sub> – desulfated	0.38	0.70	0.73
ZCuOH 673 K SO <sub>2</sub> – desulfated	0.75	0.84	0.63
Z <sub>2</sub> Cu fresh	0.00	0.30	0.02
Z <sub>2</sub> Cu 473 K SO <sub>2</sub>	0.28	0.30	0.08
Z <sub>2</sub> Cu 673 K SO <sub>2</sub>	0.47	0.30	0.00
Z <sub>2</sub> Cu 473 K SO <sub>2</sub> – desulfated	0.16	0.20	0.10
Z <sub>2</sub> Cu 673 K SO <sub>2</sub> – desulfated	0.22	0.27	0.24

**Table 18.** SCR apparent NH<sub>3</sub> orders on model catalysts after sulfation and desulfation treatments.  
(n.m. = not measured).

Sample	S:Cu	NH <sub>3</sub> order	
		SCR with 10% O <sub>2</sub>	SCR with 60% O <sub>2</sub>
ZCuOH fresh	0.00	-0.40	-0.63
ZCuOH 473 K SO <sub>2</sub>	0.59	-0.25	-0.13
ZCuOH 673 K SO <sub>2</sub>	1.44	0.00	0.00
ZCuOH 473 K SO <sub>2</sub> – desulfated	0.38	0.01	-0.09
ZCuOH 673 K SO <sub>2</sub> – desulfated	0.75	-0.20	-0.03
Z <sub>2</sub> Cu fresh	0.00	0.00	-0.04
Z <sub>2</sub> Cu 473 K SO <sub>2</sub>	0.28	-0.10	-0.15
Z <sub>2</sub> Cu 673 K SO <sub>2</sub>	0.47	-0.10	-0.16
Z <sub>2</sub> Cu 473 K SO <sub>2</sub> – desulfated	0.16	-0.09	0.06
Z <sub>2</sub> Cu 673 K SO <sub>2</sub> – desulfated	0.22	0.04	0.00

**Table 19.** SCR apparent CO<sub>2</sub> orders on model catalysts after sulfation and desulfation treatments. (n.m. = not measured).

Sample	S:Cu	CO <sub>2</sub> order	CO <sub>2</sub> order
		SCR with 10% O <sub>2</sub>	SCR with 60% O <sub>2</sub>
ZCuOH fresh	0.00	n.m.	n.m.
ZCuOH 473 K SO <sub>2</sub>	0.59	n.m.	n.m.
ZCuOH 673 K SO <sub>2</sub>	1.44	n.m.	n.m.
ZCuOH 473 K SO <sub>2</sub> – desulfated	0.38	0.01	-0.01
ZCuOH 673 K SO <sub>2</sub> – desulfated	0.75	-0.01	-0.01
Z <sub>2</sub> Cu fresh	0.00	n.m.	n.m.
Z <sub>2</sub> Cu 473 K SO <sub>2</sub>	0.28	n.m.	n.m.
Z <sub>2</sub> Cu 673 K SO <sub>2</sub>	0.47	n.m.	n.m.
Z <sub>2</sub> Cu 473 K SO <sub>2</sub> – desulfated	0.16	-0.01	-0.02
Z <sub>2</sub> Cu 673 K SO <sub>2</sub> – desulfated	0.22	-0.01	-0.01

**Table 20.** SCR apparent H<sub>2</sub>O orders on model catalysts after sulfation and desulfation treatments. (n.m. = not measured).

Sample	S:Cu	H <sub>2</sub> O order	H <sub>2</sub> O order
		SCR with 10% O <sub>2</sub>	SCR with 60% O <sub>2</sub>
ZCuOH fresh	0.00	n.m.	n.m.
ZCuOH 473 K SO <sub>2</sub>	0.59	n.m.	n.m.
ZCuOH 673 K SO <sub>2</sub>	1.44	n.m.	n.m.
ZCuOH 473 K SO <sub>2</sub> – desulfated	0.38	0.04	-0.01
ZCuOH 673 K SO <sub>2</sub> – desulfated	0.75	-0.11	0.00
Z <sub>2</sub> Cu fresh	0.00	n.m.	n.m.
Z <sub>2</sub> Cu 473 K SO <sub>2</sub>	0.28	n.m.	n.m.
Z <sub>2</sub> Cu 673 K SO <sub>2</sub>	0.47	n.m.	n.m.
Z <sub>2</sub> Cu 473 K SO <sub>2</sub> – desulfated	0.16	-0.01	0.02
Z <sub>2</sub> Cu 673 K SO <sub>2</sub> – desulfated	0.22	-0.02	0.03

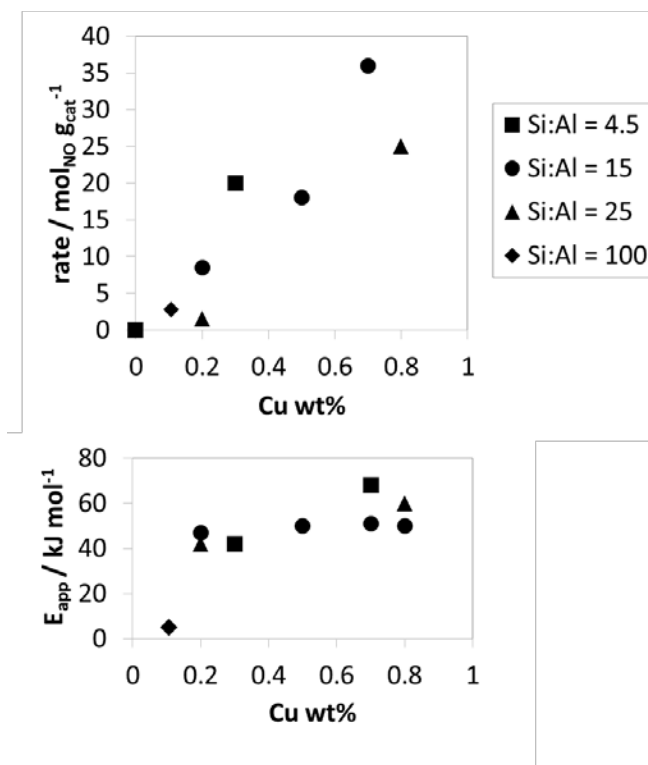


**Figure 107.** Standard SCR (300 ppm NO, 300 ppm NH<sub>3</sub>, 10% O<sub>2</sub>, 2.5% H<sub>2</sub>O, 8% CO<sub>2</sub>, in balance N<sub>2</sub>, at 200°C) rate, and apparent activation energy on unsulfated Cu-SSZ-13 samples with low Cu loadings (< 1 wt%). The catalyst with the lowest Cu and Al density (0.1 Cu wt%, Si:Al = 100) exhibited a drop in the apparent activation energy compared to other catalysts (Cu wt% from 0.2 to 0.8, Si:Al from 4.5 to 25)

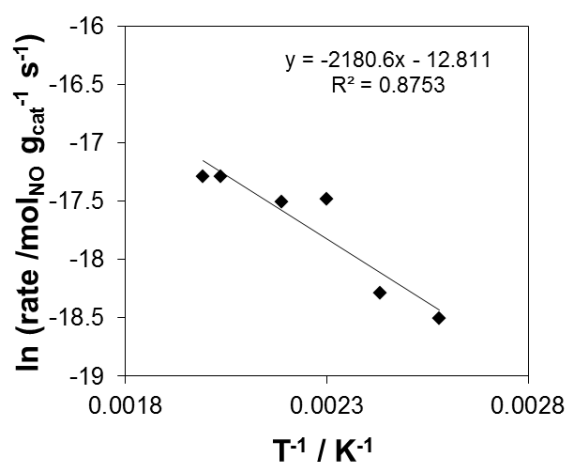


**Figure 108.** Standard SCR (300 ppm NO, 300 ppm NH<sub>3</sub>, 10% O<sub>2</sub>, 2.5% H<sub>2</sub>O, 8% CO<sub>2</sub>, in balance N<sub>2</sub>, at 200°C) Arrhenius plot of an unsulfated Cu-SSZ-13 catalysts with a low Cu and Al density (0.1 Cu wt%, Si:Al = 100).

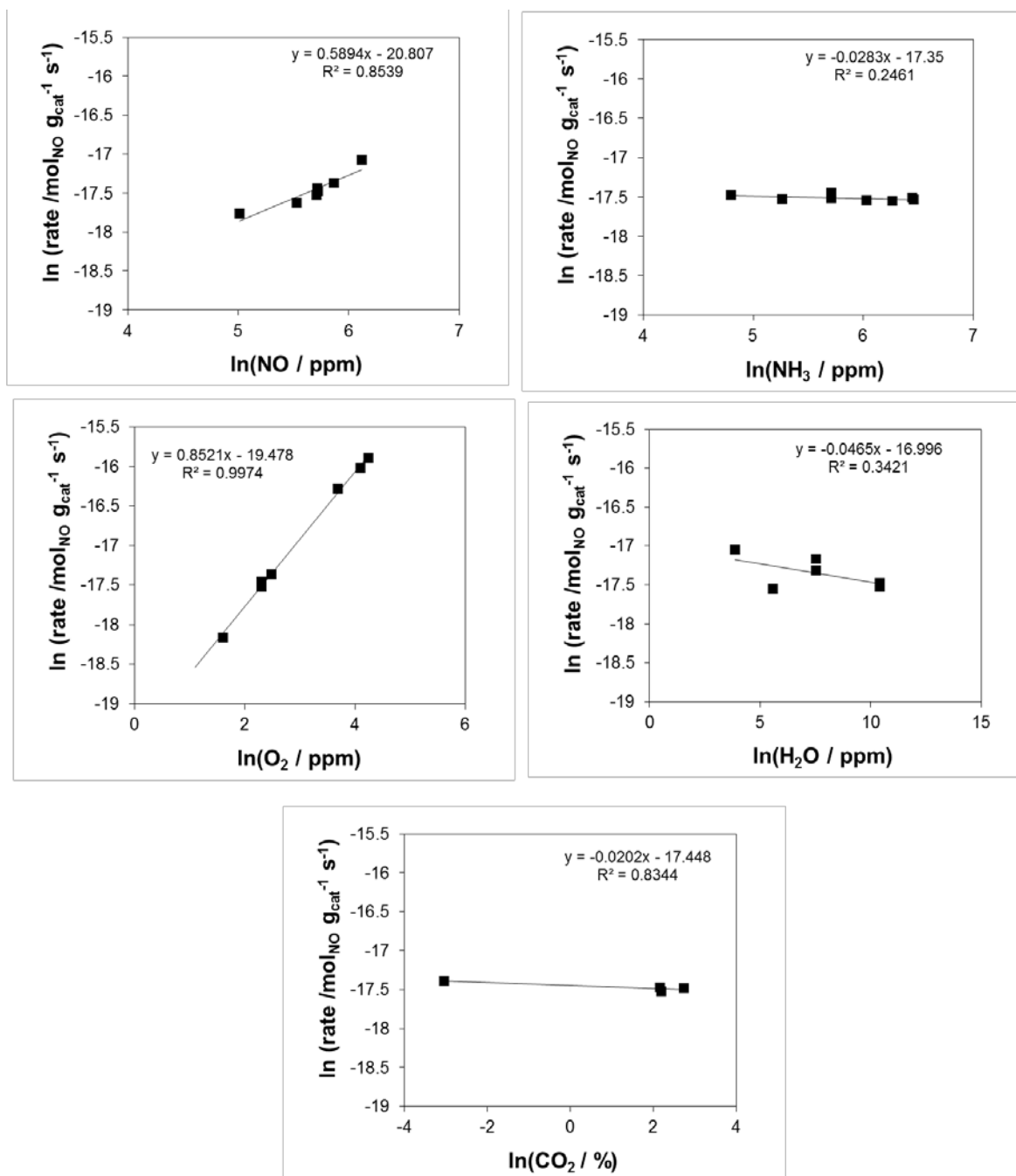


**Figure 109.** Standard SCR (300 ppm NO, 300 ppm NH<sub>3</sub>, 10% O<sub>2</sub>, 2.5% H<sub>2</sub>O, 8% CO<sub>2</sub>, in balance N<sub>2</sub>, at 200°C) order plots on an unsulfated Cu-SSZ-13 catalyst with a low Cu and Al density (0.1 Cu wt%, Si:Al = 100). The NO, NH<sub>3</sub>, O<sub>2</sub>, H<sub>2</sub>O, and CO<sub>2</sub> orders are 0.6, 0.0, 0.9, 0.0, and 0.0, respectively.

**Table 21.** Apparent activation energies and reaction orders an unsulfated Cu-SSZ-13 catalyst with a low Cu and Al density (0.1 Cu wt%, Si:Al = 100) under “10% O<sub>2</sub> SCR” conditions (300 ppm NO, 300 ppm NH<sub>3</sub>, 10% O<sub>2</sub>, 2.5% H<sub>2</sub>O, 8% CO<sub>2</sub>, balance N<sub>2</sub> at 473 K).

	E <sub>app</sub>	NO order	O <sub>2</sub> order	NH <sub>3</sub> order	CO <sub>2</sub> order	H <sub>2</sub> O order
Cu-SSZ-13 Si:Al = 100						
Cu wt% = 0.1	7	0.59	0.85	-0.03	-0.02	-0.05

### 7.7.3 Additional Characterization (TGA, NO<sub>2</sub> selectivity) on ZCuOH S:Cu = 1.44 model catalyst

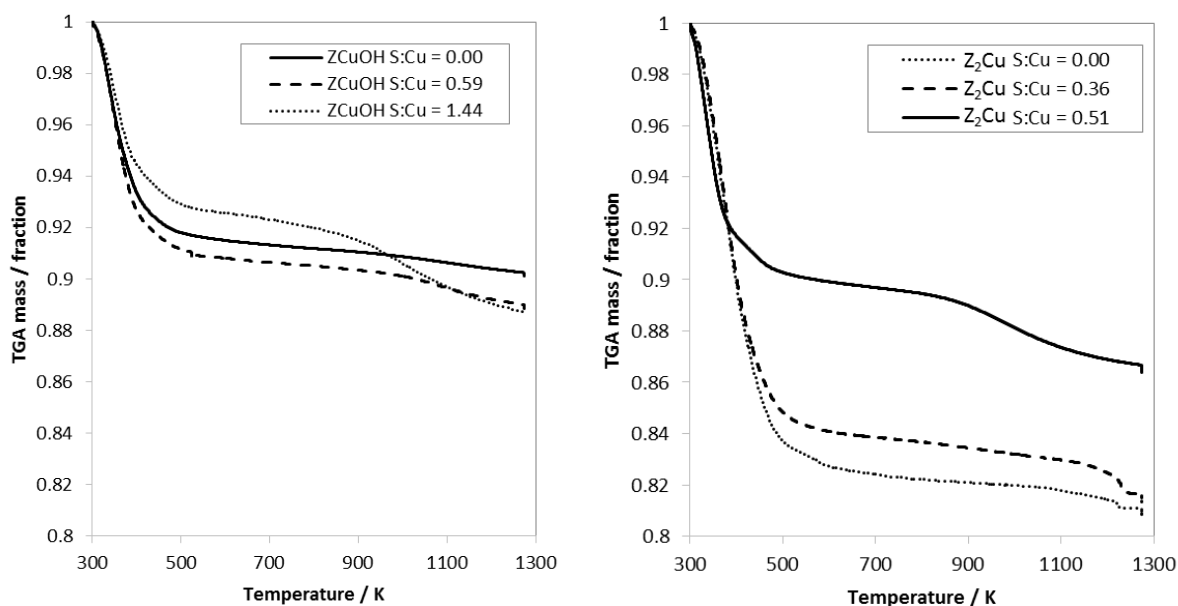


**Figure 110.** Thermogravimetric analysis (TGA) of sulfated Cu-SSZ-13 catalysts in a dry He environment (10 mg sample, ramp from ambient temperature to 1273 K with a ramp rate of 10 K min<sup>-1</sup>). Collected on a Thermal Analysis (TA) Instruments Simultaneous DSC/TGA (SDT) Q600.



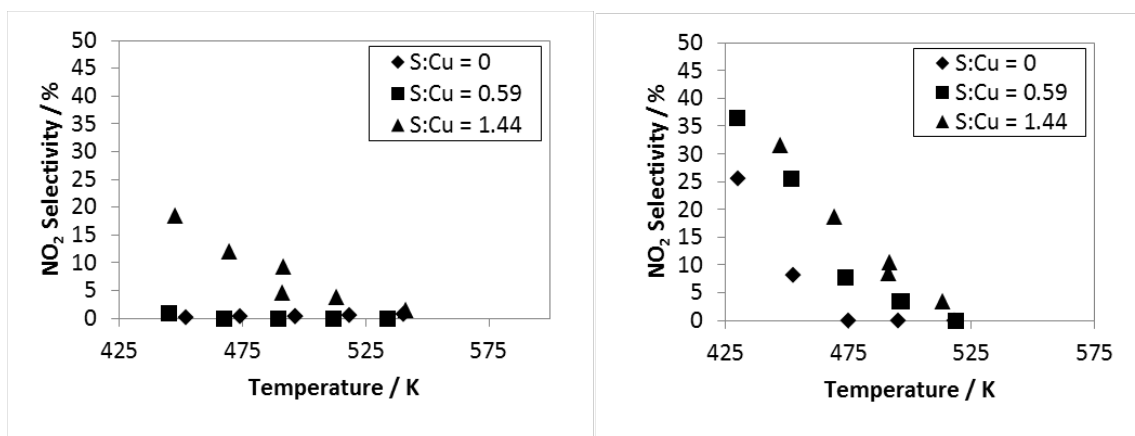


**Figure 111.** Selectivities toward NO oxidation under standard (10% O<sub>2</sub>) SCR conditions (left), and selectivities toward NO oxidation under high O<sub>2</sub> (60% O<sub>2</sub>) SCR conditions, on Cu-SSZ-13 poisoned with increasing S content.

#### 7.7.4 UV-Visible, XANES, EXAFS, N<sub>2</sub> Micropore, and Ar micropore on model ZCuOH and Z<sub>2</sub>Cu materials

##### UV-Visible results

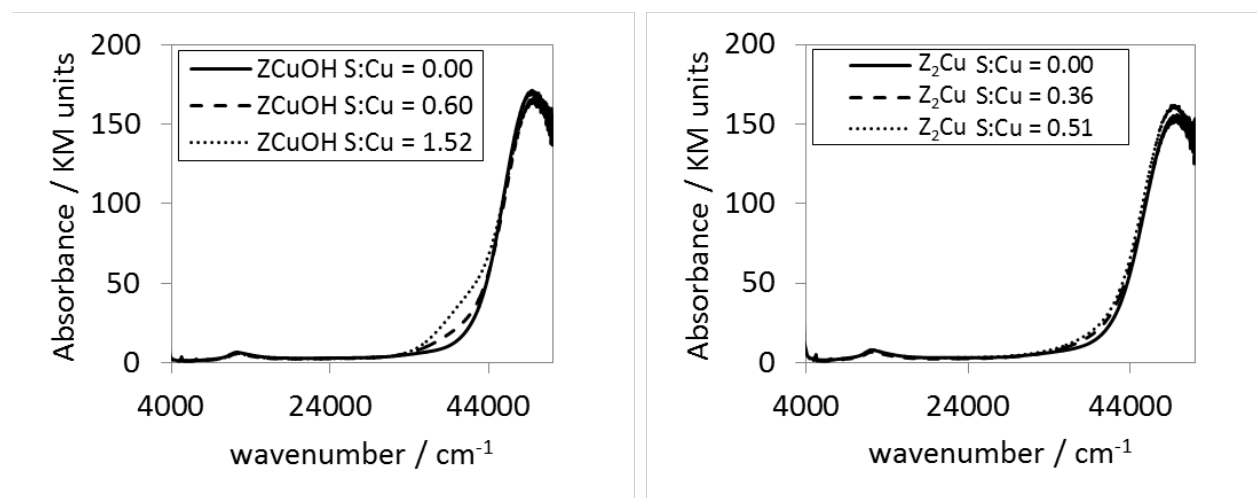


**Figure 112.** Diffuse reflectance UV-Visible spectra on ZCuOH (left) and Z<sub>2</sub>Cu (right) collected under ambient conditions (298 K, ambient air).

### XANES and EXAFS results

Quantifying Cu oxidation states using linear combination XANES is most effective when the number of species is as low as possible. The introduction of new ligands or atomic coordinations to a Cu ion will affect the intensity of the Cu(I) feature at 8.982 keV. For example, the reference used for 100% Cu(I) on  $\text{NH}_3$ -saturated Cu-SSZ-13 and Cu(I) oxide are two times different in intensity due to changes in the Cu's coordination environment [109–111]. The Cu(I)( $\text{NH}_3$ )<sub>2</sub> and Cu(II) references used in this work to quantify the Cu(II) fraction from the Cu(I) pre-edge XANES feature are described in our previous publication [109].

**Table 22.** Ambient and dehydrated (573 K in dry air) XANES Cu(II) fractions observed on fresh, sulfated, and desulfated Cu-SSZ-13 catalysts using Cu(I)( $\text{NH}_3$ )<sub>2</sub> and Cu(II) references. (n.m. not measured)

Sample	S:Cu	Ambient	573 K dehydration XANES Cu(II) fraction
ZCuOH fresh	0.00	1.00	1.00
ZCuOH 473 K $\text{SO}_2$	0.59	n.m.	1.00
ZCuOH 673 K $\text{SO}_2$	1.44	1.00	1.00
ZCuOH 473 K $\text{SO}_2$ – desulfated	0.38	n.m.	n.m.
ZCuOH 673 K $\text{SO}_2$ – desulfated	0.75	n.m.	n.m.
Z <sub>2</sub> Cu fresh	0.00	n.m.	1.00
Z <sub>2</sub> Cu 473 K $\text{SO}_2$	0.28	n.m.	1.00
Z <sub>2</sub> Cu 673 K $\text{SO}_2$	0.47	n.m.	1.00
Z <sub>2</sub> Cu 473 K $\text{SO}_2$ – desulfated	0.16	n.m.	n.m.
Z <sub>2</sub> Cu 673 K $\text{SO}_2$ – desulfated	0.22	n.m.	n.m.

**Table 23.** Operando XANES Cu(II) fractions observed on fresh, sulfated, and desulfated Cu-SSZ-13 catalysts using Cu(I)(NH<sub>3</sub>)<sub>2</sub> and Cu(II) references. (n.m. not measured).

Sample	S:Cu	SCR with 10% O <sub>2</sub> operando Cu(II) fraction	SCR with 60% O <sub>2</sub> operando Cu(II) fraction
ZCuOH fresh	0.00	0.47	0.50
ZCuOH 473 K SO <sub>2</sub>	0.59	0.71	0.98
ZCuOH 673 K SO <sub>2</sub>	1.44	0.87	0.91
ZCuOH 473 K SO <sub>2</sub> – desulfated	0.38	n.m.	n.m.
ZCuOH 673 K SO <sub>2</sub> – desulfated	0.75	1.00	1.00
Z <sub>2</sub> Cu fresh	0.00	0.92	0.98
Z <sub>2</sub> Cu 473 K SO <sub>2</sub>	0.28	0.94	0.98
Z <sub>2</sub> Cu 673 K SO <sub>2</sub>	0.47	0.93	n.m.
Z <sub>2</sub> Cu 473 K SO <sub>2</sub> – desulfated	0.16	n.m.	n.m.
Z <sub>2</sub> Cu 673 K SO <sub>2</sub> – desulfated	0.22	0.66	0.81

**Table 24.** In situ XANES Cu(II) fractions after reduction with NH<sub>3</sub> + NO and subsequent reoxidation with O<sub>2</sub> observed on fresh, sulfated, and desulfated Cu-SSZ-13 catalysts using Cu(I)(NH<sub>3</sub>)<sub>2</sub> and Cu(II) references. (n.m. not measured).

Sample	S:Cu	NO + NH <sub>3</sub> reduction XANES Cu(II) fraction	O <sub>2</sub> reoxidation XANES Cu(II) fraction
ZCuOH fresh	0.00	0.00	0.75
ZCuOH 473 K SO <sub>2</sub>	0.59	0.28	0.80
ZCuOH 673 K SO <sub>2</sub>	1.44	0.25	0.94
ZCuOH 473 K SO <sub>2</sub> – desulfated	0.38	n.m.	n.m.
ZCuOH 673 K SO <sub>2</sub> – desulfated	0.75	0.15	0.79
Z <sub>2</sub> Cu fresh	0.00	0.00	0.95
Z <sub>2</sub> Cu 473 K SO <sub>2</sub>	0.28	0.21	1.00
Z <sub>2</sub> Cu 673 K SO <sub>2</sub>	0.47	0.25	0.99
Z <sub>2</sub> Cu 473 K SO <sub>2</sub> – desulfated	0.16	n.m.	n.m.
Z <sub>2</sub> Cu 673 K SO <sub>2</sub> – desulfated	0.22	0.14	1.00

**Table 25.** Ambient and dehydrated (573 K in dry air) EXAFS Cu coordination numbers observed on fresh, sulfated, and desulfated Cu-SSZ-13 catalysts. (n.m. = not measured)

Sample	S:Cu	Ambient	573 K dehydration
			XANES Cu(II) fraction
ZCuOH fresh	0.00	3.9	3.5
ZCuOH 473 K SO <sub>2</sub>	0.59	n.m.	3.8
ZCuOH 673 K SO <sub>2</sub>	1.44	3.9	3.9
ZCuOH 473 K SO <sub>2</sub> – desulfated	0.38	n.m.	n.m.
ZCuOH 673 K SO <sub>2</sub> – desulfated	0.75	n.m.	n.m.
Z <sub>2</sub> Cu fresh	0.00	n.m.	4.0
Z <sub>2</sub> Cu 473 K SO <sub>2</sub>	0.28	n.m.	4.0
Z <sub>2</sub> Cu 673 K SO <sub>2</sub>	0.47	n.m.	4.0
Z <sub>2</sub> Cu 473 K SO <sub>2</sub> – desulfated	0.16	n.m.	n.m.
Z <sub>2</sub> Cu 673 K SO <sub>2</sub> – desulfated	0.22	n.m.	n.m.

**Table 26.** Operando EXAFS Cu coordination numbers observed on fresh, sulfated, and desulfated Cu-SSZ-13 catalysts. (n.m. = not measured)

Sample	S:Cu	SCR with 10% O <sub>2</sub>	SCR with 60% O <sub>2</sub>
		operando Cu(II) fraction	operando Cu(II) fraction
ZCuOH fresh	0.00	2.8	3.1
ZCuOH 473 K SO <sub>2</sub>	0.59	2.5	4.0
ZCuOH 673 K SO <sub>2</sub>	1.44	2.7	2.8
ZCuOH 473 K SO <sub>2</sub> – desulfated	0.38	n.m.	n.m.
ZCuOH 673 K SO <sub>2</sub> – desulfated	0.75	2.8	3.4
Z <sub>2</sub> Cu fresh	0.00	3.9	4.0
Z <sub>2</sub> Cu 473 K SO <sub>2</sub>	0.28	2.9	3.0
Z <sub>2</sub> Cu 673 K SO <sub>2</sub>	0.47	3.0	2.8
Z <sub>2</sub> Cu 473 K SO <sub>2</sub> – desulfated	0.16	n.m.	n.m.
Z <sub>2</sub> Cu 673 K SO <sub>2</sub> – desulfated	0.22	3.1	3.0

**Table 27.** In situ EXAFS coordination numbers after reduction with  $\text{NH}_3 + \text{NO}$  and subsequent reoxidation with  $\text{O}_2$  observed on Cu coordination numbers observed on fresh, sulfated, and desulfated Cu-SSZ-13 catalysts. (n.m. = not measured)

Sample	S:Cu	NO + $\text{NH}_3$ reduction XANES Cu(II) fraction	$\text{O}_2$ reoxidation XANES Cu(II) fraction
ZCuOH fresh	0.00	2.0	3.2
ZCuOH 473 K $\text{SO}_2$	0.59	2.1	2.8
ZCuOH 673 K $\text{SO}_2$	1.44	2.4	2.9
ZCuOH 473 K $\text{SO}_2$ – desulfated	0.38	n.m.	n.m.
ZCuOH 673 K $\text{SO}_2$ – desulfated	0.75	2.1	3.1
Z <sub>2</sub> Cu fresh	0.00	2.0	4.0
Z <sub>2</sub> Cu 473 K $\text{SO}_2$	0.28	2.0	3.0
Z <sub>2</sub> Cu 673 K $\text{SO}_2$	0.47	2.1	2.6
Z <sub>2</sub> Cu 473 K $\text{SO}_2$ – desulfated	0.16	n.m.	n.m.
Z <sub>2</sub> Cu 673 K $\text{SO}_2$ – desulfated	0.22	2.0	3.1

### Ar and N<sub>2</sub> micropore measurements

Sulfur uptake may lead to a decrease in micropore volume that may reflect pore blocking. Micropore volumes are reported to decrease upon co-exposure to SO<sub>2</sub> and NH<sub>3</sub> [128,131–133]. To test this behavior, we measured N<sub>2</sub> and Ar micropore volumes on sulfated catalysts before and after NH<sub>3</sub> exposure. Ar micropore volumes increase on ZCuOH samples, but not on the Z<sub>2</sub>Cu samples with increasing levels of sulfation (Figure 113). N<sub>2</sub> micropore volumes decreased after NH<sub>3</sub>-saturation of Z<sub>2</sub>Cu samples (Figure 114), consistent with literature reports [128–132]. In contrast, micropore volumes are unchanged on the sulfated and NH<sub>3</sub>-saturated ZCuOH samples (Figure 113 and Figure 114). Spectroscopic and micropore results, along with crystal unit cell sizes assessed from XRD patterns (Section S5), thus reveal differences between the ZCuOH and Z<sub>2</sub>Cu samples despite similarities in their quantitative kinetic response to sulfur exposure.

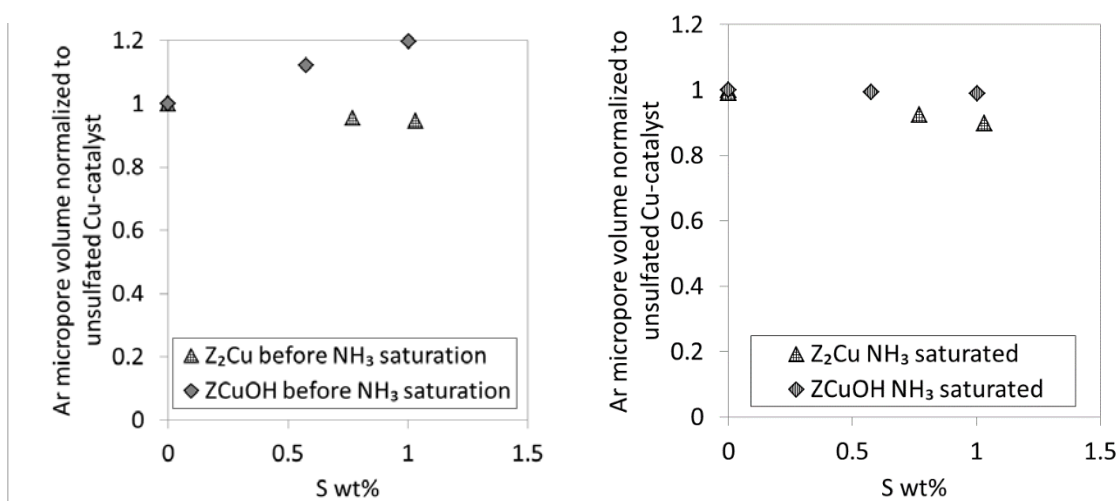


**Figure 113.** The micropore volume measured with Ar for Z<sub>2</sub>Cu invariant with increasing S wt% with increasing sulfation on sulfated materials before saturation with NH<sub>3</sub> (left), and after saturation with NH<sub>3</sub> (right).

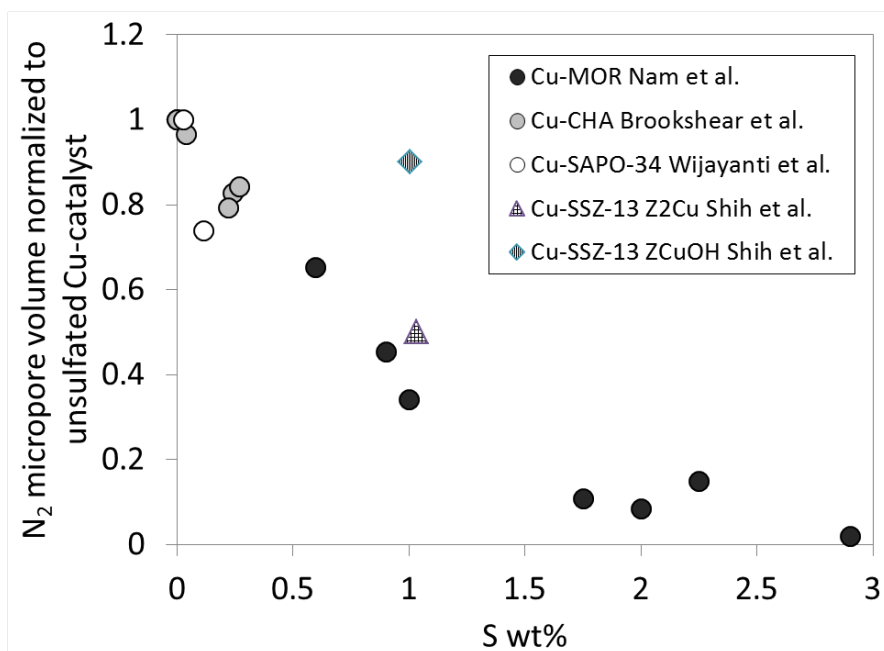


**Figure 114.** Micropore volumes measured using N<sub>2</sub> on samples that were either co-poisoned with NH<sub>3</sub> and SO<sub>2</sub>, or poisoned with SO<sub>2</sub> then saturated with NH<sub>3</sub>.



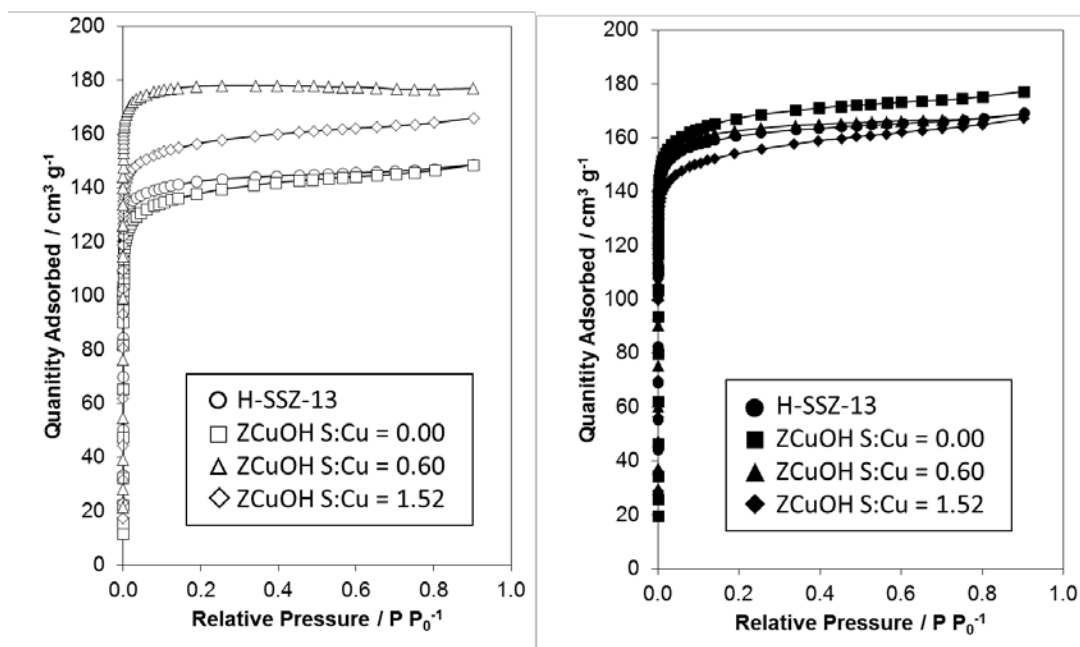


**Figure 115.** Argon adsorption isotherms (87 K) of sulfated ZCuOH model samples before NH<sub>3</sub> saturation (left) and after NH<sub>3</sub> saturation (right).

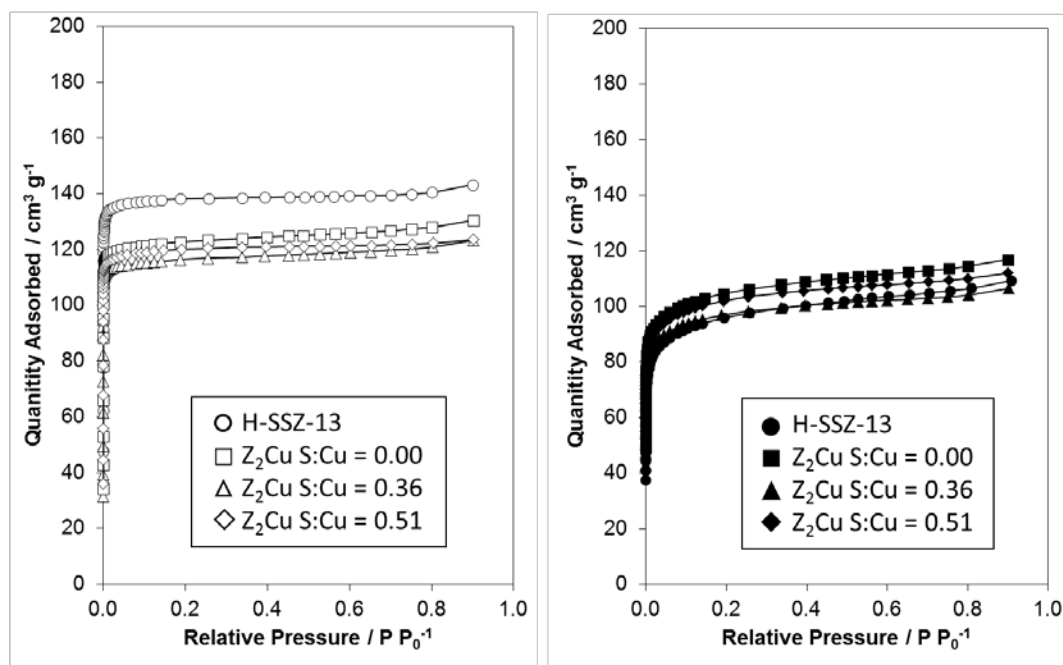


**Figure 116.** Argon adsorption isotherms (87 K) of sulfated Z<sub>2</sub>Cu model samples before NH<sub>3</sub> saturation (left) and after NH<sub>3</sub> saturation (right).

## XRD supplemental information

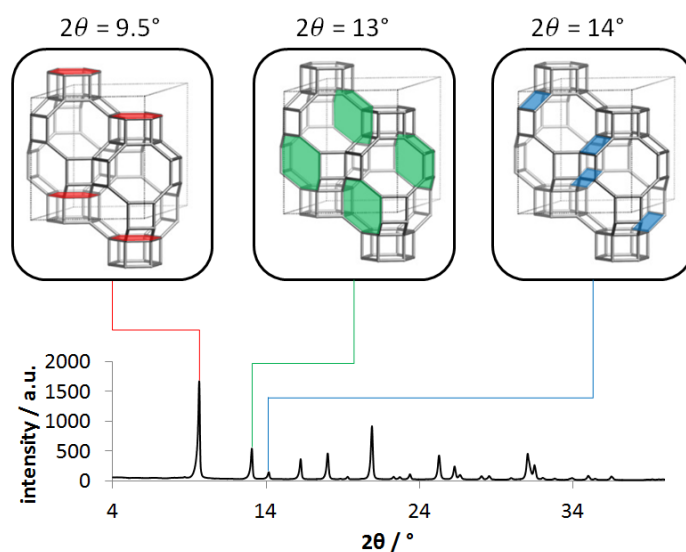
To probe the effects of sulfur exposure on crystal cell volume, XRD patterns were collected under ambient conditions before sulfation, after sulfation, and after NH<sub>3</sub> saturation of the unsulfated and sulfated samples. Shifts in the position of crystallographic planes (indexed to CHA) would indicate changes in the unit cell size and micropore volume [54,164] (Figure 117). Cu exchange and subsequent sulfur poisoning causes a shift in the 1 0 0 (9.5°), -1 1 0 (13°), and 1 1 0 (14°) peaks to lower angles (Figure 118 and Figure 119, raw XRD spectra in Figure 120 to Figure 125), indicative of an increase in spacing between crystalline planes according to Bragg's Law. NH<sub>3</sub> saturation of sulfated samples causes the peaks to revert back to their original 2θ values, indicating a relaxation of the crystal structure to its H-form under ambient conditions, possibly reflecting NH<sub>3</sub> solvation of occluded S-derived species.

The CHA cage volume was calculated by approximating it as a cylinder using Equation 27, where D is approximated as the distance between parallel diffraction planes calculated from Bragg's law using the XRD peak at 13° 2θ and h is approximated as the distance measured from the XRD peak at 9.5° 2θ.

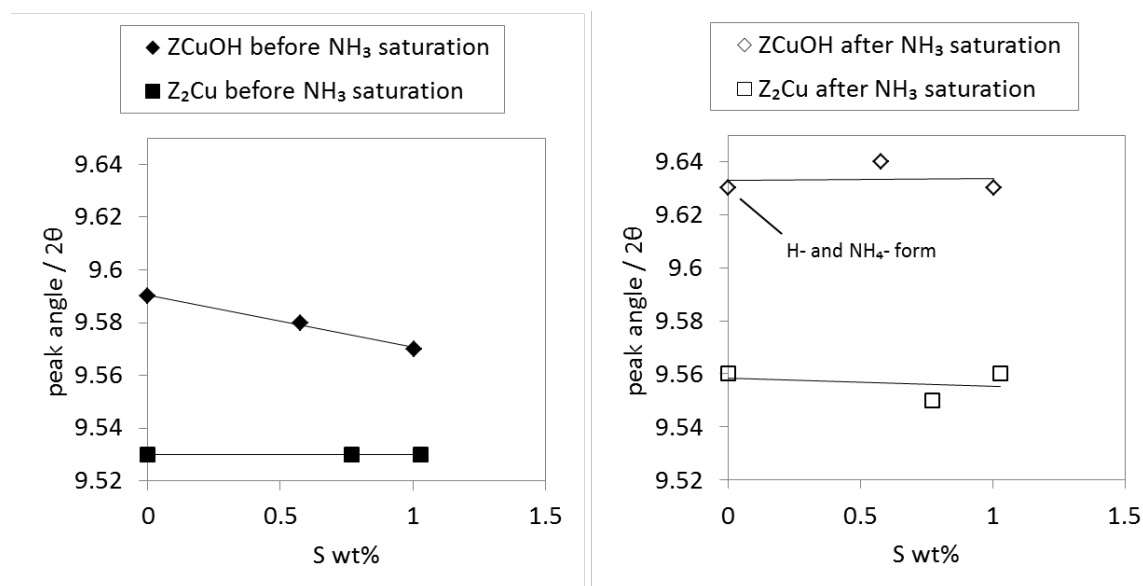
$$V_{cage} = \pi \left( \frac{D}{2} \right)^2 h \quad (\text{Equation 27})$$

The increase in cage volume scales linearly with the increase with Ar micropore volume for the Z<sub>2</sub>Cu model materials (Figure 126). We were unable to discern differences in crystallite sizes after SO<sub>2</sub> and NH<sub>3</sub> treatments using SEM (Figure 128 and Figure 129).

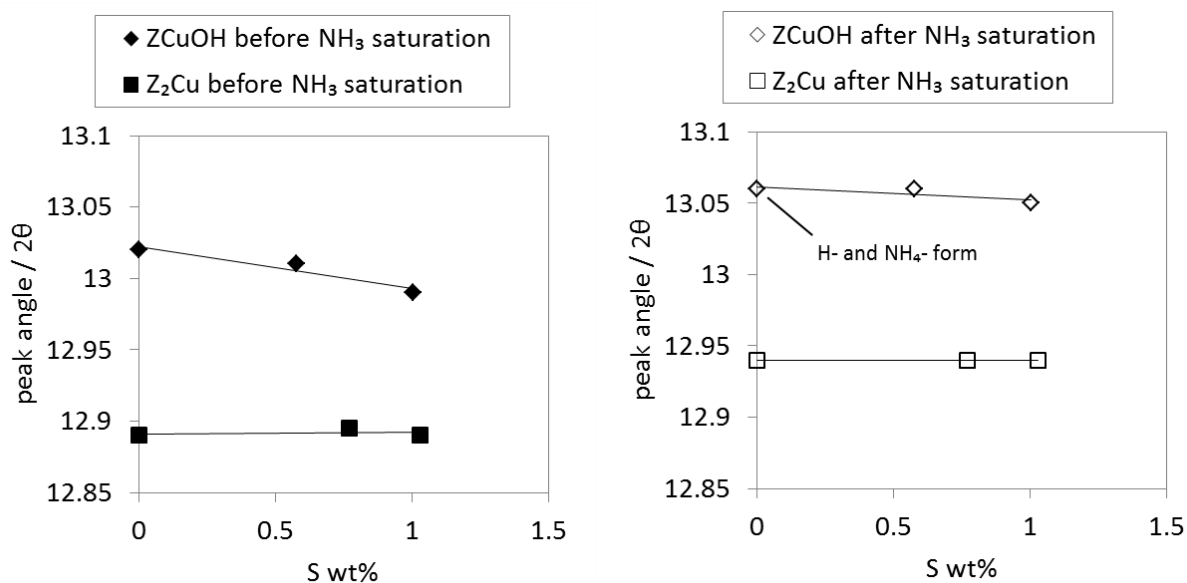
Taken together, micropore and XRD results indicate that there are two competing effects after sulfation treatments that affect the micropore volume and accessibility of Cu sites, both through increases the accessible zeolite volume due to sulfation and decreases in the micropore volume due to the addition of sulfur species.



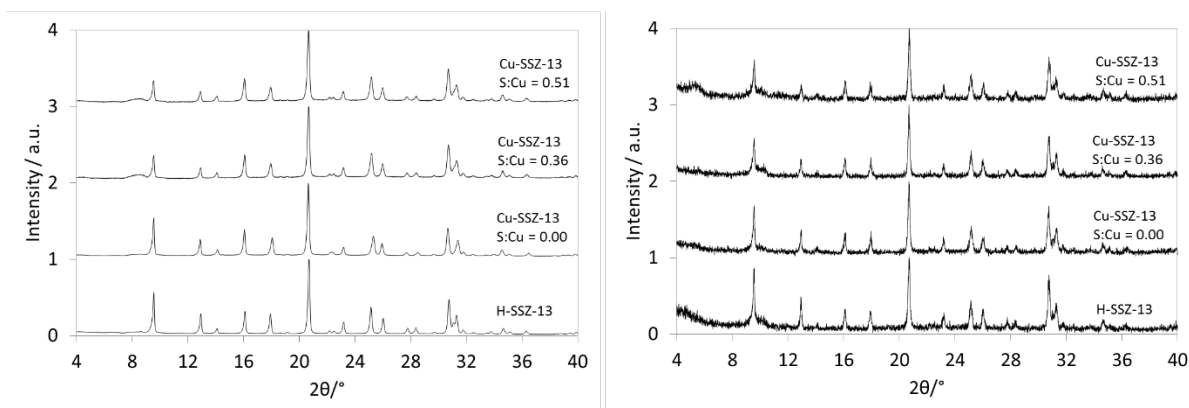
**Figure 117.** Relevant CHA XRD peaks indexed to diffraction planes for estimation of the CHA cage volume increase from XRD.



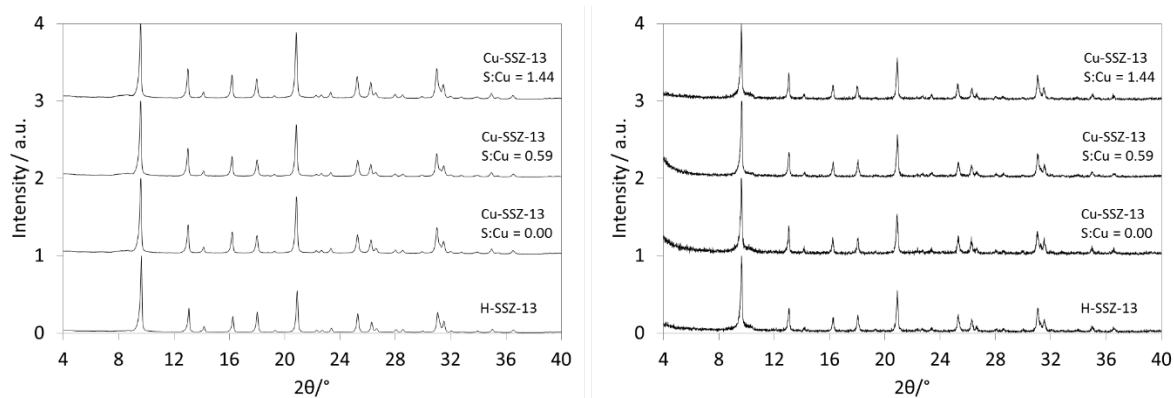
**Figure 118.** XRD peak shifts at 9.5° for Cu-SSZ-13 catalysts poisoned with only dry SO<sub>2</sub> (left) and NH<sub>3</sub> saturated after dry SO<sub>2</sub> poisoning (right) for ZCuOH (diamonds) and Z<sub>2</sub>Cu (squares).



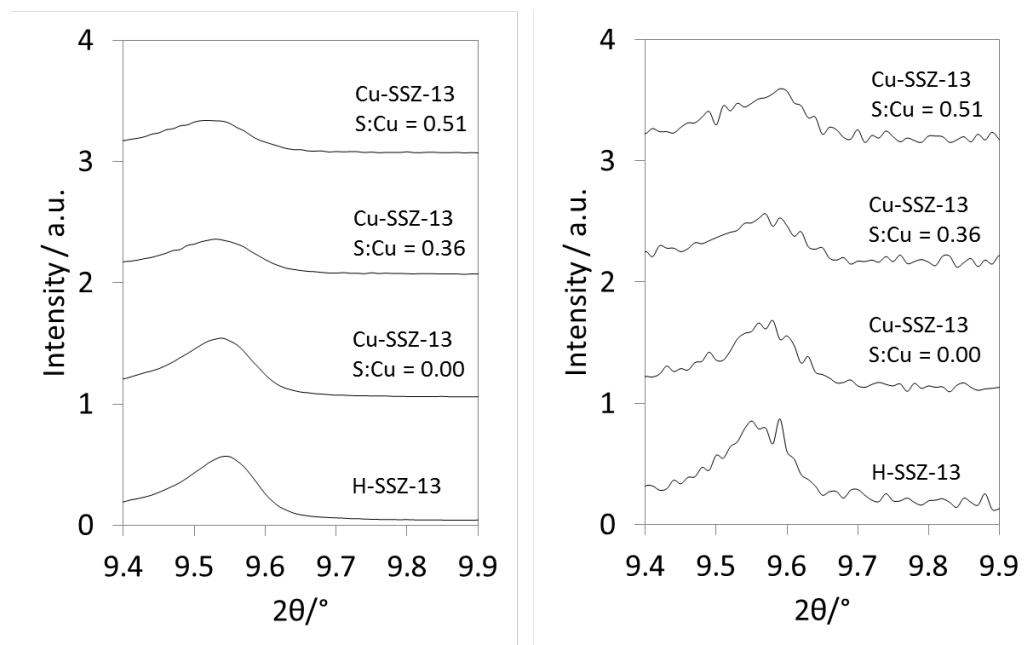
**Figure 119.** XRD peak shifts at 13° for Cu-SSZ-13 catalysts poisoned with only dry SO<sub>2</sub> (left) and NH<sub>3</sub> saturated after dry SO<sub>2</sub> poisoning (right) for ZCuOH (diamonds) and Z<sub>2</sub>Cu (squares).



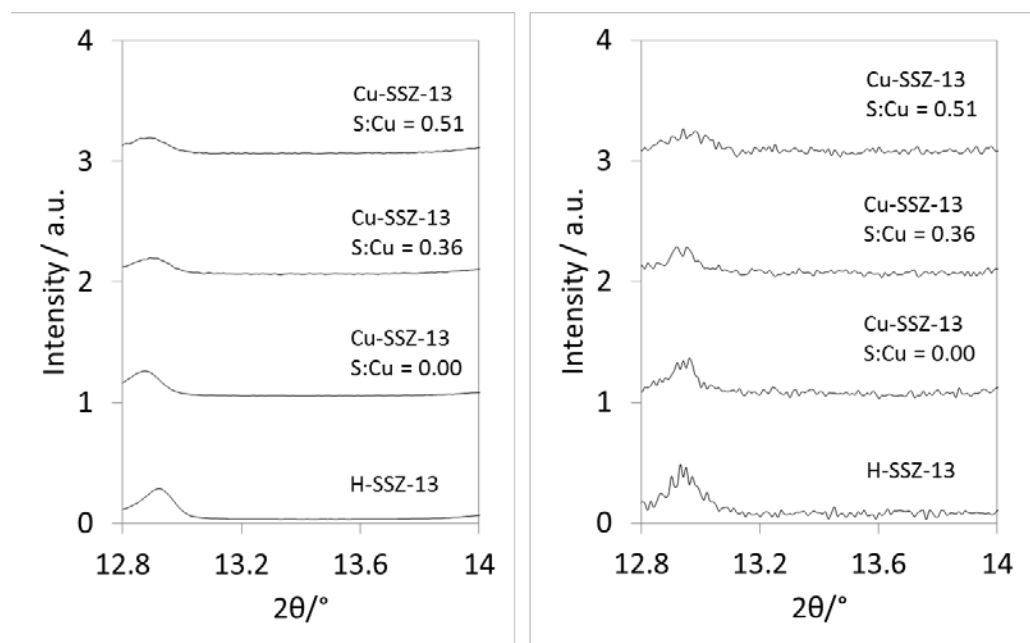
**Figure 120.** XRD patterns on  $Z_2Cu$  model catalysts after dry sulfation (left) and after  $NH_3$  saturation (right). Samples on the right were saturated with 500 ppm  $NH_3$  at 453 K until saturation, then flushed with dry  $N_2$  at 453 K and cooled to room temperature.



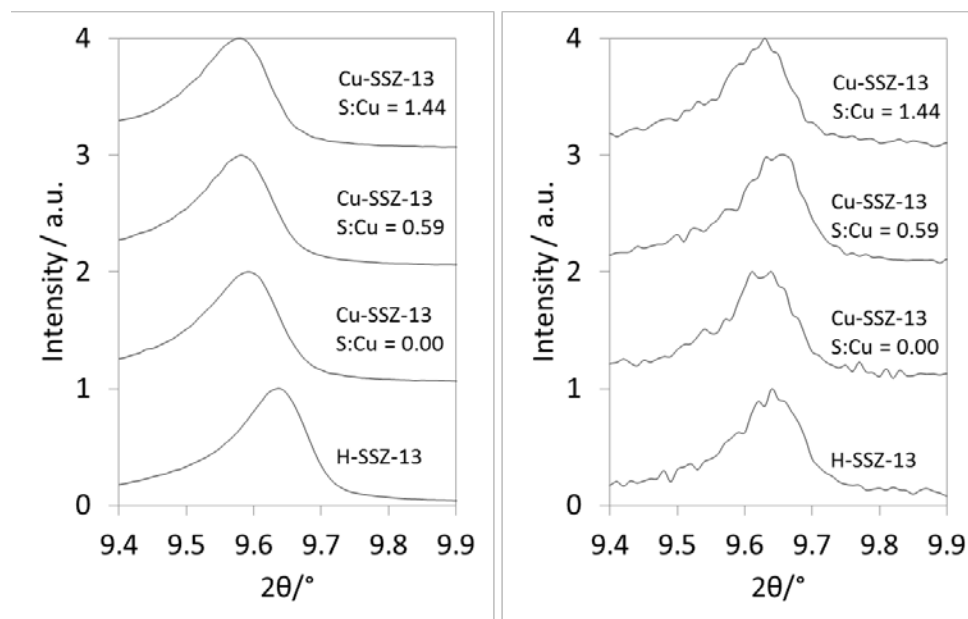
**Figure 121.** XRD patterns on  $ZCuOH$  model catalysts after dry sulfation (left) and after  $NH_3$  saturation (right). Samples on the right were saturated with 500 ppm  $NH_3$  at 453 K until saturation, then flushed with dry  $N_2$  at 453 K and cooled to room temperature.



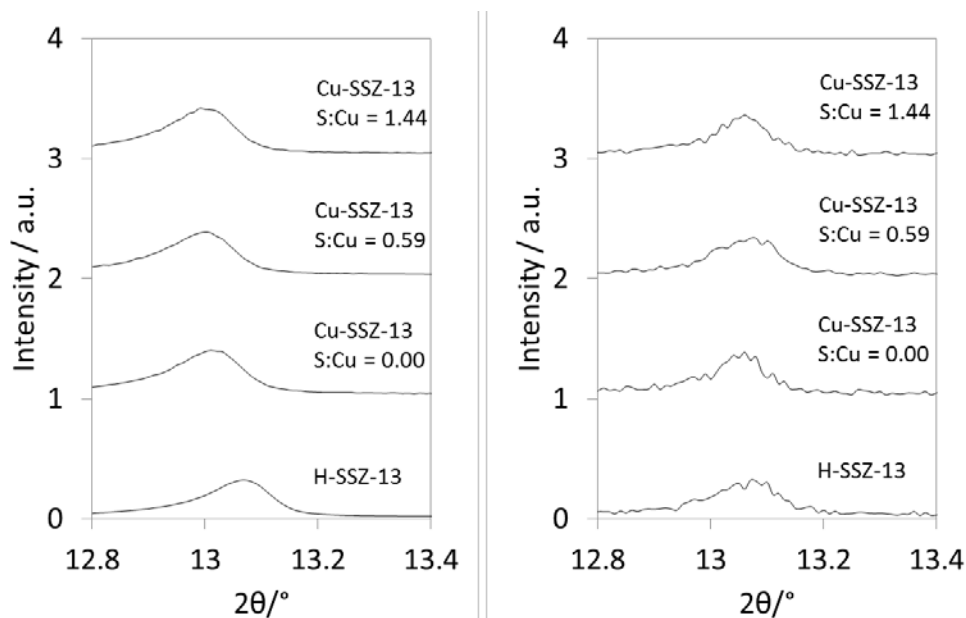
**Figure 122.** XRD patterns narrowed in on diffraction peaks at  $9.5^\circ$   $2\theta$  for  $Z_2Cu$  model catalysts after dry sulfation (left) and after  $NH_3$  saturation (right). Samples on the right were saturated with 500 ppm  $NH_3$  at 453 K until saturation, then flushed with dry  $N_2$  at 453 K and cooled to room temperature.



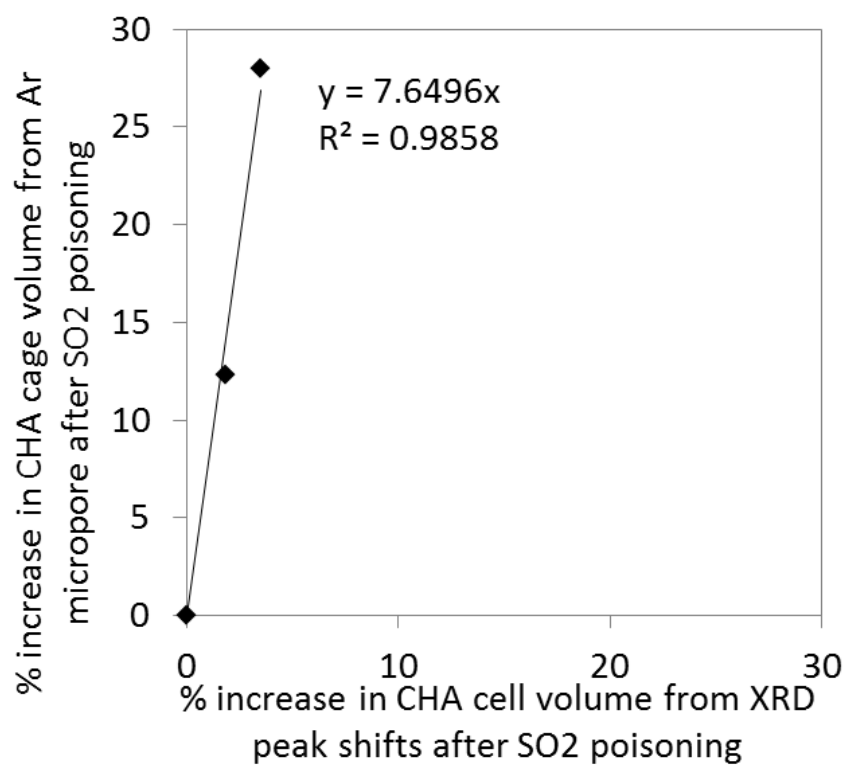
**Figure 123.** XRD patterns narrowed in on diffraction peaks at  $13^\circ$   $2\theta$  for  $Z_2Cu$  model catalysts after dry sulfation (left) and after  $NH_3$  saturation (right). Samples on the right were saturated with 500 ppm  $NH_3$  at 453 K until saturation, then flushed with dry  $N_2$  at 453 K and cooled to room temperature.



**Figure 124.** XRD patterns narrowed in on diffraction peaks at  $9.5^\circ$   $2\theta$  for ZCuOH model catalysts after dry sulfation (left) and after  $\text{NH}_3$  saturation (right). Samples on the right were saturated with 500 ppm  $\text{NH}_3$  at 453 K until saturation, then flushed with dry  $\text{N}_2$  at 453 K and cooled to room temperature.



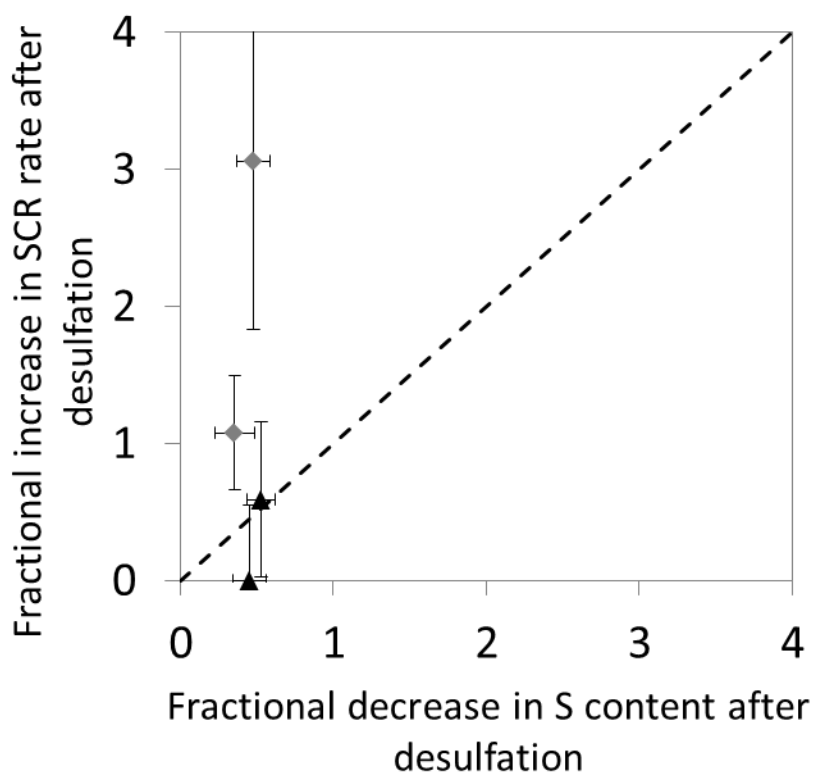
**Figure 125.** XRD patterns narrowed in on diffraction peaks at  $13^\circ$   $2\theta$  for ZCuOH model catalysts after dry sulfation (left) and after  $\text{NH}_3$  saturation (right). Samples on the right were saturated with 500 ppm  $\text{NH}_3$  at 453 K until saturation, then flushed with dry  $\text{N}_2$  at 453 K and cooled to room temperature.



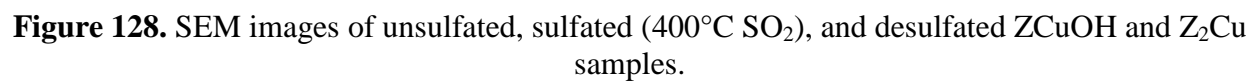
**Figure 126.** % increase in micropore volume measured using Ar micropore and XRD peak shifts on the  $Z_2Cu$  model material.



### 7.7.5 Parity plot between fractional increase in the SCR rate versus fractional decrease in sulfur content after regeneration



**Figure 127.** Fractional increase in the SCR rate after desulfation plotted versus the fractional increase in S content after desulfation. The dashed line represents parity. Error bars are 95% confidence intervals calculated from error propagation.



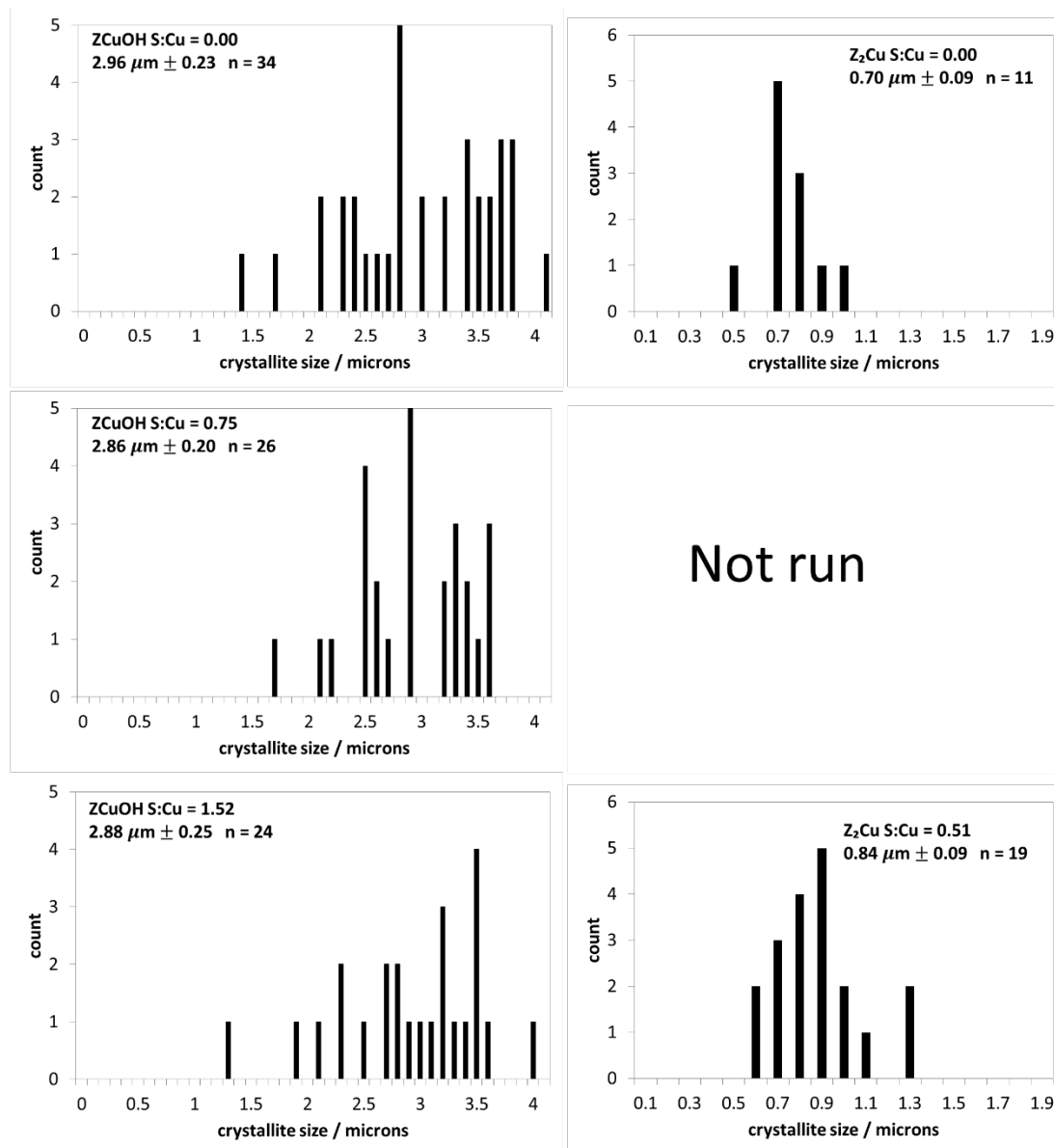


**Figure 129.** Crystallite size distribution histograms derived from SEM images. The legend reports mean average crystallite diameters with 5% confidence intervals as errors.

### 7.7.7 Transmission FTIR spectra on ZCuOH and Z<sub>2</sub>Cu model materials

Transmission FTIR was collected on a Thermo Scientific Nicolet 6700 FT-IR was used to probe changes in stretching frequencies for silanol groups, CuOH species, and Brønsted acid sites, according to the procedure used in our prior work [109]. 20 to 50 mg of sample was pelletized to prepare a 20 mm diameter wafer. All samples were dehydrated in 20% O<sub>2</sub> (99.999%, Indiana Oxygen) in balance helium (99.999 %, Indiana Oxygen) at 523 K, and cooled to room temperature before collecting spectra.

Transmission FTIR spectra collected on sulfated ZCuOH materials (Figure 130, left) reveal that silanol groups (3732 cm<sup>-1</sup>) are not perturbed upon sulfation to S:Cu values below 1, but CuOH (3650 cm<sup>-1</sup>) and Brønsted acid (3605 and 3580 cm<sup>-1</sup>) stretching frequencies shift to lower wavenumbers upon sulfation. The disappearance of the CuOH peak is consistent with the interaction of sulfur species with CuOH sites. At S:Cu values above 1, the silanol peak decreases drastically, suggesting that excess sulfur that does not poison Cu sites somehow decrease the silanol peak intensity. Transmission FTIR on sulfated Z<sub>2</sub>Cu materials (Figure 130, right) reveal that sulfur does not perturb silanol groups significantly, but does seem to decrease the intensity of Si-OH-Al groups without perturbing its stretching frequency.

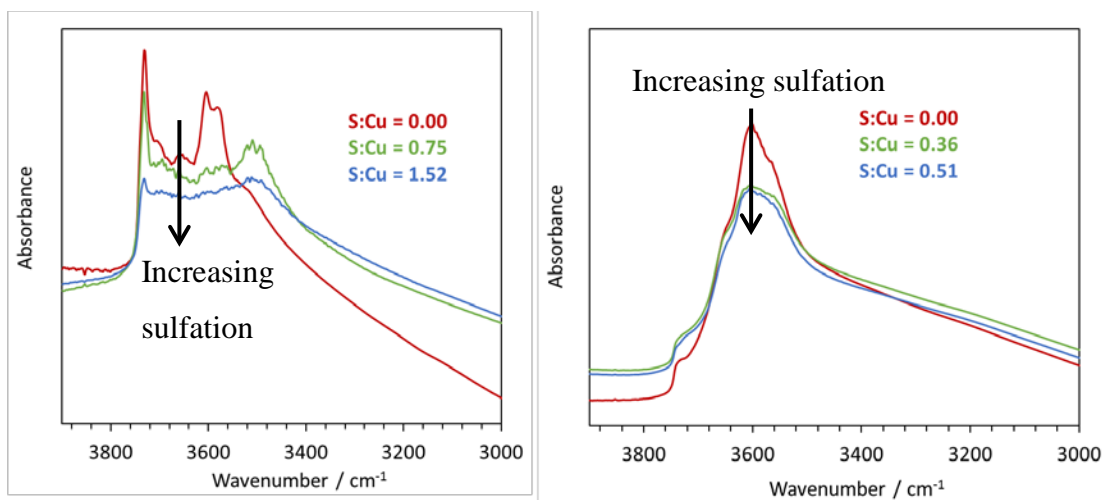


**Figure 130.** FTIR spectra normalized to mass of catalyst of ZCuOH (left) and Z<sub>2</sub>Cu (right) catalysts after sulfur poisoning.

### 7.7.8 Kinetic comparison of Cu-SAPO-34 materials in the literature to the Cu-SSZ-13 materials reported here

Several studies have been performed on sulfur-poisoned Cu-SAPO-34 catalysts [131,133,135,143,165]. Figure 131 shows the standard SCR rate and  $E_{app}$  for Cu-SAPO-34 materials plotted against the Cu-SSZ-13 materials in this study. For each equivalent of S stored on the catalysts, dry  $\text{SO}_2$  poisoning of Cu-SAPO-34 leads to more severe decreases in the turnover rate (per Cu) than for Cu-SSZ-13. In addition, the apparent activation energy on the Cu-SAPO-34 catalyst does not change with increasing S content, suggesting that the mechanism does not change with increasing sulfation.

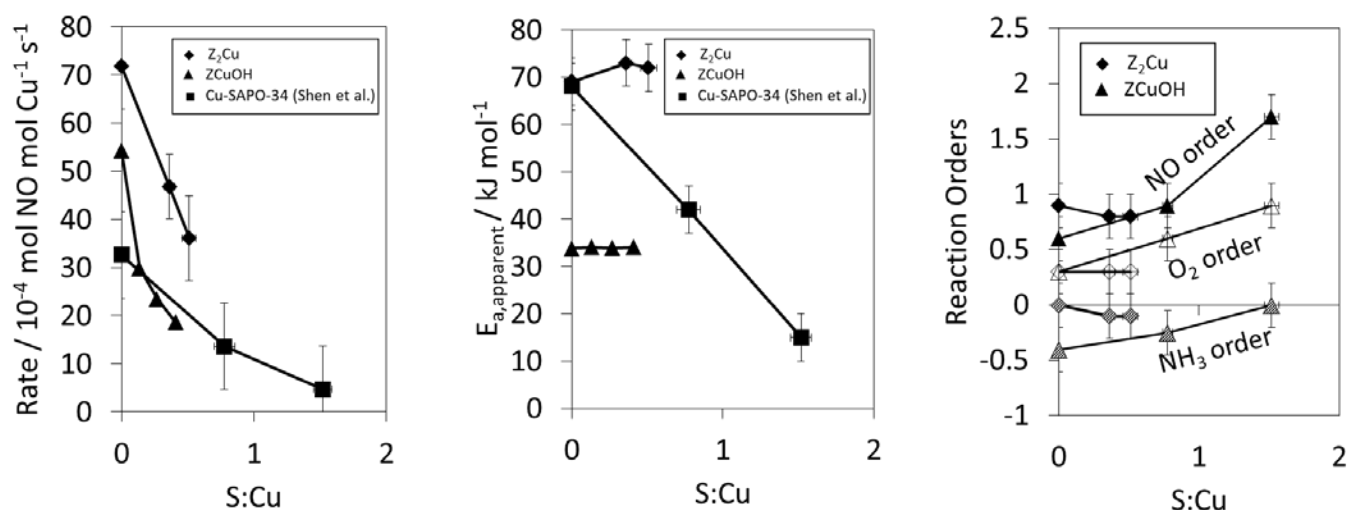


**Figure 131.** Standard SCR (300 ppm NO, 300 ppm  $\text{NH}_3$ , 10%  $\text{O}_2$ , 2.5%  $\text{H}_2\text{O}$ , 8%  $\text{CO}_2$ , in balance  $\text{N}_2$ , at 200°C) rate, apparent activation energy, and reaction orders for sulfated Cu-SSZ-13 (red and blue) and Cu-SAPO-34 (green).

### 7.7.9 Error Propagation equations used for determining reaction rate confidence intervals

**Table 28.** Governing equations used to calculate reaction rate normalized per mass catalyst, mol Cu, and (mol Cu –mol S). Concentrations of NO ( $C_{NO,in}$  and  $C_{NO,out}$ ) are in ppm.

Un-normalized rate	$-r_{NO} = \frac{(C_{NO,in} - C_{NO,out})}{1000000} \frac{P\dot{V}_{total}}{RT}$
Rate per <b>mass catalyst</b>	$-\frac{r_{NO}}{m_{cat}} = \frac{(C_{NO,in} - C_{NO,out})}{1000000} \frac{P\dot{V}_{total}}{RT} \frac{1}{m_{cat}}$
Rate per <b>mol Cu</b>	$-\frac{r_{NO}}{mol_{Cu}} = \frac{(C_{NO,in} - C_{NO,out})}{1000000} \frac{P\dot{V}_{total}}{RT} \frac{1}{m_{cat}f_{Cu} \left( \frac{1}{MW_{Cu}} \right)}$
Rate per <b>(mol Cu – mol S)</b>	$-\frac{r_{NO}}{mol_{Cu} - mol_S} = \frac{(C_{NO,in} - C_{NO,out})}{1000000} \frac{P\dot{V}_{total}}{RT} \frac{1}{m_{cat}f_{Cu} \left( \frac{1}{MW_{Cu}} \right) - m_{cat}f_S \left( \frac{1}{MW_S} \right)}$

**Table 29.** Error propagation equations used to calculate reaction rate errors normalized per mass catalyst, mol Cu, and (mol Cu –mol S). Concentrations of NO ( $C_{NO,in}$  and  $C_{NO,out}$ ) are in ppm.

Un-normalized rate	$\sigma_{r_{NO}}^2 = \left( \frac{\partial r_{NO}}{\partial C_{NO,in}} \right)^2 \sigma_{C_{NO,in}}^2 + \left( \frac{\partial r_{NO}}{\partial C_{NO,out}} \right)^2 \sigma_{C_{NO,out}}^2 + \left( \frac{\partial r_{NO}}{\partial \dot{V}_{total}} \right)^2 \sigma_{\dot{V}_{total}}^2$
Rate per <b>mass catalyst</b>	$\sigma_{r_{NO}}^2 = \left( \frac{\partial r_{NO}}{\partial C_{NO,in}} \right)^2 \sigma_{C_{NO,in}}^2 + \left( \frac{\partial r_{NO}}{\partial C_{NO,out}} \right)^2 \sigma_{C_{NO,out}}^2 + \left( \frac{\partial r_{NO}}{\partial \dot{V}_{total}} \right)^2 \sigma_{\dot{V}_{total}}^2 + \left( \frac{\partial r_{NO}}{\partial m_{cat}} \right)^2 \sigma_{m_{cat}}^2$
Rate per <b>mol Cu</b>	$\sigma_{r_{NO}}^2 = \left( \frac{\partial r_{NO}}{\partial C_{NO,in}} \right)^2 \sigma_{C_{NO,in}}^2 + \left( \frac{\partial r_{NO}}{\partial C_{NO,out}} \right)^2 \sigma_{C_{NO,out}}^2 + \left( \frac{\partial r_{NO}}{\partial \dot{V}_{total}} \right)^2 \sigma_{\dot{V}_{total}}^2 + \left( \frac{\partial r_{NO}}{\partial m_{cat}} \right)^2 \sigma_{m_{cat}}^2 + \left( \frac{\partial r_{NO}}{\partial f_{Cu}} \right)^2 \sigma_{f_{Cu}}^2$
Rate per <b>(mol Cu – mol S)</b>	$\sigma_{r_{NO}}^2 = \left( \frac{\partial r_{NO}}{\partial C_{NO,in}} \right)^2 \sigma_{C_{NO,in}}^2 + \left( \frac{\partial r_{NO}}{\partial C_{NO,out}} \right)^2 \sigma_{C_{NO,out}}^2 + \left( \frac{\partial r_{NO}}{\partial \dot{V}_{total}} \right)^2 \sigma_{\dot{V}_{total}}^2 + \left( \frac{\partial r_{NO}}{\partial m_{cat}} \right)^2 \sigma_{m_{cat}}^2 + \left( \frac{\partial r_{NO}}{\partial f_{Cu}} \right)^2 \sigma_{f_{Cu}}^2 + \left( \frac{\partial r_{NO}}{\partial f_S} \right)^2 \sigma_{f_S}^2$

## 8. SYNTHESIS OF CU-SSZ-13 MATERIALS WITH $\text{Cu}_x\text{O}_y$ SPECIES

### 8.1 Abstract

Copper speciation from aqueous ion exchange with  $\text{Cu}(\text{NO}_3)_2$  as a function of zeolite Si:Al ratio, final Cu molarity, and pH was determined from spectroscopy (UV-Visible, XAS) and selective  $\text{NH}_3$  titration of Brønsted acid (BA) sites. The following species were observed: (1) monomeric  $\text{Cu}^{2+}$  ions charged balanced by a framework O and/or an  $-\text{OH}$  ligand and (2) clustered  $\text{Cu}_x\text{O}_y$  species that are not charge-balanced by the framework. The onset of formation of  $\text{Cu}_x\text{O}_y$  species during aqueous ion exchange correlates well with Cu-precipitate formation, but not with the zeolite's point of zero charge. This study opens avenues to better understand the nature of the active site for various reactions, and to strategically synthesize Cu-zeolites with different fractions of these sites.

### 8.2 Experimental Methods

#### 8.2.1 Procedure to determine Cu-precipitation pH

$\text{Cu}(\text{NO}_3)_2$  with various molarities were prepared. 0.1 M  $\text{NH}_4\text{OH}$  was added dropwise to 10 mL of  $\text{Cu}(\text{NO}_3)_2$  while stirring until a solid precipitate was visibly observed. The mass of 0.1 M  $\text{NH}_4\text{OH}$  added was measured by difference. A calibrated Mettler Toledo S20 pH meter was used to measure the final pH. This procedure was repeated for a range of  $\text{Cu}(\text{NO}_3)_2$  molarities. The identical procedure was repeated for a range of copper acetate molarities.

### 8.3 Results and Discussion

#### 8.3.1 Effect of pH on $\text{Cu}(\text{NO}_3)_2$ precipitation with $\text{NH}_4\text{OH}$ addition

All Cu-zeolites used in SCR experiments were prepared by mixing H-zeolite with a solution of  $\text{Cu}(\text{NO}_3)_2$  then maintaining the pH of the slurry at 5 dropwise with 0.1M  $\text{NH}_4\text{OH}$  until equilibrium. As the pH is increased from acidic conditions ( $< 7$ ) at a given molarity, aqueous Cu precipitate out as  $\text{Cu}_2(\text{OH})_2$  at an intermediate pH's (hereafter called the “precipitation pH”); this phenomenon has been studied by numerous groups throughout the last century. [166–168]

A “precipitation pH” curve for  $\text{Cu}(\text{NO}_3)_2$  and  $\text{Cu}(\text{Acetate})$  shown in Figure 132 was developed using the procedure described in Appendix 7.5.1. References to literature values reported by Baes and Mesmer [168] and Regalbuto et al. [166] is also included in Figure 132. Calcination of the  $\text{Cu}_2(\text{OH})_2$  precipitate results in unsupported  $\text{Cu}_x\text{O}_y$  oxides.

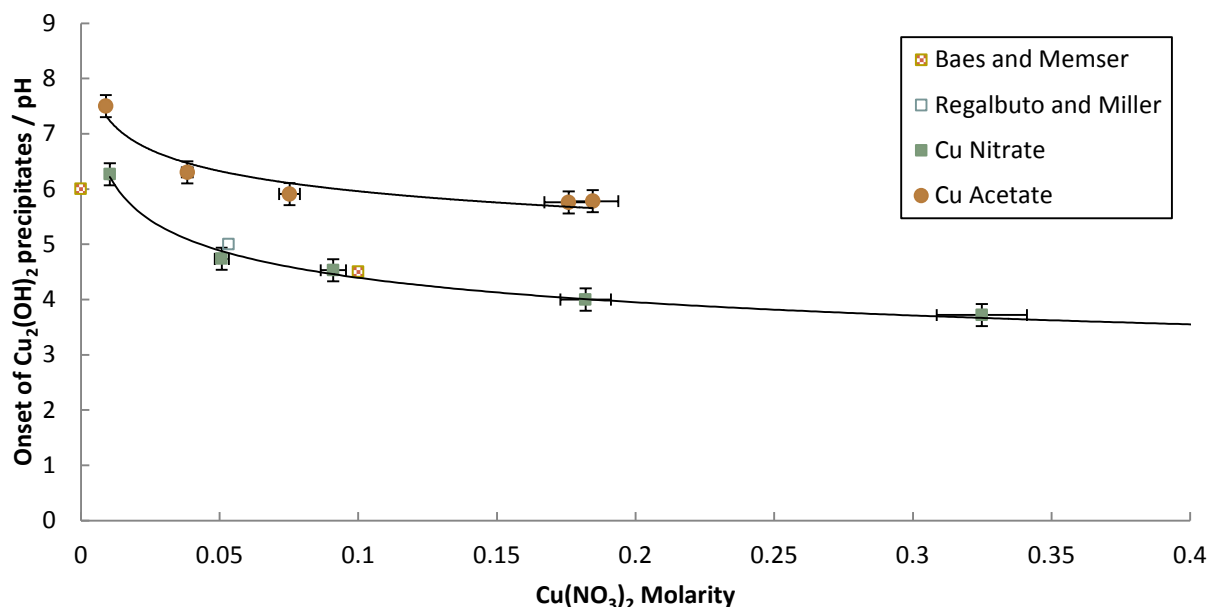


**Figure 132.** Precipitation pH curves for  $\text{Cu}(\text{NO}_3)_2$  (*black squares*) and  $\text{Cu}(\text{Acetate})$  (*black circles*) using  $\text{NH}_4\text{OH}$  as a base to increase the pH. If final equilibrium pH and Cu molarities fall above the curve,  $\text{Cu}_2(\text{OH})_2$  precipitates were observed. If final equilibrium pH and Cu molarities fall below the curve, then all Cu species are aqueous. Literature values for  $\text{Cu}(\text{NO}_3)_2$  precipitation from Baes and Mesmer ([168], *hollow square*) and Regalbuto and Miller ([166], *cross-hatched square*) are also plotted.

Combining the (1) equilibrium constant expression for the formation of  $\text{Cu}_2(\text{OH})_2$  precipitate with the (2) solubility dissociation constant of water and (3) definition of pH allows us to compute a solubility product from experimental precipitation curves in Equation 28. The derivation can be found in Appendix A.4.

$$K_{sp} = \frac{1}{[\text{Cu}^{2+}]^2 \left( \frac{K_w}{10^{-\text{pH}}} \right)^2} \quad (\text{Equation 28})$$

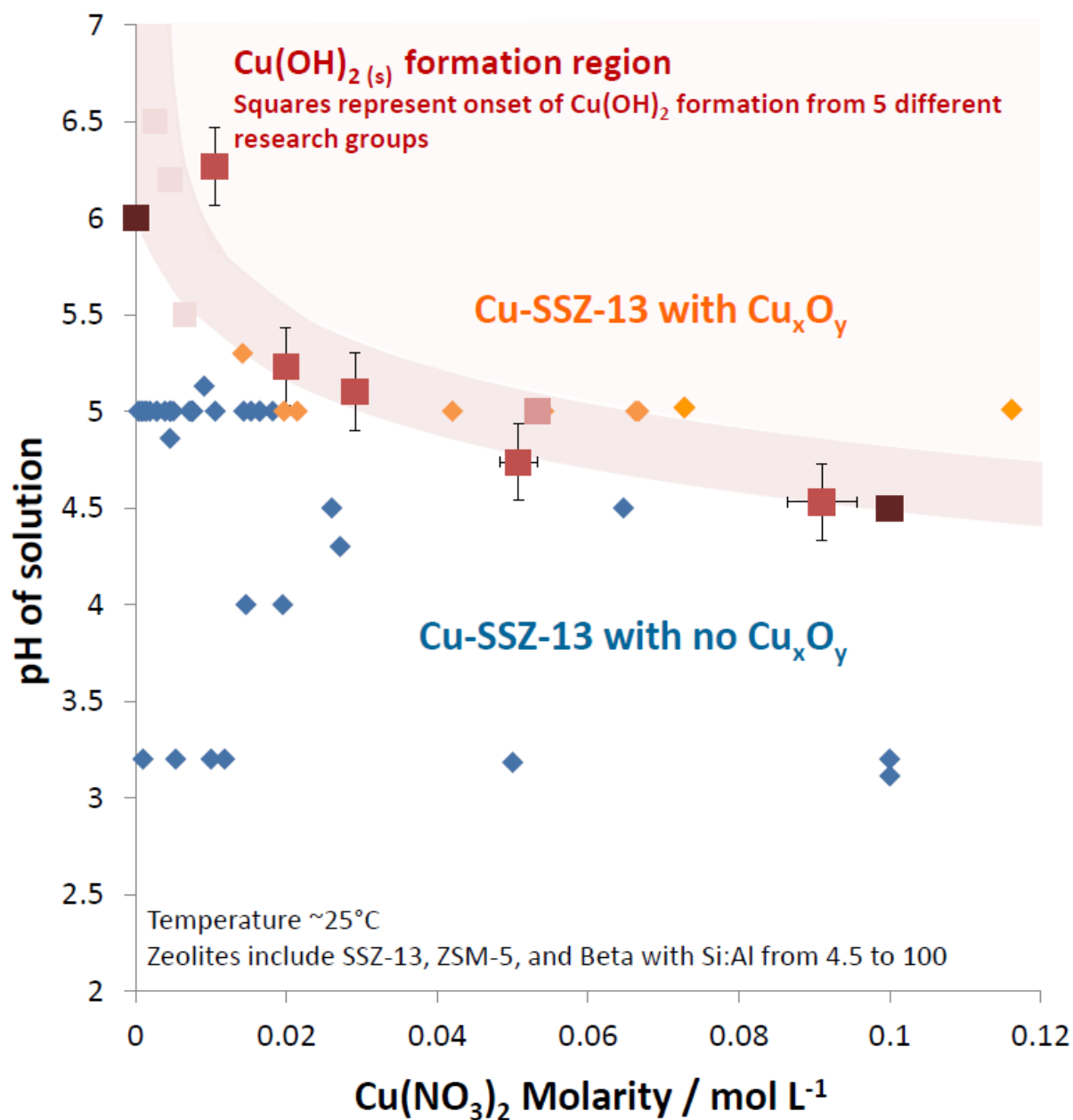
$K_{sp}$  values of  $5.5 \times 10^{20} \pm 4.5 \times 10^{20} \text{ L}^2 \text{ mol}^{-2}$  and  $4.4 \times 10^{16} \pm 3.6 \times 10^{17} \text{ L}^2 \text{ mol}^{-2}$  were obtained from the data in Figure 132 for  $\text{Cu}(\text{NO}_3)_2$  and  $\text{Cu}(\text{Acetate})$ , respectively. A reported



value for the precipitation of  $\text{Cu}_2(\text{OH})_2$  is  $2.2 \times 10^{20} \text{ L}^2 \text{ mol}^{-2}$ , which is within error of the solubility product measured for  $\text{Cu}(\text{NO}_3)_2$  [168]. Several other groups have also reported precipitation pH's and Cu molarities for  $\text{Cu}(\text{NO}_3)_2$ , of which the data is plotted in Figure 133 [166,168–170].

### 8.3.2 Effect of Cu Precipitates on Cu-speciation on Cu-zeolites

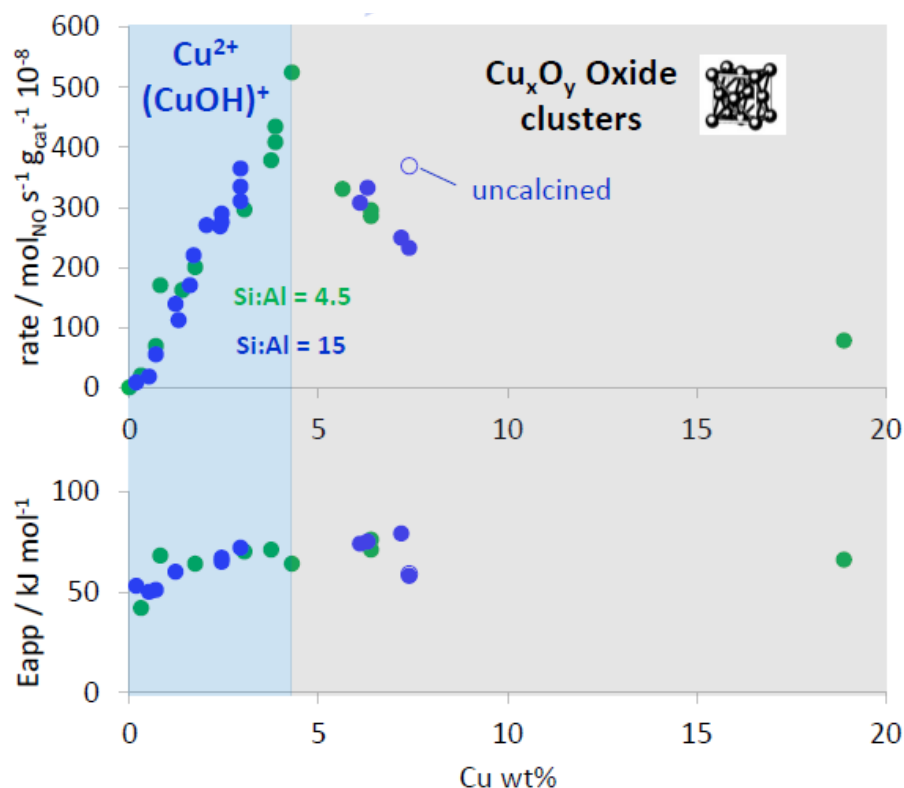
The exchange conditions for Cu-exchanged zeolites (SSZ-13, Beta, ZSM-5) using  $\text{Cu}(\text{NO}_3)_2$  as the Cu precursor and  $\text{NH}_4\text{OH}$  to control the pH were collected and plotted on the Cu-precipitation curve as shown in Figure 133. The pH of the solution (y-axis) designates the final pH of the ion-exchange slurry at equilibrium and the molarity represents the molarity of  $\text{Cu}(\text{NO}_3)_2$  in the liquid (not counting the Cu that has exchanged into the zeolite) at equilibrium. All samples that turned black after calcination (orange diamonds) appear either on or above the pH precipitation curve. All samples that exhibit no noticeable formation of  $\text{Cu}_x\text{O}_y$  clusters (blue diamonds) after calcination appear either on or below the pH precipitation curve. These results suggest the onset of undesirable black  $\text{Cu}_x\text{O}_y$  species is likely due to the collection of both Cu-zeolites and  $\text{Cu}_2(\text{OH})_2$  precipitate if Cu-exchange conditions are such that the final pH and Cu molarity at equilibrium falls above the pH precipitation curve. Upon calcination, these  $\text{Cu}_2(\text{OH})_2$  may oxidize and form black  $\text{Cu}_x\text{O}_y$  that agglomerate on and/or in the Cu-zeolite samples.



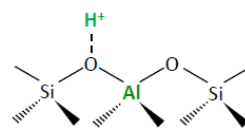
**Figure 133.** Concentration of Cu(NO<sub>3</sub>)<sub>2</sub> and pH important at equilibrium during Cu-exchange for all Cu-zeolite (SSZ-13, ZSM-5, and Beta) samples Cu-exchanged. Cu-exchanged zeolites that did not exhibit black Cu<sub>x</sub>O<sub>y</sub> clusters after calcination are represented as *blue diamonds*. Cu-exchanged zeolites that did exhibit black Cu<sub>x</sub>O<sub>y</sub> clusters after calcination are represented as *orange diamonds*. The precipitation pH for Cu(NO<sub>3</sub>)<sub>2</sub> is represented by black squares the precipitation curve model (*light red trace*).

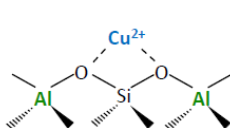
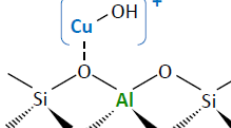
Many groups have also performed liquid Cu ion-exchange on zeolites, with and without pH control and collected UV-Visible-NIR spectra characteristic of Cu-zeolite samples without


$\text{Cu}_x\text{O}_y$  clusters. [37–42] All their equilibrium pH and solution molarities fall below the Cu-precipitation curve, indicating that  $\text{Cu}_2(\text{OH})_2$  were likely not present.



**Figure 134.** The SCR NO consumption reaction rate normalized per gram of catalyst plotted versus the Cu wt% (top) and the SCR NO consumption apparent activation energy plotted versus the Cu wt% (bottom). Standard SCR conditions (300 ppm NO, 300 ppm  $\text{NH}_3$ , 10%  $\text{O}_2$ , 7%  $\text{CO}_2$ , 2.5%  $\text{H}_2\text{O}$ , balance  $\text{N}_2$ , 200°C). Cu-SSZ-13 catalysts with Si:Al molar ratios of 4.5 and 15 and Cu wt%*s* between 0 and 19 were synthesized and used for this study. The blue shaded area between 0 to 4 wt% represents samples with all Cu as ionic  $\text{Cu}^{2+}/\text{Cu}^{1+}$  species. The grey shaded area between 4 to 19 wt% represents samples that contain bulk  $\text{Cu}_x\text{O}_y$  species.

**H<sup>+</sup> site (Brønsted acid)**  


**Cu site (Lewis acid)**  



**Cu<sub>x</sub>O<sub>y</sub> Oxide Cluster**  
  
Image from Da Costa et al. (2002)

Chemistry	H <sup>+</sup> site	Cu <sup>2+</sup> site	(CuOH) <sup>+</sup> site	Cu <sub>x</sub> O <sub>y</sub> Oxide clusters
Fast Selective Catalytic Reduction (fast SCR) $NO + NO_2 + 2NH_3 + O_2 \rightarrow 2N_2 + 3H_2O$	✓	✓	✓	?
Standard Selective Catalytic Reduction (std SCR) $4NO + 4NH_3 + O_2 \rightarrow 4N_2 + 6H_2O$	X	✓	✓	X
Dry NO Oxidation $2NO + O_2 \rightarrow 2NO_2$	X	X	?	✓
NH <sub>3</sub> Oxidation $4NH_3 + 3O_2 \rightarrow 2N_2 + 6H_2O$	X	✓	✓	?

**Key**

✓ = active

X = not active

? = uncertain

**Figure 135.** Catalytic activities of four different sites present on Cu-SSZ-13 (Brønsted acid sites, Z<sub>2</sub>Cu sites, ZCuOH sites, and Cu<sub>x</sub>O<sub>y</sub> cluster sites) for four different reactions (fast SCR [171], standard SCR [43,109], dry NO oxidation [122], NH<sub>3</sub> oxidation (Appendix H). Check marks indicate that the particular site is active for and catalyzes the particular reaction, X marks indicate that particular site is not active for the particular reaction, and question marks indicate that it is uncertain whether the particular site is active.

Figure 134 plots the SCR reaction rate as a function of Cu wt% for a series of Cu-SSZ-13 catalysts with Si:Al = 4.5 and 15. We observe that when copper exist as only ionic Cu<sup>2+</sup>/Cu<sup>1+</sup> species, the reaction rate increases nearly linearly with Cu wt%, however as Cu<sub>x</sub>O<sub>y</sub> species increase above a Cu wt% of 4, the SCR reaction rate decreases while the apparent activation energy stays constant. These kinetics suggest that Cu<sub>x</sub>O<sub>y</sub> species are inactive for SCR, and decreases the SCR reaction rate by converting ionic Cu into Cu<sub>x</sub>O<sub>y</sub> species, by pore blocking, or another comparable scenario consistent with the kinetics. The unchanged activation energy between 4 to 19 Cu wt% does suggest that the remaining Cu that's able to turnover is turning over via the same mechanistic pathway regardless of whether Cu<sub>x</sub>O<sub>y</sub> clusters are present or not. Results from Figure 133 suggest the onset of undesirable black Cu<sub>x</sub>O<sub>y</sub> species is likely due to the collection of both Cu-zeolites and Cu(OH)<sub>2</sub> precipitate if Cu-exchange conditions are such that

the final pH and Cu molarity at equilibrium falls above the pH precipitation curve. Upon calcination, these  $\text{Cu}(\text{OH})_2$  may oxidize and form unsupported black  $\text{Cu}_x\text{O}_y$  that agglomerate on the outer surface of Cu-zeolite samples, effectively preventing gas molecules from reaching the active sites. This is a possible explanation of why the SCR reaction rate normalized per gram catalyst decreases on black oxidized samples, but the apparent activation energies are the same within error when compared to blue Cu-SSZ-13 samples.

UV-Visible and XAS spectroscopic characterization on Cu-SSZ-13 catalysts with and without these  $\text{Cu}_x\text{O}_y$  species have been reported in Verma et al. [122]. From Verma et al., the appearance of UV-Visible features ( $17000$  to  $37000\text{ cm}^{-1}$ ) and XAS pre-edge features ( $8.987\text{ keV}$ ) seem to be indicative of the presence of  $\text{Cu}_x\text{O}_y$  species.

### 8.3.3 Implications of Cu-Precipitation

Commercially for the standard SCR reactor in the aftertreatment system, samples with black  $\text{Cu}_x\text{O}_y$  oxides are undesirable due to the lower SCR rate compared to samples with no  $\text{Cu}_x\text{O}_y$  clusters, as represented by all samples with Cu wt% larger than 4%. Findings from this study suggest that it may be possible for our group to synthesize Cu-SSZ-13 without black  $\text{Cu}_x\text{O}_y$  species at Cu wt% greater than 3.8 wt% (Cu-SSZ-13 Si:Al = 4.5 Cu:Al = 0.21). The sample Cu wt% of 3.8 has only titrated 50% of all its BA sites, meaning that 50% of possible Cu exchange sites can still be utilized. It is unknown when steric hinderance effects as more Cu exchange into the zeolite will play a role on the speciation of Cu or the SCR reaction rate.

## 8.4 Conclusions

The  $\text{Cu}(\text{NO}_3)_2$  molarity and pH of solution are two factors that can be utilized to control the precipitation of  $\text{Cu}(\text{OH})_2$  (s) species. During aqueous Cu-exchange, the presence of  $\text{Cu}(\text{OH})_2$  species lead to a physical mixture of  $\text{Cu}(\text{OH})_2$  particulates in presence with Cu-SSZ-13 catalysts with  $\text{Cu}^{2+}$  cations electrostatically tethered to anionic sites in the zeolite. Upon calcination, these  $\text{Cu}(\text{OH})_2$  species may solid-state exchange into the zeolite into ionic  $\text{Cu}^{2+}$  species, but a number is oxidized into  $\text{Cu}_x\text{O}_y$  species, as evidenced by UV-Visible and XAS spectroscopy. It is demonstrated that samples with a combination of different sites ( $\text{H}^+$ ,  $\text{Cu}^{2+}$ ,  $(\text{CuOH})^+$ ,  $\text{Cu}_x\text{O}_y$ ) can be

active or inactive for various different reactions, supporting the statement that “the amount of surface which is catalytically active is determined by the reaction catalyzed” by H.S. Taylor [172]. We demonstrated how the nature of the sites can be tailored during various steps of the synthesis of Cu-SSZ-13 zeolites, namely through aqueous ion-exchange. Previous chapters (3 and 4) also demonstrate that the hydrothermal zeolite synthesis and pretreatments prior to characterization or reaction can also modify the fraction and nature of sites. These three chapters collectively demonstrate that anionic Al sites in a zeolite are in general not ordered and at a given Si:Al ratio, a zeolite presents a distribution of local anionic Al sites. The density and spatial distribution of Al environment coupled with Cu-exchange conditions affects the type of Cu species, resulting in unique consequences for a rich variety of chemistries. The identification and ultimate quantification of sites will pave way for determining the nature of active sites during a number of reactions on these Cu-SSZ-13 materials, and thus accelerate mechanistic studies and the design of improved catalysts with higher fraction of active sites.

## 8.5 Acknowledgements

The author acknowledges Jonatan Albaraccin, Ishant Khurana, Lucia Perez, and Andres Pena for assistance in synthesizing Cu-SSZ-13, Cu-ZSM-5, and Cu-Beta materials used in this study. The author would also like to acknowledge Ishant Khurana, Andres Pena, and Trevor Lardinois for invaluable discussions on  $\text{Cu}_x\text{O}_y$  speciation.

**APPENDIX A. BACK-OF-THE-ENVELOPE CALCULATIONS AND DERIVATIONS**

**A.1 Energy Equivalence between gas tanks and smartphone batteries**

**Table 30.** Energy density (watt-hours) for gasoline, diesel, and a smartphone battery.

Energy Storage Item	Watt-hour
Gasoline [173]	34,000 per gallon
Diesel [173]	38,000 per gallon
Smartphone Battery [174]	11 per smartphone battery

Unit conversions tell us that the energy in 1 gallon of gasoline is enough to charge approximately 46000 smartphones.

$$\begin{aligned} & (1 \text{ gallon of gasoline}) \left( 34000 \frac{Wh}{\text{gallon}} \right) \left( 15 \frac{\text{gallons}}{\text{tank}} \right) \left( \frac{1}{11} \frac{\text{smartphone}}{Wh} \right) \\ &= 46000 \frac{\text{smartphones}}{\text{tank}} \end{aligned}$$

Since it takes approximately 3 minutes to fill up a 15 gallon tank at a gas station, the rate of energy transfer is approximately 10,000,000 watts.

**Table 31.** Rate of energy transfer for transferring energy into a gasoline automobile, electric car, and cell phone.

**\*3000 mAh \* (1 Ah /1000 mAh) \*3.7 V = 14.8 Wh**

Energy Source	Rate of energy transfer / Watts
Gasoline:	$\left(34000 \frac{Wh}{gallon}\right) \left(15 \frac{gallons}{tank}\right) \left(\frac{1}{3 minutes}\right) \left(\frac{60 minutes}{1 hour}\right)$ $= 10000000 Watts$
Electric Car [175]	1000 to 1500 Watts
Cell Phone [174]:	3 to 7 Watts

## A.2 Derivation of relation between %O<sub>2</sub> in fuel mixture and Air-to-Fuel ratio

Given the following governing equations:

Definition of the air-to-fuel ratio:

$$(A:F) = \frac{V_{air}}{V_{fuel}}$$

Definition of percent oxygen:

$$\%O_2 = \frac{V_{O_2}}{V_{total}} \cdot 100$$

O<sub>2</sub> content in air on earth:

$$V_{air} = 5V_{O_2}$$

Volume balance:

$$V_{total} = V_{air} + V_{fuel}$$

Combining the four equations above gives:

$$\%O_2 = 20 \cdot \frac{(A:F)}{(A:F) + 1}$$



### A.3 Proposed Definition of Cu-Exchange Level

Following our Cu-speciation studies, we define a new term for computing the % Cu exchange. Literature studying Cu-zeolites overwhelmingly assumes a 2:1 Cu:Al exchange ratio, defining the % Cu exchange as:

$$\% \text{ Cu Exchange} = 100(2 \text{ Cu: Al})$$

This equation does not account for the fact that Cu can speciate as  $[\text{CuOH}]^+$  and only titrate one BA site. It also assumes that the total bulk Al in the zeolite support are framework Al that give rise to sites that can be titrated by cations.

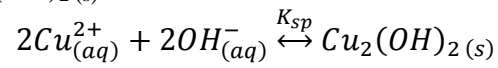
A more appropriate definition for % Cu exchange would be:

$$\% \text{ Exchange} = 100 \frac{2(\text{Co: Al}) + ((\text{Cu: Al}) - (\text{Co: Al}))}{\text{NH}_3: \text{Al}}$$

Where the Co:Al is be measured using AAS after Co-exchange to saturation of paired  $\text{Al}_f$  [105], Cu:Al is measured using AAS after Cu-exchange, and  $\text{NH}_3$ :Al can be measured using  $\text{NH}_3$ -TPD which quantifies the number of BA sites titrated by  $\text{NH}_3$  on the parent H-form [90,91]. The Co:Al can also be measured by measuring  $\text{NH}_3$ :Al ratios on a series of samples with different Cu loading and determining the inflection point between Cu siting at two Al sites and one Al site.

#### A.4 Cu<sub>2</sub>(OH)<sub>2</sub> Precipitation Equilibrium Constant (K<sub>sp</sub>) Derivation

Equilibrium constant for Cu(OH)<sub>2</sub> (s) formation:



$$K_{sp} = \frac{[Cu_2(OH)_2]}{[Cu^{2+}]^2[OH^{-}]^2} \sim \frac{1}{[Cu^{2+}]^2[OH^{-}]^2}$$

Definition of pH:

$$pH = -\log[H^{+}]$$

Solubility dissociation constant for water:

$$K_w = [OH^{-}][H^{+}] \sim 1 * 10^{-14} \frac{mol}{dm^{-6}} @ RT \rightarrow [OH^{-}] = \frac{K_w}{[H^{+}]}$$

Combine:

$$K_{sp} = \frac{1}{[Cu^{2+}]^2 \left( \frac{K_w}{10^{-pH}} \right)^2}$$

### A.5 Equations used to calculate the number of framework Al ( $Al_f$ ) from $NH_3$ TPD titration of Brønsted Acid sites on H-zeolites

#### Measuring the molar density of $H^+$ sites:

In the framework:

$$H^+:Al_f = BA:Al_f = NH_3:Al_f = 1$$

For most zeolite samples:

$$H^+:Al_t = H^+:(Al_f + Al_{ex}) < 1$$

AutoChemII-MSD BA intensity:

$$I = \frac{A_{NH_3}}{A_{Ar}} \cdot \frac{1}{m_{i,TPD} \left[ 1 - \frac{m_{i,TGA} - m_{f,TGA}}{m_{i,TGA}} \right]}$$

Calibration:

$$M_{H^+} = \frac{I}{31058} [=] \text{mol } H^+ \text{ g}^{-1}$$

#### Measuring the molar density of Cu sites (using AAS):

#### Calculate the mass density of dissolved sample

$$\left[ \frac{mg_{sample}}{L} \right] = \frac{m_{sample}}{V_{HF} + V_{water}} = \frac{m_{sample}}{m_{HF} \left( \frac{mL}{1.15g} \right) + m_{H_2O} \left( \frac{mL}{1.00g} \right)}$$

Measure the mass density of Cu in the dissolved sample solution:

$$\left[ \frac{m_{Cu}}{L} \right]$$

Cu wt%:

$$Cu \text{ wt\%} = \frac{\left[ \frac{m_{Cu}}{L} \right]}{\left[ \frac{mg_{sample}}{L} \right]}$$

**Beta Unit Cell:**  $[Al_nSi_{64-n}O_{128}]$

Atomic Balance:

$$n_{Al} = \frac{64}{1+(Si:Al)}, n_{Si} = 64 - n_{Al}, n_O = 128$$

Mass of unit cell: (coefficients are molecular masses of H, Si, Al, and O atoms):

$$m_{unit} = 1 \cdot n_H + 28 \cdot n_{Si} + 27 \cdot n_{Al} + 16 \cdot n_O$$

Molar mass of Al:

$$M_{Al_f} = \frac{n_{Al}}{m_{unit}} [=] \text{mol Al } g^{-1}$$

$$H^+: Al = \frac{M_{H^+}}{M_{Al_f}}$$

$$Cu: Al = \frac{M_{Cu}}{M_{Al_f}}$$

**Chabazite Unit Cell:**  $[Al_nSi_{36-n}O_{72}]$

Mole Balance:

$$n_{Al} = \frac{36}{1+(Si:Al)}, n_{Si} = 36 - n_{Al}, n_O = 72$$

Mass of unit cell: (coefficients are molecular masses of H, Si, Al, and O atoms)

$$m_{unit} = 1 \cdot n_H + 28 \cdot n_{Si} + 27 \cdot n_{Al} + 16 \cdot n_O$$

Molar mass of Al:

$$M_{Al_f} = \frac{n_{Al}}{m_{unit}} [=] \text{mol Al } g^{-1}$$

**MFI Unit Cell:**  $[Al_nSi_{96-n}O_{192}]$

$$n_{Al} = \frac{64}{1+(Si:Al)}, n_{Si} = 64 - n_{Al}, n_O = 128$$

$$m_{unit} = 1 \cdot n_H + 28 \cdot n_{Si} + 27 \cdot n_{Al} + 16 \cdot n_O$$

$$M_{Al_f} = \frac{n_{Al}}{m_{unit}} [=] \text{mol Al } g^{-1}$$

$$H^+: Al = \frac{M_{H^+}}{M_{Al_f}}$$

$$Cu: Al = \frac{M_{Cu}}{M_{Al_f}}$$

## APPENDIX B. HYDROTHERMAL SYNTHESIS AND CHARACTERIZATION OF CHABAZITE

### B.1 XRD

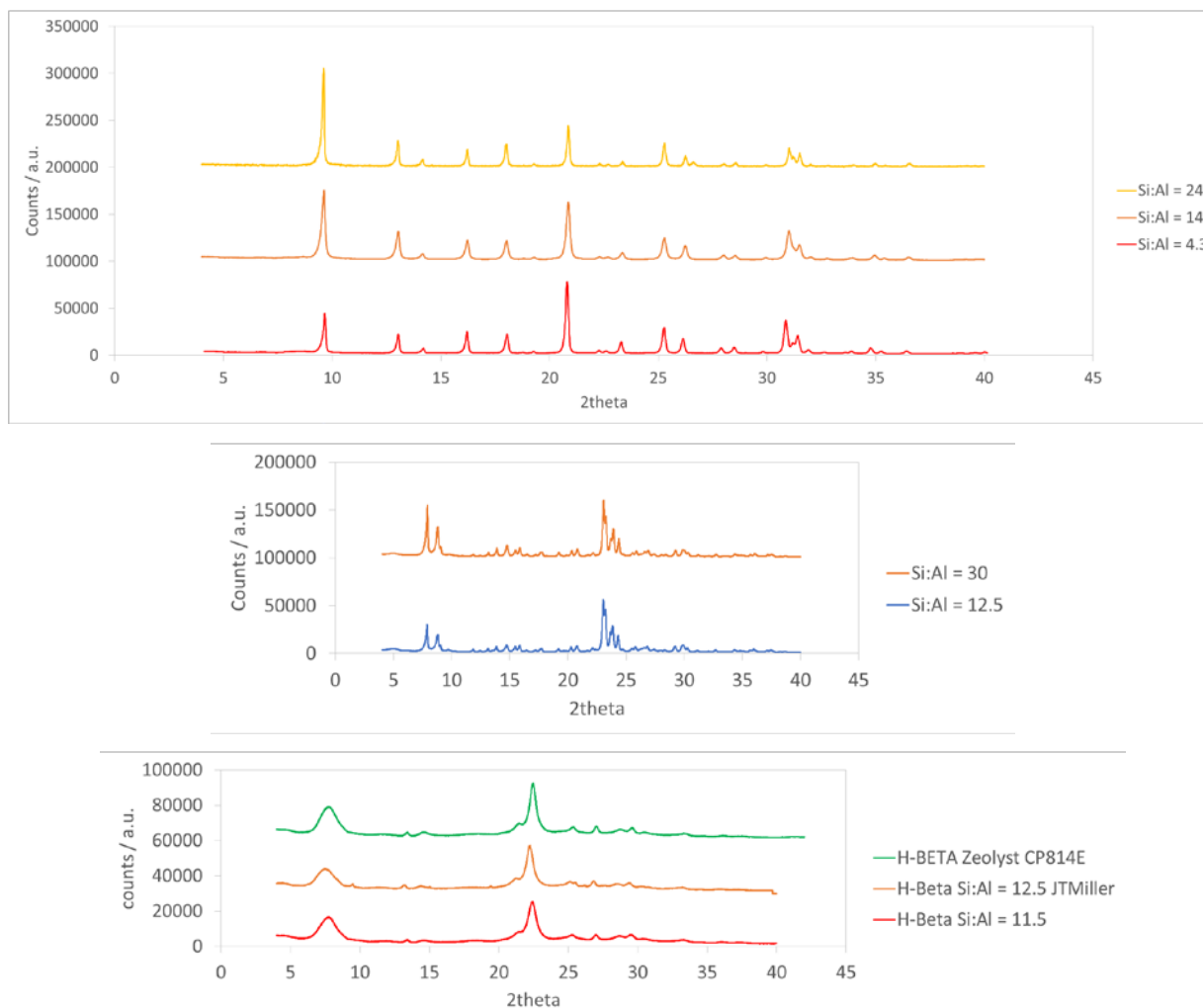


**Figure 136.** XRD spectra on the H-form of all SSZ-13 (top), ZSM-5 (middle), and Beta (bottom) zeolite supports used. Peak locations were consistent for those of SSZ-13, ZSM-5, and Beta, respectively.

## B.2 Al<sup>27</sup> NMR

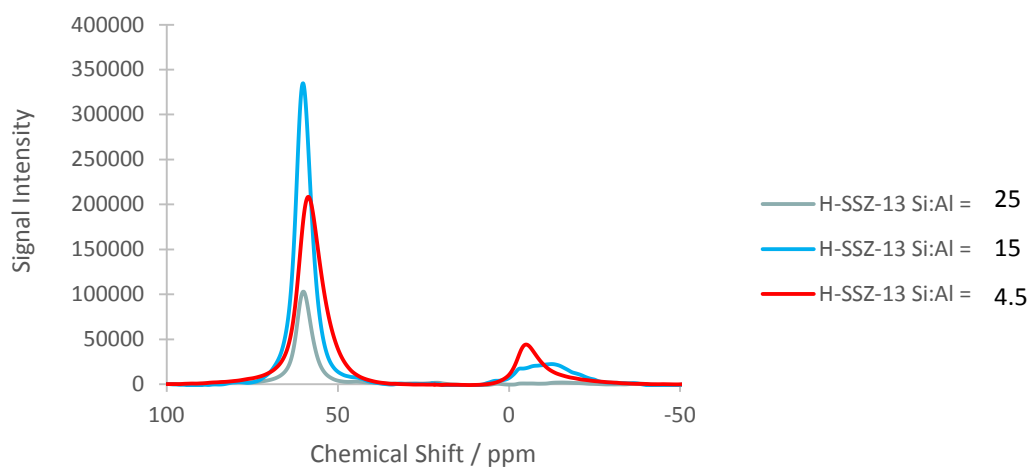


**Figure 137.** <sup>27</sup>Al-NMR spectra collected on H-SSZ-13 with Si:Al ratios of 4.5, 15, and 25.

**Table 32.** The fraction of tetrahedral and octahedral Al measured by quantifying the area under the curve for the tetrahedral feature (60 ppm chemical shift) and octahedral feature (-5 ppm chemical shift).s

	Si:Al = 4.5	Si:Al = 15	Si:Al = 25
Fraction Tetrahedral	0.85	0.95	1.00
Fraction Octahedral	0.15	0.05	0.00

### B.3 NH<sub>3</sub> TPD

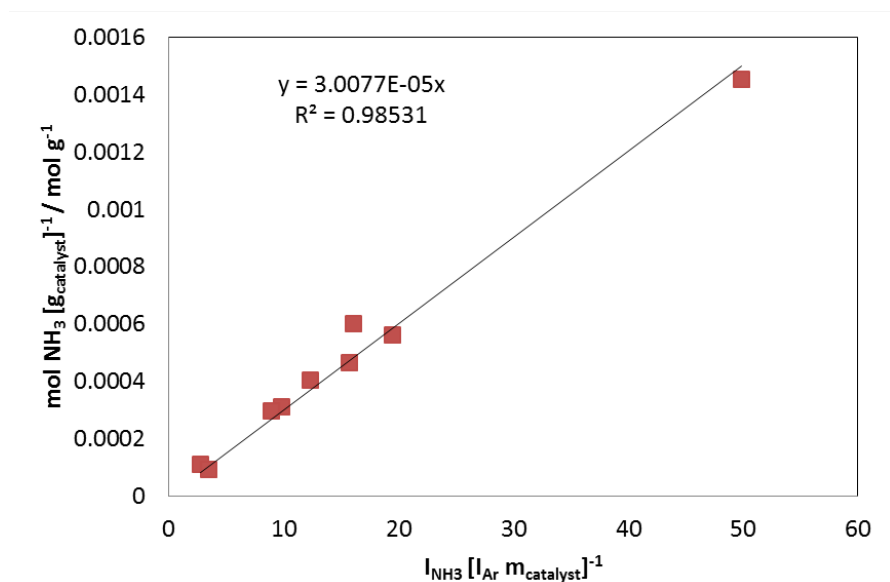


**Figure 138.** Calibration curve to convert a measured normalized intensity of NH<sub>3</sub> in the AutoChemII-MSD to the actual mol NH<sub>3</sub> g<sup>-1</sup> desorbed from the sample during TPD. The mol NH<sub>3</sub> g<sup>-1</sup> desorbed from the sample can be used to determine the NH<sub>3</sub>:Al ratio of zeolites, which is equal to the H:Al ratio assuming each NH<sub>3</sub> truly titrates one BA site during liquid NH<sub>4</sub>-exchange.

## B.4 SEM and EDS

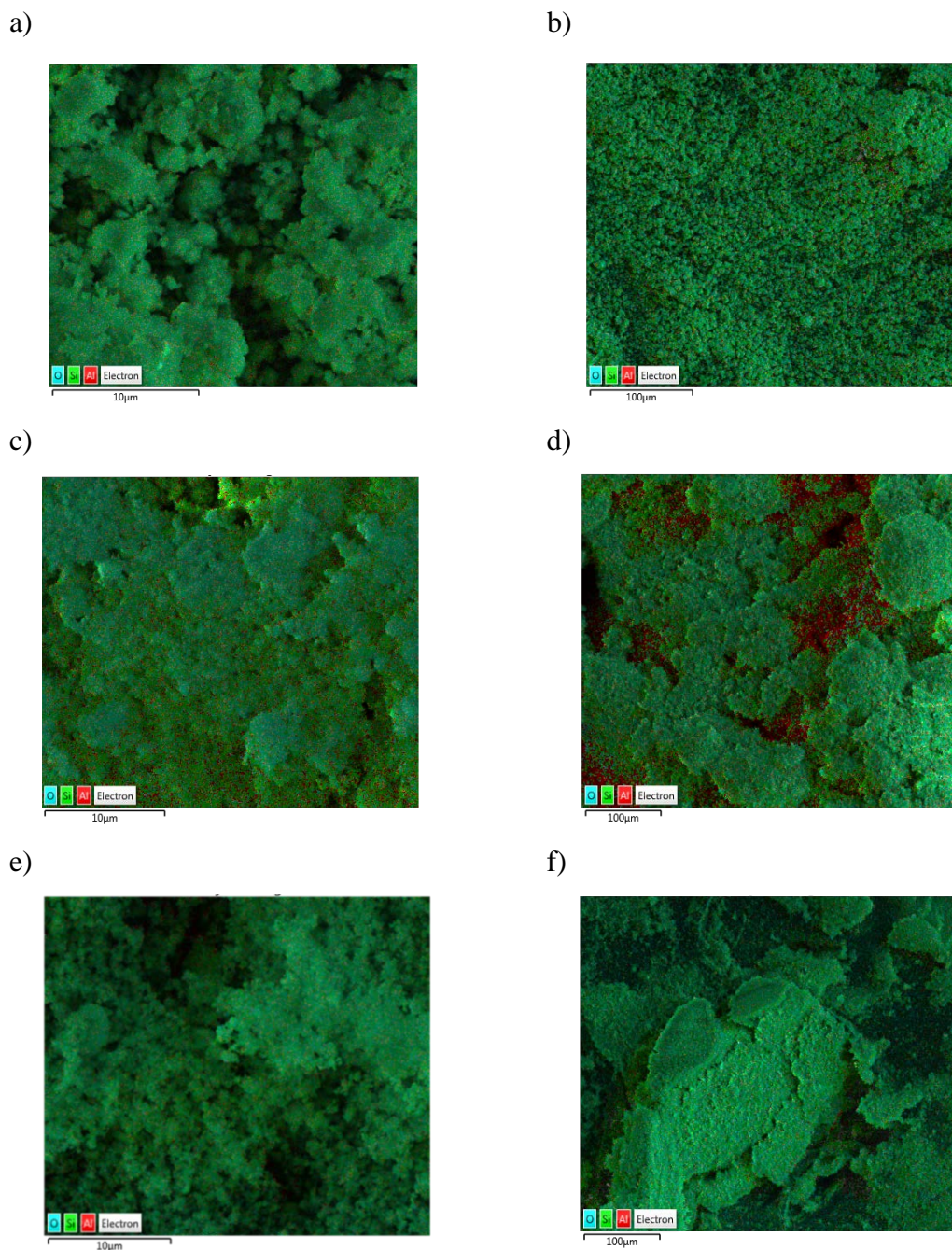


**Figure 139.** Scanning electron microscopy (SEM) and electron dispersive x-ray spectroscopy (EDS) used to determine distributions of Si and Al in the commercial H-ZSM-5 with Si:Al = 12.5 at resolutions of 10 μm (a) and 100 μm (b), Si:Al = 18 at resolutions of 10 μm (c) and 100 μm (d), and Si:Al = 30 at resolutions of 10 μm (e) and 100 μm (f). In all images, a green pixel represents the detection of Si atoms and a red pixel represents the detection of Al atoms.



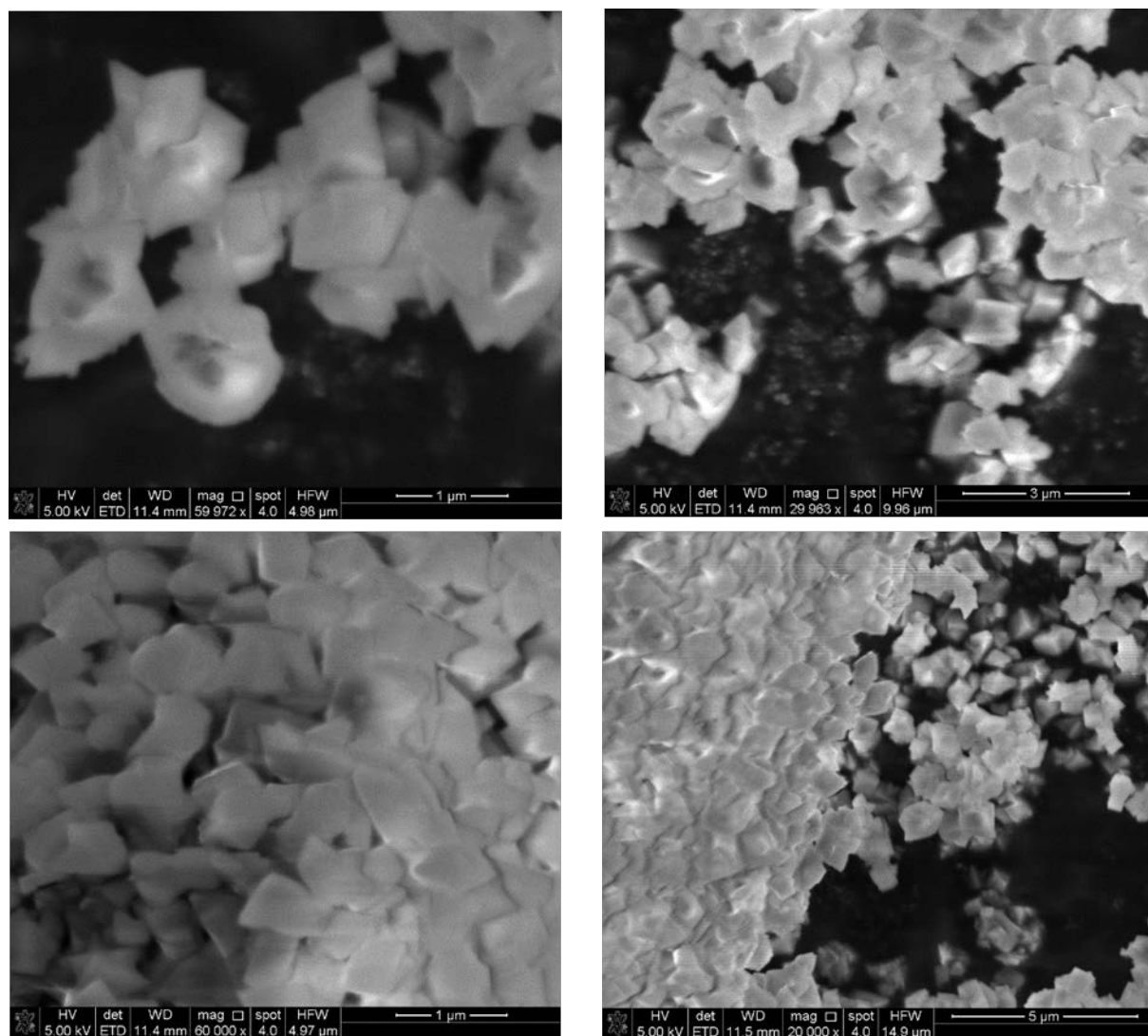


**Figure 140.** SEM images on H-SSZ-13 Si:Al = 4.5

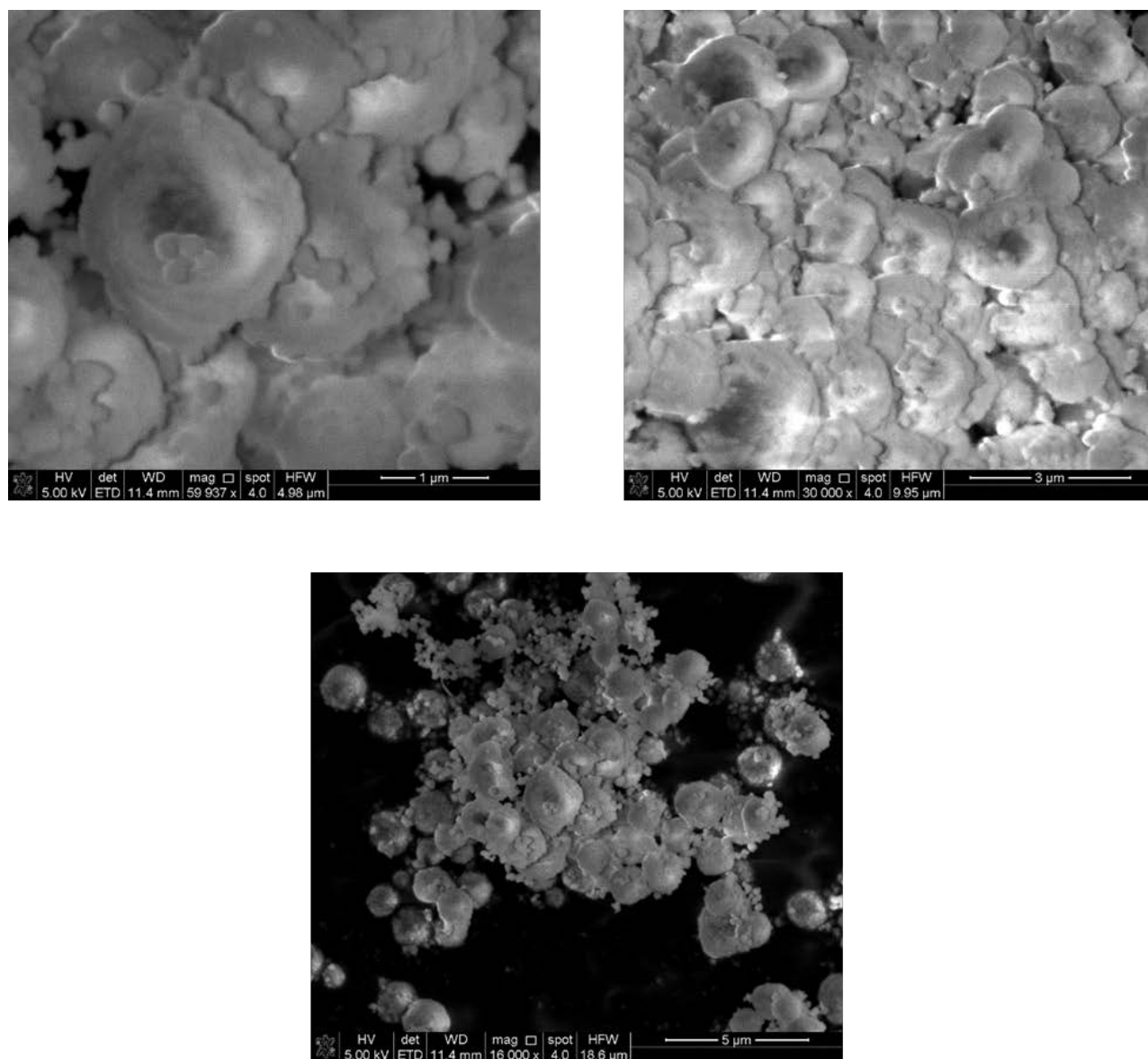


**Figure 141.** SEM images on H-SSZ-13 Si:Al = 15

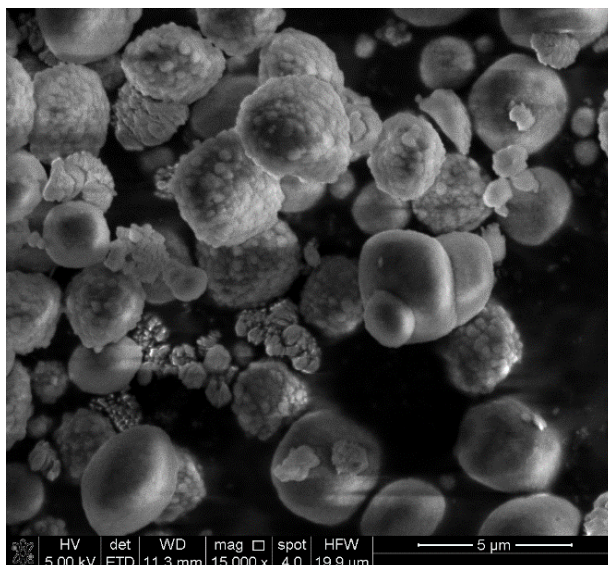


**Figure 142.** SEM images on H-SSZ-13 Si:Al = 25 synthesized via direct tumbling 10 days at 160°C.

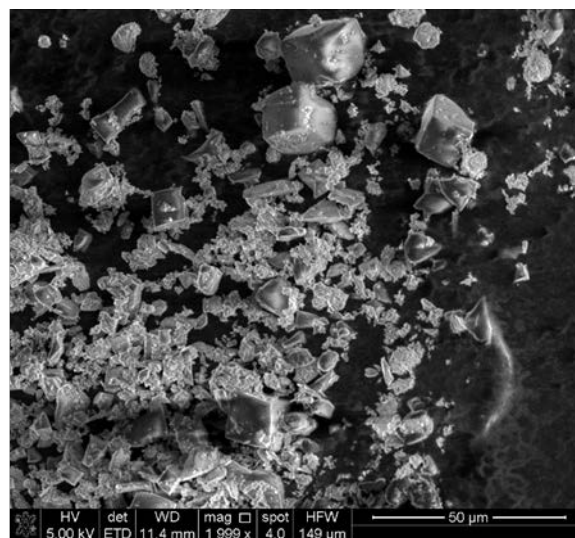
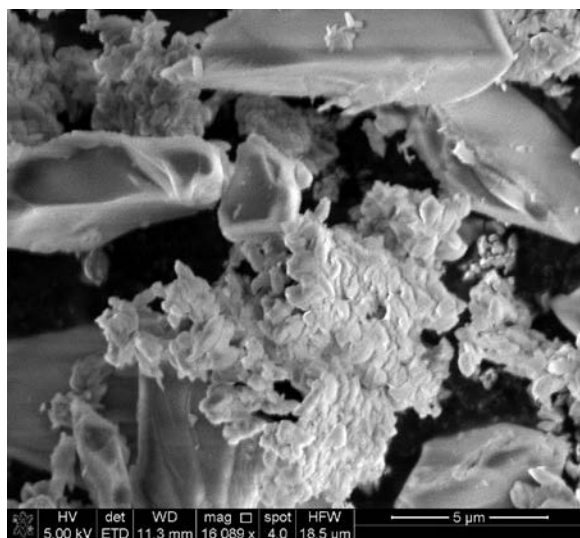


**Figure 143.** SEM images on H-SSZ-13 Si:Al = 80 synthesized in a static Parr reactor for 10 days at 160°C with stirring every 2 days via 3-minute agitation without opening the Parr reactor. HF was not added.

**Table 33.** Summary SEM results for SSZ-13

Si:Al	Synthesis Procedure	Description
$4.3 \pm 0.3$	FAU $\rightarrow$ CHA tumbling 10 days at 140°C	Crystallite diameter: ~1.2 microns Well-defined edges on crystallites No apparent presence of 2 phases
$15 \pm 2$	Direct tumbling 10 days at 160°C	Crystallite diameter: ~2 microns, smaller ones ~0.2 microns Smooth surfaces, ellipsoidal Particles of 2 different sizes (both spherical)... May be same crystallites but different size.
$24 \pm 5$	Direct tumbling 10 days at 160°C	Crystallite diameter: ~2.5 microns ellipsoidal Mix of particles with smooth and bumpy surfaces EDS shows the same Si:Al count for both particles
$80 \pm 50$	Direct static, occasional shaking (every 2 days, 3 minute agitation) 10 days at 160°C. No addition of HF.	Crystallite diameter: ~2 to 20 microns ellipsoidal Mix of particles with sharp edges and shread-like materials EDS shows: Si:Al ~30 for big cube-shaped crystals Si:Al ~70 for shread-like materials

## B.2 Centrifuge-test

We observe a correlation between the  $\text{NH}_3:\text{Al}$  ratio the presence of two phases in a Zeolyst ZSM-5 material with a bulk  $\text{Si}:\text{Al} = 18$ . Immersing the H-ZSM-5 in water and centrifuging in a clear centrifuge tube revealed the presence of two phases. Separation of the two phases revealed a Si-rich phase (bottom layer in the centrifuge tube in Figure 145(b)) and a silicoaluminate phase (top layer in the centrifuge tube in Figure 145(b)). SEM and EDS measurements on this sample also presented a un-uniform distribution of crystallites (Figure 139). Bulk  $\text{NH}_3$  on this material resulted in a  $\text{H}:\text{Al}$  of 0.55, a result from a weighted average of the two phases mixed together (Figure 144).

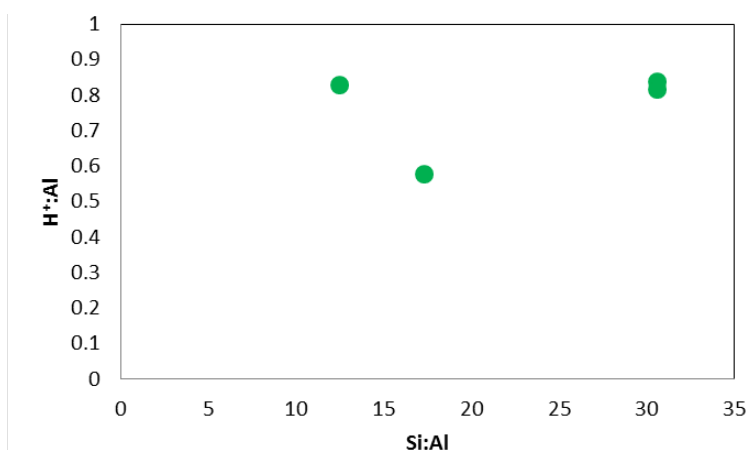


**Figure 144.** BA counts measured using liquid  $\text{NH}_4\text{NO}_3$  exchange and TPD using the AutoChemII-MSD and calibration curve for three representative commercial H-ZSM-5 samples with  $\text{Si}:\text{Al} = 12.5, 18$ , and  $30$ .

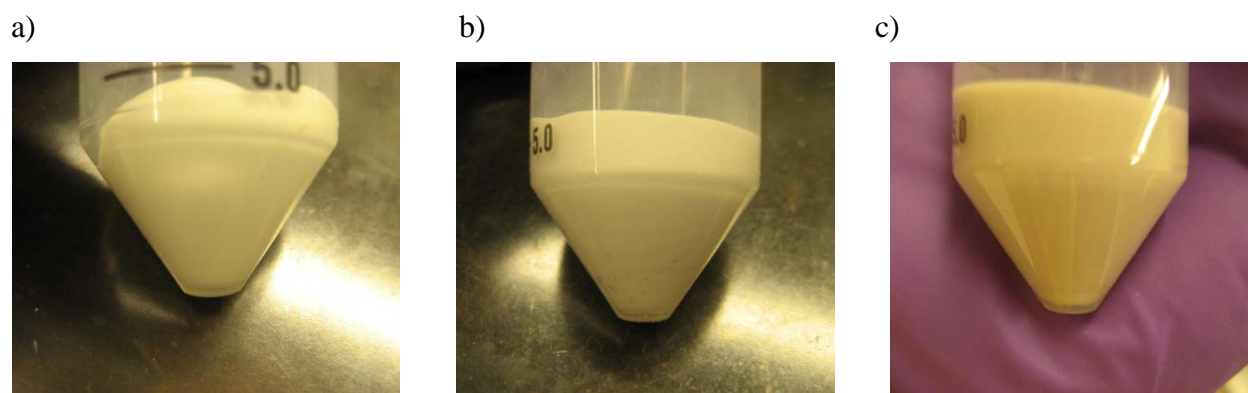


**Figure 145.** Centrifuge test performed on three representative commercial H-ZSM-5 samples with  $\text{Si}:\text{Al} = 12.5$  (a),  $\text{Si}:\text{Al} = 18$  (b), and  $\text{Si}:\text{Al} = 30$  (c).

## APPENDIX C. AQUEOUS CU-EXCHANGE OF CU INTO SSZ-13 CHABAZITE SUPPORTS

Isotherms derived for Cu-exchange with no pH control without pH control are as follows with definition of variables in the table below:

For Cu-exchange onto paired Al<sub>f</sub>: 
$$\theta_{pair}^{Cu^{2+}} = \frac{1}{2} \left( \frac{Al_f}{Al_{tot}} - \theta_{iso}^{H^+} \right) \frac{K_1 [Cu_{(aq)}^{2+}] / [H_{(aq)}^+]^2}{1 + K_1 [Cu_{(aq)}^{2+}] / [H_{(aq)}^+]^2}$$

For Cu-exchange onto isolated Al<sub>f</sub>: 
$$\theta_{iso}^{CuOH} = \left( \frac{Al_f}{Al_{tot}} - 2\theta_{pair}^{Cu^{2+}} \right) \frac{K_2 [Cu_{(aq)}^{2+}] / [H_{(aq)}^+]}{1 + K_2 [Cu_{(aq)}^{2+}] / [H_{(aq)}^+]}$$

Symbol	Meaning
$[Cu_{(aq)}^{2+}]$	Concentration of Cu <sup>2+</sup> ions in solution (not exchanged with proton)
$[H_{(aq)}^+]$	Concentration of H <sup>+</sup> ions in solution (not as BA on zeolite)
$[Al_{pair}^{Cu^{2+}}]$	Number of Al pairs titrated with isolated Cu <sup>2+</sup> already.
$[Al_{pair}^{2H^+}]$	Number of Al pairs not titrated with isolated Cu <sup>2+</sup>
$[Al_{iso}^{H^+}]$	Number of isolated unpaired Al not titrated with CuOH
$[Al_{iso}^{CuOH}]$	Number of CuOH already titrating isolated H <sup>+</sup>
$K_1$	Equilibrium Constant for exchange of paired Al with isolated Cu <sup>2+</sup>
$K_2$	Equilibrium constant for exchange of isolated Al with CuOH
$Al_{tot}$	Total number of Al in zeolite
$Al_f$	Number of Al in framework
$Al_{ex,f}$	Number of Al as extraframework species
$\theta$	Fraction of sites

The Cu-exchange isotherms for Cu-zeolite samples on SSZ-13, ZSM-5, and Beta frameworks are shown in Figure 146. Samples where primarily Cu<sup>2+</sup> species coordinated to two framework Al (top graph), and CuOH species coordinated to one framework Al (bottom graph) are shown. It should be noted that the outliers in the bottom graph were Cu-exchanged for a shorter time (3 hours vs > 6 hours) than the other samples on the isotherm, so the exchange slurry was not at

steady state, making it difficult to precisely compute  $[\text{Cu}]:[\text{H}]$ . It is observed that for all zeolite frameworks and Si:Al ratios studied (except for the SSZ-13 Si:Al = 4.5 sample), the Cu-exchange isotherm seems to overlay.

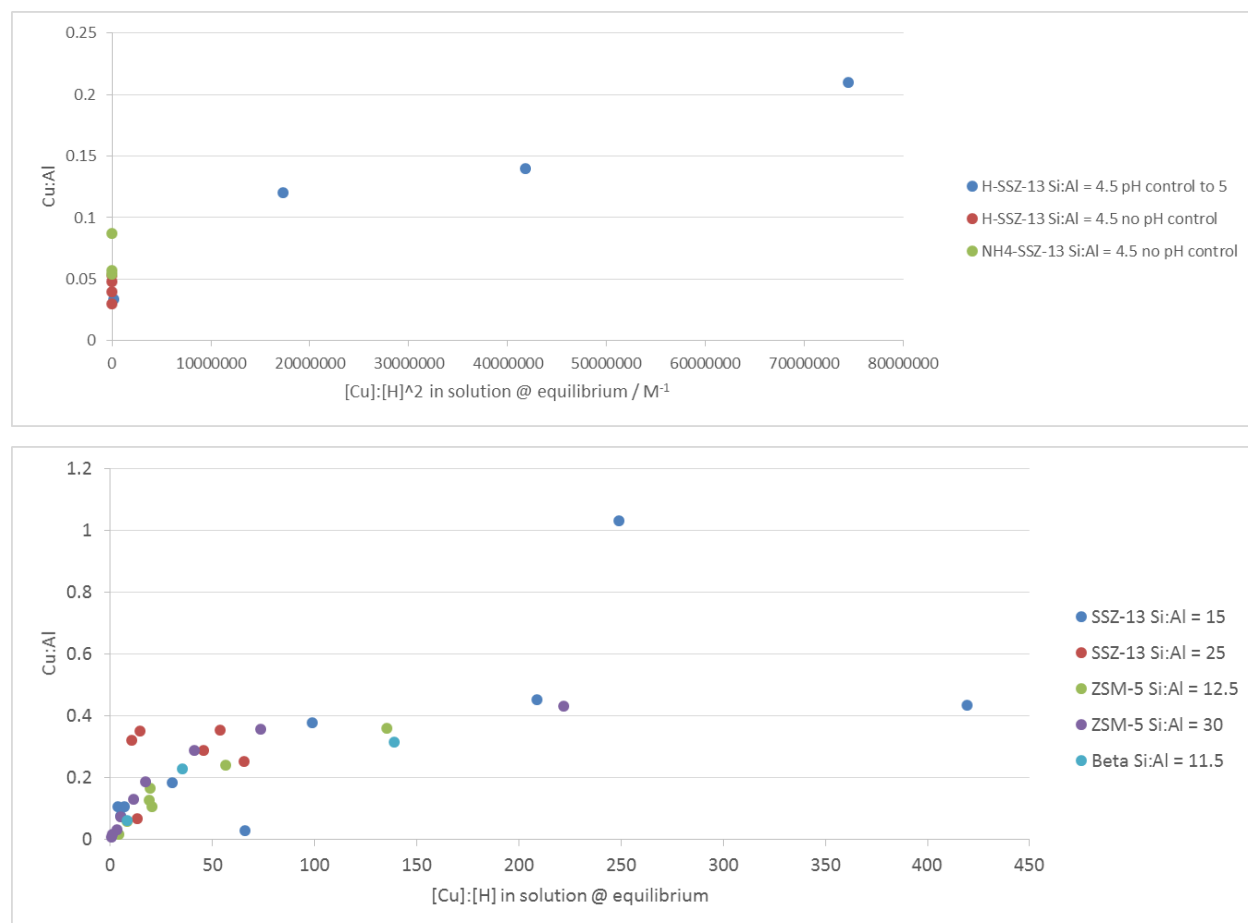


**Figure 146.** Cu-exchange isotherms for various zeolite supports for samples consisting of primarily  $\text{Cu}^{2+}$  species coordinated to two framework Al (top graph), and  $\text{CuOH}$  species coordinated to one framework Al (bottom graph).

## **APPENDIX D. LOW TEMPERATURE (30 TO 150°C) NO OXIDATION OVER H-SSZ-13 AND CU-SSZ-13 MATERIALS DURING STANDARD SCR CONDITIONS**

### **D.1 Abstract**

With increased  $\text{NO}_x$  emission regulations and improvements in the SCR catalyst performance, the fraction of the total  $\text{NO}_x$  released from an engine during start-up (outside ambient temperature to 150°C) and during its entire operating regime (150 to 600°C) is increasing. Because of this, automobile and engine manufacturers are developing technologies that will decrease the emissions of  $\text{NO}_x$  during start up. Due to the low reaction rates of SCR catalysts at temperatures lower than 150°C, the most promising technology today involves the adsorption of  $\text{NO}_x$  onto Pd/zeolites at ambient temperatures during start-up, then the subsequent desorption of  $\text{NO}_x$  and conversion of the  $\text{NO}_x$  through a Cu-SSZ-13 catalyst after temperatures have warmed up to allow for fast enough reaction rates. In this chapter we report on NO oxidation phenomenon observed when standard SCR gases are exposed to Cu-SSZ-13 catalysts at temperatures between 30 to 150°C. We observe that the selectivity to NO oxidation increases from 0 to 100% with decreasing temperatures from 150 to 30°C during standard SCR on unsulfated Cu-SSZ-13. This phenomenon is attributed to catalysis by confinement where the reaction rates and negative apparent activation energies are consistent with those reported in the literature. The phenomenon reported represents a prime example of how the selectivity of catalysts can be temperature dependent.

### **D.2 Introduction**

The purpose of Cu-SSZ-13 in the diesel exhaust aftertreatment system is to convert toxic  $\text{NO}_x$  to  $\text{H}_2\text{O}$  and  $\text{N}_2$  using  $\text{NH}_3$  as a reductant via standard SCR. With more stringent  $\text{NO}_x$  emission targets set by the government, and significant advancement in technology over the last ten years in reducing the amount of  $\text{NO}_x$  released well after the engine and aftertreatment system has warmed up (~200 to 400°C), finding solutions to decreasing the amount of  $\text{NO}_x$  released from cold start (<150°C) has become high priority [176].



### D.3 Experimental Methods

All experimental methods performed in this chapter are outlined in Section 2.6. All procedures to collect differential SCR kinetics were followed, with the temperature of the oven and catalyst as the only difference. For non-differential forward NO oxidation rates, the same gas feed rate used by Loiland et al. [177] was used (1000 ppm NO, 5% O<sub>2</sub>, in balance N<sub>2</sub> between temperature of 30 to 150°C).

### D.4 Results and Discussion

#### D.4.1 Benchmarking forward dry NO oxidation rates with Literature: bad practices and better practices

Figure 147 plots the forward NO oxidation rate for a variety of chabazite catalysts including pure-Si SSZ-13, H-SSZ-13, Na-SSZ-13, and Cu-SSZ-13. We observe that the forward NO oxidation rate increases with the addition of anionic framework sites, of which the forward NO oxidation reaction rate increases with the identity of the balanced cation H<sup>+</sup>, Na<sup>+</sup>, and Cu<sup>2+</sup>, in that order. We also notice that the apparent activation energy is negative, which means that the forward NO oxidation rate increases with decreasing temperature.

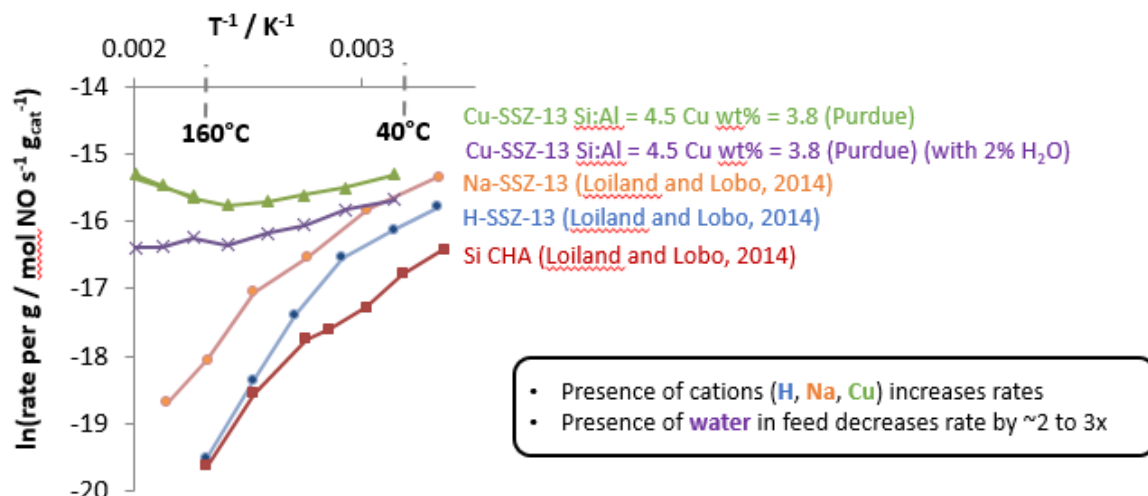


**Figure 147.** Arrhenius plot of the forward NO oxidation reaction rate between temperatures of 30 and 160°C and a feed composition of 1000 ppm NO, 5% O<sub>2</sub>, in balance N<sub>2</sub>. Forward NO oxidation rates are collected by Loiland et al. [177] on Si-CHA (red squares), H-SSZ-13 (blue circles), and Na-SSZ-13 (orange circles). Forward NO oxidation rates were also collected on Cu-SSZ-13 (Si:Al = 4.5, Cu wt% = 3.8) in the presence of 2% H<sub>2</sub>O (purples x's) and absence of H<sub>2</sub>O (green triangles).

It should be noted that forward NO oxidation reaction rates are not differential reaction rates as the concentration of NO<sub>2</sub> entering the bed is near 0 ppm and the NO<sub>2</sub> leaving the bed ranges between 0 to ~50 ppm. NO<sub>2</sub> inhibits the dry NO oxidation rate over Cu-SSZ-13 materials with Cu<sub>x</sub>O<sub>y</sub> clusters at 300°C [122], but it is uncertain whether whether NO<sub>2</sub> inhibits the NO oxidation rate at temperatures between 30 to 150°C, primarily because the active sites and mechanisms of producing NO<sub>x</sub> under the same gas feed (but different temperatures) is likely different. Thus, Figure 147 is an extremely misleading graph due to the fact that we are not measuring differential reaction rates, and thus likely not easily reproducible. To make this a reproducible differential reaction rate, we must co-feed NO<sub>2</sub> and ensure that the conversion of all reactants and products are differential (< 20% conversion) [178].

#### D.4.2 Active centers for dry NO oxidation at low temperature (30 to 150°C) and high temperature (300°C)

Verma et al. [122] experimentally and computationally demonstrated that dry NO oxidation at 300°C over Cu-SSZ-13 is inactive on H-SSZ-13 and Cu-SSZ-13 catalysts with Z<sub>2</sub>Cu sites, but is active on Cu<sub>x</sub>O<sub>y</sub> clusters. Loiland et al. [177] proposes that the mechanism of dry NO oxidation

between temperatures of 30 to 150°C is due to the confinement of the reactants within the zeolite cages and pores. DFT calculations demonstrate that the confining environment likely aid in stabilizing the transition state compared to the gas-phase NO oxidation reaction without a confining environment [177].

#### **D.4.3 Low temperature (30 to 150°C) NO oxidation over Cu-SSZ-13 catalysts during standard SCR**

With decreasing temperature from 180 to 150°C, we observe an increase in the forward rate of NO<sub>2</sub> formation while standard SCR still dominates with an activation energy of 68 kJ mol<sup>-1</sup> (Figure 148). At temperatures between 40 and 150°C, the apparent activation energy for both NO consumption and NO<sub>2</sub> formation is -5 kJ mol<sup>-1</sup>. In this temperature range it is likely that the standard SCR mechanism has been mostly or completely shut down, and the pathway NO takes to produce N<sub>2</sub> and H<sub>2</sub>O between 40 to 150°C is via fast SCR, as evidenced by the fact that the Cu-SSZ-13 material is only 70% selective toward NO<sub>2</sub> formation (Figure 149). We hypothesize that the remaining 30% selectivity is due to standard SCR and fast SCR, the latter of which uses the NO<sub>2</sub> formed as a reactant.

These results present a few possible implications that may affect our understanding of standard SCR. First, it is likely that the confinement effects observed may still play a role (albeit minor) at higher temperatures (150 to 400°C). Second, at low Cu loadings where the formation of (NH<sub>3</sub>)<sub>2</sub>Cu(I)-O<sub>2</sub>-Cu(I)(NH<sub>3</sub>)<sub>2</sub> dimers are unlikely to be a relevant or dominant intermediate in the oxidation half-cycle, the formation of NO<sub>2</sub> may also allow a higher fraction of Cu to be active since NO<sub>2</sub> reacts via fast SCR via single-site catalysis with Cu [118]. The rate of this reaction would of course be limited by the rate of NO<sub>2</sub> formation which can also be formed via other pathways other than confinement.

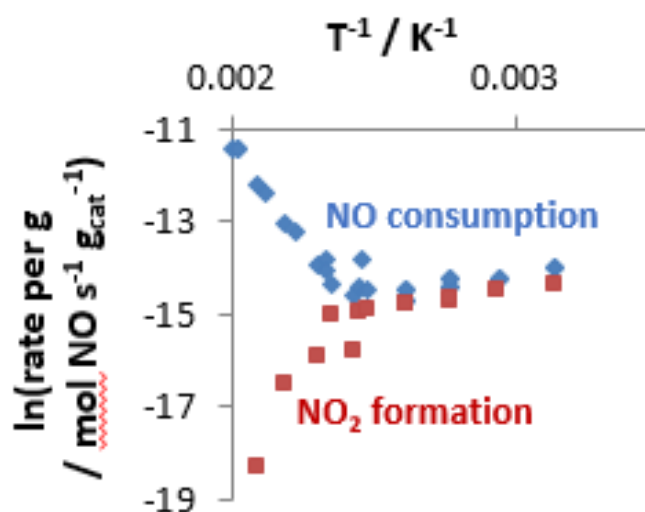


**Figure 148.** Arrhenius plots for the NO consumption rates (blue diamonds) during standard SCR gas conditions (300 ppm NO, 300 ppm NH<sub>3</sub>, 10% O<sub>2</sub>, 7% CO<sub>2</sub>, 2.5% H<sub>2</sub>O in balance N<sub>2</sub> between temperatures of 40°C and 180°C on a Cu-SSZ-13 sample (Si:Al = 4.5, Cu wt% = 3.8, Cu:Al = 0.21).

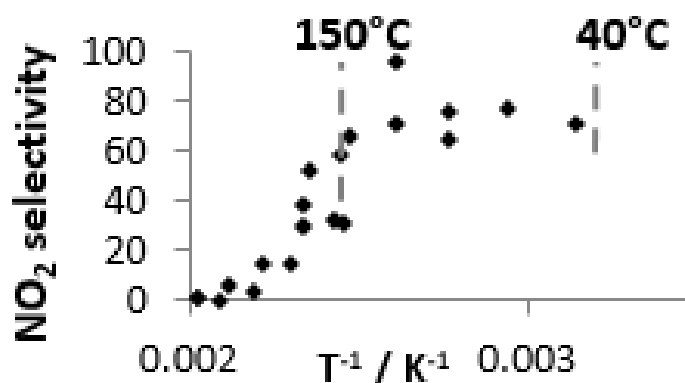


**Figure 149.** NO selectivity to NO<sub>2</sub> during standard SCR gas feed conditions between 180 to 40°C on a Cu-SSZ-13 sample (Si:Al = 4.5, Cu wt% = 3.8, Cu:Al = 0.21). NO selectivity N<sub>2</sub> and H<sub>2</sub>O via standard SCR is 100% at 180°C, but decreases to 30% at 150°C at which the selectivity stabilizes out between 150 and 40°C. Between this temperature range the NO selectivity is 70% to NO<sub>2</sub>.

For a series of samples, it has been observed the NO consumption activation energy decreases from a typical value of between 50 to 70 kJ mol<sup>-1</sup> to between -5 to 5 kJ mol<sup>-1</sup> as the standard SCR reaction temperature decreases from 180 to 30°C while the selectivity toward NO<sub>2</sub> increases from 0 to between 60 to 120% (Figure 149). Figure 150 displays the apparent activation energy

plotted versus the Cu weight % and the forward NO oxidation rate plotted versus the Cu weight %. NO conversions for these samples were all between 3 to 5% (equivalent to 9 to 15 ppm of NO converted from a 300 ppm NO feed) at 70°C, except for the Cu-SSZ-13 sample at a Cu wt% of 3.8, which exhibited a NO conversion of 15% at 70°C (45 ppm of NO converted). Because NO<sub>2</sub> is not being cofed (hence the NO<sub>2</sub> concentration through the Cu-SSZ-13 bed is not differential) and the conversions are not the same, we cannot properly compare the Cu wt% = 3.8 Cu-SSZ-13 material with the other catalysts studied [179]. We can, however, compare the other four Cu-SSZ-13 samples because the conversions are all within error (3 to 5% conversion). It should be noted that these activation energies and forward NO consumption rates will only be reproducible if another research group collects kinetics at the same conversions used in this study.

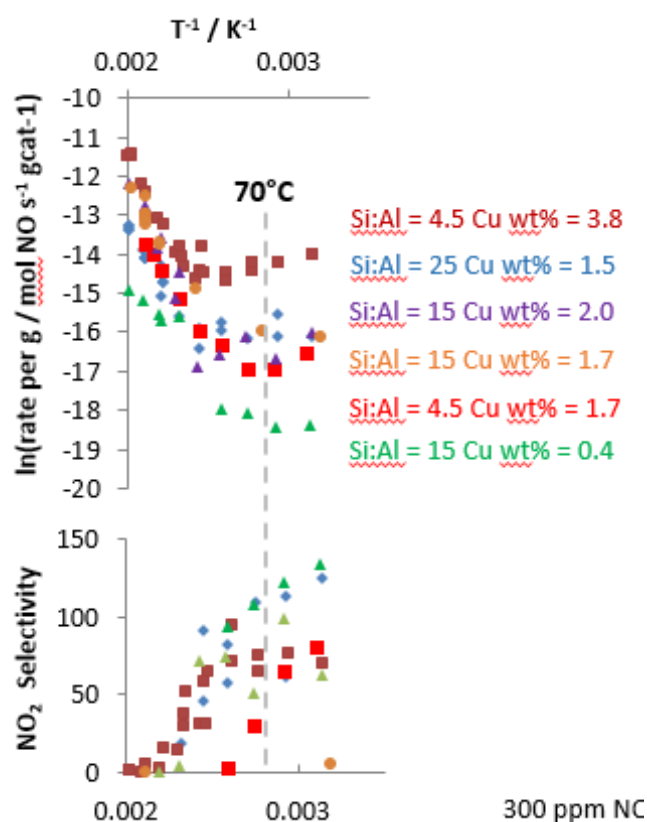


**Figure 150.** Arrhenius plots for the forward NO consumption rates during standard SCR gas conditions (300 ppm NO, 300 ppm NH<sub>3</sub>, 10% O<sub>2</sub>, 7% CO<sub>2</sub>, 2.5% H<sub>2</sub>O in balance N<sub>2</sub> between temperatures of 40°C and 180°C on a series of Cu-SSZ-13 samples with different Al and Cu densities (top graph). NO selectivity to NO<sub>2</sub> during standard SCR gas feed conditions between 180 to 40°C on a series of Cu-SSZ-13 samples with different Al and Cu densities (bottom graph).

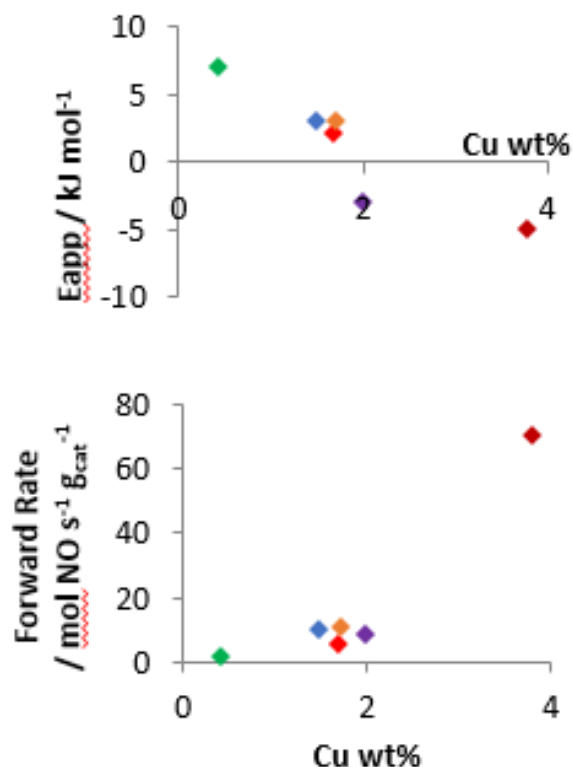


**Figure 151.** Apparent activation energies at 70°C on the series of Cu-SSZ-13 samples with varying Al and Cu densities (top graph). Forward NO reaction rates at 70°C under standard SCR gas conditions (300 ppm NO, 300 ppm  $\text{NH}_3$ , 10%  $\text{O}_2$ , 7%  $\text{CO}_2$ , 2.5%  $\text{H}_2\text{O}$  in balance  $\text{N}_2$ ) (bottom graph).

Figure 152 plots the NO consumption rate between 130 to 220°C on a  $\text{Z}_2\text{Cu}$  model Cu-SSZ-13 material ( $\text{Si:Al} = 4.5$ ,  $\text{Cu:Al} = 0.21$ ) with increasing levels of sulfation. It is observed that increasing the extent of sulfation also decrease that forward rate of NO oxidation. A possible explanation may be due to sulfur-derived species pore-blocking cages that otherwise would have been utilized for catalyzing the formation of  $\text{NO}_2$  from NO and  $\text{O}_2$  at temperatures less than 150°C.

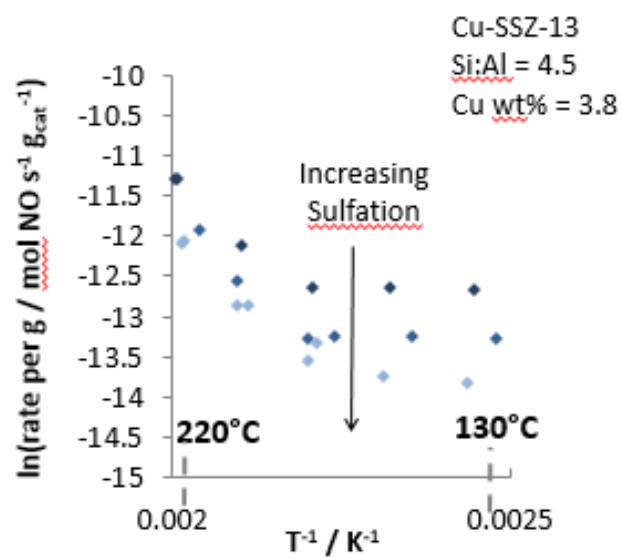


**Figure 152.** The NO oxidation rate with a standard SCR gas feed (300 ppm NO, 300 ppm NH<sub>3</sub>, 10% O<sub>2</sub>, 7% CO<sub>2</sub>, 2.5% H<sub>2</sub>O, balance N<sub>2</sub>) decreases with increasing sulfation, suggesting that sulfur species decrease the reaction rate by either removing confining environments, restricting access to Cu sites, or a combination of both.

## APPENDIX E. CU-NA-ZSM-5 CO-CATION EXCHANGE KINETICS

### E.1 Literature Review

The effect of the presence of sodium during Cu-exchange of H-ZSM-5 with a Si:Al = 12 was employed to study the influence of BA sites of Cu-zeolites on standard SCR. Sodium was considered as a poison since Na-zeolites are inactive for standard SCR and competes with Cu for BA sites on the zeolite framework. Campa et al. studied the dependence of the NO decomposition rate on the Cu loading on Cu-Y, Cu-ZSM-5, and Cu-Na-ZSM-5 catalysts [180]. Both of Campa's Cu-ZSM-5 and Cu-Na-ZSM-5 catalysts a similar increase and decrease in the rate with increasing Cu-loading, but at a given Cu loading, Cu-Na-ZSM-5 catalyst were lower than their counterpart Cu-ZSM-5 catalysts with the same Cu loading. Brandenberger et al. used Na to poison BA sites in an attempt to gain insight into the role of BA sites for the standard SCR mechanism on Fe-ZSM-5 catalysts [181] They showed using two samples with different Na contents that the light-off curve did not change significantly throughout the entire curve, including the two data points that were within the differential regime (< 20% conversion). Gao et al. also presented light-off curves for Cu-SSZ-13 and Cu-Na-SSZ-13 with the same Cu loading but different Na loadings [182]. Their results demonstrated that their Cu-Na-SSZ-13 sample exhibited higher hydrothermal stability and a higher standard SCR rate than the Na-free Cu-SSZ-13. In summary, the effects of alkali co-cations on metal-zeolite activities vary in the literature.

### E.2 Results and Discussion

A series of Cu-ZSM-5 zeolites, Cu-Na-ZSM-5 zeolites, and Na-ZSM-5 zeolites were prepared. As shown in Figure 153, the standard SCR rates per mol Cu for the series of Cu-Na-ZSM-5 with a Cu:Al = 0.10 (Cu wt% = 1.0) but varying Na:Al from 0.00 to 0.23 decrease linearly in the range studied. In addition to a decrease in the rates, the apparent activation energy ( $E_{app}$ ) also decreased with an increase Na content (Figure 153).  $E_{app}$  is the true activation energy reduced by the heat of adsorption of the adsorbed reactants. It is uncertain whether the decrease in  $E_{app}$  is due to changes in the true activation energy or the heat of adsorbed reactants. An increase in the Na content also resulted in a decrease in the  $NH_3$  order, increase in the NO order, and increase in the  $O_2$  order. Positive reactant orders (NO and  $O_2$ ) suggest that the reactant's role in the mechanism is likely interaction due with adsorbed species on the active site form the gas phase,



since an increase of these species in the gas phase increases the overall rate of reaction. Negative reaction orders ( $\text{NH}_3$ ) suggest that the reactant's role in the mechanism is as an adsorbate on the active site since an increase of these species in the gas phase decreases the overall rate of reaction. Ambient UV-Visible (Figure 155) indicate that the presence of  $\text{Na}^+$  cations does not affect the  $\text{Cu}^{2+}$  d-d transition ( $12000\text{ cm}^{-1}$ ) or ligand-metal charge transfer ( $35000\text{ cm}^{-1}$  and  $45000\text{ cm}^{-1}$ ) features, indicating that under ambient hydrated conditions, Cu does not interact with  $\text{Na}^+$ .

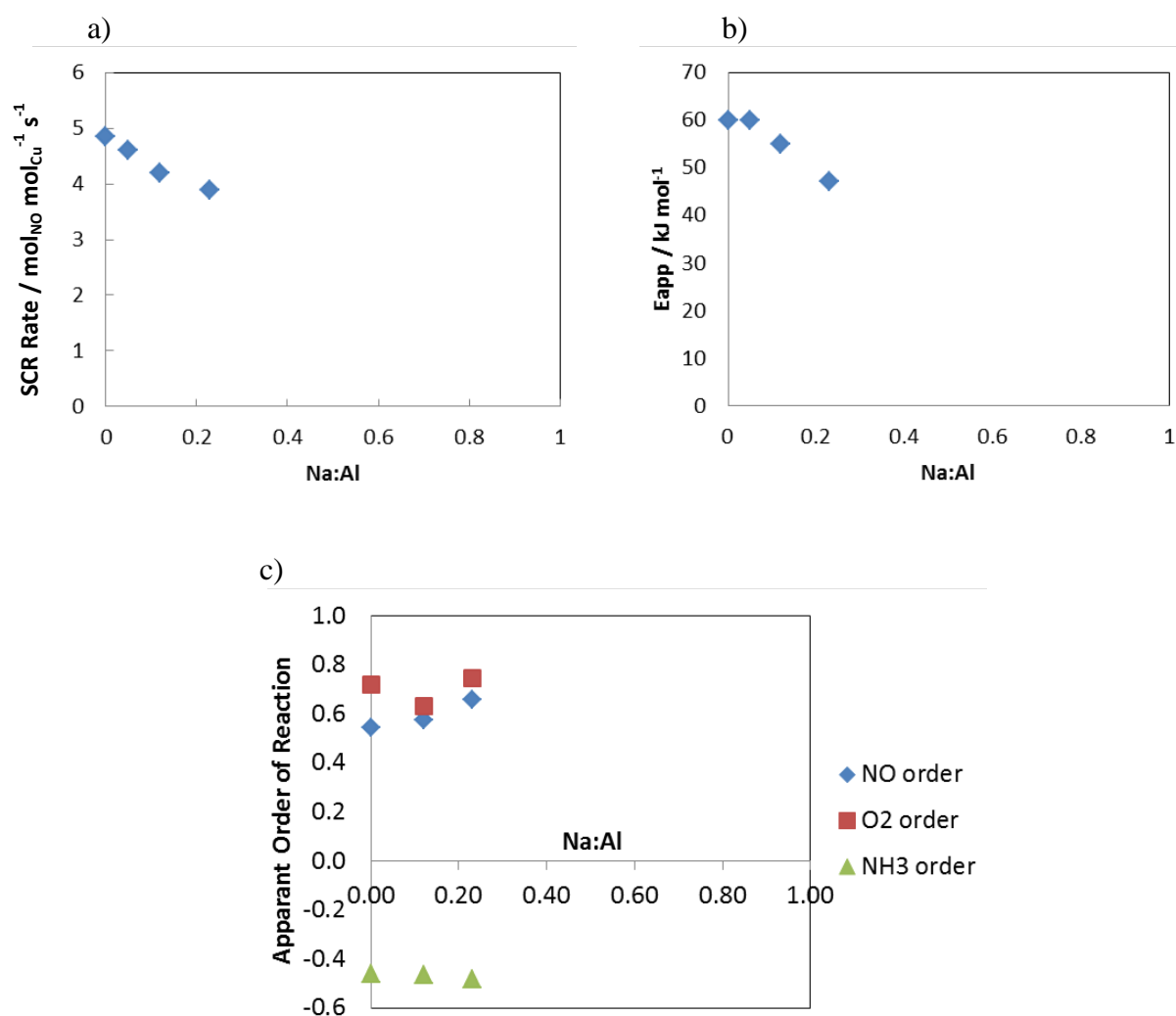


**Figure 153.** Effect of Na:Al ratio on the (a) SCR NO consumption rate normalized per mol Cu, (b)  $E_{\text{app}}$ , and (c)  $\text{NH}_3$ , NO, and  $\text{O}_2$  orders. All four samples have the same Cu wt% of  $1.00 \pm 0.05$ , but varying  $\text{Na}^+$  loadings between 0.00 to 0.25.

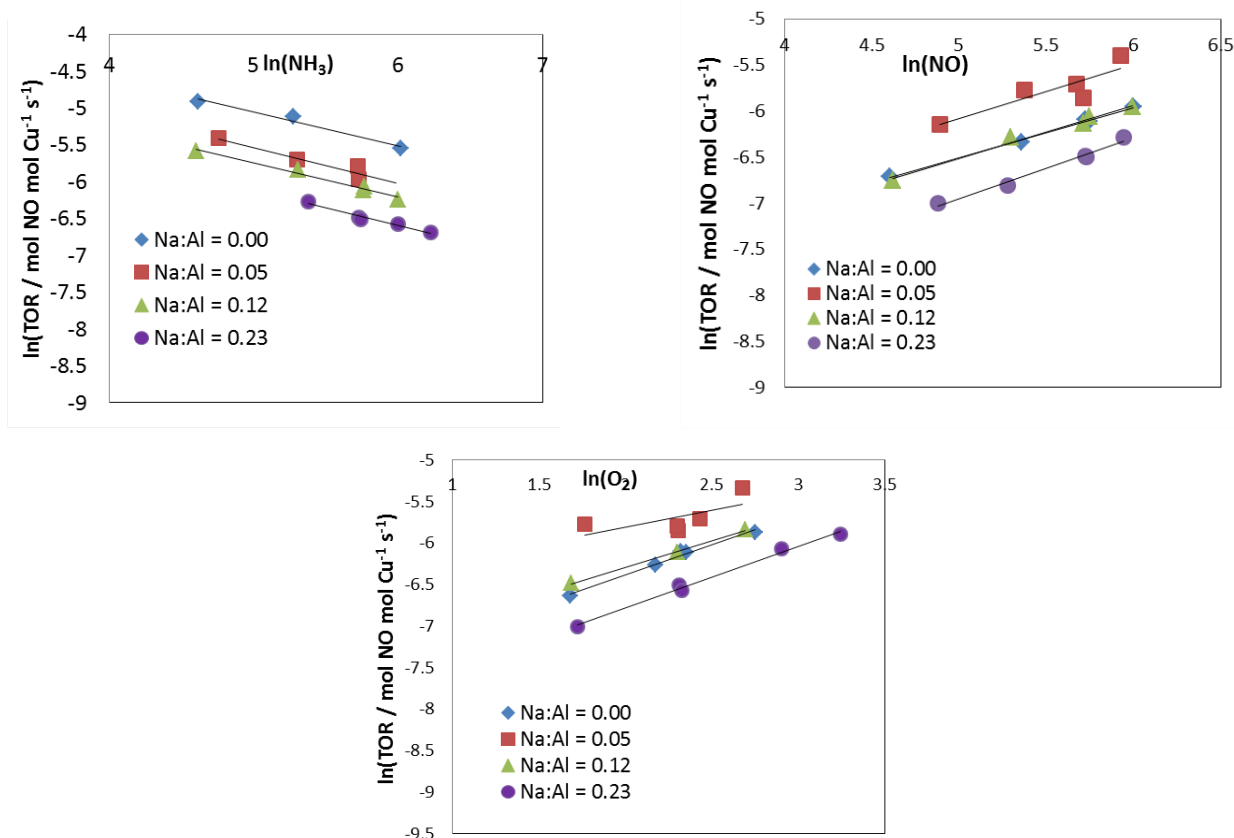


**Figure 154.** Arrhenius plots of the four Cu-Na-ZSM-5 samples tested for standard SCR rate. The temperature used was 190°C with feed conditions of 320 ppm  $\text{NH}_3$ , 320 ppm NO, 10%  $\text{O}_2$ , 7%  $\text{CO}_2$ , and 3.5%  $\text{H}_2\text{O}$ .  $\text{NH}_3$  orders were taken with  $\text{NH}_3$  concentrations ranging from 150 ppm and 500 ppm  $\text{NH}_3$ . NO orders were taken with NO concentrations ranging from 100ppm and 500 ppm NO.  $\text{O}_2$  orders were taken with  $\text{O}_2$  concentrations ranging from 2% to 15%.

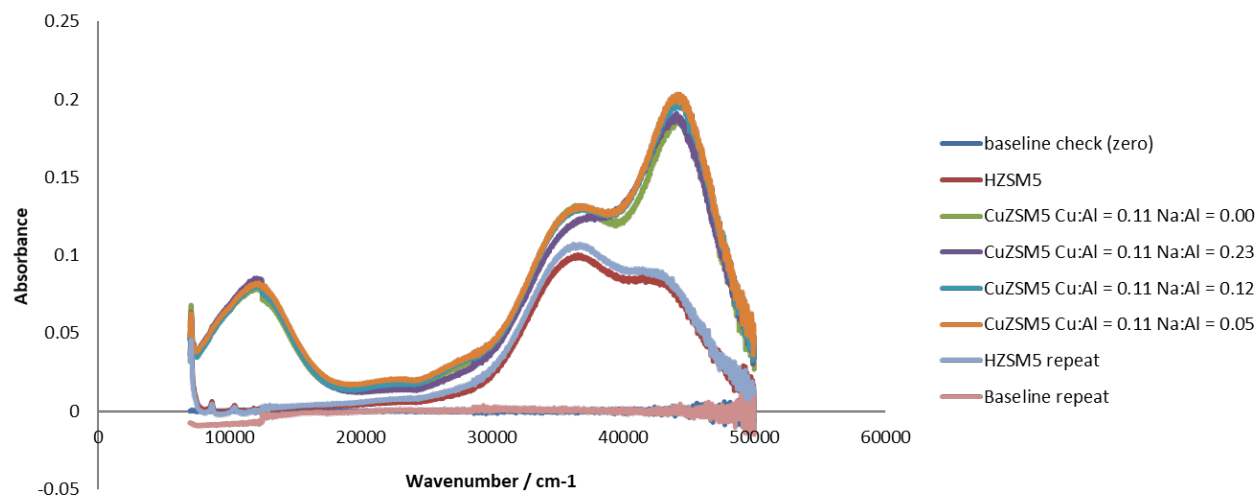


**Figure 155.** UV-Visible spectra on BaSO<sub>4</sub> baseline powder, H-ZSM-5 (Si:Al = 12.5), and four different Cu-Na-ZSM-5 materials with the same Cu:Al molar ratio of 0.11, but different Na:Al ratios ranging from 0.00 to 0.23.

## APPENDIX F. ADSORPTION ENERGIES AND SCALING RELATIONSHIPS OF $\text{NH}_x$ , $\text{NO}_x$ , $\text{SO}_x$ , AND $\text{CH}_x$ OVER METAL-SSZ-13 ZEOLITES

### F.1 Experimental Details

Crystallographic information files (.cif files) for chabazite were downloaded from the International Zeolite Association website [34], Figure 156. A full periodic unit cell for CHA (108 atoms) rather than a cluster model was used. The Grid-based Projector Augmented Wave (GPAW) method was used with a grid spacing of 0.18 Angstroms and k-points of (1,1,1). The GPAW method is a grid-based real-space implementation of DFT using the PAW method. The PAW method gets rid of core electrons, works with soft valence wave functions and all electrons are frozen (frozen core approximation), which implies no pseudo-potentials. The use of a regular 3-dimensional real space grids for representing wave functions, densities, and potentials allow for (1) efficient multi-grid algorithms for solving the Kohn-Sham equations and flexible boundary conditions.

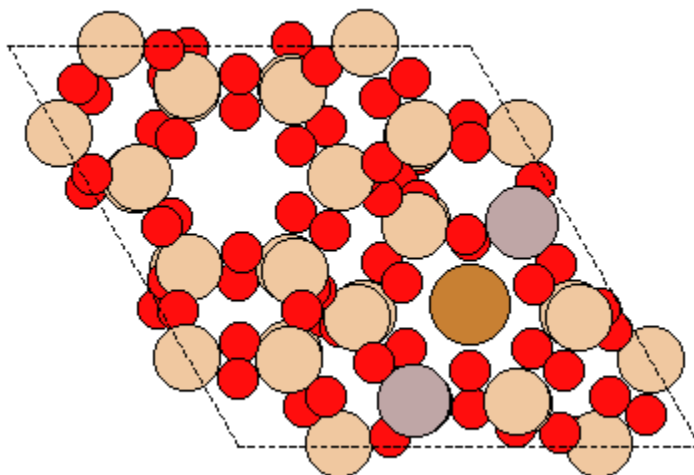


**Figure 156.** Screenshot of the CHA unit cell from the International Zeolite Association (IZA) website. Image was generated using an atomic simulation environment (ASE) python code [183].

Two modes were used, specifically (1) linear combination of atomic orbitals (LCAO) which uses a basis set of atomic orbital-like wave functions, and (2) finite difference grid mode (FD) which uses a basis set of grid-based wave functions. The basis function used is the double zeta polarized (dzp). Table 34 qualitatively compares differences between FD and LCAO modes.

**Table 34.** Qualitative comparisons between FD and LCAO modes.

	FD	LCAO
memory consumption	large	small
speed for small system	slow	fast
speed for large system	fast	very fast
absolute convergence	easy	complicated

$$E_{\text{ads}} = E_{\text{tot}}(\text{Ads/M-SSZ-13}) - E_{\text{tot}}(\text{M-SSZ-13}) - E_{\text{tot}}(\text{Ads})$$

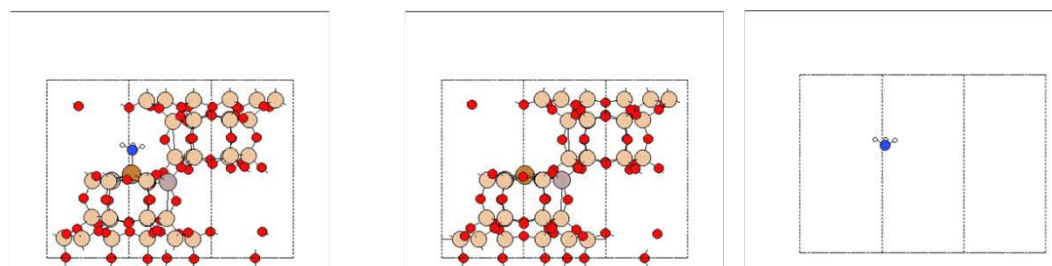
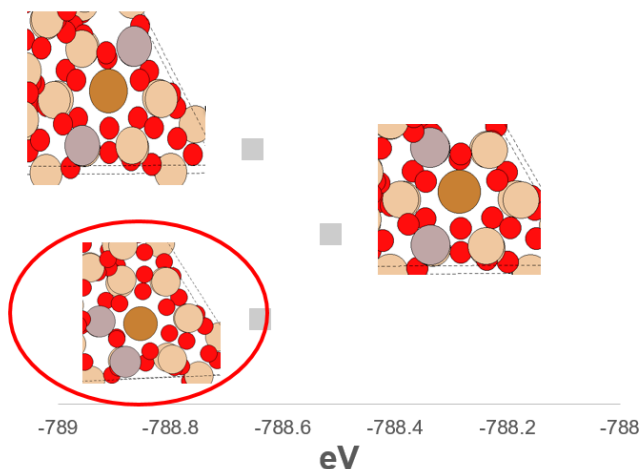


**Figure 157.** Schematic illustrating the computations necessary to determine the adsorption energy ( $\text{NH}_3$ , blue, used as illustration) of adsorbates on a Cu atom (brown) in the SSZ-13 framework (tan = silicon, dark tan = aluminum, red = oxygen).

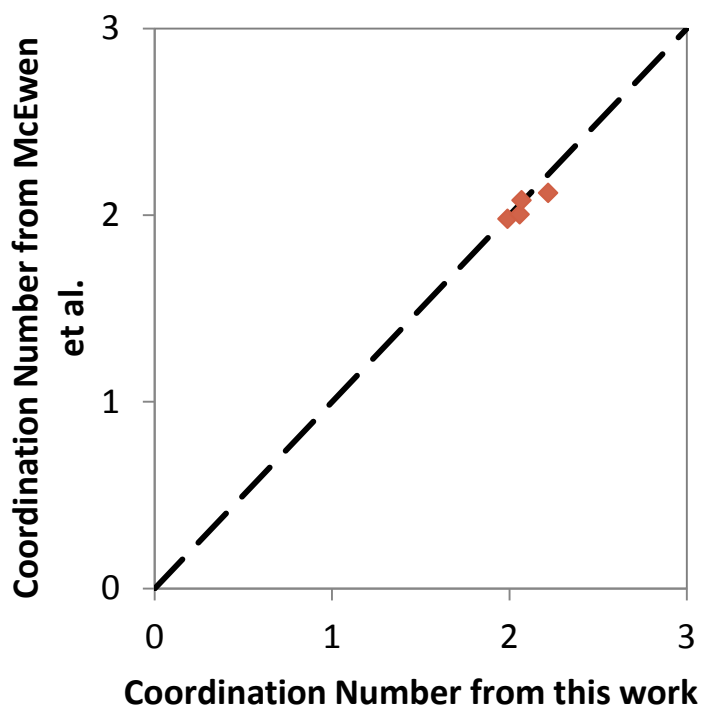
## F.2 Results

We observe that  $\text{Cu}^{2+}$  charge balanced by framework aluminum 3 nearest-neighbors (3NN) away from each other is the most stable, surprisingly followed closely by  $\text{Cu}^{2+}$  charge balanced by framework aluminum in the 1NN position, which by Lowenstein's rule should not occur due to an unfavorable electrostatic repulsion [102]. The least stable configuration is two framework

aluminum in the 2NN position. To benchmark with literature, we compared Cu-O bond distances between the  $\text{Cu}^{2+}$  and the four framework oxygen atoms that it is coordinated to with those reported by McEwen et al. [184], Figure 159.



**Figure 158.** Chabazite energies computed using LCAO for a  $\text{Cu}^{2+}$  charge balanced by two framework Al in a six membered ring at 1 nearest-neighbor (NN), 2 NN, and 3 NN positions.

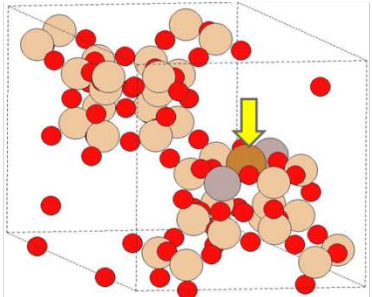


**Figure 159.** Parity plot between computed Cu-O distances between  $\text{Cu}^{2+}$  and framework O atoms in the chabazite 6 membered ring computed in this work compared to those reported by McEwen et al. [184]

The strength of the bond between adsorbates and materials scale, to a good approximation, with each other from metal to metal. Plots for  $\text{NH}_x$ ,  $\text{SO}_x$ ,  $\text{NO}_x$ , and  $\text{CH}_x$ , species ( $x = 0, 1, 2, 3, 4$ ) (result in slopes close to that determined by Equation 29 from valency rules [185], where  $x_{\max}$  is the maximum number of H or O atoms that can bind to the central atom.

$$\text{slope} = \gamma(x) = \frac{x_{\max} - x}{x_{\max}} \quad (\text{Equation 29})$$

Figure 161 to Figure 164 plot scaling relations. Although  $\text{N}_2\text{O}$  is not part of  $\text{NO}_x$  scaling relationships, it is included to verify what would be the tendency with respect to  $\Delta E_{\text{N}}$ , giving the relevance in the  $\text{NH}_3$  SCR reaction. We observe that  $\text{N}_2\text{O}$  refuses to adsorb on Pd-SSZ-13. These scaling expressions allow us to estimate all binding energy measurements for different adsorbates and their intermediates on a variety of metals with only one calculation. This allows us to crudely screen and compare reaction pathway energies quickly without depleting expensive computational time on unpromising pathways. Though this methodology is indeed powerful, researchers should be aware that under reaction conditions, the relative surface coverages of intermediates may vary across a range of environmental conditions (temperature, reactant and product concentrations), the relevant intermediates likely vary from system to system as the active metal is changed, and the rate limiting step may also vary. These complications make it difficult to compare experimental activities to computational results without rigorous and convincing experimental evidence.

Adsorbate				Metal Center
N NH NH <sub>2</sub> NH <sub>3</sub>	C CH CH <sub>2</sub> CH <sub>3</sub> CH <sub>4</sub>	S SO SO <sub>2</sub> SO <sub>3</sub>	N NO NO <sub>2</sub> N <sub>2</sub> O	Cu, Ag, Au, Co, Fe, Ir, Mo, Ni, Pd, Pt, Rh, Ru, W, Zn 

**Figure 160.** Tabulated list of adsorbates and metals used in this study. The yellow arrow points to the location of the metal center in the chabazite unit cell.

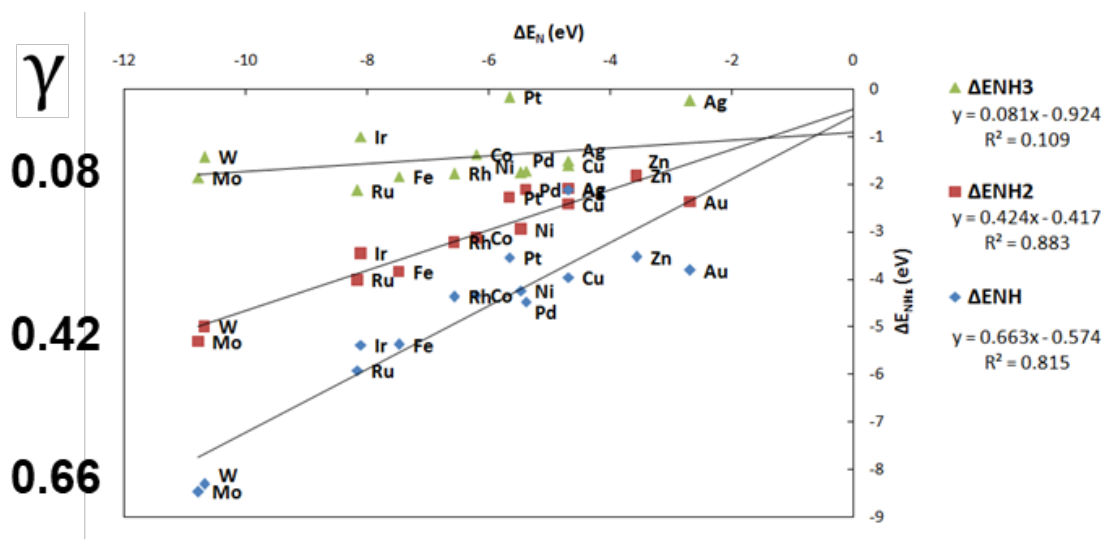


**Figure 161.** Scaling relations for  $\text{NH}_x$  on metal-SSZ-13.

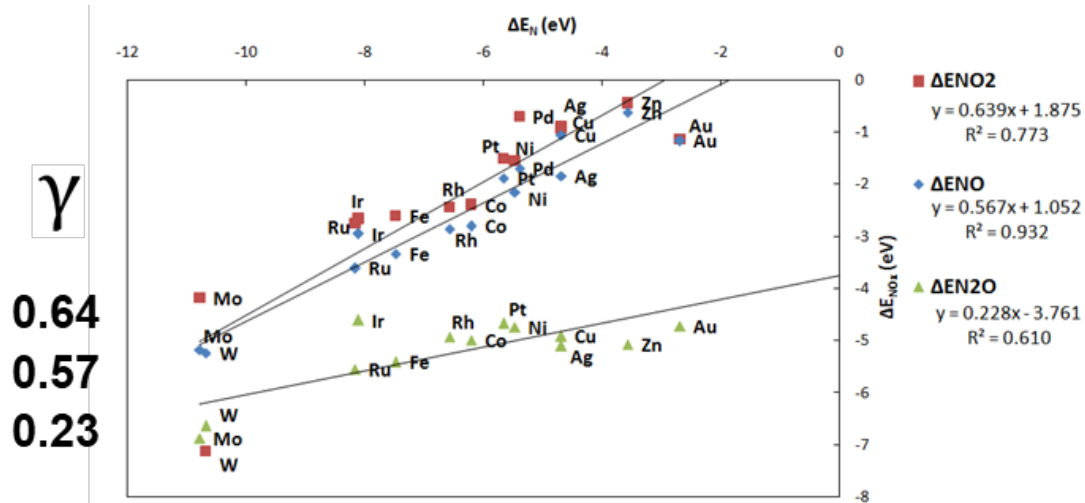


**Figure 162.** Scaling relations for  $\text{NO}_x$  and  $\text{N}_2\text{O}$  on metal-SSZ-13.



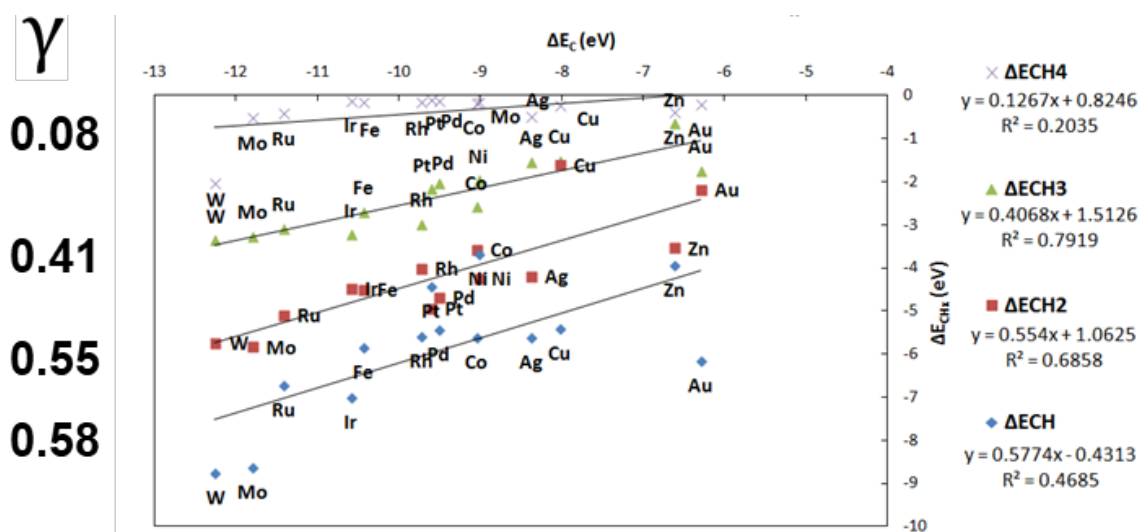


Figure 163. Scaling relations for  $CH_x$  on metal-SSZ-13.

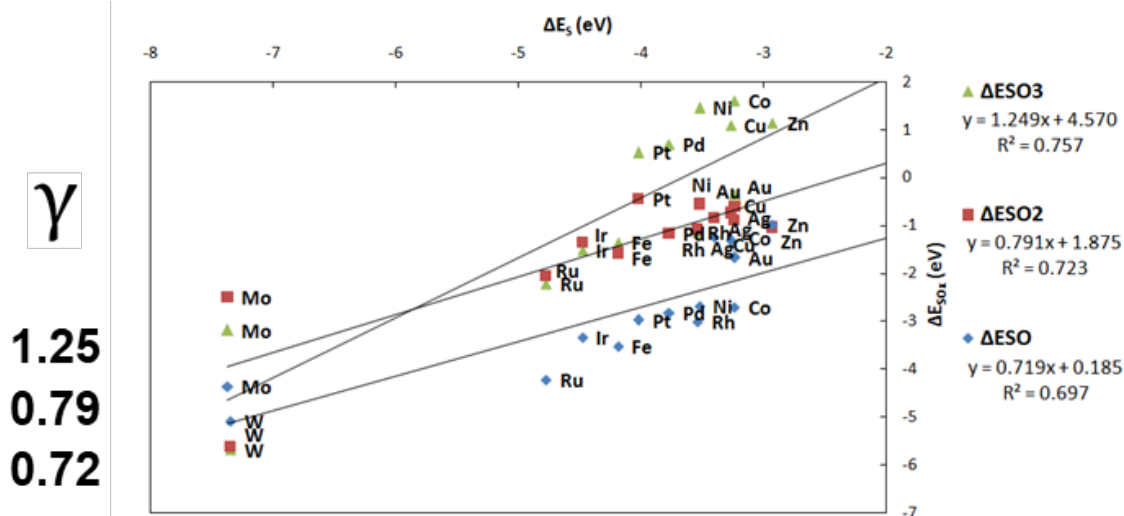


Figure 164. Scaling relations for  $SO_x$  on metal-SSZ-13.

## **G.2 Acknowledgements**

We acknowledge Professor Jeffrey Greeley for his guidance during his density functional theory (DFT) methods course in 2015. The author also acknowledges teammates Jonatan Albarracin-Caballero, James W. Harris, and Han-Ting Tseng for designing this project and calculating a number of the binding energies in the scaling relationship plots. The author also acknowledges Zhenhua Zeng, Joseph Kubal, and Tej Choksi for assistance in getting our DFT calculations to run on the Purdue University supercomputers.

## APPENDIX G. CU- AND FE-ZEOLITES AT THE TOP OF THE VOLCANO

### G.1 Introduction

The literature is laden with improper comparison of catalytic activities, specifically comparing maximum conversions across a temperature range. Other reports compare catalytic conversions at a set temperature. These means of comparison are flawed since the amount of catalyst (hence amount of active sites) and flow rates are not taken into consideration. One can easily artificially increase their catalytic conversions by simply loading more catalyst, decreasing the flow rate, or modifying the feed composition, thus leading to improper comparison true catalyst activity.

Lightoff curves (conversions plotted versus the catalyst temperature) are easy to collect and have value in demonstrating the economics and potential commercialization of the catalyst.

Reproducible and proper comparison of true catalytic activity, however, requires a measurement called the turnover rate is the, and takes into account the amount of catalyst loaded, the number of active sites, flow rates, and feed compositions.

$$\text{Turnover rate} = \frac{\text{intrinsic rate}}{\text{number of active sites}} \quad (\text{Equation 30})$$

### G.2 Experimental

Data extracted from literature light-off curves that were differential (<20% conversion) were used to calculate the reaction rate using CSTR design equations. The SCR rate per mol Cu was then re-adjusted to standard NH<sub>3</sub> SCR (200°C, 300 ppm NO, 300 ppm NH<sub>3</sub>, 10% O<sub>2</sub>) conditions assuming an activation energy of 60 kJ mol<sup>-1</sup>, O<sub>2</sub> order of 0.5, NO order of 0.5, NH<sub>3</sub> order of 0, CO<sub>2</sub> order of 0, and H<sub>2</sub>O order of 0. Though the reaction orders will not be exactly the same across all samples, using these values will allow us to better compare rates collected under the same standard SCR condition.

Several studies have measured the conversions of Fe-zeolites [186–189], Ag-zeolites, [190], Cu-zeolites [43,57,115,118,191–193], Co-zeolites [194], Ru-zeolites [195], and W-zeolites [196]

under differential standard SCR conditions but did not report reaction rates. All of these studies measured activities using sieved powder catalysts in a fixed bed reactor and provided the necessary information required to calculate reaction rates: flow rates, mass of catalyst loaded, metal loading on the zeolite, and the conversion versus temperature lightoff curves. Literature that collected conversions through a monolith or failed to report one or more of the variables listed above were not considered. Of the papers that did, differential conversions were extracted and converted to standard SCR reaction rates at 200°C. We observe in Figure 165 that a constant turnover rate is achieved for Cu-, Fe-, and Co-zeolites with different metal loadings when normalized to the mols of metal on the sample.

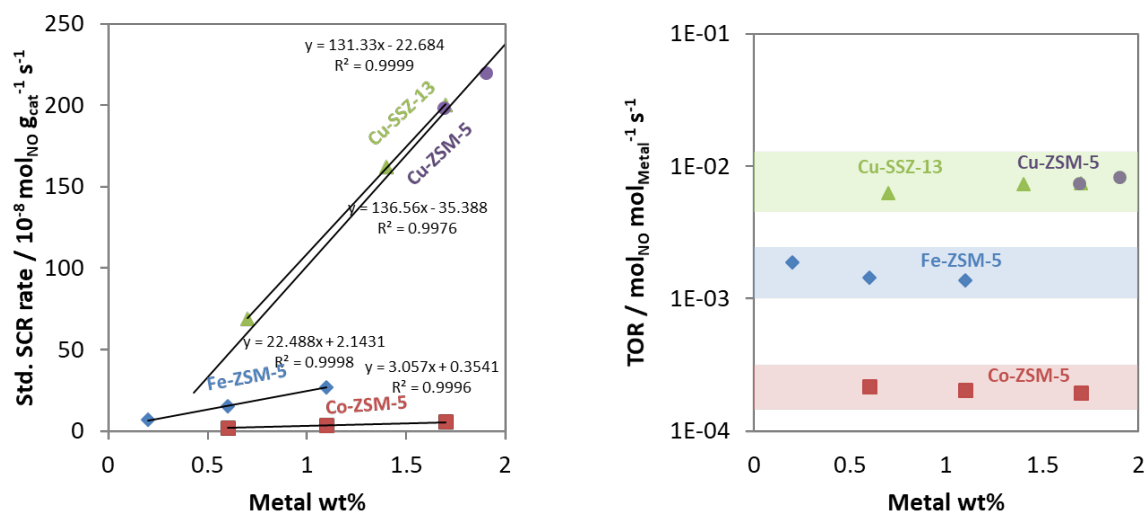


**Figure 165.** NO consumption SCR reaction rates normalized per gram of material plotted versus the metal wt% (left). NO consumption SCR reaction rates normalized per mol metal loaded versus the metal wt%.

We then use the DFT methods in Appendix F to calculate  $\text{NH}_3$  binding energies to  $\text{M}^{2+}$  species charged balance by two 3NN framework Al on a number of metals, summarized in Figure 166.

Metal	$E_{\text{NH}_3} / \text{eV}$		
Ru	-2.14		
Mo	-1.86		
Fe	-1.84		
Zn	-1.81	too strong	
Rh	-1.78		
Ni	-1.76		
Pd	-1.73		
Cu	-1.61	just right	
Ag	-1.51		
W	-1.43		
Co	-1.38	too weak	
Ir	-1.00		
Au	-0.25		
Pt	-0.18		



**Figure 166.** DFT-computed  $\text{NH}_3$  binding energies onto a variety of  $\text{M}^{2+}$  sites charged balanced by two anionic sites on a SSZ-13 framework.

Plotting the standard SCR reaction rate per mol metal on the zeolite against the computed  $\text{NH}_3$  binding energy results in a volcano-type plot with Cu-zeolites at the peak. This correlation is possibly coincidence, but, if true, suggests that  $\text{NH}_3$  binding energies is descriptor that can be used to predict how the nature of the metal in metal-exchanged zeolites affect the standard SCR reaction rate. The Sabatier principle [197] is prevalent in this volcano-type plot;  $\text{NH}_3$  that binds to metal zeolites weaker than -1.6 eV result in  $\text{NH}_3$  failing to bind to the metal site, resulting in slower reactions, and  $\text{NH}_3$  that binds to metal zeolites stronger than -1.6 eV results in  $\text{NH}_3$  or products binding too strong to the metal site, resulting the poisoning of the metal sites and a decrease in the reaction rate.

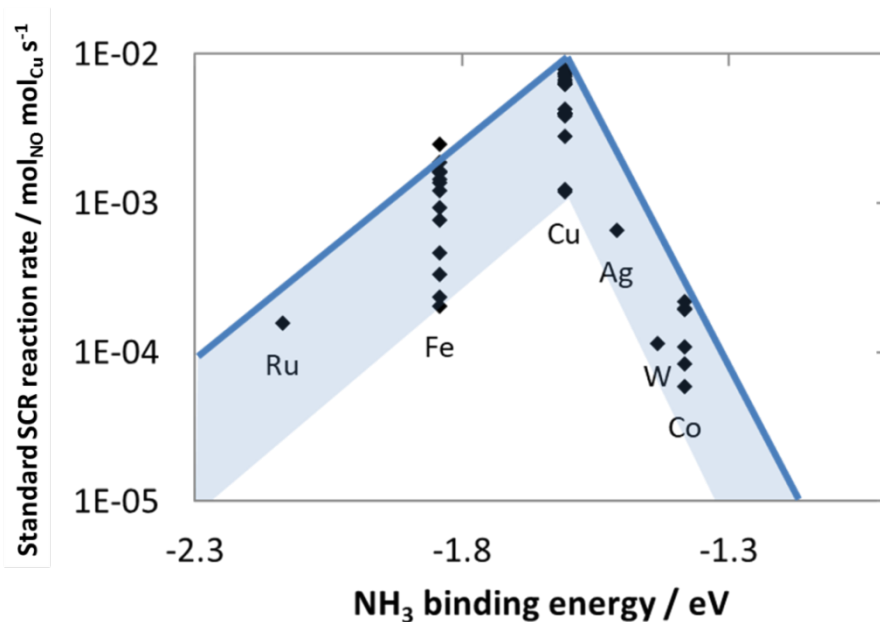


**Figure 167.** Experimentally measured standard SCR reaction rates normalized per mol active metal plotted versus the DFT-computed binding energies. Cu-zeolites turns over the fastest, Fe- and Ag- with mediocre rates, and Ru-, W-, and Co- with poor rates.

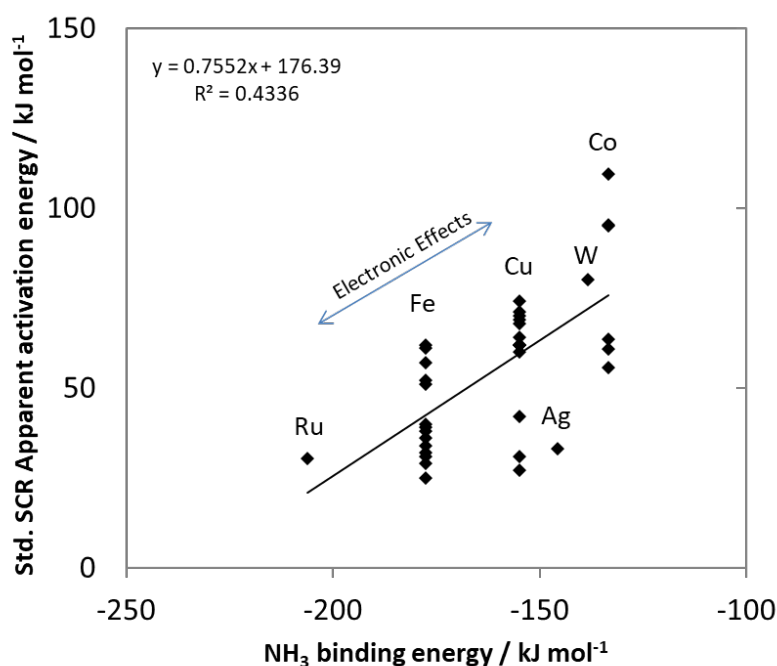


**Figure 168.** Experimentally measured standard SCR apparent activation energies plotted versus the DFT-computed binding energies. The increase in apparent activation energy with increasing binding energy may be due to electronic effects of isolated metal active sites.

Fitting Figure 168 to Equation 31, we obtain best fit values of  $\gamma_{NH_3} = 0.76 \pm 0.29$  and  $\xi = 176.4 \pm 46.2$ .

$$E_{app} = \Sigma \gamma_{NH_3} \Delta E_{NH_3} + \xi \text{ (Equation 31)}$$

This linear equation is a scaling relationship and demonstrates the power of scaling relations – the  $NH_3$  binding energy computed from DFT is able to predict the experimental apparent activation energy to a certain degree of accuracy.

## G.2 Acknowledgements

We acknowledge Professor Jeffrey Greeley for his guidance in introducing us to density function theory (DFT) methods during his course in 2015. The author also acknowledges Brandon Bukowski, Joseph Kubal, Arthur Dysart, and Ishant Khurana for insights, discussion, and input into this work.

## APPENDIX H. NH<sub>3</sub> OXIDATION KINETICS OVER CU-SSZ-13

### H.1 Introduction

Ammonia slip is an issue in commercial diesel aftertreatment systems. Ammonia injected into the system is intended to react stoichiometrically with the toxic NO and NO<sub>2</sub> in the exhaust stream to form clean water and nitrogen, however if too much NH<sub>3</sub> is injected, NH<sub>3</sub> (which is corrosive) may be released into the atmosphere. Some of this ammonia oxidation could occur at the end of the SCR Cu-SSZ-13 catalyst monolith, but most occurs in an ammonia-slip catalyst placed downstream of the SCR catalyst. Commercially, the ammonia slip catalyst consists of a physical mixture of platinum/palladium and Cu-SSZ-13 zeolite catalysts. The purpose of the platinum/palladium is to oxidize some NH<sub>3</sub> to N<sub>2</sub>, NO, NO<sub>2</sub>, and/or N<sub>2</sub>O, and the purpose of the SCR catalyst is to react the residual NH<sub>3</sub> with NO<sub>x</sub>.

NH<sub>3</sub> oxidation typically occurs and competes with SCR at temperatures exceeding 350°C, leading to a decrease in NH<sub>3</sub> available to stoichiometrically catalyze SCR and also possibly forms NO which would subsequently be then. Although ammonia oxidation on Cu-SSZ-13 catalysts do not occur appreciably in the commercial system, studying this reaction on Cu-SSZ-13 opens up avenues to better understand fundamentals of how ammonia affects the mobility and reactivity of the ionic Cu active centers in Cu-SSZ-13 materials. In this chapter, results on the kinetics of NH<sub>3</sub> oxidation over Cu-SSZ-13 catalysts.

Kwak et al. [198] suggested that the high SCR selectivity to N<sub>2</sub> could possibly be related to Cu-SSZ-13's ability to oxidize NH<sub>3</sub>. Gao et al. [63] observed that the NH<sub>3</sub> oxidation rate increases linearly with increasing Cu wt% at 350 and 400°C, but parabolically at 250 and 300°C. Gao et al. [57] also observed an inflection in the apparent activation energy at 250°C, likely due to the material's inability to store NH<sub>3</sub> at temperatures above 250°C. In addition, Piubello et al. [199] claimed that NH<sub>3</sub> oxidation occurs via the formation of NO, which gets consumed via standard SCR from NH<sub>3</sub> cutoff experiments.



### H.3 Results

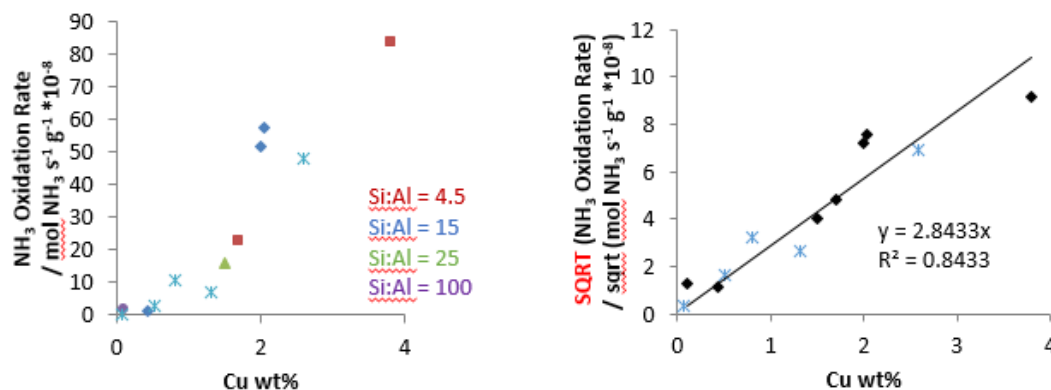


**Figure 169.**  $\text{NH}_3$  oxidation rates (300 ppm  $\text{NH}_3$ , 10%  $\text{O}_2$ , 2.5%  $\text{H}_2\text{O}$ , in balance  $\text{N}_2$ , 300°C) as a function of the Cu wt% collected on Cu-SSZ-13 materials with different Al and Cu densities (left graph). The square root of the  $\text{NH}_3$  oxidation rate plotted versus the Cu wt% results in a linear relationship (right graph).

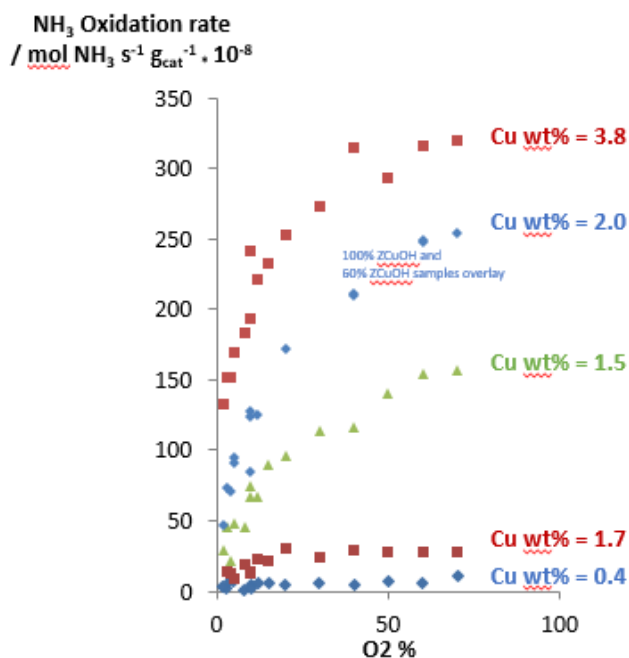


**Figure 170.**  $\text{NH}_3$  oxidation rates normalized per gram of catalyst as a function of  $\text{O}_2$  concentration on a series of Cu-SSZ-13 catalysts with varying Cu densities. Samples with Si:Al ratios of 4.5 (red), 15 (blue), and 25 (green) were tested. Two Cu-SSZ-13 Si:Al = 15 catalysts with the same Al density and Cu density, but different Al distributions were also tested --  $\text{NH}_3$  reaction rates between these two samples matched within error.

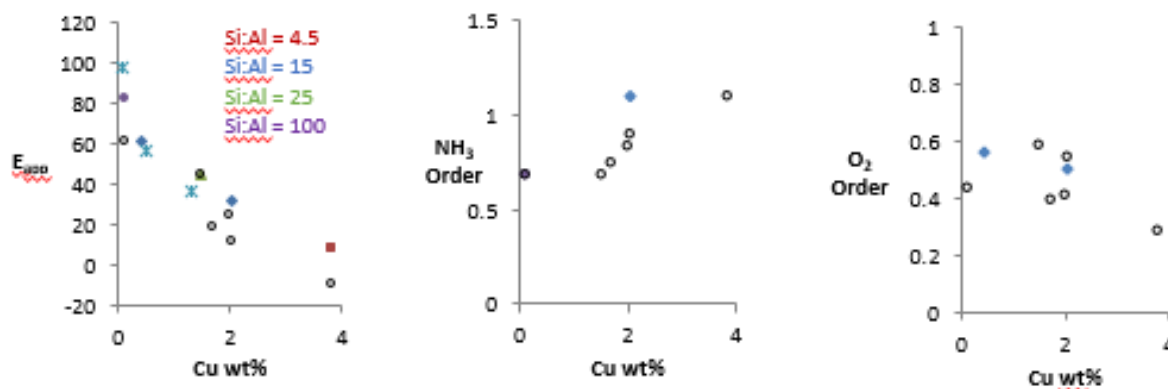


**Figure 171.** Apparent activation energies, NH<sub>3</sub> order, and O<sub>2</sub> orders for NH<sub>3</sub> oxidation (300 ppm NH<sub>3</sub>, 10% O<sub>2</sub>, balance N<sub>2</sub>, 300°C) on a series of Cu-SSZ-13 materials without co-feeding H<sub>2</sub>O (solid shapes) and with co-feeding 2.5% H<sub>2</sub>O (hollow shapes).

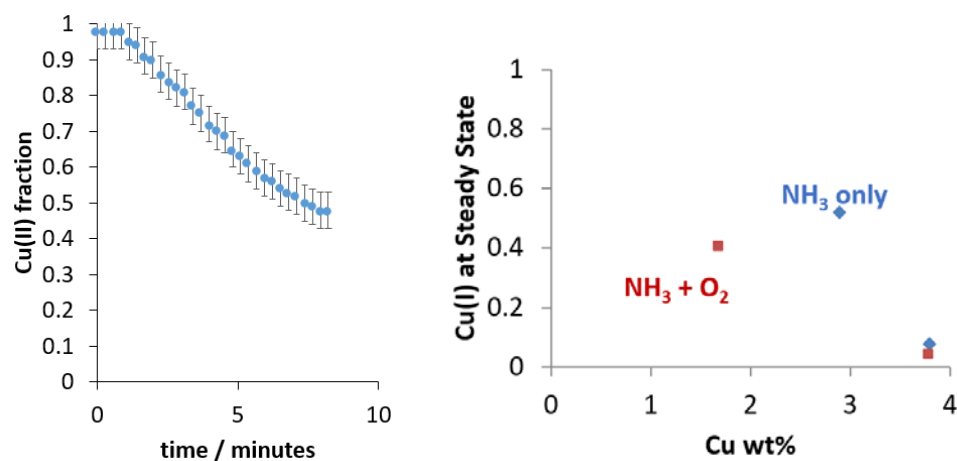


**Figure 172.** Cu(II) fraction transients measured as a function of time on a Cu-SSZ-13 catalyst (Si:Al = 15, Cu wt% = 3) during NH<sub>3</sub> saturation at 200°C of a calcined catalyst with only Cu(II) (left graph). Steady state Cu(I) fractions after NH<sub>3</sub> saturation with O<sub>2</sub> (red squares) and with only NH<sub>3</sub> (blue diamonds) (right graph).

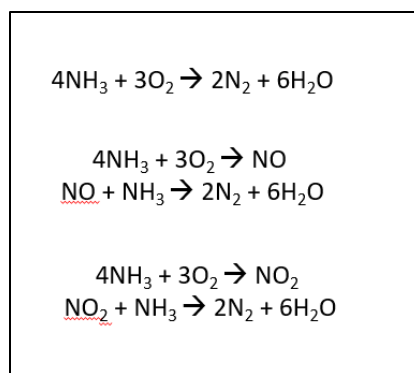


**Figure 173.** Three possible pathways for  $\text{NH}_3$  oxidation: (1) direct oxidation to  $\text{N}_2$  and  $\text{H}_2\text{O}$ , (2) Oxidation to  $\text{NO}$ , then to  $\text{N}_2$  and  $\text{H}_2\text{O}$  via standard SCR, (3) oxidation to  $\text{NO}_2/\text{NO}$ , then to  $\text{N}_2$  and  $\text{H}_2\text{O}$  via fast SCR.

## APPENDIX I. CU-ION MOBILITY AND KINETIC STUDIES

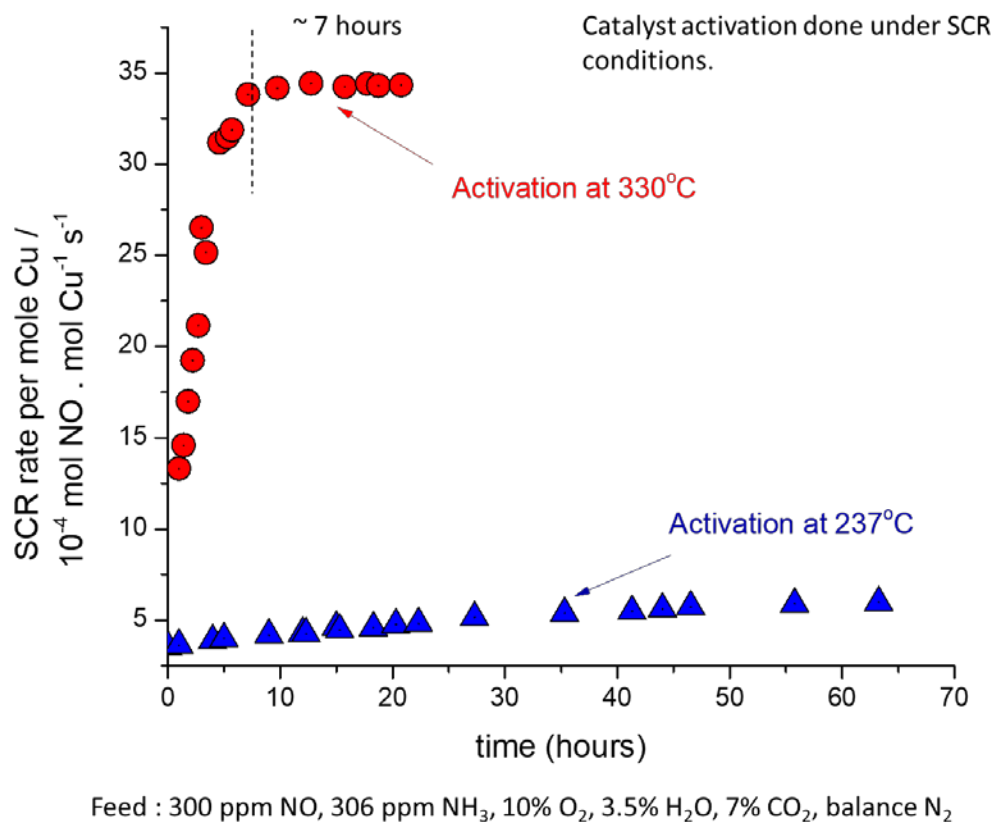


**Figure 174.** SCR reaction rate on a physical mixture of Cu-SiO<sub>2</sub> and H-SSZ-13 as a function of time. The physical mixture was activated at 237°C (blue triangles) and 330°C (red circles).

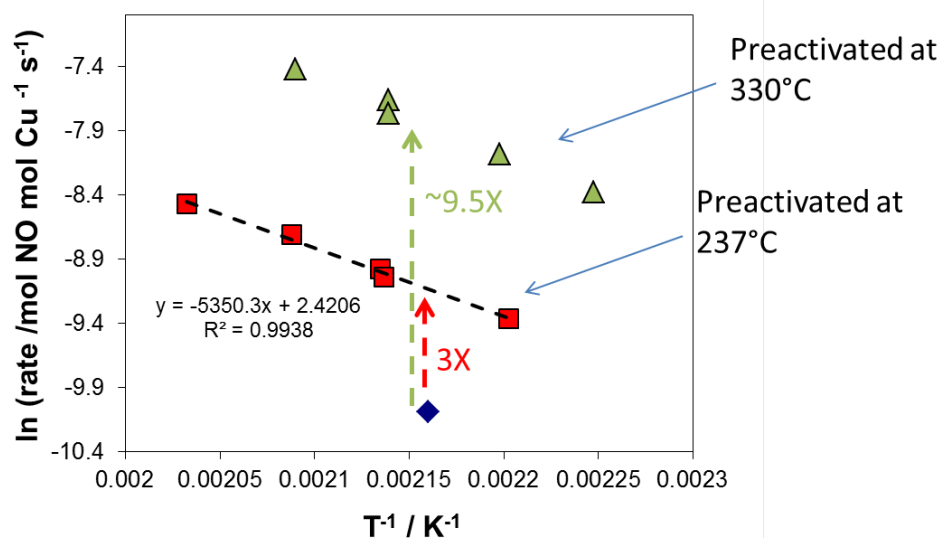


**Figure 175.** Arrhenius plots of activated Cu-SiO<sub>2</sub> and H-SSZ-13 physical mixtures after activation at 237°C (red squares) and 330°C (green triangles). The reaction rate on Cu-SiO<sub>2</sub> is represented by the blue diamond.

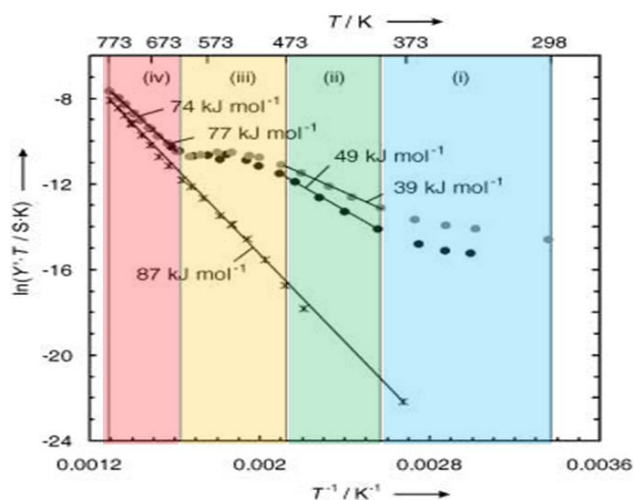


**Figure 176.** Arrhenius plot for the proton transport rate measured from Impedance Spectroscopy (IS) over a H-ZSM-5 material (Si:Al = 60) in the presence of 1% H<sub>2</sub>O (grey circles), 100 ppm NH<sub>3</sub> (black circles), and dehydrated (black x's). Figure adapted from Franke et al. [200,201].

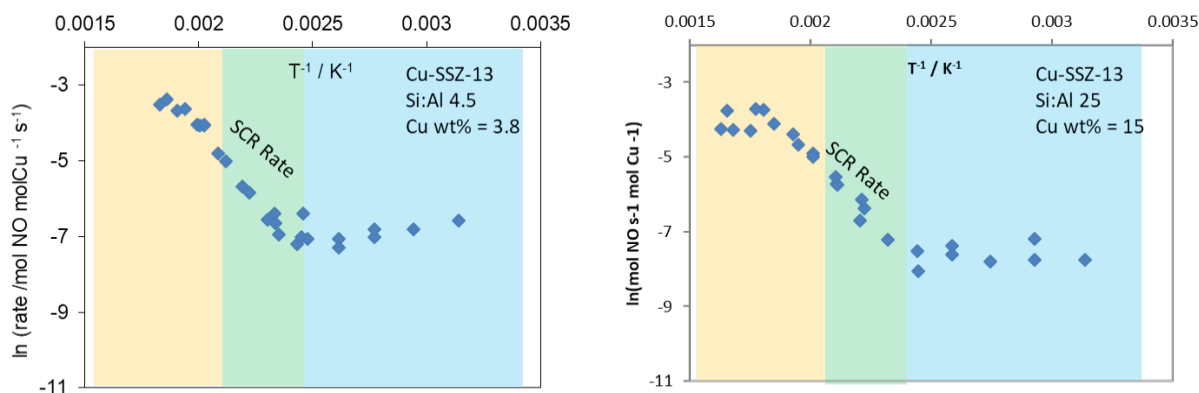
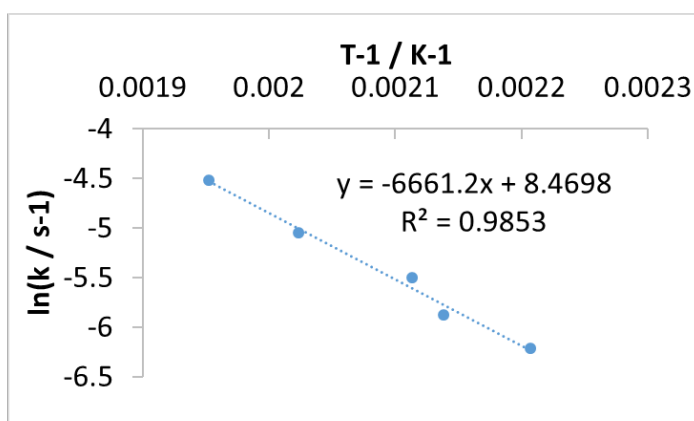


**Figure 177.** Arrhenius plots for the consumption of NO during standard SCR feed conditions for a Cu-SSZ-13 catalyst with most Cu ions as  $Z_2Cu$  (left) and as  $ZCuOH$  (right).

1<sup>st</sup> Order Fit  
 $E_{app} = 54 \text{ kJ mol}^{-1}$



2<sup>nd</sup> Order Fit  
 $E_{app} = 139 \text{ kJ mol}^{-1}$

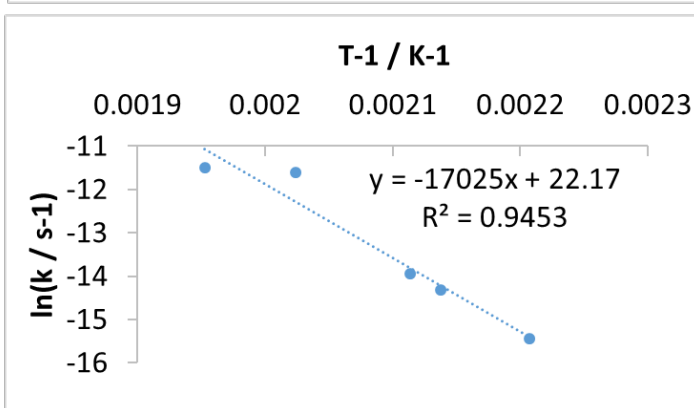


**Figure 178.** Arrhenius plots for the initial rate of decrease after cutting off  $NH_3$  from a catalyst operating at differential steady state under standard SCR conditions (300 ppm  $NH_3$ , 300 ppm NO, 10%  $O_2$ , 7%  $CO_2$ , 2.5%  $H_2O$ , balance  $N_2$  at temperatures between 160 to 240°C) on a Cu-SSZ-13 material (Si:Al = 4.5, Cu:Al = 0.21). Fitting the initial rate to a first order rate law gives a better fit than fitting it to a second order rate law.

## APPENDIX J. DEACTIVATION OF CU-ZSM-5

An experiment to test the hydrothermal stability of Cu-ZSM-5 (Si:Al = 12.5, Cu wt% = 1.26) at 400°C was performed. Figure 171 shows the  $\text{NH}_3$  concentration as the Cu-ZSM-5 catalyst was subjected to standard SCR conditions (300 ppm  $\text{NH}_3$ , 300 ppm NO, 10%  $\text{O}_2$ , 8%  $\text{CO}_2$ , 2.5%  $\text{H}_2\text{O}$ , balance  $\text{N}_2$ ) at 400°C for 40 hours. We observe a 80% decrease in the reaction rate at 200°C and a decrease in the apparent activation energy from 60  $\text{kJ mol}^{-1}$  to 30  $\text{kJ mol}^{-1}$  (Figure 180).

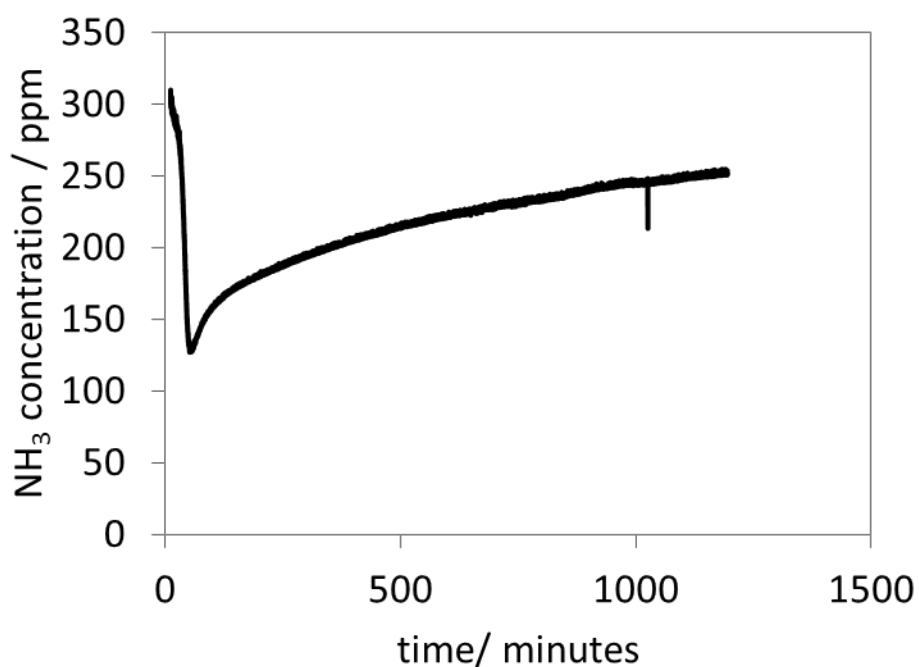


**Figure 179.**  $\text{NH}_3$  concentration over an initially fresh Cu-ZSM-5 catalyst over the course of exposure to standard SCR conditions (300 ppm  $\text{NH}_3$ , 300 ppm NO, 10%  $\text{O}_2$ , 8%  $\text{CO}_2$ , 2.5%  $\text{H}_2\text{O}$ , balance  $\text{N}_2$ ) at 400°C for 40 hours.

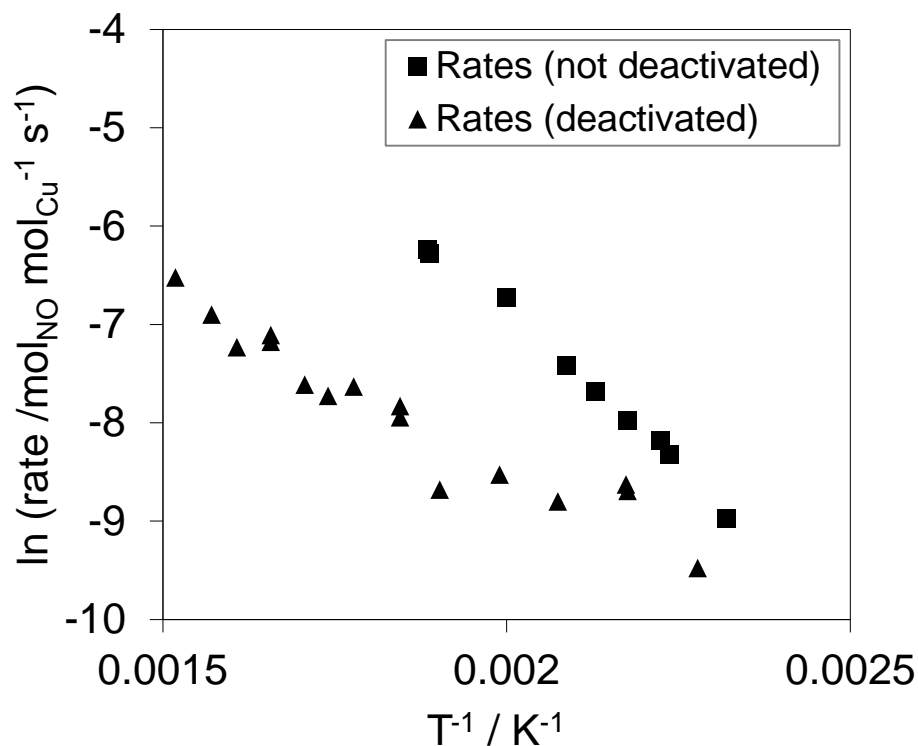


**Figure 180.** Standard SCR reaction rates on fresh Cu-ZSM-5 catalyst after exposure to standard SCR conditions (300 ppm  $\text{NH}_3$ , 300 ppm  $\text{NO}$ , 10%  $\text{O}_2$ , 7%  $\text{CO}_2$ , 2.5%  $\text{H}_2\text{O}$ , balance  $\text{N}_2$ ) at 400°C for 40 hours. The apparent activation energy at 200°C decreases from 60  $\text{kJ mol}^{-1}$  to 30  $\text{kJ mol}^{-1}$



## **APPENDIX K. N<sub>2</sub>O FORMATION ON CUXOY, Z<sub>2</sub>Cu, AND ZCuOH SITES DURING STANDARD SCR AND IMPACT OF SULFUR POISONS**

### **K.1 Introduction**

N<sub>2</sub>O is regulated due to its estimated global warming potential of ~300 times that of CO<sub>2</sub> [202,203]. It is produced from the combustion of fossil fuels and also from the aftertreatment process, especially over SCR catalysts because it deals with converting NO<sub>x</sub> gases [204–206]. It has been proposed that the production of N<sub>2</sub>O occurs via two pathways: (1) The decomposition of ammonium nitrate species formed from NH<sub>3</sub> and NO<sub>x</sub>, and (2) The oxidation of NH<sub>3</sub> with O<sub>2</sub> to N<sub>2</sub>O [29,206–208]

### **K.2 Results and Discussion**

The N<sub>2</sub>O formation rate during standard SCR at 200°C is three to four times higher on ZCuOH and Cu<sub>x</sub>O<sub>y</sub> model Cu-SSZ-13 than on the Z<sub>2</sub>Cu model Cu-SSZ-13 (Table 36). We also observe no significant difference between the standard SCR apparent activation energies and the N<sub>2</sub>O formation activation energies. This suggests that the N<sub>2</sub>O formation pathway is likely directly dependent on the rate of SCR, and is mechanistically an offshoot from the standard SCR mechanism. This suggests that it's unlikely that the formation of N<sub>2</sub>O is from NH<sub>3</sub> oxidation, but rather than the formation of ammonium nitrates during standard SCR cycle.

The impact of sulfur poisons using the same sulfur poisoned materials prepared in Chapter 7 on the N<sub>2</sub>O formation rate were also studied. Table 37 summarizes the standard SCR reaction rates and apparent activation energies in addition to the N<sub>2</sub>O formation rates and apparent activation energies on unsulfated, sulfated, and desulfated model Z<sub>2</sub>Cu and model ZCuOH Cu-SSZ-13. The N<sub>2</sub>O formation rate on plotted versus the molar S:Cu ratio (Figure 182) indicates that an increase in sulfur suppresses the N<sub>2</sub>O formation rate on both model ZCuOH and model Z<sub>2</sub>Cu materials, with the rate suppressed more on the model ZCuOH Cu-SSZ-13. We observe a decrease in the ratio of the rates with increasing sulfur loading on both materials (Figure 183), this indicates that the fractional decrease in the N<sub>2</sub>O formation rate is much larger than the fractional decrease in the standard SCR rate after sulfur poisoning.

The presence of sulfur poisons does not change the  $\text{N}_2\text{O}$  formation apparent activation energy, on both  $\text{Z}_2\text{Cu}$  and  $\text{ZCuOH}$  model catalysts after sulfation and desulfation (Figure 184). The standard SCR apparent activation energy does not change for  $\text{Z}_2\text{Cu}$  model catalysts after sulfation and desulfation, but decreases for  $\text{ZCuOH}$  model catalysts after sulfation and desulfation. We previously interpreted the parity in standard SCR and  $\text{N}_2\text{O}$  formation energies as evidence that the rate of formation of  $\text{N}_2\text{O}$  is linked with how fast the standard SCR catalytic cycle turns over. However, if the two apparent activations are just coincidentally the same within error, then it could indicate that the formation of  $\text{N}_2\text{O}$  mechanistically occurs via a different pathway with a similar activation barrier independent of the rate of standard SCR. It is also possible that because sulfur species that poison  $\text{ZCuOH}$  sites directly interact with the Cu ions (unlike  $\text{Z}_2\text{Cu}$ , where sulfur simply blocks the sites), that these species continue contributing to  $\text{N}_2\text{O}$  formation, but not to standard SCR.

### **K.3 Recommendations**

We recommend to co-feed  $\text{N}_2\text{O}$  during standard SCR to determine the  $\text{N}_2\text{O}$  order since the  $\text{N}_2\text{O}$  concentration through the catalyst bed is not differential during these studies. In addition, a better model  $\text{Cu}_x\text{O}_y$  material would be  $\text{Cu}_x\text{O}_y$  deposited onto pure-silica SSZ-13. The pure silica SSZ-13 can be synthesized hydrothermally in fluoride media [209,210], and  $\text{Cu}_x\text{O}_y$  species can be deposited onto the support using pH-controlled  $\text{Cu}(\text{OH})_2$  precipitation methods described in Chapter 8. After calcination, the resulting Cu-SSZ-13 material will have 100%  $\text{Cu}_x\text{O}_y$  species with no ionic Cu.

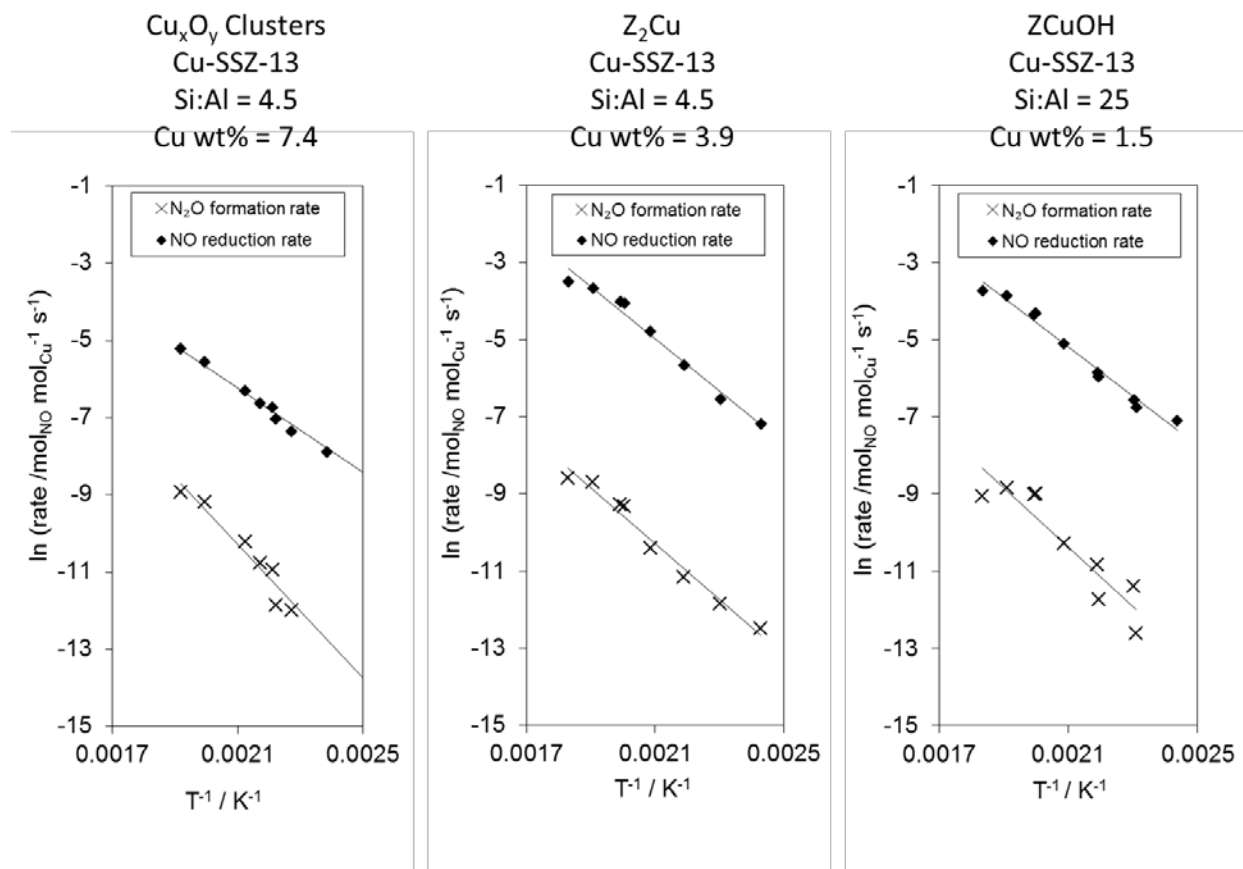


**Figure 181.** Arrhenius plots for the SCR NO reduction rate (black diamonds) and the N<sub>2</sub>O formation rate during SCR (black crosses) on model Cu<sub>x</sub>O<sub>y</sub>, Z<sub>2</sub>Cu, and ZCuOH Cu-SSZ-13 materials. Standard SCR conditions were used (300 ppm NH<sub>3</sub>, 300 ppm NO, 10% O<sub>2</sub>, 8% CO<sub>2</sub>, 2.5% H<sub>2</sub>O, balance N<sub>2</sub>, 150 to 250°C).

**Table 35.** Fraction of Cu species on  $\text{Cu}_x\text{O}_y$ ,  $\text{Z}_2\text{Cu}$ , and  $\text{ZCuOH}$  model materials.

\*The fraction of  $\text{Cu}_x\text{O}_y$  sites were estimated from differential SCR rates. The ratio of the actual measured SCR rate on the material with  $\text{Cu}_x\text{O}_y$  to the expected SCR rate assuming all its Cu were  $\text{Z}_2\text{Cu}$  was used to estimate the fraction of  $\text{Cu}_x\text{O}_y$ .

Model Material	Si:Al	Cu wt%	Fraction $\text{Z}_2\text{Cu}$	Fraction $\text{ZCuOH}$	Fraction $\text{Cu}_x\text{O}_y$
$\text{Cu}_x\text{O}_y^*$	4.5	7.43	0.3	0.0	0.7
$\text{Z}_2\text{Cu}$	4.5	3.86	1.0	0.0	0.0
$\text{ZCuOH}$	25	1.50	0.2	0.8	0.0

**Table 36.** SCR reaction rates and apparent activation energies compared to the  $\text{N}_2\text{O}$  formation rates and activation energies on  $\text{Cu}_x\text{O}_y$ ,  $\text{Z}_2\text{Cu}$ , and  $\text{ZCuOH}$  model materials (300 ppm  $\text{NH}_3$ , 300 ppm  $\text{NO}$ , 10%  $\text{O}_2$ , 8%  $\text{CO}_2$ , 2.5%  $\text{H}_2\text{O}$ , balance  $\text{N}_2$ , 200°C). The ratio of the  $\text{N}_2\text{O}$  formation rate and SCR  $\text{NO}$  reduction rate is tabulated in the right-most column.

Model Material	Cu wt%	SCR NO reduction kinetics		$\text{N}_2\text{O}$ formation kinetics		$\text{rate}_{\text{N}_2\text{O}}:\text{rate}_{\text{SCR}}$
		$E_{\text{app}}$ / $\text{kJ mol}^{-1}$	Rate / $\text{mol}_{\text{NO}}$ $\text{mol}_{\text{Cu}}^{-1} \text{s}^{-1}$	$E_{\text{app}}$ / $\text{kJ mol}^{-1}$	Rate / $\text{mol}_{\text{N}_2\text{O}}$ $\text{mol}_{\text{Cu}}^{-1} \text{s}^{-1}$	
$\text{Cu}_x\text{O}_y$	7.43	58	$1.8 \cdot 10^{-3}$	76	$3.0 \cdot 10^{-5}$	0.017
$\text{Z}_2\text{Cu}$	3.86	63	$6.9 \cdot 10^{-3}$	60	$5.6 \cdot 10^{-5}$	0.008
$\text{ZCuOH}$	1.50	58	$5.1 \cdot 10^{-3}$	64	$3.4 \cdot 10^{-4}$	0.067

**Table 37.** Impact of sulfation and desulfation on N<sub>2</sub>O formation rates on model Z<sub>2</sub>Cu and ZCuOH Cu-SSZ-13.

Material	S:Cu	SCR NO reduction		N <sub>2</sub> O formation		rate <sub>N<sub>2</sub>O</sub> : rate <sub>SCR</sub>
		E <sub>app</sub> / kJ mol <sup>-1</sup>	Rate / mol <sub>NO</sub> mol <sub>Cu</sub> <sup>-1</sup> s <sup>-1</sup>	E <sub>app</sub> / kJ mol <sup>-1</sup>	Rate / mol <sub>N<sub>2</sub>O</sub> mol <sub>Cu</sub> <sup>-1</sup> s <sup>-1</sup>	
Z <sub>2</sub> Cu unsulfated	0.00	69	6.9·10 <sup>-3</sup>	60	5.6·10 <sup>-5</sup>	0.0081
Z <sub>2</sub> Cu 200°C SO <sub>2</sub>	0.28	73	4.7·10 <sup>-3</sup>	62	2.0·10 <sup>-5</sup>	0.0043
Z <sub>2</sub> Cu 400°C SO <sub>2</sub>	0.47	72	3.6·10 <sup>-3</sup>	61	2.9·10 <sup>-6</sup>	0.0008
Z <sub>2</sub> Cu 200°C SO <sub>2</sub> desulfated	0.38	62	6.1·10 <sup>-3</sup>	66	3.3·10 <sup>-5</sup>	0.0054
Z <sub>2</sub> Cu 400°C SO <sub>2</sub> desulfated	0.75	61	4.3·10 <sup>-3</sup>	75	1.2·10 <sup>-5</sup>	0.0028
ZCuOH unsulfated	0.00	52	5.1·10 <sup>-3</sup>	64	3.4·10 <sup>-4</sup>	0.067
ZCuOH 200°C SO <sub>2</sub>	0.59	42	1.4·10 <sup>-3</sup>	59	6.9·10 <sup>-6</sup>	0.0049
ZCuOH 400°C SO <sub>2</sub>	1.44	15	4.7·10 <sup>-4</sup>	59	1.1·10 <sup>-6</sup>	0.0023

ZCuOH						
200°C SO <sub>2</sub>	0.38	38	$1.9 \cdot 10^{-3}$	64	$8.9 \cdot 10^{-6}$	0.0047
desulfated						
ZCuOH						
400°C SO <sub>2</sub>	0.75	34	$1.1 \cdot 10^{-3}$	57	$1.5 \cdot 10^{-5}$	0.0136
desulfated						

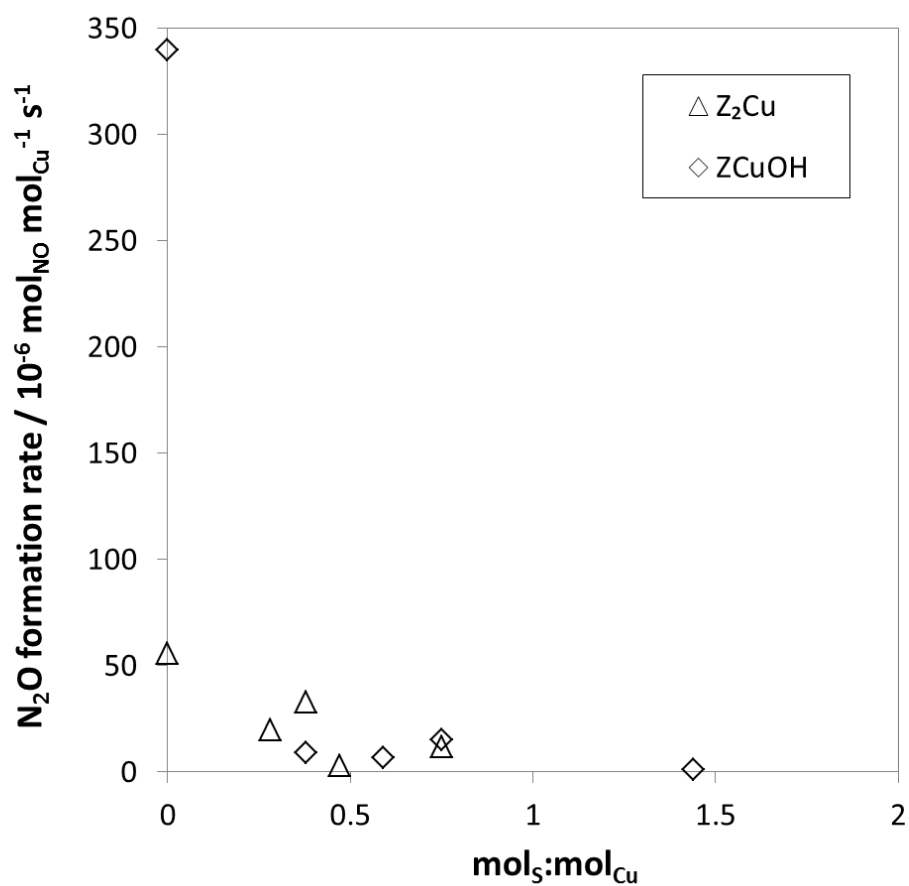


**Figure 182.** The N<sub>2</sub>O formation rate over Z<sub>2</sub>Cu (hollow triangles) and ZCuOH (hollow diamonds) Cu-SSZ-13 catalysts before and after sulfur poisoning and after desulfation. The presence of sulfation suppresses the N<sub>2</sub>O formation rate with ZCuOH exhibiting the largest decrease in N<sub>2</sub>O formation after sulfur poisoning.

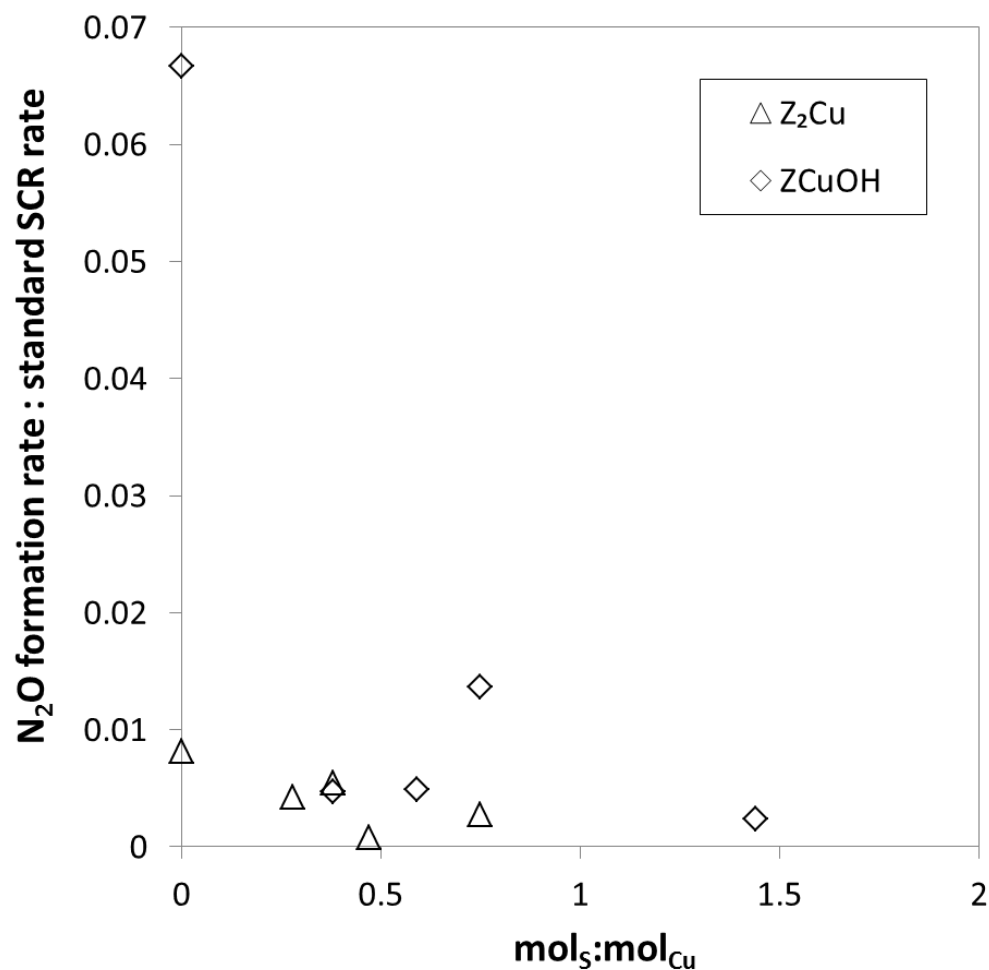


**Figure 183.** Although the presence of sulfur suppresses both the standard SCR and  $\text{N}_2\text{O}$  formation rate, the  $\text{N}_2\text{O}$  formation rate is suppressed to greater extents than the standard SCR rate after sulfation and desulfation on the model  $\text{ZCuOH}$  Cu-SSZ-13 (diamonds). Sulfation suppresses the  $\text{N}_2\text{O}$  formation rate and standard SCR rate by approximately equal extents on model  $\text{Z}_2\text{Cu}$  Cu-SSZ-13 (triangles).

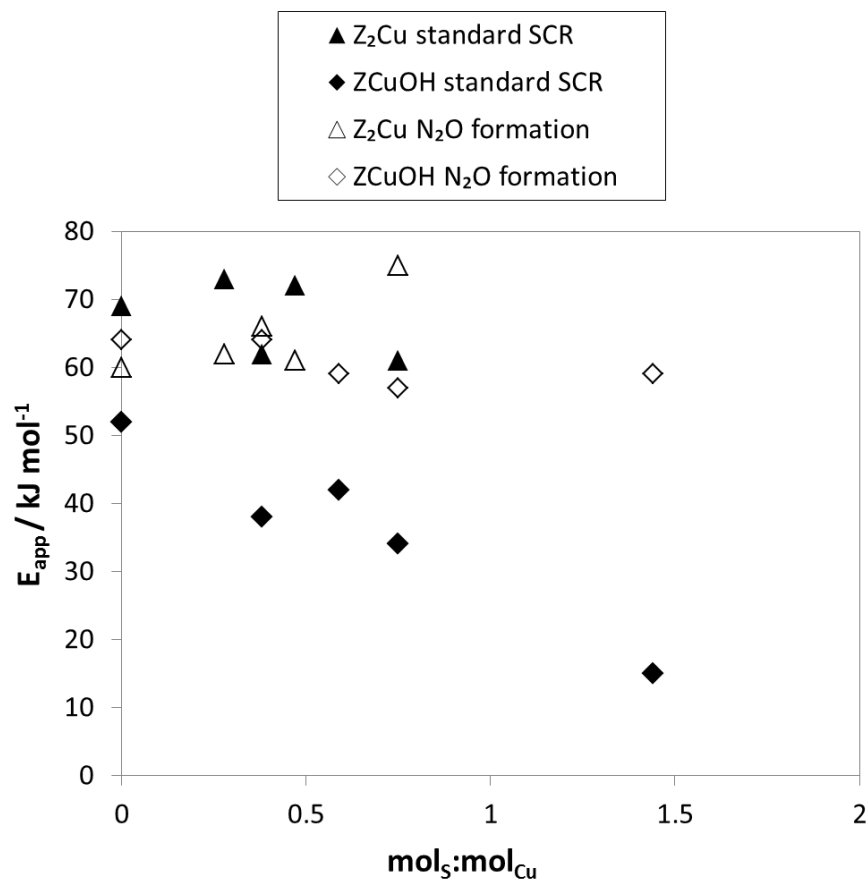


**Figure 184.** The N<sub>2</sub>O formation apparent activation energy does not change within error with increasing sulfur poisoning on both model Z<sub>2</sub>Cu (hollow triangles) and ZCuOH (hollow diamonds) Cu-SSZ-13 materials. The standard SCR apparent activation energy decreases with increasing sulfur poisoning on ZCuOH model Cu-SSZ-13 (solid diamonds), but does not change with increasing sulfur poisoning on Z<sub>2</sub>Cu model Cu-SSZ-13 (solid triangles).



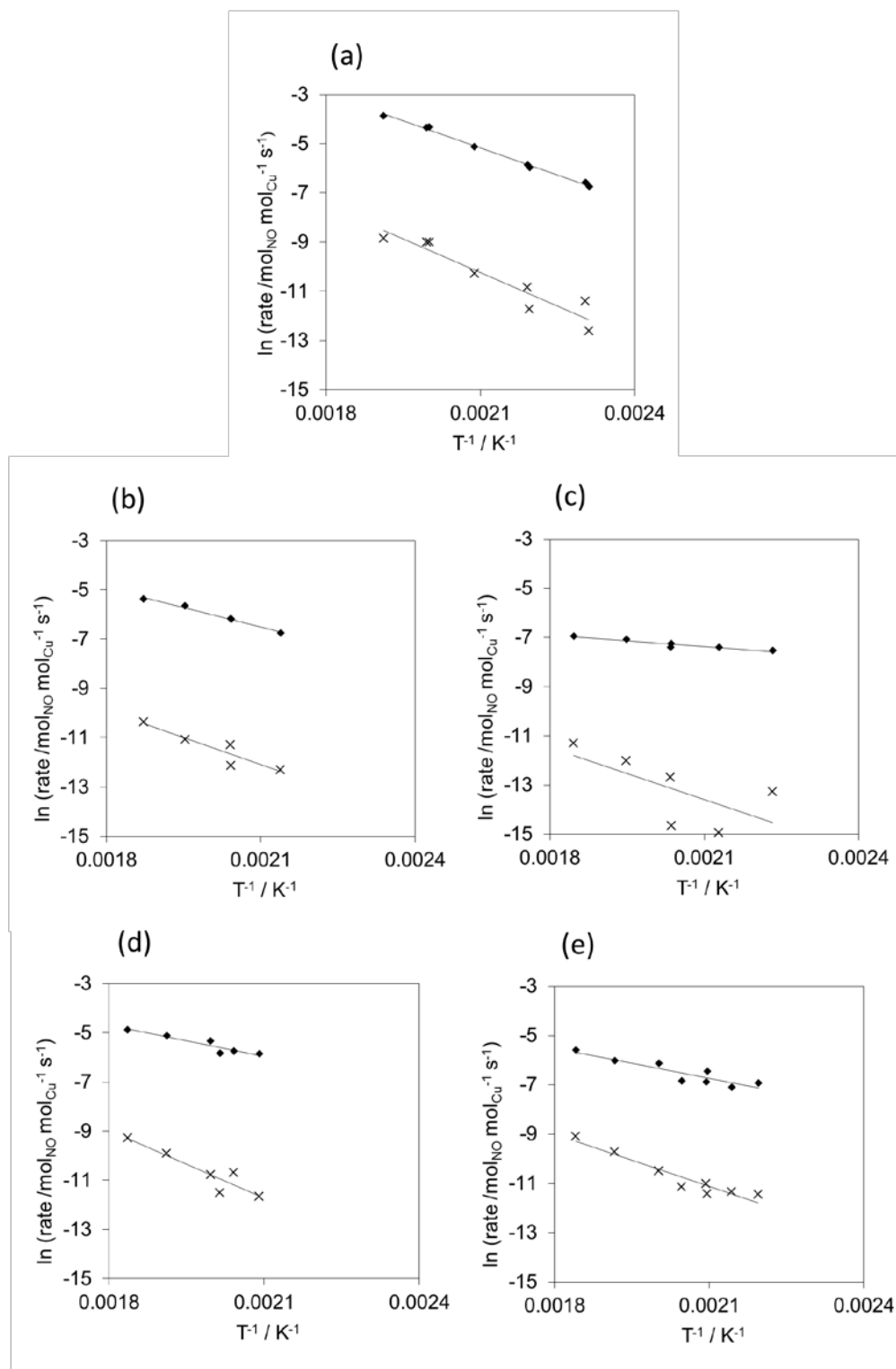


**Figure 185.** Arrhenius plots of standard SCR rates (black diamonds) and  $N_2O$  formation rates during standard SCR (crosses) on (a) unsulfated, (b) 200°C  $SO_2$ , (c) 400°C  $SO_2$ , (d) 200°C  $SO_2$  desulfated, (e) 400°C  $SO_2$  desulfated model ZCuOH catalysts.

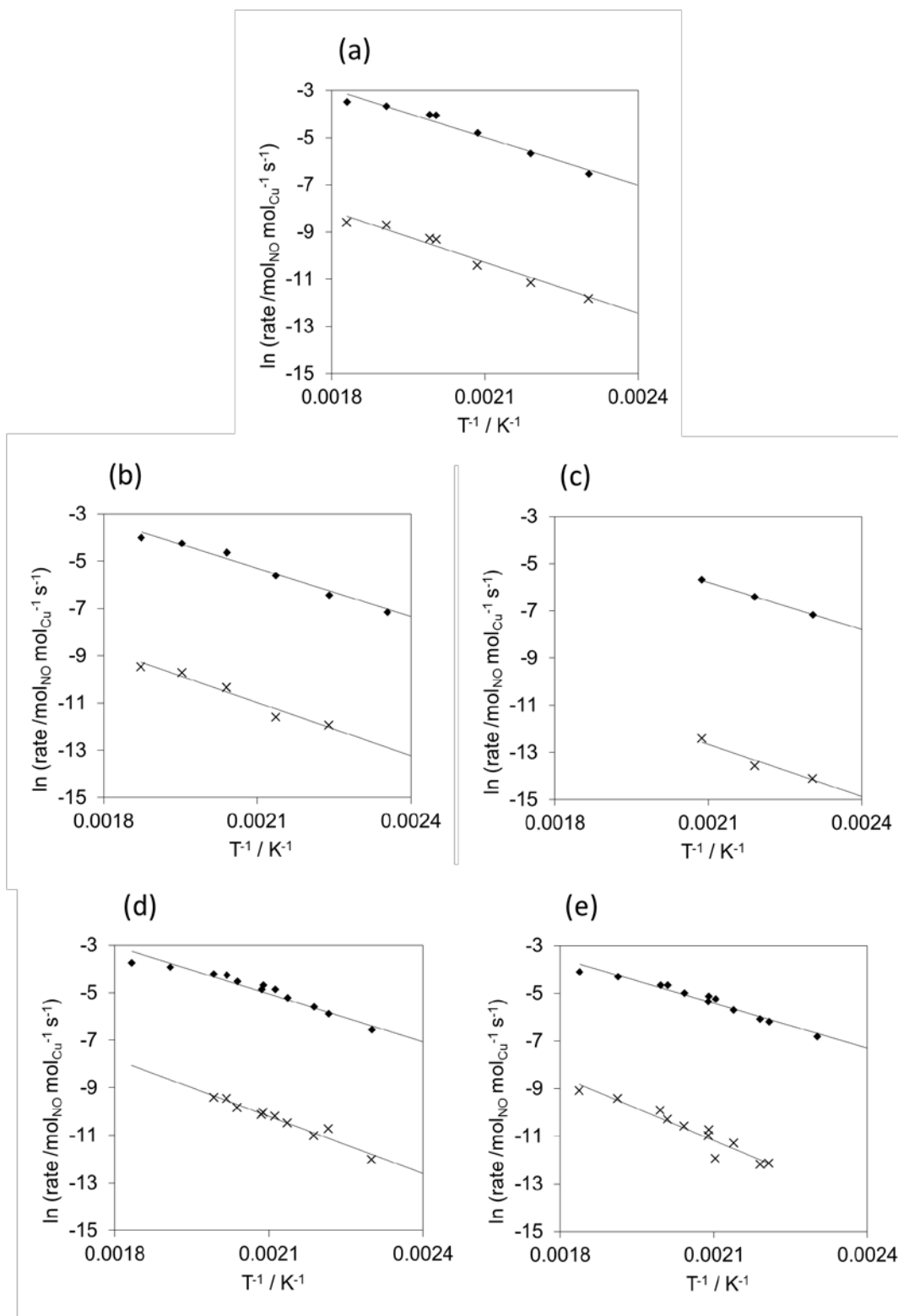


**Figure 186.** Arrhenius plots of standard SCR rates (black diamonds) and  $\text{N}_2\text{O}$  formation rates during standard SCR (crosses) on (a) unsulfated, (b) 200°C  $\text{SO}_2$ , (c) 400°C  $\text{SO}_2$ , (d) 200°C  $\text{SO}_2$  desulfated, (e) 400°C  $\text{SO}_2$  desulfated model  $\text{Z}_2\text{Cu}$  catalysts.

## APPENDIX L. OBSERVED PHENOMENON WHEN STANDARD SCR GASES ARE BUBBLED THROUGH AQUEOUS $\text{Cu}(\text{NO}_3)_2$

### L.1 Experimental

In lieu of a packed bed reactor, the standard SCR mixture (300 ppm  $\text{NO}$ , 260 ppm  $\text{NH}_3$ , 10%  $\text{O}_2$ , 2.5%  $\text{H}_2\text{O}$ , 8%  $\text{CO}_2$ , in balance  $\text{N}_2$  at  $20^\circ\text{C}$ ) was bubbled through a stir-bar agitated aqueous solution (100 mL, or none for blank runs) in a 250 mL vacuum filter Erlenmeyer flask. The gaseous products after bubbling were analyzed using a MKS FTIR 2030. After loading the aqueous solution, the Erlenmeyer flask was assembled and pressure tested with Helium for 30 minutes at 5 psig. SCR gases were flown only if the pressure did not decrease.

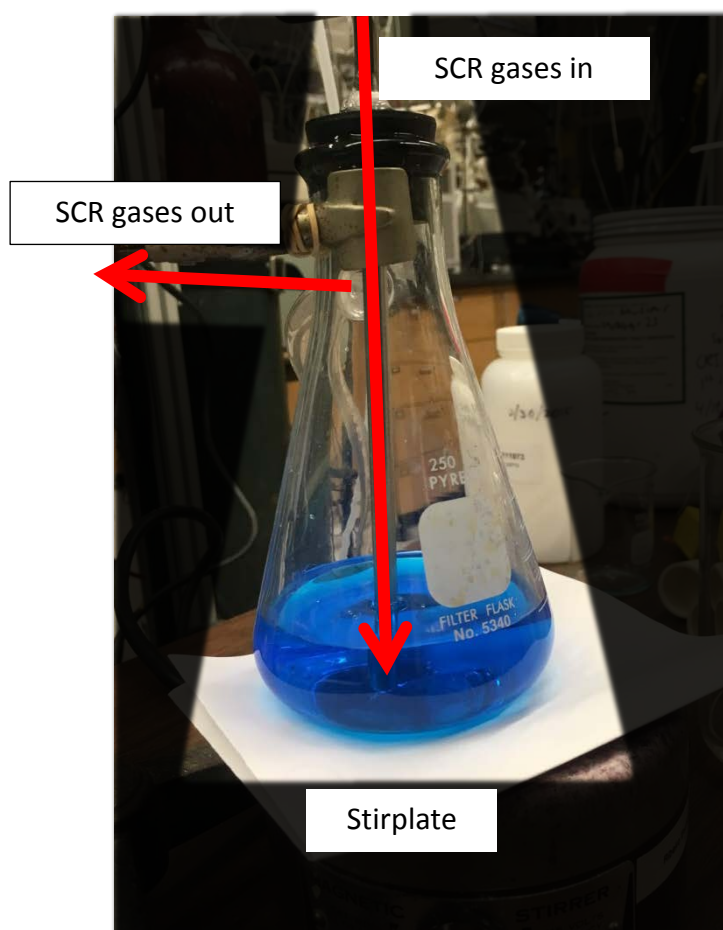


**Figure 187.** Photo of the vacuum filter Erlenmeyer flask setup for bubbling SCR gases through a  $\text{Cu}(\text{NO}_3)_2$  solution.

## L.1 Results and Discussion

We first observe that when there is no liquid in the Erlenmeyer flask, the  $\text{NH}_3$  concentration increases to its steady state value of 260 ppm, indicating that the  $\text{NH}_3$  is not converted or being accumulated anywhere in the piping system. Regardless of whether the standard SCR mixture is bubbled through water or 1.0 M  $\text{Cu}(\text{NO}_3)_2$ , we observe that  $\text{NH}_3$  does not break through, indicating that the  $\text{NH}_3$  is accumulating in the aqueous solution (Figure 183). During this process the  $\text{NH}_3$  reacts with  $\text{H}_2\text{O}$  to ammonium hydroxide, thereby increasing the pH, resulting in the formation of solid  $\text{Cu}(\text{OH})_2$  precipitates [168]. These  $\text{Cu}(\text{OH})_2$  precipitates are visually observed as the  $\text{Cu}(\text{NO}_3)_2$  solution transitions from a clear see-through blue solution to an opaque light-blue slurry over the course of 30 minutes.

The NO concentration temporal profile is the same for the first 8 minutes regardless of whether the Erlenmeyer flask was unfilled or filled with water or 1.0 M  $\text{Cu}(\text{NO}_3)_2$ . This indicates that NO does not appreciably dissolve in  $\text{H}_2\text{O}$  or adsorb to the  $\text{Cu}^{2+}$  ions in the solution. We do observe that NO cyclically adsorbed and desorbed in pulses when bubbled through the  $\text{Cu}(\text{NO}_3)_2$  solution, with the magnitude of NO adsorption and desorption increasing as the pH of the solution increases. We do not measure the formation of  $\text{N}_2\text{O}$  or  $\text{NO}_2$ , ruling out the possibility of side reactions. We do not have sufficient evidence to confidently pinpoint the identity or nature of the adsorption or desorption sites, but speculate that the NO adsorption may be due to the  $\text{Cu}(\text{OH})_2$  precipitates. With regards to how NO desorbs, it is possible that NO desorbs when  $\text{Cu}(\text{OH})_2$  precipitates that store the NO is physically perturbed in the stirred slurry either through exposure to the walls of the flask, exposure to the liquid-gas interface, or when  $\text{Cu}(\text{OH})_2$  species crystallize and break off the end the stainless steel bubbler where the  $\text{NH}_3$  concentration is the highest. We observed a deposits of  $\text{Cu}(\text{OH})_2$  precipitates at then end of the stainless steel bubbler when cleaning the flask for repeat measurements.

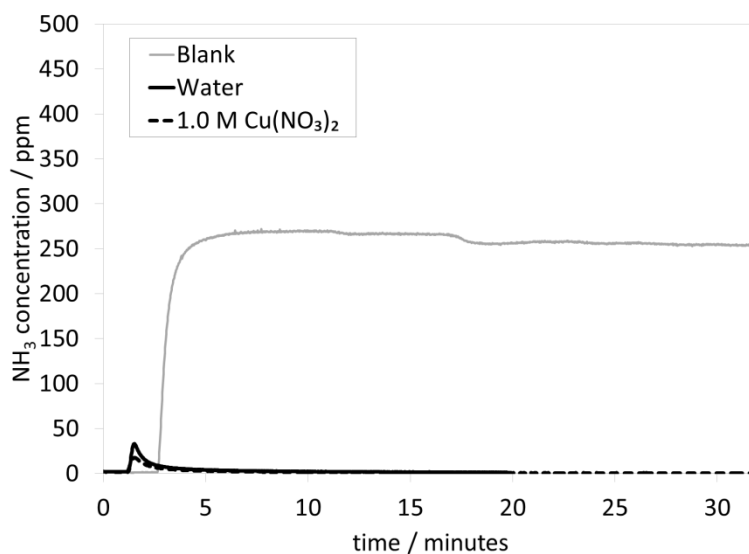


**Figure 188.**  $\text{NH}_3$  concentration as a function of time through a blank Erlenmeyer flask (grey trace), water (black trace), and 1.0 M  $\text{Cu}(\text{NO}_3)_2$  (dashed black trace). At time zero the SCR mixture started flowing at time zero. The breakthrough time delay before appearance of  $\text{NH}_3$  into the MKS FTIR 2030 is due to  $\text{NH}_3$  displacing the inert  $\text{N}_2$  in the piping and Erlenmeyer flask.

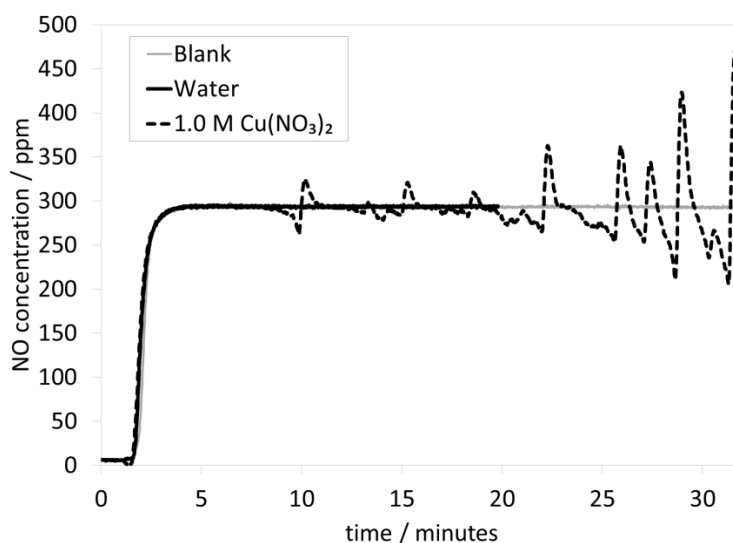


**Figure 189.**  $\text{NO}$  concentration as a function of time through a blank Erlenmeyer flask (grey trace), water (black trace), and 1.0 M  $\text{Cu}(\text{NO}_3)_2$  (dashed black trace). The standard SCR mixture started flowing at time zero. The breakthrough time delay before appearance of  $\text{NO}$  into the MKS FTIR 2030 is due to  $\text{NO}$  displacing the inert  $\text{N}_2$  in the piping and Erlenmeyer flask.

## REFERENCES

- [1] BP, 1965-2018 BP Statistical Review of World Energy, (n.d.).
- [2] BP, BP Energy Outlook 2018, (2018).  
<https://www.bp.com/content/dam/bp/en/corporate/pdf/energy-economics/energy-outlook/bp-energy-outlook-2018.pdf>.
- [3] G. Zuckerman, *The Frackers: The Outrageous Inside Story of the New Billionaire Wildcatters*, 2013. doi:10.1016/S0092-8674(00)80317-7.
- [4] P. Varey, *100-Octane: The Story Behind the Fuel*, Peter Varey Associates, 2017.
- [5] M.I. Goldman, *Controlling Pollution: The Economics of a Cleaner America*, 1st ed., Prentice Hall, Inc., 1967.
- [6] D.C. Williams, *The Guardian: EPA's Formative Years, 1970-1973*, EPA 202-K-93-002 Sept. (1993).
- [7] 2017 Sustainability Progress Report, (2017).
- [8] P. Taylor, R. Burch, *Catalysis Reviews : Science and Engineering Knowledge and Know - How in Emission Control for Mobile Applications Knowledge and Know-How in Emission Control*, (2011) 37–41. doi:10.1081/CR-200036718.
- [9] T. V. Johnson, *Diesel Emissions in Review*, (2011). doi:10.4271/2011-01-0304.
- [10] C.P. Generation, *EPA emissions regulations : What they mean for standby , prime and distributed power systems*, (2007).
- [11] United States Environmental Protection Agency, *Our Nation's Air - Status and Trends through 2010*, (2012).
- [12] United States Environmental Protection Agency, *The History of Reducing Tailpipe Emissions*, (1999).
- [13] United States Environmental Protection Agency, *Risk and Exposure Assessment to Support the Review of the NO<sub>2</sub> Primary National Ambient Air Quality Standard*, (2008).
- [14] W. Cheng, D. Hamrin, J. Heywood, S. Hochgreb, K. Min, M. Norris, *An Overview of Hydrocarbon Emissions Mechanisms in Spark-Ignition Engines*, SAE Tech. Pap. (1993) 1–16. doi:<https://doi.org/10.4271/932708>.

- [15] M. Littman, Introduction to Combustion Chemistry EMISSIONS #1-COMBUSTION CHEMISTRY, 2012. <https://www.princeton.edu/ssp/64-tiger-cub-1/64-data/combustion-chemistry.pdf>.
- [16] M. Takeuchi, S. Matsumoto, NO<sub>x</sub>storage-reduction catalysts for gasoline engines, *Top. Catal.* 28 (2004) 151–156. doi:10.1023/B:TOCA.0000024344.91688.e4.
- [17] P.G. Blakeman, A.F. Chiffey, P.R. Phillips, M. V Twigg, A.P. Walker, Developments In Diesel Emission Aftertreatment Technology, SAE Tech. Pap. (2003). doi:10.4271/2003-01-3753.
- [18] S. Bhattacharyya, R.K. Das, Catalytic Control of Automotive NO: A Review, *Int. J. Energy Res.* 369 (1999) 351–369.
- [19] D. Upadhyay, M. Goebelbecker, M.J. van Nieuwstadt, W.C. Ruona, Diesel Aftertreatment Systems, US 6,895,747 B2, 2006. doi:10.1038/incomms1464.
- [20] L.J. Woodrow, M.J. van Nieuwstadt, Diesel Aftertreatment Systems, US 6,983,589 B2, 2006. doi:10.1016/j.(73).
- [21] Z. Liu, S. Ihl Woo, Recent Advances in Catalytic DeNO<sub>x</sub> Science and Technology, *Catal. Rev.* 48 (2006) 43–89. doi:10.1080/01614940500439891.
- [22] W.E. Farneth, R.J. Gorte, Methods for Characterizing Zeolite Acidity, *Chem. Rev.* 95 (1995) 615–635. doi:10.1021/cr00035a007.
- [23] P. Grange, B. Delmon, V.I. Pa, Catalytic removal of NO, *Catal. Today.* 46 (1998) 233–316.
- [24] R.H. Linnell, W.E. Scott, Diesel exhaust composition and odor studies, *J. Air Pollut. Control Assoc.* 12 (1962) 510–545. doi:10.1080/00022470.1962.10468121.
- [25] A.W. Date, Analytic Combustion: With Thermodynamics, Chemical Kinetics and Mass Transfer, (2011) 2014. <http://www.amazon.com/exec/obidos/redirect?tag=citeulike07-20&path=ASIN/1107002869>.
- [26] R.H. Gonzalez, Diesel Exhaust Emission System Temperature Test, *United States Technol. Dev. Progr.* (2008).
- [27] J. Hussain, K. Palaniradja, N. Alagumurthi, R. Manimaran, Effect of Exhaust Gas Recirculation (EGR) on performance and emission characteristics of a three cylinder direct injection compression ignition engine, *Alexandria Eng. J.* 51 (2012) 241–247. doi:10.1016/j.aej.2012.09.004.

- [28] M. Koebel, M. Elsener, M. Kleemann, Urea-SCR: a promising technique to reduce NO<sub>x</sub> emissions from automotive diesel engines, *Catal. Today*. 59 (2000) 335–345.  
doi:10.1016/S0920-5861(00)00299-6.
- [29] D. Zhang, R.T. Yang, N<sub>2</sub>O Formation Pathways over Zeolite-Supported Cu and Fe Catalysts in NH<sub>3</sub>-SCR, *Energy and Fuels*. 32 (2018) 2170–2182.  
doi:10.1021/acs.energyfuels.7b03405.
- [30] G. Busca, L. Lietti, G. Ramis, F. Berti, Chemical and mechanistic aspects of the selective catalytic reduction of NO<sub>x</sub> by ammonia over oxide catalysts : A review, 18 (1998).
- [31] J. Li, H. Chang, L. Ma, J. Hao, R.T. Yang, Low-temperature selective catalytic reduction of NO<sub>x</sub> with NH<sub>3</sub> over metal oxide and zeolite catalysts—A review, *Catal. Today*. 175 (2011) 147–156. doi:10.1016/j.cattod.2011.03.034.
- [32] S. Brandenberger, O. Kröcher, A. Tissler, R. Althoff, The State of the Art in Selective Catalytic Reduction of NO<sub>x</sub> by Ammonia Using Metal-Exchanged Zeolite Catalysts, *Catal. Rev. Sci. Eng.* 50 (2008) 492–531. doi:10.1080/01614940802480122.
- [33] F. Gao, J.H. Kwak, J. Szanyi, C.H.F. Peden, Current Understanding of Cu-Exchanged Chabazite Molecular Sieves for Use as Commercial Diesel Engine DeNO<sub>x</sub> Catalysts, *Top. Catal.* 56 (2013) 1441–1459. doi:10.1007/s11244-013-0145-8.
- [34] IZA, International Zeolite Association, Int. Zeolite Assoc. (2016). <http://www.iza-online.org/>.
- [35] I. Kiricsi, C. Flego, G. Pazzuconi, W.O.J. Parker, R. Millini, C. Perego, G. Bellussi, Progress toward Understanding Zeolite .beta. Acidity: An IR and <sup>27</sup>Al NMR Spectroscopic Study, *J. Phys. Chem.* 98 (1994) 4627–4634. doi:10.1021/j100068a024.
- [36] G.L. Woolery, G.H. Kuehl, H.C. Timken, A.W. Chester, J.C. Vartuli, On the nature of framework Lewis acid sites in ZSM-5 Brønsted and, 2449 (1997) 288–296.
- [37] O. Mihai, C.R. Widyastuti, A. Kumar, J. Li, S.Y. Joshi, K. Kamasamudram, N.W. Currier, A. Yezerets, L. Olsson, The Effect of NO<sub>2</sub>/NO<sub>x</sub> Feed Ratio on the NH<sub>3</sub>-SCR System Over Cu–Zeolites with Varying Copper Loading, *Catal. Letters*. 144 (2013) 70–80.  
doi:10.1007/s10562-013-1133-0.



- [38] O. Mihai, C.R. Widyastuti, S. Andonova, K. Kamasamudram, J. Li, S.Y. Joshi, N.W. Currier, A. Yezerets, L. Olsson, The effect of Cu-loading on different reactions involved in NH<sub>3</sub>-SCR over Cu-BEA catalysts, *J. Catal.* 311 (2014) 170–181. doi:10.1016/j.jcat.2013.11.016.
- [39] P.J. Carl, S.C. Larsen, EPR study of copper-exchanged zeolites: effects of correlated g- and A-strain, Si/Al ratio, and parent zeolite, *J. Phys. Chem. B.* 104 (2000) 6568–6575. doi:10.1021/jp000015j.
- [40] W. Griinert, N.W. Hayes, R.W. Joyner, E.S. Shpiro, M.R.H. Siddiqui, G.N. Baevras, Structure , Chemistry , and Activity of Cu-ZSM-5 Catalysts for the Selective Reduction of NO , in the Presence of Oxygen, (1994) 10832–10846.
- [41] J. Hun Kwak, H. Zhu, J.H. Lee, C.H.F. Peden, J. Szanyi, Two different cationic positions in Cu-SSZ-13?, *Chem. Commun. (Camb).* 48 (2012) 4758–60. doi:10.1039/c2cc31184d.
- [42] J.H. Kwak, T. Varga, C.H.F. Peden, F. Gao, J.C. Hanson, J. Szanyi, Following the movement of Cu ions in a SSZ-13 zeolite during dehydration, reduction and adsorption: A combined in situ TP-XRD, XANES/DRIFTS study, *J. Catal.* 314 (2014) 83–93. doi:10.1016/j.jcat.2014.03.003.
- [43] S.A. Bates, A.A. Verma, C. Paolucci, A.A. Parekh, T. Anggara, A. Yezerets, W.F. Schneider, J.T. Miller, W.N. Delgass, F.H. Ribeiro, Identification of the active Cu site in standard selective catalytic reduction with ammonia on Cu-SSZ-13, *J. Catal.* 312 (2014) 87–97. doi:10.1016/j.jcat.2014.01.004.
- [44] I. Lezcano-Gonzalez, U. Deka, B. Arstad, a Van Yperen-De Deyne, K. Hemelsoet, M. Waroquier, V. Van Speybroeck, B.M. Weckhuysen, a M. Beale, Determining the storage, availability and reactivity of NH<sub>3</sub> within Cu-Chabazite-based Ammonia Selective Catalytic Reduction systems., *Phys. Chem. Chem. Phys.* 16 (2014) 1639–50. doi:10.1039/c3cp54132k.
- [45] O.P. Krivoruchko, T. V. Larina, R.A. Shutilov, V.Y. Gavrilov, S.A. Yashnik, V.A. Sazonov, I.Y. Molina, Z.R. Ismagilov, Effect of the electronic state and copper localization in ZSM-5 pores on performance in NO selective catalytic reduction by propane, *Appl. Catal. B Environ.* 103 (2011) 1–10. doi:10.1016/j.apcatb.2010.12.046.

- [46] B.M. Abu-zied, W. Schwieger, *Applied Catalysis B : Environmental* Nitrous oxide decomposition over transition metal exchanged ZSM-5 zeolites prepared by the solid-state ion-exchange method, 84 (2008) 277–288. doi:10.1016/j.apcatb.2008.04.004.
- [47] A.K.S. Clemens, A. Shishkin, P.A. Carlsson, M. Skoglundh, F.J. Martínez-Casado, Z. Matej, O. Balmes, H. Härelind, Reaction-driven Ion Exchange of Copper into Zeolite SSZ-13, *ACS Catal.* 5 (2015) 6209–6218. doi:10.1021/acscatal.5b01200.
- [48] H.G. Karge, *Solid-state Reactions of Zeolites*, (n.d.).
- [49] S. Shwan, M. Skoglundh, L.F. Lundegaard, R.R. Tiruvalam, V.W. Ton, Solid-State Ion-Exchange of Copper into Zeolites Facilitated by Ammonia at Low Temperature Supporting information, (n.d.) 3–6.
- [50] S. Li, A. Zheng, Y. Su, H. Fang, W. Shen, Z. Yu, L. Chen, F. Deng, Extra-framework aluminium species in hydrated faujasite zeolite as investigated by two-dimensional solid-state NMR spectroscopy and theoretical calculations., *Phys. Chem. Chem. Phys.* 12 (2010) 3895–903. doi:10.1039/b915401a.
- [51] L. Ren, L. Zhu, C. Yang, Y. Chen, Q. Sun, H. Zhang, C. Li, F. Nawaz, X. Meng, F.-S. Xiao, Designed copper-amine complex as an efficient template for one-pot synthesis of Cu-SSZ-13 zeolite with excellent activity for selective catalytic reduction of NO(x) by NH<sub>3</sub>., *Chem. Commun. (Camb)*. 47 (2011) 9789–9791. doi:10.1039/c1cc12469b.
- [52] L. Xie, F. Liu, K. Liu, X. Shi, H. He, Inhibitory effect of NO<sub>2</sub> on the selective catalytic reduction of NO<sub>x</sub> with NH<sub>3</sub> over one-pot-synthesized Cu–SSZ-13 catalyst, *Catal. Sci. Technol.* 4 (2014) 1104. doi:10.1039/c3cy00924f.
- [53] I. Lezcano-Gonzalez, D.S. Wragg, W.A. Slawinski, K. Hemelsoet, A. Van Yperen-De Deyne, M. Waroquier, V. Van Speybroeck, A.M. Beale, Determination of the Nature of the Cu Coordination Complexes Formed in the Presence of NO and NH<sub>3</sub> within SSZ-13, *J. Phys. Chem. C*. 119 (2015) 24394–24403. doi:10.1021/acs.jpcc.5b06875.
- [54] D.W. Fickel, R.F. Lobo, Copper Coordination in Cu-SSZ-13 and Cu-SSZ-16 Investigated by Variable-Temperature XRD, *J. Phys. Chem. C*. 114 (2010) 1633–1640. doi:10.1021/jp9105025.
- [55] S.T. Korhonen, D.W. Fickel, R.F. Lobo, B.M. Weckhuysen, A.M. Beale, Isolated Cu<sup>2+</sup> ions: active sites for selective catalytic reduction of NO., *Chem. Commun. (Camb)*. 47 (2011) 800–2. doi:10.1039/c0cc04218h.

- [56] U. Deka, E.A. Eilertsen, H. Emerich, M.A. Green, S.T. Korhonen, B.M. Weckhuysen, A.M. Beale, P. Cedex, Confirmation of Isolated Cu<sup>2+</sup> Ions in SSZ-13 Zeolite as Active Sites in, *J. Phys. Chem. C*. 116 (2012) 4809–4818.  
<http://pubs.acs.org/doi/abs/10.1021/jp212450d>.
- [57] F. Gao, E.D. Walter, E.M. Karp, J. Luo, R.G. Tonkyn, J.H. Kwak, J. Szanyi, C.H.F. Peden, Structure–activity relationships in NH<sub>3</sub>-SCR over Cu-SSZ-13 as probed by reaction kinetics and EPR studies, *J. Catal.* 300 (2013) 20–29. doi:10.1016/j.jcat.2012.12.020.
- [58] E. Borfecchia, K. a. Lomachenko, F. Giordanino, H. Falsig, P. Beato, a. V. Soldatov, S. Bordiga, C. Lamberti, Revisiting the nature of Cu sites in the activated Cu-SSZ-13 catalyst for SCR reaction, *Chem. Sci.* 6 (2014) 548–563. doi:10.1039/C4SC02907K.
- [59] F. Göltl, J. Hafner, Structure and properties of metal-exchanged zeolites studied using gradient-corrected and hybrid functionals . III . Energetics and vibrational spectroscopy of adsorbates Structure and properties of metal-exchanged zeolites studied using gradient-corrected, 64503 (2012). doi:10.1063/1.3676410.
- [60] R.E. Buló, P. Sautet, What Makes Copper-Exchanged SSZ-13 Zeolite Efficient at Cleaning Car Exhaust Gases?, *J. Phys. Chem. Lett.* (2013).
- [61] U. Deka, I. Lezcano-gonzalez, B.M. Weckhuysen, A.M. Beale, Local Environment and Nature of Cu Active Sites in Zeolite-Based Catalysts for the Selective Catalytic Reduction of NO<sub>x</sub>, *ACS Catal.* 3 (2013) 413–427. dx.doi.org/10.1021/cs300794s.
- [62] J. Sarkany, J.L. Itri, W.M.H. Sachtler, Redox chemistry in excessively ion-exchanged Cu / Na-ZSM-5, *Catal. Letters.* 16 (1992) 241–249.
- [63] F. Gao, E.D. Walter, M. Kollar, Y. Wang, J. Szanyi, C.H.F. Peden, Understanding ammonia selective catalytic reduction kinetics over Cu/SSZ-13 from motion of the Cu ions, *J. Catal.* 319 (2014) 1–14. doi:10.1016/j.jcat.2014.08.010.
- [64] R.Q. Long, R.T. Yang, Catalytic Performance of Fe – ZSM-5 Catalysts for Selective Catalytic Reduction of Nitric Oxide by Ammonia, 339 (1999) 332–339.
- [65] T. Günter, H.W.P. Carvalho, D.E. Doronkin, T. Sheppard, P. Glatzel, A.J. Atkins, J. Rudolph, C.R. Jacob, M. Casapu, J.-D. Grunwaldt, Structural snapshots of the SCR reaction mechanism on Cu-SSZ-13., *Chem. Commun. (Camb).* 51 (2015) 9227–30. doi:10.1039/c5cc01758k.

- [66] S.Y. Joshi, A. Kumar, J. Luo, K. Kamasamudram, N.W. Currier, *Applied Catalysis B : Environmental* New insights into the mechanism of  $\text{NH}_3$ -SCR over Cu- and Fe-zeolite catalyst : Apparent negative activation energy at high temperature and catalyst unit design consequences, *Appl. Catal. B Environ.* 226 (2018) 565–574.  
doi:10.1016/j.apcatb.2017.12.076.
- [67] T. Yu, T. Hao, D. Fan, J. Wang, M. Shen, W. Li, Recent  $\text{NH}_3$  - SCR Mechanism Research over Cu / SAPO-34 Catalyst, (2014).
- [68] C. Paolucci, A.A. Verma, S.A. Bates, V.F. Kispersky, J.T. Miller, R. Gounder, W.N. Delgass, F.H. Ribeiro, W.F. Schneider, Isolation of the Copper Redox Steps in the Standard Selective Catalytic Reduction on Cu-SSZ-13, *Angew. Chemie Int. Ed.* 53 (2014) 1–7. doi:10.1002/anie.201407030.
- [69] H.Y. Huang, R.Q. Long, R.T. Yang, Kinetics of selective catalytic reduction of NO with  $\text{NH}_3$  on Fe-ZSM-5 catalyst, 235 (2002) 241–251.
- [70] N.W. Cant, I.O.Y. Liu, The mechanism of the selective reduction of nitrogen oxides by hydrocarbons on zeolite catalysts, 63 (2000) 133–146.
- [71] Y. Hoon, J. Henao, M. Jun, W.M.H. Sachtler, E. Weitz, The role of NO in the mechanism of  $\text{NO}_x$  reduction with ammonia over a BaNa – Y catalyst, 231 (2005) 181–193.  
doi:10.1016/j.jcat.2005.01.014.
- [72] J. Szanyi, J.H. Kwak, H. Zhu, C.H.F. Peden, Spectroscopy Studies on Cu-SSZ-13  $\text{NH}_3$  SCR Catalysts : mechanistic implications, (2013) 3–4.
- [73] W.M. Heijboer, a. a. Battiston, A. Knop-Gericke, M. Havecker, H. Bluhm, B.M. Weckhuysen, D.C. Koningsberger, F.M.F. de Groot, Redox behaviour of over-exchanged Fe/ZSM5 zeolites studied with in-situ soft X-ray absorption spectroscopy, *Phys. Chem. Chem. Phys.* 5 (2003) 4484. doi:10.1039/b306130m.
- [74] B.J. Adelman, T. Beutel, G. Lei, W.M.H. Sachtler, Mechanistic Cause of Hydrocarbon Specificity over Cu / ZSM-5 and Co / ZSM-5 Catalysts in the Selective Catalytic Reduction of  $\text{NO}_x$ , *J. Catal.* 335 (1996) 327–335.
- [75] M. Inomata, A. Miyamoto, Y. Murakami, Mechanism of the reaction of NO and  $\text{NH}_3$  on vanadium oxide catalyst in the presence of oxygen under the dilute gas condition, *J. Catal.* 62 (1980) 140–148. doi:10.1016/0021-9517(80)90429-7.

- [76] M. Inomata, A. Miyamoto, T. Ui, K. Kobayashi, Y. Murakami, Activities of vanadium pentoxide/titanium dioxide and vanadium pentoxide/aluminum oxide catalysts for the reaction of nitric oxide and ammonia in the presence of oxygen, *Ind. Eng. Chem. Prod. Res. Dev.* 21 (1982) 424–428. doi:10.1021/i300007a014.
- [77] W. Wong, K. Nobe, Kinetics of nitric oxide reduction with ammonia on “chemical mixed” and impregnated vanadium(V) oxide-titanium(IV) oxide catalysts, *Ind. Eng. Chem. Prod. Res. Dev.* 23 (1984) 564–568. doi:10.1021/i300016a010.
- [78] J. Marangozis, Comparison and Analysis of Intrinsic Kinetics and Effectiveness Factors of the Catalytic Reduction of NO with Ammonia in the Presence of Oxygen, *Ind. Eng. Chem. Res.* 31 (1992) 987–994.
- [79] I. Odenbrand, S.T. Lundin, L. Anderson, Catalytic Reduction of Nitrogen Oxides - 1. The Reduction of NO, *Appl. Catal.* (1985) 335–352. doi:10.1017/CBO9781107415324.004.
- [80] G. Tuenter, W.F. Van Leeuwen, L.J.M. Sneyers, Kinetics and Mechanism of the NO, Reduction with NH<sub>3</sub> on V<sub>2</sub>O<sub>5</sub>-WO<sub>3</sub>-TiO<sub>2</sub> Catalyst, *Ind. Eng. Chem. Prod. Res. Dev.* 25 (1986) 633–636.
- [81] F. Kapteijn, L. Singoredjo, N.J.J. Dekker, J.A. Moulijn, Kinetics of the Selective Catalytic Reduction of NO with NH<sub>3</sub> over Mn<sub>2</sub>O<sub>3</sub>-WO<sub>3</sub>-Al<sub>2</sub>O<sub>3</sub>, *Ind. Eng. Chem. Res.* 32 (1993) 445–452. doi:10.1021/ie00015a007.
- [82] A. M.D., F. Puglisi, J.A. Dumesic, W.S. Millman, N. Topsoe, Kinetic and Infrared Spectroscopic Studies of Fe-Y Zeolites for the Selective Catalytic Reduction of Nitric Oxide by Ammonia, *J. Catal.* (1993).
- [83] M. Azhar Uddin, T. Komatsu, T. Yashima, Selective catalytic reduction of nitric oxide with ammonia on copper (II) ion-exchanged zeolite, *Catal. Commun.* (1995). doi:10.1016/j.catcom.2005.01.009.
- [84] T. Komatsu, Kinetic Studies of Reduction of Nitric Oxide with Ammonia on Cu<sup>2+</sup>-Exchanged Zeolites, *J. Catal.* 148 (1994) 427–437. doi:10.1006/jcat.1994.1229.
- [85] S.I. Zones, Conversion of Faujasites to High-silica Chabazite SSZ-13 in the Presence of N,N,N-Trimethyl-1-adamantanammonium Iodide, *J. Chem. Soc. Faraday Trans.* 87 (1991) 3709–3716.

- [86] D.W. Fickel, E. D'Addio, J. a. Lauterbach, R.F. Lobo, The ammonia selective catalytic reduction activity of copper-exchanged small-pore zeolites, *Appl. Catal. B Environ.* 102 (2011) 441–448. doi:10.1016/j.apcatb.2010.12.022.
- [87] S.I. Zones, Zeolite SSZ-13 and its Method of Preparation, 4,544,538, 1985.
- [88] S.I. Zones, R.A. Van Nordstrand, Novel zeolite transformations: The template-mediated conversion of Cubic P zeolite to SSZ-13, *Zeolites*. 8 (1988) 166–174. doi:10.1016/S0144-2449(88)80302-6.
- [89] C.-C. Chang, Z. Wang, P. Dornath, H. Je Cho, W. Fan, Rapid synthesis of Sn-Beta for the isomerization of cellulosic sugars, *RSC Adv.* 2 (2012) 10475. doi:10.1039/c2ra21381h.
- [90] J.R. Di Iorio, S.A. Bates, A.A. Verma, W.N. Delgass, F.H. Ribeiro, J.T. Miller, R. Gounder, The Dynamic Nature of Brønsted Acid Sites in Cu–Zeolites During NO<sub>x</sub> Selective Catalytic Reduction: Quantification by Gas-Phase Ammonia Titration, *Top. Catal.* 58 (2015) 424–434. doi:10.1007/s11244-015-0387-8.
- [91] S.A. Bates, W.N. Delgass, F.H. Ribeiro, J.T. Miller, R. Gounder, Methods for NH<sub>3</sub> titration of Brønsted acid sites in Cu-zeolites that catalyze the selective catalytic reduction of NO<sub>x</sub> with NH<sub>3</sub>, *J. Catal.* 312 (2014) 26–36. doi:10.1016/j.jcat.2013.12.020.
- [92] M.H. Groothaert, J. a van Bokhoven, A. a Battiston, B.M. Weckhuysen, R. a Schoonheydt, Bis(mu-oxo)dicopper in Cu-ZSM-5 and its role in the decomposition of NO: a combined in situ XAFS, UV-vis-near-IR, and kinetic study., *J. Am. Chem. Soc.* 125 (2003) 7629–40. doi:10.1021/ja029684w.
- [93] J. Wang, V.F. Kispersky, W.N. Delgass, F.H. Ribeiro, Determination of the Au active site and surface active species via operando transmission FTIR and isotopic transient experiments on 2 . 3 wt .% Au / TiO<sub>2</sub> for the WGS reaction, *J. Catal.* 289 (2012) 171–178. doi:10.1016/j.jcat.2012.02.008.
- [94] C.U. Segre, N.E. Leyarowska, L.D. Chapman, W.M. Lavender, P.W. Plag, A.S. King, A.J. Kropf, B.A. Bunker, K.M. Kemner, P. Dutta, R.S. Duran, J. Kaduk, The MRCAT insertion device beamline at the Advanced Photon Source, *AIP Conf. Proc.* 521 (2000) 419–422. doi:10.1063/1.1291825.

- [95] A.J. Kropf, J. Katsoudas, S. Chattopadhyay, T. Shibata, E.A. Lang, V.N. Zyryanov, B. Ravel, K. McIvor, K.M. Kemner, K.G. Scheckel, S.R. Bare, J. Terry, S.D. Kelly, B.A. Bunker, C.U. Segre, The new MRCAT (Sector 10) bending magnet beamline at the advanced photon source, *AIP Conf. Proc.* 1234 (2010) 299–302. doi:10.1063/1.3463194.
- [96] V.F. Kispersky, A.J. Kropf, F.H. Ribeiro, J.T. Miller, Low absorption vitreous carbon reactors for operando XAS: a case study on Cu/Zeolites for selective catalytic reduction of NO<sub>x</sub> by NH<sub>3</sub>, *Phys. Chem. Chem. Phys.* 14 (2012) 2229–38. doi:10.1039/c1cp22992c.
- [97] V.F. Kispersky, A.J. Kropf, F.H. Ribeiro, J.T. Miller, Low absorption vitreous carbon reactors for operando XAS: a case study on Cu/Zeolites for selective catalytic reduction of NO<sub>x</sub> by NH<sub>3</sub> - Supplementary Material, *Phys. Chem. Chem. Phys.* 14 (2012).
- [98] D.J. Parrillo, A.T. Adamo, G.T. Kokotailo, R.J. Gorte, Amine adsorption in H-ZSM-5, *Appl. Catal.* 67 (1990) 107–118. doi:10.1016/S0166-9834(00)84435-8.
- [99] O. Kresnawahjuesa, R.J. Gorte, D. De Oliveira, L.Y. Lau, A simple, inexpensive, and reliable method for measuring Brønsted-acid site densities in solid acids, *Catal. Letters.* 82 (2002) 155–160. doi:10.1023/A:1020514911456.
- [100] A.G. Palkhiwala, R.J. Gorte, Characterization of H-FER and H-TON using temperature-programmed desorption of alkylamines, *Catal. Letters.* 57 (1999) 19–23. doi:10.1023/A:1019010624157.
- [101] L. Chen, T.V.W. Janssens, M. Skoglundh, H. Grönbeck, Interpretation of NH<sub>3</sub>-TPD Profiles from Cu-CHA Using First-Principles Calculations, *Top. Catal.* 0 (2018) 0. doi:10.1007/s11244-018-1095-y.
- [102] M. Lowenstein, The Distribution of Aluminium in the Tetrahedra of Silicates and Aluminates, (n.d.) 92–96.
- [103] B.J. Aylett, Chemistry of the elements, *Polyhedron.* 4 (1985) 1799–1800. doi:10.1016/S0277-5387(00)84180-7.
- [104] J. Dedecek, L. Capek, P. Sazama, Z. Sobalík, B. Wichterlová, Control of metal ion species in zeolites by distribution of aluminium in the framework : From structural analysis to performance under real conditions of SCR-NO<sub>x</sub> and NO, N<sub>2</sub>O decomposition, *Appl. Catal. A Gen.* 391 (2011) 244–253. doi:10.1016/j.apcata.2010.06.026.

- [105] J.R. Di Iorio, R. Gounder, Controlling the Isolation and Pairing of Aluminum in Chabazite Zeolites Using Mixtures of Organic and Inorganic Structure-Directing Agents J. R. Di Iorio and R. Gounder\* Chemistry of Materials , ( 2016 ) submitted, Chem. Mater. (2016) Submitted.
- [106] F. Giordanino, P.N.R. Vennestrøm, L.F. Lundegaard, F.N. Stappen, S. Mossin, P. Beato, S. Bordiga, C. Lamberti, Characterization of Cu-exchanged SSZ-13: a comparative FTIR, UV-Vis, and EPR study with Cu-ZSM-5 and Cu- $\beta$  with similar Si/Al and Cu/Al ratios., Dalton Trans. 42 (2013) 12741–61. doi:10.1039/c3dt50732g.
- [107] F. Giordanino, E. Borfecchia, K. a. Lomachenko, A. Lazzarini, G. Agostini, E. Gallo, A. V. Soldatov, P. Beato, S. Bordiga, C. Lamberti, Interaction of NH<sub>3</sub> with Cu-SSZ-13 Catalyst: A Complementary FTIR, XANES, and XES Study, J. Phys. Chem. Lett. 5 (2014) 1552–1559. doi:10.1021/jz500241m.
- [108] J. Luo, F. Gao, K. Kamasamudram, N. Currier, C.H.F. Peden, A. Yezerets, New insights into Cu/SSZ-13 SCR catalyst acidity. Part I: Nature of acidic sites probed by NH<sub>3</sub> titration, J. Catal. 348 (2017) 291–299. doi:10.1016/j.jcat.2017.02.025.
- [109] C. Paolucci, A.A. Parekh, I. Khurana, J.R. Di Iorio, H. Li, J.D. Albarracin Caballero, A.J. Shih, T. Anggara, W.N. Delgass, J.T. Miller, F.H. Ribeiro, R. Gounder, W.F. Schneider, Catalysis in a cage: Condition-dependent speciation and dynamics of exchanged copper cations in ssz-13 zeolites, J. Am. Chem. Soc. 138 (2016) 6028–6048. doi:10.1021/jacs.6b02651.
- [110] A. Gaur, B.D. Shrivastava, S. Khalid, Copper K-edge XANES of Cu ( I ) and Cu ( II ) oxide mixtures, (2009). doi:10.1088/1742-6596/190/1/012084.
- [111] J. Boita, L. Nicolao, M.C.M. Alves, J. Moralis, Controlled growth of metallic copper nanoparticles, New J. Chem. 41 (2017) 16–18. doi:10.1039/c7nj03056h.
- [112] P. Atkins, T. Overton, J. Rourke, M. Weller, F. Armstrong, M. Hagerman, Inorganic Chemistry, 2009.
- [113] J. Song, Y. Wang, E.D. Walter, N.M. Washton, D. Mei, L. Kovarik, M.H. Engelhard, S. Proding, Y. Wang, C.H.F. Peden, F. Gao, Toward Rational Design of Cu / SSZ-13 Selective Catalytic Reduction Catalysts : Implications from Atomic-Level Understanding of Hydrothermal Stability, (2017) 8214–8227. doi:10.1021/acscatal.7b03020.



- [114] V.L. Sushkevich, J.A. Van Bokhoven, Revisiting copper reduction in zeolites: The impact of autoreduction and sample synthesis procedure, *Chem. Commun.* 54 (2018) 7447–7450. doi:10.1039/c8cc03921f.
- [115] C. Paolucci, I. Khurana, A.A. Parekh, S. Li, A.J. Shih, H. Li, J.R. Di Iorio, J.D. Albarracin-Caballero, A. Yezerets, J.T. Miller, W.N. Delgass, F.H. Ribeiro, W.F. Schneider, R. Gounder, Dynamic multinuclear sites formed by mobilized copper ions in NO<sub>x</sub> selective catalytic reduction, *Science* (80-. ). 357 (2017) 898–903.
- [116] H.G. Karge, Characterization by IR Spectroscopy, *Verif. Synth. Zeolitic Mater.* (2001) 69. doi:http://dx.doi.org/10.1016/B978-044450703-7/50113-7.
- [117] W.N. Delgass, Truth and Beauty in 50 years of Catalysis Research, *Purdue Univ. Sch. Chem. Eng. Truth Beauty Semin.* (n.d.) 2015.
- [118] T.V.W. Janssens, H. Falsig, L.F. Lundegaard, P.N.R. Vennestrom, S. Rasmussen, P.G. Moses, F. Giordanino, E. Borfecchia, K. a. Lomachenko, C. Lamberti, S. Bordiga, A. Godiksen, S. Mossin, P. Beato, A consistent reaction scheme for the selective catalytic reduction of nitrogen oxides with ammonia, *ACS Catal.* (2015) 150319102200004. doi:10.1021/cs501673g.
- [119] B.J. Adelman, T. Beutel, G. Lei, W.M.H. Sachtler, On the mechanism of selective NO<sub>x</sub> reduction with alkanes over Cu /vZSM-5, *Appl. Catal. B Environ.* 11 (1996) L1–L9.
- [120] R. Long, Reaction Mechanism of Selective Catalytic Reduction of NO with NH<sub>3</sub> over Fe-ZSM-5 Catalyst, *J. Catal.* 207 (2002) 224–231. doi:10.1006/jcat.2002.3528.
- [121] E. Tronconi, I. Nova, C. Ciardelli, D. Chatterjee, M. Weibel, Redox features in the catalytic mechanism of the “standard” and “fast” NH<sub>3</sub>-SCR of NO<sub>x</sub> over a V-based catalyst investigated by dynamic methods, *J. Catal.* 245 (2007) 1–10. doi:10.1016/j.jcat.2006.09.012.
- [122] A.A. Verma, S.A. Bates, T. Anggara, C. Paolucci, A.A. Parekh, K. Kamasamudram, A. Yezerets, J.T. Miller, W.N. Delgass, W.F. Schneider, F.H. Ribeiro, NO oxidation: A probe reaction on Cu-SSZ-13, *J. Catal.* 312 (2014) 179–190. doi:10.1016/j.jcat.2014.01.017.

- [123] C. Paolucci, I. Khurana, A.A. Parekh, S. Li, A.J. Shih, H. Li, J.R. Di Iorio, J.D. Albarracin-Caballero, A. Yezerets, J.T. Miller, W.N. Delgass, F.H. Ribeiro, W.F. Schneider, R. Gounder, Dynamic multinuclear sites formed by mobilized copper ions in NO<sub>x</sub> selective catalytic reduction, *Science* (80-. ). 357 (2017) 898 LP-903.
- [124] A. Marberger, A.W. Petrov, P. Steiger, M. Elsener, O. Kröcher, M. Nachtegaal, D. Ferri, Time-resolved copper speciation during selective catalytic reduction of NO on Cu-SSZ-13, *Nat. Catal.* 1 (2018) 221–227. doi:10.1038/s41929-018-0032-6.
- [125] F. Gao, D. Mei, Y. Wang, J. Szanyi, C.H.F. Peden, Selective Catalytic Reduction over Cu/SSZ-13: Linking Homo- and Heterogeneous Catalysis, *J. Am. Chem. Soc.* 139 (2017) 4935–4942. doi:10.1021/jacs.7b01128.
- [126] I. Bull, W. Xue, P. Burk, R.S. Boorse, W.M. Jaglowski, G.S. Koermer, A. Moini, J.A. Patchett, J.C. Dettling, M.T. Claude, United State Patent No: US 7,601,662 B2, 7,601,662 B2, 2009.
- [127] United States Environmental Protection Agency, Diesel Fuel Standards and Rulemakings, Diesel Fuel Stand. (2017).
- [128] S.W. Ham, H. Choi, I.S. Nam, Y.G. Kim, Effect of Copper Contents on Sulfur Poisoning of Copper Ion-Exchanged Mordenite for NO Reduction by NH<sub>3</sub>, *Ind. Eng. Chem. Res.* 34 (1995) 1616–1623. doi:10.1021/ie00044a014.
- [129] S.-W. Ham, I.-S. Nam, Y.G. Kim, Activity and durability of iron-exchanged mordenite-type zeolite catalyst for the reduction of NO by NH<sub>3</sub>, *Korean J. Chem. Eng.* 17 (2000) 318–324. doi:10.1007/BF02699047.
- [130] M.H. Kim, I.S. Nam, Y.G. Kim, Characteristics of mordenite-type zeolite catalysts deactivated by SO<sub>2</sub> for the reduction of NO with hydrocarbons, *J. Catal.* 179 (1998) 350–360. doi:10.1006/jcat.1998.2230.
- [131] K. Wijayanti, S. Andonova, A. Kumar, J. Li, K. Kamasamudram, N.W. Currier, A. Yezerets, L. Olsson, Impact of sulfur oxide on NH<sub>3</sub>-SCR over Cu-SAPO-34, *Appl. Catal. B Environ.* 166–167 (2015) 568–579. doi:10.1016/j.apcatb.2014.11.043.
- [132] D.W. Brookshear, J.G. Nam, K. Nguyen, T.J. Toops, A. Binder, Impact of sulfation and desulfation on NO<sub>x</sub> reduction using Cu-chabazite SCR catalysts, *Catal. Today.* 258 (2015) 359–366. doi:10.1016/j.cattod.2015.04.029.

- [133] M. Shen, H. Wen, T. Hao, T. Yu, D. Fan, J. Wang, W. Li, J. Wang, Deactivation mechanism of SO<sub>2</sub> on Cu/SAPO-34 NH<sub>3</sub>-SCR catalysts: structure and active Cu<sup>2+</sup>, Catal. Sci. Technol. 5 (2015) 1741–1749. doi:10.1039/C4CY01129E.
- [134] A. Kumar, K. Kamasamudram, N. Currier, A. Yezerets, Effect of Transition Metal Ion Properties on the Catalytic Functions and Sulfation Behavior of Zeolite-Based SCR Catalysts, SAE Int. J. Engines. 10 (2017) 9. doi:10.4271/2017-01-0939.
- [135] L. Zhang, D. Wang, Y. Liu, K. Kamasamudram, J. Li, W. Epling, SO<sub>2</sub> poisoning impact on the NH<sub>3</sub>-SCR reaction over a commercial Cu-SAPO-34 SCR catalyst, Appl. Catal. B Environ. 156–157 (2014) 371–377. doi:10.1016/j.apcatb.2014.03.030.
- [136] A. Kumar, J. Li, J. Luo, S. Joshi, A. Yezerets, K. Kamasamudram, N. Schmidt, K. Pandya, P. Kale, T. Mathuraiveeran, Catalyst Sulfur Poisoning and Recovery Behaviors: Key for Designing Advanced Emission Control Systems, in: Symp. Int. Automot. Technol., 2017. doi:10.4271/2017-26-0133.
- [137] A. Kumar, M.A. Smith, K. Kamasamudram, N.W. Currier, H. An, A. Yezerets, Impact of different forms of feed sulfur on small-pore Cu-zeolite SCR catalyst, Catal. Today. 231 (2014) 75–82. doi:10.1016/j.cattod.2013.12.038.
- [138] T. Hamzehlouyan, C. Sampara, J. Li, A. Kumar, W. Epling, Sulfur Poisoning of a Pt/Al<sub>2</sub>O<sub>3</sub> Oxidation Catalyst: Understanding of SO<sub>2</sub>, SO<sub>3</sub> and H<sub>2</sub>SO<sub>4</sub> Impacts, Top. Catal. 59 (2016) 1028–1032. doi:10.1007/s11244-016-0592-0.
- [139] Y. Cheng, C. Lambert, D. Heui, J. Hun, S. June, C.H.F. Peden, The different impacts of SO<sub>2</sub> and SO<sub>3</sub> on Cu / zeolite SCR catalysts, Catal. Today. 151 (2010) 266–270. doi:10.1016/j.cattod.2010.01.013.
- [140] P.S. Hammershøi, Y. Jangjou, W.S. Epling, A.D. Jensen, T.V.W. Janssens, Reversible and irreversible deactivation of Cu-CHA NH<sub>3</sub>-SCR catalysts by SO<sub>2</sub> and SO<sub>3</sub>, Appl. Catal. B Environ. 226 (2018) 38–45. doi:10.1016/j.apcatb.2017.12.018.
- [141] K. Wijayanti, K. Xie, A. Kumar, K. Kamasamudram, L. Olsson, Effect of gas compositions on SO<sub>2</sub> poisoning over Cu/SSZ-13 used for NH<sub>3</sub>-SCR, Appl. Catal. B Environ. 219 (2017) 142–154. doi:10.1016/j.apcatb.2017.07.017.

- [142] P.S. Hammershøi, P.N.R. Vennestrom, H. Falsig, A.D. Jensen, T.V.W. Janssens, Importance of the Cu oxidation state for the SO<sub>2</sub>-poisoning of a Cu-SAPO-34 catalyst in the NH<sub>3</sub>-SCR reaction, *Appl. Catal. B Environ.* 236 (2018) 377–383. doi:10.1016/j.apcatb.2018.05.038.
- [143] Y. Jangjou, D. Wang, A. Kumar, J. Li, W.S. Epling, SO<sub>2</sub>Poisoning of the NH<sub>3</sub>-SCR Reaction over Cu-SAPO-34: Effect of Ammonium Sulfate versus Other S-Containing Species, *ACS Catal.* 6 (2016) 6612–6622. doi:10.1021/acscatal.6b01656.
- [144] Y. Jangjou, Q. Do, Y. Gu, L.G. Lim, H. Sun, D. Wang, A. Kumar, J. Li, L.C. Grabow, W.S. Epling, Nature of Cu Active Centers in Cu-SSZ-13 and Their Responses to SO<sub>2</sub>Exposure, *ACS Catal.* 8 (2018) 1325–1337. doi:10.1021/acscatal.7b03095.
- [145] Y. Cheng, C. Lambert, D.H. Kim, J.H. Kwak, C.H.F. Peden, The Different Impacts of SO<sub>2</sub> and SO<sub>3</sub> on Cu / Zeolite SCR Catalysts, 48124 (2008) 48124.
- [146] Z. Zhang, J.D. Atkinson, B. Jiang, M.J. Rood, Z. Yan, NO Oxidation by Microporous Zeolites: Isolating the Impact of Pore Structure to Predict NO Conversion, *Appl. Catal. B Environ.* 164 (2015) 573–583. doi:10.1016/j.apcatb.2014.06.044.
- [147] A. Kumar, M.A. Smith, K. Kamasamudram, N.W. Currier, A. Yezerets, Chemical deSO<sub>x</sub>: An effective way to recover Cu-zeolite SCR catalysts from sulfur poisoning, *Catal. Today.* 267 (2016) 10–16. doi:10.1016/j.cattod.2016.01.033.
- [148] R. Ando, T. Hihara, Y. Banno, M. Nagata, Detailed Mechanism of S Poisoning and De-Sulfation Treatment of Cu-SCR Catalyst, in: WCX<sup>TM</sup> 17 SAE World Congr. Exp., 2017. doi:10.4271/2017-01-0944.Copyright.
- [149] T.V.W. Janssens, H. Falsig, L.F. Lundegaard, P.N.R. Vennestrom, S.B. Rasmussen, P.G. Moses, F. Giordanino, E. Borfecchia, K.A. Lomachenko, C. Lamberti, S. Bordiga, A. Godiksen, S. Mossin, P. Beato, A consistent reaction scheme for the selective catalytic reduction of nitrogen oxides with ammonia, *ACS Catal.* 5 (2015) 2832–2845. doi:10.1021/cs501673g.
- [150] J. Luo, D. Wang, A. Kumar, K. Kamasamudram, N. Currier, A. Yezerets, Identification of two types of Cu sites and their unique responses to hydrothermal aging and sulfur poisoning, *Catal. Today* 2. (2015) 47201. doi:http://dx.doi.org/10.1016/j.cattod.2015.12.002.

- [151] C. Paolucci, I. Khurana, A.A. Parekh, S. Li, A.J. Shih, H. Li, J.R. Di Iorio, J.D. Albarracin-caballero, A. Yezerets, J.T. Miller, W.N. Delgass, F.H. Ribeiro, W.F. Schneider, R. Gounder, Dynamic multinuclear sites formed by mobilized copper ions in NO<sub>x</sub> selective catalytic reduction, 903 (2017) 898–903.
- [152] R.M. Koros, E.J. Nowak, A diagnostic test of the kinetic regime in a packed bed reactor, *Chem. Eng. Sci.* 22 (1967) 470. doi:10.1016/0009-2509(67)80134-9.
- [153] IBM Corporation, S. Max-Planck Institut, Carr-Parrinello Molecular Dynamics Code, (2016). <http://www.cpmc.org/>.
- [154] J.P. Perdew, Y. Wang, Accurate and simple analytic representation of the electron-gas correlation energy, *Phys. Rev.* 45 (1992) 244. doi:10.1007/978-3-540-78648-1\_7.
- [155] J.P. Perdew, K.A. Jackson, M.R. Pederson, D.J. Singh, C. Fiolhais, Atoms, molecules, solids, and surfaces: Applications of the GGA for exchange and correlation, *Phys. Rev. B.* 46 (1992) 6671. doi:10.1103/PhysRevB.48.4978.2.
- [156] J.P. Perdew, K. Burke, M. Ernzerhof, Generalized Gradient Approximation Made Simple, *Phys. Rev. Lett.* 77 (1996) 3865–3868. doi:10.1103/PhysRevLett.77.3865.
- [157] K. Laasonen, A. Pasquarello, R. Car, C. Lee, D. Vanderbilt, Car-Parrinello molecular dynamics with Vanderbilt ultrasoft pseudopotentials, *Phys. Rev. B.* 47 (1993) 10142–10153. doi:10.1103/PhysRevB.47.10142.
- [158] Vienna ab-initio Software Package, Vienna Ab-Initio Softw. Packag. (2018). [www.vasp.at](http://www.vasp.at).
- [159] H. Li, C. Paolucci, W.F. Schneider, Zeolite Adsorption Free Energies from ab Initio Potentials of Mean Force, *J. Chem. Theory Comput.* 14 (2018) 929–938. doi:10.1021/acs.jctc.7b00716.
- [160] N.I. of S. and T.-J.A.N.A.F. (NIST-JANAF), Thermochemical Tables, (2013). <http://kinetics.nist.gov/janaf/>.
- [161] G. Yang, X. Du, J. Ran, X. Wang, Y. Chen, Understanding SO<sub>2</sub> Poisoning over Different Copper Species of Cu- SAPO-34 Catalyst : A Periodic DFT Study, *J. Phys. Chem. C.* 122 (2018) 21468–21477. doi:10.1021/acs.jpcc.8b06765.
- [162] P.S. Hammershøi, A.D. Jensen, T.V.W. Janssens, Impact of SO<sub>2</sub> -poisoning over the lifetime of a Cu-CHA catalyst for NH<sub>3</sub> -SCR, *Appl. Catal. B Environ.* 238 (2018) 104–110. doi:10.1016/j.apcatb.2018.06.039.

- [163] P.S. Hammershøi, Y. Jangjou, W.S. Epling, A.D. Jensen, T.V.W. Janssens, Reversible and irreversible deactivation of Cu-CHA NH<sub>3</sub>-SCR catalysts by SO<sub>2</sub> and SO<sub>3</sub>, *Appl. Catal. B Environ.* 226 (2018) 38–45. doi:10.1016/j.apcatb.2017.12.018.
- [164] R.F. Lobo, M.J. Annen, M.E. Davis, Zeolite phi: a physical mixture of chabazite and offretite, *J. Chem. Soc. Faraday Trans.* 88 (1992) 2791. doi:10.1039/ft9928802791.
- [165] M. Shen, X. Li, J. Wang, C. Wang, J. Wang, Nature Identification of Cu Active Sites in Sulfur-Fouled Cu/SAPO-34 Regeneration, *Ind. Eng. Chem. Res.* 57 (2018) 3501–3509. doi:10.1021/acs.iecr.7b05053.
- [166] M. Schreier, S. Teren, L. Belcher, J.R. Regalbuto, J.T. Miller, The nature of “overexchanged” copper and platinum on zeolites., *Nanotechnology.* 16 (2005) S582-91. doi:10.1088/0957-4484/16/7/036.
- [167] P. Chemistry, By s. mahapatra and, (1966).
- [168] C.F. Baes, R.E. Mesmer, *The Hydrolysis of Cations*, Wiley, New York, 1976.
- [169] T. William, J. Albrecht, J. Addai-mensah, D. Fornasiero, Effect of pH, concentration and temperature on copper and zinc hydroxide formation in solution, (n.d.) 1–10. <http://www.conference.net.au/chemeca2011/papers/477.pdf>.
- [170] L. Hidmi, M. Edwards, Role of Temperature and pH in Cu(OH)<sub>2</sub> Solubility, *Environ. Sci. Technol.* 33 (1999) 2607. doi:10.1021/es981121q.
- [171] S. Li, Y. Zheng, F. Gao, J. Szanyi, W.F. Schneider, Experimental and Computational Interrogation of Fast SCR Mechanism and Active Sites on H-Form SSZ-13, *ACS Catal.* 7 (2017) 5087–5096. doi:10.1021/acscatal.7b01319.
- [172] H.S. Taylor, The Mechanism of Activation at Catalytic Surfaces, *Proc. R. Soc. A Math. Phys. Eng. Sci.* 113 (1926) 77–86. doi:10.1098/rspa.1926.0140.
- [173] D. Pimentel, Ethanol fuels: Energy balance, economics, and environmental impacts are negative, *Nat. Resour. Res.* 12 (2003) 127–134. doi:10.1023/A:1024214812527.
- [174] D. Ferreira, A.K. Dey, V. Kostakos, Understanding human-smarthpone concerns: a study of battery life, in: *Pervasive Comput.*, 2011. doi:10.1016/j.arr.2010.02.003.
- [175] P.A. Bauerle, L. Newhouse, Vernon, J.T. Wolak, System and Method for Charging a Plug-In Electric Vehicle, US 8,054,039 B2, 2011.

- [176] D. Mei, F. Gao, J. Szanyi, Y. Wang, Mechanistic insight into the passive NO<sub>x</sub> adsorption in the highly dispersed Pd/HBEA zeolite, *Appl. Catal. A Gen.* 569 (2019) 181–189. doi:10.1016/j.apcata.2018.10.037.
- [177] J. a. Loiland, R.F. Lobo, Low temperature catalytic NO oxidation over microporous materials, *J. Catal.* 311 (2014) 412–423. doi:10.1016/j.jcat.2013.12.013.
- [178] H.A. Massaldi, J.A. Maymo, Error in Handling Finite Conversion Reactor Data by the Differential Method, *J. Catal.* 14 (1969) 61–68.
- [179] G. Noh, Z. Shi, S.I. Zones, E. Iglesia, Isomerization and  $\beta$ -scission reactions of alkanes on bifunctional metal-acid catalysts: Consequences of confinement and diffusional constraints on reactivity and selectivity, *J. Catal.* (2018). doi:10.1016/j.jcat.2018.03.033.
- [180] M.C. Campa, V. Indovina, G. Minelli, G. Moretti, I. Pettiti, P. Porta, a. Riccio, The catalytic activity of Cu-ZSM-5 and Cu-Y zeolites in NO decomposition: dependence on copper concentration, *Catal. Letters.* 23 (1994) 141–149. doi:10.1007/BF00812142.
- [181] S. Brandenberger, O. Kröcher, A. Wokaun, A. Tissler, R. Althoff, The role of Brønsted acidity in the selective catalytic reduction of NO with ammonia over Fe-ZSM-5, *J. Catal.* 268 (2009) 297–306. doi:10.1016/j.jcat.2009.09.028.
- [182] F. Gao, Y. Wang, N.M. Washton, M. Kollr, J. Szanyi, C.H.F. Peden, Effects of Alkali and Alkaline Earth Cations on the Activity and Hydrothermal Stability of Cu/SSZ-13 NH<sub>3</sub>-SCR Catalysts, *ACS Catal.* 5 (2015) 6780–6791. doi:10.1021/acscatal.5b01621.
- [183] A. Larsen, M. Jens, B. Jakob, C. Ivano, C. Rune, D. Marcin, F. Jesper, G. Michael, H. Bjork, H. Cory, The Atomic Simulation Environment - A Python library for working with atoms, *J. Phys. Condens. Matter.* 29 (2017) 27. doi:10.1088/1361-648X/aa680e.
- [184] J.-S. McEwen, T. Anggara, W.F. Schneider, V.F. Kispersky, J.T. Miller, W.N. Delgass, F.H. Ribeiro, Integrated operando X-ray absorption and DFT characterization of Cu–SSZ-13 exchange sites during the selective catalytic reduction of NO<sub>x</sub> with NH<sub>3</sub>, *Catal. Today.* 184 (2012) 129–144. doi:10.1016/j.cattod.2011.11.037.
- [185] F. Abild-Pedersen, J. Greeley, F. Studt, J. Rossmeisl, T.R. Munter, P.G. Moses, E. Skulason, T. Bligaard, J.K. Nørskov, Scaling Properties of Adsorption Energies for Hydrogen-Containing Molecules on Transition-Metal Surfaces, *Phys. Rev. Lett.* 99 (2007) 16105. doi:10.1103/PhysRevLett.99.016105.

- [186] Z. Li, K. Xie, W. Huang, W. Reschetilowski, Selective Catalytic Reduction of NO<sub>x</sub> with Ammonia over Fe-Mo/ZSM-5 Catalysts, *Chem. Eng. Technol.* 28 (2005) 797–801. doi:10.1002/ceat.200500113.
- [187] K. Rahkamaa-tolonen, T. Maunula, The effect of NO<sub>2</sub> on the activity of fresh and aged zeolite catalysts in the NH<sub>3</sub>-SCR reaction, 100 (2005) 217–222. doi:10.1016/j.cattod.2004.09.056.
- [188] G. Qi, R.T. Yang, Ultra-active Fe/ZSM-5 catalyst for selective catalytic reduction of nitric oxide with ammonia, *Appl. Catal. B Environ.* 60 (2005) 13–22. doi:10.1016/j.apcatb.2005.01.012.
- [189] M. Schwidder, S. Heikens, A. De Toni, S. Geisler, M. Berndt, A. Brückner, W. Grünert, The role of NO<sub>2</sub> in the selective catalytic reduction of nitrogen oxides over Fe-ZSM-5 catalysts: Active sites for the conversion of NO and of NO/NO<sub>2</sub> mixtures, *J. Catal.* 259 (2008) 96–103. doi:10.1016/j.jcat.2008.07.014.
- [190] M. Moreno-González, B. Hueso, M. Boronat, T. Blasco, A. Corma, Ammonia-Containing Species Formed in Cu-Chabazite As Per In Situ EPR, Solid-State NMR, and DFT Calculations, *J. Phys. Chem. Lett.* (2015) 1011–1017. doi:10.1021/acs.jpcclett.5b00069.
- [191] J. Wang, D. Fan, T. Yu, J. Wang, T. Hao, X. Hu, M. Shen, W. Li, Improvement of low-temperature hydrothermal stability of Cu/SAPO-34 catalysts by Cu<sup>2+</sup> species, *J. Catal.* 322 (2015) 84–90. doi:10.1016/j.jcat.2014.11.010.
- [192] Y.J. Kim, J.K. Lee, K.M. Min, S.B. Hong, I.S. Nam, B.K. Cho, Hydrothermal stability of CuSSZ13 for reducing NO<sub>x</sub> by NH<sub>3</sub>, *J. Catal.* 311 (2014) 447–457. doi:10.1016/j.jcat.2013.12.012.
- [193] D. Wang, F. Gao, C.H.F. Peden, J. Li, K. Kamasamudram, W.S. Epling, Selective catalytic reduction of NO<sub>x</sub> with NH<sub>3</sub> over a Cu-SSZ-13 catalyst prepared by a solid-state ion-exchange method, *ChemCatChem*. 6 (2014) 1579–1583. doi:10.1002/cctc.201402010.
- [194] F. Bin, C. Song, G. Lv, J. Song, X. Cao, H. Pang, K. Wang, Structural Characterization and Selective Catalytic Reduction of Nitrogen Oxides with Ammonia : A Comparison between Co / ZSM - 5 and Co / SBA-15, *J. Phys. Chem. C*. 116 (2012) 26262–26274.
- [195] S. Heylen, N. Delcour, C.E.A. Kirschhock, J.A. Martens, Selective Catalytic Oxidation of Ammonia into Dinitrogen over a Zeolite-Supported Ruthenium Dioxide Catalyst, *ChemCatChem*. 4 (2012) 1162–1166. doi:10.1002/cctc.201100489.



- [196] A. Väliheikki, T. Kolli, M. Huuhtanen, T. Maunula, T. Kinnunen, R.L. Keiski, The effect of biofuel originated potassium and sodium on the NH<sub>3</sub>-SCR activity of Fe-ZSM-5 and W-ZSM-5 catalysts, *Top. Catal.* 56 (2013) 602–610. doi:10.1007/s11244-013-0012-7.
- [197] P. Sabatier, *La catalyse en chimie organique*, Berange, Paris. (1920).
- [198] J.H. Kwak, R.G. Tonkyn, D.H. Kim, J. Szanyi, C.H.F. Peden, Excellent activity and selectivity of Cu-SSZ-13 in the selective catalytic reduction of NO<sub>x</sub> with NH<sub>3</sub>, *J. Catal.* 275 (2010) 187–190. doi:10.1016/j.jcat.2010.07.031.
- [199] F. Piubello, Y. Jangjou, I. Nova, W.S. Epling, Study of NO Formation During NH<sub>3</sub> Oxidation Reaction Over a Cu-SAPO-34 SCR catalyst, *Catal. Letters.* 146 (2016) 1552–1561. doi:10.1007/s10562-016-1783-9.
- [200] M.E. Franke, U. Simon, R. Moos, A. Knezevic, R. Mu, C. Plog, D. Gmbh, Development and working principle of an ammonia gas sensor based on a refined model for solvate supported proton transport in zeolites  $\gamma$ , (2003) 5195–5198. doi:10.1039/b307502h.
- [201] M.E. Franke, U. Simon, Solvate-Supported Proton Transport in Zeolites, (2004) 465–472. doi:10.1002/cphc.200301011.
- [202] Overview of Greenhouse Gases, United States Environ. Prot. Agency. (2018). <http://www.epa.gov/climatechange/ghgemissions/gases/co2.html>.
- [203] Inventory of U.S. Greenhouse Gas Emissions and Sinks 1990 - 2016, United States Environ. Prot. Agency. (2018). [www.epa.gov/ghgemissions/inventory-us-greenhouse-gas-emissions-and-sinks](http://www.epa.gov/ghgemissions/inventory-us-greenhouse-gas-emissions-and-sinks).
- [204] T. Huai, T.D. Durbin, J. Wayne Miller, J.M. Norbeck, Estimates of the emission rates of nitrous oxide from light-duty vehicles using different chassis dynamometer test cycles, *Atmos. Environ.* 38 (2004) 6621–6629. doi:10.1016/j.atmosenv.2004.07.007.
- [205] L.A. Graham, S.L. Belisle, P. Rieger, Nitrous oxide emissions from light duty vehicles, *Atmos. Environ.* 43 (2009) 2031–2044. doi:10.1016/j.atmosenv.2009.01.002.
- [206] K. Kamasamudram, C. Henry, N. Currier, A. Yezerets, N<sub>2</sub>O Formation and Mitigation in Diesel Aftertreatment Systems, *SAE Int. J. Engines.* 5 (2012) 688–698. doi:10.4271/2012-01-1085.

- [207] H.-Y. Chen, Z. Wei, M. Kollar, F. Gao, Y. Wang, J. Szanyi, C.H.F. Peden, A comparative study of N<sub>2</sub>O formation during the selective catalytic reduction of NO<sub>x</sub> with NH<sub>3</sub> on zeolite supported Cu catalysts, *J. Catal.* 329 (2015) 490–498.  
doi:10.1016/j.jcat.2015.06.016.
- [208] M. Konsolakis, Recent Advances on Nitrous Oxide (N<sub>2</sub>O) Decomposition over Non-Noble-Metal Oxide Catalysts: Catalytic Performance, Mechanistic Considerations, and Surface Chemistry Aspects, *ACS Catal.* 5 (2015) 6397–6421.  
doi:10.1021/acscatal.5b01605.
- [209] E. a. Eilertsen, M.H. Nilsen, R. Wendelbo, U. Olsbye, K.P. Lillerud, Synthesis of high silica CHA zeolites with controlled Si/Al ratio, Elsevier B.V., 2008. doi:10.1016/S0167-2991(08)80193-0.
- [210] E. a. Eilertsen, B. Arstad, S. Svelle, K.P. Lillerud, Single parameter synthesis of high silica CHA zeolites from fluoride media, *Microporous Mesoporous Mater.* 153 (2012) 94–99. doi:10.1016/j.micromeso.2011.12.026.

## VITA

Arthur Jayang Shih was born in 1991 in Columbus, Indiana. After 7 years immersed in the smell of midwestern forests and diesel engines, his family moved to Raleigh, North Carolina where he lived for 5 years before moving to Ann Arbor, Michigan in 2003. Throughout his high school years, he embarked on a number of science projects ranging from toasting marshmallows to predicting musical pitches of the tuba using a ruler and governing equations derived from acoustics to modeling and experimentally testing the motion of a pendulum. He enrolled in the College of Engineering at the University of Michigan in 2009. In route to earning a BSE in chemical engineering, Arthur was a vagabond researcher. He performed biomedical cancer research in Professor Tom Wang and Professor Raoul Kopelman's research groups, flow cell battery computational fluid mechanics research in Professor Charles Monroe's group, polymer film development research with Dr. Rishikesh Bharadwaj at Avery Dennison, and carbon capture research with Professor Ralph Yang. In 2013 he joined Purdue University where he worked with Professor Fabio H. Ribeiro on heterogeneous catalysis for reducing NO<sub>x</sub> from diesel engine exhaust. Upon earning his Ph.D. in 2018, he will join Professor Marc Koper's research group at Leiden University to perform fundamental electrocatalysis research applied to fuel cells.

## PUBLICATIONS

### **NH<sub>3</sub>-titration method:**

Di Iorio et al., *Top. Catal.* **58**, 424-434 (2015)

### **SCR Active Site Speciation and Proposed Mechanism:**

Paolucci et al., *Angew. Chem. Int. Ed.* **53**, 11828-11833 (2014)

Paolucci et al., *J. Am. Chem. Soc.* **138**, 2236-2247 (2016)

Paolucci et al., *Science* **357**, 898–903 (2017)

Li et al., *J. Am. Chem. Soc.* Submitted

### **Hydrothermal Deactivation:**

Albarracin-Caballero et al., *Reac. Chem. & Eng.* **2**, 168-179 (2017)

### **Sulfur-Poisoning:**

Shih et al., *Appl. Cat. A*, submitted